Vols. 134, Nos. 1–4 (1995)

REDSEI 134(1–4) 1–498 (1995)
ISSN 1042-0150
ISBN 2-919875-16-7

— and —

EDITOR IN CHIEF
Jochen P. Biersack

REGIONAL EDITORS
N. Itoh/H. Kronmüller/M. A. Kumakhov/N. Tolk

Proceedings of the
Seventh Europhysical Conference on
Defects in Insulating Materials Eurodim 94

Lyon 1 – University

July 5–8, 1994

Part I

Guest Editors:

M. G. Blanchin, J. Davenas, B. Moine,
C. Pédrini and M. Treilleux

DISTRIBUTION STATEMENT A
Approved for public release
Distribution Unlimited

GORDON AND BREACH PUBLISHERS

DTIC QUALITY INSPECTED 1

19970516 054

Radiation Effects and Defects in Solids

EDITOR IN CHIEF

Jochen P. Biersack — Hahn-Meitner-Institut, Glienickerstrabe 100, 14109 Berlin, Germany

REGIONAL EDITORS

N. Itoh — Department of Physics, Faculty of Science, Nagoya University, Furo-cho, Chikusa-ku, Nagoya 464, Japan

H. Kronmuller — Max-Planck-Institut für Metallforschung, Institut für Physik, Heisenbergstrabe 1, 70569 Stuttgart 80, Germany

M. A. Kumakhov — Russian Research Center, "I. V. Kurchatov Institute", Kurachatov Sq, Moscow 123182 Russia

N. Tolk — Department of Physics and Astronomy, Vanderbilt University, P.O. Box 1807-B, Nashville, Tennessee 37325, USA

FOUNDING EDITORS

L. T. Chadderton (Radiation Effects)

R. R. Hasiguti (CLDAM)

EDITORIAL BOARD

V. V. Beloshitsky, I. V. Kurchatov Research Center, Russia
S. Datz. Oak Ridge National Laboratory, USA
L. C. Feldman, AT & T Bell Laboratories, USA
A. Gras-Marti, Universitat d'Alacant, Spain
E. Kaufmann, Argonne National Laboratory, USA
M. Kiritani, Nagoya University, Japan
F. F. Komarov, Shevchenko NIIPF, Minsk, Belarus
A. I. Kupchishin, Kirov University, Alma Ata, Kazakhstan
G. Margaritondo, Institut de Physique Appliquee, Switzerland
W. Möller, Forschungszentrum Rossendorf, Germany
J. W. Rabalais, University of Houston, USA
S. Radhakrishna, Indian Institute of Technology, India
E. Rimini, Universita di Catania, Italy
W. A. Sibley, National Science Foundation, USA
P. D. Townsend, University of Sussex, UK
J. C. Tully, AT & T Bell Laboratories, USA
Z.-L. Wang, Shandong University, China
G. Watkins, Lehigh University, USA
J. Williams,The Australian National University, Australia

AIMS AND SCOPE

Radiation Effects and Defects in Solids publishes experimental and theoretical papers of both a fundamental and applied nature that contribute to the understanding of either phenomena induced by the interaction of radiation with condensed matter or defects in solids introduced not only by radiation but also by other processes. Papers are categorised in three groups.

Section A: Radiation Effects — Suitable topics include, but are limited to, atomic collisions, radiation induced atomic and molecular processes in solids, the stopping and range of ions and radiation damage, sputtering and mixing in solids, radiation-induced transport phenomena and the role of defects and impurities introduced by radiation. Papers in ion implantation in metals and semiconductors as well as on radiation effects in insulators and superconductors, in fusion and fission devices and in space research are considered. Studies on fission tracks, isotope dating and ion beam analytic techniques are also welcome.

Section B: Crystal Lattice Defects and Amorphous Materials — Topics covered include atomic and electronic properties of defects, influence of defects on lattice properties and processes, the latice-defect approach to solid state reactions such as clustering, precipitation, laser annealing and the role of impurities, the defects dynamics in a non-steady state such as under particle or electromagnetic irradiation or during a rapid temperature change and problems associated with the metastable nature of amorphous materials.

Section C: Radiation Effects and Defects in Solids Express — This section is available separately on subscription and presents significant short notes and communications in camera-ready form from the above fields for the fastest possible publication.

Notes for contributors can be found at the back of the journal.

(Continued on inside back cover)

Proceedings of the Seventh Europhysical Conference on Defects in Insulating Materials Eurodim 94

Lyon 1 – University

July 5–8, 1994

Part I

Guest Editors:

M. G. Blanchin, J. Davenas, B. Moine,
C. Pédrini and M. Treilleux

DISTRIBUTION STATEMENT A
Approved for public release;
Distribution Unlimited

Radiation Effects and Defects in Solids Volume 134 (1995)

CONTENTS – PART I

Note on Pagination, Author Index and Table of Contents

The Proceedings of the EURODIM 94 Conference is being published in four volumes of Radiation Effects and Defects in Solids (Volume 134, Part I, Volume 135, Part II, Volume 136, Part III and Volume 137, Part IV). To facilitate indexing and referring to this Proceedings, the page numbers of Volume 135, Volume 136 and Volume 137 will run continuously from the end of Volume 134. An author index will appear at the end of Volume 137. A complete table of contents will appear in Volume 134, Part I and Volume 137, Part IV.

Preface xxiii

Computer Simulation of the Thermodynamics and Diffusion in Nonstochiometric Materials 1
G. E. MURCH

Defects in Glasses 7
A. R. SILINS

Optical Properties of Oxide Glasses Doped by Semiconductor Nanocrystals 11
A. I. EKIMOV

Scintillators and Applications: Cerium-Doped Materials 23
M. J. WEBER, M. BLISS, R. A. CRAIG, and D. S. SUNBERG

The Sol-Gel Method for the Synthesis of Glasses, Ceramics and Hybrid Materials 31
M.GUGLIELMI and P. BARBOUX

Ultrafast Spectroscopy of Defects 39
M. LEBLANS

1 Calculations and Theory

Static Simulations of Cu^+ Centers in Alkali Halides 47
V. LUAÑA, M. A. BLANCO, M. FLÓREZ, A. MARTÍN PENDÁS and L. PUEYO

Investigation of the Electronic Structure of Point Defects in Ionic Crystals by the Cluster Scattered Wave Method with the Self-Consistent Calculation of the Lattice Distortion and Long-Range Polarization 51
A. B. SOBOLEV

Protons in Oxides 57
C. R. A. CATLOW, P. S. BARAM, S. C. PARKER, J. PURTON and K. V. WRIGHT

Electronic Structure of Intrinsic and Impurity Mn-Centres in A_2BX_4 Crystals with β-K_2SO_4 Type Structure 65
I. BOLESTA, I. KITYK, Y. FURGALA and S. VELGOSH

Electronic Structure of a LiB_3O_5 Nonlinear Optical Crystal 69
A. Yu. KUZNETSOV, A. B. SOBOLEV, I. N. OGORODNIKOV and A. V. KRUZHALOV

Oxygen Vacancy in Perovskite Oxides: Electron Structure Calculation by the SCF Xα SW Technique 75
M. A. BUNIN, S. A. PROSANDEYEV, I. I. GEGUSIN and I. M. TENNENBOUM

Radiative and Nonradiative Tunneling Processes in Silicon 79
A. J. ZAKRZEWSKI, A. M. FRENS, M. T. BENNEBROEK and J. SCHMIDT

Theoretical Simulations of I-Center Annealing in KCl Crystals 83
A. I. POPOV, E. A. KOTOMIN and R. I. EGLITIS

Modelling of Point Defects in α-AL203 87
E. A. KOTOMIN, A. STASHANS and P.W. M. JACOBS

A Combined Computer Simulation and EXAFS Study of Dopant Clustering in Lanthanum Oxide 91
A. V. CHADWICK, G. MORRISON and R. RAFIUDDIN

Cluster Calculation of Impurity-Induced Core-Valence Transitions 95
A. S. VOLOSHINOVSKII, V. B. MIKHAILIK and P. A. RODNYI

Calculation of the Mollwo-Ivey Parameters in the Point-Ion Approximation 101
M. S. MALGHANI and D. Y. SMITH

Dynamics of Lithium Ions in Lithium Oxide 107
J. L. GAVARTIN, C. R. A. CATLOW, A. L. SHLUGER, P.W. M. JACOBS and Z. A. RYCERZ

Computer Modelling and Brillouin Scattering Studies of High Temperature Disorder in CdF_2 111
T. T. NETSHISAULU, P. E. NGOEPE, J. D. COMINS and C. R. A. CATLOW

Mixed Dimers in Rare-Earth-Doped Fluorides 117
S. S. DE SOUZA and A. R. BLAK

Theoretical Study of the Coordination of the Cr^{3+} Ion in α-Al_2O_3 123
R. FRANCO, J. M. RECIO, A. MARTÍN PENDAS, E. FRANCISCO, V. LUAÑA and L. PUEYO

Local Relaxations and Optical Properties of Cr^{3+} in MgO 127
D. J. GROH, R. PANDEY and J. M. RECIO

Anomalous Charge Screening in the Radiation-Induced Recombination of Charged Defects in Ionic Solids 133
V. N. KUZOVKOV

The Kinetics of Defect Aggregation: A Novel Lattice Formalism 137
V. N. KUZOVKOV

Electric Field Induced Energy Shift in F-Centre Emission 141
M. J. PONNAMBALAM

Semi-Empirical Analysis of the Quantum Yield of the Three Center Auger Effect 145
A. J. ZAKRZEWSKI

On the Error in the Activation Energy Obtained by the Initial Rise Method for Thermally Stimulated Processes in Dielectrics 147
ANTÔNIO E. DO NASCIMENTO, PIOTR TRZESNIAK, MÁRIO E. G. VALERIO and JOSÉ F. DE LIMA

***ab initio* Molecular-Cluster Modelling of a Paramagnetic Excess-Electron Vacancy Center in Paratellurite** 153
D. P. MADACSI and K. RAKSÁNY

Point Defect Modelling and Transport Processes in AgBr 157
RADHA D. BANHATTI and Y. V. G. S. MURTI

Computer Simulation of Uranium Oxide Phases 161
R. A. JACKSON, J. E. HUNTINGTON and R. G. J. BALL

Shell Model and Embedded Cluster Calculations of Hole Bipolarons in $BaTiO_3$ 165
H. DONNERBERG and A. BIRKHOLZ

Atomistic Lattice Simulations of Dopant Migration in Planar-and Helical-Chain Conductive Polymers 171
J. CORISH, D. A. MORTON-BLAKE, KALYANI VELURI and F. BÉNIÈRE

Optical Proteties of Cr^{3+} and Ni^{2+} Ions in MgO, $LiNbO_3$ and LMA 175
F. MICHEL-CALENDINI

Simulation of Oxygen Vacancies at the Si-SiO_2 Interface 179
S. CARNIATO, G. BOUREAU and J. HARDING

Why is 10Dq so useful for Measuring Changes of the Impurity-Ligand Distance? 185
M. T. BARRIUSO, J. A. ARAMBURU and M. MORENO

The Jahn-Teller Effect in the Excited States of MnF_6^{4-} and CrF_6^{3-} Complexes 189
J. A. ARAMBURU, M. T. BARRIUSO and M. MORENO

Energetics of the RbF + CaF_2 → $RbCaF_3$ Solid State Reaction: A First-Principle Study 193
M. FLÓREZ, J. M. RECIO, A. M. PENDÁS, E. FRANCISCO and V. LUAÑA

Effects of a Quantum Crystal Potential on the Derivation of Electron Gas Interionic Energies 197
E. FRANCISCO, J. M. RECIO, M. A. BLANCO, A. M. PENDÁS and L. PUEYO

Stability of B1 and B2 Phases from Electronic Density Topology Considerations 201
A. M. PENDÁS, J. M. RECIO, M. FLÓREZ, M. A. BLANCO and E. FRANCISCO

Physical Properties of the Ground State of a Tunnelling Particle in a Phonon Field in the Intermediate Coupling Regime 205
G. BENIVEGNA, A. MESSINA and E. PALADINO

2 Defects in Oxides

Microstructure of Single-Crystal Sillenite Fibers 209
V. V. PROKOFIEV, J. P. ANDREETA, C. J. DE LIMA, M. R. B. ANDREETA, A. C. HERNANDES, J. F. CARVALHO, A. A. KAMSHILIN and T. JÄÄSKELÄINEN

OH Vibrational Modes in Sillenites 213
P. BENEVENTI, R. CAPELLETTI, L. KOVÁCS, Á. PÉTER and F. UGOZZOLI

On the Substitution Site of Cr and Fe in $LiNbO_3$: An EXAFS Study 219
G. CORRADI, A. V. CHADWICK, A. R. WEST, K. CRUICKSHANK and M. PAUL

Magnetic Bistability and Memory of Conduction Electrons Released from Oxygen Vacancies in Gallium Oxide 223
D. GOURIER, L. BINET and E. AUBAY

Second Harmonic Generation and Thermally Stimulated Depolarization Current Investigation of $K_{1-x}Li_xTaO_3$ 229
P. VOIGT, S. KAPPHAN, L. OLIVEIRA and M. S. LI

Influence of Yttrium and of the Oxygen Pressure on α Alumina Microstructure. Relation with Mechanical Properties 233
M. K. LOUDJANI, C. HAUT and S. PARISOT

The Gigantic Ions of Chromium in Ruby 239
V. I. FLEROV and A. V. FLEROV

The Short Life-Time Defect Formation in α-Al_2O_3 Under the Synchrotron Radiation 243
V. V. HARUTUNYAN, A. N. BELSKY, V. A. GEVORKYON, V. V. MIKHAILIN and G. N. YERITSIAN

Thermal Depolarization Spectroscopy for Probing the Contribution of $CaCO_3$ to the Dielectric Relaxation of Dolomite ($CaMg(CO_3)_2$) 247
A. N. PAPATHANASSIOU, J. GRAMMATIKAKIS, V. KATSIKA and A. B. VASSILIKOU-DOVA

Defects and Features of Ion-Electron Processes in Garnets 251
A. E. NOSENKO and V. N. SHEVCHUK

Dielectric Response of Natural Zeolite (Stilbite) Single Crystals 257
J. M. KALOGERAS and A. VASSILIKOU-DOVA

EPR Spectra of Cr^{3+} Ions in $LiNbO_3$:ZnO and $LiNbO_3$:CaO 261
D. BRAVO, A. MARTÍN, M. VODA and F. J. LÓPEZ

Tunneling Afterglow and Point Defects in Feldspars 265
R. VISOCEKAS and A. ZINK

Evidence for Schottky Barrier Formation Due to Hole Centers in Al_2O_3: and MgO:Li with Metal Contacts 273
R. VILA and M. JIMÉNEZ DE CASTRO

Nuclear Magnetic Resonance and Electrical Conductivity in Single-Crystalline Paratellurite 277
J. WEGENER, O. KANERT, R. KÜCHLER and A. WATTERICH

Vibration + Libration Absorption Bands of OH Centres in $LiNbO_3$ 283
A. GRÖNE and S. KAPPHAN

OH^- Absorption in $Bi_4Si_3O_{12}$ Single Crystals 287
L. KOVÁCS, P. BENEVENTI and R. CAPELLETTI

Anharmonic Effects on Lattice Vibration Modes of Sillenites 293
P. BENEVENTI, R. CAPELLETTI and L. KOVÁCS

On the Dielectric Relaxations in Crystalline Insulators and Amorphous Systems 299
E. LAREDO, M. ALDANA and A. BELLO

Lattice Defects in Beryllium Oxide 303
I. N. ANTSIGIN and A. V. KRUZHALOV

Effects of the Microindentation, X-Irradiation and Annealing on the F-Centre-Like Defects Production in MgO 307
T. A. NAZAROVA and M. V. NAZAROV

Optically Stimulated Luminescence in Anion-Defective Carbon Doped α-Al_2O_3 Crystals 311
N. KRISTIANPOLLER and L. OSTER

Thermally Stimulated Depolarization Currents in Natural Beryl 315
C. VIANNA and A. R. BLAK

Crystal Structure Perfection and Domain Structure Revealing in Epitaxial Ferroelectric Thin Films 321
V. A. ALYOSHIN, E. V. SVIRIDOV, I. N. ZAKHARCHENKO and V. P. DUDKEVICH

The Effect of Local Ordering in a System of Defects in Weakly Doped $KTaO_3$: Dielectric Anomalies and Their Origin 325
V. TREPAKOV, F. SMUTNÝ, V. VIKHNIN, V. BURSIAN, L. SOCHAVA, L. JASTRABÍK and P. SYRNIKOV

A Cation Vacancy Center in Crystalline Al_2O_3 329
B. D. EVANS and L. S. CAIN

3 Colour Centers

Optical Spectra of Cu^{2+} Ions in LiF Crystals 333
A. SCACCO, C. MARASCA, U. M. GRASSANO and N. ZEMA

Nature of Uncommon Nuclear Spin Relaxation in NaCl with High Concentration of Reorienting OH- Impurities at Low Temperatures 337
O. KANERT, M. BACKENS, M. FRICKE, S. KAPPHAN, R. KÜCHLER and V. S. VIKHNIN

Relaxation and IR Spectroscopic Properties of the CN^- Stretching Mode in Silver Halides 341
C. E. MUNGAN, U. HAPPEK, W. VON DER OSTEN and A. J. SIEVERS

Time-resolved Picosecond Spectroscopy of the Resonant Secondary Radiation of F Centers in KCl 345
N. AKIYAMA, F. NAKAHARA and H. OHKURA

Four-wave Phase Conjugation with F_3^+ Color Centers in LiF 349
T. TSUBOI and H. E. GU

Cu^+ and OH^- Pairs Defects Interaction in NaF Crystals 353
J. L. FABRIS, M. MÜLLER, A. C. HERNANDES, M. SIU-LI and S. KAPPHAN

Cu^+ High Doping Effects in KCl and KBr Films 357
L. OLIVEIRA, C. M. G. S. CRUZ, M. A. P. SILVA and M. SIU-LI

Radiation Induced Colour Centres in Cerium Fluoride 361
E. APOSTOL, I. DAFINEI, GH. MITROAICA, T. TANASE and V. TOPA

Up-Conversion and Relaxation Kinetics among CN^- Vibrational States After Single Pulse 0→1 Excitation in Rubidium-Halide-Cyanide Crystals 367
H. NAKAGAWA and F. LÜTY

The Estimation of Size of Gigantic Ions of Chromium in Corundum Lattice 371
V. I. FLEROV, A. V. FLEROV and S. I. FLEROV

Off-Centre Effects in the Triplet Relaxed Excited State of Impurity ns^2 Ions in Alkali Halides 375
V. HIZHNYAKOV, K. KALDER, V. KORROVITS, V. NAGIRNYI, A. STOLOVICH and S. ZAZUBOVICH

Anharmonicity Effects and Phonon Coupling of OH-Divalent Impurity Complexes in Alkali Halides 379
P. BENEVENTI, R. CAPELLETTI, M. DARRA, R. FIESCHI, W. B. FOWLER and A. GAINOTTI

Structure and Thermodynamic Behavior of In^{3+}–$2V_{Ag}$ DEFECTS IN AgBr 385
J. C. AUSTIN, K. J. PRICE, B. K. PATNAIK and M. L. SWANSON

Color Centers in Mixed Crystals of Alkali Silver Halides and Ammonium Silver Halides 389
T. AWANO and T. MATSUYAMA

On F-Aggregate Centre Formation in KCl Crystals Containing O^{2-}-Vacancy Complexes 395
P. RAERINNE and P. KETOLAINEN

A Light Induced Configurational Change of F_A Centres in Li Doped KCl-KBr Crystals 401
P. KETOLAINEN and P. SILFSTEN

E-V Energy Transfer in the F_H(CN) Center in KCl and CsCl 405
L. F. CHEN and K. S. SONG

Point Defect Interaction in Alkali Halide Crystals 411
A. V. GEKTIN, V. YA. SEREBRYANNY and N. V. SHIRAN

Ultrafast Relaxation of F_H-Centre in KBr:OH^- 417
P. PROSPOSITO, M. CASALBONI, F. IGNOZZA and U. M. GRASSANO

Configuration of F_A (Na) Defects in KF Crystals 421
A. SCACCO, C. GILIBERTI, U. M. GRASSANO, G. BALDACCHINI, M. CREMONA, R. M. MONTEREALI and A. SHPAK

Triplet State of F_3^+ in LiF 425
G. BALDACCHINI, M. CREMONA, G. D'AURIA, V. KALINOV and R. M. MONTEREALI

Optical Properties of F and F^+ Type Centers in Barium β-Alumina 431
D. GOURIER, B. VIANA, P. BELLENOUE, J. THERY and D. VIVIEN

Identification of I_3^- AND I_5^- Clusters in Irradiated KI by X-Ray Photoelectron, Raman and Optical Absorption Spectroscopies 437
J. D. COMINS, T. P. NGUYEN, M-A. PARISELLE, S. LEFRANT and A. M. T. ALLEN

Vibronic Scheme of the Franck-Condon State of F Centers that Consistently Elucidates MCD and Resonance Raman Scattering 443
S. MURAMATSU, Y. MORI and H. OHKURA

Luminescence of Defect Centres in Hg_2Cl_2 447
Z. BRYKNAR, P. PEKA, A. KOŇÁKOVÁ, J. KRÁL and H.-J. SCHULZ

Autler-Townes Splittings of Photo-Excited Point Defects 453
M. GLASBEEK, C. J. M. TAVARES, M. A. COSTA NETO and R. SITTERS

Photoinduced Color Centers Creation in Superionic Crystals $RbAg_4I_5$ 457
N. KOVALEVA, A. BORIS, S. BREDIKHIN and T. AWANO

M-Centre Luminescence in NaF and LiF: Towards a Comprehensive Interpretation of the M-centre Emission Properties in Alkali Halides 461
L. BOSI and D. GALLO

Investigation of the Dynamical Behaviour of the $F_H(CN^-)$ Centre in KCl with Temperature Dependent ENDOR Spectroscopy 465
TH. PAWLIK, R. BUNGENSTOCK, J. M. SPAETH and F. LÜTY

ODEPR of Indium Colour Centres in the X-Irradiated Storage Phosphor KBr:In 471
U. ROGULIS, J. -M. SPAETH, I. TALE and E. RUZA

Thermoactivated Spectroscopy of Heterovalent Impurity Traps in $CdWO_4$ 477
V. TĀLE, I. TĀLE and L. L. NAGORNAYA

Point Defects Related to 260 K Thermostimulated Luminescence in α-Al_2O_3 481
M. SPRINGIS, P. KULIS and I. TALE

A Defect Model for the Optical and EPR Activity of the T-Center in Yttrium-Stabilized Zirconia 485
C. B. AZZONI, L. BOLIS, P. CAMAGNI, G. C. CAMPAGNOLI and M. DE SIMONE

Influence of OH^- Impurities on the Relaxation of F Centers Studied with Picosecond Optical Pulses 489
E. GUSTIN, W. WENSELEERS, M. LEBLANS, A. BOUWEN and D. SCHOEMAKER

Stabilization of H Centres in Irradiated LiF:Mg Crystals 493
S. MYSOVSKY, B. ROGALEV and V. CHERNOV

Radiation Effects and Defects in Solids Volume 135 (1995)

CONTENTS – PART II

Note on Pagination, Author Index and Table of Contents

The Proceedings of the EURODIM 94 Conference is being published in four volumes of Radiation Effects and Defects in Solids (Volume 134, Part I, Volume 135, Part II, Volume 136, Part III and Volume 137, Part IV). To facilitate indexing and referring to this Proceedings, the page numbers of Volume 135, Volume 136 and Volume 137 will run continuously from the end of Volume 134. An author index will appear at the end of Volume 137. A complete table of contents will appear in Volume 134, Part I and Volume 137, Part IV.

4 Spectroscopy luminescence

X-Ray Storage Phosphors 1/[499]
J. M. SPAETH, TH. HANGLEITER, F. K. KOSCHNICK and TH. PAWLIK

Fluorescence Line Narrowing in Mn^{4+} Doped Gadolinium Gallium Garnet[1] 11/[509]
A. SUCHOCKI, M. POTEMSKI, A. BRENIER, C. PEDRINI and G. BOULON

Fine Structure of the Absorption and Emission Spectra of Ni^{2+}-Ions in $BaLiF_3$ 15/[513]
E. MARTINS, S. L. BALDOCHI, S. P. MORATO, N. D. VIEIRA JR., A. LUCI, M. CASALBONI, U. M. GRASSANO, G. BALDACCHINI, M. CREMONA, R. M. MONTEREALI, E. KRAUSZ and M. RILEY

Spectroscopic Study of Cr^{3+} in New Elpasolites 19/[517]
M. C. MARCO DE LUCAS, J. M. DANCE, F. RODRÍGUEZ, A. TRESSAUD, M. MORENO and J. GRANNEC

Time Resolved Spectroscopy of Ni^{2+} Doped Fluoroclorozirconate Glasses 23/[521]
M. A. BUÑUEL, R. ALCALA and R. CASES

Charge Exchange Processes between Impurity Ions and the Host Crystal in Wide Band-Gap Crystals 27/[525]
DONALD S. McCLURE, WING C. WONG and SERGEI A. BASUN

The Role of Different Charge States of Impurity Ions in Photoconductivity of Insulators 37/[535]
S. A. BASUN

Two-Photon Laser Spectroscopy of Ce^{3+} in $LiYF_4$ 41/[539]
J. C. GÂCON, J. BAUDRY, C. GARAPON and G. W. BURDICK

Optical Spectroscopy of Yb^{3+} Ions in $Ca_xCd_{1-x}F_2$ 45/[543]
K. ŚWIATEK

ENDOR-Investigations of Rare Earth and Transition Metal Ions in the Cubic Elpasolite Crystal Cs_2NaYF_6 49/[547]
TH. PAWLIK, J.-M. SPAETH, M. OTTE and H. OVERHOF

Optical and EPR Spectroscopy of Impurity Manganese Ions in Disordered $Ca_3Ga_2Ge_4O_{14}$ Single Crystals 55/[553]
A. E. NOSENKO, R. YE. LESHCHUK and B. V. PADLYAK

Interaction of Impurity Centres in Cs_2CdI_4-Mn Crystals 61/[559]
I. BOLESTA and Y. FURGALA

Blue Avalanche Upconversion in YAG:Tm 65/[563]
S. GUY, M. F. JOUBERT, B. JACQUIER and C. LINARÉS

New Spectroscopic Effects of Ferroelectric Phase Transition in $Li_2Ge_7O_{15}$ Crystals Doped with $3d^3$-Ions 69/[567]
A. A. KAPLYANSKII, S. A. BASUN and S. P. FEOFILOV

Excited State Absorption in Holmium Doped $Gd_3Ga_5O_{12}$ Garnet 73/[571]
A. BRENIER, C. MADEJ, C. PÉDRINI and G. BOULON

Luminescence of Ytterbium Doped $LiNbO_3$:MgO under UV Excitation 77/[575]
A. BRENIER, C. MADEJ, C. PÉDRINI and G. BOULON

Optical Detection of Eu^{3+} Sites in $Gd_3Ga_5O_{12}:Eu^{3+}$ 81/[579]
L. C. COURROL, L. GOMES, A. BRENIER, C. PÉDRINI, C. MADEJ and G. BOULON

Study of Bistable (Shallow-Deep) Defect Systems in $CdF_2:M^{3+}$ (M: In, Ga) 85/[583]
YANG CAI and K. S. SONG

Polarized Charge Transfer Spectra of Cu^{2+} Doped Perovskite Layers $(RNH_3)_2Cd_xMn_{1-x}Cl_4 (x = 0-1)$ 89/[587]
B. BATICLE, F. RODRÍGUEZ and R. VALIENTE

Optical Properties and Local Structure of $MnCl_6^{4-}$ in $ABCl_3:Mn^{2+}$ 95/[593]
M. C. MARCO DE LUCAS, F. RODRÍGUEZ, C. PRIETO, M. VERDAGUER, M. MORENO and H. U. GÜDEL

Photo-EPR Studies of Electron and Hole Trapping by $[Fe(CN)_6]^{4-}$ Complexes in Silver Chloride 101/[599]
M. T. OLM and R. S. EACHUS

Site Selective Spectroscopy of Eu^{3+} and Eu^{3+}-Ho^{3+} Doped Glasses 105/[603]
V. D. RODRÍGUEZ, V. LAVÍN, U. R. RODRÍGUEZ-MENDOZA, I. R. MARTÍN and P. NUÑEZ

Thermoluminescence of Brazilian Topaz 109/[607]
DIVANÍZIA DO N. SOUZA, JOSÉ F. DE LIMA and MÁRIO ERNESTO G. VALERIO

Point Defects Produced by Grinding of CaS Phosphors: An Electron Spin Resonance Study 115/[613]
D. CAURANT, D. GOURIER, N. DEMONCY and M. PHAM-THI

Thermally Stimulated Depolarization Current of Monovalent Copper Ions in Calcium Fluoride 121/[619]
L. OLIVEIRA, O. R. NASCIMENTO, M. SIU LI, C. PÉDRINI and H. BILL

Photostimulated Luminescence of KBr-In Crystals 125/[623]
I. PLAVINA, A. I. POPOV and A. TALE

Energy Transfer and Up-Conversion in Yb-Tm Codoped Fluorindate Glasses 129/[627]
V. D. RODRÍGUEZ, I. R. MARTÍN, R. ALCALÁ and R. CASES

Spectrally Resolved Thermoluminescence of Cu and Eu Doped $Li_2B_4O_7$ 133/[631]
M. MARTINI, C. FURETTA, C. SANIPOLI, A. SCACCO and K. SOMAIAH

Reversible Photoionization Process in Luminescent Ce^{3+} Doped Elpasolite-Type Fluoroindates 137/[635]
J. P. CHAMINADE, A. GARCIA, T. GAEWDANG, M. POUCHARD, J. GRANNEC and B. JACQUIER

Excited Levels of the 2.56 eV Emission in Synthetic Diamond 143/[641]
E. PEREIRA, L. PEREIRA, D. M. HOFMANN, W. STADLER and B. K. MEYER

Er^{3+} Ion Concentration and Annealing Temperature Effect on the Fluorescence of Er^{3+}: TiO_2 Planar Waveguides Prepared by the Sol-Gel Process 149/[647]
A. BAHTAT, M. BOUAZAOUI, M. C. MARCO DE LUCAS, M. BAHTAT, B. JACQUIER and J. MUGNIER

EPR and Photoluminescence of Cr^{3+} Ions in $CsCdF_3$ and $CsCaF_3$ 157/[655]
B. VILLACAMPA, R. CASES and R. ALCALÁ

Spectroscopic Properties of Mn^{2+} Ions in Mixed Fluoroperovskites 163/[661]
F. LAHOZ, P. J. ALONSO, B. VILLACAMPA and R. ALCALÁ

EPR Study of Concentration Dependence in Ce, Ce:La and Ce:Y Doped SrF_2 169/[667]
O. DANKERT, D. VAINSHTEIN, H. C. DATEMA and H. W. DEN HARTOG

Differential Spectroscopic Properties of Nd^{3+} in $NdGaO_3$ and $LaGaO_3$ 173/[671]
V. M. ORERA, L. E. TRINKLER and R. I. MERINO

EPR of Jahn-Teller Cr^{2+} in CaF_2, BaF_2 and $SrCl_2$ 179/[677]
P. B. OLIETE, V. M. ORERA and P. J. ALONSO

Nd^{3+} Centres in Highly Neodymium Doped $LaBGeO_5$ Crystals 183/[681]
L. BITAR, J. CAPMANY, L. E. BAUSÁ, J. GARCÍA-SOLÉ, R. MONCORGÉ and A. A. KAMINSKII

Energy Levels of the Eu^{3+} Centers in $LiNbO_3$ 187/[685]
J. E. MUÑOZ SANTIUSTE, I. VERGARA and J. GARCÍA SOLÉ

EPR Study of Nd^{3+} Ions in $Bi_4Ge_3O_{12}$ Single Crystals 191/[689]
D. BRAVO, A. MARTÍN, A. A. KAMINSKII and F. J. LÓPEZ

Light-Induced NIR-Absorption in $Sr_{0.61}Ba_{0.39}Nb_2O_6$: Ce at Low Temperatures 195/[693]
G. GRETEN, S. KAPPHAN and R. PANKRATH

Sharp R-Lines in Absorption and Emission of Cr^{3+} in Stoichiometric (VTE) $LiNbo_3$ 199/[697]
C. FISCHER, S. KAPPHAN, XI-QI FENG and NING CHENG

Clustering Processes in CaF_2:Gd+Lu and CaF_2:Gd+Sm 203/[701]
N. SUÁREZ

New Symmetry Properties of the Cubic Rare-Earth Centers in Crystals 207/[705]
V. LUPEI

Nonradiative Recombination Processes in Wide Band Gap II-VI Phosphor Materials 213/[711]
M. SURMA and M. GODLEWSKI

Upconversion Luminescence Properties of Er^{3+} Ions Doped in Lithium Niobate Single Crystals 217/[715]
H. J. SEO, T. P. J. HAN, G. D. McCLURE and B. HENDERSON

EPR and Optical Spectroscopy of Cr^{3+} Doped $CaYAlO_4$ 223/[721]
M. YAMAGA, H. TAKEUCHI, K. HOLLIDAY, P. MACFARLANE, B. HENDERSON, Y. INOUE and N. KODAMA

Optical Properties of Cr^{3+}-Ions in $LaSr_2Ga_{11}O_{20}$ 227/[725]
A. LUCI, M. CASALBONI, T. CASTRIGNANÒ, U. M. GRASSANO and A. A. KAMINSKII

Nonlinear Transmission in Cr^{4+}-Doped Silicates 231/[729]
V. P. MIKHAILOV, N. I. ZHAVORONKOV, N. V. KULESHOV, A. S. AVTUKH, V. G. SHCHERBITSKY and B. I. MINKOV

Photo-Stimulated X-Ray Luminescence in $LiTaO_3$:Tb^{3+} Based Green Emitting Phosphors 237/[735]
R. BRACCO, C. MAGRO and R. MORLOTTI

Absorption and Luminescence Spectroscopy of Zinc Borate Glasses Doped with Trivalent Lanthanide Ions 243/[741]
LUIGI AMBROSI, MARCO BETTINELLI, GUY CORMIER and MAURIZIO FERRARI

Optical Energy Transfer in Rare Earth Doped Silica Gels 247/[745]
A. BOUAJAJ, A. MONTEIL, M. FERRARI and M. MONTAGNA

Samarium Doped Alkaline Earth Halide Thin Films as Spectrally Selective Materials for Hole Burning? 253/[751]
A. MONNIER, M. SCHNIEPER, R. JAANISO and H. BILL

5 Excited States

Upconversion in $CsCdBr_3$:Pr^{3+} 257/[755]
J. NEUKUM, N. BODENSCHATZ and J. HEBER

Metastable One-Halide Self-Trapped Excitons in Alkali Halides 263/[761]
A. LUSHCHIK, CH. LUSHCHIK, F. SAVIKHIN and E. VASIL'CHENKO

Optical Studies of Self-Trapped Holes and Excitons in Beryllium Oxide 269/[767]
S. V. GORBUNOV, S. V. KUDYAKOV, B. V. SHULGIN and V. YU. YAKOVLEV

The Experimental Observation of the Potential Barrier for Self-Trapped Exciton Decay into F-H Pair in KCl-Na in Crystals 275/[773]
S. A. CHERNOV and V. V. GAVRILOV

Luminescence of ON- And OFF-Center STE In ABX_3 Crystals 281/[779]
A. S. VOLOSHINOVSKII, V. B. MIKHAILIK and P. A. RODNYI

Phonon Assisted Excitonic Luminescence In $CsPbCl_3$ 285/[783]
I. BALTOG, S. LEFRANT, C. DIMOFTE, and L. MIHUT

Optical Properties Of Pb^{2+}-Based Aggregated Phase In NaCl And CsCl Alkali Halide Hosts 289/[787]
M. NIKL, K. POLAK, K. NITSCH, G. P. PAZZI, P. FABENI and M. GURIOLI

Dynamical Processes of Ortho- and Para-Excitons in Alkali Iodides 295/[793]
KOICHI TOYODA, TORU TSUJIBAYASHI and TETSUSUKE HAYASHI

Defects and Luminescence In Pure and I-Doped AgBr Crystals 301/[799]
L. NAGLI, A. SHMILEVICH, A. KATZIR and N. KRISTIANPOLLER

6 Scintillators

Scintillation Mechanisms in Rare Earth Orthophosphates 305/[803]
A. J. WOJTOWICZ, D. WISNIEWSKI, A. LEMPICKI, and L. A. BOATNER

Scintillation Properties of $Lu_3Al_{5-x}Sc_xO_{12}$ Crystals[1] 311/[809]
N. N. RYSKIN, P. DORENBOS, C. W. E. VAN EIJK and S. KH. BATYGOV

Monte-Carlo Simulation of the Creation of Excited Regions in Insulators by a Photon 315/[813]
R. A. GLUKHOV and A. N. VASIL'EV

Scintillation Properties of $GdAlO_3$:Ce Crystals[1] 321/[819]
P. DORENBOS, E. BOUGRINE, J. T. M. DE HAAS, C. W. E. VAN EIJK and M. V. KORZHIK

Scintillation Properties of Y_2SiO_5:Pr Crystals[1] 325/[823]
P. DORENBOS, M. MARSMAN, C. W. E. VAN EIJK, M. V. KORZHIK and B. I. MINKOV

Scintillation Mechanism In $CsGd_2F_7:Ce^{3+}$ and $CsY_2F_7:Ce^{3+}$ Crystals† 329/[827]
D. R. SCHAART, P. DORENBOS, C. W. E. VAN EIJK, R. VISSER, C. PEDRINI, B. MOINE and N. M. KHAIDUKOV

Nanosecond UV-Scintillation in Cesium Iodide Crystals 333/[831]
S. CHERNOV and V. GAVRILOV

Defects Induced by Irradiation at Room Temperature in Cerium Fluoride 337/[835]
E. AUFFRAY, I. DAFINEI, P. LECOQ and M. SCHNEEGANS

Local Trap Centres in $PbWO_4$ Crystals 343/[841]
E. AUFFRAY, I. DAFINEI, P. LECOQ and M. SCHNEEGANS

Temperature Dependence of Crossluminescence Characteristics in CsCl and CsBr in the 20–300 K Range 349/[847]
V. MAKHOV, J. BECKER, L. FRANKENSTEIN, I. KUUSMANN, M. RUNNE, A. SCHRÖDER and G. ZIMMERER

Time-Resolved Studies Of Fast Scintillating Crystals Under VUV And X-Ray Synchrotron Radiation Excitation 355/[853]
E. G. DEVITSIN, N. M. KHAIDUKOV, N. YU. KIRIKOVA, V. E. KLIMENKO, V. A. KOZLOV, V. N. MAKHOV and T. V. UVAROVA

ODMR of CD Impurity Centers in GG Irradiated BaF_2 Crytals 361/[859]
U. ROGULIS, J. TROKŠS, Ā. VEISPĀLS, I. TĀLE, P. KŪLIS and M. SPRIŅĢIS

Colour Cathodoluminescence from $Bi_4[GeO_4]_3$ Crystals **367/[865]**
T. A. NAZAROVA, M. V. NAZAROV, G.V. SAPARIN and S. K. OBYDEN

Further Results on $GdAlO_3$:Ce Scintillator **369/[867]**
J. A. MAREŠ, M. NIKL, C. PEDRINI, D. BOUTTET, C. DUJARDIN, B. MOINE, J. W. M. VERWEIJ and J. KVAPIL

Multiplication of Anion and Cation Electronic Excitations in Alkali Halides **375/[873]**
M. KIRM, A. FRORIP, R. KINK, A. LUSHCHIK, CH. LUSHCHIK and I. MARTINSON

Peculiarities of the Triplet Relaxed Excited State Structure in Thallium-Doped Cesium Halide Crystals **379/[877]**
V. NAGIRNYI, A. STOLOVICH, S. ZAZUBOVICH, V. ZEPELIN, M. NIKL, E. MIHOKOVA and G. P. PAZZI

The Role of Cation Vacancies in Excitation Mechanism of Re-Ions in Alkaline-Earth Sulphides **383/[881]**
A. N. BELSKY, V. V. MIKHAILIN and A. N. VASIL'EV

LSO-Ce Fluorescence Spectra and Kinetics for UV, VUV and X-Ray Excitation **391/[889]**
I. A. KAMENSKIKH, V. V. MIKHAILIN, I. H. MUNRO, D. Y. PETROVYKH, D. A. SHAW, P. A. STUDENIKIN, A. N. VASIL'EV, I. A. ZAGUMENNYI and YU. D. ZAVARTSEV

Luminescence and Scintillation Properties of $In_2Si_2O_7$ **397/[895]**
A. GARCIA, T. GAEWDANG, J. P. CHAMINADE, C. FOUASSIER, B. VARREL, B. JACQUIER, M. MESSOUS, B. CHAMBON and D. DRAIN

Thermoluminescence of Doped $Gd_3Ga_5O_{12}$ Garnet Ceramics **401/[899]**
A. JAHNKE, M. OSTERTAG, M. ILMER and B. C. GRABMAIER

Luminescence Decay of Rare Earth Ions in an Orthophosphate Matrix **407[905]**
B. FINKE and L. SCHWARZ

Radiation Effects and Defects in Solids Volume 136 (1995)

CONTENTS – PART III

Note on Pagination, Author Index and Table of Contents

The Proceedings of the EURODIM 94 Conference is being published in four volumes of Radiation Effects and Defects in Solids (Volume 134, Part I, Volume 135, Part II, Volume 136, Part III and Volume 137, Part IV). To facilitate indexing and referring to this Proceedings, the page numbers of Volume 135, Volume 136 and Volume 137 will run continuously from the end of Volume 134. An author index will appear at the end of Volume 137. A complete table of contents will appear in Volume 134, Part I and Volume 137, Part IV.

7 Laser Materials

On The Temperature Dependence of the Rate of Energy Transfer between Rare Earth Ions in Solids 1/[911]
B. DI BARTOLO, G. ARMAGAN and M. BUONCRISTIANI

Progress in Ultrafast Color Center Lasers 7/[917]
K. MÖLLMANN and W. GELLERMANN

The Release of Stored Energy in Heavily Irradiated NaCl Explosive Reactions. 11/[921]
D. VAINSHTEIN, M. VAN DEN BEMT, J. SEINEN, H. C. DATEMA and H. W. DEN HARTOG

On the Mechanism of Contrast in the Cathodoluminescence Imaging of Laser Crystals 15/[925]
V. LUPEI

Excited State Absorption Of Fe^{3+} In Garnet Crystals 19/[929]
V. LUPEI, S. HARTUNG and G. HUBER

Thermal Effects on the Quantum Efficiency of 3 μm Erbium Lasers 23/[933]
S. GEORGESCU, V. LUPEI, T. J. GLYNN and R. SHERLOCK

Mn^{2+} Luminescence in Mg-Al Spinels 29/[939]
U. R. RODRÍGUEZ-MENDOZA, V. D. RODRÍGUEZ and A. IBARRA

Inhomogeneous Broadening Of The V^{4+} Luminescence In $CaYAlO_4$ 33/[943]
M. YAMAGA, T. YOSIDA, Y. INOUE, N. KODAMA and B. HENDERSON

Multisite Structure of Nd^{3+} in YAG 37/[947]
A. LUPEI, C. TISEANU and V. LUPEI

Cr^{3+}-Doped Borates—Potential Tunable Laser Crystals? 43/[953]
G. WANG, H. G. GALLAGHER, T. P. J. HAN and B. HENDERSON

Nd^{3+} Strontium Fluorovandate (SVAP) – A Promising Crystal for Diode Pumped Lasers at 1.06 μm and 1.34 μm 47/[957]
M. A. SCOTT, H. G. GALLAGHER, T. P. J. HAN and B. HENDERSON

Charge Compensation and The Spectroscopy of Cr^{3+} in $KMgF_3$ 51/[961]
D. R. LEE, T. P. J. HAN and B. HENDERSON

Perspective Laser Infrared Optics Material Cesium Iodide 57/[967]
I. ANTONIV, I. GARAPYN and R. DIDYK

Laser Diode Pumping of a Colour Centre Laser with Emission in the 1.5 μm Wavelength Domain 61/[971]
A. KONATÉ, J. L. DOUALAN and J. MARGERIE

Ni^{2+}:$BaLiF_3$: A Promising R. T. Tunable Solid State Laser Material 65/[975]
M. MORTIER, J. Y. GESLAND, M. ROUSSEAU, F. AUZEL, and D. MEICHENIN

Ag^+ Center in Alkaline-Earth Fluorides: New UV Solid State Lasers? 69/[979]
P. BOUTINAUD, A. MONNIER and H. BILL

8 Photorefractive and non linear materials

Photorefractive Crystals—The Role of Defects 73/[983]
ECKHARD KRÄTZIG

Hydrogen Defects in $LiNbO_3$ and Applications 79/[989]
J. M. CABRERA

Luminicence and Optical Second Harmonic Generation by Dipolar Microregions in $KTaO_3$ 85/[995]
C. FISCHER, C. AUF DER HORST, P. VOIGT, S. KAPPHAN and J. ZHAO

Non-Linear and Fractal Dynamic Processes in Superionics 91/[1001]
A. E. UKSHE and N. G. BUKUN

Magnetic Circular Dichroism and Absorption Study of Photochromism in Mn– Doped $Bi_{12}GeO_{20}$ 99/[1009]
F. RAMAZ, A. HAMRI, B. BRIAT, V. TOPA and G. MITROAICA

R B S Study of Defect Profiles in Proton Implanted $LiNbO_3$ 103/[1013]
S. OULD SALEM, B. CANUT, P. MORETTI, J. MEDDEB, S. M. M. RAMOS, and P. THEVENARD

XPS Studies of Europium Implanted $LiIO_3$ 107/[1017]
S. M. M. RAMOS, C. ROSSO, P. MORETTI, C. GALEZ, B. CANUT and P. THEVENARD

Characterisation of Planar Waveguides Formed by Proton Implantation in Lithium Iodate 111/[1021]
C. ROSSO, P. MORETTI, J. MUGNIER and J. BOUILLOT

Structural and Optical Characteristics of Crystallized $PbTiO_3$ Waveguides Prepared by Sol-Gel Process 115/[1025]
C. URLACHER, E. BERNSTEIN, J. SERUGHETTI and J. MUGNIER

SHG Phase Matching Conditions For Undoped and Doped Lithium Niobate 119/[1029]
U. SCHLARB, A. REICHERT, K. BETZLER, M. WÖHLECKE, B. GATHER, T. VOLK and N. RUBININA

Phase-Conjugate Waves Generated by Anisotropic Four-Wave Mixing in $LiNbO_3$ and $LiTaO_3$ Optical Waveguides 123/[1033]
D. KIP and E. KRÄTZIG

Photoinduced Linear Dichroism in Sillenite Crystals and in Diamond 129/[1039]
H.-J. REYHER, J. RUSCHKE, and F. MERSCH

Absorption Spectral Changes with Ultraviolet-Illumination in GeO_2-SiO_2 Glass Films Prepared by Sputtering Deposition 133/[1043]
JUNJI NISHII, HIROSHI YAMANAKA, HIDEO HOSONO and HIROSHI KAWAZOE

Ion-Beam/Channeling Characterization of $LiNbO_3$: Interaction between Impurity Sites 137/[1047]
L. REBOUTA, M. F. DA SILVA, J. C. SOARES, M. T. SANTOS, E. DIÉGUEZ and F. AGULLÓ LÓPEZ

Manifestation of a Confinement-Type Lattice Anharmonicity in the Emission Spectra of Niobate Glass 141/[1051]
M. GRINBERG, W. JASKÓSKI, CZ. KOEPKE, J. PLANELLES, and M. JANOWICZ

9 Radiation Defects

The Effect of the Relaxation of 4d I^- Hole on the Formation of Emission Centers in Alkali Halides 145/[1055]
A. N. BELSKY, S. KLIMOV, E. I. ZININ, P. MARTIN, C. PEDRINI and A. V. GEKTIN

SEM-Analysis of Fracture Features Formed in Excimer-Laser Induced Surface Damage of CaF_2 151/[1061]
H. JOHANSEN, S. GOGOLL, E. STENZEL, M. REICHLING, and E. MATTHIAS

Electron Self-Trapping and Photolysis in $PbCl_2$ Crystals 157/[1067]
S. V. NISTOR, E. GOOVAERTS and D. SCHOEMAKER

NaF Films: Growth Properties and Electron Beam Induced Defects 163/[1073]
M. CREMONA, A. P. SOTERO, R. A. NUNES, M. H. DO PINHO MAURICIO, L. C. SCAVARDA DO CARMO, R. M. MONTEREALI, S. MARTELLI, and F. SOMMA

Defects in Ion Implanted and Electron Irradiated MgO and Al_2O_3 169/[1079]
R. S. AVERBACK, P. EHRHART, A. I. POPOV and A. v. SAMBEEK

EPR-Study of Electron-Radiation Induced Ca Colloids in CaF_2 Crystals 175/[1085]
F. BEUNEU, C. FLOREA and P. VAJDA

Defect Mechanisms in the Thermoluminescence of LiF:Mg, Cu, P 181/[1091]
S. MAHAJNA, D. YOSSIAN and Y. S. HOROWITZ

Photoinduced Phenomena in $RbAg_4I_5$ Superionic Crystals 187/[1097]
S. BREDIKHIN, N. KOVALEVA, T. HATTORI and M. ISHIGAME

EPR vs. Temperature of Fe^{3+} ions Produced by Radiolysis in $CdCl_2$:Fe Crystals 191/[1101]
S. V. NISTOR, E. GOOVAERTS and D. SCHOEMAKER

Radiation Effects in Pure and Re Doped $KMgF_3$ 197/[1107]
N. V. SHIRAN, V. K. KOMAR, V. V. SHLYAKHTUROV, A. V. GEKTIN, N. P. IVANOV, V. A. KORNIENKO, I. M. KRASOVITSKAYA and Y.A. NESTERENKO

Simulation of the Build-Up Radiation Damage in NaCl:Initial Stages of Colloid Formation 201/[1111]
W. J. SOPPE and J. PRIJ

Theory of Diffusion-Controlled Defect Aggregation under Irradiation: A Comparative Study of Three Basic Approaches 209/[1119]
E. A. KOTOMIN, V. N. KUZOVKOV, M. ZAISER and W. SOPPE

Thermoluminescence of Pure and Eu-Doped $NaZnF_3$ 217/[1127]
C. FURETTA, M. GRAZIANI, C. SANIPOLI, and A. SCACCO

Peculiarities of a Radiation Defect Creation in Beryllium Oxide Crystals 221/[1131]
S. V. KUDYAKOV, I. N. ANTSIGIN, S. V. GORBUNOV and A. V. KRUZHALOV

Interpretation of the Extralarge Inhomogeneous Broadening in the Optical Spectra of Heavily Neutron-Irradiated IaB-Type Diamond 227/[1137]
A. OSVET and I. SILDOS

Point Defects and Short-Wavelength Luminescence of LiB_3O_5 Single Crystals 233/[1143]
I. N. OGORODNIKOV, A. Yu. KUZNETSOV, A. V. KRUZHALOV and V. A. MASLOV

Some Specific Features of TL-Output Storage in MgO:Fe Crystals 239/[1149]
V. S. KORTOV and A. V. MONAKHOV

Optical Damage of W-Doped $KTiOPO_4$ Non Linear Single Crystals 243/[1153]
M. J. MARTÍN, C. ZALDO, F. DÍAZ, R. SOLÉ, D. BRAVO and F. J. LÓPEZ

Low Temperature Photostimulated Luminescence of KBr–In Crystal After UV Irradiation 249/[1159]
L. E. TRINKLER and M. F. TRINKLER

Peculiarities of Interstitials in a Simple Cubic CsCl Crystal 253/[1163]
A. LUSHCHIK, K. IBRAGIMOV, I. KUDRJAVTSEVA and L. PUNG

Radiation Processes on the Surface of Irradiated Corundum Monocrystals 257/[1167]
V. V. HARUTUNYAN, A. K. BABAYAN, V. A. GEVORKYAN and V. N. MAKHOV

Influence of the Crystallographic Orientation of the Surface on Damage and Chemical Effects in Ion-Implanted MgO **261/[1171]**
L. GEA, P. THEVENARD, R. BRENIER, B. CANUT, S. M. M RAMOS and M. BERANGER

ESR Study of the Insulator-Conductor Transition in Polyimide Kapton Induced by Swift Heavy Ion Irradiations **267/[1177]**
J-P. SALVETAT, A. BERTHAULT, F. BRISARD, J-M. COSTANTINI, and J. DAVENAS

The Exfoliation of LiF Implanted with Alkali Ions at Low Temperature **273/[1183]**
J. DAVENAS and B. V. THIEN

Europium Diffusion in Y- and Z-Cut $LiNbO_3$ Pre-Irradiated by Gev Uranium Ions **279/[1189]**
S. M. M. RAMOS, R. BRENIER, B. CANUT, G. FUCHS, A. MEFTAH, P. MORETTI, S. OULD SALEM, P. THEVENARD, M. TOULEMONDE and M. TREILLEUX

Optical Study of Defects in RbI and KI Bombarded With High Energy Argon Ions at Temperatures between 20 K and 300 K **283/[1193]**
M. A. PARISELLE, E. HOURDEQUIN, J. D. COMINS, E. BALANZAT, S. LEFRANT and B. RAMSTEIN

Self-Trapped Exciton Luminescence Under Dense Electronic Excitations: Ion-Induced Transient Thermal Effects **287/[1197]**
L. PROTIN, E. BALANZAT, S. BOUFFARD, A. CASSIMI, E. DOORYHEE, J.L. DOUALAN, C. DUFOUR, J. P. GRANDIN, J. MARGERIE, E. PAUMIER, and M. TOULEMONDE

Raman and Optical Absorption Studies of the Annealing of γ-Irradiated KI and KI (Sr) **295/[1205]**
J. D. COMINS, A. M. T. ALLEN, E. RZEPKA and S. LEFRANT

A Comparative Study of Glow Curves in Photo-Transferred and Pre-Dose Sensitized Thermoluminescence (PTTL and TL) in LiF:Mg, Ti **301/[1211]**
T. M. PITERS, E. M. YOSHIMURA, C. M. SUNTA, E. OKUNO, N. K. UMISEDO and M. P. DIAZ

Latent Track Formation in $LiNbO_3$ Single Crystals Irradiated by GeV Uranium Ions **307/[1217]**
B. CANUT, R. BRENIER, A. MEFTAH, P. MORETTI, S. OULD SALEM, M. PITAVAL, S. M. M. RAMOS, P. THEVENARD and M. TOULEMONDE

Modification of Magnesium Phosphate Glass by H^+ Irradiation: Formation of OH-Bond and Phosphorus-Colloid **311/[1221]**
N. MATSUNAMI, K. KAWAMURA and H. HOSONO

Radiation Effects and Defects in Solids Volume 137 (1995)

CONTENTS – PART IV

Note on Pagination, Author Index and Table of Contents

The Proceedings of the EURODIM 94 Conference is being published in four volumes of Radiation Effects and Defects in Solids (Volume 134, Part I, Volume 135, Part II, Volume 136, Part III and Volume 137, Part IV). To facilitate indexing and referring to this Proceedings, the page numbers of Volume 135, Volume 136 and Volume 137 will run continuously from the end of Volume 134. An author index will appear at the end of Volume 137. A complete table of contents will appear in Volume 134, Part I and Volume 137, Part IV.

10 Surface Defects

Topography and Dynamics of Surface Defects on Ionic Crystals 1/[1227]
R. T. WILLIAMS, R. MARK WILSON, and A. L. SHLUGER

Influence of the Mismatch Dislocations on the Elastic Properties of the Insulating Fluoride Films Deposited on Si(111) 11/[1237]
V. V. ALEKSANDROV and N. L. YAKOVLEV

Analysis of the Propagation of Strongly Attenuated Leaky Acoustic Modes as Method of the Detection of the Low Scale Interface Defects in the Layered Structures 15/[1241]
V. V. ALEKSANDROV, V. R. VELASCO, and N. L. YAKOVLEV

Bulk and Surface Metallization of CaF_2 under Low Energy Electron Irradiation 19/[1245]
R. BENNEWITZ, C. GÜNTHER, M. REICHLING, E. MATTHIAS, R. M. WILSON and R. T. WILLIAMS

Surface Modification of Polymers Indused by Ion Implantation 25/[1251]
RENÉ ENDRŠT, VÁCLAV ŠVORČÍK, VLADIMÍR RYBKA and VLADIMÍR HNATOWICZ

The Behaviour of Pure and K^+ Implanted LiF Surfaces under Electron Bombardment 29/[1255]
C. JARDIN, P. DURUPT and J. DAVENAS

Investigation of ZnSe Films Grown on GGG, YIG 35/[1261]
P. KOSOBOUTSKI and P. VODOLAZSKI

Investigation of the Thermochemical Reaction in ZnSe Crystals from Action by Infrared Light 39/[1265]
P. KOSOBOUTSKI, R. KIJAK and R. BIBIKOV

11 Nanomaterials

Effects of Resonance on Low-Frequency Raman Scattering from Semiconductor Nanocrystals 45/[1271]
L. SAVIOT, B. CHAMPAGNON, E. DUVAL and A. I. EKIMOV

Nanocrystalline Copper Doped Zinc Oxide Gas Sensors 51/[1277]
A. V. CHADWICK, A. HARSCH, N. V. RUSSELL, K. F. TSE, A. R. WHITHAM and A. WILSON

Clustering in NaCl:Pb 57/[1283]
K. POLAK, M. NIKL and K. NITSCH

Optical Study of the Phase Separation in Alkali Halide Solid Solutions 63/[1289]
M. INABA and S. HASHIMOTO

Metallic Na Formation in NaCl Crystals by Electron and VUV Photon Irradiation 69/[1295]
S. OWAKI, S. KOYAMA, M. TAKAHASHI, T. OKADA, R. SUZUKI and M. KAMADA

Nano-Structures and Quantum Size Effects in Heavily Irradiated NaCl 73/[1299]
D. VAINSHTEIN, H. P. DEN HARTOG, H. C. DATEMA, J. SEINEN and H. W. DEN HARTOG

Stacking Fault Excitons in AgBr Microcrystals with Twin Planes 77/[1303]
A. MARCHETTI

Optical Properties of Metallic Nanoparticles Synthesized by Implantation of Alkali Ions in LiF 81/[1307]
J. DAVENAS and C. JARDIN

Nanometric Metallic Particles in Insulating Materials:Bi-SiOx 89/[1315]
C. MARTET, J. F. ROUX, M. TREILLEUX, B. CABAUD, J. C. PLENET and G. FUCHS

Electronic Structure and Optical Spectra of Overstoichiometric Cadmium Atoms in CdI_2 Crystals 95/[1321]
I. BOLESTA, I. KITYK, V. KOVALISKO and R. TURCHAK

Enhanced Raman Scattering of Phonons in CaF_2 and MgO Containing Ca and Li Colloids 99/[1325]
P. B. OLIETE, M. L. SANJUÁN and V. M. ORERA

TEM Study of FE-Co Oxides System of Ammonia Catalyst 105/[1331]
V. S. TEODORESCU and L. C. NISTOR

Optical Non Linear Measurements in CdS Doped Silica Films 109/[1335]
A. OTHMANI, J. C. PLENET, E. BERNSTEIN, F. PAILLE, C. BOVIER, J. DUMAS, P. RIBLET, J. B. GRÜN, P. GILLIOT and R. LEVY

12 Carbon and Polymers

EPR Study of the Hole Paramagnetic Center in C_{70} Fullerite 115/[1341]
L. S. SOCHAVA, V. S. VIKHNIN, YU. S. GRUSHKO, S. N. KOLESNIK and M. V. KORNIENKO

Carbon Nanostructures in Implanted Nonconjugated Polymers 119/[1345]
O. YU. POSUDIEVSKY

Compensation Effects in C_{60} Doped by Ion Implantation 123/[1349]
P. TROUILLAS, B. RATIER and A. MOLITON

High Temperature Behaviour of Thermoelectric Power of Implanted Polymer Films 129/[1355]
C. MOREAU, B. RATIER, A. MOLITON and B. FRANÇOIS

Optical Properties Induced by the Formation of Carbon Nanoparticles in Irradiated Polyimide 135/[1361]
J. DAVENAS and J. P. SALVETAT

13 Disordered Systems

Low-Frequency Excitations in Fluoride Glass Studied by Nuclear Spin Relaxation and Electrical Conductivity 141/[1367]
J. DIECKHÖFER, O. KANERT, R. KÜCHLER and H. JAIN

Conductivity and Structure Relations in Polycrystalline α/β-Lead Fluoride Doped with Scandium Fluoride 147/[1373]
A. MEYER, J. TEN EICKEN, O. V. GLUMOV, W. GUNSSER, M. KARUS, and I. V. MURIN

Photovoltaic Effect and Electronic Transitions in $RbAg_4I_5$ 153/[1379]
A. BORIS, T. HATTORI and M. ISHIGAME

EXAFS Studies of Disorder in CdF_2-PbF_2 Systems 159/[1385]
T. T. NETSHISAULU, C. R. A. CATLOW, A. V. CHADWICK, G. N. GREAVES and P. E. NGOEPE

Amorphous Sol-Gel Derived Lead Titanate Thin Films used as Passive Waveguides 165/[1391]
C. URLACHER, A. BAHTAT, J. MUGNIER, C. BOVIER and J. SERUGHETTI

Ultrasonic Attenuation Measurements In Neutron-Irradiated Quartz: The Influence of Heat Treatment for a Dose of 4.7×10^{19} N/CM^2 169/[1395]
V. KEPPENS and C. LAERMANS

Study of the $K_{4.2}Ti_{1.2}(PO_4)_3$ Glass by Dielectric and Raman Spectroscopy 173/[1399]
C. Z. TAN, O. KANERT and R. KÜCHLER

Laser Irradiation Induced Structural Relaxation in the Densified SiO_2 Glass and SiO_2 Thin Film 179/[1405]
C. Z. TAN, Z. L. WU, and J. ARNDT

Optical Band-Gap and Activation Energy of Thin Films from the Se-Ag-I and Te-Ag-I Systems 183/[1409]
T. PETKOVA and M. MITKOVA

Effect of Ionic Exchange upon the Behaviour of Soda Lime Silicate Glass 187/[1413]
R. CAPELLETTI, P. GRAU, P. VAN HOI, and M. SUSZYNSKA

Polarization and Depolarization in Silica by Migration of Electric Charge Carriers 191/[1417]
M. BARLAND, E. DUVAL, T. ACHIBAT and A. BOUKENTER

The Polar Transition Of Li-Doped and Nb-Doped $KTaO_3$: Comparative Analysis from Hard-Phonon Raman Spectra 199/[1425]
P. CALVI, P. CAMAGNI, E. GIULOTTO and L. ROLLANDI

14 Dislocation, Plasticity

Plastic Deformation and Dislocations in Ceramic Materials 205/[1431]
J. RABIER

Plastic Deformation of CaF_2 Single Crystals 213/[1439]
A. MUÑOZ, A. DOMINGUEZ RODRIGUEZ and J. CASTAING

A Material Science Approach for the Evaluation of the Rheological State into the Earth's Lower Mantle 217/[1443]
F. VALLIANATOS, K. EFTAXIAS and A. VASSILIKOU-DOVA

Diffusion-Controlled Transitory Creep in Binary Oxides 223/[1449]
M. JIMÉNEZ-MELENDO, A. DOMÍNGUEZ-RODRÍGUEZ and J. CASTAING

Creep Behaviour of 21 Mole% Y_2O_3-Fully Stabilized Zirconia Single Crystals 227/[1453]
D. GÓMEZ-GARCÍA, J. MARTÍNEZ-FERNÁNDEZ, A. DOMÍNGUEZ-RODRÍGUEZ, P. EVENO and J. CASTAING

Microscopical Studies of Dislocations and Plasticity in Deformed Ionic Crystals 231/[1457]
M. V. NAZAROV and T. A. NAZAROVA

15 Transport Phenomena

Atomic Transport of Oxygen in Nonstoichiometric Oxides 233/[1459]
J. L. ROUTBORT and G. W. TOMLINS

Defect Interactions, Statistical Thermodynamic and Electronic Transport in Ionic Nonstoichiometric Oxides 239/[1465]
R. TETOT and G. BOUREAU

Defect Parameters for Rubidium Chloride from Ionic Conductivity Measurements 247/[1473]
PATRICK W. M. JACOBS and MARCIA L. VERNON

Transport Processes in Fluoride Crystals under High Pressure 251/[1477]
I. V. MURIN, O. V. GLUMOV, W. GUNSSER and M. KARUS

Transport Phenomena in Alkali Halide Mixed Crystals 255/[1481]
F. BÉNIÈRE, V. H. BABU, M. BÉNIÈRE and K. V. REDDY

Local Structure and Oxygen Transport in Transition Metal Doped YSZ 259/[1485]
N. NICOLOSO, J. MAIER, F. K. KOSCHNICK and J. M. SPAETH

Anomalous Point Defect Formation and Phase Transitions: The Significance of a Cube Root Law 267/[1493]
N. HAINOVSKY and J. MAIER

Intrinsic Electron Traps and Electronic Conduction in YSZ 273/[1499]
R. I. MERINO and V. M. ORERA

High Temperature Annealing Effects on the A.C. Conductivity of Swept Synthetic Quartz 277/[1503]
P. CAMPONE, M. MAGLIOCCO, G. SPINOLO and A. VEDDA

Diffusion of ^{18}O in Cr_2O_3: Bulk and Scales and Relation with Oxidation Kinetics 285/[1511]
S. C. TSAI, A. M. HUNTZ, C. DOLIN and C. MONTY

Influence of Yttrium on Transport Properties of α Alumina Scales Developed on Yttrium Implanted β NiAl 291/[1517]
J. BALMAIN, M. K. LOUDJANI and A. M. HUNTZ

Effective Diffusion Coefficient and Diffusion-Controlled Reactions in Insulating Solids with Defects 295/[1521]
YU. H. KALNIN and P. ZAPOL

Fast Diffusion of the Off-Center Impurities Cu^+ and Li^+ in the KCl Lattice 299/[1525]
F. DESPA and V. TOPA

Internal Reduction of Polycrystalline Cr-Doped Alumina 305/[1531]
M. BACKHAUS-RICOULT and A. PEYROT

The Second-Order Elastic Constants of AgBr from 20°C to 400°C 309/[1535]
L. S. CAIN and GANG HU

Schottky Barriers in Superionic Crystals 313/[1539]
S. BREDIKHIN, T. HATTORI and M. ISHIGAME

Electrical Conductivity of a α-$LiIO_3$:Cr^{3+} Single Crystal 319/[1545]
R. L. MOREIRA, P. BOURSON, C. ROSSO, C. GALEZ, A. RIGHI and J. M. CRETTEZ

A Renewed Approach of Hopping Conduction in Amorphous Materials 323/[1549]
R. ONGARO and M. GAROUM

16 Superconductivity

Transport Properties and Defect Chemistry of High-Tc-Superconductors 327/[1553]
M. QUILITZ and J. MAIER

Laser-Heating and Phonon Moeds in $YBa_2Cu_3O_x$ 331/[1557]
L. GASPAROV

The $YBa_2Cu_3O_z$ Phase Diagram 337/[1563]
C. PICARD, P. GERDANIAN, A. H. MOUDDEN and M. G. BLANCHIN

Density of Electron States near Surfaces of Layered Copper Oxides 343/[1569]
S. A. PROSANDEYEV and I. M. TENNENBOUM

Increasing of T_c in the New HTSC $HgBa_2CuO_{4+\lambda}$ PROMOUTED BY DEFECTS 347/[1573]
YU. N. MYASOEDOV, R. V. LUTCIV, I. V. KITYK, V. N. DAVYDOV, and YA. V. BOYKO

Large Local Distortions Introduced by Defects in $YBa_2Cu_3O_7$ Superconductors: An X-Ray-Absorption Study 351/[1577]
FRANK BRIDGES, G. G. LI, C. H. BOOTH, J. B. BOYCE and T. CLAESON

Author Index i

PREFACE

The Seventh Europhysical Conference on Defects in Insulating Materials (EURODIM 94) was held in the 'Ecole Normale Supirieure' de Lyon. The conference has been organized by the 'Laboratoire de Physico-Chimie des Matiriaux Luminescents' and the 'Departement de Physique des Matiriaux' of the University Claude Bernard Lyon I.

EURODIM 94 follows the so-called LATDIM 90 europhysical conference of the same series held in Groningen (The Netherlands) and the ICDIM 92 international conference held in Germany. The aim of such conferences is to bring together scientists from academic institutions and industry to discuss about the physics and chemistry of defects in insulating solids and their role in the properties of materials. It is clear that the numerous applications and the quest for new and better materials make this field of research very active.

EURODIM 94 received more than 600 contributions and more than 500 demands of participation, a large number of which coming from scientists of Eastern Europe. Following the example of ICDIM 92, we did a strong effort to financially support many of them with the help of various institutions and private contributions. We want to gratefully acknowledge all the sponsors who participated in the financial support of the conference and more especially the local institutions who were particularly generous.

The final scientific program included 23 invited papers, 57 oral contributions and around 400 poster presentations. We wish to acknowledge the members of the International Advisory Committee for their help in the choice of the invited talks and the members of the Program Committee who had the difficult task to review more than 300 papers and to select the oral contributions of the conference. On behalf of the Organizing Committee we now express our thanks to all the authors and the referees, who have contributed to the Proceedings of EURODIM 94.

Marie-Genevihve BLANCHIN
Christian PEDRINI
Conference Chairmen

Jokl DAVENAS

Publication Committee

Radiation Effects and Defects in Solids, 1995, Vol. 134 pp. 1–6
Reprints available directly from the publisher
Photocopying permitted by license only

© 1995 OPA (Overseas Publishers Association)
Amsterdam B.V. Published under license by
Gordon and Breach Science Publishers SA
Printed in Malaysia

COMPUTER SIMULATION OF THE THERMODYNAMICS AND DIFFUSION IN NONSTOICHIOMETRIC MATERIALS

G. E. MURCH

Department of Mechanical Engineering, The University of Newcastle, Callaghan, NSW 2308, Australia

(Received July 1, 1994)

In this brief review recent progress in the application of computer simulation techniques to the thermodynamics and diffusion processes in highly nonstoichiometric materials is discussed. For the discussion of thermodynamics we review the application of the Monte Carlo method and its recent full integration with lattice relaxation methods. For the discussion of diffusion we also review the application of the Monte Carlo method with special emphasis on concentrated as well as defective systems and also its integration with lattice relaxation methods. Testing of relations among phenomenological coefficients, tracer diffusivities and ionic conductivities is also commented on.

Key words: thermodynamics, diffusion, Monte Carlo, computer simulation.

1 INTRODUCTION

From an experimental point of view there is an abundance of high quality thermodynamic data for numerous nonstoichiometric pure materials, though rather less so for mixed systems. A similar situation also exists for diffusion data, both tracer and chemical. In spite of these data an understanding beyond the mass action law approach has been rather slow in coming. In this brief overview we will focus on the problems, how they can be tackled by computer simulation and review some of the progress made to date.

2 COMPUTER SIMULATION OF THE THERMODYNAMICS OF NONSTOICHIOMETRIC MATERIALS

In order to describe the thermodynamics of the nonstoichiometric phase it has been usual to address two formally separate problems. The first is the free energy of formation of the defect. The second is the calculation of the free energy of interaction of those defects.The very well-known Mott-Littleton approach as embodied in such codes as HADES III[1] and CASCADE[2] has enjoyed widespread success in the calculation of formation (and migration) internal energies, these are closely equal to the constant pressure defect formation (and migration) enthalpies in many cases. We might mention that binding energies of a defect to a dopant can also be calculated in much the same way.[4] The entropies of defect production and migration are also accessible using such quasi-harmonic programs as SHEOL.[3] For an excellent review of the recent progress, see Harding.[5,6]

Computer calculation of the free energy of interactions requires a statistical mechanical approach, in particular the Monte Carlo method. In order to discuss the computer calculation of the interactions it is useful to use $Co_{1-\delta}O$ as a concrete example. We write for the Hamiltonian H of the defective oxide in the grand canonical ensemble assuming that only doubly ionized vacancies and electron holes localised on the metal lattice exist.

$$H = E_I - N_M\left[H^F_{V''} - TS^F_{V''} + \text{constant} - \frac{c}{2}dG(O_2)\right] \quad (1)$$

where E_I is the interaction internal energy, this includes both electrostatic and short range interactions, N_M is the number of metal ions, $c = 1/(1-\delta)$ is the composition of the oxide and $d\Delta G(O_2) = \Delta G(O_2)_c - \Delta G(O_2)_{c=1}$ with $\Delta G(O_2) = RTlnPo_2$. $H^F_{V''}$ and $S^F_{V''}$ are the formation enthalpy and entropy of one doubly ionized vacancy and two holes at infinite dilution respectively.

It has long been known that $\Delta G(O_2)$ is not particularly sensitive to the details of the model. Much more sensitive are its components, the partial molar enthalpy $\Delta H(O_2)$ and entropy $\Delta S(O_2)$. In the grand canonical ensemble $\Delta G(O_2)$ versus c is immediately available in a Monte Carlo simulation ($\Delta G(O_2)$ is specified and the lattice equilibrates to the appropriate composition). The partial molar enthalpy can be calculated from the fluctuations in the internal energy, see for example.[7] The entropy and enthalpy can, of course, be found from the temperature dependence of $\Delta G(O_2)$. At very low defect concentrations the grand canonical ensemble becomes unworkable because of the low probability of defect insertion/removal.[8]

The petit canonical ensemble is a reasonable alternative in a Monte Carlo simulation. $\Delta G(O_2)$ can be calculated readily by using the so-called particle insertion method first introduced by Widom[9] and adapted to Monte Carlo simulation by Murch and Thorn.[10] The chemical potential μ (the quantity in square brackets in Eqn. 1) is written as

$$\mu = -kTln\left[\frac{B}{(N_M+1)} < \exp(-\Delta E_M/kT) >\right] \quad (2)$$

where B is the number of sites in the lattice and ΔE_M is the change in energy on the addition of the $N_M + 1$ ion. A better numerical result is obtained by appropriately averaging over the particle insertion process and particle removal process.[7] It is worth mentioning that the particle insertion method can also be used in a Molecular Dynamics simulation by freezing a given configuration.[11] The partial molar enthalpy and entropy can be obtained from the temperature dependence of μ. The enthalpy can be calculated directly using the insertion method described by Tétot *et al.*[8] or by numerically differentiating the internal energy, see for example ref 7.

The first Monte Carlo calculations in the area made use of blocking models in a rigid lattice: a defect blocks a given number of neighbouring sites from occupation by other defects.[12] This model has seen considerable success in interstitial solid solutions in metals where long range interactions are not important. Even in oxides such as UO_{2+x} the partial molar entropy of oxygen is quite nicely described by defect clusters blocking a small number of sites. Being athermal, such models are, of course, incapable of describing a dependence of the partial molar enthalpy of solution.[13] Later Monte Carlo calculations used 'soft' nearest neighbour interactions, the model now being the lattice gas analogue of the Ising ferromagnet. The agreement with experiment in systems such as UC_x $1 \leq x \leq 2$ where long range interactions are relatively unimportant is surprisingly good.[14]

Two areas clearly needed improvement. For application to systems with low dielectric constants one needs to include the long range Coulombic interactions. And of course one needs to remove the rigid lattice assumption. Many years earlier Atlas[15] had attempted to describe analytically the thermodynamics of the nonstoichiometric phase in terms of Coulombic interactions. The Monte Carlo implementation was rather a long time in coming though preliminary calculations were described by Murch.[16] The difficulty comes about because of the large amount of computer time required to recompute the interactions at

each Monte Carlo step. In an important series of Monte Carlo papers Tétot, Boureau and coworkers[8,17,18,19,20] have recently explored the thermodynamic properties of Coulombically interacting defects in applications to CeO_{2-x},[17,19], $Co_{1-\delta}O$,[8,20] $Mn_{1-\delta}O$[8] and $Ni_{1-\delta}O$[8]. Among other things it was shown that the approximations employed by Atlas[15] have artifically given a good description of the partial molar enthalpy in CeO_{2-x},. Such Monte Carlo calculations have also been especially useful in determining the limits of applicability of the widely used ideal mass action law[18] and the Debye-Hückel formalism.[19] These calculations employed only Coulombic interactions and so are inappropriate for wide departures from stoichiometry where the defects will frequently be in close proximity.

This brings us back also to the problem of moving beyond the rigid lattice. There are two ways of proceeding in order to include the effect of short range interactions, assuming of course that they are known. The first (non rigorous) way is to employ a pattern recognition scheme in the Monte Carlo program in conjunction with energies calculated in a separate relaxation/Mott-Littleton program. The pattern could extend over, say, 20 or 30 sites. This idea has been used in a diffusion context[21] but so far has not been employed for thermodynamic properties. Probably the particle insertion method in the petit canonical ensemble for calculating the chemical potential would be the simplest to implement. The second way to proceed is to integrate the Monte Carlo and relaxation methods in an exact calculation fully in the spirit of the zero Kelvin formalism. At every Monte Carlo step a full relaxation of the entire lattice is required. Of course a great deal of computer time is required for such calculations. On present machines it is virtually out of the question to even contemplate a 3D calculation involving Coulombic interactions and short range forces and a Mott-Littleton approach for the polarisation response! So far, two far more limited calculations have been reported.[22,23] The first was a Monte Carlo calculation in the grand canonical ensemble for a 1D interstitial solid solution model. The second, in the same ensemble, was an extensive calculation of the chemical potential/phase diagram of the well-known Frenkel-Kontorova model. Some representative isotherms from the second study are shown in Figure 1. It is worth noting that the Monte Carlo/relaxation calculation can remove the articificial distinction between formation and interaction of the defects.

3 COMPUTER SIMULATION OF DIFFUSION IN NONSTOICHIOMETRIC MATERIALS

In order to understand the overall diffusion process in a highly condensed system where the hopping model is applicable one has to deal with two rather distinct components of that process. The first is the calculation of the activation enthalpy and entropy for the individual jumps, and therefore the jump frequency, the other is the calculation of the correlations in directions between those jumps as reflected in such quantities as the correlation factors. For self diffusion in **stoichiometric** ionic solids both of these components can be dealt with readily. The well-known Mott-Littleton calculations of defect formation and migration enthalpies with HADES III[1] and CASCADE[2] and the SHEOL[3] calculation of entropies have been especially significant in providing quantitative contact with experiment. And the calculation of correlation factors has been an active subject for over 40 years.The accurate calculation of these factors by Monte Carlo for instance is done so routinely that it is even used as an undergraduate experiment at the author's university among others, see especially ref. 24.

The introduction of a single impurity can be handled along similar lines, this has been nicely demonstrated by Harding and coworkers[25,26] for impurity diffusion in CoO and NiO. Increasing the concentration of dopant atoms, in other words to enter the concentrated regime, represents a formidable obstacle. One now needs to average over a very large

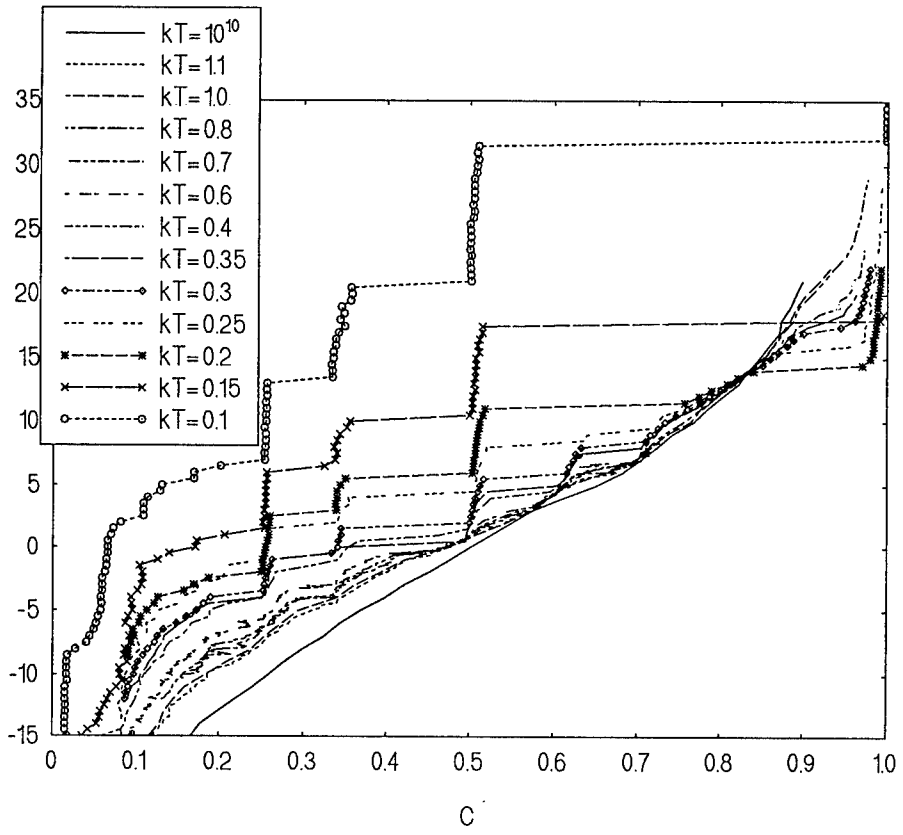

FIGURE 1 The chemical potential μ divided by the cage potential V_o versus concentration in the Frenkel-Kontorova model at various values of kT. The interactions between particles, as expressed by αb^2 (where α is the force constant and b is the average distance between the particles) was put equal to 0.4 π.

number of different environments encountered by a given atom. In principle there appear to be two computer simulation approaches to the problem. The first is to use Molecular Dynamics. This is certainly the preferred method for the problem, partly because it avoids the hopping model formalism, and partly because all dynamical information is accessible. But at present it is not a viable method in highly condensed systems. In liquids, at high temperatures, or in fast ion conductors, it is of course a well established technique. Even there, the number of calculations in mixed systems still remains small. The other approach is to use a Monte Carlo method combined with a lattice relaxation calculation. In this, there are two options.

One can first calculate defect migration (and formation) energies for the relatively small number of distributions in a local region, perhaps involving 20 or 30 sites. With these energies in hand, one can then do a 'standard' Monte Carlo diffusion simulation:[27] at each attempted move of the defect, the distribution of atoms in the immediate region is scanned, recognised and the appropriate energy looked up and used to form a jump probability. Computer generated random numbers are then used to determine the outcome. One can calculate the average jump frequency and the tracer correlation factors from the mean squared displacements and number of jumps in time t. If an electric field is imposed, it will also be possible to calculate what are now called collective correlation factors.[28] After the

initial calculation for CeO_2 doped with Y_2O_3[16] there has been little further progress. The main difficulties appear to be the very large investment in time in assembling the energies from the Mott-Littleton program and the need to conceive an efficient pattern recognition scheme for each new problem in addition to a new Monte Carlo lattice program. The neglect of the background outside the local region is a rather worrying assumption that is difficult to evaluate.

The Monte Carlo/relaxation scheme above was basically a tandem calculation: the energies were calculated beforehand and used as required in the Monte Carlo calculation. The second option is to integrate them into a single program. The general idea is that at each **attempted** move, the energy barrier is calculated hypothetically by moving, in increments, the atom from its site towards the vacancy with lattice relaxation at each point. This is of course how migration energies are calculated in Mott-Littleton programs. Something like 10 relaxations are required in order to reasonably establish the energy barrier. A computer generated random number is then used to establish the outcome of the proposed jump. Naturally, this type of simulation is extremely slow. Various preliminary unpublished calculations by the author in alloy systems have all shown that it is far too slow to be useful at this time except in one dimensional models such as the Frenkel-Kontorova model.

Rather more progress, but of a completely different kind, has been made by using Monte Carlo computer simulation of diffusion in rigid lattice models. The intent here is not so much to model real systems accurately, but to test analytical relations using models showing various degrees of non-ideality in the distributions of the components. A series of papers by Lidiard and Murch and coworkers[29,30] dealing with relations between the phenomenological coefficients of irreversible thermodynamics and measurable atomic transport coefficients such as tracer diffusivities and ionic conductivities showed that computer simulation, even of rigid lattice models, could be very useful in delineating the range of validity of the derived relations. Results of these simulations should give one the confidence to use such relations in an experimental context.

ACKNOWLEDGEMENTS

I wish to thank Professor Boureau and Dr Tétot for sending preprints of their recent work. This work was supported by the Australian Research Council.

REFERENCES

1. C. R. A. Catlow, W. C. Mackrodt and R. F. Stewart, *Phys. Rev. B.*, **25**, 1006 (1982).
2. M. Leslie, *SERC Daresbury Lab. Report*—DL/SCI/TM31T, (1982).
3. J. H. Harding, *Phys. Rev. B.*, **32** 6861 (1985).
4. A. Dwivedi and A. N. Cormack, *Phil. Mag. A.*, **61**, 1 (1990).
5. J. H. Harding, *Cryst. Latt. Def. and Amorph. Mat.* **18**, 247 (1989).
6. J. H. Harding, *Rep. Prog. Phys.* **53**, 1403 (1990).
7. S. H. Lim, M. Hasebe, G. E. Murch and W. A. Oates, *Phil. Mag. B.*, **61**, 173 (1990).
8. R. Tétot, B. Nacer and G. Boureau, *J. Phys. Chem. Solids*, **54**, 517 (1993).
9. B. Widom, *J. Chem. Phys.*, **39**, 2808 (1963).
10. G. E. Murch and R. J. Thorn, *J. Comput. Phys.* **29**, 237 (1978).
11. U. Heinbach and J. Fisher, *Molec. Simul.*, **1**, 109 (1987).
12. B. G. Baker, *J. Chem. Phys.*, **45**, 2694 (1966).
13. G. E. Murch, *Phil. Mag.*, **32**, 1129 (1975).
14. G. E. Murch and R. J. Thorn, *Phil. Mag.*, **34**, 299 (1976).
15. L. M. Atlas, *J. Phys. Chem. Solids*, **29**, 91 (1968).
16. G. E. Murch, PhD Thesis, The Flinders University of South Australia, 1973.

17. M. Benzakour, R. Tétot and G. Boureau, *J. Phys. Chem. Solids*, **49**, 381 (1988).
18. R. Tétot and G. Boureau, *J. Phys. Chem. Solids*, in press, 1994.
19. R. Tétot, M. Benzakour and G. Boureau, *J. Phys. Chem. Solids*, **51**, 545 (1990).
20. R. Tétot, B. Nacer and G. Boureau, *J. Phys. Chem. Solids*, in press (1994).
21. A. D. Murray, G. E. Murch and C. R. A. Catlow, *Solid State Ionics*, **18–19**, 196 (1986).
22. G. E. Murch and W. A. Oates, *Phil. Mag. Lett.*, **56**, 187 (1987).
23. G. E. Murch, S. Zhong and C. M. Bruff, *Defect and Diffussion Forum, in press.*
24. G. E. Murch and S. J. Rothman, in *Nontraditional Methods in Diffusion*, ed. G. E. Murch, H. K. Birnbaum and J. R. Cost, (TMS-AIME, PA, 1984), Chapter 12, p. 281.
25. J. H. Harding, *Advanced Ceramics*, **23**, 229 (1987).
26. J. H. Harding, M. J. L. Sangster, A. M. Stoneham and K-J. Tarento, *Phil. Mag. A.* **62**, 473 (1990).
27. G. E. Murch in *Diffusion in Crystalline Solids*, ed. G. E. Murch and A. S. Nowick, (Academic Press, Orlando FL, 1984), Chapter 7, p. 379.
28. G. E. Murch and Z. Qin, *Defect and Diffusion Forum*, **109**, 1, (1994).
29. A. B. Lidiard, G. E. Murch, Z. Qin and L. Zhang, *Phil. Mag. A.*, **62**, 595 (1990).
30. Z. Qin and G. E. Murch, *Phil. Mag. A.*, **67**, 757 (1993).

Radiation Effects and Defects in Solids, 1995, Vol. 134, pp. 7–10
Reprints available directly from the publisher
Photocopying permitted by license only

© 1995 OPA (Overseas Publishers Association)
Amsterdam B.V. Published under license by
Gordon and Breach Science Publishers SA
Printed in Malaysia

DEFECTS IN GLASSES

A. R. SILINS

Institute of Solid State Physics, University of Latvia, Kengaraga iela 8, Riga, LV-1063, LATVIA

(Received July 1, 1994)

The absence of long range order in the glass structure allows to define only point defects in these materials. They are: 1) intrinsic defects—atomic size local deviation from short range order; 2) impurity defects—isolated impurity atoms or ions in the glass network; 3) intrinsic impurity defects—complexes consisting of the impurity atoms chemically bonded to one of the intrinsic defect atoms. The latter defects are characteristic for the doped glasses. Presence of point defects in glasses introduces new spectroscopic properties of these solid materials. Defect generation, interaction and recombination reactions resulting from the external influence causes the glass spectroscopic property changes.

Key words: glass structure, point defects, spectroscopic properties.

1 INTRODUCTION

Point defects in glasses are atomic size local absences (deviations) of short range order (intrinsic defects) and the presence of the isolated impurity atoms or ions (impurity defects) in the glass network. When both mentioned types of point defects exist in the glass network they could under external influence interact with each other and create new type of point defects, the so called intrinsic-impurity defects. As in the real glasses there always exist at least the equilibrium, but mainly frozen in intrinsic defects in high enough concentrations, therefore usually all technological impurities could create intrinsic-impurity type defects. These defects are characteristic for the glassy state of solid materials, because intrinsic defects are chemically active sites in the network and in the glass preparation process they with large probability react with technological impurities.

In glasses intrinsic defects play much more important role than in crystals of the same chemical composition, because in the glassy state there exists different type of elementary intrinsic defects than in the crystalline state and the frozen in concentrations of 'glassy state' defects are much higher than frozen in concentrations of 'crystalline state' defects. This happens, because the 'glassy state' elementary intrinsic defects, e.g., the ends of broken chemical bond, do have strong chemical interaction with glass network, but 'crystalline state' elementary intrinsic defects, e.g., the interstitial atoms or ions have much smaller interaction with the surroundings atoms. It leads to the situation that intrinsic defect creation energy in glass is smaller than in crystal, but intrinsic defect diffusion energy in glass is much higher than in crystal with the same chemical composition. As a result in glassy state it is easier to generate elementary intrinsic defects in high concentrations, but below glass transition temperature they are not able to recombine and remain frozen in intrinsic defects.

To investigate defects in glasses it is necessary to find out precisely which spectroscopic or other properties of the material are determined by definite point defects. This problem is common for point defects investigations in any solid state material. Among optical glasses the most investigated material is fused silica, in which as the result of long-term experimental work the spectroscopic properties of elementary intrinsic defects, some of its aggregates and main impurity defects are determined. Therefore later in this review the fused silica will be used as an example to approve one or another common suggestion.

2 STRUCTURE OF IDEAL GLASS

In order to find out point defects in any of glasses it is necessary to define the ideal structure of glass. Usually this structure is defined as solid network, in which each atom has the same short range order (the same type of geometry of surrounding atoms). In the ideal fused silica (SiO_2) glass network each silicon atom is tetrahedraly surrounded by four oxygen atoms and each oxygen atom is surrounded by two silicon atoms. Such structure is determined by direct methods: x-ray or neutron difraction. The main part (more than 99%) of each glass usually consists of ideal structure. The chemical composition of glass together with its ideal part of structure determines the so called fundamental physical properties of each concrete glass. For optical glasses the main practical role plays fundamental ultraviolet (electronic) and infrared (vibronic) absorption, as well as the transparency region between the absorptions.

Usually the short range order of atoms in ideal glass is similar, but not equal to the short range order of the relevant atoms in crystals of the same chemical composition. To obtain disordered material (glass) absolute similarity of short range order is not possible. The deviations are mainly placed in the geometry of surrounding atoms around the atom with the smallest coordination number. These deviations cause also slight differences of fundamental physical properties between glass and crystal with the same chemical composition.

3 THERMALLY INDUCED DEFECTS

The ideal glass does not exist (as well as the ideal crystal), because as the result of thermal influence in this structure there always exists equilibrium or frozen in imperfections (intrinsic defects). Usually in the optical glasses definite concentrations of high temperature (glass preparation conditions) intrinsic defects are frozen in. The glass transition temperature is the reference point below which the frozen in intrinsic defects appear. In fact each glass in ordinary conditions (room temperature) has the frozen in intrinsic defect concentrations which reflect the thermal equilibrium defect concentrations at glass transition temperature. Above transition temperature different defect generation, interaction and recombination reactions take place and elementary intrinsic defects and their aggregates appear in the glass network. It is important to estimate the types of concentrations of these high temperature intrinsic defects in glasses, because afterwards they are frozen in.

Our efforts used to estimate the concentrations of frozen in thermal defects in fused silica show, that in the stoichiometric glass the main defects are non-bridging oxygen atoms and three-fold-coordinated silicon atoms. Deviations from stoichiometry lead to the increase of two-fold-coordinated silicon atoms (oxygen deficit) or increase of non-bridging oxygen atoms (oxygen excess). These defects play an important role in the optical waveguides made from fused silica because the high cooling rate in preparation increases the glass transition temperature for fused silica in waveguides.

4 SPECTROSCOPIC PROPERTIES OF DEFECTS

The existence of point defects in glass usually appears as changes of the material spectroscopic properties in the transparency regions. It is very hard to find out the defects in glasses from changes of spectroscopic properties in the fundamental physical property regions, because the defect concentrations are at least three orders of magnitude less than the concentrations of ideal network atoms which determine the fundamental physical

properties of the glass. Therefore we can conclude that, if the spectroscopic characteristics of several types of point defects coincide with the glass fundamental spectroscopic properties, the presence of such defects cannot appear as an essential physical property change of the glass. In fused silica to this type of point defects belong oxygen vacancies, peroxy bridges and chlorine atoms chemically bonded to the three-fold-coordinated silicon atoms.

From the practical viewpoint the most important are point defects which are changing the spectroscopic properties of the glass in the transparency regions. Usually it is necessary to reduce the concentration of such type defects, but sometimes they could be used as activators. In fused silica to this type of point defects belong non-bridging oxygen atoms, three-fold-coordinated silicon atoms, two-fold-coordinated silicon atoms and hydrogen atoms chemically bonded to the non-bridging oxygen atoms.

It is necessary to remind that there are almost different intrinsic defects in the glass and crystal with the same chemical composition. It is reflected also in the differencies of the material spectroscopic properties caused by the presence of point defects. For example, the point defect related spectroscopic properties in fused silica are almost different from those in crystalline quartz.

5 DEFECT GENERATION, INTERACTION AND RECOMBINATION

When the spectroscopic characteristics of point defects are determined, it is possible to investigate the defect generation, interaction and recombination reactions in the glass network resulting from the external influence by the detection of changes in glass spectroscopic properties. Thus in the fused silica it is found out, that radiation created exciton decay leads to the generation of elementary intrinsic defects with small probability. Much easier is to create non-bridging oxygen atoms from hydroxyl bonded to the glass network by breaking off O-H chemical bond under vacuum-ultraviolet light irradiation. Isolated hydrogen atoms are also generated in this process. These impurity defects (hydrogen atoms) are stable in the fused silica glass network only at temperatures below 100 K. The small activation energy for diffusion of hydrogen atoms allows them to move in the glass network at higher temperatures than 100 K and recombine with non-bridging oxygen atoms. Such recombination reactions restore the intrinsic-impurity type hydroxyl point defects in the fused silica glass network.

Very high intensity light irradiation leads to the glass density changes. It could be caused by intrinsic defect generation and interaction reactions. In fused silica, where defect interactions reduce the free volume in the glass network, the material density increases, but in sodium silicate glasses, where charged defects are created, the material density decreases (materials expand). Such density changes are connected with the changes of other glass main physical properties, for example, light refraction index.

6 PRACTICAL USE OF DEFECTS

The presence of point defects in glasses is widely used to solve practical tasks. Mainly all glass-based lasers act on electronic transitions between impurity defect (activator) levels. In similar way impurity and sometimes intrinsic defects are used in glass luminofors, scintilators, optical filters and other devices. Large popularity has obtained the refractive grating writing possibilities in the glass waveguides. This process is connected with the charge state and geometrical structure changes of the existing point defects caused by the light influence.

In the photo- and electrochromic glasses point defect generation and recombination reactions, caused by light or electric field influence, also plays an essential role in the practical use of these materials. As the glass chemical composition variation possibilities are infinite, there are great chances to choose appropriate glass to solve the pointed out practical problem.

7 CONCLUSIONS

1. Thermally induced point defects play much more important role in the glassy state than in the crystalline state of the material with the same chemical composition.
2. Impurities in glasses mainly exist as intrinsic-impurity defect complexes, where impurity atom is chemically bonded to one of the intrinsic defect atoms.
3. Defect generation, interaction and recombination reactions in the glass network change the spectroscopic and sometimes basic physical properties of the material.

This work is funded by the Latvian Council of Science, Grant # 93.656.

Radiation Effects and Defects in Solids, 1995, Vol. 134, pp. 11–22
Reprints available directly from the publisher
Photocopying permitted by license only

© 1995 OPA (Overseas Publishers Association)
Amsterdam B.V. Published under license by
Gordon and Breach Science Publishers SA
Printed in Malaysia

OPTICAL PROPERTIES OF OXIDE GLASSES DOPED BY SEMICONDUCTOR NANOCRYSTALS

A. I. EKIMOV

A. F. Ioffe Physical-Technical Institute, 194021 St. Petersburg, Russia

Process of diffusion controlled phase decomposition of oversaturated solid solution, which makes it possible to grow semiconductor nanocrystals in a glass matrix and to vary the size of them in a controlled manner, is reviewed. It is demonstrated that optical properties of semiconductor-doped glasses are governed by quantum confinement of electronic and vibronic excitations in the nanocrystals. Manifestations of the quantum size effect in absorption, luminescence and Raman scattering spectra of these composite materials are regarded.

Key words: semiconductor, glass, exciton, quantum size effect, Raman scattering.

At the beginning of 80's it was understood that optical properties of semiconductor-doped glasses are determined by very special kind of defects—by nanometre scale size semiconductor particles embedded in a host matrix of glass.[1–3] It was found that semiconductor nanocrystal embedded in a wide gap matrix of oxide glass represents a three dimensionally confined quantum well for electronic excitations (electrons, holes, excitons). Therefore, the energy spectrum of the excitations is governed by quantum size effect and depends strongly on the size of the particles.

Since that time the semiconductor-doped glasses have been a subject of very intensive investigations. It was demonstrated that due to the quantum confinement effect these composite materials demonstrate novel linear, non-linear and electro-optical properties, not available in bulk materials (for recent review see [4]). Recent advances in technology of these composite materials show that semiconductor-doped waveguides can be fabricated with the use of high-frequency sputtering and/or ion implantation techniques. Progress in the both fundamental and technological aspects makes semiconductor-doped glasses an attractive material for practical applications in the fields of optoelectronics, integrated optics, all-optical switching devices and so on.

This paper is aimed at reviewing of state of art and recent advances in technology and physics of semiconductor-doped glass materials.

1 THERMODYNAMICS OF SEMICONDUCTOR NANOCRYSTALS GROWTH

Growth of semiconductor particles in solid state matrices is based on the process of diffusion controlled phase decomposition of oversaturated solid solution. Three methods of creation of the oversaturated solution of semiconductor phase in a solid state matrix are used now: co-melting of glass and semiconductor at high temperature, high-frequency co-sputtering of glass and semiconductor and method of implantation of semiconductor phase ions into the glass matrix.

The growth of the particles is performed in a course of the phase decomposition process at annealing of samples at temperature sufficiently high to obey effective diffusion of semiconductor ions in a matrix. It is well known[5] that this process can be divided onto three stages: nucleation, stage of growth at the expense of solved matter and stage of recondensational growth. In a course of the first stage the nuclei appear but do not grow in size. The dependence of critical radius of the nuclei on temperature of annealing can be described by the following expression:[4]

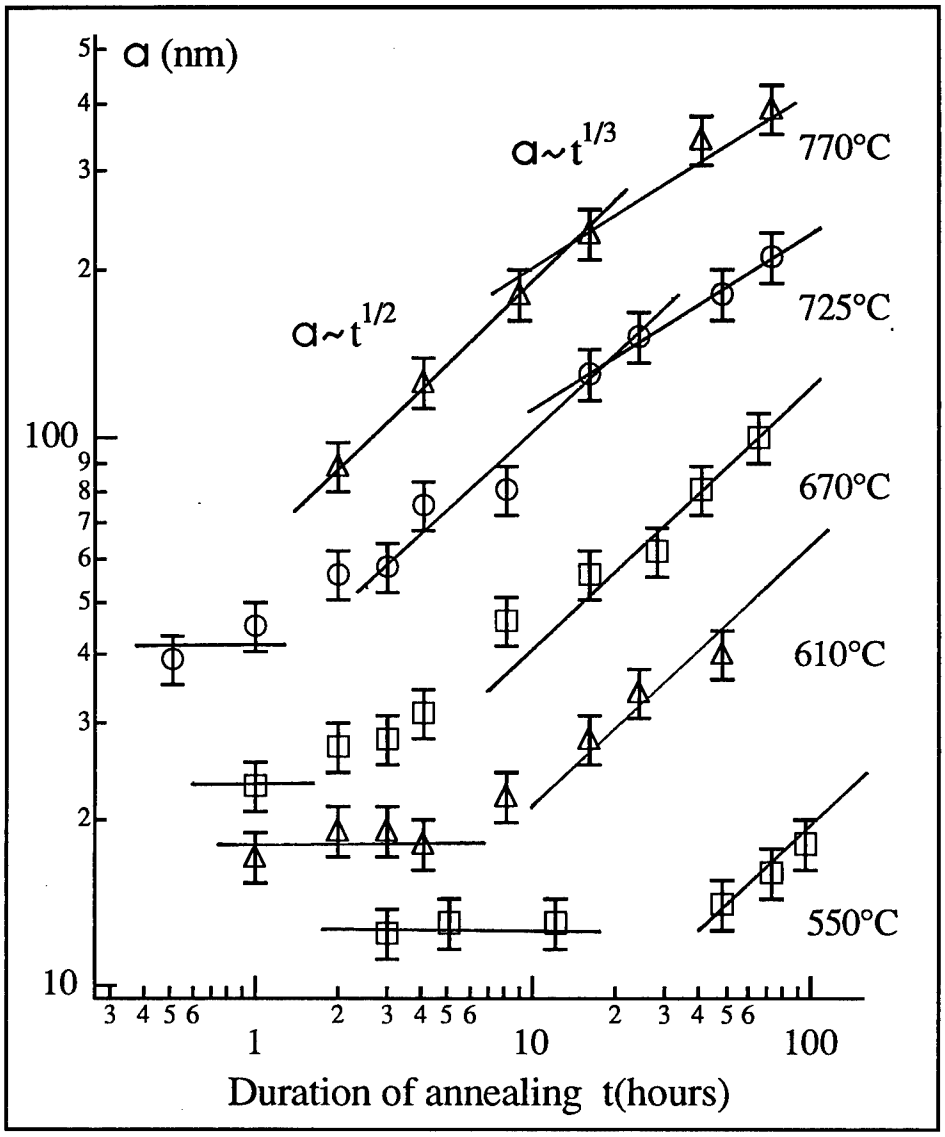

FIGURE 1 Dependence of mean radius of CdS nanocrystals as a function of annealing duration at various temperatures. Solid lines show slope of the dependencies for different stages of phase decomposition process (see text).

$$a_{cr} = 2\sigma T_o v/\delta H(T_o - T) \quad (1)$$

where: σ is a coefficient related to interfacial surface tension, T is an annealing temperature, T_o is a temperature of equilibrium solution, v is a mean specific volume of the particles and ΔH is a mean specific entalphy.

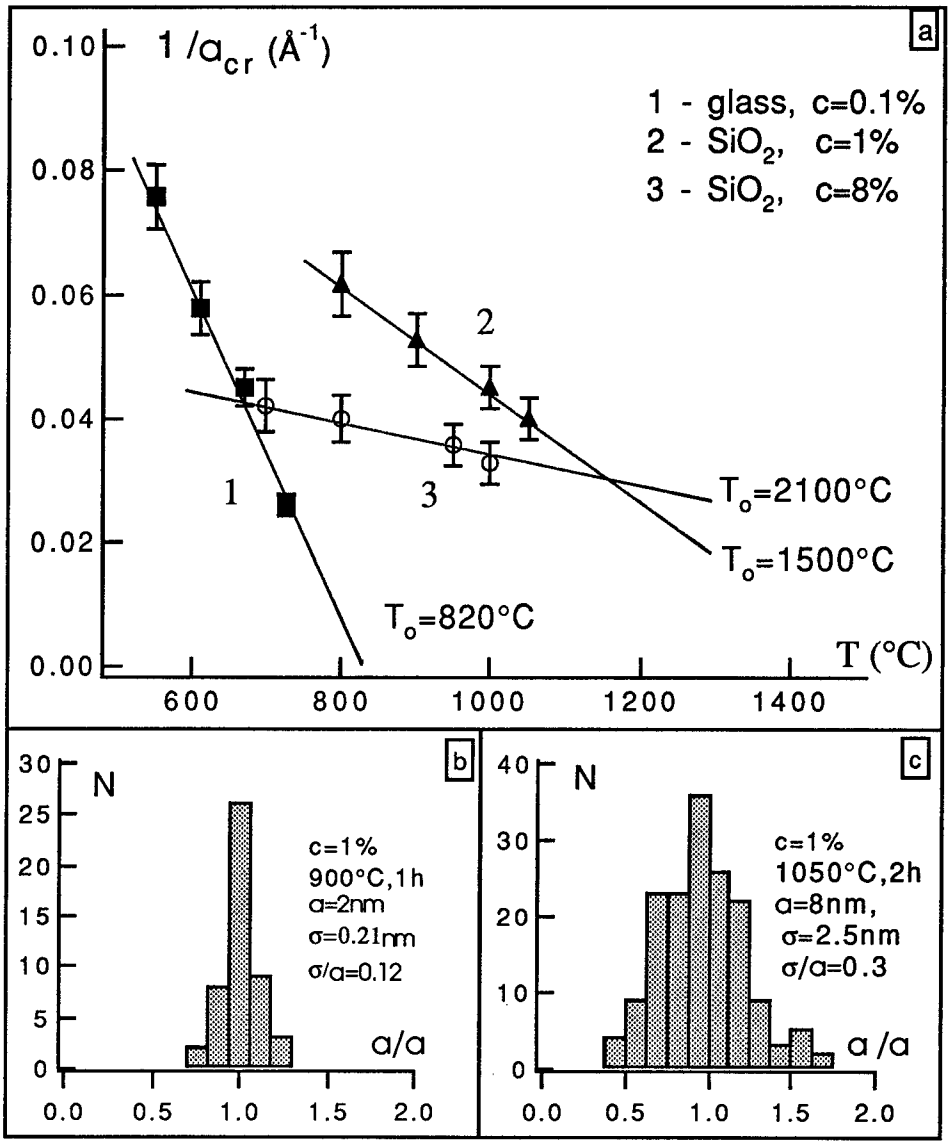

FIGURE 2 (a) – Dependence of critical radius of CdS nucleation in multicomponent glass matrices (1) and SiO_2 thin films (2.3) on annealing temperature; (b) and (c) – size distribution functions of nanocrystals grown in SiO_2 film at nucleation –(b) and second –(c) stages of phase decomposition process (size distributions are normalised to mean radius).

The nucleation process is accompanied by decreasing of the solution oversaturation and this initiates the second stage of the growth process. Kinetics of the particles growth at the expense of solved matter can be described by the following expression:[5]

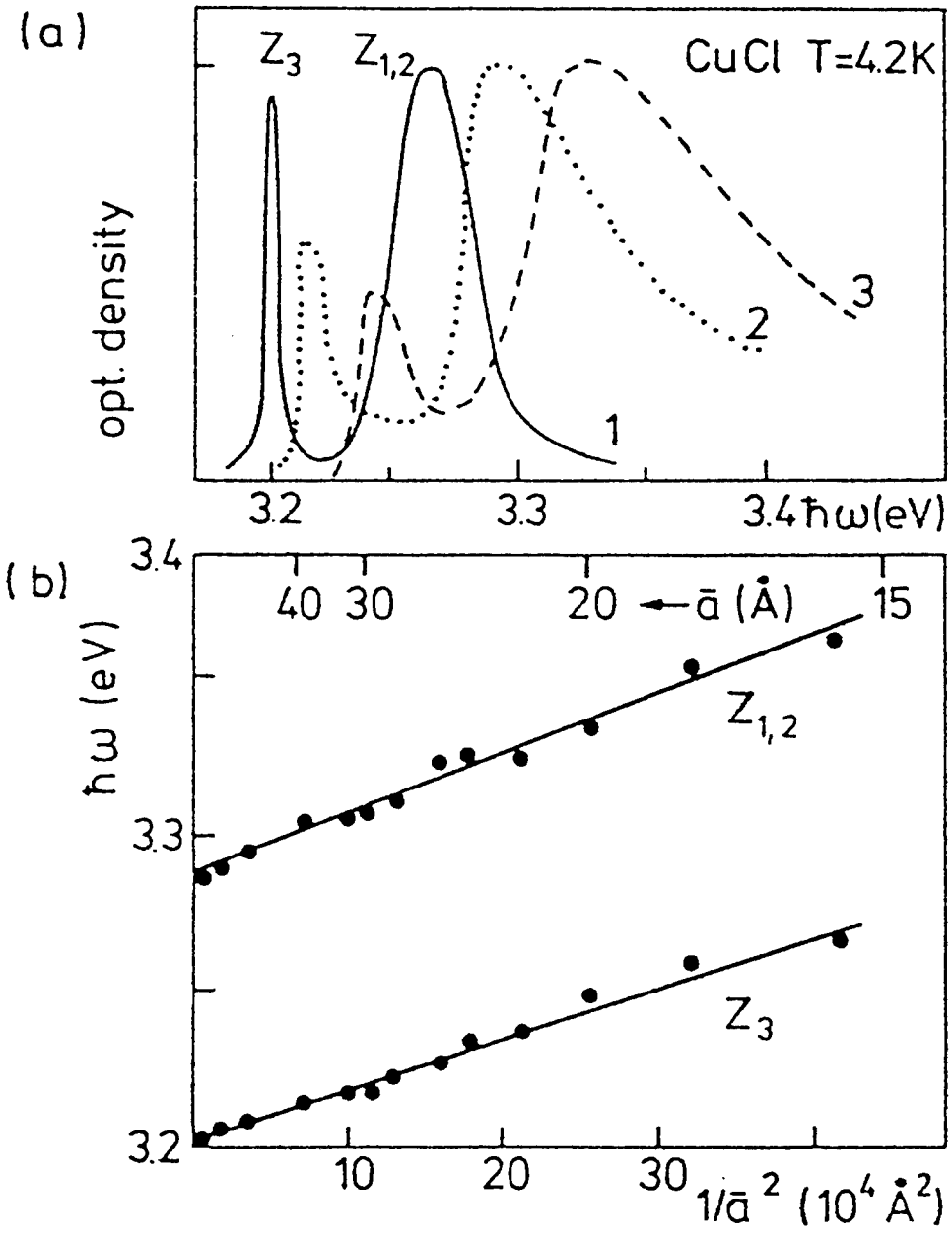

FIGURE 3 (a) – Low temperature (4.2 K) absorption spectra of CuCl nanocrystals with different mean radius: a = 310 Å-(1,) a = 29 Å-(2), a = 20 Å-(3); (b) – comparison of experimental size dependence of spectral position of excitonic lines (shown by points) with theoretical dependencies.

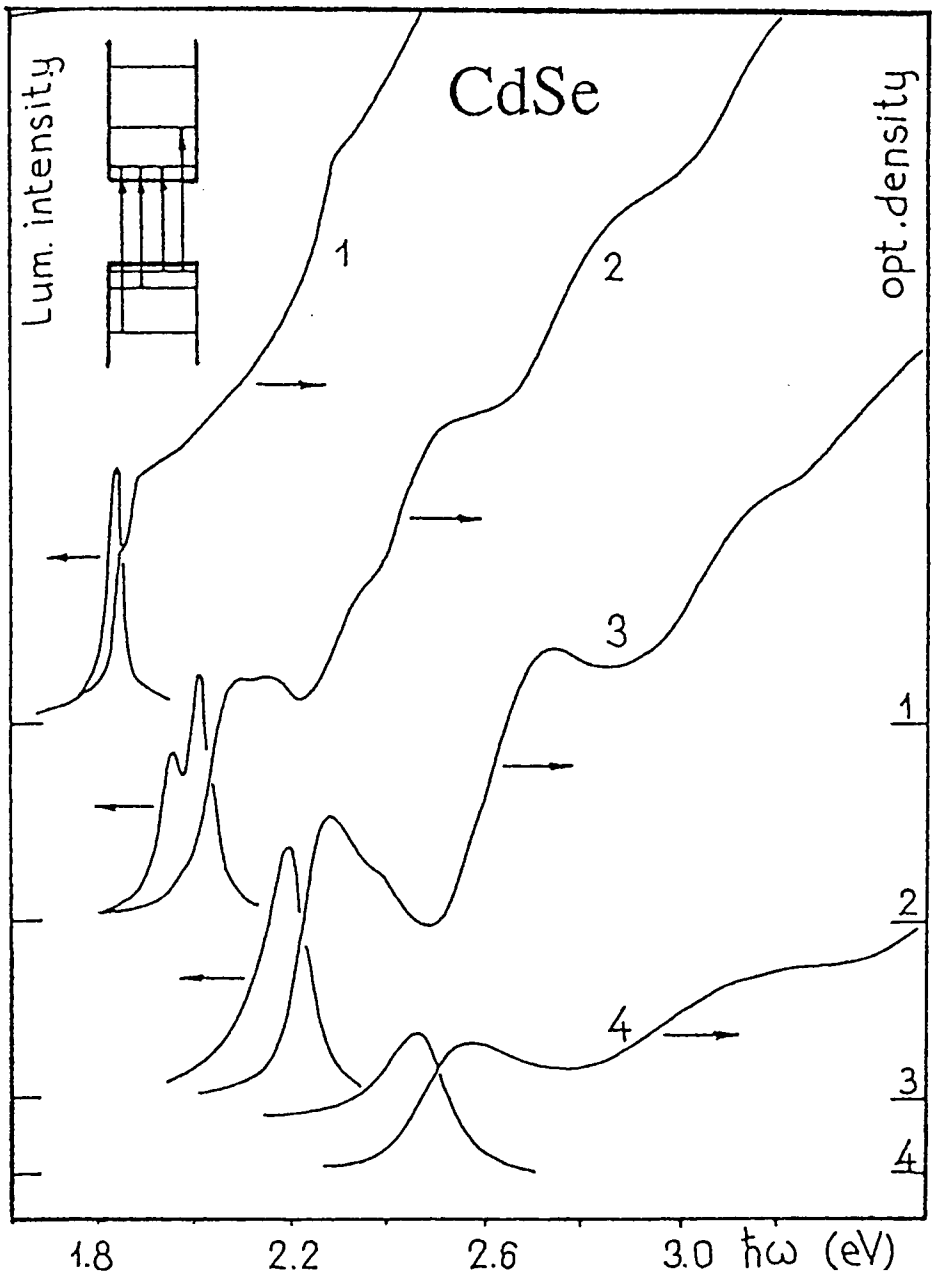

FIGURE 4 Low temperature (4.2 K) absorption spectra and luminescence spectra obtained under pulsed laser excitation of CdSe nanocrystals with mean radius a = 250 Å – (1), 38 Å – (2), 26 Å – (3) and 21 Å – (4).

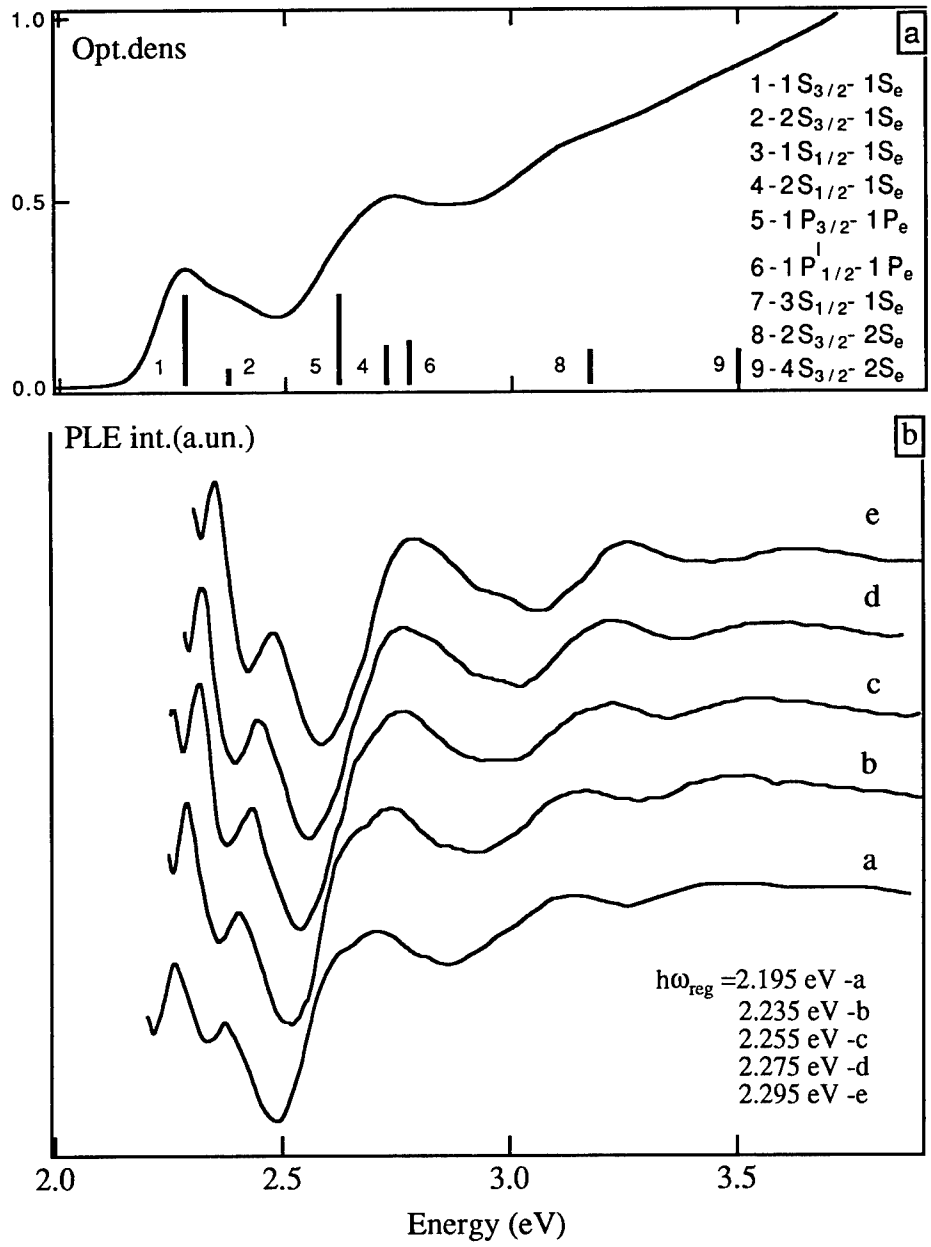

FIGURE 5 (a) – Absorption spectrum of CdSe nanocrystals with a = 26 Å. Vertical bars show calculated energies and relative intensities of electron-hole transitions (the assignment of the transitions is the same as in [11]); (b) – PLE spectra at various energies of luminescence registration obtained for the sample.

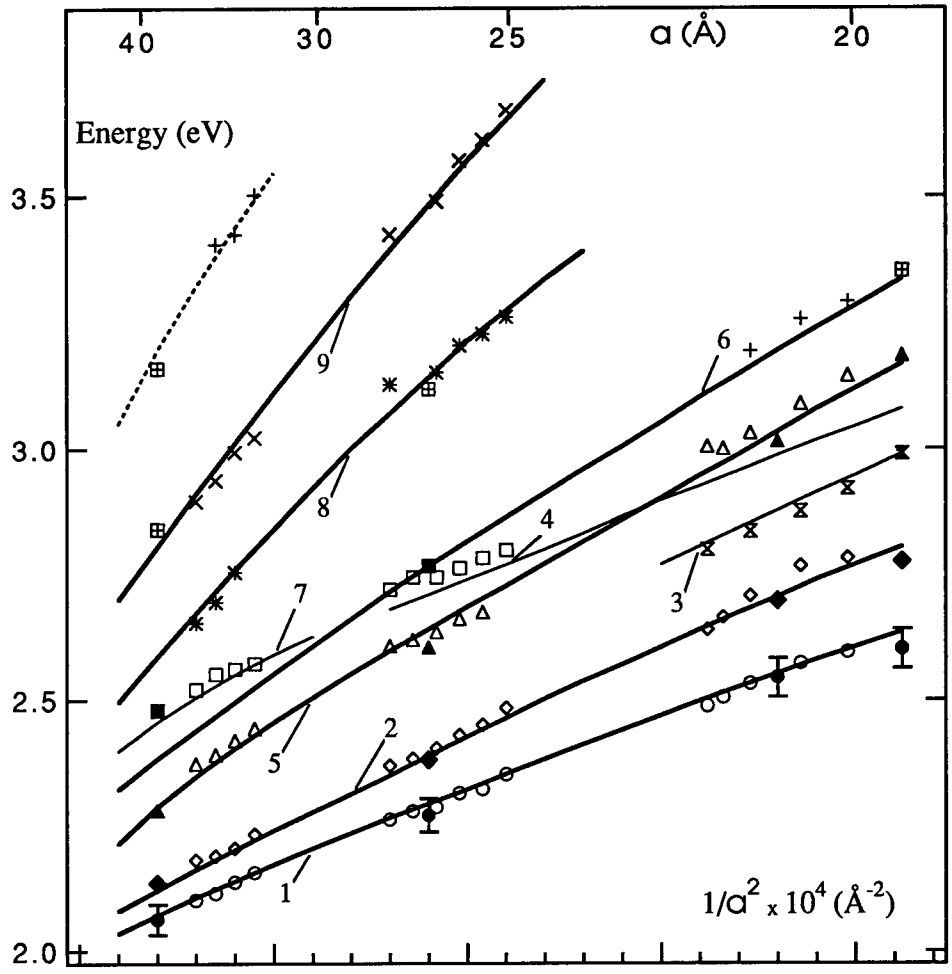

FIGURE 6 Size dependence of energy of optical transitions between electron and hole quantum levels in CdSe nanocrystals. Filled marks show energies obtained from second derivative of absorption spectra for samples with mean radius a = 38, 26, 21 and 19 Å; empty marks show the energies obtained from PLE spectra. Theoretical dependencies[11] are shown by solid lines for transitions with significant strength and by thin lines for transitions with the strength drastically increasing or decreasing within of interval of investigated sizes. Dot line show the dependence for high energy transition not calculated in.[11]

$$a = (2(c_o - c_e)/(c_p - c_e))^{1/2} \cdot (D\tau)^{1/2} \quad (2)$$

where: a is a mean radius of the particles, τ is a duration of annealing process, c_o is initial concentration of semiconductor phase, c_e is equilibrium concentration and $D = D_o\exp(\Delta E/kT)$ is the diffusion coefficient.

The following expression for the kinetics of the particles growth at recondensation

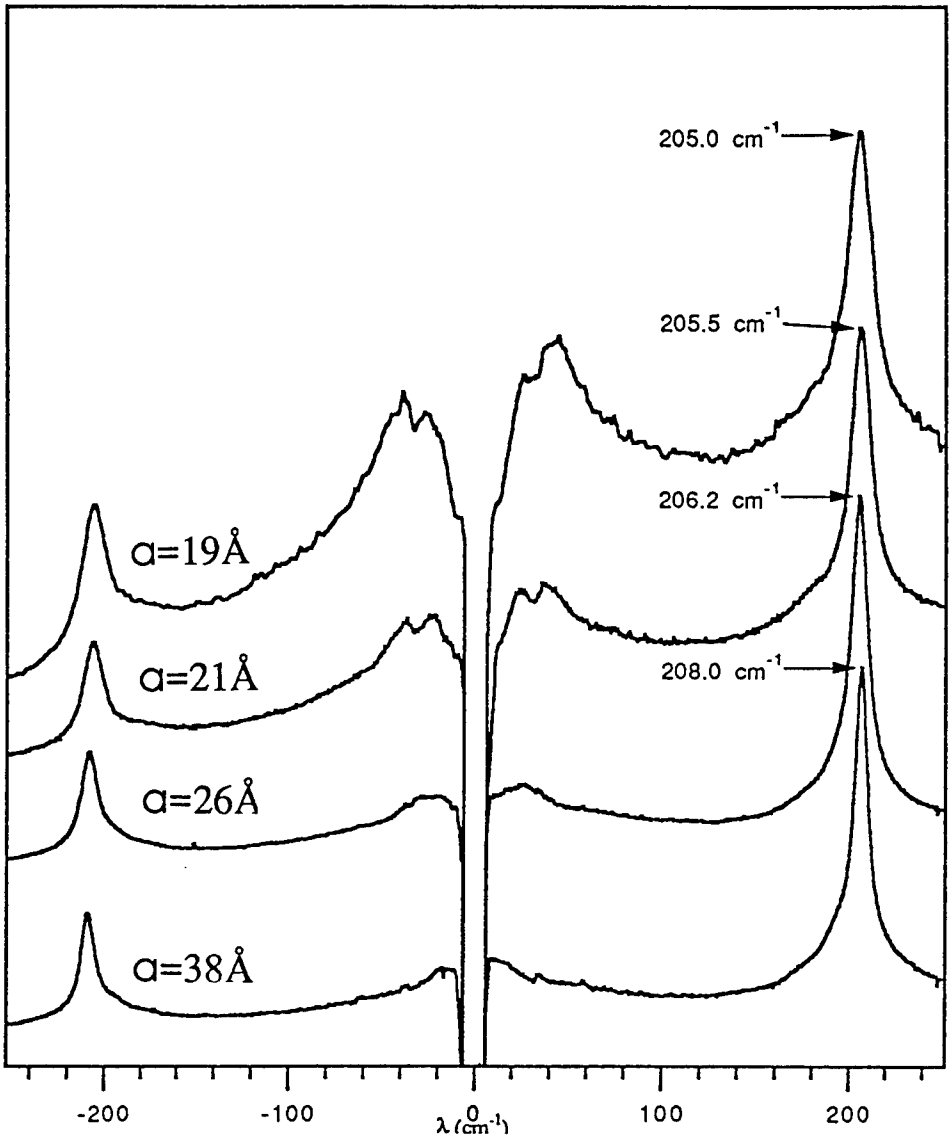

FIGURE 7 Raman scattering spectra from CdSe nanocrystals of various size at room temperature. Frequencies of LO phonons averaged over Stokes and anti-Stokes components are shown.

stage of phase decomposition process was obtained by Lifshits and Slesov:[6]

$$a = (4\sigma/9)^{1/3} \cdot (D\tau)^{1/3} \tag{3}$$

Experimental dependence of mean radius of the particles as a function of duration of

annealing at various temperatures are shown in Figure 1 for the case of CdS-doped multicomponent oxide glass. The mean radius of the particles was measured by small angle X-ray scattering.[7] The three stages of diffusion controlled phase decomposition process are seen in the figure. Plateau at the beginning of the process correspond to the nucleation stage. One can see that critical radius of nuclei increases with increasing of annealing temperature. The nucleation stage is followed by growth of the particles at the expense of solved matter. It is seen from the figure that growth of the particles follow to the square root dependence of the mean radius on duration of annealing. The recondensation stage which is characterised by cubic root dependence of mean size on the annealing duration can be seen in the figure at highest temperatures of annealing.

These data show that the growth of the particles in a course of diffusion controlled phase decomposition of oversaturated solid solution makes it possible to vary their size in a controlled manner starting from a few manometers by choosing of temperature or/and duration of heat treatment. Each stages of the phase decomposition process is characterised by own kinetics of particles growth and by own size distribution function of them. Therefore it is interesting to know which stage of phase decomposition process is characterised by narrowest size distribution function of the particles. As it was shown theoretically[6] and experimentally,[8] growth of particles at recondensation stage is characterised by steady-state size distribution function with a half width about 30% of mean radius of the particles.

Detailed studies of nanocrystals growth at first and second stages of phase decomposition process have been performed recently for the case of CdS-doped SiO_2 thin films deposited on quartz or/and silicon substrates with the use of high frequency co-sputtering technique.[9] Experimental dependencies of critical radius of nuclei on annealing temperature are shown in Figure 2a for multicomponent oxide glass sample with concentration of semiconductor phase 0.1% and for samples with concentration 1% and 8% in SiO_2 matrix. Solid lines are plotted in accordance with equation (1). One can see that even at nucleation stage of phase decomposition process it is possible to vary the mean size of nanocrystals in a controlled manner by choosing of annealing temperature.

The comparison of size distribution functions of CdS nanocrystals grown in SiO_2 film, measured by HRTEM method for the particles grown at first and second stages of phase decomposition process is shown in Figure 2b, c. Half width of the size distribution function obtained for the second stage (Figure 2c) is about 30% of a mean radius and it is similar to the one at recondensation stage. At the same time, the half width of size distribution function for particles grown at nucleation stage is significantly narrower. This shows that the nucleation stage of diffusion controlled phase decomposition process is more preferable from viewpoint of the width of size distribution function.

2 ENERGY SPECTRUM OF ELECTRONIC EXCITATIONS

The energy spectrum of electronic excitations in semiconductor nanocrystal is determined by the quantum size effect as well as by Coulomb interaction of electron and hole in the nanocrystal. Both the energies depend on the size of nanocrystals. Therefore, two different situations, depending on relationship of nanocrystal radius a and bulk exciton Bohr radius R_{ex}, should be regarded: so called 'weak' confinement regime, when $a \gg R_{ex}$, and regime of 'strong' confinement when $a \ll R_{ex}$.

An example of size dependence of low temperature absorption spectra ($T = 4.2$ K) for the 'weak' confinement regime is shown in Figure 3 for the CuCl nanocrystals (bulk exciton Bohr radius is about 7 Å). The nanocrystals were grown in a matrices of

multicomponent oxide glass in a course of phase decomposition process.[7] As it is seen from Figure 3a, the absorption spectra are of excitonic nature down to the smallest investigated sizes a $\sim$ 15 Å. The decrease of nanocrystal size is accompanied by a blue shift of both excitonic lines due to quantum confinement of exciton as a whole. For the exciton originating from the upper, non degenerate valence subband (Z_3 line) the size dependence of the exciton line spectral position can be described by the following expression:

$$h\varpi_{Z_3} = E_g - E_{ex} + 0.67h^2\pi^2/2M_s a^2 \quad (5)$$

were: E_g, E_{ex} and M_s are forbidden gap width, exciton binding energy and exciton translation mass in bulk CuCl. Numerical coefficient takes into account shift of optical lines due to Lifhitz-Slesov size distribution function.[8] Taking into account the influence of the size distribution function on determination of mean radius of nanocrystals from low angle X-ray scattering data,[10] the experimental slope of size dependence of Z_3 line spectral position can be described with the use of well known bulk value of Z_3 exciton mass $M_s = (2.3+/-0.2)m_o$, were m_o is free electron mass. These shows that energy spectrum of confined exciton can be described in frame of effective mass approximation with the use of simple model of quasiparticle with nondegenerate parabolic band down to smallest investigated sizes of the nanocrystals. Size dependence of Z_{12} exciton spectral position can be described also in frame of effective mass approximation with taking into account of real structure of the spin-orbit splitted subband.[8]

CdSe, for which bulk exciton Bohr radius is R_{ex} = 56 Å, is a good example of a 'strong' confinement regime. Low temperature absorption spectra and luminescence spectra at pulsed laser excitation of CdSe-doped glass samples with various mean radius of the nanocrystals are shown in Figure 4. It is seen that the decrease of nanocrystals size leads to significant blue shift of the both absorption edge and interband luminescence. The decrease of nanocrystal size leads also to appearance of a smoothed structure in the absorption spectra, which originates from optical transitions between quantum levels of electron in conduction band and hole in valence band (see inset in the figure). Theory of electron-hole pairs energy spectrum quantization in 'strong' confinement regime, which takes into account a nonparabolicity of electronic band and real structure of valence band in CdSe, has been developed in[11,12] to describe the experimental results. Figure 5a shows absorption spectrum of CdSe-doped glass sample with mean radius of nanocrystals a = 26 Å. Energies and relative intensities of optical transitions between quantum levels of electron and hole calculated for the sample, are shown in Figure 5a by vertical bars. Notation of the transitions is the same as in.[12]

The structure of electron-hole optical transitions is smoothed in the absorption spectra by inhomogeneous broadening coursed by size distribution of the nanocrystals. Methods of size selective spectroscopy makes it possible to reveal this structure. Figure 5b shows set of Photoluminescence Excitation (PLE) spectra obtained for the same sample at various energies of luminescence registration. It is seen that the PLE spectra demonstrate well resolved structure of electron-hole optical transitions at registration of the luminescence from within of inhomogeneously broadened near band-gap luminescence. More of this, a spectral shift of the luminescence registration leads to the spectral shift of the PLE structure. This shows that PLE technique makes it possible to investigate size dependence of energies of the optical transitions from within of size distribution function of each sample. Figure 6 summarise the size dependence of energies of electron-hole optical transitions in CdSe nanocrystals. Filled marks show energies of the transitions obtained from second derivative of absorption spectra for the samples with various mean radius of the nanocrystals, empty marks show the energies obtained from PLE spectra for the same

samples. As it was shown in,[12] relative intensities of the transitions depend strongly on nanocrystal size. Thick solid lines show theoretical dependencies for transitions with significant oscillator strength within of interval of investigated sizes. Thin lines show the dependencies for transitions with oscillator strength drastically depending on size. The theoretical dependencies were obtained at the following set of energy-band parameters:[12] $E_g = 1.84$ eV, $\Delta_{so} = 0.42$ eV, $\gamma_1 = 2.1$, $\gamma = 0.55$, $E_p = 17.5$ eV and $f = -0.42$. As it is seen from Figure 6, a good agreement of the theoretical dependencies with experimental data can be achieved in frame of effective mass approximation for 'strong' confinement regime also, if real band structure of semiconductor material is taken into account.

3 ENERGY SPECTRUM OF VIBRONIC EXCITATIONS

The progress in the studies of electronic excitation spectra has opened the door for investigation of energy spectrum of phonons in semiconductor quantum dot structures. Figure 7 shows spectra of resonant Raman scattering obtained at $T = 300$ K from CdSe-doped glass samples with different mean radius of the nanocrystals. The spectra were measured at excitation by different lines of Ar and Kr-ion lasers in the vicinity of absorption tail for each sample. The frequencies of LO Raman lines obtained from the averaging over Stokes and anti-Stokes components are shown in the figure for each sample. It is seen that the decreasing of the nanocrystal size leads to decreasing of LO phonon frequency in accordance to negative dispersion of LO phonon in CdSe. One can see also that decreasing of nanocrystal size is accompanied by significant increasing of scattering intensity in a low-frequency region. This effect is due to the increasing of strength of electron-hole pairs coupling with acoustic modes of the nanocrystals at the decreasing of their size. One can see also that decreasing of nanocrystal size leads to significant increasing of acoustic modes frequencies in accordance to positive dispersion of acoustic phonons. These data show that energy spectra of acoustic and optical phonons in the nanocrystals are quantized. Size dependence of frequencies of the phonons can be described in frame of a model of size quantization of phonon energy spectrum in semiconductor quantum dot structures.

4 CONCLUSION

The results reviewed show that developed technologies make it possible to grow nanocrystals of various semiconductor compounds in bulk and thin film matrices of wide gap materials. These techniques permit to vary in a controlled manner mean size of nanocrystals and their concentration in a matrices. Energy spectra of electronic and vibronic excitations in the semiconductor quantum dot structures are governed by fundamental quantum size effect. Therefore, optical properties of these composite materials can be varied by controllable variation of size of nanocrystals in a course of their growth. This makes them promising for various practical applications in the fields of optoelectronics and integrated optics.

REFERENCES

1. A. I. Ekimov and A. A. Onushchenko, *Sov. JETP Lett.* **34**, 345 (1981).
2. Al. L. Efros and A. L. Efros, *Sov. Phys. Semicond.* **16**, 772 (1982).
3. L. E. Brus, *J. Chem. Phys*, **80**, 4403 (1984).

4. A. D. Yoffe, *Adv. Phys.* **42**, 173 (1993).
5. R. Kampmann and R. Wagner, in '*Decomposition of Alloys*' (Oxford, 1983).
6. I. M. Lifshits and V. V. Slesov, *Sov. JETP*, **35**, 479 (1958).
7. V. V. Golubkov, A. I. Ekimov, A. A. Onushchenko and V. A. Tsehomskii, *Sov. Phys. and Chem. of Glass*, **7**, 397 (1981).
8. A. I. Ekimov, A. A. Onushchenko, A. G. Pluhin and Al. L. Efros, *Sov. JETP*, **61**, 891 (1985).
9. S. A. Gurevich, A. I. Ekimov, I. A. Kudriavtsev, O. G. Lublinskaya, A. V. Osinskii, A. S. Usikov, N. N. Faleev, Semicond. **28**, 486 (1994).
10. A. I. Ekimov, Al. L. Efros, Proc. of XII winter school on Phys. of Sem. Leningrad, USSR, 66 (1985).
11. G. B. Grigorian, E. M. Kazaryan, Al. Efros, T. V. Yaseva, *Sov. Phys. Sol. St.* **32**, 1031 (1990).
12. A. I. Ekimov, F. Hache, M. C. Shanne-Klein, D. Ricard and C. Flytzanis, I. A. Kudriavtsev, T. V. Yaseva, A. V. Rodina, Al. L. Efros, JOSA B, **10**, 101 (1993).

Radiation Effects and Defects in Solids, 1995, Vol. 134, pp. 23–29
Reprints available directly from the publisher
Photocopying permitted by license only

© 1995 OPA (Overseas Publishers Association)
Amsterdam B.V. Published under license by
Gordon and Breach Science Publishers SA
Printed in Malaysia

SCINTILLATORS AND APPLICATIONS: CERIUM-DOPED MATERIALS

M. J. WEBER, M. BLISS, R. A. CRAIG, and D. S. SUNBERG

Pacific Northwest Laboratory, Richland, WA 99352 USA

Scintillator materials are widely used for the detection of ionizing radiation in a variety of applications including high energy and nuclear physics, astrophysics, geophysical exploration, medical imaging, security inspection, and industry. Research involving the use of photoluminescence, radioluminescence, thermoluminescence, and synchrotron radiation is underway to further our fundamental understanding of the factors affecting scintillator performance and to discover improved materials. The importance of defects and their effects on energy transfer and overall scintillation efficiency are illustrated by considering recent results for cerium-activated crystals and glasses.

Key words: scintillation, efficiency, cerium, crystal, glass, thermoluminescence.

1 INTRODUCTION

Since the first use of scintillator materials about one century ago, many materials have been discovered and used in the applications noted above. Although most of the essential physics of the scintillation process has been known and understood for several decades,[1] the need for improved materials in many of these applications has created a renaissance in research and development of scintillator materials. This interest and activity is well documented in the proceedings of two recent international conferences devoted to scintillator materials.[2,3] These review the requirements for scintillator materials in various applications, the characterization and properties of scintillators, and the status of our understanding of the factors affecting scintillator performance.

Today we have a large number of known and well-characterized scintillator materials including crystals, glasses, plastics, and liquids.[4] No single material is superior for all applications; in most cases improvements in one or more properties are desirable. A number of the properties that one must keep in mind in selecting a material for a specific application are given in Figure 1. The material may be in the form of a bulk crystal or glass, fiber, sheet, or liquid. The photodetector to be used will depend on the emission wavelength and light yield. The decay time is important for fast timing and high repetition rate applications; the absence of afterglow is important in medical imaging. Stability includes several factors that must be known or controlled, for example, environmental or chemical durability, ruggedness and mechanical shock resistant, and variation of light output with temperature and time. Radiation damage is particularly important in high radiation environments such as in detectors for use with proposed high luminosity colliders. Whereas for detecting very energetic particles light yield may not be too important, for applications where the particle energy is smaller and fixed, e.g., in positron emission tomography, increased light yield is important for improving spatial resolution. Energy resolution is also dependent on light yield. The price of raw materials, preparation of the scintillator material, and fabrication into the desired size and shape all enter into the final cost. Cost is a major consideration for proposed detectors for high energy physics experiments which may incorporate thousands of crystals with total crystal volumes measured in cubic meters. These and other factors not included in Figure 1, such as high density for good stopping power, differ in their relative importance in selecting materials

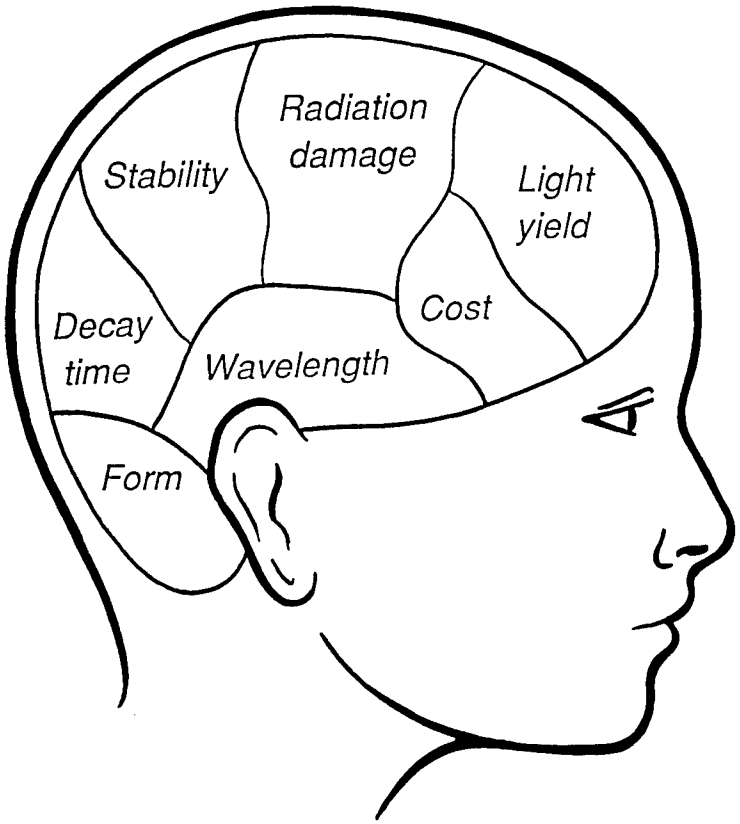

FIGURE 1 Properties of scintillator materials to be considered when selecting materials for different applications.

for specific applications. Here we examine briefly the question of improving the scintillation light output. Can scintillators be made more efficient and what are the factors limiting efficiency?

2 SCINTILLATION PROCESS AND EFFICIENCY

The basic processes in scintillation may be divided into three stages:[5] (i) the absorption of the incident radiation or particle by the host and conversion of the energy into thermalized electrons and holes, (ii) transfer of some fraction of the electron and hole excitation to luminescence centers, and (iii) the luminescence process. The quantum efficiency is given by

$$\eta = \beta \bullet S \bullet Q, \tag{1}$$

where β is the conversion efficiency for creating electron-hole pairs, S is the transfer efficiency, and Q is the radiative efficiency of the luminescence centers. Because the

incident energy E_{in} of a particle will usually be very much bigger than the band gap E_g of the material, the number of electron-hole pairs and of resultant scintillation photons may be very large, thus yielding huge quantum efficiencies. In terms of energy efficiency, however, the performance of scintillators is less impressive. For a scintillation photon of energy E_s, this efficiency is given by

$$\eta(E_s/E_{in}) \sim (E_{in}/\alpha E_g) \bullet S \bullet Q \bullet (E_s/E_{in}) = (E_s/\alpha E_g)S \bullet Q \qquad (2)$$

In Eq. (2) it is assumed that it takes on the average an energy α times the band gap to create a thermalized electron-hole pair. Various treatments of polaron and plasmon models and electron-phonon scattering losses show that α is typically about 2–3 for semiconductor and insulator materials (see Ref. 6 for an excellent review of this problem). Thus from Eq. (2), for a material having transfer and luminescence efficiencies of unity and an emission energy approaching that of the band gap, the energy efficiency should be $\sim 25\%$, which is about what has been obtained for the best phosphors. For one of the best scintillators, NaI(Tl), E_s is equal to approximately $E_g/2$ and the reported efficiency is 12%, therefore S and Q must again be near unity. Therefore scintillator materials already exist with near maximum achievable efficiency and only small improvements in their light yield are possible.

3 CERIUM SCINTILLATOR MATERIALS

Cerium-activated scintillator materials have been known and used for several decades[4] but have received renewed interest because of the favorable spectroscopic properties of Ce^{3+} and the ability to incorporate Ce^{3+} into many different host materials. Among the attractive properties of Ce^{3+} are (1) its luminescence, which occurs in the visible-near ultraviolet region and is well matched to the spectral response of high efficiency photodetectors, (2) the emission involves an allowed transition and thus is fast for good time resolution, (3) the luminescence intensity and decay time are stable and insensitive to temperature for many hosts at room temperatures, (4) there are no long-lived radioactive isotopes, and (5) Ce is the least rare of the rare earths. The density, dominant decay time, and relative light output of a number of Ce^{3+} activated materials are given in Table I. There is a large variation in Ce^{3+} scintillator efficiencies, ranging from values approaching that of NaI(Tl) for Lu_2SiO_5 to values orders of magnitude smaller for some glasses. The materials all exhibit intense photoluminescence (except for PbF_2) with luminescence lifetimes characteristic of radiative decay, thus their radiative quantum efficiencies Q are high. The conversion efficiency β is not expected to differ greatly for crystals and glasses of different chemical compositions. Therefore the large variation in Ce^{3+} scintillation efficiency is due to differences in the transfer efficiency S. Electrons and holes created in the conduction and valence bands may combine radiatively or nonradiatively, be trapped by various defects, form mobile or trapped excitons, or migrate to the vicinity of a Ce^{3+} ion and excite it. The relative probabilities of these processes enter into the transfer efficiency and are material dependent.

Recently, excitation spectra recorded with synchrotron radiation have been used to examine the relative differences in light output resulting from direct excitation into the 5d bands of Ce^{3+} and from excitation of valence band and core electrons. Large differences in excitation spectra associated with the transfer process are observed[7] for the two extreme cases in Table I—crystalline lutetium orthosilicate and glasses.

Table I
Comparison of properties of cerium scintillator materials (from Refs. 2 and 5)

Material	Density (g/cm^3)	Decay time (ns)	Relative light yield
Reference			
NaI(Tl)	3.67	230	100
Crystals			
Lu_2SiO_5(LSO)	7.4	$\sim$ 40	75
Gd_2SiO_5(GSO)	6.71	30–60	20–25
$LuPO_4$	6.53	24	33
$YAlO_3$	5.55	30	40
CeF_3	6.16	$\sim$ 5, 30	5–9
$CsGd_2F_7$	5.5	40	16
PbF_2	8.24		$\sim$ 0
Glasses			
silicate (GS1)	2.5–2.7	$\sim$ 60	7–9
phosphate	$\sim$ 2.6	$\sim$ 30	< 1
fluoride (HfF_4)	$\sim$ 6-7	10, 30	< 1

3.1 *Lutetium Orthosilicate*

The scintillation efficiency of lutetium orthosilicate (LSO) is the highest reported for any Ce^{3+} activated material and nearly equal to that of NaI(Tl). Since $E_s \sim 1/(2E_g)$, this efficiency suggests high values for both S and Q. The scintillation output of LSO has, however, been found to vary significantly with growth and annealing conditions. Measurements of light output for a number of different samples have shown a convincing anti-correlation between integrated thermoluminescence output and scintillation light output over a range of several orders of magnitude.[8] Thus defects and their effect on transfer efficiency can account for the large variation in scintillation found for different LSO crystals. The existence of very deep traps is also evident from the report[9] of phosphorescence lasting for >2000 s.

The best LSO crystals are grown in an atmosphere containing oxygen. Annealing the crystals in a reducing atmosphere decreases the scintillation light output whereas annealing in an O_2 atmosphere increases the output and introduces an absorption band attributed to Ce^{4+}.[8] Thermally-induced luminescence experiments show the existence of five peaks in the glow curve between 300 and 650 K.[9] Although the origin and nature of defects associated with these charge traps were not identified, oxygen vacancies are one possibility. Lutetium orthosilicate has a complex crystal structure with two inequivalent sites for Ce^{3+} that contribute about equally to the scintillation at low temperatures[10] and with five different oxygen sites. The substitution of Ce^{3+} at a Lu^{3+} site involves a large mismatch of ionic radii, 18 pm (the mismatch for Ce^{4+} is only 1 pm). Also, whereas the two Ce sites in Ce_2SiO_5 have 8- and 9-fold oxygen coordination, the two Lu^{3+} sites in LSO have 6- and 7-fold oxygen coordination. Thus preparation of Ce-doped LSO in an O_2 atmosphere provides oxygen to satisfy the coordination needs of Ce^{3+}, reduces the number of oxygen vacancies, and changes the oxidation state of some ions to Ce^{4+}.

3.2 *Silicate Glass*

The best cerium-activated glasses (silicates) have efficiencies of only about 1/10 that of

NaI(Tl) and LSO; other glasses (phosphates, heavy metal fluorides) are reported to have much lower efficiencies.[2] This is not surprising given that glass is a disordered medium and the importance of defects and traps in reducing the transfer efficiency. Defects in glass are defined as deviations from short-range order and may be intrinsic (for example, three-coordinated Si, oxygen vacancies, or interstitial oxygen in the case of SiO_2), broken bonds, or extrinsic defects such as impurities. Many different thermally-induced defects are also possible.

Several years ago Spowart,[11] in an investigation of Ce^{3+}-activated Li-Mg-Al silicate glasses, reported two broad peaks in thermoluminescence curves, one below and one above room temperature. The scintillation efficiency and thermoluminescence glow curves varied with glass composition but no detailed study was made. Recently we have begun a systematic investigation of the effects of composition and microstructure on the scintillation efficiency of Ce-doped silicate glasses.[12] Table II shows a large systematic

Table II
Scintillation efficiency of alkaline-earth glasses (2 μs integration time).[12]

Glass composition (mol. %)	Light output (%NaI)
$64.4SiO_2-20Li_2O-15MgO-0.6Ce_2O_3$	8.14
$64.4SiO_2-20Li_2O-15CaO-0.6Ce_2O_3$	6.22
$64.4SiO_2-20Li_2O-15SrO-0.6Ce_2O_3$	5.20
$64.4SiO_2-20Li_2O-15BaO-0.6Ce_2O_3$	3.18

variation in scintilllation efficiency found by varying the alkaline earth component in otherwise identical glasses. Measurements of the absorption and emission spectra and decay curves for these glasses show only small changes, as expected for such small ompositional changes. That the change in scintillation efficiency is related to defects and their effect on the transfer efficiency is demonstrated by the low-temperture thermoluminescence curves in Figure 2 for the two extreme materials in Table II. The glow curves were obtained using annealed samples of a uniform size of $5 \times 5 \times 1$ mm, irradiating them with 325-nm light from a He-Cd laser while the samples were held at low temperatures, and then heated at a rate of 0.9°C/s. The larger integrated intensity and more pronounced high temperature peak for the Ba containing glass is qualitatively consistent with its reduced scintillation efficiency in Table II.

Although the principal decay of Ce^{3+} scintillation from the silicate glasses in Table II is $\sim$ 50 ns characteristic of radiative 5d–4f transitions, the overall decay is non-exponential with a long tail extending to tens of μs. Measurements of a Li-Mg-Al silicate glass (GS1) by Angelini *et al.*[13] were fitted with decay components having characteristic times approaching 1 ms. This indicated that much of the excitation in glass was stored in deep traps. They also showed that only about one-half of the light was emitting in the first microsecond following excitation. Thus when comparing the scintillation light output of materials, it is important to note the integration time used.

The small scintillation efficiency of Ce^{3+} glasses is due to the large number of defects that trap electrons and holes and prevent or delay the excitation of the activator. The number and type of traps vary with the glass composition and structure and the thermal treatment. The lower efficiency of fluoride glasses is probably associated with the more ionic, weaker bonding in these glasses. For silicate glasses we have observed an increase in light following annealing in air. Measurements of the Ce^{3+} L_{III} x-ray absorption near edge structure (XANES) of annealed samples[14] reveal the presence of Ce^{4+}, an effective

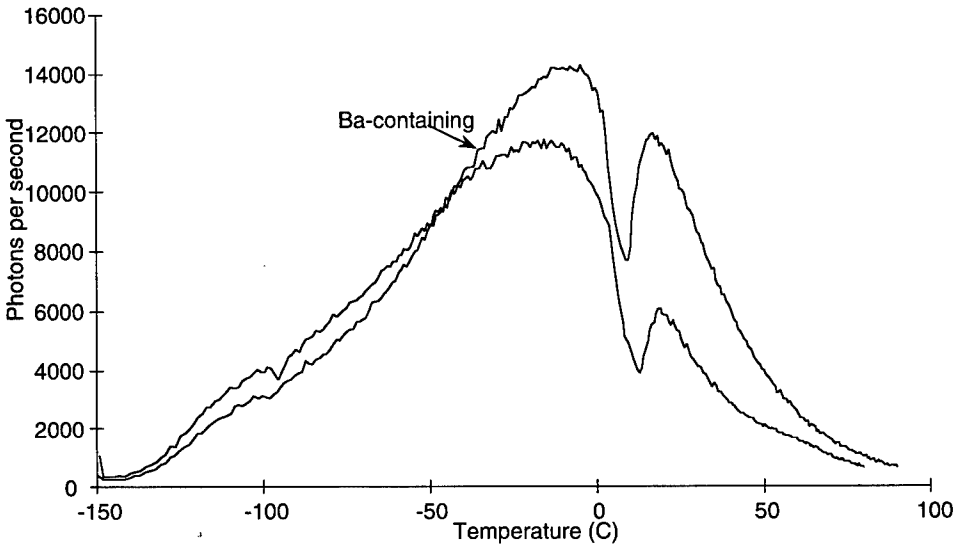

FIGURE 2 Thermoluminescence glow curves for Mg-containing and Ba-containing Ce^{3+}-doped silicate glasses in Table II.

electron trap. Further studies of the scintillation yield and thermoluminescence of glasses are planned.

4 CONCLUDING COMMENTS

Defects play a dominant role in determining the scintillation efficiency of many Ce^{3+} activated materials. This may be particularly important for disordered materials. The overall scintillation process can best be investigated and understood by a combination of photoluminescence, radioluminescence and thermo-luminescence measurements, excitation spectra using synchrotron radiation, and theoretical calculations of electronic structure of the host, defects, and luminescence centers. These should guide the discovery of new scintillator materials and improve the ability to tailor their chemical composition and structure for specific applications.

ACKNOWLEDGEMENTS

We thank W. C. Richey for his excellent help in developing the thermo-luminescence apparatus and C. L. Melcher and J. S. Schweitzer for valuable discussions of the properties of LSO. This work was supported in part by the Pacific Northwest Laboratory's Laboratory Directed Research and Development Program. Pacific Northwest Laboratory is operated by Battelle Memorial Institute for the U.S. Department of Energy under contract DE-AC06-76RLO 1830.

REFERENCES

1. See, for example, G. F. Garlick, in *Luminescence of Inorganic Solids*, ed. P. Goldberg (Academic Press, New York, 1966), and G. W. Ludwig and J. D. Kingsley, *J. Electrochem*, Soc. **117**, 348 and 353 (1970).

2. *Heavy Scintillators*, eds. F. De Notoristefani, P. Lecoq and M. Schneegans (Editions Frontieres, Gif-sur-Yvette, 1993).
3. *Scintillator and Phosphor Materials*, eds. M. J. Weber, P. Lecoq, R. C. Ruchti, C. Woody, W. M. Yen and R. Y. Zhu, *Materials Research Society Symposium Proceedings* Vol. 348 (1994).
4. G. F. Knoll, *Radiation Detection and Measurement* (John Wiley & Sons, New York, 1989), 2nd edition.
5. See A. Lempicki, A. J. Wojtowicz and E. Berman, *Nucl. Instr. and Meth.* **A333**, 304 (1993) and G. Blasse, *J. Lumin*, **60 & 61**, 930 (1994).
6. P. A. Rodnyi, P. Dorenbos and C. W. E. van Eijk, in *Materials Research Society Symposium Proceedings* Vol. 348, 379 (1994) and references cited therein.
7. C. Pedrini, A. N. Belsky, A. N. Vasil'ev, D. Bouttet, B. Moine, P. Martin, and M. J. Weber, in *Materials Research Society Symposium Proceedings* Vol. 348, 225 (1994).
8. R. Vissor, C. L. Melcher, J. S. Schweitzer, H. Suzuki and T. A. Tombrello, *IEEE Trans. Nucl. Sci.* **42** (in press).
9. P. Dorenbos, C. W. E. van Eijk, A. J. J. Bos and C. L. Melcher, *J. Lumin.* **60 & 61**, 979 (1994).
10. H. Suzuki, T. A. Tombrello, C. L. Melcher and J. S. Schweitzer, *IEEE Trans. Nucl. Sci.* **40**, 380 (1993).
11. A. R. Spowart, *J. Phys. C: Solid State Phys.* **12**, 3369 (1979).
12. M. Bliss, R. A. Craig, D. S. Sunberg and M. J. Weber, in *Materials Research Society Symposium Proceedings* Vol. 348, 195 (1994).
13. C. Angelini, W. Beusch. *et al.*, *Nucl. Instr. and Meth.* **A281**, 50 (1989).
14. D. L. Blanchard, D. S. Sumberg, R. A. Craig, M. Bliss and M. J. Weber, *Materials Research Society Symposium Proceeding's* Vol. 375, 241 (1995).'

Radiation Effects and Defects in Solids, 1995, Vol. 134, pp. 31–37
Reprints available directly from the publisher
Photocopying permitted by license only

© 1995 OPA (Overseas Publishers Association)
Amsterdam B.V. Published under license by
Gordon and Breach Science Publishers SA
Printed in Malaysia

THE SOL-GEL METHOD FOR THE SYNTHESIS OF GLASSES, CERAMICS AND HYBRID MATERIALS

M. GUGLIELMI* and P. BARBOUX**

**Dipartimento di Ingegneria Meccanica Universitá di Padova, Via Marzolo 9, 35100 Padova (Italy); **Chimie de la Matiére Condensée, Université Pierre et Marie Curie, 75252 Paris (France)*

(Received July 1, 1994)

The sol-gel method is firstly described taking the TiO_2-SiO_2 system as an example of the chemical procedure and its effect on the structure of the obtained material. The possibilities given by this low temperature synthesis are briefly described giving particular emphasis on so-called hybrid materials. The second part of the paper is devoted to defects in sol-gel materials. Studies on Raman active defects and paramagnetic states are reviewed. A brief discussion on crystallization defects is also presented.

Key words:sol-gel method, glasses, ceramics, hybrid materials, defects.

1 THE SOL-GEL METHOD

Sol-gel is a low temperature method for the synthesis of inorganic networks. Suitable monomeric or oligomeric precursors of the network forming oxides, generally alkoxides, are reacted with water in a common solvent (normally alcohol) and gelation occurs due to hydrolysis and polycondensation reactions. Different precursors can be added to the same solution and a high degree of homogeneity should be obtained upon gelation. However, homogeneity of multicomponent gels depends on the nature of precursors, on their reactivities and on the chemical route followed for the preparation of gels, as explained in 1.1. The gel, which is constituted of interconnected solid and liquid phases, has to be dried to eliminate the liquid and to obtain a porous xerogel. This can be densified by suitable thermal treatment and transformed into a glass or, if crystallization takes place, into a ceramic. Chemical modification of the precursors or mixing with organic moieties allow the preparation of hybrid organic-inorganic materials with interesting tunable properties.

1.1 *Sol-Gel Glasses and Ceramics*

An important and characteristic feature of the sol-gel process is that the glassy state is obtained without reaching temperatures higher than Tg. About fifty among binary, ternary and multicomponent glasses have been obtained by the sol-gel method[1,2] and it has been shown that, in general, gels-derived glasses become indistinguishable from ordinarily melted glasses when they are heated to Tg.[3] At lower temperatures, amorphous glasslike solids are obtained which may have very attractive properties. Differently from melted glasses, these glassy solids have a structure and properties that depend not only on their thermal history, but also on their 'chemical history'. Features like porosity, OH content, skeletal density, homogeneity and the tendency to crystallize, are strongly dependent on the reactants and the chemical path followed for the synthesis.

The low temperature sol-gel process allows to prepare glasses not obtainable from melt. A very interesting example is the preparation of alkaline-earth silicate glasses. Homogeneous glasses of this type are impossible to prepare from the melt because of a stable liquid immiscibility which extends up to very high temperatures, but they were successfully prepared from gels.[4,5]

Ceramics are obtained when crystallization takes place during heat treatment of the gel. Crystallization can be only partial, thus giving glass-ceramic materials. Many different oxide systems have been explored, looking for specific properties[1] (ferroelectricity, piezoelectricity, electrical conductivity, high Tc superconductivity, optical nonlinearity, catalytic properties). The potential capability to control the composition, the amount of dopants, the structure and the microstructure through the chemical synthesis make sol-gel a very interesting method for ceramic processing. Furthermore, the specific feature of starting from liquid solutions allows the production of different types of ceramic products: powders, hollow spheres, fibers, coatings, membranes. Powders with controlled size and shape, good homogeneity, high purity and reactivity can be produced by different sol-gel techniques. This possibility attracts the attention of ceramists,[6,7] but low yields and lengthy processing times are still critical drawbacks. Therefore, this method is mostly used for preparing high added value materials, such as coatings. Ceramic coatings have been produced mainly for electronic applications (for example, conductive, ferroelectric, ferromagnetic, superconducting films), optical applications, chemical protection. Membranes could be produced taking advantage of the high surface area and small size porosity achievable by sol-gel.[8]

In general, compositional defects like residual organics, carbon, OH groups, are introduced by the sol-gel route. These must be taken into account when optical and electronic materials have to be produced. For example, OH groups may generate foaming during the thermal treatment or may affect negatively the optical losses of sol-gel derived fibers or monoliths. Special procedures, like a treatment with Cl_2, have to be adopted to avoid this problem.

1.2 *The TiO_2-SiO_2 System as an Example of Sol-Gel Synthesis*

Titania-silica sols, gels and glasses have been studied by many researchers, from the point of view of both the chemical synthesis and the characterization of products. A detailed bibliography may be found in ref. 1. The TiO_2-SiO_2 system offers a good example of a sol-gel processing where precursors with different hydrolysis rates are used. The main reactions occurring in a solution where silicon and titanium alkoxides are mixed with alcohol and water are reported in the figure. If the hydrolysis reactions have the same rate, the number of hydrolyzed groups should be statistically distributed between the two precursors and, depending on the relative amounts of silicon and titanium alkoxides, homocondensation of the more abundant species (reaction c or d) should occur together with heterocondensation (reaction e). However, as titanium alkoxides are much easier hydrolyzable than the corresponding silicon alkoxides, reaction d anticipates the hydrolyis of the silicon alkoxide and homocondensation is preferred, leading to an inhomogeneous gel. This happens whenever two or more alkoxides with different reactivities are mixed together and hydrolyzed. In order to limit phase separation different routes have been proposed in the literature: sequential hydrolysis,[9] where the less hydrolyzable alkoxide is allowed to react with water before the addition of the 'fast' alkoxide; selection of precursors with similar reactivities (changing of the alkyl group changes the reactivity of the alkoxide);[10] use of hybrid alkoxides containing different elements in the same molecule; control of reactivity by chemical methods by using, for example, chelating agents.[11]

The achievement of an apparently homogeneous solution without precipitation of a second phase is not necessarily a proof that heterocondensation was preferred to homocondensation. In the specific case of the TiO_2-SiO_2 system, the sequential method gives clear solutions. However $Ti(OR)_4$ is known to catalyze the condensation of silanol groups and it was demonstrated that its addition to a solution of pre-hydrolyzed $Si(OR)_4$ gives only a limited amount of Si-O-Ti bonds.[12] The control of the reaction rate by chelating

Silica-titania gels

1) Hydrolysis

$$Si(OR)_4 + n\,H_2O \longrightarrow Si(OH)_n(OR)_{4-n} + n\,ROH \qquad (a)$$

$$Ti(OR)_4 + m\,H_2O \longrightarrow Ti(OH)_m(OR)_{4-m} + m\,ROH \qquad (b)$$

2) Condensation

$$\equiv Si{-}OH + HO{-}Si\equiv \longrightarrow \equiv Si{-}O{-}Si\equiv + H_2O \qquad (c)$$

$$\equiv Ti{-}OH + HO{-}Ti\equiv \longrightarrow \equiv Ti{-}O{-}Ti\equiv + H_2O \qquad (d)$$

$$\equiv Si{-}OH + HO{-}Ti\equiv \longrightarrow \equiv Si{-}O{-}Ti\equiv + H_2O \qquad (e)$$

3) Chelation by acetylacetone (acacH)

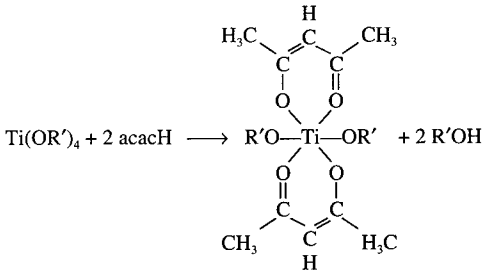

FIGURE 1 Reactions occurring in a precursor solution for silica-titania gel. Chelation (3) is used to decrease the hydrolysis rate of titanium alkoxides.

agents, such as acetylacetone, is a common method to avoid the precipitation of titanium species. Acetylacetone, as all β-diketones, exhibits keto-enol tautomerism and the enol form reacts promptly with titanium alkoxides, giving more stable structures (see figure). Clear gels can be obtained in this way, but again, this does not mean that gels are really homogeneous.[11] Sometimes, sophisticated analytical techniques are necessary to detect such inhomogeneities, which, however, do not seem to affect the macroscopic properties of the material. In fact, titania-silica glasses almost identical to commercial products (obtained by the flame hydrolysis process at about 1800°C) were prepared by the sol-gel route at much lower temperature.

XRD[11,13] and TEM[14] studies have shown that crystallization of gels takes place at a temperature that depends on the TiO_2 concentration. This agrees with the fact that TiO_2 is not a glass forming oxide and the larger is its amount, the easier is its separation as a crystalline phase. However, the 'stability' of amorphous gels is somewhat surprising. Gels

with very high titania percentage, up to at least 60 mol%, remained amorphous after treatment at 500°C[15] and those with 25 mol% showed no crystalline phases after heating at 900°C,[16] while traditional glass cannot dissolve more than 10 mole % of titania. The resulting structure is, however, dependent on the chemical history and gels with the same composition, but obtained by a different procedure, may exhibit different crystallization temperatures.[11]

Thin sol-gel coatings may be obtained on glass or other substrates by depositing a liquid film of the precursor solution on the substrate and allowing it to gel and dry. Thermal treatment is then performed to densify the layer. Coatings in the TiO_2-SiO_2 binary system are particularly interesting because the refractive index can be tuned with the composition. Schröder[17] was the first to show that the refractive index of TiO_2-SiO_2 sol-gel coatings changes linearly from 1.46 to about 2.2. This type of coatings can be used in integrated optics for producing planar and strip optical waveguides, as very low optical losses (0.3 dB/cm) can be obtained.[18,19,20]

2 HYBRID MATERIALS.

Most difficulties in sol-gel processing of monoliths or thick films derive from the strain built-up during drying and densification heat treatment. A possible way to by-pass this problem is to increase the structural compliance. This can be done by introducing organic moieties in the sol-gel processing, due to the soft chemistry involved. Moreover, new interesting hybrid materials can be synthesized by the way.[21] Organic molecules, oligomers or low molecular weight polymers can be simply embedded in the inorganic matrix (Class I hybrids, following Sanchez and Ribot[22] classification). Organic and inorganic components can be bounded through covalent or iono-covalent bonds (Class II) playing the role of network formers or network modifiers.

The synthesis of hybrid materials is interesting as it offers several possibilities: improvement of coatings, fibers, monoliths processing; microstructural control (i.e. porosity, hydrophobicity/hydrophilicity); adjustment of mechanical and thermal properties (elastic moduli, toughness, thermal expansion coefficient). Moreover, new specific properties (optical, electrical, chemical, biochemical) can be obtained by the organic component.

A drawback of organic-inorganic materials is their thermal lability. Generally, they cannot be used at temperatures higher than 200–300°C, even if temperature stability can be slightly increased by chosing thermally resistant components.[23] This is not always a disadvantage, as it can be used to eliminate the organic components for obtaining an inorganic material. For example, the use of trifunctional alkoxysilanes (for example, $CH_3Si(OC_2H_5)_3$, that has a non-hydrolizable Si-C bond) reduces the connectivity of the silica gel network and enables to obtain thicker inorganic films after treatment at 500°C.[24]

3 DEFECTS IN GELS AND GEL-DERIVED MATERIALS

The low synthesis temperature of gel derived materials could lead to think that a low concentration of thermally activated defects should be present. However, in analogy with glass formation from melts upon freezing of the liquid structure, the gelation process may be thought as a chemical 'freezing' where the species in solution suddenly loose their freedom by the progress of condensation reactions. At the low temperatures of synthesis non-equilibrium structure can be kinetically stable and structural relaxation is hindered. Furthermore, gel-derived materials are usually highly porous before thermal densification and defects associated to surface structures should be expected to be present in significant concentrations. As an example, localized defects in silica gels have been studied by Raman spectroscopy and ESR.

3.1 *ESR Studies*

Paramagnetic defects are not present in silica gels. However, they form upon irradiation and their study can add information on the thermal evolution and on the effect of chemical processing.[25,26,27] Organic radical species $CH_3CH\bullet OH$, $\bullet CH_3$) were observed in dried gels and their reduction during thermal treatment could be followed. The presence of O_2^- centers was observed in irradiated silica gels by Kordas *et al.*[25] and Wolf *et al.*[26] The last authors irradiated the gels with X-rays and, as the energy involved was not sufficient to create a Si-O-O-Si peroxy linkage, they deduced that it was existing in the gel prior to irradiation. They probably form as condensation products in solution or in the dried gel. Griscom *et al.*,[27] studying silica gels prepared in THF solution (instead of ethanol, as in ref. 26) by using ^{17}O-enriched water, did not observe the characteristic ^{17}O hyperfine signature of the peroxy radical. Instead, they obtained the characteristic spectrum of the non-bridging oxygen hole centers (NBOHC).

Although the reason for such a discrepancy was not clear, it was pointed out that the different procedure used for the preparation of gels could change the condensation reactions and the resulting products. Non-bridging oxygens are also reported in ref. 25 for gels treated at 900°C prior to irradiation.

The E′center (Si•) is reported in all the cited works and is likely due to hole trapping at the sites of oxygen vacancies.

3.2 *Raman Studies*

Raman spectra of vitreous silica (v-SiO_2) exhibit two narrow bands at ca. 490 and 608 cm^{-1}, named D_1 and D_2, respectively, and ascribed to structural defects. These D_1 and D_2 bands are also present in gel-derived silica, but their intensity changes independently with thermal treatment, indicating an unrelated origin.[28,29] Several defect models have been proposed by different authors for v-SiO_2 and were considered by Brinker and coworkers:[30] (1) broken or missing bonds, which associate both D_1 and D_2 bands with a dangling Si-O bond; (2) silanols periodically arranged on paracrystalline surfaces, where D_1 is related to silanones and D_2 to cyclic tetrasiloxanes resulting from silanone reaction; (3) 2,3 4-fold rings; (4) peroxy linkages. They studied a ^{18}O-enriched silica gel by Raman spectroscopy and DSC. The results brought the authors to assign D_1 and D_2 in agreement with Galeener,[31] to ring breathing of 4-fold and 3-fold siloxane rings, respectively.

The thermal evolution of the two bands in gels can be explained by the different stability expected for strained and unstrained species. The 4-fold ring (D_1) is relatively unstrained and thus it is present both in solution and at high temperature. Instead, the strained 3-fold ring (D_2) is not stable in solution nor at high temperatures, but it may form by condensation on the surface. This would explain the absence of D_2 in dried gels, its appearance at $T > 250°C$, when hydroxyls condense in the rigid structure, and its sudden decrease at $T > 700°C$, when breaking and reforming of bonds can occur.

Although the genesis of D_1 and D_2 is likely to be very different in v-SiO_2 (high temperature processing, $T \gg Tg$) and in gel-derived SiO_2 (low temperature processing, $T < Tg$), their structural nature is certainly the same. Thus, this result is valid for both type of glasses.

3.3 *Crystallization Defects*

As previously discussed, the low temperature gelation process corresponds to a 'chemical freezing' which does not give the possibility to the forming solid structure to organize in an ordered network. As a matter of fact, dried gels are almost always amorphous. Lange *et al.*[32] pointed out that when the synthesis temperature is very low the driving potential for crystallization is very large and the critical nucleus size required for

spontaneous crystallization is very small. However, diffusion in strongly inhibited. Thus, crystallization is thermodynamically favoured, but kinetically hindered. This accounts for the formation of unexpected amorphous or metastable structures. As diffusion can occur only on very short range, small nuclei may form, but the degree of homogeneity in multicomponent systems will strongly influence the nature of crystalline phases. At intermediate temperature phase ordering on the short range will be preferred to long range diffusion. For example, if the mixture is homogeneous with a composition close to an existing crystalline phase, this phase will crystallize even if it is not in its temperature range of stability as compared to phase separation. However, if the composition is different or the system is non-homogeneous, the phase should not form. On the opposite, in a binary system where two phases coexist at equilibrium, these will crystallize easier if the amorphous material is already phase separated. Instead, homogeneity will hinder the achievement of equilibrium, and metastable or non equilibrium structures could form. Several examples can be cited, but we will limit to one, particularly clear and significant, recently presented by Bonhomme-Coury *et al.*[33] Al_2O_3-TiO_2 gels with a composition corresponding to Al_2TiO_5 were prepared following two procedures. In the first preparation no precaution was taken to control the hydrolysis kinetics of the titanium alkoxide and a gel with separate condensation of titanium oxide and alumina was obtained. By heating this non-homogeneous gel, rutile-TiO_2 and α-Al_2O_3 crystallized below 1000°C and reacted at T > 1280°C to give β-Al_2TiO_5, in agreement with the equilibrium phase diagram. In the second procedure acetic acid was used to slow down the reaction rates. The crystallization behaviour of this 'homogeneous' gel was quite different from the previous one. In fact, a crystalline aluminium titanate very similar to β-Al_2TiO_2 was observed below 800°C. As discussed above, this phase was obtained by a local ordering of the homogeneous mixture. However, it was metastable as compared to the phase separation of simple oxides and, indeed, at higher temperatures the higher diffusion kinetics allowed this phase to decompose into rutile-TiO_2 and α-Al_2O_3. Only above 1280°C the stable β-Al_2TiO_5 formed again.

The low temperature synthesis methods should affect also the amount of structural defects. The concentration of equilibrium defects (vacancies, interstitials) should be small if the crystallization occurs under equilibrium conditions. But this is not the case, at least in sol-gel processes, because of the sudden change of chemical potential (and viscosity). So, kinetic reasons justify the presence of non-equilibrium defects. Unfortunately, only few experimental evidences have been published on this subject on gel materials. For example, Barboux *et al.*[34] found microtwinning phenomena in the $YBa_2Cu_3O_{7-x}$ phase of superconductive ceramics. This phase can be described as Ba- and Y-containing perovskite blocks ordered along the c axis. Its formation requires a quite long range ordering, that is not achieved at low temperatures. Partial disordering of the alignments results in such microtwinning. Similarly, the low temperature synthesis of many materials leads to structures which appear to have higher symmetry (as observed by X-ray diffraction) than the regular ones. As well known examples, tetragonal ZrO_2 is obtained instead of monoclinic;[35] cubic-like $PbTiO_3$ is obtained instead of tetragonal.[36] This higher symmetry relates to a higher disorder coming from the gel precursors. In this hypothesis, we are explaining high symmetry through an order which has not been completely obtained for kinetic reasons. Another explanation, given by many authors, relates on thermodynamical considerations taking into account the effect of the surface energy.

Certainly, more extensive research should be addressed to this important field. From this point of view, sol-gel should be considered an experimental procedure for studying the more general aspects of low temperature synthesis and the effects it may have on structure and defects.

REFERENCES

1. C. J. Brinker and G. W, Scherer, *Sol-Gel Science* (Academic Press, San Diego, 1990).
2. P. J. James. *J. Non-Cryst. Solids*, **100**, 93 (1988).
3. J. D. Mackenzie. *Ultrastructure Processing of Advanced Ceramics*, eds. J. D. Mackenzie and D. R. Ulrich (Wiley, New York, 1988) p. 589.
4. T. Hayashi and H. Saito. *J. Mater. Sci.*, **15** 1971 (1980).
5. M. Yamane and T. Kojima. *J. Non-Cryst. Solids*, **44** 181 (1981).
6. E. Matijevic and P. Gherardi. *Transformation of Organometallics into Common and Exotic Materials: Design and Activation, Nato ASI series E, no. 141*, ed. R. M. Laine (Martinus Nijhoff, Dordrecht, 1988) p. 279.
7. E. Barringer, N. Jubb, B. Fegley, R. L. Pober, H.K. Bower. *Ultrastructure Processing of Glasses, Ceramics, and Composties*, eds. L. L. hench and D. R. Ulrich (Wiley, New york, 1984) p. 315.
8. L. Cot, A. Larbot, and C. Guizard. *Ultrastructure Processing of Advanced Ceramics*, eds. J. D. Mackenzie and D. R. Ulrich (Wiley, New York, 1988) p. 211.
9. M. Emili, L. Incoccia, S. Mobilio, G. Fagherazzi and M. Guglielmi. *J. Non-Cryst. Solids*, **74** 129 (1985).
10. M. Yamane, S. Inoue, and K. Nakazawa. *J. Non-Cryst. Solids*, **48** 153 (1982).
11. L. Armelao, P. Colombo, G. Granozzi and M. Guglielmi. *J. Non-Cryst.Solids*, **139** 198 (1992).
12. J. D. Basil and C. C. Lin. *Ultrastructure Processing of Advanced Ceramics*, eds. J. D. Mackenzie and D. R. Ulrich (Wiley, New York, 1988) p. 783.
13. J. Cheng and D. J. Wang. *J. Non-Cryst. Solids,* **48** 153 (1982).
14. E. Breval, Z. Deng and C. G. Pantano. *J. Non-Cryst. Solids*, **125** 50 (1990).
15. K. Kamiya, S. Sakka and I. Yamanaka. *Tenth International Congress on Glass* (The Ceramic Society of Japan, 1974), **13**, p. 44.
16. C. J. R. Gonzales-Oliver, P. F. James and H. Rawson, *J. Non-Cryst. Solids*, **48** 129 (1982).
17. H. Schröder. *Physics of Thin Films: Advances in Research and Development*, vol. 5, eds. G. Hass and R. E. Thun (Academic Press, New York, 1969), p. 87.
18. M. Guglielmi, P. Colombo, L. Mancinelli Degli Esposti, G. C. Righini, S. Pelli. *Proc. SPIE Vo. 1513 Glasses for Optoelectronics II* (1991) p. 44.
19. M. Guglielmi, P. Colombo, L. Mancinelli Degli Esposti, G. C. Righini, S. Pelli and V. Rigato, *J. Non-Cryst. Solids* (1992).
20. B. D. Fabes, B. J. J. Zelinski D. J. Taylor, L. Weisenbach, S. Boggavarapu and D. Z. Dent. *Sol-Gel Optics II:SPIE Proceedings Vol. 1758* (1992) p. 277.
21. H. Schmidt. *J. Sol-Gel Sci. Tech.*, **1** 217 (1994).
22. C. Sanchez and F. Ribot. *Proceedings of the First European Workshop on Hybrid Organic-Inorganic Materials*, eds. C. Sanchez and F. Ribot (Paris, 1993) p. 9.
23. M. Guglielmi, P. Colombo, G. Brusatin, G. Facchin and M. Gleria, *J. Sol-Gel Sci. and Tech.*, **2** 109 (1994).
24. M. Guglielmi, A. Martucci, P. Innocenzi. To be published.
25. G. Kordas, R. A. Weeks and L. C. Klein. *J. Non-Cryst.Solids*, **71** 327 (1985).
26. A. A. Wolf, E. J. Friebele and D. C. Tran. *J. Non-Cryst.Solids*, **71** 345 (1985).
27. D. L. Griscom, C. J. Brinker and C. S. Ashley. *J. Non-Cryst.Solids*, **92** 295 (1987).
28. A. Bertoluzza, C. Fagnano, M. A. Morelli, V. Gottardi and M. Guglielmi. *J. Non-Cryst.Solids*, **48** 117 (1982).
29. V. Gottardi, M. Guglielmi, A. Bertoluzza, C. Fagnano and M. A. Morelli. *J. Non-Cryst.Solids*, **63** 71 (1984).
30. C. J. Brinker, D. R. Tallant, E. P. Roth and C. S. Ashley. *Defects in Glasses*, eds. F. L. Galeener, D. L. Griscom and M. J. Weber (Mat.Res.Soc., Pittsburgh, Pa., 1986) p. 387.
31. F. L. Galeener. *J. Non-Cryst.Solids*, **49** 53 (1982).
32. F. F. Lange, M. L. Balmer and C. G. Levi. *J. Sol-Gel Sci. and Tech.*, **2** 317 (1994).
33. L. Bonhomme-Coury, N. Lequex, S. Mussotte and P. Boch. *J.Sol-Gel Sci. and Tech.*, **2** 371 (1994).
34. P. Barboux, I. Campion, S. Daghish and J. Livage. *J. Non-Cryst.Solids*, **147&148**, 704 (1992).
35. R. C. Garvie. *J. Phys. Chem.*, **82** 218 (1978).
36. Y. Xu and J. D. Mackenzie, *Integrated Ferroelectrics*, **1** 17 (1992).

Radiation Effects and Defects in Solids, 1995, Vol. 134, pp. 39–45
Reprints available directly from the publisher
Photocopying permitted by license only

© 1995 OPA (Overseas Publishers Association)
Amsterdam B.V. Published under license by
Gordon and Breach Science Publishers SA
Printed in Malaysia

ULTRAFAST SPECTROSCOPY OF DEFECTS

M. LEBLANS

Physics Department, University of Antwerp (U.I.A.), Universiteitsplein 1, B-2610 Wilrijk (Antwerp), Belgium

The intrinsic luminescence quenching of the F center in NaI and NaBr has been the subject of discussion for many years. The key question was whether the nonradiative electronic transition to the ground state after optical excitation occurs during or after lattice relaxation in the excited electronic state. Ultrafast time resolved techniques showed that in the case of NaBr the electronic transition predominantly occurs from the relaxed excited state (RES), whereas in NaI the electronic transitions during and after lattice relaxation have a comparable efficiency. A similar question raises when the luminescence is quenched by aggregation of the F-center with a molecular impurity. In addition one wants to characterize the electronic-vibrational (e-v) energy transfer associated with the nonradiative *F*-center relaxation by measuring the population of the vibrational levels after the transfer. Ultrafast spectroscopy can contribute to a better understanding of the e-v transfer process in particular in the case of the OH^-perturbed *F* center: Because of the stronger quenching of electronic luminescence and the much faster (nonradiative) vibrational decay for OH^-, much fewer information is available yet than in the case of CN^-.

1 INTRODUCTION

In most of the alkali halides the *F* center possesses a high emission efficiency after optical excitation. For NaBr, NaI and the lithium halides very weak or no luminescence was observed. Bartram and Stoneham[1] noticed that the luminescence quenching in these cases agrees with the Dexter-Klick-Russell (DKR) criterion: when the crossing point between the potential curves of the ground and excited electronic state lies below the energy reached after optical excitation, the system makes a nonradiative transition near the crossing point during the vibrational relaxation in the excited state (Figure 1). Although this interpretation was supported by several theoretical estimates of the efficiency of the crossover process, experimental evidence was provided on the basis of emission-efficiency measurements that the nonradiative transition occurred from the RES.[2] In the case of impurity-induced luminescence quenching due to e-v transfer, the excitation spectra for vibrational luminescence of $F_H(CN^-)$ in CsBr and KCl showed that electronic relaxation of the *F* center during vibrational relaxation is a possible relaxation channel.[3] However, a splitting of the RES could be an alternative explanation. As will be explained in Sec. III the timescale of the electronic relaxation can distinguish between the two processes. The interpretation of experimental data is complicated by thermal ionization at higher temperatures, by electron tunneling at higher F-center concentrations,[2] and by electronic energy transfer[4] when F_n centers are present. Essential information on the nature of the interaction between the *F*-center electron and the impurity vibration is contained in the energy distribution over the vibrational levels after the electronic relaxation.[3,5] Due to the radiative nature of the CN^- vibrational relaxation on a ms timescale, the e-v transfer of the $F_H(CN^-)$ center is already well-documented and reviewed in Ref. 3. The OH^- impurity is experimentally a more difficult case, since its stretch vibration decays nonradiatively on ns timescale.[6]

2 EXPERIMENTAL TECHNIQUES

Detection of weak picosecond luminescence decay is possible with a streak-camera.

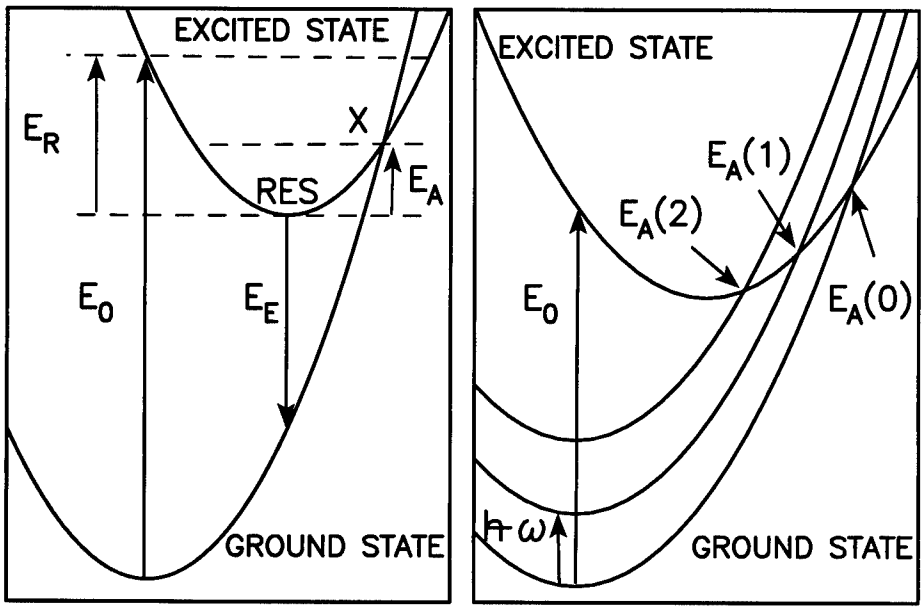

FIGURE 1 Configurational coordinate diagram in the case of intrinsic luminescence quenching and the introduction of new crossing points $E_A(n)$ when energy transfer to a molecular vibrational level $n\hbar\omega$ occurs.

Time-resolved hot luminescence of the *F*-center in KCl was measured in this way.[7] The spectral range of the ordinary electronic luminescence does not allow to study the electronic F-center relaxation to the ground state with this technique.

Pulsed pump-probe laser techniques offer an alternative to measure ultrafast time response. The time resolution is determined by the width of the excitation pulses. A first pulse (pump) excites the system and changes its response on a second pulse (probe), which can be delayed variably with respect to the first one. The probed response can be, e.g., the Raman or absorption spectrum of a transient state prepared by the pump pulse,[8,9] stimulated emission,[10] or temporal bleaching of an absorption band (induced transparency).[11,12] For most of the data discussed here the increased transmittance of a probe pulse induced by the pump pulse is measured. As a function of the time delay between pump and probe pulse one thus obtains the ground-state recovery of an excited color center, independent of the relaxation mechanism. A double modulation scheme with phase-sensitive detection can be used at high pulse repetition rates.[11] This is advantageous for the elimination of unwanted pump-beam intensity and noise reduction. The resulting sensitivity of the technique allows for low power excitation and can be advantageous to avoid, e.g., non-linear effects, heat dissipation, and additional relaxation channels occurring at high saturation.[12] The interpretation of the decay scans with the modulation technique are, however, not always straightforward when in addition to a fast channel also relaxation components are present slower than the modulation period.[13] The high repetition rate can also considerably complicate the problem, if a slowly decaying

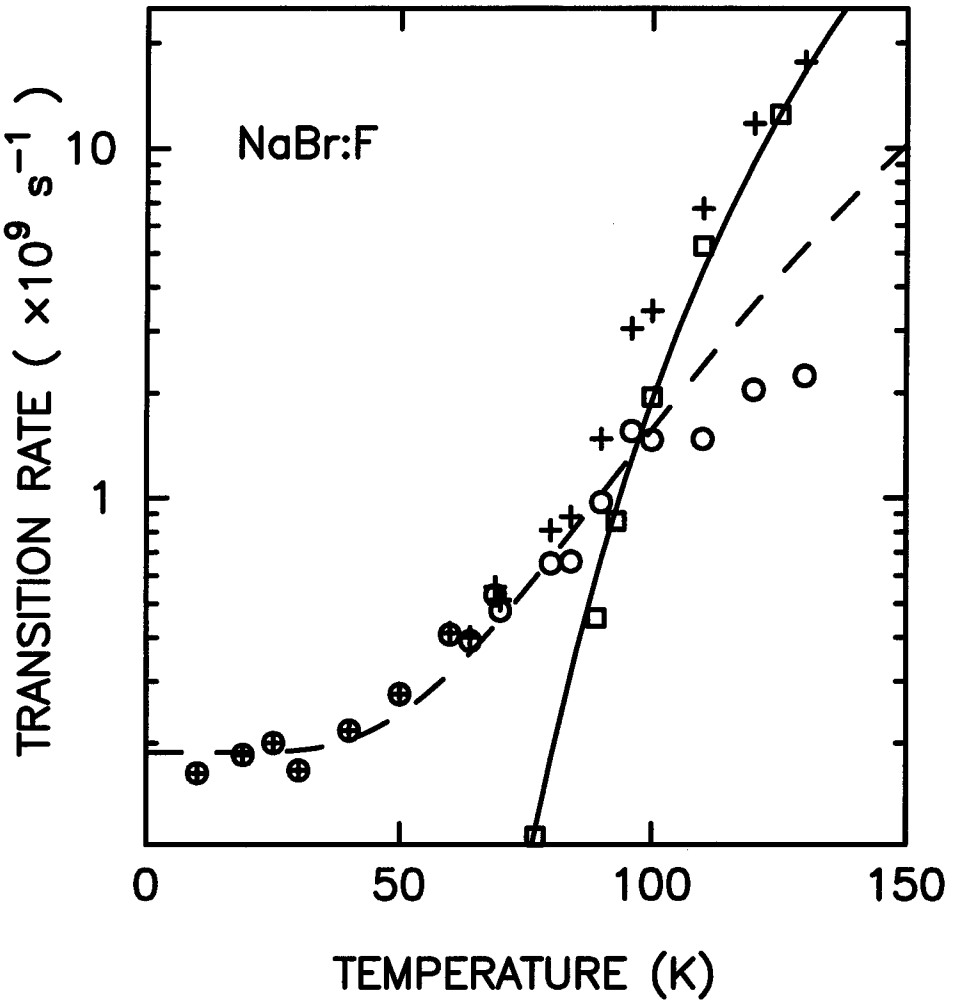

FIGURE 2 The ionization rate (□) and the nonradiative transition rate (○) of the RES of the *F* center in NaBr, derived from the ionization efficiency data of Ref. 2 and total transition rate of the ground-state recovery measurements (+). The full line is a fit of the ionization rate to an Arrhenius behavior. The dashed curve is a fit of the nonradiative transition rate to Eq. 2.

excitation, involved in the relaxation cycle, gets saturated:[3] Repumping of the *F*-center electron in the $F_H(CN^-)$ center when the CN^- is still vibrating after a previous deexcitation of the electron, creates definitely a different situation than an electronic excitation with the CN^- at rest. In such a case it may be more advantageous to use highly energetic pulses at a much lower repetition rate. Such pulses can also be used to generate in a transparent medium an ultrafast spectrally broad continuum. Used as a probe beam, this supercontinuum can be used to monitor with ultrashort time resolution the pump-beam induced absorption changes over a broad spectrum.[3,9,14]

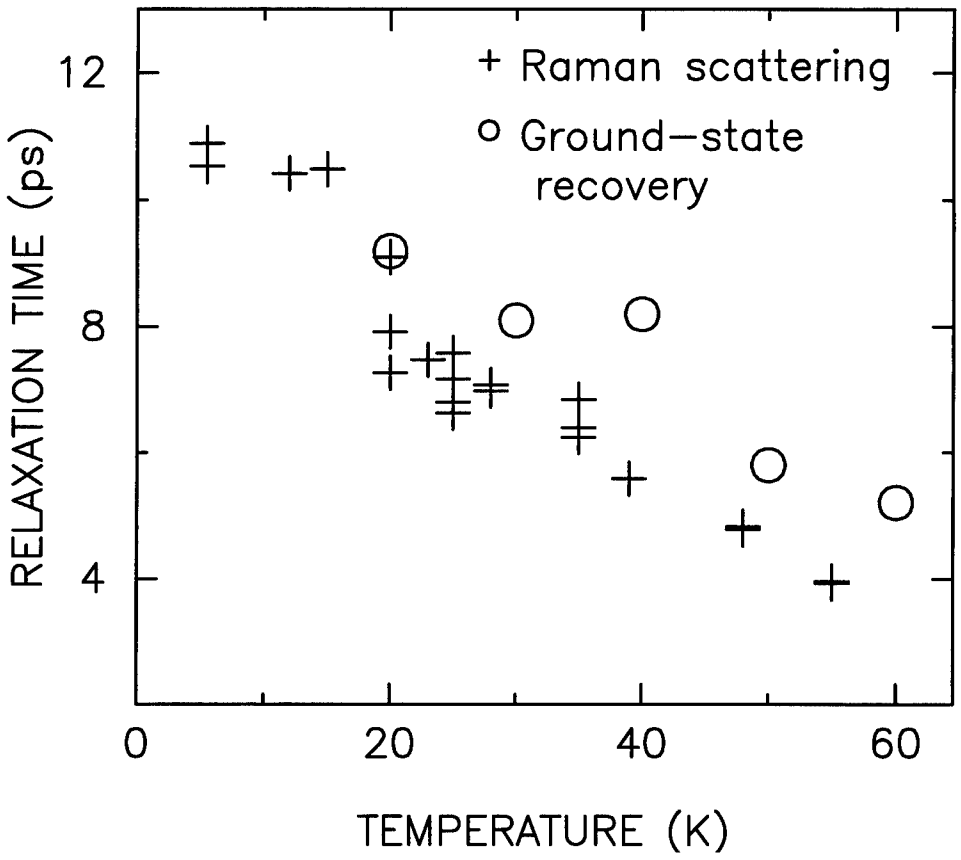

FIGURE 3 Decay time of the fast relaxation channel of the F center in NaI as a function of the temperature (○). The values of the inverse linewidth of the gapmode dominating the vibrational resonant Raman spectrum in NaI[10] are also shown for comparison (+).

3 INTRINSIC QUENCHING OF F-CENTER LUMINESCENCE

An important consideration is that the ground-state recovery of the F center occurs on the timescale of the vibrational relaxation in the case of the crossover process. The lattice relaxation in the excited state of the KCl: $F_A(Li^+)$ has been established to be 13 ps from the risetime of stimulated emission after a pulsed excitation in the absorption band.[10] For the F center in NaI and NaBr the vibrational lifetime was estimated from linewidth measurements of the resonant Raman spectrum to be 10.5 ps and 0.6 ps, respectively.[15] If the nonradiative transition occurs only from the RES, the time constant of the ground-state recovery τ_o at low temperatures can be derived from the expected radiative lifetime τ_r and the emission efficiency η_e:

$$\tau_0 = \eta_e \, \tau_r \tag{1}$$

Thus, a nonradiative lifetime of 5.4 ns is expected for NaBr and 27 ns for NaI.

Induced-transparency measurements were performed on the F center in NaBr and NaI with 10-ps time resolution and yielded at 10 K a relaxation component of 6 ns and in the

order of tens of ns, respectively.[11,13] Being in good agreement with Eq. 1 and much slower than the vibrational lifetime, one concludes that the F center in NaBr and NaI reaches the RES with a high efficiency, from which nonradiative decay occurs. A theoretical expression for the latter process fits well the temperature dependence observed for this decay component in NaBr (Figure 2):[11]

$$\tau_{nr}^{-1} = \frac{C^2\sqrt{2\pi}}{\hbar\sqrt{E_R\kappa_B T^*}} \exp\left(-\frac{E_A}{\kappa_B T^*}\right), \tag{2}$$

with T* an *effective* temperature, which is nonzero at zero temperature.

In the case of NaBr also a slower decay channel related to the recapture of conduction electrons is observed, with an increasing amplitude at higher temperatures. This decay channel can not be clearly distinguished in NaI, which is possibly due to the fact that the maximum available time delay between pump and probe pulses is considerably shorter than the ground-state recovery in the temperature range in which the dominant contribution changes from the component related to the RES lifetime to the retrapping component.

The uncertainty on the values for Eq. 1 are large enough to allow for a contribution from the crossover process with a comparable efficiency as the transition from the RES, and its contribution could occur faster than the 10-ps time resolution. Measurements on NaI with 200-fs time resolution show indeed an additional relaxation component of 10.5 ps. The temperature dependence of its time constant follows closely the vibrational lifetime derived from linewidth measurements of the resonant Raman spectrum (Figure 3). Apparently, the interstate electronic transition is sufficiently fast to allow for a $\sim 33\%$ efficiency of the crossover process during lattice relaxation.

4 IMPURITY-INDUCED NONRADIATIVE RELAXATION

When the F center is perturbed by an impurity, the parameters in Eq. 2 can be modified, due to (static) changes, e.g., of the electronic wavefunctions and the effective phonon frequency. Alternatively or additionally, the vibrational excitation of the impurity may interact with the F-center electron, so that energy transfer to the impurity vibration occurs.[3] If during the nonradiative electronic relaxation a particular vibrational level n of the impurity is populated, the transition rate from the RES has an activation energy which can be determined by the crossing-point energy of the potential curve of the excited state and the one of the ground electronic state moved upwards $n\hbar\omega_v$ in energy (Figure 1). The lowering of the activation energy implies the necessity of considering again electronic transitions during lattice relaxation and from the RES. The lowering of the activation energy is a result of the fact that due to energy conservation less energy is to be dissipated into phonons when the impurity vibration is excited in the electronic relaxation process.

Without clarifying the interaction between the F-center electron and the impurity vibration, it explains why e-v transfer can be efficient in the case high-frequency intramolecular vibrations, such as is the case of CN^- and OH^-. It was concluded from a study of H_s^--induced nonradiative relaxation of the F center in NaBr that it might considerably affect the intrinsic nonradiative relaxation rate due to e-v transfer even for relatively low vibrational energies.[16] Nevertheless, it was also clear from this study that static perturbations of the F center due to the presence of the impurity influence the nonradiative relaxation rate in this case.

Although their energy is much lower, rotational or librational excitations of a molecular impurity may play a similar role in the nonradiative relaxation as the internal vibration.

They may efficiently promote the electronic transition as was suggested by the activation energy derived from induced-transparency measurements of the (unaggregated) F center in OH^--doped KCl, which was close to the librational frequency.[12,17] Induced-transparency measurements on KBr:$F_H(OH^-)$ revealed a 300-ps relaxation component at low temperatures with an activation energy considerably lower than the librational frequency.[18,19] It was suggested that phonons are responsible to stimulate the nonradiative relaxation.[18] This activation energy may also be explained in terms of low-lying crossing points: An activation energy in the order of 100 cm^{-1} would be obtained for both hosts when the vibrational level $n = 2$ of OH^- is excited. With this respect the ground-state recovery of KBr:$F_H(OD^-)$ would be very important, since the vibrational energy levels are significantly different in this case. Our induced-transparency measurements show,[19] however, that the temperature dependence of the relaxation should be considered with care, because two different configurations of KBr: $F_H(OH^-)$ exist depending on the OH^- orientation. They possess a different absorption band, strongly overlapping with each other. Their equilibrium populations depend on the temperature and each configuration may have its own nonradiative relaxation rate. A conversion of one of the centers to the other configuration due to OH^- reorientation during the nonradiative relaxation processes after optical excitation, would be detected as an absorption increase (negative signal) or an increased transparency (positive signal), depending on which absorption band is probed. Decay scans for different pump and probe wavelengths reveal indeed two components with a sign change when the excitation wavelength is varied: one with a decay constant longer than several ns at all temperatures and a strongly temperature-dependent one, decaying in $\sim$ 300 ps at 50 K. They may therefore be related to reorientation of the OH^- impurity after optical excitation and may offer an interesting way to studying the possible interrelation between molecular reorientation and nonradiative relaxation. Since the observed sign changes can also be due to modification of the ground-state absorption by vibrational excitation of OH^-[20], a comparative study is indicated with KCl, in which only one configuration is observed for $F_H(OH^-)$.

Also, a relaxation component faster than 10 ps was observed for KBr: $F_H(OH^-)$,[19] which lies in the timescale of lattice relaxation. It is therefore probably related to electronic transitions at the new crossing points. In contrast to this observation, transient absorption measurements with a white-light continuum on CsBr: $F_H(CN^-)$ yielded an electronic relaxation component on ns timescale.[3] The results on NaI: F (Sec. II) show, however, that the 60-ps resolution of those experiments was very probably insufficient to observe a contribution arising from electronic transitions during lattice relaxation.

In the case of $F_H(OH^-)$ very little is known yet about the efficiency of the e-v transfer and the energy distribution over the vibrational levels after the electronic relaxation. Only for KCl the population of the vibrational levels by anti-Stokes Raman scattering has been measured after pulsed excitation of the F-center electron.[5] For both OH^- and OD^- the largest population was observed for $n = 1$. However, the data were analyzed in the assumption of steady-state conditions, whereas the pump and probe pulse consisted of the same 60 ps pulse train of 76 MHz repetition rate and both the nonradiative relaxation and the vibrational relaxation are expected to occur on a timescale faster than 13 ns. Due to the high excitation power used in this experiment, it is also not clear whether one can exclude repumping of $F_H(OH^-)$ centers, which are not yet relaxed vibrationally from previous e-v transfer events.

REFERENCES

1. R. H. Bartram and A. M. Stoneham, *Solid State Commun.* **17**, 1593 (1975).

2. G. Baldacchini, D. S. Pan, and F. Lüty. *Phys. Rev.* **B24**, 2174 (1981).
3. F. Luty and V. Dierolf, in *Proceedings of the International Conference on Defects in Insulating Materials, SchloßNordkirchen, Germany, 1992*, edited by O. Kanert and J. M. Spaeth (World Scientific, Singapore), Vol. 1, p. 17; D. Samiec, A. Katerkamp, H. Stolz, and W. von der Osten, p. 548.
4. J. De Kinder, W. Joosen, and D. Schoemaker, *Phys. Rev.* **B42**, 9674 (1990).
5. G. Halama, K. T. Tsen, S. H. Lin, F. Lüty, and J. B. Page, *Phys. Rev.* **B39**, 13457 (1989) .
6. C. E. Mungan, U. Happek, and A. J. Sievers, *J. Luminescence* **58**, 33 (1994).
7. N. Akiyama and H. Ohkura, *J. Luminescence* **60 & 61**, 713 (1994).
8. T. Suzuki, K. Tanimura, and N. Itoh, *Phys. Rev.* **B49**, 7233 (1994).
9. T. Makimura, K. Tanimura, N. Itoh, T. Tokizaki, A. Nakamura, *J. Phys. Cond. Matter* **6**, 4581 (1994).
10. J. M. Wiesenfeld, L. F. Mollenauer, and E. P. Ippen, *Phys. Rev. Lett.* **47**, 1668 (1981).
11. F. De Matteis, M. Leblans, W. Joosen, and D. Schoemaker, *Phys. Rev.* **B45**, 10377 (1992).
12. D. Jang, T. C. Corcoran, M. A. El-Sayed, L. Gomes, and F. Lüty, in *Ultrafast Phenomena V*, edited by G. R. Fleming (Springer-Verlag, Berlin, 1986).
13. F. De Matteis, M. Leblans, W. Slootmans, and D. Schoemaker, *Phys. Rev.* **B50**, 13186 (1994).
14. R. Dorsinville, P. P. Ho, J. T. Manassah, and R. R. Alfano, in *The Supercontinuum Lasersource*, edited by R. R. Alfano (Springer, New York, 1989).
15. F. De Matteis, M. Leblans, and D. Schoemaker, *Phys. Rev.* **B49**, 9357 (1994).
16. E. Gustin, M. Leblans, A. Bouwen, and D. Schoemaker, *Phys. Rev.* **B49**, 916 (1994).
17. L. Comes and F. Lüty, *Phys. Rev.* **B30**, 7194 (1984) .
18. P. Prosposito, M. Casalboni, F. Ignozza, and U. M. Grassano, *Proceedings of this Conference.*
19. E. Gustin, W. Wenseleers, M. Leblans, A. Bouwen, and D. Schoemaker, *Proceedings of this Conference.*
20. Y. Yang and F. Lüty, *Bull. Am. Phys. Soc.* **31**, 699 (1986).

1 CALCULATIONS AND THEORY

Radiation Effects and Defects in Solids, 1995, Vol. 134, pp. 47–50
Reprints available directly from the publisher
Photocopying permitted by license only

© 1995 OPA (Overseas Publishers Association)
Amsterdam B.V. Published under license by
Gordon and Breach Science Publishers SA
Printed in Malaysia

STATIC SIMULATIONS OF Cu^+ CENTERS IN ALKALI HALIDES

V. LUAÑA, M. A. BLANCO, M. FLÓREZ, A. MARTÍN PENDÁS and L. PUEYO

Departamento de Química Física y Analítica. Facultad de Química; Universidad de Oviedo, 33006-Oviedo, Spain

Quantum-mechanical calculations and atomistic simulations have been used to characterize the local geometry, stability and resonant vibrations of Cu_A centers in alkali halides

Key words: Impurities, Cu^+ centers, Vibrations in crystals.

1 INTRODUCTION

The Cu_A centers in alkali halides appear to be quite simple closed shell impurity systems. They present, however, important difficulties both from the experimental and from the theoretical points of view. The detailed geometry for most centers has not been established, and quite significant differences exist among theoretical calculations.[1,2] Vibration frequencies computed from cluster calculations are usually far different from the values determined upon the analysis of electronic spectra.[3,4] Cu^+ exhibits on some crystals (NaBr, KCl, and KBr) an off-center equilibrium position, for which the mechanism is yet unknown.

2 METHOD AND MODELING

The above questions have been investigated with the *ab initio* Perturbed Ion (aiPI) quantum-mechanical methodology.[4] Thus cluster-in-the-lattice calculations have been done, in which the local wavefunction of a given cluster (C) is self-consistently solved, and the classical and quantum effects provided by a frozen lattice (L) are taken into account. An initial aiPI calculation on the pure host crystal provides the wavefunctions to represent the lattice, that is going to be frozen, both electronically and geometrically, during the cluster calculation.

We have observed the convenience to separate the cluster C region into two parts: an innermost region, C_1, made of all ions that are geometrically as well as electronically relaxed, and the border region, C_2, collecting the ions that suffer only electronic relaxation. In this paper the notation ***Cn-m*** is used to indicate that C is made up of the central substituted position and the ***n*** nearest neighbors, the first ***m*** of them being the C_1 region.

The presence of the C_2 region improves the calculation by interfacing the cluster wavefunction to the fixed lattice density. As an example, the nearest-neighbor (nn) Cu-F distance in Cu^+:NaF passes from 2.14 Å in the Cl-1 model (7 ions), to 2.18 Å in C2-1 (13 ions), and to 2.20 Å in C3-1 (25 ions) and C4-1 (33 ions). Even more important, neglecting the C_2 region has produced, in some cases, rather unphysical energy functions.

3 LOCAL GEOMETRY OF THE Cu_A CENTERS

C12-4 models (179 ions, 33 of them being moved) have been used to determine the local geometry of Cu_A centers in nine alkali halides. Totally symmetric (breathing) displacements of the shells have only been permitted at this point. Equivalent C12-4 models of the pure hosts have also been solved, and the local relaxations due to the impurity have been computed as the difference $\Delta R^i = R^i_{th}(Cu_A) - R^i_{th}(A_A)$, in order to avoid systematic errors in the calculation. Interestingly, we have found that it is only the first shell of neighbors that appreciably relax upon substitution. The nn relaxations (See Table I) depend mostly on the cation being substituted. Negligible or very small inwards relaxations are obtained for Cu:Li*X*, inwards relaxations close to –0.1 Å are obtained for Cu:Na*X*, and values around –0.3 Å are encountered for Cu:KX. These results follow the tendency that should be expected according to Shannon's octahedral ionic radii[5]: 0.90 (Li^+), 1.16 (Na^+), 1.52 (K^+), and 0.91 Å (Cu^+). Moreover, Emura *et al.*[6] did EXAFS measurements on Cu:NaCl and found an inwards relaxation of –0.10 ± 0.02 Å, in excellent agreement with our calculations.

4 STABILITY OF THE Cu_A CENTERS

The formation energy of the Cu_A centers is quite dependent on the size of the C_1 and C_2 regions. For instance, Cu:LiF is unstable by 1.10 eV in the C0-0 model (*C* only contains the substituted position), by 0.21 eV in C12-0, and it turns to be stable by –0.25 eV in the C12-4 model.

According to the C12-4 model, substituting Cu^+ for the cation is energetically favored in the nine alkali halides. As Table II shows, the formation energies are mainly determined by the cation being substituted, Cu_{Li} being the less stable and Cu_K the most stable centers. The aiPI values can be compared with the results from atomistic HADES simulations also presented in Table II. The HADES and aiPI results are rather coincident for the three fluorides, but the atomistic simulation predicts the Cu_A centers in the three chlorides to be 1–2 eV more stable than the aiPI calculation. The origin of this significant difference remains yet unknown.

Table I
Theoretical Cu-*X* distances and relaxations, in Å, for the Cu_A centers.

	LiF	LiCl	LiBr	NaF	NaCl	NaBr	KF	KCl	KBr
R_{th}(Cu-*X*)	2.021	2.522	2.734	2.201	2.706	2.906	2.276	2.769	3.004
ΔR	0.000	–0.033	–0.020	–0.124	–0.105	–0.086	–0.378	–0.365	–0.299

Table II
Formation energies (in eV) of the Cu_A centers.

	LiF	LiCl	LiBr	NaF	NaCl	NaBr	KF	KCl	KBr
aiPI	–0.252	–0.688	–0.392	–1.022	–0.867	–0.684	–1.771	–1.646	–1.377
HADES[a]	–0.200	–2.704		–1.598	–3.200		–1.978	–3.123	

(a) Using set II potentials and shell parameters from Ref. 7 and Cu-*X* potentials from Ref. 8.

5 RESONANT VIBRATIONS OF Cu^+:NaF

The 138 independent O_h force constants corresponding to the vibration of $Cu^+$and its first

four shells of neighbors have been numerically computed from the aiPI energy, according to the procedure described in Ref. 4. These force constants give the vibrational modes of the impurity, under the harmonic approximation. The C12-4 of both the impurity center and the pure host crystal have been examined in parallel, and from the comparison of the results of both we have determined that the only modes truly characteristic of the impurity center are the lowest a_{1g}, e_g, and t_{1u} vibrations. Strong couplings are found among vibrational modes of adjacent shells, showing that theoretical frequencies derived from small cluster calculations should be checked for convergence before being compared to the experimental values. As an example, the t_{1u} vibration appears at 155 cm^{-1} when the movement of Cu^+ is considered alone, and drops to 108 cm^{-1} when the coupled movement of the 33 innermost ions is calculated (See Table III). Vibration frequencies having a localized character in the doped system are obtained at 206 cm^{-1} ($1a_{1g}$), 108 cm^{-1} ($1t_{1u}$), and 173 cm^{-1} ($1e_g$). The eigenvector analysis shows that the associated modes are dominated by the motion of the impurity and its first shell of neighbors. These frequencies can be compared with the experimentally observed t_{1u} frequency of 93 cm^{-1},[3] the value of 168 ± 10 cm^{-1} empirically estimated for $1a_{1g}$ upon the shape of the ${}^1A_{1g} \leftarrow T_{1g}({}^3E_g)$ electronic band,[3] and the speculative $1e_g$ frequency of 150 cm^{-1}.[9] On the other hand, we have done a preliminary test on the influence of the ionic polarization on the resonant vibrations. To this end we have implemented a classical linear model of point dipoles, self consistently computed in the electrical field provided by the ions, each carrying an electrical charge and a point dipole. This model has been included as an optional correction to the aiPI calculations. Results in Table III show that the lattice polarization does not significantly affect the coupled a_{1g} vibration, but it lowers as much as 23 cm^{-1} the $1t_{1u}$ mode, consistently with the relatively large polarizability of Cu^+.

Table III
Frequencies (in cm^{-1}) of the vibrational modes having a localized character for the Cu_{Na} center in NaF.

		$\omega(1a_{1g})$	$\omega(1e_g)$	$\omega(1t_{1u})$
aiPI	Uncoupled[(a)]	263	197	155
	Coupled[(a)]	206	173	108
+Polarization[(b)]	Uncoupled	239		126
	Coupled	201		85

(a) A single diagonal force constant is used in the *uncoupled* calculations, whereas the complete matrix is diagonalized in the *coupled* ones.
(b) Using fixed polarizability values of 1.67 (Cu^+), 0.147 (Na^+), and 1.02 $Å^3$ (F^-). Polarization is only accounted for in the C_1 region.

ACKNOWLEDGEMENTS

Most calculations have been done on the Centro de Cálculo Científico of the Universidad de Oviedo. HADES calculations were done at Michigan Technological University during a visit of VL made possible under NATO Grant CRG-921348. Financial support has been provided by the Spanish DGICyT under Grant PB93/0327.

REFERENCES

1. V. Luaña and M. Flórez, *J. Chem. Phys.* **97**, 6544 (1992).
2. M. Flórez,, M. A. Blanco, V. Luaña, and L. Pueyo, *Phys. Rev.* **B49**, 69 (1994).
3. D. S. Mc Clure and S. C. Weaver, *J. Phys. Chem. Solids* **52**, 81 (1991).
4. V. Luaña, M. Flórez, and L. Pueyo, *J. Chem. Phys.* **99**, 7979 (1993).
5. R. D. Shannon, *Acta Crystallogr.* **A32**, 751 (1976).

6. S. Emura, T. Moriga, T. Murata, H. Maeda, A. Koizumi, and M. Nomura, in *X-ray absorption fine structure*, ed. by S. Samar Hosmain (Ellis Horwood, England, 1991), p. 432.
7. C. R. A. Catlow, K. M. Diller, and M. J. Norgett, *J. Phys.* **C10**, 1395 (1977).
8. J. Meng, R. Pandey, J. M. Vail, and A. B. Kunz, *Phys. Rev.* **B38**, 10083 (1988).
9. S. A. Payne, A. B. Goldberg, and D. S. Mc Clure, *J. Chem. Phys.* **78**, 3688 (1983).

Radiation Effects and Defects in Solids, 1995, Vol. 134, pp. 51–55
Reprints available directly from the publisher
Photocopying permitted by license only

© 1995 OPA (Overseas Publishers Association)
Amsterdam B.V. Published under license by
Gordon and Breach Science Publishers SA
Printed in Malaysia

INVESTIGATION OF THE ELECTRONIC STRUCTURE OF POINT DEFECTS IN IONIC CRYSTALS BY THE CLUSTER SCATTERED WAVE METHOD WITH THE SELF-CONSISTENT CALCULATION OF THE LATTICE DISTORTION AND LONG-RANGE POLARIZATION

A. B. SOBOLEV

Experimental Physics Department,
Urals State Technical University, 620002 Ekaterinburg, Russia

(Received 1 July 1994)

This paper describes the calculations of the electronic structures of the F-center in NaCl, pure anion vacancy, F^+ and *F*-centers in MgO by the embedded cluster method. This work is an alternative approach relative to the ICECAP method within which the embedded cluster model based on Johnson's Scattered Wave method is combined with the Mott-Littleton method. The main features of the model are: self-interaction correction of single-particle energies in the case of perfect crystals and point defects whose states are in the band gap of a perfect crystal; Mott-Littleton method modification allowing for the description of the defect wave function in the analytical form; construction of the cluster one-electron potential when describing the rest of the crystal in shell model terms.

Key words: Electronic structure; embedded cluster; point defect.

1 INTRODUCTION

The available theoretical methods for the defect electronic structure calculations provide contradictory results even in the case of the simplest defects (*F*-center in *NaCl* and *MgO*)[1–4]. The contradictions are due to the absence of a satisfactory solution of the problem of the self-consistent calculation of electron distribution and lattice distortion near the defect.

If we consider concrete computation methods we can see that the most effective way of investigating the defect electronic structure is the use of the embedded cluster models based on this or that cluster method (CM) and the Mott-Littleton method (MLM) or the molecular statics method for the description of displacement and polarisation of the main crystal region. The greatest progress in the development of the embedded cluster model has been made by Vail and Harding with co-workers (program ICECAP[1,2]).

The disadvantages of this approach are: (1) the use of the Hartree-Fock method without taking into account the electronic correlation is too rough but when taking into account the electronic correlation this method is not efficient from the computation point of view; (2) the problem of association between MLM and CM has not been solved satisfactorily due to different treatment of the charge of an ion in the shell model (SM) and CM.

If we proceed with the consideration of the studies based on the local density approximation (LDA) we should note the studies made in Brazil,[5] France[6] and Russia.[3] These cluster methods are based on Johnson's scattered wave (SW) method,[7] and the rest of the crystal is described in the 'muffin-tin' approximation. The lattice deformation is an input parameter but, to be more exact, the introduction of ion displacements from equilibrium

is incorrect as the contribution of the rest of the crystal is calculated only for a perfect lattice.

2 EMBEDDED CLUSTER METHOD FOR CALCULATION OF THE ELECTRONIC STRUCTURE OF POINT DEFECTS IN IONIC CRYSTALS

This section describes the embedded cluster method based on the LDA with a self-consistent calculation of the lattic distortion and polarisation.[8] We have chose the scattered wave method with an original programmed realization of the MUSCAT[9] and the Mott-Littleton method with the shell model (original molecular statics program—MOLSTAT[10]) as the base for our model. Our approach consists in the following.

2.1 *Modification of the MOLSTAT Program*

MLM has been modified to describe the defect wave function as hydrogenic function with variational parameters. Let's consider it by the example of the *F*-center. We use hydrogenic functions of the type:

$$\Psi = N(f/\Theta, \phi) \cdot R(f/\lambda, r), \tag{1}$$

where N is the angle part, R is the radial part, λ is the variational parameter.

Energy of interaction of the defect electronic density with the point lattice ions E_f^{dl} can be written as follows:

$$E_f^{dl} = \sum_l \left\{ q_i^s V_f^d\left(r_i^s, \lambda\right) + q_i^c V_f^d\left(r_i^c, \lambda\right) \right\} \tag{2}$$

where q_i^c, q_i^s—is the charges of the nuclei and shells of the lattice ions in the 'shell model', $V_f^d(r)$—is the Coulomb potential created by the defect inpoint r.

For the ground state ($f \rightarrow 1s$) it looks like:

$$V_{1s}^d = (r, \lambda) = \frac{e}{r}\left\{1 - \left[1 + \lambda \frac{r}{a}\right] \cdot exp\left(-\left(2\lambda \frac{r}{a}\right)\right)\right\}, \tag{3}$$

where a is the interionic distance, e—charge of electron. For the exited state it is given elsewhere.[11] Then the total energy of a defected crystal will be written as:

$$Ef(\lambda) = E_f^d(\lambda) + E_f^{dl}(\lambda, \xi) + E_f^{def}(\lambda, \xi) \tag{4}$$

where ξ are crystal lattice ions displacements corresponding to value λ, E_f^{def}—energy of the defected crystal distortion (including crystal polarization energy and short-range part of energy changes), E_f^d—kinetic energy of the *F*-center electron.

Tests. To test the proposed model we calculated energy of absorption, emission and lattice distortions for the *F*-center in the *NaCl* crystal. Dependence of the total energy of the *F*-center for ground and excites states on parameter λ has been obtained. Calculations of E_f^{def} and minimization of E_f by displacements ξ at present λ was performed by the gradient method in the framework of MLM according to MOLSTST,[10,11] and the optimum value λ_{opt} was determine from the position of the total energy dependence minimum. A

satisfactory agreement with the data available[12] speaks of the correctness of the modification proposed.

2.2 *Quantum-Chemical calculations*

To connect the muffin -tin description of electron density (the SW method) with hydrogenic form Löwdin's partitional procedure was used. This procedure allow us to connect the many-center representation of density with the once-center representation. This function by the least square method fitted to the hydrogenic form which enabled us to determine variational parameter λ, and, thus, to proceed with the calculations of the displacements and potential contributions of the ML method, closing the circle of combining the models.

2.3 *Construction of the Potential*

The formalism of the construction of the cluster one-electron potential when describing the rest of the crystal in ML terms consist in the following. Cluster one-electron states for the defect can be divided into two groups: energies and wave functions of the defect and energies and wave functions corresponding to the valence band (VB) of a perfect crystal. At this point the electron density can be represented in the form of two charge distributions: the charge density of the lattice regular ion and the density corresponding to the defect. By introducing the 'atomic spheres' approximation the part of the Coulomb potential from the first charge distribution (infinite) can be easily calculated by the ML method. The cluster part of the Coulomb potential for the second charge distribution is calculated as in 'muffin-tin' models.

2.4 *Self-interaction Correction*

A scheme taking into account the self-interaction correction for the defect states and perfect crystal states has been realised in the Perdew–Zunger approximation[13]. For the cluster one-electron states, modelling the valence band of a perfect crystal we used the averaged exchange—correlation potential with the self-interaction correction in accordance with.[9]

2.5 *Self-consistency*

The described procedure appears to be self-consistent, and when self-consistency having been achieved we have a one-electron spectrum obtained in the framework of CM and a lattice configuration obtained by the Ml method. The parameter of self-consistency of this models is the defect electron density fitted to hydrogenic form.

3 RESULTS

3.1 *F-center in NaCl*

F-center in quantum chemical calculations was simulated by clusters including six coordination spheres of the vacancy (V): $[VNa_{38}Cl_{42}]$. Details and parameters of calculations are described elsewhere.[8]

For the ground state of the F-center in $NaCl$ relaxations of neighboring ions were: $\xi_1 = +0.0001$, $\xi_2 = -0.011$, $\xi_3 = -0.004$ and for the relaxed exited state they were $\xi_1 = +0.068$, $\xi_2 = -0.018$, $\xi_3 = -0.005$. Relaxation is given in the units of the shortest interionic distance

a = 2.79 Å. With ξ '+' corresponds to ion relaxation from the vacancy (outward), and '–' corresponds to ion relaxation to the vacancy (inward).

The calculated value of the isotropic part of hyperfine splitting a in accord with to experimental data as well as the pseudopotential calculation data.[14] Absorption energy Eab, calculated as different between one-electron energies of empty state t_{1u}^{*} and occupied state a_{1g} was E^{ab} = 3.08 eV (E_{ab}^{exp} = 2.77 eV) and E_{em} = 1.69 eV (E_{em}^{exp} = 0.98 eV).

3.2 *F-like centers in MgO*

From the point of view of the theoretical methods the interest for investigation of F-like centers is due to their ability to be modelled for the better understanding of F-like center structures in compound oxide crystals. Within the framework of the developed model calculations of the electronic structure of the F-center in NaCl, pure anion vacancy, F^+ and *F*-centers in *MgO* were made. Clusters [$VMg_{38}O_{42}$] were examined.[15]

The calculated relaxation values were: for pure vacancy (*V*), ξ_1 = +0.087, ξ_2 = –0.053, ξ_3 = +0.015, ξ_4 = –0.004, ξ_5 = +0.015, ξ_6 = –0.010 for the F^+ center: ξ_1 = +0.052, ξ_2 = –0.028, ξ_3 = +0.003, ξ_4 = +0.002, ξ_5 = +0.011, ξ_6 = –0.006 and for the *F*-center ξ_1 = +0.032, ξ_2 =–0.012, ξ_3 = –0.005, ξ_4 = +0.006, ξ_5 = +0.007, ξ_6 = +0.011 in *MgO*. (Values of relaxations are given in units from a = 2.106 Å).

In general the data obtained agree with the data provided in.[1,16] It should be noted that the relaxation values of the nearest neighbours for the *F*-center in *MgO* are rather significant compared to its analogue on alkali-halides. This is due to a greater delocalization wave function of the *F*-center in *MgO* in comparison with the *F*-center in alkali-halides (*NaCl*), which is testified by the results of the partial charge distribution analysis.[15] Calculation within the given model permits to determinate the position of defect ground state a_{1g} relative to the bands of a perfect crystal. According to cluster calculations ($VMg_{38}O_{42}$) the main electronic vacancy state a_{1g} is displaced by the amount of ~2.8 eV from *VB*, F^+ center ~0.45 eV, *F*-center ~2.9eV.

This results show that the presence of the ground state of a pure anion vacancy in the *VB* of a perfect Crystal, which is typical of the methods based on the local density approximation[3,4] is an error of LDA models and is associated with the fact that SIC and ion relaxation in the vicinity of the defect are not taken into account.

The obtained absorption energies were: the F^+ center E_{ab} = 6.2 eV, *F* center E_{ab} = 5.5 eV. The transistion state procedure provides values F^+ center E_{ab}^{ts} = 5.6 eV, *F*-center E_{ab}^{ts} = 5.2 eV, which also do not agree with the experimental data: F^+ center E_{ab} = 4.95 eV, *F* center E_{ab} = 5.0 eV. Over-estimated values of E_{ab} are characteristic of the *F*-center calculations in alkali-halides too and are associated with of the roughness the description of *F*-center exited states in a cluster model.

SUMMARY

The efficiency of the proposed variant of combination of the cluster method of scattered waves and the method of molecular statics in the investigation of the electronic structure of point defects in ionic crystals is demonstrated by the example of calculations of the *F* center electronic structure in ionic crystals.

ACKNOWLEDGEMENTS

The author has benefited from fruitful discussions with Dr. Varaksin A. N.

REFERENCES

1. Vail J. M., Pandey R., Harker A. H., *Cryst. Latt. Def. and Amorf. Mater.* 1987. **V.15**. p. 13.
2. Vali J. M., *J. Phys. Chem. Solids*. 1990. **V.51**. N 7. p. 589–607.
3. Bezel A. V., Lobatch V. A., *Sov. Phys. Sol. State*. 1991. **V. 33**. N. 4. p. 1312–1314.
4. Choi S., Takeushi. T., *Phys. Rev. Lett*. 1983. **V.50**. N 19 p. 1474–1477.
5. Ferreira L. G., De Sigueira M. L., *Phys. Rev. B*. 1986. N. 8. p. 5351–5319.
6. Chermette M., Pedrini C. , *J. Chem. Phys*. 1981. **V.75**. N. 4. p. 1869–1875.
7. Johnson K. H., *Adv. Quant. Chem*. 1973. **V.7**. p. 143–185.
8. Sobolev A. B.., *Sov. Phys. Sol. State*. 1994. **V.36**. N. 6. (in press).
9. Sobolev A.B.., *Sov. Phys. Sol. State*. 1994. **V.36**. N. 9. p. 2509–2518.
10. Gavartin J. L., Catlow C. R. A., Shuluger A. L., Varaksin A. N., *Kolmogorov Yu. N. Modelling Simul. Mater. Sci. Eng*. 1992. **V.1**. N. 1. p. 29–38.
11. Sobolev A. B., Varaksin A. N., *Sov. Phys. Sol. State*. 1994. **V.36**. N. 2. p. 275–283.
12. Mejila C. R., *Cryst. Latt. Def. and Amorf. Mater*. 1986. **V.13**. p. 137–147.
13. Perdew J. P., Zunger M. R., *Phys. Rev. B*. 1981. **V.23**. N. 10. p. 5048–5079.
14. Zwicker R. D., *Phys. Rev. B*. 1978. **V.18**. N. 4. p. 2004–2010.
15. Sobolev A. B., *Sov. Phys. Sol. State*. 1994. **V.36**. N. 10 (in press).
16. Halliburton L. E., Cowan D. L., Hollroyd L., *Phys. Rev. B*., 1975. **V.12**. N. 8. p. 3408–3419).

Radiation Effects and Defects in Solids, 1995, Vol. 134, pp. 57–64
Reprints available directly from the publisher
Photocopying permitted by license only

© 1995 OPA (Overseas Publishers Association)
Amsterdam B.V. Published under license by
Gordon and Breach Science Publishers SA
Printed in Malaysia

PROTONS IN OXIDES

C. R. A. CATLOW,[1] P. S. BARAM,[2] S. C. PARKER,[2] J. PURTON[2] and K. V. WRIGHT[3]

[1]Davy Faraday Research Laboratory, The Royal Institution of Great Britain, 21 Albemarle Street, London W1X 4BS, U.K.; [2]Department of Chemistry, University of Bath, Claverton Down, Bath, U.K.; [3]Materials Science Centre, University of Manchester and UMIST, Grosvenor Street, Manchester, M1 7HS, UK

(Received July 1, 1994)

We discuss the nature of the defects involved in the incorporation of hydrogen in oxides and silicates. We describe how computational techniques may be used to investige the structures and energies of hydrogen containing defects in these materials.

Key words: Hydrogenic defects; oxides; silicates; computer simulation

1 INTRODUCTION

There is a particularly rich and fascinating defect chemistry associated with hydrogen in oxides and silicates. Such defects may exert a controlling influence on both the chemical and physical properties of these materials. Examples include solid state proton conduction,[1] the crucial yet poorly understood mechanisms of the reaction of water with quartz[2,3] and other minerals including olivine, $[(Mg/Fe)_2SiO_4]$ where the nature and mechanisms of water dissolution are of considerable geochemical significance[4,5,6] and the role of Brønsted acid hydroxyl groups in catalytic aluminosilicates.[7] There is nevertheless relatively little knowledge of the atomistic structures and reaction mechanisms involved in water and hydrogen dissolution in these materials. This paper will describe the types of defect and defect reactions which may occur when hydrogen is incorporated in oxide and silicate systems and will emphasise the rôle computational techniques—both simulations, based on interatomic potentials and *ab initio* quantum mechanical techniques—in providing valuable quantitative information as to both the structure and stabilities of the hydrogen containing defects and to the energetics of the corresponding defect reactions. We will consider binary oxides, (specifically MgO), and a range of minerals, notably quartz, garnets, olivine and microporous catalytic aluminosilicates, which exhibit a rich variety of hydrogen containing defect chemistry.

2 REACTION MECHANISMS

Let us consider first the mechanisms whereby water may dissolve in these materials, for which there are the following five broad classes of reactions (in describing which the Kröger-Vink notation will be used):

(i) Interstitial formation

$$(H_2O)_g \rightarrow (H_2O)_I,$$

in which the water is incorporated at an interstitial site without reaction. This simple process may be of considerable importance in more open structures, especially zeolitic materials, and may be of significance in quartz.

(ii) Reaction with oxygen vacancies

$$O_0 + V_O^{\cdot\cdot} H_2O \rightarrow 2(OH)^{\cdot}.$$

Here, and incoming water molecule fills an oxygen vacancy creating an OH group after donation of a proton to another oxygen ion.

(iii) Hydrolysed cation vacancy formation

$$M_M + nO + \frac{n}{2} H_2O \rightarrow [V_M^{n+}(OH)_n] + 'MO'_{n/2},$$

where n is the charge state/valence of the cation. In these reactions, cations are displaced to the surface to form new oxide material and the appropriate number of surrounding oxygen ions are protonated (by the dissolution of water molecules) to achieve electroneutrality.

(iv) Bridging oxygen hydrolysis

$$M\diagup\!\!\!\diagup^{O}\diagdown\!\!\!\diagdown M + H_2O \rightarrow M\text{—}OH\ HO\text{—}M,$$

in which water attacks an oxygen bridging two metal atoms in a framework structure, e.g. a silicate, with resulting bond rupture and the creation of two hydroxyl groups.

(v) Protonation of basic sites

$$A'_M + O_o^x + H_2O \rightarrow (A\ OH) + OH^-,$$

where A corresponds to a low valence substitutional creating an effective negative charge which enhances the basicity of the neighbouring oxygen site which may then accept a proton from a water molecule. The remaining hydroxyl group is likely to occupy a nearby position in the structure.

We should contrast these mechanisms with those operative for hydrogen molecule incorporation for which we propose three principal classes of mechanism:

(i) Interstitial formation

$$(H_2)_g \rightarrow (H_2)_I,$$

which is of course exactly analogous to the corresponding reaction involving water, unlike the case for the following two incorporation mechanisms, which involved oxidative processes.

(ii) Oxidation of hydrogen with hole annihilation

$$2h^{\cdot} + 2O_0 + H_2 \rightarrow 2(OH)^{\cdot},$$

which requires the presence of excess holes due to acceptor impurities. Alternatively we may have:

(iii) Oxidation of hydrogen by electron creation

$$2O_0 + H_2 \rightarrow 2(OH)^{\cdot} + 2e',$$

which will of course necessitate the presence of low energy states for conduction band electrons.

We should emphasise the contrast between the *redox* processes compared with the *protonation* acid/base reactions involved in water incorporation. The remainder of this paper will concentrate on the latter reactions; but the theoretical and computational approaches described are generally applicable.

3 THEORETICAL METHODS

We use standard Mott Littleton techniques[8,9,10] and *ab initio* cluster calculations to evaluate the structures and energies of the hydrogen containing defects. The former calculations employed well establish interatomic potentials (see references 10,11,12) and the latter, *ab initio* pseudopotential LDF techniques on clusters containing between 30 and 60 atoms, with hydrogen termination of the outermost oxygen atoms. Detailed discussions are given in references 13 and 14. We note that the Mott Littleton simulations of OH containing groups treated the latter using a standard Morse potential.[15]

4 CASE STUDIES

(i) MgO

The relevant reactions here are oxygen vacancy filling and hydrolysed cation vacancy formation, which we can represent as follows:

$$V_O^{\cdot\cdot} + O_0 + H_2O \rightarrow 2(OH)^{\bullet},$$

$$Mg_{Mg} + 2O_0 + H_2O \rightarrow [V_{Mg}(OH)_2] + MgO.$$

The hydrolysed cation vacancy has two possible structures as shown in Figure 1. Calculations indicate that the linear structure has a lower energy, and the reaction energetics reported subsequently are based on the calculated energy for this species. We note that an interesting decomposition mechanism, also shown in Figure 1, has been suggested by Freund[16] for the non-linear species; it involves loss of hydrogen molecule with resulting creation of a peroxy ion trapped at the cation vacancy.

Evaluation of the energies of reaction requires use of Born-Haber cycles in which the energy of the proton transfer reaction: $O^{2-} + H_2O \rightarrow 2OH^-$, plays a key rôle. The latter energy is taken from standard theremochemical data, as discussed by Wright and Catlow[12], where there are also further details of the construction of the thermodynamic cycles.

Our Mott-Littleton calculations yield reaction of 5.8 eV for the hydrolysed cation vacancy formation reaction and 4.9 eV for the oxygen vacancy filling. We conclude therefore that even in the presence of 'acceptor' impurities, such as Li^+, which promote oxygen vacancy formation, water solubility will be low in MgO. Very low levels of $(OH)^{\bullet}$ and of $[V_{Mg}(OH)_2]$ species would, however, be expected at higher temperatures. We note also that the latter species is very strongly bound with the energy required to effect dissociation into component V''_{Mg} and OH′ defects being ~3.5 eV.

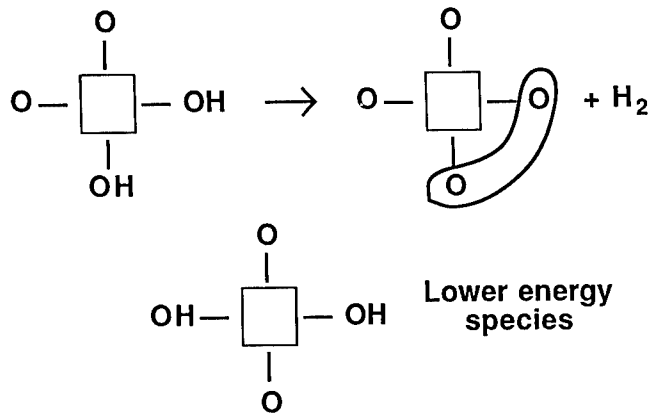

FIGURE 1 Cation vacancy—hydroxyl clusters in MgO. The proposed mechanism of H_2 loss for the non-linear cluster is indicated.

(ii) Hydrogarnet

This system acts as a test case for the ability of our methodologies to investigate vacancy defects in silicates. The hydrogarnet structure contains hydrolysed silicon vacancies. We therefore calculated the energetics of formation of these species in the grossular end member of the series.(*i.e.* $Ca_3Al_2Si_3O_{12}$)

The reaction involved can be represented as

$$Si_{Si} + 4O_0 + 2H_2O \rightarrow [V_{si}(OH)_4]$$

The relevant defect reaction energy is calculated as 0.5 eV per water molecule.[23] This low value is compatible with the ready solution of water into this material to form the hydrogarnet species. We will consider below the comparison between energy minimised structures for this defect, and those determine by crystallographic studies of hydrogarnet.

(iii) Quartz

The question of the mechanism of water incorporation in SiO_2 quartz has been extensively debated (see for example Hobbs,[2] Cordier *et al.*[3]). Several reactions are possible, of which the following are the most important: (i) hydrogarnet defect formation, (ii) bridging oxygen hydrolysis, (leading to the formation of the so-called 'Griggs defect'), (iii) the incorporation of water molecules in the channels of the quartz structure and (iv) oxygen vacancy filling. The presence of water related species is also important when considering the oxidation of silicon (Hagon *et al.*[17,18]) and the dissolution of minerals.[19]

Purton *et al.*[20] performed LDF cluster calculations, to determine the structure of the hydrogarnet defect within α-quartz. They took an $Si_5O_{16}H_{12}$ cluster constructed so that a Si atom lay at the centre. This central silicon atom was removed and each of the four surrounding oxygen atoms was protonated. The defect cluster was then relaxed to give the equilibrium configuration in Figure 2. The resulting configuration is consistent with that observed in the crystallographic studies of hydrogarnet (see reference 23.) The H atoms lie outside the volume of the oxygen tetrahedron and each H is associated with one face of the O tetrahedron. Thus two O-H distances can be observed—one at 0.99 Å and another at 1.87–1.92 Å.

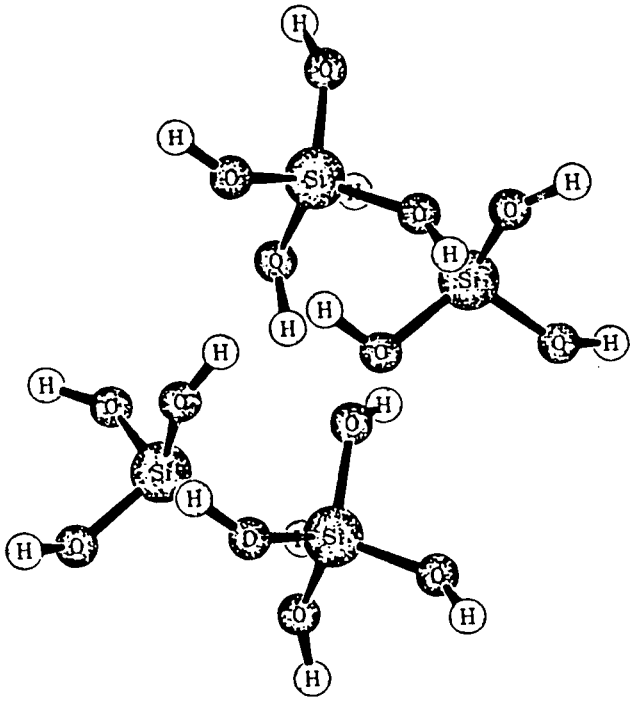

FIGURE 2 The calculated equilibrium geometry for the hydrogarnet defect.

LDF cluster calculations were also performed on a 54 atom ($Si_8O_{26}H_{20}$) cluster constructed to simulate the 'Griggs defect', (Heggie *et al.*,[21]). The central bridging oxygen atom was hydrolysed as discussed in section 2. The equilibrium structure obtained has the two hydroxyl groups in a plane with the hydrogen atoms pointing away from one another. By calculating the total energy of the cluster containing the 'Griggs' defect and that of a cluster of ideal quartz and an isolated molecule, an energy for the hydrolysis of the bridging oxygen bond was determined to be 2.3 eV. Further calculations involving larger clusters (approximately 150 atoms) are being undertaken to exclude effects due to boundary conditions.

Atomistic simulations were performed on the hydrogarnet and 'Griggs' defects in α-quartz and in both cases an equilibrium geometry similar to the *ab initio* calculations was observed. One advantage of the atomistic simulations is that defect formation energies are readily obtainable. Furthermore, because of the consistent nature of the parameters used, we may compare the two formation energies in order to determine which of the competing species is likely to be the most stable. The defect reaction energies for formation of the hydrogarnet and 'Griggs' defects are 2.86 and 3.52 eV per H_2O indicating that the hydrogarnet defect is the more stable. Further work is, however, needed on this problem.

If 'acceptor' (i.e. low valence) cationic impurities such as Al, are present, incorporation of water by oxygen vacancy filling becomes a possibility. We therefore investigated the energetics of this reaction:

$$O_O + V_O^{\cdot\cdot} + H_2O \rightarrow 2(OH)^{\cdot},$$

for which we calculated a negative energy (–2.01 eV). Thus in the presence of even low partial pressures of water vapour, Al impurities in quartz will in effect be compensated by

OH species. An extensive study of these species was reported by Sim *et al.*[22] They found that the proton is strongly stabilised on oxygen sites adjacent to the Al; its energy on more distant sites is ~1.8 eV higher. Interestingly the proton can be exchanged for other cation species e.g. Li^+ and Na^+.

Finally we should consider dissolution of water molecules in the channels of the quartz structure. Quantum mechanical studies of the structures and energies of water molecules in quartz were reported by Hagon *et al.*[17,18] Energies of ~2 eV were calculated for the dissolution energy suggesting that such processes could be significant.

(iv) Olivine

The extent of water solubility in olivine has been extensively debated, as has the nature of the resulting defect species (Miller *et al.*,;[4] Bell and Rossman;[5] Bai and Kohlstedt.[6] Let us consider first the three obvious reactions; i.e. hydrogarnet defect formation, vacancy filling and hydrolysed magnesium vacancy formation, for which the calculated energies per incorporated water molecule are given in Table I.

The energies of reaction for the formation of the two hydrolysed vacancy defects are high (>3 eV per water molecule). Oxygen vacancy filling is again an exothermic process; but since this material is not normally significantly contaminated with acceptor impurities, oxygen vacancy concentrations are expected to be low.

We therefore considered a fourth possible mechanism for the solution of water in this material. It involves a redox process in which Fe^{3+} at magnesium sites (a species which is known to be present in appreciable concentrations) is reduced to Fe^{2+} by the dissolving water, i.e.

$$2Fe^{\cdot}_{Mg} + 2O_o + H_2O \rightarrow 2Fe_{Mg} + 2(OH)^{\cdot} + \frac{1}{2}O_2$$

The calculated energy of 0.46 eV is substantially lower than that calculated for formation of either of the hydrolysed cation vacancies, and we suggest that this process is the main mechanism of water incorporation in olivine. Our suggestion is consistent with the observed enhancement of water solubility in olivine by iron impurities. Further discussion of these calculations is given by Wright and Catlow.[23]

(v) Pervskite structured oxides

Acceptor doped materials with the persovskite or related crystal structures are being used increasingly as proton conductors—materials which are of considerable importance in

TABLE I
Defect reactions (eV) for H_2O incorporation in olivine

1.	Hydrogarnet defect formation: $2H_2O + Si_{Si} \rightarrow [V_{Si}(OH)_4] + \text{'}SiO_2\text{'}$	E = 6.1 (= 3.05 per H_2O)
2.	Vacancy filling: $O_o + V_{\ddot{O}} + H_2O \rightarrow 2(OH)^{\cdot}$	E = –1.24
3.	Hydrolysed cation vacancy formation $Mg_{Mg} + 2O_o + H_2O \rightarrow [V_{Mg}(OH)_2] + \text{'}MgO\text{'}$	E = 3.7
4.	Reduction of Fe^{3+} with protonation of oxygen $2Fe^{\cdot}_{Mg} + 2O_o + H_2O \rightarrow 2Fe_{Mg} + 2(OH)^{\cdot} + \frac{1}{2}O_2$	E = 0.46

fuel cell technology. Examples are provided by Yb doped $SrCeO_3$ (Iwahara *et al.*[24]) and Fe^{3+} doped $KTaO_3$ (Scherban and Nowick[25]) which show proton conductivity after reaction with water. OH groups are introduced by the standard vacancy filling reaction (the vacancies being present as charge compensators for the dopants). Protons can the migrate between oxygen ions by a tunnelling process. Recent calculations of Cherry *et al.*[26] have suggested that the barrier for proton transfer between neighbouring oxygen ions is low. Embedded quantum mechanical cluster techniques were used to investigate the processes in $LaAlO_3$ with the two nearest neighbour oxygens ions and neighbouring Al ions being described quantum mechanically using high quality basis sets. Hartree-Fock CI calculations were performed, and yielded migration barriers of <0.1 eV. Tunnelling through such small barriers would be expected to be a rapid process. The activation energy cannot be equated with the barrier energy discussed above; rather, it is associated with the lattice relaxation energy required to create an equivalent environment around both the sites involved in the tunnelling process. Calculations of this energy term are in progress.

(vi) Acidic Sites in Aluminosilicates and Related Materials

We have seen that Al doped quartz will normally contain charge compensating protons present in well defined Al-OH complexes. The same species are found in the fascinating group of microporous aluminosilicates known as zeolites which have been extensively studied over many years owing to their unique catalytic properties (see e.g. Thomas,[7] and Newsam[27]). Much of the catalytic behaviour of these materials can be attributed to the presence of Brønsted acid centres; the microporous architecture, however, controls the nature of the reactions and products giving rise to the phenomenon of shape selective acid catalysis. For this reason the properties the Brønsted acid centres in these materials have been intensively studied by both theoretical and experimental techniques. For example, work of Schroder *et al.*[28] used Mott-Littleton techniques to characterise the Al-OH centre in Zeolite Y—the widely used hydrocarbon cracking catalyst. Calculations of vibrational frequencies of the OH group are in good agreement with the experimental data. Quantum mechanical techniques have also been extensively used in modelling acid centres in zeolites and their interaction with small molecules (see, for example, the review of Sauer,[29] and the recent work of Gale *et al.* [30]).

There has also been speculation on the rôle of hydrogarnet defects (referred to in the context of zeolite science as 'proton nests') in these solids. Further experimental and theoretical studies will be needed to assess the importance of such species in Zeolites.

5 SUMMARY AND CONCLUSION

This paper has illustrated the important and pervasive nature of hydrogen containing defects in oxide materials. It has also demonstrated the significant contribution which can be made by theoretical and computational techniques in advancing our understanding of these complex defects.

ACKNOWLEDGEMENTS

We are grateful to several colleagues for useful discussion, notably A. M. Stoneham, J. M. Thomas, G. D. Price, D. W. Lewis, M. Cherry and M. S. Islam. We are also grateful to R. Jones and M. Heggie for permission to quote unpublished results.

REFERENCES

1. H. Iwahara, *Solid State Ionics*, **53–56**, 575, 1992.
2. B. E. Hobbs, *J. Geophysical Research*, **89**, 4026, 1984.
3. P. Cordier, B. Boulogne and J. C. Doukhan, *Bull. Mineral*, **111**, 113, 1988.
4. G. H. Miller, G. R. Rossman and G. E. Harlow, *Phys. Chem. Minerals*, **14**, 461, 1990.
5. D. R. Bell and G. R. Rossman, *Science*, **225**, 1391, 1990.
6. Q. Bai and D. L. Kohlstedt, *Nature*, **357**, 672, 1992.
7. J. M. Thomas, April issue 1992 *Scientific American*, **266**, 85–88.
8. N. F. Mott and M. J. Littleton, *Trans. Farad. Soc.* **34**, 485, 1938.
9. C. R. A. Catlow and W. C. Mackrodt, (Eds) 1982, 'Computer Simulation of Solids', Lecture Notes in Physics vol. **166** (Springer, Berlin).
10. J. H. Harding, *Rep. Prog. Physics*, **53**, 1403, 1990.
11. M. J. Sanders, M. Leslie and C. R. A. Catlow, *Chem. Soc., Chem. Comm.* **1271**, 1984.
12. K. V. Wright and C. R. A. Catlow, *Phys. Chem. Mineral*, **20**, 515, 1994.
13. R. Jones, *J. Phys. C.* **21**, 5735, 1988.
14. R. Jones, *Molecular Simulation*, **4**, 113, 1989.
15. P. Saul, C. R. A. Catlow and J. Kendrick, *Phil. Mag.* **B51**, 107, 1985.
16. F. Freund, 1989, *Advances in Solid State Chemistry* (ed. C. R. A. Catlow) vol. I. JAI Press.
17. J. P. Hagon, A. M. Stoneham and M. Jaros, *Phil. Mag.* **55**, 221, 1978a.
18. J. P. Hagon, A. M. Stoneham and M. Jaros, *Phil. Mag.* **55**, 225, 1987a.
19. A. C. Lasaga, *Reviews of Geophysics*, **30**, 269, 1992.
20. J. Purton, R. Jones, M. Heggie, S. Öberg and C. R. A. Catlow, *Phys. Chem. Minerals*, **18**, 389, 1992.
21. M. Heggie, R. Jones and J. Purton, 1995, to be published.
22. Sim F.& Catlow CRA., Int. J. Quantum Chem (Quantum Chem Symp), **23**, 651 (1989)
23. K. V. Wright, R. Freer and C. R. A. Catlow, *Phys. Chem. Mineral*, **20**, 500, 1994.
24. H. Iwahara, T. Esaka, H. Uchida and N. Maeda, *Solid State Ionics*, **3–4**, 359, 1984.
25. J. Scherban and A. S. Nowick, *Solid State Ionics*, **53–56**, 1004, 1992.
26. M. Cherry, M. S. Islam and C. R. A. Catlow—to be published.
27. J. M. Newsam, 1992 in 'Solid State Chemistry—Techniques: (eds. Cheetham, A. K. and Day, P.), Oxford University Press.
28. K-P. Schröder, J. Sauer, M. Leslie, C. R. A. Catlow and J. M. Thomas, *Chem. Phys. Lett.* **188**, 320, 1992.
29. J. Sauer, 1992, in 'Modelling of Structure and Reactivity in Zeolites' (ed. C. R. A. Cartlow) p. 183 Academic Press, London.
30. J. D. Gale, C. R. A. Catlow and J. R. Carruthers, *Chem. Phys. Lett.*, **216**, 155–161, 1993.

Radiation Effects and Defects in Solids, 1995, Vol. 134, pp. 65–68
Reprints available directly from the publisher
Photocopying permitted by license only

© 1995 OPA (Overseas Publishers Association)
Amsterdam B.V. Published under license by
Gordon and Breach Science Publishers SA
Printed in Malaysia

ELECTRONIC STRUCTURE OF INTRINSIC AND IMPURITY Mn-CENTRES IN A_2BX_4 CRYSTALS WITH β-K_2SO_4 TYPE STRUCTURE

I. BOLESTA, I. KITYK, Y. FURGALA and S. VELGOSH

Department of Physics, Lviv State University, 50, Dragomanova St., Lviv, UA290005, UKRAINE

A_2BX_4 single crystals (A = Cs, Rb, $N(CH_3)_4$; B = Cd, Zn, Mn, Fe; X = Cl, Br, I) with β-K_2SO_4 type structure belong to the compounds with the different phase transitions (PT), including PT into incommensurate structure. The persistence of the transitions metals play an important role in the investigations of PT by the ligands field in the types of crystals, in particular, in the vicinity of phase transition. The nature of the corresponding phase transitions is closely connected with the tetrahedral complexes $[B^{2+}X_4]^{2-}$ bounded by A^- cations. The Mn^{2+} ions were chosen due ithe persistence of the five external d-electrons, which are highly sensitive to the external fields. The present work deal with experimental and theoretical investigation of the electronic band structure and optical parameters of $[N(CH_3)_4]_2$ $MnCl_4$ and Cs_2CdI_4 single crystals.

Key words: Band structure, impurity and intrincis centres.

1 INTRODUCTION

The energy parameters of $[N(CH_3)_4]_2$ $MnCl_4$ and Cs_2CdI_4 single crystals were calculated using the tight binding method. Exchange-correlational effects were treated within the local density approximation. Interpolation formulas were used for the exchange-correlation potential obtained for $r_s > 1$ in[1] and for $r_s < 1$ in[2] in a form parametrized by Perdew, where tivistic effects (mass velocity and Darvin terms) were also in the calculation.

The crystal volume was subdivided into Wigner-Seitz spheres which surrounded each atom. Within each sphere the potential was taken spherically symmetric. The set of basis functions which have been used consisted of 2s, 2p N; 2s, 2p C; 3s, 3p Cl; $3d^5$ Mn^{2+} functions for $[N(CH_3)_4]_2MnCl_4$ and 5s, 5p I; 5s, 5p Cd; 6s Cs for Cs_2CdI_4. Atomic positions, crystal structure, radial atomic functions and Wigner-Seitz radii, which were equal to 0.192 nm for N, to 0.180 nm for C, 0.176 nm for Mn and to 0.210 nm for Cl were used as the input parameters. The coincidence of the two following energy values within 0.019 a.u. was chosen as a concordance criterion. Phonon subsystem was taken into account using Green function technique.

The potentials were presented as superpositions of the ion potentials and the selfconsistent potential due to the existence of the others electrons. The latter is formed by the Hartree term V_m obtained exactly from Poissons equation and the Slater exchange-correlation term V_{xc}. The starting potential was unscreened. Simultaneously the contribution of the electron-phonon interaction was investigated.

2 RESULTS AND DISCUSSION

Figure 1 and Figure 2 show the energy band structure of Cs_2CdI_4 single crystals for β-K_2SO_4 and Sr_2GeS_4 crystalline type respectively. One can see, that the valence band of these crystals are formed by s^- and p^- iodine orbitals, while the conduction bands are connected with s^- orbitals of ceasium and s^- and p^- orbitals of cadmium. The calculated

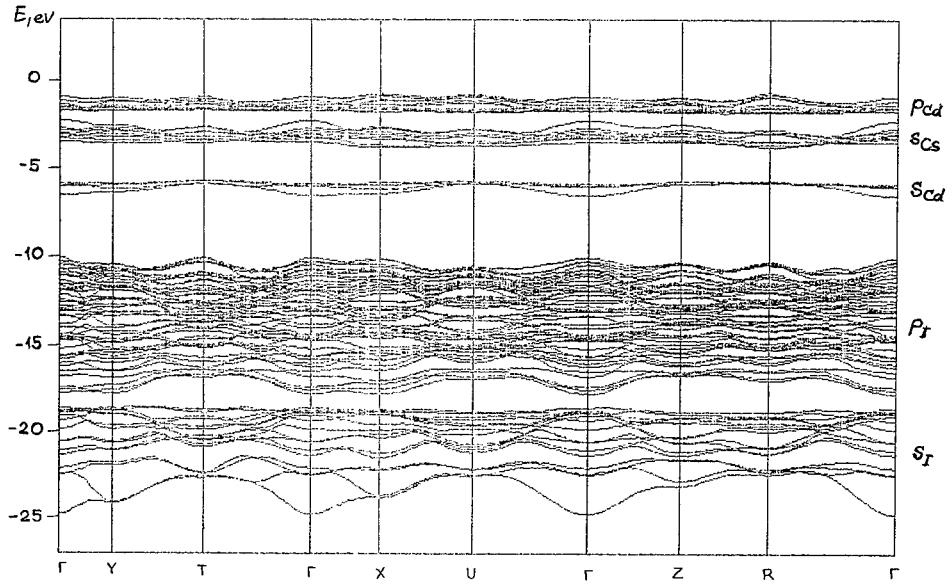

FIGURE 1 Electronic band structure of Cs_2CdI_4 single crystals with β-K_2SO_4 crystalline type.

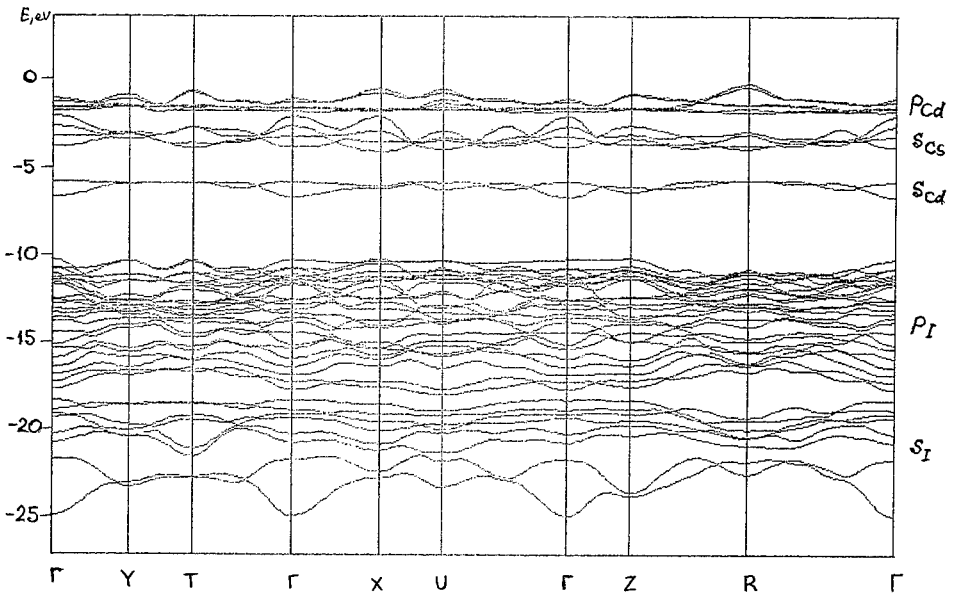

FIGURE 2 Electronic band structure Cs_2CdI_4 single crystals with Sr_2GeS_4 crystalline type.

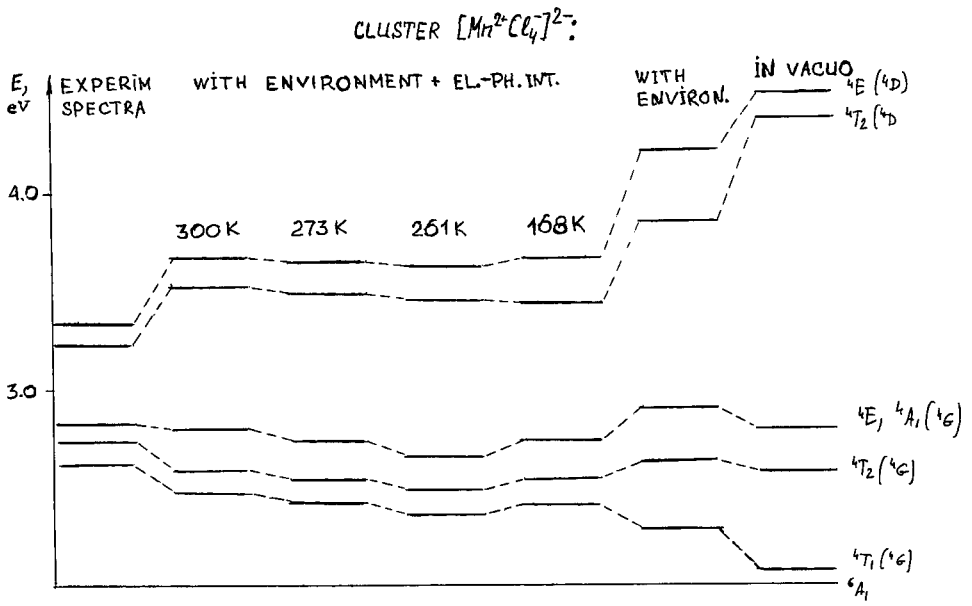

FIGURE 3 Electronic structure of $[Mn^{2+}Cl_4^-]^{2-}$ cluster in $[N(CH_3)_4]_2\ MnCl_4$ single crystals.

results show, that Cs_2-CdI_4 single crystals posses indirect interband transitions, since, the maximum of valence band is located in Γ-point in Brilluwen zone and the minimum of conductive band near T-point for β-K_2SO_4 type structure and near Z-point for Sr_2GeS_4 type structure. The calculated value of E_g is equal: 3.53 and 3.59 eV in Γ-point for β-K_2SO_4 and Sr_2GeS_4 crystalline type respectively, and 3.51 for both type structures for the shortest interband transitions. The PT in Cs_2CdI_4 from β-K_2SO_4 to Sr_2GeS_4 crystalline type causes the shift of valence band maximum from Z- to T-point.

$[Mn^{2+}Cl_4]^{2-}$ clusters are the structure elements of $[N(CH_3)_4]_2\ MnCl_4$. The calculations were performed for the different types of the clusters: cluster in vacuo, cluster with environment and the clusters with the accounting of the electron-phonon interaction. Besides the positions of the energy terms for different temperatures T = 273 K, T = 261 K and T = 168 K, which correspond to the different crystalline phases was investigated. The obtained results are presented in Figure 3. Coming out from the obtained results the main features of the optical spectra were calculated. It was revealed that only the accounting of the electron-phonon interaction can give the results which are in good accordance with experiment. From the same figure one can see that all the optical transitions occur from the ground state $^6A_1$. The phase transitions have a great influence on the positions of the main term energy positions.

All the obtained data indicate an important role of the electron-phone interaction in the formation of the optical spectra in A_2BX_4 single crystals with the transitional metals.

ACKNOWLEDGMENT

This work was supported by the State Commetee of Science and Technology of Ukraine.

REFERENCES

1. D. M. Ceperley, B. J. Alder, *Phys. Rev. Letters*, **45**, 566 (1988).
2. M. Gell-Mann, K. A. Brueckner, *Phys. Rev.*, **106**, 364 (1957).

Radiation Effects and Defects in Solids, 1995, Vol. 134, pp. 69–73
Reprints available directly from the publisher
Photocopying permitted by license only

© 1995 OPA (Overseas Publishers Association)
Amsterdam B.V. Published under license by
Gordon and Breach Science Publishers SA
Printed in Malaysia

ELECTRONIC STRUCTURE OF A LiB_3O_5 NONLINEAR OPTICAL CRYSTAL

A. Yu. KUZNETSOV, A. B. SOBOLEV, I. N. OGORODNIKOV
and A. V. KRUZHALOV

Experimental Physics Department, Urals State Technical University, 620002 Ekaterinburg, Russia

(Received July 1, 1994)

The electronic bands of a LiB_3O_5 (LBO) crystal with excellent nonlinear optical properties have been studied using the scattered-wave method in embedded-cluster model. Calculations were carried out for a $[B_3O_7]^{5-}$ cluster, as this anionic group is the crystal basic structural unit. The interpretation of experimental photoemission spectra is based on electronic structure cluster calculations. From calculation performed, it follows that the contribution of trigonal and tetrahedral boron-oxygen groups dominates in the electronic structure of LBO, the contribution of $2p$-boron states is immaterial.

Key words: Lithium triborate, LiB_3O_5, electronic structure, cluster calculation.

1 INTRODUCTION

Lithium triborate LiB_3O_5 (LBO) is a new nonlinear optical material enjoying different applications such as second harmonic generation, optical parametric oscillators, optical wave-guide devices, etc. Another important characteristic of LBO is the extent of its transparency range, from 160 to 3500 nm, which makes it useful for application in the deep ultraviolet range. LBO crystallizes in a complex orthorhombic cell with four formula units per cell.[1] The space group is $Pna2_1$, with the crystal parameters $a = 8.46$ Å, $b = 5.13$ Å, and $c = 7.38$ Å. It is well known that boron can be bound by either three or four oxygen atoms to form two structurally different molecular units, a trigonal BO_3 group and a tetrahedral BO_4 group. Nonlinear optical and spectroscopic properties of a number of borate materials depend largely on the unique way in which the two base units combine because of different electronic bonding characteristics of these base groups. Therefore, a thorough understanding of the relationship between the electronic bands and the crystal structure is very important.

2 CALCULATION DETAILS

We studied the valence-band (VB) structure of LBO by X-ray photoemission spectroscopy (XPS) using large crystals of high optical quality.[2] The interpretation of photoelectron spectra is based on the electron structure cluster calculations. We used a scattered-wave method in an embedded-cluster model[3,4] to determine the VB density of electronic states. Since the crystal structure of LBO is not simple, the cluster approach is the preferred method for analyzing the electronic bands of this material.[5] Calculations were carried out on $[B_3O_7]^{5-}$ cluster, as this anionic group is a basic structural unit of the crystal being studied (C_{2v} point group symmetry) (Figure 1). This anionic group consists of one tetrahedral BO_4 unit and two plane trigonal BO_3 units. These two types of borate group are linked to form a B—O network, the Li atoms are located at a open interstitial site of the network. The nearest-neighbor (NN) B—O bonding distance is between 1.37 (trigonal bonds B—O) and 1.47 (tetrahedral bonds B—O) Å. The NN Li—O bonding distance are much larger, ranging

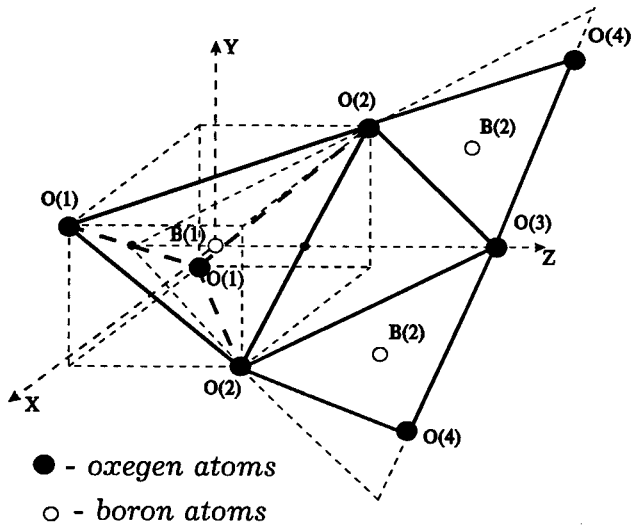

FIGURE 1 The anionic group of $[B_3O_7]^{5-}$ for LiB_3O_5.

from 1.98 to 2.18 Å. The interaction between the *Li* cation and the $[B_3O_7]^{5-}$ group is neglected in our analysis. The cluster potential was taken in the 'muffin-tin' (MT) approach. The radii of cluster MT-spheres were taken R_O=1.06 Å and R_B=0.40 Å. The self-interaction correction potential was performed in the Vosko-Vilk-Nusair form.[6] The calculations were self-consistent.

3 CALCULATION RESULTS AND DISCUSSION

In Figure 2 we show the energy levels of cluster molecular orbitals (MO). From Figure 2 it follows that the filled states the MO of a $[B_3O_7]^{5-}$ cluster form two well-defined groups. One includes MO lowest energy ($1a_1$, $2b_1$,...,$4a_1$) and is due to the hybridization *O2s* MO (core-like states). The second group of MO ($1a_2$, $5a_1$,...,$3a_2$) is formed by *O2p* states split in the crystal field and belong to the 'upper' VB (UVB) of a perfect crystal. The whole UVB can be subdivided into three subgroups. A dominant contribution to the orbitals of the top UVB is made by nonboding π-type 2*p* MO ($6b_1$,...,$3a_2$) of *O*(1) and *O*(2) atoms. The middle UVB orbitals is constituted mainly by different types of 2*p* MO ($4b_2$,...,$7b_2$) of *O*(3) and *O*(4) atoms. Finally, the bottom UVB consist of bonding σ-type 2*p* MO ($1a_2$,..., $3b_2$) of *O*(1) and *O*(2) atoms.

Our results agree qualitatively with other cluster calculation.[7] Our data and the results of Ref. 7 coincide in the numbers of identical symmetry states for each group but differ in sequence within each group. In contradistinction to our conclusions, the authors of Ref. 7 have interpreted the MO $2b_2$, $4a_1$, $7b_2$,..., $3a_2$ as formed by dangling bonds due to the bonds of quantum cluster and the rest of crystal. Therefore the above authors exclude the contribution that these states make to the formation of the electronic structure of the crystal as a whole. The discrepancies that have arisen can be explained by features peculiar to the models used. Thus Ref. 7 disregarded the Coulomb contributions by the rest of crystal, a fact which should lead to distortion of the Coulomb potential for periphery cluster ions.[5]

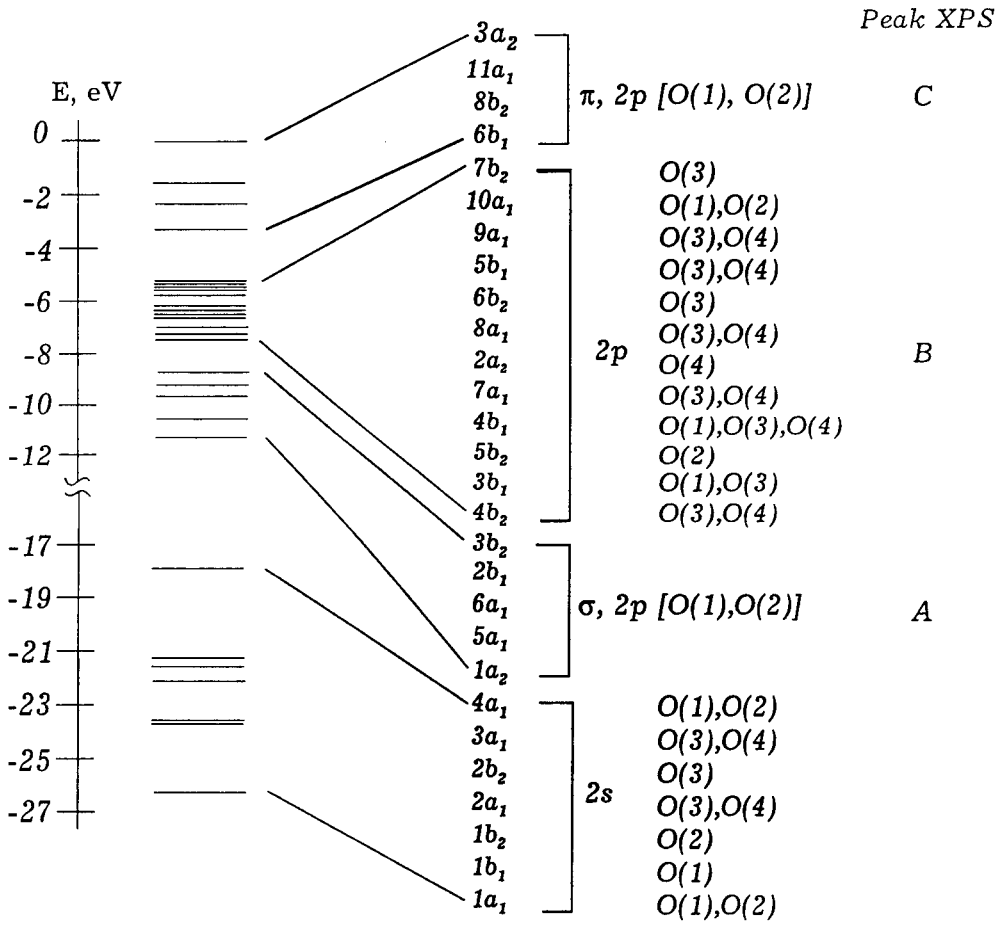

FIGURE 2 The energy diagram of the $[B_3O_7]^{5-}$ cluster.

The calculation that we have performed shows that the partial densities of states (PDOS) of $O(1)$ and $O(2)$ atoms (tetrahedral position) are close to one another, Figure 3. An analogous conclusion may be drawn about the similarity of the PDOS of $O(3)$ and $O(4)$ atoms (trigonal position). At the same time the PDOS of $O(1)$ atoms differs considerable from that of $O(3)$ atoms. In terms of the energy band structure one can talk of the nonequivalence of pairs of oxygen atoms in tetrahedral and trigonal positions. To prove this, we calculated Madelung-type potential contributions, witch are an anion-position potential induced by a point lattice. The data obtained ($O(1)$, $O(2)$ and $O(3)$—31.4 eV, $O(4)$—32.7 eV) show that the Coulomb contributions to the anion-position potentials of an LBO crystal are approximately the same, a circumstance that does not permit one to speak of the nonequivalence of the energy structure of anions. Therefore, nonequivalence of the DOS of oxygen ions occupying tetrahedral and trigonal positions stems from the peculiar position of ions in a $[B_3O_7]^{5-}$ cluster or, put in other words, from features peculiar to the structure of the base crystal unit of LBO, i.e., the anion group $[B_3O_7]^{5-}$. This assumption agrees with the conclusions of Ref. 8. Note also that according to calculation, the boron atoms make only an immaterial contribution to the formation of LBO crystal's valence band.

The charge distribution corresponding to a $[B_3O_7]^{5-}$ cluster is presented in the below Table. The charges for the corresponding region have been obtained by integration of the electron density function determined for these regions. The electronic charge equal to 8.52 is localized in the intersphere region. Such electron density behavior comes from a relatively large charge delocalization in the anion MT-spheres. The anion sphere effective charge ranges from 0.73 to 0.91, values which differ from the hypothetic oxygen ionic charge in this material, –2. A tendency for a greater delocalization of the anion electronic charge is also observed at other values of MT-radius. The greater delocalization of the anion electronic charge may be connected with an electron that has left an anion sphere, as it is the case with *MgO*.[9]

TABLE I
The electronic charge distributions $[B_3O_7]^{5-}$ cluster (in electron charge unit)

region	nuclear charge	electronic charge	MT-radius, Å
B(1)	5	1.98	0.40
B(2)	5	1.98	0.40
O(1)	8	8.73	1.06
O(2)	8	8.73	1.06
O(3)	8	8.86	1.06
O(4)	8	8.92	1.06
Q_i	0	8.52	—
Q_{out}	0	0.01	4.94

Q_i—intersphere charge; Q_{out}—outside cluster charge

The data on molecular orbitals (Figure 2) forming the electron structure of a $[B_3O_7]^{5-}$ cluster permit unambiguous identification of XPS data. In Figure 3 we show DOS a PDOS of a $[B_3O_7]^{5-}$ cluster against experimental valence band XPS. The cluster's energy structure give a good fit to experiment. Thus, the gap between the 'lower' VB and the UVB is equal 6.54 eV. The centre of the 'lower' VB lies near energies ~ –24 eV with respect to 'absolute' zero. This is in quantitative agreement with XPS data. The top-middle and middle-bottom gaps in the UVB are equal to 1.83 and 1.19 eV, respectively. In according calculation, the width of the UVB is ~11.5 eV Such a structure of the UVB good fits with the XPS spectrum. Peak A (Figure 3 (a)) is due mainly to the superposition of the bonding σ-type $2p$ MO of tetrahedral-coordination anions. A dominant to peak B is made by trigonal-coordination anions, while peak C is formed chiefly by nonbonding π-type MO of tetrahedral-coordination anions. The contribution to the XPS peak due to core-like states $O2s$ comes from the MO formed by the $O2s$-states of all anion type. Note that according to calculations, a minigap of 1 eV exists between the $2s$ MO of tetrahedral- and trigonal-coordination anions. Possibly, it is fact that explains the presence in the XPS spectrum of a 'shoulder' in core-like $O2s$ band from the lower-energy side (Figure 3 (a)).

4 CONCLUSIONS

Thus the energy band structure calculations performed in this study of a perfect crystal LBO give a good fit to experimental data, permitting us to assert that the proposed model and the scattered-wave method are adequate in simulating the electronic structure of the crystal involved. The computed electronic structure shows a close relationship between energy band structure and crystallography structure for LBO. The results obtained

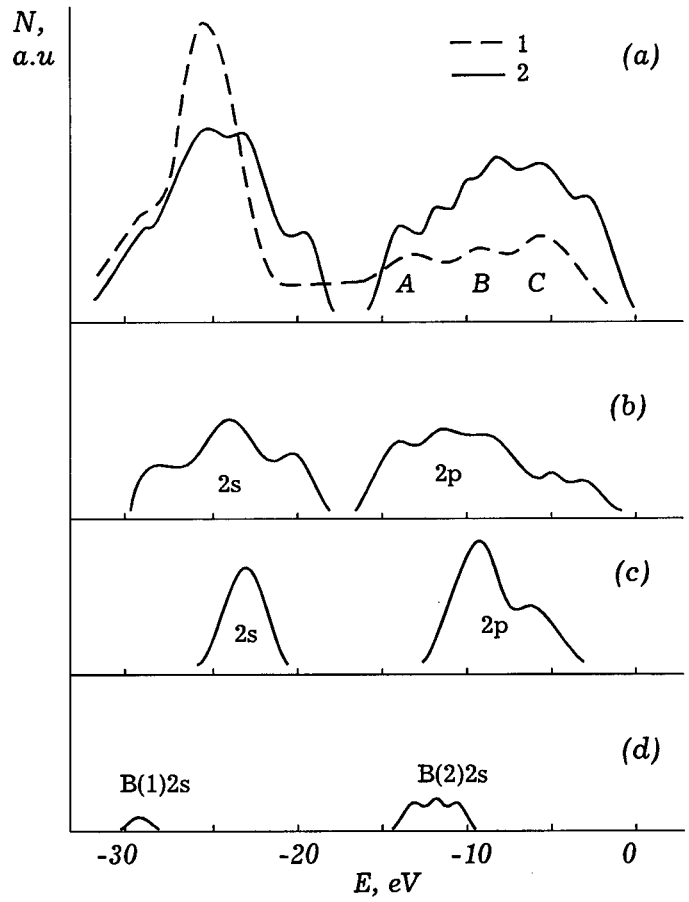

FIGURE 3 (a) Valence band XPS spectrum for LBO (1) and culculated valence band (2). Calculated PDOS: (b) $O(1)$, $O(2)$ atoms, (c) $O(3)$, $O(4)$ atoms, and (d) $B(1)$, $B(2)$ atoms.

substantiate the possibility of extending our models to include point defects calculations for LBO crystals, the goal of our subsequent research.

REFERENCES

1. H. König and A. Hoppe, *Z. Anorg. Allg. Chem.* **439**, 71 (1978).
2. A. Yu. Kuznetsov, M. V. Kuznetsov, I. N. Ogorodnikov, A. V. Kruzhalov A. V., and V. A. Maslov. *Fizika Tverdogo Tela.* **36**, 845 (1994).
3. V. A. Lobatch, A. B. Sobolev, I. R. Rubin. *Phys. Stat. Sol. (b).* **60**, 165 (1990).
4. A. B. Sobolev, S. M. Erukhimovich, V. S. Startsev, and O. A. Keda . *Zurnal strykturnoy khimii.* **32**, 17 (1991).
5. K. H. Jonson *Adv. Quant. Chem.* **7**, 143 (1973).
6. S. H. Vosko, L. Vilk, and N. Nusair. *Can. J. Phys.* **58**, 1200 (1980).
7. R. H. French, J. W. Ling, F. S. Ohuchi, and C. T. Chen *Phys. Rev. B.* **44**, 8496 (1991).
8. W. Y. Hsu, R. V. Kasowski *J. Appl. Phys.* **73**, 4101 (1993).
9. V. A. Lobach and I. R. Rubin *Phys. Stat. Sol. B.* **160**, 505 (1990).

Radiation Effects and Defects in Solids, 1995, Vol. 134, pp. 75–77
Reprints available directly from the publisher
Photocopying permitted by license only

© 1995 OPA (Overseas Publishers Association)
Amsterdam B.V. Published under license by
Gordon and Breach Science Publishers SA
Printed in Malaysia

OXYGEN VACANCY IN PEROVSKITE OXIDES: ELECTRON STRUCTURE CALCULATION BY THE SCF Xα SW TECHNIQUE

M. A. BUNIN, S. A. PROSANDEYEV, I. I. GEGUSIN, I. M. TENNENBOUM

Institute of Physics, Rostov State University, 194 Stachky Ave, Rostov on Don 344104, Russia

(Received July 1, 1994)

The electron structure of the oxygen vacancy in $SrTiO_3$ has been computed for the first time in frames of the approach that does not use a basis. The SCF Xα SW technique is used for this purpose. The clusters considered have 4 coordination spheres included. A satisfactory agreement with experiment is obtained for the cluster modeling the ideal crystal.

It is found that the lowest unoccupied state of the cluster modeling the double-charged oxygen vacancy V_o^{++} is of the a1g symmetry, and it is localized in the sphere of vacant site for 34%, in cation spheres -for 20%. The potential reaches its maximum value in the vicinity of vacancy center. It means that a strong localization of an a_{1g}-state in the vicinity of V_o^{++} is possible only due to the multiple scattering of the electron wave at the nearest neighbors. Perovskite, oxygen vacancy, electronic structure.

Key words: Oxygen vacancy, oxides, electronic structure

The outstanding importance of the oxygen vacancies (V_o) in the formation of numerous significant features of perovskite oxides has been repeatedly confirmed by the experiments. Still there are only few theoretical studies implemented mainly by the tight-binding or by the discrete variational Xα methods [1–4]. We are aware of the only calculation of the V_o-features in $YBa_2Cu_3O_7$ [5] that has been performed non-selfconsistently and in frames of an approach that makes no use of a basis. The merits of tight binding method are well known, however the choice of a proper basis poses a difficult problem (for discussion of this point, see [6]). Here, the first results of a V_o-calculation in $SrTiO_3$ by the SCF Xα SW technique that makes no use of a basis, are presented. Recently this approach has been successfully applied by us to the KCl F-center calculation [7].

The clusters $(OTi_2O_8Sr_4O_2)^{6-}$ and $(Ti_2O_8Sr_4O_2)^{(6+n)-}$ considered, consist of: the central oxygen atom or an empty sphere of the same radius replacing it, and 16 atoms of its nearest neighbourhood. The charge of the whole cluster depends on the number of electrons at the V_o site: n = 1 for the single-charged vacancy V_o^+ occupied by 1 electron; n = 2 for the double-charged vacancy V_o^{++}. The α-constants for exchange are taken from the well known paper by Schwarz. The value of α used for the empty sphere is the same as for the oxygen atom. The computations had been carried out until the electron density difference at two subsequent iterations is less than 0.01 a.u. The MT-spheres radii for O-, Ti-, and Sr-atoms are equal to 2.14, 1.55, and 2.98 a.u., respectively. The cores had not been frozen.

The core energies of oxygen atoms entering the different co-ordination spheres of the cluster that models the ideal crystal, differ less than for 0.03%. The energies of the semicore levels Sr 4p, O2s, Sr4s, and Ti 3p agree satisfactorily with the experiment (theoretical values 1.11, 1.06–1.21, 2.33, 2.56 Ry may be compared with the experimental ones [8] 1.20, 1.18–1.27, 2.48, 2.51, respective to the valence band top). The with 3.0 eV of the forbidden gap computed for this cluster is close to the experimental value of 3.2 eV.

The one-electron level diagrams for all clusters considered are displayed in Figure 1. The uppermost occupied levels of the valence 'bands' are coincided. The corresponding

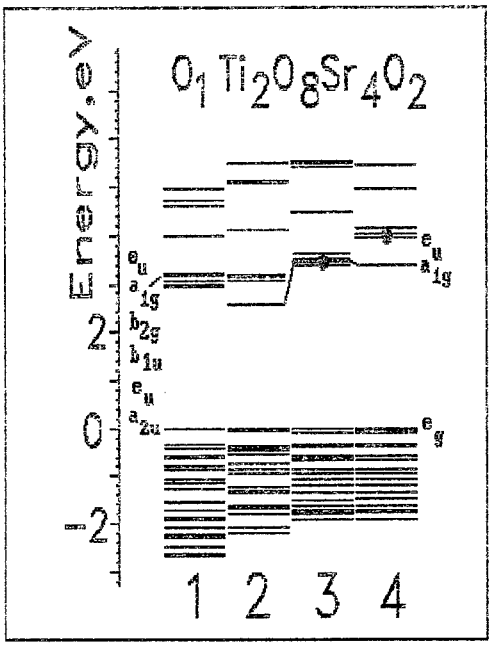

FIGURE 1. One-electron level diagram for the cluster $OTi_2O_8Sr_4O_2$, that models the ideal crystal (1), and for the cluster , $\square Ti_2O_8Sr_4O_2$, that models the crystal with V_o^{++} (2), and with V_o^+ in the state a_{1g}^1 (3) and e_u^1 (4).

absolute energies computed are as follows: –0.41, –0.67, –0.63, –0.62 Ry. The constant values of the potential within the cluster intersphere region are equal to –0.45, –0.45, –0.47, –0.47 Ry, respectively.

The lowest unoccupied state is featured by a_{1g}-symmetry for the V_o^{++} -cluster. Its wave function is localized in the central sphere for 34% (s-type relative to the center), in the Ti-spheres for 20% (dσ-states), in oxygen spheres for 26% and in the intersphere region for 16%. Since there is no positive charge within the central sphere V_o, the potential reaches its local maximum value at the center (Figure 2).

The electron structure of V_o^+-cluster is featured by the following peculiarity: if a_{1g} state is occupied by an electron, its energy is slightly (for 0.006 Ry) higher than the unoccupied, dπ–states energy (Figure 1), while if the lowest dπ -state is occupied, it appears higher than the a_{1g}-level (Figure 1). It is clear that these results must be made more accurate by means of a computation accounting for the spin. This work is now in progress.

As a result of these computations, an unique situation is revealed. It appears that two, closely lying quantum states of different origin may co-exist in the electron spectrum of $SrTiO_3$. One of them is mainly formed by multiple scattering of electron wave at the atoms surrounding the V_o-center. This scattering ensures a state localized predominantly in the central empty sphere and at the two nearest cations may exist, despite the potential reaches its maximum value in the vicinity of V_o. On the contrary, the second state assumed cannot be featured by s-type symmetry respective the central sphere. It is formed chiefly as a result of V_o electric field acting on the nearest cations [1,2]. This state is predominantly localized at the cations which are the nearest ones to the V_o-center. Apparently, the further experimental and theoretical developments of this topic are desirable.

This work is partially supported by the National Program on HTSC within the frames of the Project 92068.

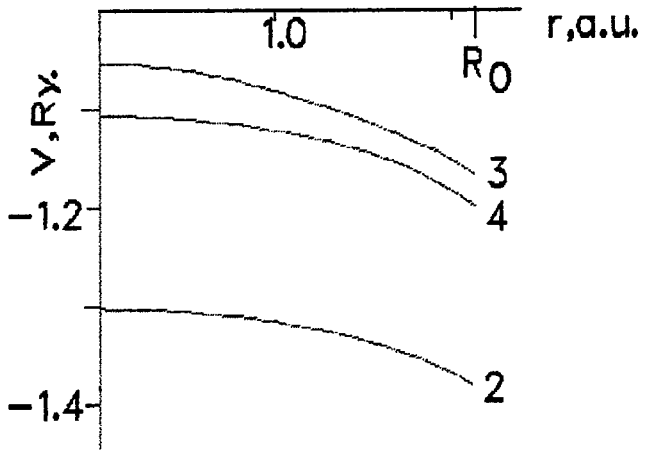

FIGURE 2. One-electron potential in the central MT sphere vs. radii for the variants referred to in the capture to Figure 1.

REFERENCES

1. M. O. Selme and P. Pecheur *J. Phys.* **C.6**, 2559 (1983).
2. A. V. Fisenko, S. A. Prosandeyev, and V. P. Sachenko, *phys. status solidi (b)* **137**, 187 (1986).
3. M. Tsukada, C. Satoko and H. Adachi, *J. Phys. Soc. Japan* **47**, 1610 (1979).
4. V. M. Loktev, S. A. Prosandeyev and Yu. Yu. Tarasevich, *phys. status solidi (b)* **174**, 141 (1992).
5. A. B. Sobolev, P. V. Lushnikov, V. A. Lobach et. al., *superconductivity*, **4**, 487 (1991) (in. russ.).
6. P. Rubin N. and N. Kristoffel, *Solid State Communications* **87**, 1121 (1993).
7. M. A. Bunin, I. I. Gegusin, S. A. Prosandeyev, *Solid State Phys.*, **35**, 841 (1993) (in russ.).
8. S. P. Kowalszyk, F. R. McFreely, L. Ley *et al.*, *Solid State Communication.* **23**, 161 (1977).

Radiation Effects and Defects in Solids, 1995, Vol. 134, pp. 79–81
Reprints available directly from the publisher
Photocopying permitted by license only

© 1995 OPA (Overseas Publishers Association)
Amsterdam B.V. Published under license by
Gordon and Breach Science Publishers SA
Printed in Malaysia

RADIATIVE AND NONRADIATIVE TUNNELING PROCESSES IN SILICON*

A. J. ZAKRZEWSKI,** A. M. FRENS,*** M. T. BENNEBROEK,*** and J. SCHMIDT***

***Institute of Physics, Polish Academy of Sciences, Al. Lotnikow 32/46; 02–668 Warsaw, Poland; ***Huygens Laboratory, P.O. Box 9504, 2300 RA Leiden, The Netherlands*

(Received July 1, 1994)

An excitation transfer among carbon-oxygen and vacancy-oxygen defects in electron irradiated silicon was studied by means of the photo-Electron Spin Echo (photo-ESE) technique. Analysis of the appropriate rate equations enabled us to estimate quantum yield of nonradiative tunneling among (C–O) and (V–O) centers. These processes were found to be several orders of magnitude more efficient than donor-acceptor pair radiative recombination and bound exciton radiative transitions.

Key words: carrier generation-recombination, irradiated silicon.

1 INTRODUCTION

It is known that the vacancy-oxygen (V–O) complex is one of the dominant paramagnetic center formed in electron irradiated silicon. The chemical nature and the point symmetry of this defect is now well understood.[1] On the other hand, its role in the carrier generation-recombination processes has not been determined until recently. The first observation that (V–O) is a really effective recombination center was made by Chen *et al.*[2] They found that the tunneling process among shallow phosphorus donors and (V–O) complexes is very fast (nanosecond time-scale) and even much faster than other recombination processes involving phosphorus donors, like the capture and recombination of free electrons and holes, donor-acceptor transitions or bound excitons formation and recombination processes.

In this communication we present phenomenological analysis of the kinetics of the magnetic resonance signals related to phosphorus donors, (V–O) and (C–O) (i.e. carbon-oxygen) complexes. We focus here mainly on the photo-ESE technique, but other experimental methods were also employed, including photoluminescence, photoconductivity, electron spin resonance (ESR) and optically detected magnetic resonance. It should be mention here, that similarly to the previous photo-ESR studies on II—VI and III—V semiconductors,[3] also the photo-ESE technique is a very convenient tool for studying excitation transfer phenomena, especially in those cases, when direct ESR measurement are very difficult. It was shown,[3] that under proper experimental conditions (temperature, excitation range, intensity, *etc.*) one can often pick up a given recombination process and study it 'separately' from the others. In many cases this is the only way to analyze the role of a particular recombination channel and to compare its efficiency with other recombination transitions.

2 RESULTS AND DISCUSSION

Our experiments were performed on electron irradiated silicon undoped and doped with carbon. Excitation transfer phenomena among (C–O) and (V–O) defects were studied via

*This work was supported in part by research grant of KBN No. 02 0493 91 01

monitoring ESE signal of the first excited triplet state of neutral $(V–O)^T$ complex in K-band spectrometer at 1.2 K under selective (0.785 and 0.793 eV) pulsed laser excitation. In this communication we limit our analysis to the recombination processes taking place under the experimental conditions listed above. In this way it was possible to neglect thermally stimulated processes and also direct excitation of other centers.

A one-to-one correspondence between excitation spectrum of the $(V–O)^T$ and (C–O) related luminescence clearly indicates that the excitation transfer among these centers occurs (detailed discussed of these spectra is given in the recent publications.[4,5] This excitation transfer process (from (C–O) to (V–O)) was found to be very fast, i.e., at time-scale less than 50 ns. In principle several mechanisms may be responsible for a such effective excitation transfer: energy transfer processes, exciton and electron tunneling. In the following we focus ourselves on the nonradiative electron tunneling, as proposed recently by Frens *et al*.[4,5]. The sequence of the involved transitions is given by the following scheme:

$$(C–O) + h\nu_{0.79} \Rightarrow (C–O)^* \quad \text{(photo-excitation)}$$
$$(V–O) + h\nu_{0.79} \Rightarrow (V–O)^+ + e_{CB} \quad \text{(direct photoionization)}$$
$$(C–O)^* + (V–O) \Rightarrow (C–O)^+ + (V–O)^- \quad \text{(primary electron tunneling)}$$
$$(C–O)^+ + (V–O)^- \Rightarrow (V–O)^0 + (V–O)^T \quad \text{(secondary electron tunneling leaving (V–O) center in the excited triplet state)}$$

Due to high anisotropy of the $(V–O)^-$ electron wave function only a fraction of the $(C–O)^+$ and $(V–O)^-$ pairs recombine quickly. Moreover, some of the electrons excited directly from (V–O) to the conduction band are captured by C_i (interstitial carbon) centers. In such a way we could explain not only a very fast creation of the $(V–O)^T$ excited triplet state, but also the experimentally detected $(V–O)^-$, $(C–O)^+$ and C_i^- centers.

The lower limit of the tunneling rate can be estimated via the analysis of the kinetic rate equation describing the $(V–O)^-$ creation process:

$$dn/dt = <\beta>*n_{CO}*(N–n) \tag{1}$$

where N and n denote the total concentration of $(V–O)^0$ and $(V–O)^-$ respectively, n_{co} the concentration of (C–O)* and $<\beta>$ the tunneling rate.

Under following approximations: $N >> n$ and n_{co} = const one can obtain:

$$dn/dt = <\beta>*n_{CO}*N \tag{2}$$

From experiment, the excitation time of $(V–O)^T$ is less than 50 ns. hence:

$$dn/dt \approx \Delta n/\Delta t = n_f/50 \text{ ns} \tag{3}$$

where n_f denotes the numbers of (V–O) centers taking part in tunneling transitions. Then

$$<\beta> \approx 10^7 * \gamma/N \tag{4}$$

where the coefficient γ indicates, how many excited (C–O)* decay nonradiatively via electron tunneling to (V–O). Based on the experimental results we can assume that $N \approx 10^{16}$ cm $^{-3}$ and y = 0.01–01. Hence, $<\beta> \approx 10^{-10}$–10^{-11} cm^3/s.

To estimate value of the coefficient $<\beta>$ for radiative phosphor donor-boron acceptor transitions we utilized results of Dirksen *et al*.[6] They measured decay kinetics of the photo-induced ESE signal of phosphorus donors in Si:P,B crystals. Bearing in mind that

concentrations of donors and acceptors were nearly equal, this kinetics can be described by the following equation:

$$dn/dt = -\langle\beta\rangle n^2 \tag{5}$$

where n(t) denote concentration of neutral donors at time t after pulsed excitation. Comparing experimental data of Dirksen *et al.* with the solution of the above equation we estimated that $\langle\beta\rangle = 10^{-18}$–$10^{-20}$ cm^3/s.[8]

In conclusion, we have shown the importance of the nonradiative tunneling inter-defect processes, which were found to be several orders of magnitude more efficient than radiative ones.

REFERENCES

1. K. L. Brower, *Phys. Rev.* **B4**, 1968 (1971).
2 W. M. Chen, B. Monemar, E. Janzen and J. L. Lindström, *Phys. Rev. Lett.* **67**, 1914 (1991).
3. M. Godlewski, *Phys. Stat. Sol.* (a) **91**, 11 (1985).
4. A. M. Frens, M. T. Bennebroek, A. Zakrzewski, J. Schmidt, M. W. Chen, E. Janzen, J. L. Lindström, B. Monemar, *Phys, Rev. Lett.* **72**, 2939 (1994).
5. A. M. Frens, M. T. Bennebroek, A. Zakrzewski, J. Schmidt, M. W. Chen, E. Janzen, J. L. Lindström, B. Monemar, *Mat. Sci. Forum,* **143–147**, 1371 (1994).
6. P. Dirksen, A. Henstra and W. Th. Wenckebach, *J. Phys.: Condens. Matter* **1**, 7085 (1989).
7. The ESE signal is directly proportional to n(t).
8. Note that in such systems $\langle\beta\rangle$ is a time-dependent quantity.

Radiation Effects and Defects in Solids, 1995, Vol. 134, pp. 83–86
Reprints available directly from the publisher
Photocopying permitted by license only

© 1995 OPA (Overseas Publishers Association)
Amsterdam B.V. Published under license by
Gordon and Breach Science Publishers SA
Printed in Malaysia

THEORETICAL SIMULATIONS OF I-CENTER ANNEALING IN KCl CRYSTALS

A. I. POPOV, E. A. KOTOMIN and R. I. EGLITIS

Institute of Solid State Physics, University of Latvia, 8 Kengaraga str., Riga LV1063, Latvia

(Received July 1, 1994)

This paper focus on theory of diffusion-controlled annealing of the most mobile radiation-induced defects—I centers—in KCl crystals. The kinetics of annealing of pairs of close oppositely charged defects—α-I centers (arising as a result of the tunnelling recombination of primary Frenkel defects—F and H centers) and F-I centers (when H center trap electrons) is calculated taking into account defect diffusion and Coulomb/elastic interaction. Special attention is paid to the conditions under which multi-stage annealing arises; theoretical results are compared with the relevant experimental data.

Key words: Alkali halides, Frenkel defects, diffusion, tunneling, recombination kinetics, color centers, F-center, I-center.

1 INTRODUCTION

I centers (interstitial halide ions) are known to be the most mobile radiation-induced defects in alkali halides and therefore they play an important role in the low-temperature defect annealing processes. The experimental data analysis [1] shows that I centers recombine not only with their complementary α centers (anion vacancies), but also with F,F′ and V_k centers.

In this paper we consider briefly the kinetics of correlated annealing of radiation-induced pairs of close α-I and F-I centers in KCl crystals, stimulated by I-center diffusion and Coulomb or elastic attraction, respectively. Some preliminary results for F, I annealing were presented by us recently for KBr [2], in which study I center was assumed to lie at the cube center. However, as follows from the double-force tensor analysis of I centers in KBr [3], it is more likely to form a split interstitial (dumbbell) along the <100> axis. Therefore in this paper we assume I centers to be situated in the middle of the Me-X distance as is shown in Figure 1a.

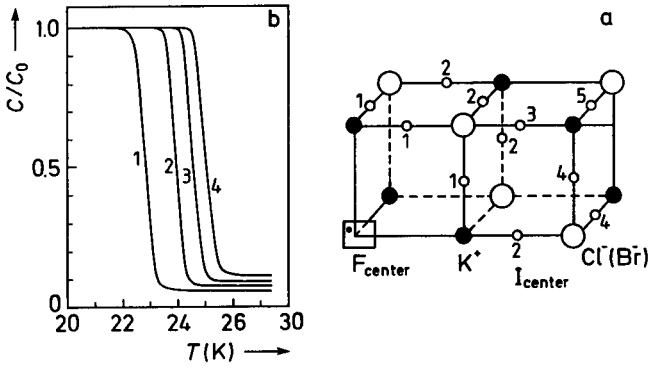

FIGURE 1 (a) Spatial position of several types of I centers (marked 1 to 5) with respect to the close F center in KCl. (b) the calculated correlated annealing of the four types of such close F-I centers (1NN–4NN) in KCl, as controlled by I center diffusion and the elastic attraction to F center (1_1 = 3.51 Å; 1_2 = 4.71 Å; 1_3 = 5.66 Å and 1_4 = 6.47 Å).

2 RESULTS AND DISCUSSION

The model used was described in details in [4,5]; it should be only noted here that we incorporate therein the elastic and Coulomb interactions of close and mobile defects. The former interaction is characterized by the interaction energy of $\varphi(r) = -\alpha/r^3$ [6], where α is the elastic interaction constant and r the relative distance between defects. We have found that $\alpha \simeq 4$ eV Å^3 for F, I centers for both KCl and KBr (see [2] for more details). The annihilation radius $r_0 = 3$ Å, which is close to the interionic spacing, was earlier used in the kinetics of F,H recombination [4,5]. The activation energy for I center hopping is $E_a = 0.08$ eV [7]; The pre-exponential factor in the diffusion coefficient $D = D_0 \exp(-E_a/kT)$ is $D_0 = 8\ 10^{14}$ Å^2 s^{-1}, and the results of our calculations are presented in Figures 1 to 4. The conclusion we draw from Figure 1 (b)

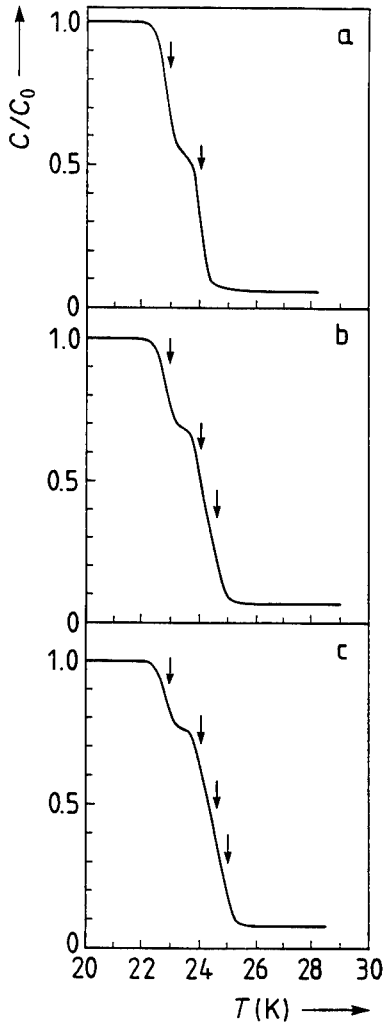

FIGURE 2 The kinetics of simultaneous annealing of several kinds of NN F,I defects presented in equal concentrations: (a) 1NN + 2NN; (b) 1NN + 2NN + 3NN; (c) 1NN + 2NN + 3NN + 4NN. The arrows show the step temperatures for individual defects, as in Figure 1 (b).

is that an increase of the initial distance l between the partners within close F,I pairs from the nearest-neighbour distance (1NN) to the fourth—nearest neighbours (4NN) results in an increase of both the corresponding annealing temperature (by about 1 K per one-step increase of the degree of neighbourhood) and in a higher survival probability, i.e. higher fraction of I centers not recombining with their 'own' F centers.

Figure 2 shows the F-I center annealing for *different* spatial distributions. The obvious result is that a *well-pronounced* recovery stages step structure are observed only for two first nearest-neighbour pairs, whereas badly-resolved stages emerge already for 3 NN and 4 NN. Figure 3 shows theoretical results for α-1 center annealing. It shows that the several well-pronounced stages are observed in the case of simultaneous annealing of 1 NN–3 NN

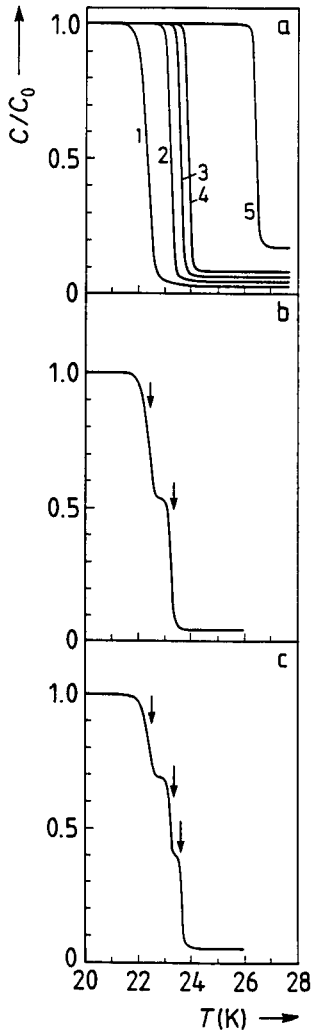

FIGURE 3 The kinetics of the individual (1NN–4NN) (a) and simultaneous (b, c) annealing of several kinds of NN α,I-defects present in equal concentrations. (b) –1NN + 2NN (c) 1NN + 2NN + 3NN. Curve 5 in (a) corresponds to very-well separated defects (distance between α,I centers is 23.3 Å, i. e. they are 5th neigbours along the <110> axis).

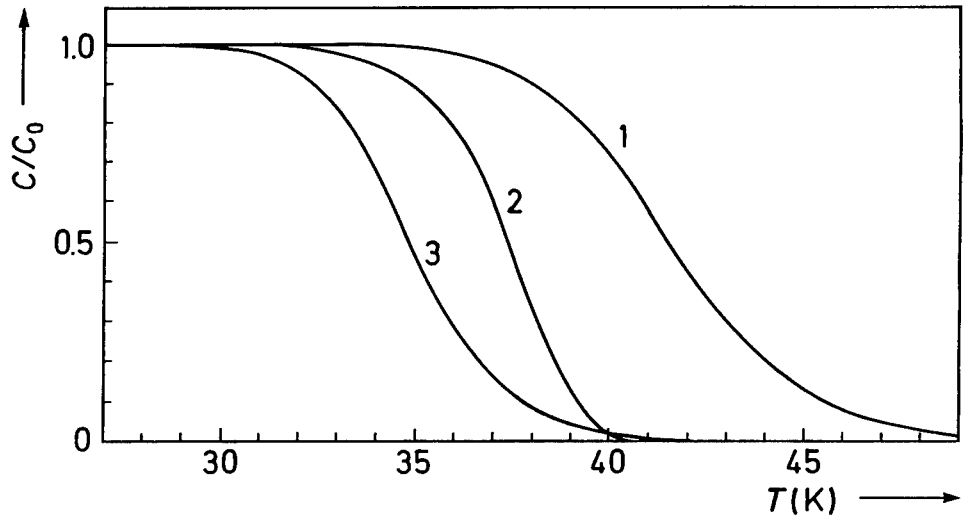

FIGURE 4 Uncorrelated annealing of I centers in KCl for different concentrations of defects: curve $C_o(I) = 10^{16}$ cm^{-3}; $C_o(F) = 10^{16}$ cm^{-3}. Curve 2–$C_o(I) = 10^{15}$ cm^{-3}; $C_o(F) = 10^{17}$ cm^{-3}. Curve 3–$C_o(I) = 10^{18}$ cm^{-3}; $C_o(F) = 10^{18}$ cm^{-3}.

of α, I defects present in equal concentrations, whereas more distant defects are badly resolved.

Lastly, computer simulations of the *free* I center annealing demonstrates clearly how the annealing temperature depends on the initial defect concentration (i. e. irradiation dose)—the effect observed experimentally more than once [see [7] and reference therein].

We would like to stress in conclusion that the problem of the correlated annealing of spatially correlated Frenkel defects is very universal and actual not only for ionic solids, but also for rare-gas solids [8] and metals [9]. We believe that the use for these materials of the correct mathematical formalism presented by us in [4,5] (and applied there to KBr and in this paper—to KCl crystals) could get more useful information about first stages of the radiation damage of materials.

The research described in this publication was made possible in part by Grant LB2000 from International Science Foundation.

REFERENCES

1. V. E. Zirap, *Phys. Status Solidi* **B 119**, 49 (1983).
2. A. I. Popov, E. A. Kotomin and R. I. Eglitis, *Phys. Status Solidi* **B 175**, K39 (1993).
3. H. Lohstoter, H. Spalt and H. Peisl, *Phys. Rev. Lett.* **2**, 224 (1972).
4. E. A. Kotomin, A. I. Popov and R. I. Eglitis, *J. Phys.: Condens. Matter* **4**, 5901 (1992); *Nucl. Instr. Method Phys. Research* **B 65**, 512 (1992).
5. E. A. Kotomin, A. I. Popov and M. Hirai, *J. Phys. Soc. Japan* **63**, 2602 (1994).
6. W. Schen, W. Frank and H. Kronmuler, *Phys. Status Solidi* **B 82**, 523 (1977).
7. A. I. Popov, E. A. Kotomin and R. I. Eglitis, *Phys. Status Solidi* **B** 1994 (in press).
8. R. Balzer, O. Kroggler and H. Spalt, *J. Phys. C: Solid St. Phys.*, **13**, 6349 (1980).
9. W. Schilling, K. Sonnenberg and H. I. Dibbert, *Radiation Effects* **16**, 57 (1972); R. Lennartz, F. Dworschak and H. Wollenberger, *J. Phys. F., Metal. Phys.* **7**, 2011 (1977).

Radiation Effects and Defects in Solids, 1995, Vol. 134, pp. 87–90
Reprints available directly from the publisher
Photocopying permitted by license only

© 1995 OPA (Overseas Publishers Association)
Amsterdam B.V. Published under license by
Gordon and Breach Science Publishers SA
Printed in Malaysia

MODELLING OF POINT DEFECTS IN α-AL2O3

E. A. KOTOMIN[a], A. STASHANS[a,b] and P. W. M. JACOBS[c]

[a]Institure for Solid State Physics, University of Latvia, Rainis Blvd. 19, Riga LV1050 Latvia; [b]Department of Quantum Chemistry, Uppsala University Box 578, S-757 20 Uppsala, Sweden; [c]Department of Chemistry, The University of Western Ontario London, Ontario N6A 5B7, Canada

(Received July 1, 1994)

The semiempirical method of the Intermediate Neglect of Differential Overlap (INDO), in the program SYM-SYM, has been used for calculations on perfect and imperfect corundum crystals. For the perfect crystal the periodical Large Unit Cell (LUC) model was used while the Molecular Cluster (MC) model was used in defect calculations. By means of the MC model, we have investigated the optical properties of electronic centers (F^+, F, F^-, F_{Mg}, F^-_{Mg}) in corundum. Calculated optical properties of these defects are compared with experimental values and new bands are predicted to exist in the absorption spectrum of Mg-doped corundum. The energy levels of F-type and Mg-impurity related centers are found to lie in the gap between the upper valence band and conduction band, as for similar centers in MgO and alkali halides.

Key words: alumina, F centre, point defects

1 INTRODUCTION

Corundum (α-Al_2O_3), or sapphire, is probably the most important ceramic material and its technological importance has stimulated numerous studies of its optical and magnetic properties.[1,2] However, only a few attempts have been made to understand theoretically the geometry and electronic structure of electron and hole centers created in corundum under irradiation. This is due primarily to the complicated structure of corundum, its large unit cell and the semi-ionic character of chemical bonding. The INDO method has been widely applied previously to point defects in a number of ionic crystals, including oxides.[3,4] This method[5] allows one to construct defective clusters containing up to several tens of atoms and to carry out automated geometry optimization.[6]

2 RESULTS AND DISCUSSION

Results for a family of hole centers have already been published;[4,7] in this paper we focus on electronic centers-both intrinsic F^+, F and the hypothetical F^- (respectively, one, two and three electrons trapped by an O vacancy), and centers associated with Mg-impurity (F_{Mg} and F^-_{Mg} in which an Mg^{2+} ion substitutes for Al^{3+} nearby an F^+ or F center). To extend our basis set for F-type calculations, additional 2s, 2p Slater-type atomic orbitals were centered at the O vancancy. The only fitting done was for the orbital exponents of the F^+ wave function in order to reproduce the experimental energy of the central absorption band at 5.5 eV(1A → 2A transition). The same basis set was used for calculations on all the other electron centers. An enlarged 65-atom ($Al_{26}O_{39}$) stoichiometric quantum cluster was used for these electron-type defect studies, this being embedded in the electrostatic field of the rest of the crystal.

Table I shows calculated absorption and luminescence energies. The calculated absorption energy of the F center (5.9 eV) is in good agreement with the experimental value of 6.1 eV; the same is true for the luminescence energies for both F^+ and F centers. These

TABLE I

Calculated absorption and luminescence energies. Optical transitions are calculated as the difference of total self-consistent energies in the ground and excited states (ΔSCF method). Due to low C_2 point symmetry the threefold degenerate 2p excited state of the F^+ center is split by the crystalline field into three states: $1B(p_z)$, $2A(p_y)$, and $2B(p_x)$.

Defect	Absorption, eV		Luminescence, eV	
	Theory	Expt.	Theory	Expt.
	5.2(1A → 1B)	4.8		
F^+	5.5(1A → 2A)	5.4[8]	4.0(1B → 1A)	3.8[8]
	5.8(1A → 2B)	6.0		
F	5.9(1A → 2A)	6.1[8]	2.8(2A → 1A)	3.0[8]
	5.1(1A → 2A)	4.95		
F_{Mg}	5.3(1A → 3A)	5.70[9]	4.2(2A → 1A)	4.1[10]
	5.9(1A → 4A)			
F^-_{Mg}	6.4(1A → 2A)		3.5(2A →1A)	

calculations, especially for the excited states, are non-trivial since optimisation of the geometry for several groups of atoms is required. Figure 1 shows the displacements of atoms nearest to the O vacancy the nearest anions O_1 and O_2 (shifted by σ at an angle α with respect to the line connecting O–O atoms) and two kinds of A*l* atoms forming the so-called short bonds (Al_3 and Al_4, shifted by Δ) and those forming long bonds (Al_1, and Al_2, shifted by δ). The optimized inward relaxations σ of the two nearest oxygen atoms towards the vacancy are 4.6% and 2.2% for the F^+ and F ground states, respectively (in units of the O–O distance in the perfect corundum). This occurs at angles $\alpha = 5°$ and 25°, respectively. The displacements of O atoms for the charged F^+ center naturally are larger than for a netural F center due to electrostatic effects; the same is true for the outward A1 displacements (5.5% for F^+ and 2.3% for F, respectively). The wavefunctions of the ground states are well localized within a vacancy but that of the excited state of the F center is delocalized on to the nearest cations. However, the adiabatic potential energy curve of the excited F center has a minimum, from which the radiative transition to the ground state occurs. The calculated luminescence energy of 3.0 eV is close to the experimentally observed 2.8 eV. The energy of thermal quenching of luminescence, E_a was calculated to be ≈0.5 eV, in good agreement with the experimental value of 0.4 eV[8]. In the neutral F_{Mg} center the nearest O atoms are displaced slightly more that in the F center but less than in F^+. Observed displacements of A1 atoms are larger due to the Coulomb repulsion from the vacancy. The Mg^{2+} ion itself is displaced towards the F^+ center, since it is oppositely charged with respect to the perfect crystal lattice. Calculated absorption energies for Mg-impurity related centers (Table I) shows that only the neutral center F_{Mg} fits the experimental values. We predict additionally a third absorption band to exist for this center at a photon energy of approximately 6.0 eV.

Energy levels of the F-type centers fall into the gap between the upper valence band and the conduction band as in the alkali halides and MgO. Excited states of the one-electron F^+ and F_{Mg} centers are well localized whereas those for two-electron centers F and F^-_{Mg} are delocalized,being degenerate with the conduction band. The observed 1.2 eV splitting of the low (C_2) symmetry excited F^+ center state is due to the deep position of its levels in the energy gap. We came to this conclusion by simulating the delocalization of the wave function of the excited F^+ center state as a function of its orbital exponentζ; when reducing ζ the distance between the F^+ center excited-state level and the conduction band diminishes and the wave function becomes more diffuse with a simultaneous reduction

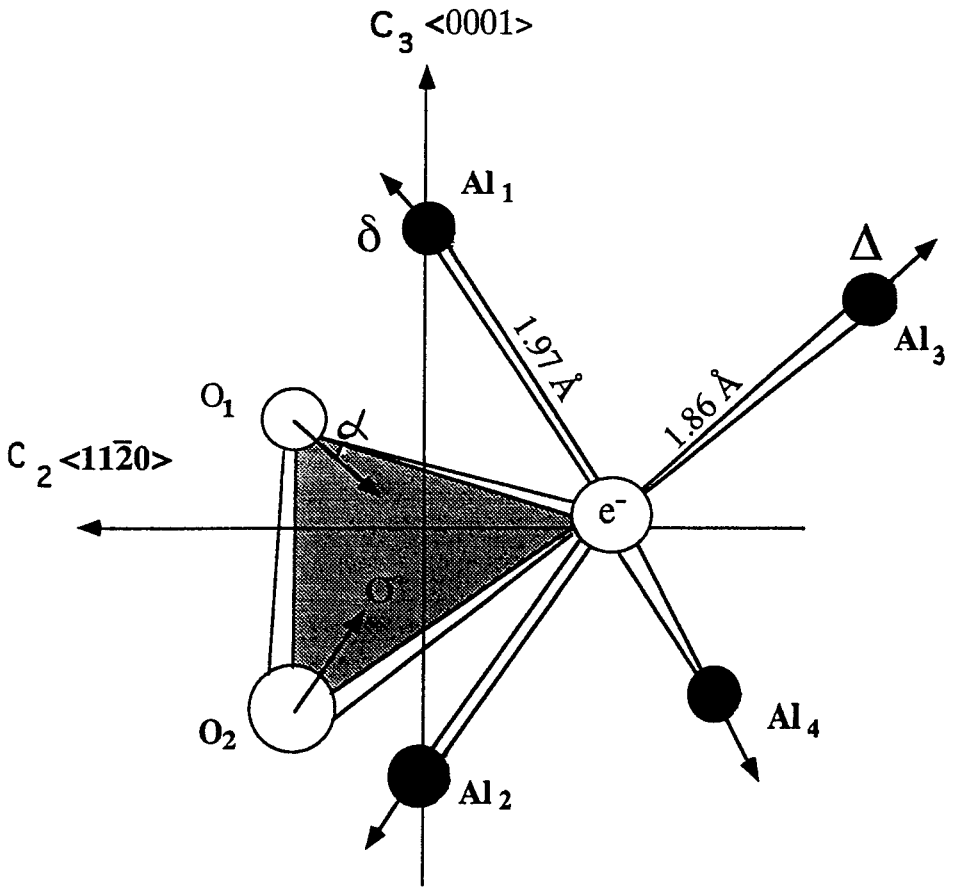

FIGURE 1 The displacements of atoms optimised in the calculations of the spectroscopic properties of F-type centers.

of the splitting of the excited state. This is exactly what happens in $F(F_{Mg})$ centers. We have also obtained F^+-induced states split off from the conduction band, which could be observed as new absorption bands at ≈ 8 eV additional to the three 'classical' bands around 5–6 eV. Lastly, we simulated the hypothetical F^- center in corundum and found that the third electron indeed occupies the local level split off from the conduction band by ≈ 1 eV. This confirms the idea[9] that such defects (similar to the F^- centers in alkali halides) could exist and be responsible for the thermostimulated luminescence peaks observed in corundum at 260 K.

ACKNOWLEDGEMENTS

Financial support from ISF (grant LB20007) to EAK is greatly appreciated. A. S. thanks the Nordic Council of Ministers for the financial support and the members of the Department of Quantum Chemistry at Uppsala University for their warm hospitality during his stay there in 1993–1994. Stimulating discussions with J.-L. Calais, A. Popov, I. Tale are also appreciated. The program SYM-SYM was written by L. N. Kantorovich and A. I. Livshicz and we are grateful to them for making it available for our use.

REFERENCES

1. J. Valbis and N. Itoh, *Rad. Eff and Def. in Solids*, **116**, 171(1991); J. -M. Spaeth and F. K. Koschnick, *J. Phys. Chem. Solids*, **52**, 1 (1991).
2. K. J. Caulfield, R. Cooper, and J. F. Boad, *Phys. Rev.*, **B47**, 55 (1993).
3. P. W. M. Jacobs, E. A. Kotomin, A. Stashans, E. V. Stefanovich, and I. Tale, *J. Phys.: Cond. Matter*, **4**, 7531 (1992); A. L. Shluger and E. S. Stefanovich, *Phys. Rev.*, **B42**, 9646 (1990); A. L. Shluger, R. W. Grimes, C. R. A. Catlow and N. Itoh, J. *Phys: Cond. Matter*, **3**, 8027 (1991).
4. L. Kantorovich, A. Stashans, E. Kotomin, P. W. M. Jacobs, *Int. J. Quant. Chem.*, **52**, 1177 (1994).
5. E. Stefanovich, E. Shidlovskaya, A. Shluger, and M. Zakharov, *Phys. Stat. Sol.*, **B160**, 529 (1990); A. Shluger and N. Itoh, *J. Phys.: Cond. Matter*, **2**, 4119 (1990); E. A. Kotomin and A. L. Shluger, *Phys. Stat. Sol.*, **B109**, 75 (1982).
6. L. N. Kantorovich and A. I. Livshicz, *Phys. Stat. Sol.*, **B174**, 79 (1992).
7. P. W. M. Jacobs and E. A. Kotomin, *Phys. Rev. Lett.*, **69**, 1411 (1992); P. W. M. Jacobs, E. A. Kotomin, A. Stashans, and I. A. Tale, *Phil. Mag.*, **B67**, 557 (1993).
8. J. H. Crawford Jr., *Nucl. Instr. Meth.*, **B1**, 159 (1984).
9. V. S. Kortov, T. S. Bessonova, M. S. Akselrod, and I. I. Milman, *Phys. Stat. Sol.* (a) **87**, 629 (1985).
10. P. A. Kulis, M. J. Springsis, I. A. Tale, V. S. Vainer, and J. A. Valbis, *Phys. Stat. Sol.*, **B104**, 719 (1981); M. J. Springis and J. A. Valbis, *Phys. Stat. Sol.*, **B123**, 335 (1984).
11. S.-I. Choi and T. Takenchi, *Phys. Rev. Lett.*, **50**, 1479 (1983).

Radiation Effects and Defects in Solids, 1995, Vol. 134, pp. 91–94
Reprints available directly from the publisher
Photocopying permitted by license only

© 1995 OPA (Overseas Publishers Association)
Amsterdam B.V. Published under license by
Gordon and Breach Science Publishers SA
Printed in Malaysia

A COMBINED COMPUTER SIMULATION AND EXAFS STUDY OF DOPANT CLUSTERING IN LANTHANUM OXIDE

A. V. CHADWICK, G. MORRISON and R. RAFIUDDIN

Chemical Laboratory, University of Kent, Canterbury, Kent CT2 7NH, U.K

Atomistic computer modelling and Extended X-ray Absorption Fine Structure (EXAFS) measurements were used in a study of the mode of solution of Sr^{2+} ions in La_2O_3. The results are in agreement with previous modelling studies which show that the most favourable mode of solution is cation substitution with anion vacancy charge compensation. The energy of solution was found to be 1.3 eV. The Sr K-edge EXAFS results for 10 and 20 mole percent Sr^{2+} doped La_2O_3 were consistent with cation substitution. For both doped samples the EXAFS indicate the presence of a defect cluster containing $2Sr_{La}$ ions adjacent to a $V_O^{\cdot\cdot}$.

Key words: Lanthanum oxide, computer modelling, EXAFS, dopant clusters.

1 INTRODUCTION

Lanthanum oxide (La_2O_3) doped with divalent cations, notably Sr^{2+} and Ca^{2+}, is a good O^{2-} ion conductor[1] and a useful catalyst for oxidative coupling of methane.[2] The understanding of both the catalytic activity and the ionic motion is dependent on a knowledge of the defect structure. There have been very few studies of the defect properties of La_2O_3, the most notable being the very recent computer simulations by Ilett and Islam.[3] This work showed that (i) the intrinsic defects were anion-Frenkel pairs (ii) O^{2-} were the mobile defects and (iii) the alkaline earth ions dissolved substitutionally on the La^{3+} sites with the formation of charge compensating O^{2-} vacancies.

We report a study of the defects in Sr^{2+} doped La_2O_3 using a combination of computer modelling and *E*xtended *X*-ray *A*bsorption *F*ine *S*tructure (EXAFS). The computer code was the same as that employed by Ilett and Islam,[3] however the parameters for the hexagonal La_2O_3 structure were those of Aldebert and Traverse[4] and the interatomic potentials were those recently developed by Bush *et al.*[5] Since the level of doping employed to obtain high ionic conductivity is high, typically several mole percent, defect clustering is expected and the calculation of various cluster binding energies were undertaken. EXAFS is a powerful method of investigating local structures[6] and measurements were used to identify the nature of the defect clusters.

2 METHODS

2.1 *Computer Simulations*

Calculations were performed with the CASCADE code[7] running on the University of Kent Meiko parallel processing computer. The interatomic potentials were those reported recently by Bush *et al.*[5]

2.2 *EXAFS*

Samples of 10 and 20 mole per cent Sr^{2+} doped La_2O_3 (based on moles SrO to moles of

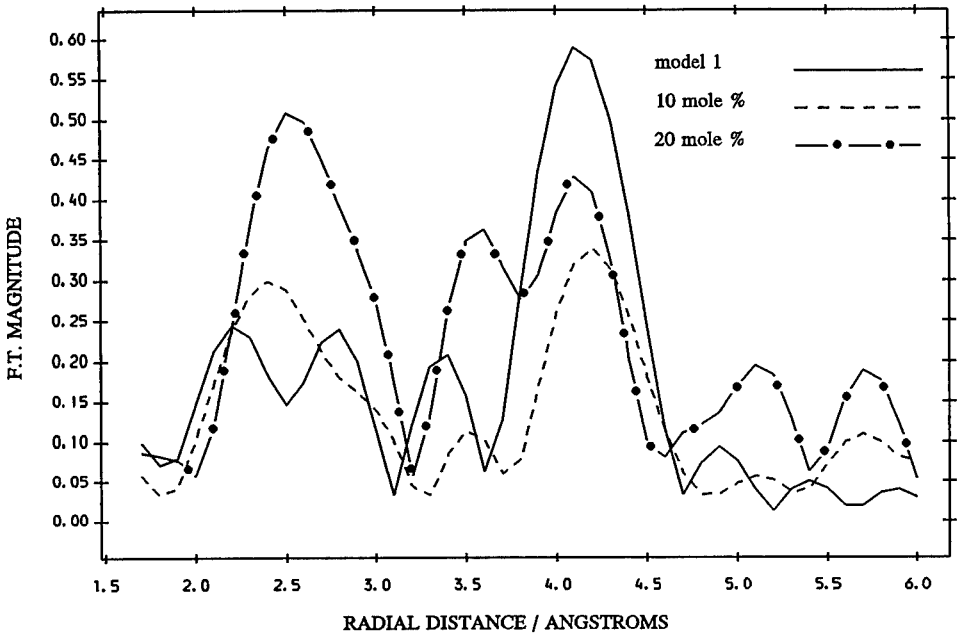

FIGURE 1 Radial distribution functions for Sr^{2+} doped La_2O_3.
- - - - - - - 10 mole per cent; – • – • – • – • – 20 mole per cent;
———— model 1 (see text).

La_2O_3) were prepared by a high temperature solid state reaction.[1] Sr K-edge EXAFS were collected at room temperature in transmission mode on station 9.2 at the SERC Daresbury Synchrotron Radiation Source. The spectra were analysed using the Daresbury EXAFS suite of computer programs.[8]

3 RESULTS AND DISCUSSION

Computer simulations were used to calculate the energies of the possible intrinsic defects in La_2O_3. In the present work the anion-Frenkel and Schottky quintet were found to be almost equally favourable, the energies of formation being 2.41 and 2.37 eV per defect, respectively. In the La_2O_3 structure there are two non-equivalent anion sites, O^1 and O^2, and siting the vacancy at the O^1 position is energetically favoured to the extent 1.02 eV. The cation-Frenkel pair was not energetically favourable with a calculated formation energy of 5.95 eV per defect. In previous calculations[3] the anion-Frenkel pair was found to be strongly favoured over the Schottky quintet, the energies per defect being 2.57 and 3.34 eV, respectively. The differences between the two sets of calculations originate from the use of different interatomic potentials. Calculations of defect migration energies show that the most mobile defect is the anion vacancy, moving between O^1 sites, which agrees with previous calculations.[3]

All possible modes for solution of La_2O_3 were considered and the most energetically favourable is cation substitution with anion vacancy compensation. Using the equation

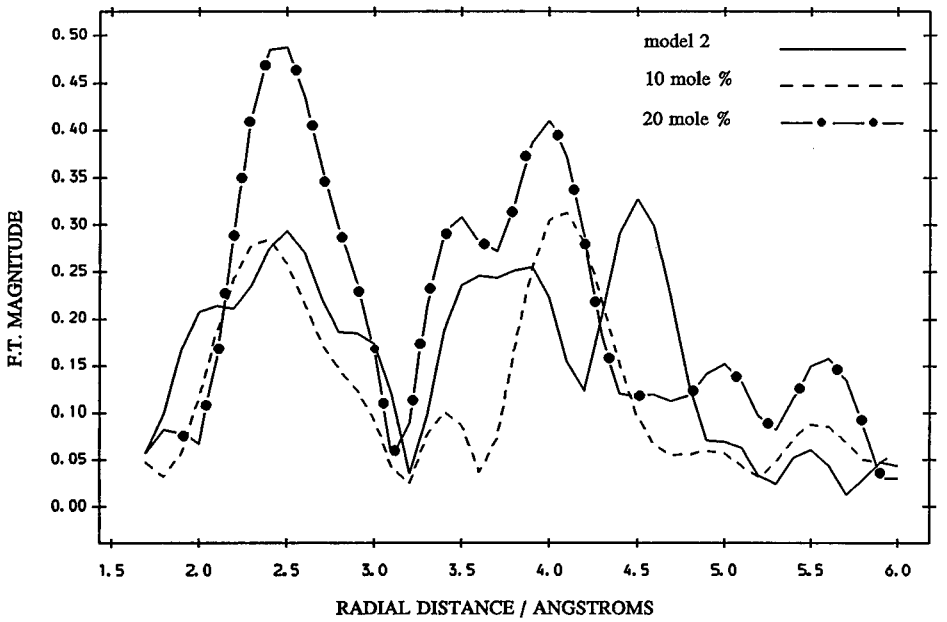

FIGURE 2 Radial distribution functions for Sr^{2+} doped La_2O_3.
- - - - - - - 10 mole per cent; — • — • — • — • — 20 mole per cent;
———— model 2 (see text).

below the energy of solution is calculated to be 1.31 eV.

$$SrO + La_{La}^{x} + 1/2O_o \rightarrow Sr_{La}' + 1/2V_o^{\cdot\cdot} + 1/2La_2O_3$$

This energy is based on two assumptions, the first assumption, which is inherent in the methodology used by the CASCADE code,[7] is that the defects are present at infinite dilution. The second assumption is that the defects are isolated; this assumption is not valid at high dopant concentrations or at low temperatures as the defects will be associated into clusters.

The level of Sr^{2+} doping in La_2O_3 used as an O^{2-} ion conductor is up to 20 mole per cent. At these high levels of doping it is expected that there will be defect clustering. Calculations of the binding energy of several simple clusters were performed. The binding energy is defined as the energy of the cluster minus the sum of the energies of the isolated defects; a negative binding energy indicating a stable cluster. The results from these calculations can be seen in Table I.

Table I

Cluster	Binding Energy (eV)	Binding Energy/Defect (eV)
$Sr_{La} + V_{o(I)}$	−0.46	−0.23
$2Sr_{La} + V_{o(I)}$	−1.23	−0.41
$4Sr_{La} + 2V_{o(I)}$	−2.34	−0.39

It can be seen that the simple charge compensated cluster, $2Sr^{2+}$ ions on La^{3+} sites adjacent to an O^{2-} vacancy (termed *model* 1) is the most favourable cluster; being slightly more favourable than the larger, $4Sr^{2+}$ adjacent to O^{2-} vacancies, cluster (termed *model* 2). It should be noted that the above clusters have many possible geometries and the results given in Table I are only those for the most energetically favourable geometries for each cluster. However these results do not rule out the formation of even larger and more complex clusters, especially at high dopant concentrations. The radial distribution functions (rdf), from the EXAFS experiments on the two samples are shown in Figures 1 and 2. The plots were obtained by a Fourier transform of the normalised EXAFS spectra and as phase shifts[8] have been employed the radial distances should be realistic. Also shown on the plots are the rdf's the clusters, model 1 (Figure 1) and model 2 (Figure 2), studied in the computer simulations. These were obtained by using the atomic occupancies and positions from the CASCADE calculations with the default value of the Debye-Waller factor (0.01 $Å^2$). Therefore the magnitudes of the theoretical models are not directly comparable with the experimental values, however, radial distances for the techniques should correspond to real distances.

The experimental rdf's show peaks at ~ 2.5 (with a shoulder at ~ 3.0), ~ 3.5 and ~ 4.2 Å. Preliminary fitting of the EXAFS shows the first of these peaks is due to O^{2-} ions and that at ~ 4.2 Å is due to cations. The peak at ~ 3.5 Å has not yet been assigned and detailed fitting is still in progress. It can be seen from Figure 1 that the model 1 cluster reproduces well the peak positions in the experimental rdf's. In contrast inspection of Figure 2 indicates that cluster model 2, although comparable in energy to cluster model 1, does not reproduce the experimental peak positions; in particular the cation shell position is very different. This qualitative analysis clearly indicates that the dominant cluster in the 10 and 20 mole per cent samples is the smaller model 1 cluster.

4 CONCLUSIONS

The calculations indicate that the Schottky quintet and the anion-Frenkel pair in La_2O_3 have similar energies. The mode of solution of Sr^{2+} ions is substitutional with the formation of O^{2-} charge compensating vacancies. The binding energies of Sr^{2+} ions and oxygen vacancies indicate that defect clusters are energetically favourable, the most favoured being that formed by 2 Sr^{2+} ions and an O^{2-} vacancy on adjacent sites. Comparison of the calculations and the EXAFS measurements indicate that this cluster is dominant in both 10 and 20 mole per cent Sr^{2+} doped La_2O_3.

REFERENCES

1. S. J. Milne, R. J. Brook and Y. S. Zhen, *Br. Ceram. Proc.*, **41**, 243 (1989).
2. Z. Kalenik and E. E. Wolf, *Catal. Lett.*, **9**,441 (1991); *Catalysis*, **13**, 255 (1992).
3. D. J. Ilett and M. S. Islam, *J. Chem. Soc., Faraday Trans.*, **89**, 3833 (1993).
4. P. Aldebert and J. P. Traverse, *Mat. Res. Bull.*, **14**, 303(1979).
5. T. S. Bush, J. D. Gale, C. R. A. Catlow and P. D. Battle, *J. Mater. Chem.* **4**, 831 (1994).
6. A. V. Chadwick, *Solid State Ionics*, **63–65**, 721, (1993).
7. M. Leslie, *SERC Darebury Laboratory Report*, No. DL/SCI/TM31T (1982).
8. N. Binsted, S. J. Gurman, J.W. Campbell and P. Stephenson, *SERC Daresbury EXAFS Programs, EXCALIB, EXBACK and EXCURV92*, (1992).

Radiation Effects and Defects in Solids, 1995, Vol. 134, pp. 95–100
Reprints available directly from the publisher
Photocopying permitted by license only

© 1995 OPA (Overseas Publishers Association)
Amsterdam B.V. Published under license by
Gordon and Breach Science Publishers SA
Printed in Malaysia

CLUSTER CALCULATION OF IMPURITY-INDUCED CORE-VALENCE TRANSITIONS

A. S. VOLOSHINOVSKII,* V. B. MIKHAILIK* and P. A. RODNYI**

* *Physics Department, Lviv State University, Lomonosov st. 8, Lviv, 290005, Ukraine;*
** *Experimental Physics Department, Technical University, Politekhnicheskaya st. 29, St. Petersburg, 195251, Russia*

The electronic structure of $[CsCl_n]$ molecular cluster and possible radiative transitions between crystal valence band and impurity core states are calculated with self-consistent field X_α scattering wave method. Correlation of experimental and theoretical data confirms the local cluster-type nature of the radiative core-valence transitions.

Key words: Crossluminescence, self-consistent field X_α scattering wave method, cluster approach.

1 INTRODUCTION

Specific intrinsic emission caused by radiative transitions of valence electrons to empty (hole) states in the outermost core band has been widely studied in some ionic crystals for which the Auger transitions between the valence and upper core bands are completely energetically forbidden (see e.g. review).[1] In other words the effect is detectable when $E_c > 2E_g$, where E_c is the energy distance from the bottom of the conduction band to the upper core band and E_g the band gap energy (Figure 1). The general features of radiative core-valence transitions (CVT) are i) the short decay time (10^{-9}s), ii) the existence of threshold excitation energy coinciding with that of the transitions from the upper core band to the conduction band, and iii) the high thermal stability of the emission intensity and decay time. Certain correlation is considered to exists between the density of the valence band electron states and the emission spectra of CVT.[2]

Up to now the intrinsic emission has been observed and identified for halide compounds containing Ba^{2+}, K^+, Rb^+ and Cs^+ cations. This is due to the abovementioned specific energy condition for detecting the CVT. In wide-gap halides are doped with these cations, the radiative recombination of the valence electrons with holes originating from the uppermost impurity core level can occur.[3] In this case the characteristic energy condition has the similar form $E_c' > 2E_g$, where E_c' is the impurity core hole energy from the bottom of the conduction band. Thus the corresponding impurity-induced CVT occur under high-energy excitation (Figure 1).

Here we report the results of calculation studies of the impurity-induced CVT in the framework of cluster approach and the comparison with the relevant experimental data for the crystals doped with Cs which have different structure of the emission cluster $[CsCl_n]$ (n denotes coordination number). Some preliminary results of our investigations may be found in Ref.[3,4]

2 CALCULATION PROCEDURES

The electronic structure of $[CsCl_n]$ molecular cluster was calculated with the self-consistent field (SCF) X_α scattering wave method. The molecular cluster approach used does not take into account the crystal field influence. Geometry of the nearest anion surrounding of Cs in

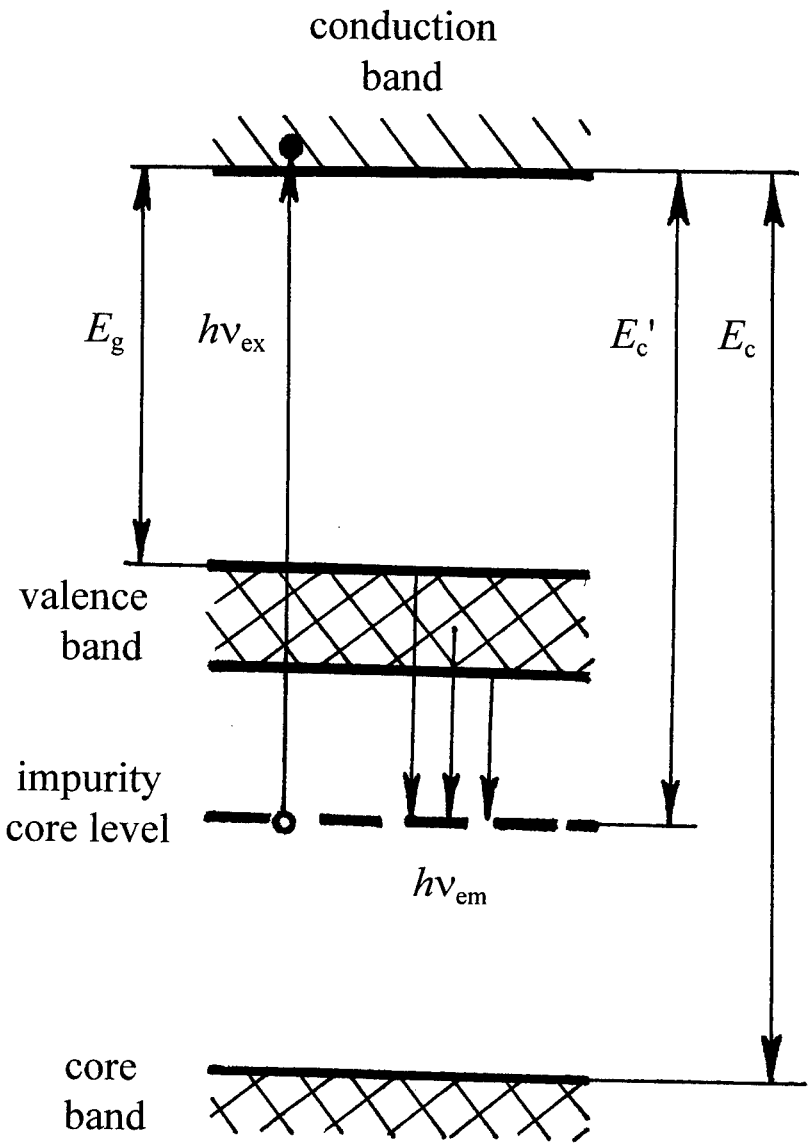

FIGURE 1 Energy band diagram and possible electron transitions responsible for impurity-induced core-valence emission. E_g denotes band gap energy, E_c and E_c' the energy distances between conduction band and core band and between conduction band and impurity core levels resp.

the structures considered is specified by coordination number n = 6, 8, 12 being octahedral, cubic or cubooctahedral respectively. Cs-Cl distance was adopted to be equal to 0.32 nm for all types of clusters. It is equal to cation-anion distance in KCl crystal. MT-radii were picked out under the condition of minimum for one-electronic potential

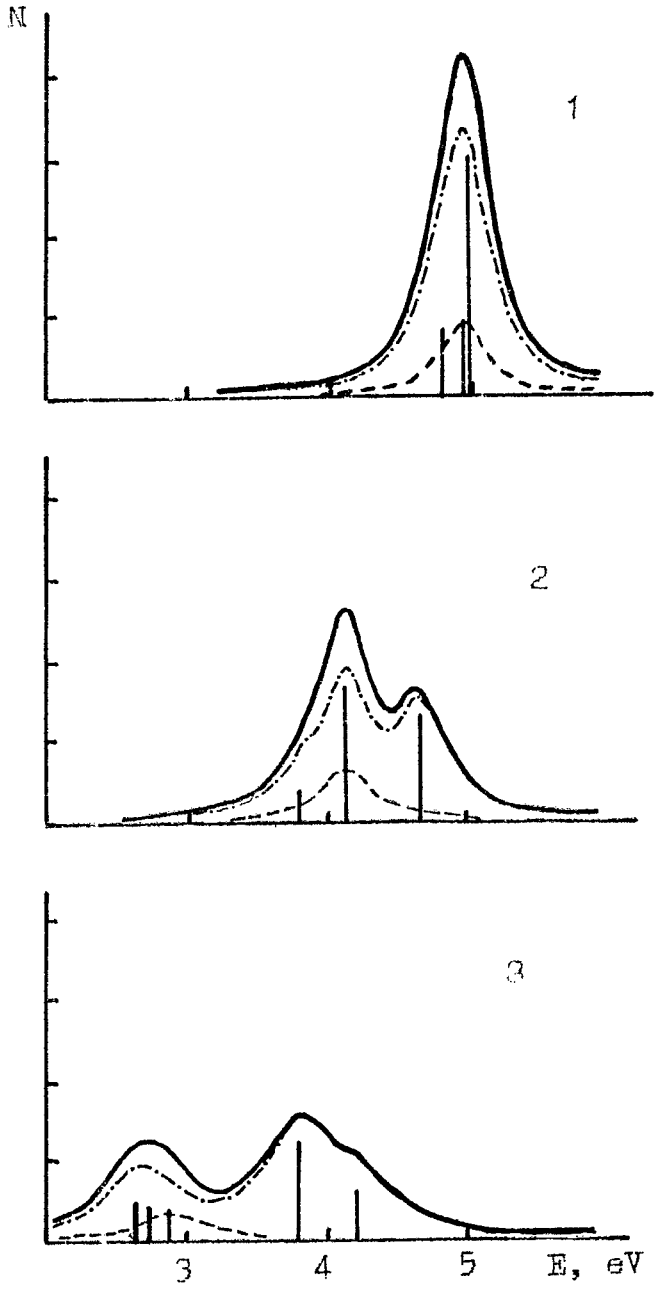

FIGURE 2 Calculated spectra (full line) of radiative transitions between chlorine electronic states and impurity core hole states of cesium for clusters $[CsCl_6]$ (1), $[CsCl_8]$ (2) and $[CsCl_{12}]$ (3). Dashed and point-dashed lines display the deposits of the transitions in the s- and d-symmetry states.

jump at the MT-spheres. Start functions for the charge densities and potentials in MT-spheres were constructed using s-, p- and d-wave functions of the electronic shells Cs and Cl atoms. The cluster electronic wave function was written as a superposition of the solutions of one-electronic Shroedinger equation for different regions. Then the solution was used for further iterations. The matrix elements for dipole transitions were calculated between the initial core hole states and the final valence electron states.

3 RESULTS AND DISCUSSION

The data obtained show that the upper group of filled levels which corresponds to the crystal valence band is formed, in principal, by the states with p-symmetry of chlorine ions. The results of calculation demonstrate that the cesium d- and s-states also contribute to the full density of electron states in the valence band which is of primary importance for understanding of the emission nature. The density of the d- and s-states of cesium is more than order of magnitude less than that for chlorine p- states. The cesium s- and d-states form a group of levels in the valence band, of which number and energy location depend on the coordination number n of $[CsCl_n]$ cluster. the cesium d-state splitting is defined by chlorine wave function overlapping. The outermost core band is formed by 5pCs states centered nearly 5 eV deeper than the top of the valence band. The electron states of 5pCl core band are located at 12 eV.

Keeping in mind the data obtained, the emission spectra of the radiative CVT were calculated in frame of a dipole approach as the non-forbidden transitions between s- plus d- valence states on Cs and 5pCs core states. Energy location and arbitrary intensities for these transitions are displayed in Figure 2 (vertical lines). The simulation of the corresponding radiative CVT spectra was performed using Gaussian widening (half-width 0.3 eV) of the energy levels.

We use the relevant experimental data of our studies of the impurity-induced CVT in Cs-doped KCl, RbCl, $SrCl_2$ and $RbCaCl_3$ halide crystals[3,4] in order to comparison with the results of theoretical calculations. Figure 3 presents the X-ray excited spectra of fast emission components of the investigated crystals. One can observe the characteristic features of the investigated emission noted in Sec. 1. Such peculiarities allowed us to identify the emission as the radiative impurity-induced CVT of valence electrons to impurity 5pCs core levels.[3]

The experimental results indicate the crystals with the octahedral anion environment (coordination number $n = 6$) exhibit one emission band (KCl:Cs, RbCl:Cs). Two bands are observed in $SrCl_2$:Cs crystals with the cubic anion surrounding ($n = 8$). In perovskite-like $RbCaCl_3$:Cs crystals ($n = 12$) the spectrum structure is more complicated. The changes in the profile of the fast emission spectrum are known to occur in CsCl crystals at the phase transition from the structure with $n = 8$ to the rock salt structure ($n = 6$). In this case the emission spectrum is transformed from the two-band to the one-band form.[5]

Good agreement of experimental and theoretical results follows from comparison of the calculated (Figure 2) and measured (Figure 3) spectra. In the case of $n = 6$ the allowed transitions form only a single peak. For $n = 8$ the dipole transitions are grouped in two well defined peaks. In cubouctahedral perovskites ($n = 12$) complicated spectrum shape is realized.

4 CONCLUSION

Theoretical-experimental agreement of the results derived for the crystals investigated

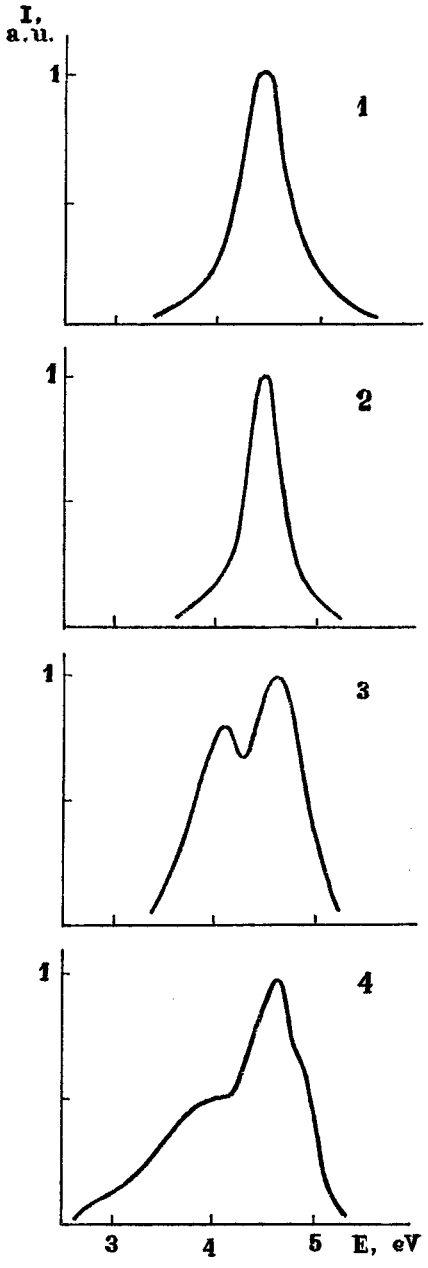

FIGURE 3 Normalized spectra of the impurity-induced CVT for KCl:Cs (1), RbCl:Cs (2), $SrCl_2$:Cs (3) and $RbCaCl_3$:Cs (4) crystals.

draws the conclusion[3,4] that the recombination of the valence electron with core hole involves mainly the nearest-neighbor ions of the opposite sign. Therefore the emission spectrum of the CVT is defined mainly by the energy characteristics and the mutual positions of the ion pairs participating in recombination processes. This situation implies that the radiative core-valence transitions have a local cluster-type nature. A relation between emission spectrum profile and structure of cluster $[CsCl_n]$ obtained here confirms validity of the cluster approach to the CVT nature interpretation.

REFERENCES

1. P. A. Rodnyi, Sov. *Phys. Solid. State*, **34** (1992) 1053.
2. J. Jansons, Z. Rachko, J. Valbis, J. Andriessen, P. Dorenbos, C. W. E. van Eijk and M. N. Khaidukov., *J. Phys. Condens. Matter* **5** (1993) 1589.
3. A. S. Voloshinovskii, V. B. Mikhailik, S. V. Syrotyuk and P. A. Rodnyi, *Sov. Phys. Sol. State,* **34** (1992) 1916.
4. A. S. Voloshinovskii, V. B. Mikhailik, P. A. Rodnyi and S. V. Syrotyuk, *Phys. Stat. Sol.* **B173** (1992) 739.
5. S. G. Akerman, *Opt. Spectrosc.* (USSR), **51** (1981) 515.

Radiation Effects and Defects in Solids, 1995, Vol. 134, pp. 101–106
Reprints available directly from the publisher
Photocopying permitted by license only

© 1995 OPA (Overseas Publishers Association)
Amsterdam B.V. Published under license by
Gordon and Breach Science Publishers SA
Printed in Malaysia

CALCULATION OF THE MOLLWO-IVEY PARAMETERS IN THE POINT-ION APPROXIMATION†

M. S. MALGHANI and D. Y. SMITH

Department of Physics, University of Vermont, Burlington, VT 05405, U.S.A.

We report the first general calculation of the empirical parameters appearing in the Mollwo-Ivey relation between absorption energy and interionic spacing for defects in ionic solids. The calculation is based on the Vinti sum-rule formulation of the Mollwo-Ivey law [Phys. Rev. Lett. *69*, 184 (1992)], a self-consistent Hartree-Fock-Slater procedure for defect ions, and a host-crystal environment modeled in the point-ion approximation. The Ivey exponent is reproduced in most cases to within better than 20% using this model in the alkali halides. The wide range of Ivey exponents can be qualitatively understood in terms of the compressibility of the defect.

Key words: Color Centers, Electron-Excess Centers, F Center, U Center, Mollwo-Ivey, Ivey Law.

1. INTRODUCTION

The oldest and best known empirical relation used in studies of defects in insulators is the Mollwo-Ivey power-law relation[1] between a defect's optical absorption energy, E_d, and the host-crystal interionic spacing, a:

$$E_d = Ca^{-n}, \tag{1}$$

where C is an energy-scale factor, and n is the Ivey exponent. While originally proposed for F centers, this relation holds for many electron-excess defects in ionic or partially ionic hosts. Examples[2,3] include F and F-aggregate centers, and substitutional s^2-configuration ions including H^- (U centers), Cu^-, Ag^- and Au^- in the alkali halides.

Despite its long history and wide applicability, the physical basis of the Mollwo-Ivey 'law' has long remained incompletely understood. It was recently shown[4] that the Mollwo-Ivey relation holds for defects whose ground-state rms radii have a linear dependence on the host-crystal interionic separation. The key to this insight is the Vinti sum rule,[5] which relates the mean-square radius of a quantum mechanical system's ground state to the inverse first moment of the system's dipole absorption spectrum. That is,

$$\langle 0 \mid r^2 \mid 0 \rangle = \frac{3\hbar}{2m_e} \frac{\mu_{-1}}{\mu_0}, \tag{2}$$

where m_e is the free-electron mass and

$$\mu_n = \int_0^\infty \omega^n K(\omega) d\omega \tag{3}$$

is the n^{th} moment of the absorption spectrum, $K(\omega)$. Since the dipole oscillator strength of many defects in ionic materials is largely concentrated in a single band, the Vinti sum rule takes the approximate form

† This work was supported in part by the State of Vermont and the National Science Foundation under EPSCoR Grant RII—8610679.

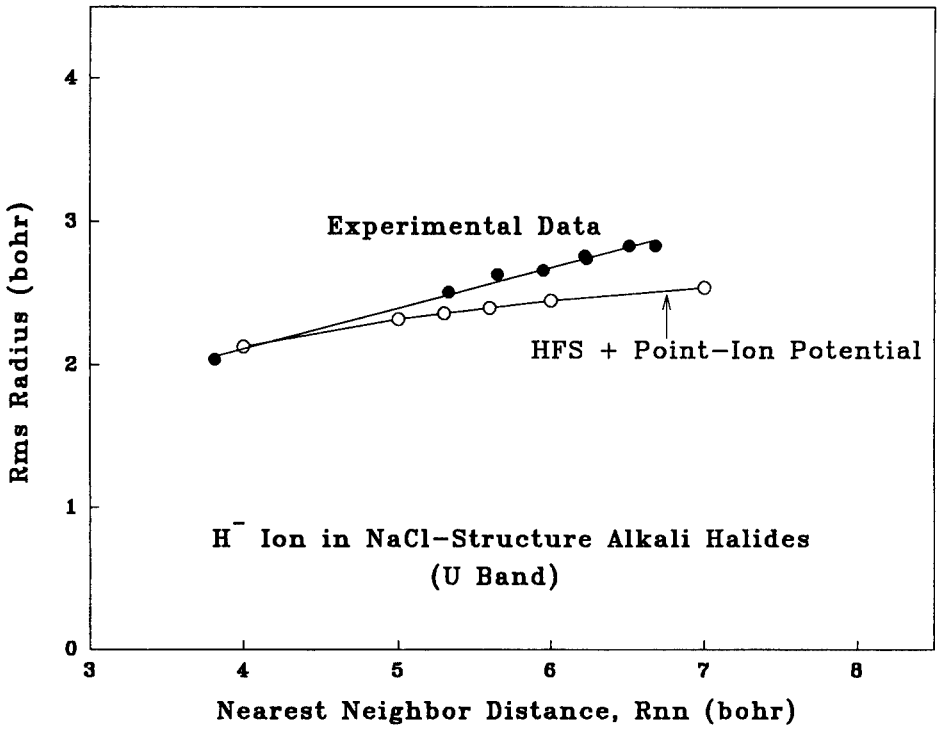

FIGURE 1. The root-mean-square radius of the U center in NaCl-structure alkali halides as a function of host-crystal interionic spacing. Solid circles: radii derived *via* the Vinti sum-rule from measured U-band spectra. Open circles: radii calculated from ground-state wave functions calculated in the Hartree-Fock-Slater approximation for H^- ions in a spherically averaged point-ion crystal field. Note: one bohr unit equals 0.529 Å.

$$\langle 0 \mid r^2 \mid 0 \rangle \approx \frac{3\hbar^2}{2m_e E_d} \tag{4}$$

for many color centers. Corrections to this simplified form have been studied[4] by including the F center's weak high-energy transitions, but the radii found by including all known absorption bands are only 2 to 5% less than those found using the F band alone. We will, therefore, use Eq. 4 here.

2. GROUND-STATE RADII

The rms radii found by applying Eq. 4 to a number of centers that show Mollwo-Ivey behavior are given in Table I for representative alkali halides. In all these cases the rms ground-state radius is considerably less than the normal host-crystal interionic separation: F-center radii are some 70 to 74% of the interionic distance; substitutional ionic defects are significantly smaller, some 40 to 50% of the interionic distance. This provides strong verification of the conventional picture for these defects as having highly localized ground states that are not significantly mixed with the host-crystal electronic levels.

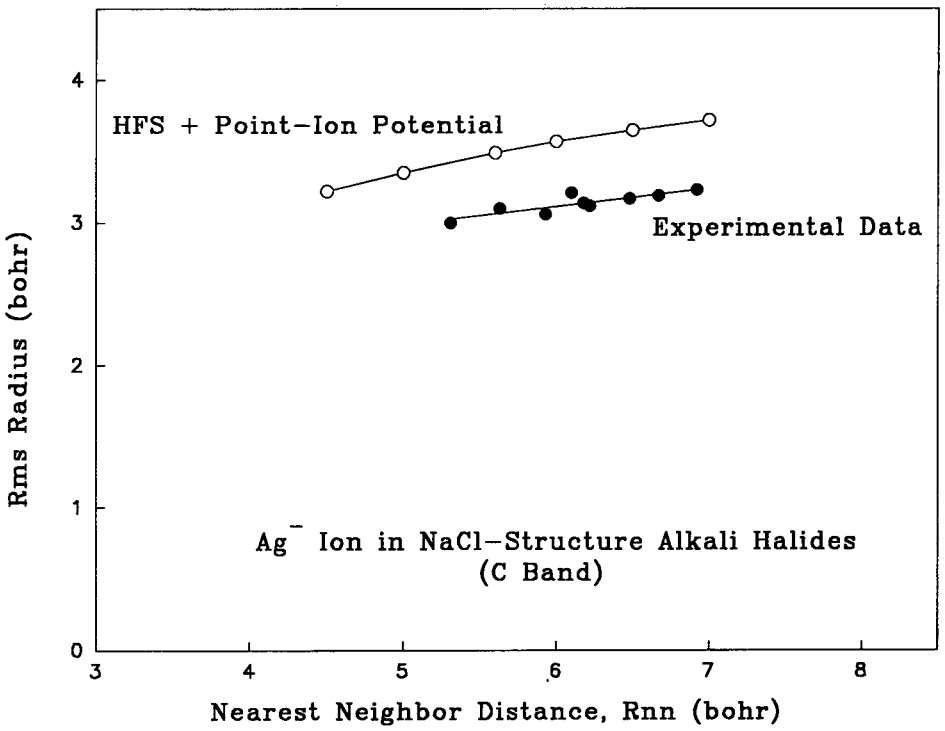

FIGURE 2. The root-mean-square radius of substitutional Ag^- ions in NaCl-structure alkali halides as a function of host-crystal interionic spacing. Solid circles: radii derived *via* the Vinti sum-rule from measured Ag^- C-band spectra. Open circles: radii calculated from ground-state ion wave functions calculated in the Hartree-Fock-Slater approximation for Ag^- ions in a spherically averaged point-ion crystal field.

A second conclusion is that the rms radii of this group of defects is very nearly a linear function of the host-crystal interionic spacing. This was first recognized for the F center (See Ref, 4, Figure 1). Here we illustrate it for the substitutional H^- (U center) and Ag^- centers in NaCl-structure alkali halides.

3. MOLLWO-IVEY PARAMETERS

A formal theory of the Mollwo-Ivey relation for defects with the majority of their oscillator strength concentrated in a single band has been developed by, in essence, inverting the above procedure. One assumes the linear relation,

$$\langle 0 \mid r^2 \mid 0 \rangle^{\frac{1}{2}} = \xi a + \eta. \tag{5}$$

Then, by using the Vinti sum rule in its approximate form, Eq. 4, and performing a Taylor-series expansion in the variable a about a convenient average interionic spacing, a_{av}, one finds [see Ref. 4 for details]

$$C \approx \frac{3\hbar^2 a_{av}^n}{2m r_{av}^2}, \tag{6}$$

and

$$n = 2\left(\frac{a_{av}}{r_{av}}\right)\frac{d\langle 0 \mid r^2 \mid 0\rangle^{\frac{1}{2}}}{da} \approx \frac{2}{1+\eta/\xi a_{av}}. \tag{7}$$

Here r_{av} is the rms radius corresponding to the average interionic spacing, a_{av}.

The high degree of ground-state localization of the centers we are considering allows us to model them in a crystal-field approximation. To test the predictive powers of the sum-rule theory of the Mollwo-Ivey relation, we have calculated the ground electronic states of the F, U, and noble-metal centers in the Hartree-Fock-Slater approximation[7] using a spherically averaged point-ion potential to model the surrounding host lattice for this initial test of the theory. Examples of the resulting radii are given for the H^- and Ag^- ions in Figures 1 and 2. Comparison of these calculated radii with those derived from absorption spectra *via* the Vinti sum rule shows that the calculations reproduced the 'observed' radii to within 16%.

Table I

Root-mean-square radii of selected electron-excess centers in NaCl-structure alkali halides that satisfy Mollwo-Ivey relations. These values were calculated from the approximate form of the Vinti sum rule, Eq. 4, which assumes all the defect's oscillator strength is concentrated in a single symmetric band; absorption-band energies were taken from Ref. 3. The nearest-neighbor interionic separation is given for comparison. The estimates of the ionic radii for s^2 ions derived from crystallographic data for similar ions are given for comparisons.

	Defect Radii in Å for Various Hosts								Crystal Data
Defect	NaCl	NaBr	KCl	KBr	KI	RbCl	RbBr	RbI	Estimates[b] Å
F Centers	2.04	2.23	2.23	2.36	2.47	2.37	2.48	2.59	
U Centers (Sub. H^-)	1.33	1.39	1.41	1.45	1.50	1.46	1.50	—	2.08
Substitutional Cu^-	—	—	1.67	1.70	1.73	—	—	—	1.4–1.8
Substitutional Ag^-	1.59	1.64	1.62	1.65	1.69	1.66	1.68	1.71	1.5–2.0
Substitutional Cu^-	—	—	1.45	1.47	1.50	1.47	1.49	1.52	1.5–1.7
Interionic Spacing[a] Å	2.81	2.98	3.14	3.29	3.53	3.27	3.43	3.66	

a. From Singh, Ref. 6.
b. From Shimanuki and Nishimaki, Ref. 3.

Eqs. 6 and 7 for the parameters in the Mollwo-Ivey relation involve both the rms radius of the defect and its derivative with respect to a. We have determined the derivative by fitting the calculated rms radii with a polynomial in a and evaluating its derivative at the Taylor-series expansion point, a_{av}, which was normally taken as the mid-point of the range of interionic separations for which data on the defect in question are available. Table II summarizes the results of evaluating Eq. 7. Here we have treated all the NaCl-structure alkali halides as a group.[8] Experimental values of the exponent derived from Mollwo-Ivey plots of observed spectra are given for comparison. Agreement between calculated and experimental values of n is quite good considering the approximations made. More importantly, the results allow us to interpret the physical meaning of the Ivey exponent.

According to Eq. 7, the Ivey exponent is (to within a factor of two) a measure of the spatial 'compressibility', $d(r/r_{av})/d(a/a_{av})$, i.e. the rate of change in the reduced rms

radius, r/r_{av}, with respect to changes in the reduced host-crystal spacing, a/a_{av}. But this derivative depends on the slope and intercept parameters, ξ and η, in Eq. 5, according to which the defect behaves as though it contained a hard core of radius η.

Applying this notion to the present data, we see that both experiments and our calculations yield Ivey exponents that divide naturally into three groups; the F center with $n \simeq 2$; the U center with $n \simeq 1$; and the negative noble-metal ions with $n \simeq 0.5$. Table II shows that a similar division holds for η; the F center has the smallest value of η, less than 0.3 Å; the U center has $\eta \simeq$ 1.0 Å; and the noble-metal centers have $\eta \simeq$ 1.5 Å. If η is interpreted as representing an effective defect core radius, it is reasonable to compare the calculated values with the atomic core involved—a hydrogen atom for the U center and the corresponding atoms for the noble metals. Table II shows there is very good correspondence between η and the radii of these atoms. In the case of the F center there is no 'core', so one might expect $\eta = 0$, not the observed value of $\sim$ 0.3 Å. However, calculation of the F center's electronic structure for small lattice spacings show that as the interionic separation, a, decreases, the kinetic energy of confinement ($\sim a^{-2}$) increases faster than the potential well's depth ($\sim a^{-1}$). As a result, the F-center electron delocalizes below a critical radius a_c, which can be estimated by equating the Madelung energy to the kinetic energy of an electron confined to a cubic box with side $2a_c$. The result is $a_c = 3\pi^2/8\alpha$ bohr units (α = Madelung constant) or approximately one Ångstrom which is very nearly the point at which our numerical calculations show the rms radius starts to diverge. Extrapolation of the calculations to zero lattice constant yields an apparent hardcore size of approximately 0.3 Å.

Table II

Experimental and calculated values of the Ivey exponent, n, for defects in NaCl-structured alkali halides. Observed atomic radii are given for comparison with the apparent core radius, η. Values of the average interionic spacing, a_{av}, used in the calculation are given since n is weakly dependent on the value chosen.

Defect	Fit to Experiment[a]			Atomic Radii[b]	HFS-Point-Ion Model[c]	
	n	ξ	η(Å)	Å	n	a_{av}(Å)
F Centre	1.77	0.64	0.27	—	1.67	2.84
U Centre (Sub. H^-)	1.10	0.28	0.52	0.78	0.65_o	2.84
Substitutional Cu^- (C band)	0.65_4	0.15	1.20	1.27	0.57	3.32
Substitutional Ag^- (C band)	0.54	0.13	2.35	1.44	0.62	3.24
Substitutional Au^- (C band)	0.58_3	0.13	0.97	1.44	0.53	3.40

a) Absorption band energies taken from Ref. 3.
b) From Ref. 9, Appendix B.
c) Based on a parabolic fit to calculated rms radii *vs.* interionic spacing. Full Slater exchange used in HFS computations.

In summary, we have calculated the ground-state radii of a number of typical color centers in the alkali halides which are known to obey Mollwo-Ivey relations. We find that all ground-state radii are significantly smaller than the interionic spacing. Such centers can be treated in a crystal-field model. Accordingly, we have calculated the defect rms radii using the Hartree-Fock-Slater procedure and, for this initial test, a point-ion crystal field. From the predicted radii we then calculated the Ivey-exponent using the Vinti sum-rule theory of the Mollwo-Ivey relation. The results are in good agreement with experiment and lead to the interpretation of the Ivey exponent as a measure of a defect's spatial compressibility. Small, but systematic, differences between the present results and experiment are attributed to ion-size effects, which we plan to investigate in the future.

REFERENCES

1. E. Mollwo, Nachr. Ges. Wiss. Göttingen, Heft 1, 97 (1931); H. F. Ivey, *Phys. Rev.* **72,** 341 (1947).
2. See, for example, W. B. Fowler, *Physics of Color Centers* (Academic, New York, 1968).
3. S. Shimanuki and N. Nishimaki, *Phys. Status Solidi* **B122**, 269 (1984).
4. M. S. Malghani and D. Y. Smith, *Phys. Rev. Lett.* **69**, 184 (1992).
5. J. P. Vinti, *Phys. Rev.* **41**, 432 (1932).
6. B. P. Singh, *Phys. Stat. Sol.* **B162**, 329 (1990).
7. F. Herman and S. Skillman, *Atomic Structure Calculations* (Prentice-Hall, Englewood Cliffs, 1963).
8. Somewhat better fits are obtained if separate Mollwo-Ivey plots are made for each alkali family of salts. We have shown that this arises in part from nonlinear dependence of rms radii on a. Details of this will be discussed elsewhere.
9. J. H. Schulman and W. D. Compton, *Color Centers in Solids* (MacMillan, New York, 1962), Appendix B.

Radiation Effects and Defects in Solids, 1995, Vol. 134, pp. 107–110
Reprints available directly from the publisher
Photocopying permitted by license only

© 1995 OPA (Overseas Publishers Association)
Amsterdam B.V. Published under license by
Gordon and Breach Science Publishers SA
Printed in Malaysia

DYNAMICS OF LITHIUM IONS IN LITHIUM OXIDE

J. L. GAVARTIN, C. R. A. CATLOW, A. L. SHLUGER, P. W. M. JACOBS*
and Z. A. RYCERZ*

The Royal Institution of Great Britain, 21 Albemarle Street, London W1X 4BS, U.K.
**Centre for Chemical Physics, University of Western Ontario, London, Canada*

It is known that high ionic conductivity in fluorite-structured materials is associated with thermally created Frenkel-type disorder at temperatures well-below the melting point. Using crystalline Li_2O as a model system, we studied the mechanism of formation of Frenkel pairs at temperatures close to the transition to the fast-ionic phase, and ionic motion at temperatures above the transition point. The dynamical behaviour of lithium oxide has been studied using both lattice dynamics within the quasi-harmonic (QH) approximation and molecular dynamics (MD).

The QH approximation allows one to evaluate the Helmholtz free energy of a crystal in a microscopic model, while neglecting configurational entropy effects. The temperature dependence of the lattice parameter, elastic constants, heat capacity and vibrational spectra were calculated within this approximation and compared with available experimental data. This comparison proved the ability of both the shell-model and rigid ion model to describe not only static but also thermodynamic properties of crystalline lithium oxide. The phonon dispersion $w(q)$ and phonon density of states were calculated at various temperatures, simulated by lattice expansion. Figure 1 shows the phonon dispersion at 10 K and at 1000 K, as well as the corresponding density of states obtained within the QH approximation. The remarkable feature of these results is the peak in the transverse Raman (TR) mode and the minimum in the longitudinal optical (LO) mode, which occur at the same k-point, namely (0.66, 0.66, 0). Futhermore, these branches approach one another as the temperature increases, and have a tendency to cross near this k-point. Therefore, we calculated the dispersion along the [0.66, 0.66, k_z] direction and found considerable softening of the modes as the temperature approaches the fast-ionic phase transition point. Analysis of vibrational data provides the following scenario for Frenkel pair formation. Mode softening leads to the loss of relative phase of Li^+ ions moving along the [100] crystal direction (as the TR mode disappears), so that the ionic motion can be considered as that of a set of coupled oscillators. As soon as a few neighbouring ions get in phase, a large amplitude coherent motion rapidly develops along ⟨100⟩ direction. Such fluctuations propagate a caterpillar-like mechanism, whereby a Li^+ ion moves into the cube-interstitial position, while the rest of the chain of ions moves simultaneously along ⟨100⟩, each ion filling the site vacated by its nearest-neighbour. Thus an interstitial ion and a cation vacancy, separated by a few unit cells, can be created within the same elementary act.

To verify our deductions from the QH approximation we employed the MD method, which follows the time evolution of the positions and velocities of a small ensemble of particles at constant N,V,E. These MD simulations have revealed a remarkable justification of the model for Frenkel defect formation suggested by lattice dynamics. Figure 2, illustrates the coherent motion of three Li^+ ions involved in the formation of a stable interstitial. Ions 1,2,3 show positive X displacements between time steps $\Delta t = 3230$ and 3300. Simultaneously ion 1 undergoes displacements in the Y^- and Z^+ directions which result in the the formation of an interstitial. The MD simulation of a Li_2O crystal at T = 1000 K shows a large number of such fluctuations involving highly coherent motion of 2 or 3 Li ions.

In the fast ionic regime, simulated at 1700 K, radial distribution functions (RDF) show

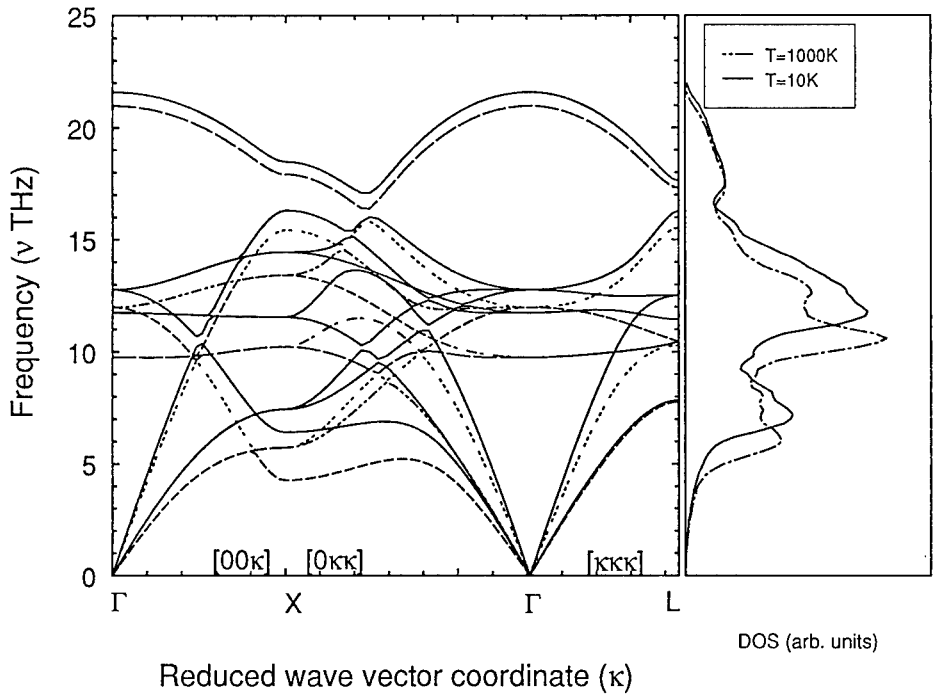

FIGURE 1 Phonon dispersion curves together with the phonon DOS calculated at 10 K and 1000 K, using the shell-model within the quasi-harmonic approximation.

for O-O a succession of well-defined peaks, while for Li-O RDF peaks are less-well defined from 3^{rd} nearest neighbours onwards, and for Li-Li they are much more diffuse. This indicates a well-defined O sublattice but a more diffuse Li sub-lattice because of intensive ionic motion. The time-averaged Li^+ density function n(r) shows non-zero values between ion sites along ⟨100⟩, confirming motion is mainly along ⟨100⟩, but n(r) is extremely small between ion sites along ⟨110⟩ due to relatively few ⟨110⟩ jumps. Along ⟨111⟩ n(r) is significant between ion sites, suggesting interstitials and ionic motion by the non-collinear interstitialcy mechanism. Projections of particle positions on XY, YZ or ZX planes, and also single-ion trajectories, show that vacancy jumps occur in about 0.2 ps, that is in about 5 vibrational periods, in contrast to Frenkel defect formation, which occurs in two vibrational periods, due to the concerted motion of ⟨ 100 ⟩ chains of 2,3 .. Li^+ ions. Three-dimensional plots of the density in (100) planes show Li^+ ions concentrated on lattice sites but with significant density along ⟨ 100 ⟩ directions due to ions in motion between sites. Similar plots in (400) planes show zero Li^+ density at the two cube-centre sites occupied by O^{2-}, but significant density (Figure 3) in the two alternate cube-centre sites and along ⟨110⟩ directions connecting these sites, suggesting ⟨110⟩ direct jumps. Thus the consistent application of lattice dynamics and molecular dynamics is proving a valuable aid to understanding the details of defect formation and motion.

Finally, comparison of the phonon dispersion curves for several other crystals with the fluorite structure show similar features in the behaviour of TR and LO modes. Therefore, we believe that the same fluctuations are responsible for the fast-ionic phase transition in

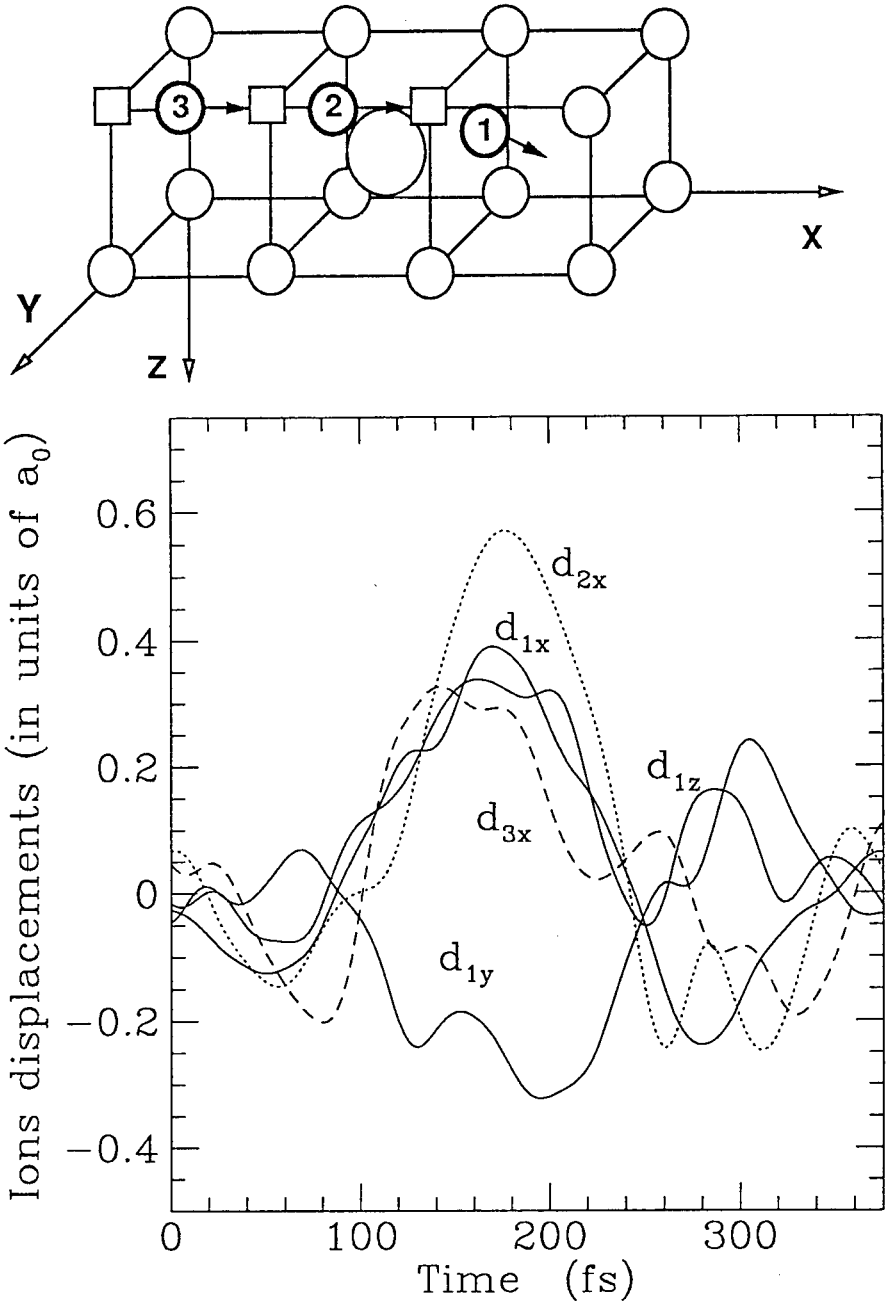

FIGURES 2 A particular example of coherent ionic motion in real time, extracted from a rigid ion (NVE) MD run at 1000 K. Simulation box of 324 ions with a density taken from the quasi-harmonic estimate of the thermal lattice expansion. These are the fluctuations responsible for the creation of spatially separated Frenkel defects, by the first ion moving into the interstitial position and the other 2, 3 or even more ions following simultaneously into their nn-site along the ⟨100⟩ direction. (Time interval = 2.5 fs)

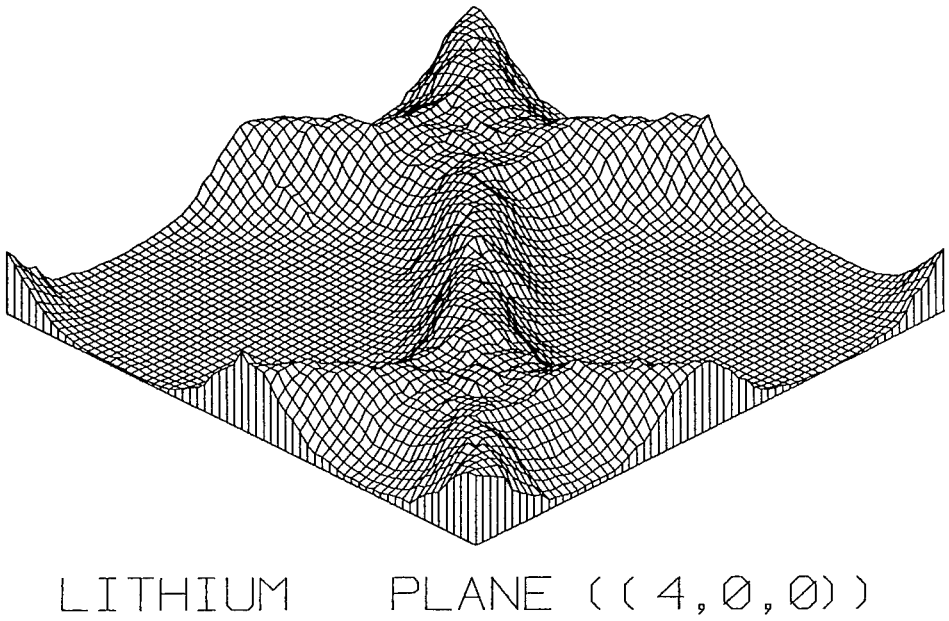

FIGURE 3 Density of Li^+ ions in the (400) plane. In a perfect Li_2O crystal at low T this plane would contain only a pair of O^{2-} ions.

all materials with this structure. Indeed, a similar mechanism for Frenkel defect formation has been observed in MD of $SrCl_2$.

ACKNOWLEDGEMENTS

PJ thanks NSERC for a Research Grant; JG thanks The Royal Society for financial support; ALS and JG thank the Royal Institution of Great Britain for hospitality and financial support.

Radiation Effects and Defects in Solids, 1995, Vol. 134, pp. 111–115
Reprints available directly from the publisher
Photocopying permitted by license only

© 1995 OPA (Overseas Publishers Association)
Amsterdam B.V. Published under license by
Gordon and Breach Science Publishers SA
Printed in Malaysia

COMPUTER MODELLING AND BRILLOUIN SCATTERING STUDIES OF HIGH TEMPERATURE DISORDER IN CdF_2

T. T. NETSHISAULU[†], P. E. NGOEPE[‡], J. D. COMINS and C. R. A. CATLOW*

[†]*Department of Physics, University of North, Sovenga 0727, South Africa;*
[‡]*Department of Physics, University of the Witwatersrand, P.O. Wits 2050, South Africa;*
**The Royal Institution, 21 Albermarle Street, London W1X 4BS, U.K*

The reliability of the lattice simulations depends on the quality of the potentials used. Hence, the interionic potentials of CdF_2 were derived and used in the calculations of the crystal bulk data. The temperature dependences of elastic constants is investigated. Elastic properties are predicted. The complementary studies using Brillouin scattering methods, show that the disorder at the transition temperature ($T_c \approx 900$ K) results in an abrupt decrease in the elastic constant C_{11}. Both methods show that the elastic constants linearly decrease with increasing temperature within the low temperature region. Similar trends have been observed in other fluorites. This shows that our interionic potentials reproduce the behaviour of CdF_2 reasonably well.

Key words: CdF_2, elastic constants, lattice simulation, interionic potentials, lattice parameter, Brillouin scattering.

1 INTRODUCTION

Compounds with a fluorite structure have been extensively studied both experimentally and theoretically. Most of these fluorites (e.g. CaF_2, PbF_2, etc) undergo a transition to a fast-ion phase, above a characteristic temperature T_c, where a significant reduction in certain elastic constants and a substantial rise in ionic conductivity occur on the fluorine sublattice.[1]

Although pure CdF_2 has a fluorite structure, its high temperature behaviour is still not well known. However, an addition of CdF_2 to fluorites like PbF_2, reduces the transition temperature of the latter quite considerably.[2] Hence, a better understanding of the elastic properties of this compound is necessary.

In the present work we present the empirically derived shell model and rigid ion potentials of CdF_2, for molecular statics studies. This will be followed by calculated bulk crystal data such as the elastic constants. To complement these studies, we have conducted Brillouin scattering measurements on this compound in order to study the effect of disorder on the elastic constants of CdF_2. The results obtained are also compared with those of other alkaline-earth fluorides to check whether the same behaviour is observed.

2 INTERIONIC POTENTIALS

Interionic potentials are used in predicting structural and thermodynamic data of ionic crystals. The lattice energy of the crystal is given by

$$U_L(r_{ij}) = \sum_{i>j} \frac{q_i q_j}{r_{ij}} + \sum_{i>j} \phi_{ij} \qquad (1)$$

where q_iq_j/r_{ij} and ϕ_{ij}, are the Coulomb and the short-range interactions, respectively. The latter describes the effects of overlap of the electron charge clouds of the interacting ions. The most popularly used expression in simulating ionic solids has the Buckingham form

$$\phi_{ij}(r) = A_{ij} \exp(-r/\rho_{ij}) - C_{ij}/r^6 \tag{2}$$

Ionic polarisability is treated using the shell model, where an ion is simulated by a massless shell linked to a core by a harmonic spring. The free-ion polarisability is defined by

$$\alpha_i = Y_i^2e^2/k_i \tag{3}$$

where Y_ie is the shell charge and k_i is the spring constant. Polarisation and short-range interactions are coupled by allowing repulsive forces to act only between the shells.[3] The reliability of the simulation depends on the appropriate determination of the potential parameters in equations (2) and (3).

3 COMPUTATIONAL PROCEDURE

Short-range potential parameters of CdF_2 were derived empirically using a THBFIT code.[4] The least-squares fitting procedure was used where potential parameters were adjusted to the crystal bulk data (i.e. elastic and dielectric constants).

Perfect lattice calculations were computed using the basic principles embodied in the THBREL code.[4] Firstly, a fluorite unit cell was specified and repeated infinitely in space. Furthermore, the elastic constants were calculated from the second derivatives of the lattice energy with respect to lattice strains. Finally, the temperature dependence of the elastic constants were simulated from the change of the lattice parameter of CdF_2 with temperature.[2]

4 EXPERIMENTAL PROCEDURE

In the present investigation, the Brillouin scattering measurements were carried out using the 488 nm line from an argon-ion laser operated in a single mode and analysed with a triple-pass Fabry-Perot interferometer. The Brillouin shift ν and the velocity of the acoustic phonons V are related by

$$\nu = (2nVw_o/c) \sin(\theta/2) \tag{4}$$

where n is the refractive index of the material, w_o is the frequency of the incident light, and θ is the scattering angle, chosen to be 90°.

Cadmium fluoride samples typically of the size $3 \times 3 \times 3$ mm^3, were cut out from the single boules which had been oriented using the Laue back-reflection technique. The procedure followed is outlined elsewhere.[5]

In the present report the samples were prepared for studies along the [100] phonon propagation. Acoustic mode frequencies associated with C_{11} were measured in the temperature range 300 – 1100 K. The temperature dependence of the elastic constants could be related to ν^2 provided that changes in ν^2 dominate those in ρ/n^2, so that $C_{11}\alpha(\rho/n^2)\nu^2$ becomes $C_{11}\alpha\nu^2$.

5 RESULTS AND DISCUSSIONS

Figure 1 shows the lack of anomaly in the temperature variation of the lattice parameter with temperature for CdF_2 in the temperature range 300–800 K.

The calculated lattice properties evaluated from the potential models are given in table I. Most of these properties are fairly reproduced by these models, with the exception of C_{12} which is underestimated by the rigid-ion model. However, the latter potentials have been found to be satisfactory in molecular dynamics simulations provided that static dielectric constants are correctly predicted.[6]

It is evident from our simulation studies that linear reductions occur in the temperature dependence of the elastic constants (Figure 2). The calculations were based on the quasi-harmonic theory of Garber and Granato.[7]

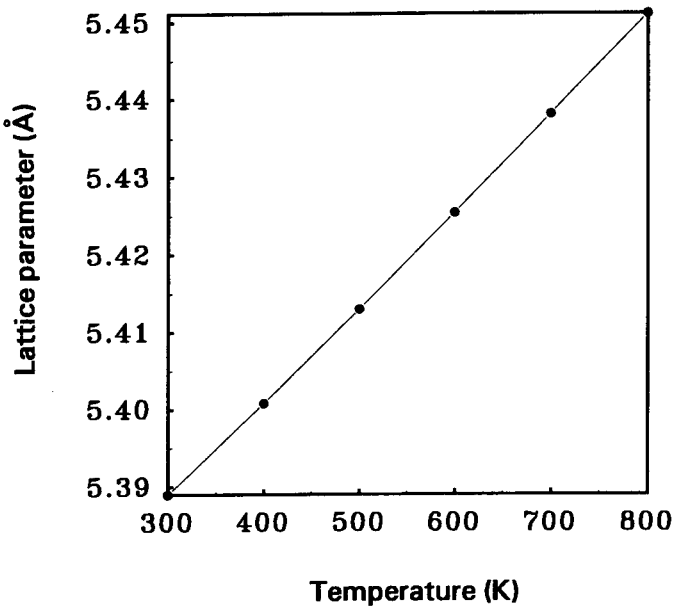

FIGURE 1 The variation of the lattice parameter of CdF_2 with temperature[2].

TABLE I
Crystal bulk data of cadmium fluoride at room temperature.

	Elastic constants			Dielectric constants	
	C_{11}(Gpa)	C_{12}(GPa)	C_{44}(GPa)	ϵ_0	ϵ_∞
Calculated					
Shell model	188.10	48.10	19.60	9.46	2.23
Rigid-ion	182.60	20.83	20.97	8.95	0.00
Experiment	184.00 (183.8)*	67.00	21.80	9.00	2.43

*Our Brillouin scattering experimental value.

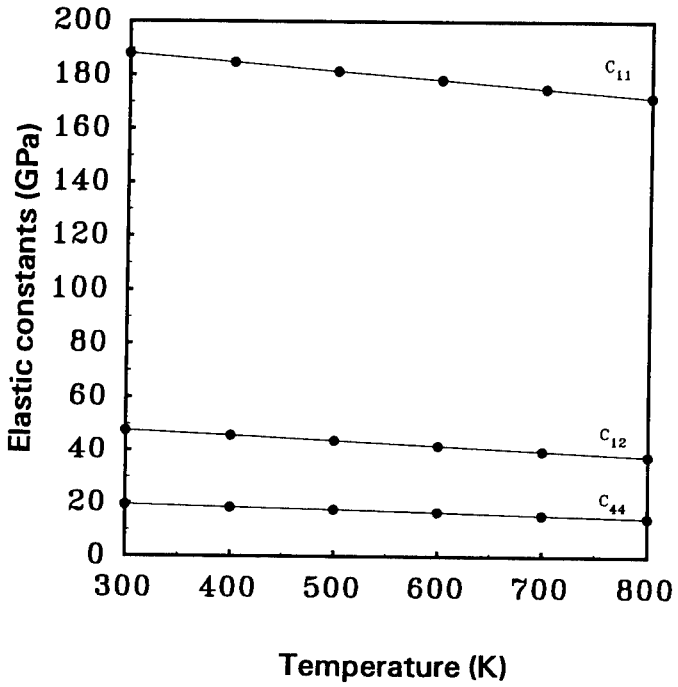

FIGURE 2 The temperature dependence of the calculated elastic constants of CdF_2.

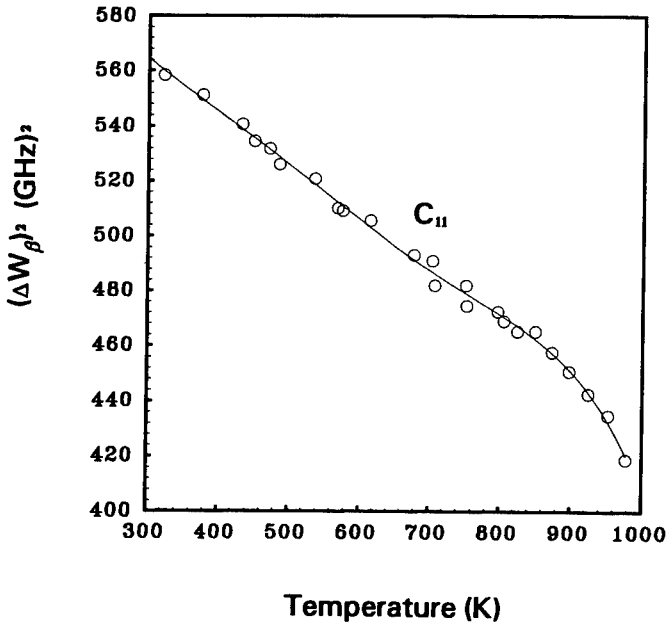

FIGURE 3 The temperature dependence of the square of Brillouin-scattering frequency in CdF_2.

TABLE II
A comparison of the calculated and experimental temperature gradients dC_{ij}/dT of the various elastic constants of CdF_2 below 800 K.

C_{ij}	Calculated	Experimental	% Deviations
	(MPa/K)	(MPa/K)	
C_{11}	33.9	62.8	46.0
C_{12}	20.6		
C_{44}	9.7		

The behaviour of the mode frequency ν^2 and its associated elastic constant C_{11} is shown in Figure 3. A clear linear initial fall in the mode frequency with temperature persists up to about 900 K and is followed by an abrupt reduction. These substantial reductions in the mode frequency marks the onset of the diffuse superionic transition. We also note in comparing our room-temperature values with the Brillouin scattering results that, the value of C_{11} is well reproduced by our interionic potentials.

Further support is provided by our molecular dynamics results,[8] which predicted the diffuse transition temperature to the fast-ion phase ($T_c \approx 993$ K), and also highlighted that migration in CdF_2 occurs via a fluorine vacancy mechanism.

Estimates of the elastic constants gradients are given in table II. Our calculations show large variations in C_{11}, whereas for C_{12} and C_{44}, smaller variations were obtained. Our calculated linear reduction in C_{11} is smaller than the experimentally observed value. This discrepancy arise from the difference between theory and experiment for the elastic constants themselves.

The present investigation strongly indicates that our data for CdF_2 are typical of those of other fluorites. Hence, this study has provided further supporting evidence that CdF_2 is a superionic conductor.

REFERENCES

1. J. D. Comins, P. E. Ngoepe and C. R. A. Catlow, *J. Chem. Soc. Faraday Trans.* **86**, 1183 (1990).
2. I. Kosacki, *Appl. Phys.* **A49**, 413 (1989).
3. B. G. Dick and A. W. Overhauser, *Phys. Rev.* **112**, 90 (1958).
4. C. R. A. Catlow, *Annu. Rev. Mater. Sci.* **16**, 517 (1986).
5. P. E. Ngoepe, *Ph.D. Thesis* (University of Witwatersrand, Johannesburg, 1987).
6. C. R. A. Catlow and M. L. Wolf, *Proc. R. Soc. Lond.* **A413**, 201 (1987).
7. J. A. Garber and A. V. Granato, *Phys. Rev.* **B11**, 3990 (1975).
8. T. T. Netshisaulu, P. E. Ngoepe, J. D. Comins and C. R. A. Catlow, *Proceedings of the International Conference on Defects in Insulating Materials*, ed. O. Kanert and J. M. Spaeth (World Scientific Publishers, 1993, 979–981).

Radiation Effects and Defects in Solids, 1995, Vol. 134, pp. 117–121
Reprints available directly from the publisher
Photocopying permitted by license only

© 1995 OPA (Overseas Publishers Association)
Amsterdam B.V. Published under license by
Gordon and Breach Science Publishers SA
Printed in Malaysia

MIXED DIMERS IN RARE-EARTH-DOPED FLUORIDES

SAULO SOARES DE SOUZA and ANA REGINA BLAK[#]

Instituto de Física—Universidade de São Paulo, C.P. 20516, CEP 01452–990, São Paulo, Brazil

(Received July 1, 1994)

Dipole aggregation in rare-earth-doped fluorides, using the HADES code to calculate the energies of the defects was extensively studied. The binding energy values determined for dipoles and dimers agree quite well with published data. The possibility of creation of mixed dimers took into account the size of the impurities and also the electronic configuration. The results obtained confirmed that binding energies depend upon the ionic radius of the impurities and revealed a preferential order for the formation of mixed dimers. For the impurities with ionic radii larger than or very near to that for calcium the chance of forming mixed dimers is greater than for smaller impurities. The obtained values of the energies confirm the possibility of mixed dimer creation although simple dimers are preferentially formed first.

Key words: fluorides, dipoles, dimers binding energy and static simulation.

1 INTRODUCTION

Calcium fluoride solutions with trivalent rare-earth-fluorides were extensively investigated using Static Defect Simulations. Nevertheless, the occurence of dimers of different impurities has never been considered. It is well known that calcium fluoride forms a wide range of solid solutions with other fluorides, referred to as 'anion excess fluorides', whose predominant defects are dipolar complexes formed by substitutional trivalent ions in a Ca^{2+} site (M^{3+}) and an interstitial fluorine (F_i^-) in the nearest neighbour (nn) site.[1] In spite of several studies dealing with the theory of defect aggregation in fluorides[2,3,4,5] the contribution of this work was to calculate the activation energies of the aggregation processes originated by the presence of two different impurities in the crystal structure forming the dimer. The calculations allow distinction to be made among various possible configurations of small dipole clusters, like dimers, and the variation of the stability of these dimers with the size of the dopant ion.

2 METHOD OF CALCULATION

The defect simulation procedures programmed in the Harwell Automatic Defect Examination System (HADES) code, provided by the Harwell Laboratory, U.K., include an accurate treatment of lattice relaxation. The total energy of the system is minimized by a relaxation of the ions surrounding a defect. This relaxation decreases fairly rapidly for distances away from the defect. The method generally adopted is based on the 'two regions strategy', where the crystal surrounding the defect is divided into two regions. In the inner region (region I), immediately surrounding the defect, atoms interact atomistically, through interatomic potentials and outside this region, the forces become relatively weak and a dielectric continuum approximation following Mott and Littleton[6] is employed. In the present calculations, consistent region I sizes of 90 ions were used.

[#] The participation in the conference was supported by Fundação de Amparo à Pesquisa do Estado de São Paulo (FAPESP).

3 RESULTS

3.1 *Homogeneous Dimers*

The first calculations were done assuming two dipoles of the same kind of impurity in four different configurations, as is shown in Figure 1. According to the results, all four models may occur but the first one is the most stable. Analysing the binding energy it is possible to conclude that only the first configuration is permitted, transforming the binding energy into a very important parameter in this study. This energy is obtained subtracting the formation energy of the two individual dipoles from the formation energy of the dimer.

3.2 *Mixed Dimers*

The possibility of a dimer formation from two dipoles of two different impurities has been considered, following the same four configurations used in the case of homogeneous dimers and combining the seven lanthanide ions: Lu, Yb, Er, Tb, Gd, Eu and La. All the parameters were taken from the work done by the group of Catlow[2,4] on defects formed with M^{3+} ions in fluorides. The calculation followed the same procedure as before, first obtaining the formation energy and then the binding energy. All the possible configurations of dimers were considered, a total of 21 combinations in five different situations. In the case of configuration 2, for two different impurities, there are now two different possibilities. Again, configuration 1 is the most favourable one, followed by the second one where the larger dopant ion is situated between two fluorine ions. In general, the configuration presenting higher energy values always contain one La^{3+} ion and the lower energy values, one Yb^{3+} ion, suggesting that the formation energy values are dependent on the size of the rare-earth dopant. On the other hand, for the binding energies, dimers containing La^{3+} present the lowest values, reinforcing the correlation between energy values and ionic radii of the dopant ion. In an attempt to correlate formation and binding energies with the ionic radius of the second dopant ion, Figures 2 and 3 were done. In general, the formation energy increases with the ionic radius of the second dopant ion (Figure 2), but the binding energy of the dimers decreases (Figure 3). When the two impurities have approximately the same

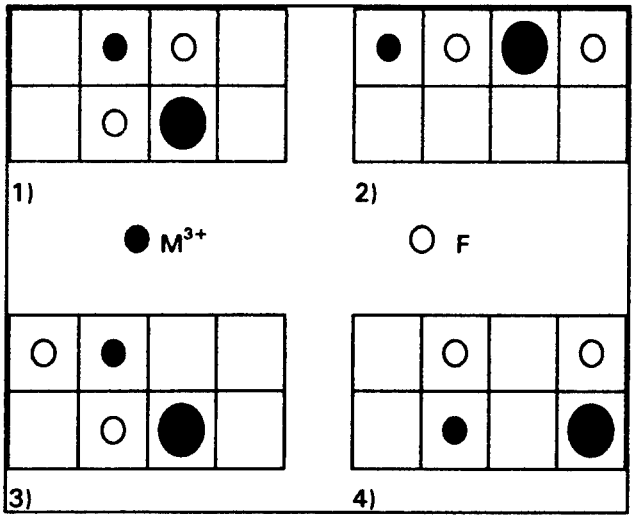

FIGURE 1 The four models suggested for dimers.

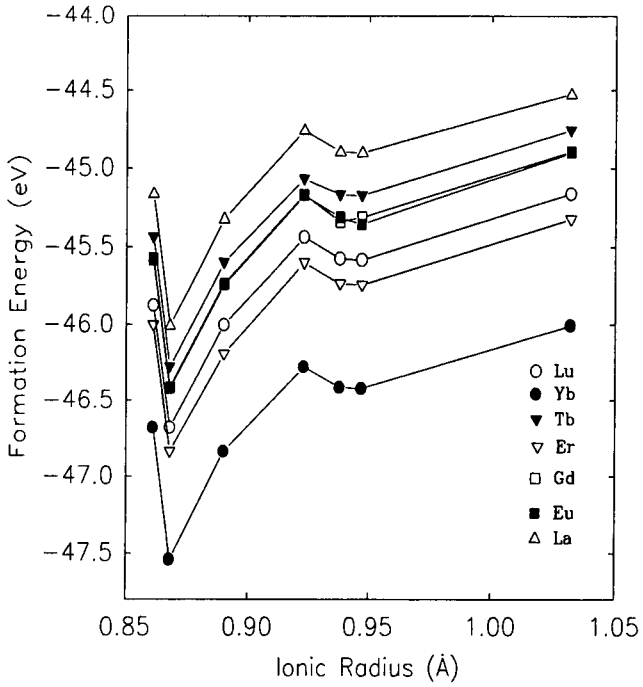

FIGURE 2 Formation energy for all the dimers formed with Lu, Yb, Er, Tb, Gd, Eu and La.

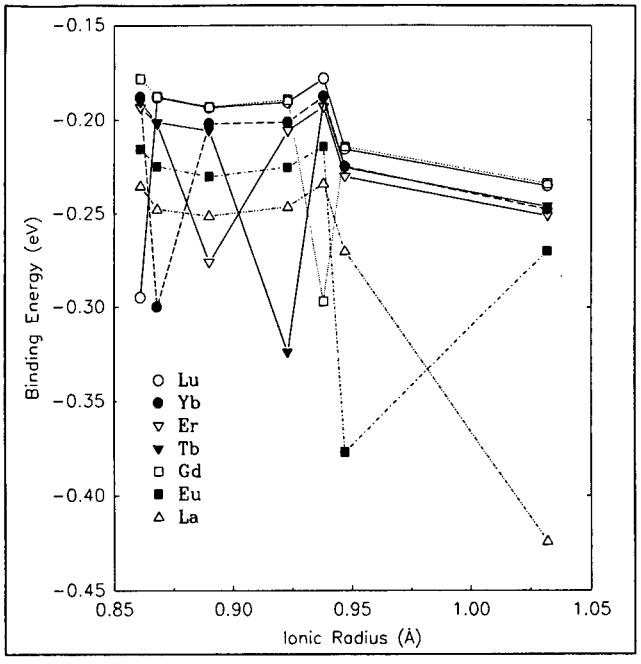

FIGURE 3 Binding energy for all the dimers formed with Lu, Yb, Er, Tb, Gd, Eu and La.

size, this effect is not observed. In Table I the order of formation of dimers is presented, taking as a guide the binding energies. In all cases, the homogeneous dimers come in the first place followed by the mixed dimers where Lanthanum is one of the M^{3+} impurity ions. This confirms the tendency of ions larger than calcium to form small aggregates of dipoles. The examination of the dipoles in pairs originated Table II. After each pair there are sets of three numbers, the first and the second ones, representing, respectively, the simple dimer of the larger impurity ion (1) and the simple dimer of the smaller impurity ion (2) and the third one representing the dimer of both impurity ions (3). The mixed dimers are always in last place in the preference order. For Gd-Tb, Gd-Yb, Er-Yb and Er-Lu, an inversion in the preferential order is observed, the smaller dimer coming before the larger one. From Figure 2 one perceives that the energy values are minimum for Lu, Yb and Tb. This means that the expected behaviour is not always that strictly related to the ion sizes.

4 CONCLUSIONS

Although two dipoles with two different M^{3+} impurity ions can form a dimer without violating stability conditions, simple dimers with two dipoles of the same impurity ion are frequently formed first. Among the four configurations for dimers considered in this work,

TABLE I
The preferential order of dimers in terms of binding energies.

order	dimer	order	dimer
1	La-La	15	Tb-Eu
2	Eu-Eu	16	Yb-Eu
3	Tb-Tb	17	Lu-Eu
4	Yb-Yb	18	Gd-Eu
5	Gd-Gd	19	Er-Tb
6	Lu-Lu	20	Yb-Er
7	Er-Er	21	Yb-Tb
8	Eu-La	22	Lu-Er
9	Er-La	23	Er-Gd
10	Yb-La	24	Lu-Tb
11	Tb-La	25	Tb-Gd
12	Lu-La	26	Lu-Yb
13	Gd-La	27	Yb-Gd
14	Er-Eu	28	Lu-Gd

TABLE II
Formation order of dimers. (1) Simple dimer of the larger impurity ion, (2) simple dimer of the smaller impurity ion and (3) dimer of both impurity ions.

dimer	formation order	dimer	formation order	dimer	formation order
La-Eu	1,2,3	Eu-Tb	1,2,3	Gd-Lu	1,2,3
La-Gd	1,2,3	Eu-Er	1,2,3	Tb-Er	1,2,3
La-Tb	1,2,3	Eu-Yb	1,2,3	Tb-Yb	1,2,3
La-Er	1,2,3	Eu-Lu	1,2,3	Tb-Lu	1,2,3
La-Yb	1,2,3	Gd-Tb	2,1,3	Er-Yb	2,1,3
La-Lu	1,2,3	Gd-Er	1,2,3	Er-Lu	2,1,3
Eu-Gd	1,2,3	Gd-Yb	2,1,3	Yb-Lu	1,2,3

the number 1, where the two dipoles are parallel, side by side in opposite directions turn out to be the most stable in all cases. Analysis of the formation energies showed that Yb presents the lowest values although being one of the smallest ions considered in the calculation. It is well known that for large ions the tendency in forming small aggregates, like dimers, is increased. One possible explanation is that Yb is the only element from the lanthanide series presenting closed shells. The analysis of the binding energies showed that La has preference upon all the other ions in forming dimers. In this case, ion size explains this behaviour, because this is the only impurity ion larger than Ca, confirming that large ions preferentially form small aggregates.

ACKNOWLEDGMENTS

The authors are grateful to the Harwell Laboratory, UK, for providing HADES II code.

REFERENCES

1. M. E. G. Valério, A. R. Blak and A. Chadwick, *Rad. Eff. Def. Sol.* **119–121**, 393 (1991).
2. J. Corish, C. R. A. Catlow, P. W. M. Jacobs and S. H. Ong, *Phys. Rev. B* **25**, 6425 (1982).
3. C. R. A. Catlow, M. J. Norgett and T. A. Ross, *J. Phys. C* **10**, 1627 (1977).
4. P. J. Bendall, C. R. A. Catlow, J. Corish and P. W. M. Jacobs, *J. Sol. Stat. Chem.* **51**, 159 (1984).
5. P. W. M. Jacobs and S. H. Ong, *J. de Physique* **37**, 331 (1976).
6. N. F. Mott and M. J. Littleton, *Trans. Faraday Soc.* **34**, 485 (1938).

Radiation Effects and Defects in Solids, 1995, Vol. 134, pp. 123–126
Reprints available directly from the publisher
Photocopying permitted by license only

© 1995 OPA (Overseas Publishers Association)
Amsterdam B.V. Published under license by
Gordon and Breach Science Publishers SA
Printed in Malaysia

THEORETICAL STUDY OF THE COORDINATION OF THE Cr^{3+} ION IN α-Al_2O_3

R. FRANCO, J. M. RECIO, A. MARTÍN PENDAS, E. FRANCISCO, V. LUAÑA and L. PUEYO

Departamento de Química Física y Analítica, Universidad de Oviedo, E-33006 Oviedo, España

The local arrangement of a substitutional Cr^{3+} ion for an Al^{3+} ion in corundum is studied by means of first-principles pairwise simulations and quantum-mechanical *ab initio* Perturbed Ion calculations. Our investigation is organized in two steps. First, we determine the cohesive properties of the host lattice by calculating the set of four crystalline parameters that makes minimum the total energy of corundum. Secondly, we solve cluster models of increasing complexity centered at the Cr^{3+} site and embedded in the previously computed crystal potential. This is a consistent strategy that contributes to determine the local geometry of Cr^{3+} in α-Al_2O_3.

Key words: Corundum, Ruby, Cluster-in-the-lattice, Ab initio calculations, Local geometry.

1 INTRODUCTION

There exists experimental controversy and limited data concerning the position of the substitutional Cr^{3+} ion and its local environment in the ruby crystal. From the analysis of x-ray,[1] ENDOR,[2] and optical spectra,[3] the values reported for the displacement of the Cr^{3+} along the C_3 axis spread a range from –0.06 Å to +0.13 Å, with respect to the position of the Al^{3+} ion in the perfect lattice of corundum. From the XAFS measurements,[4] the two shortest Cr-O distances have been determined to be 1.95 Å and 2.04 Å, but the three dimensional distribution of the six oxygens surrounding Cr^{3+} has only been tentatively suggested.

It is our aim in this contribution to present the preliminary results of an investigation directed to the theoretical determination of the Cr^{3+} coordination in ruby. To this end we make use of a first-principles strategy that consists in cluster-in-the-lattice calculations combining atomistic simulations and a quantum-mechanical *ab initio* technique.

2 COMPUTATIONAL TECHNIQUES AND CLUSTER MODELLING

To determine the local relaxation around a given impurity (I) embedded in a crystalline field, it is necessary to compute the effective energy of a set of ions formed by the impurity and the ions affected electronically or geometrically by it. That set of ions constitutes the cluster (C), whereas the rest of the crystal forms the lattice environment (L). In this work, we have considered clusters containing from one to seven ions (CrO_6:α-Al_2O_3) and including up to five different geometrical degrees of freedom (the z coordinate of all the ions, and the x coordinates of the two triangles of oxygens, see Figure 1). We start our study by performing total energy calculations in the perfect α-Al_2O_3 crystal. The first computational tool used has been a Hartree-Fock local scheme, the aiPI model.[5] After the optimization of the four crystal parameters that define the unit cell of corundum ($\mathbf{a}$, $\mathbf{c}$, $\mathbf{x_o}$, and $\mathbf{z_{Al}}$) we have the ionic electronic densities (IEDs) and the crystalline positions of the ions, which are necessary to modelize the L region in the cluster-in-the-lattice calculations. Furthermore, the IEDs provide the input to generate crystal consistent interionic potentials

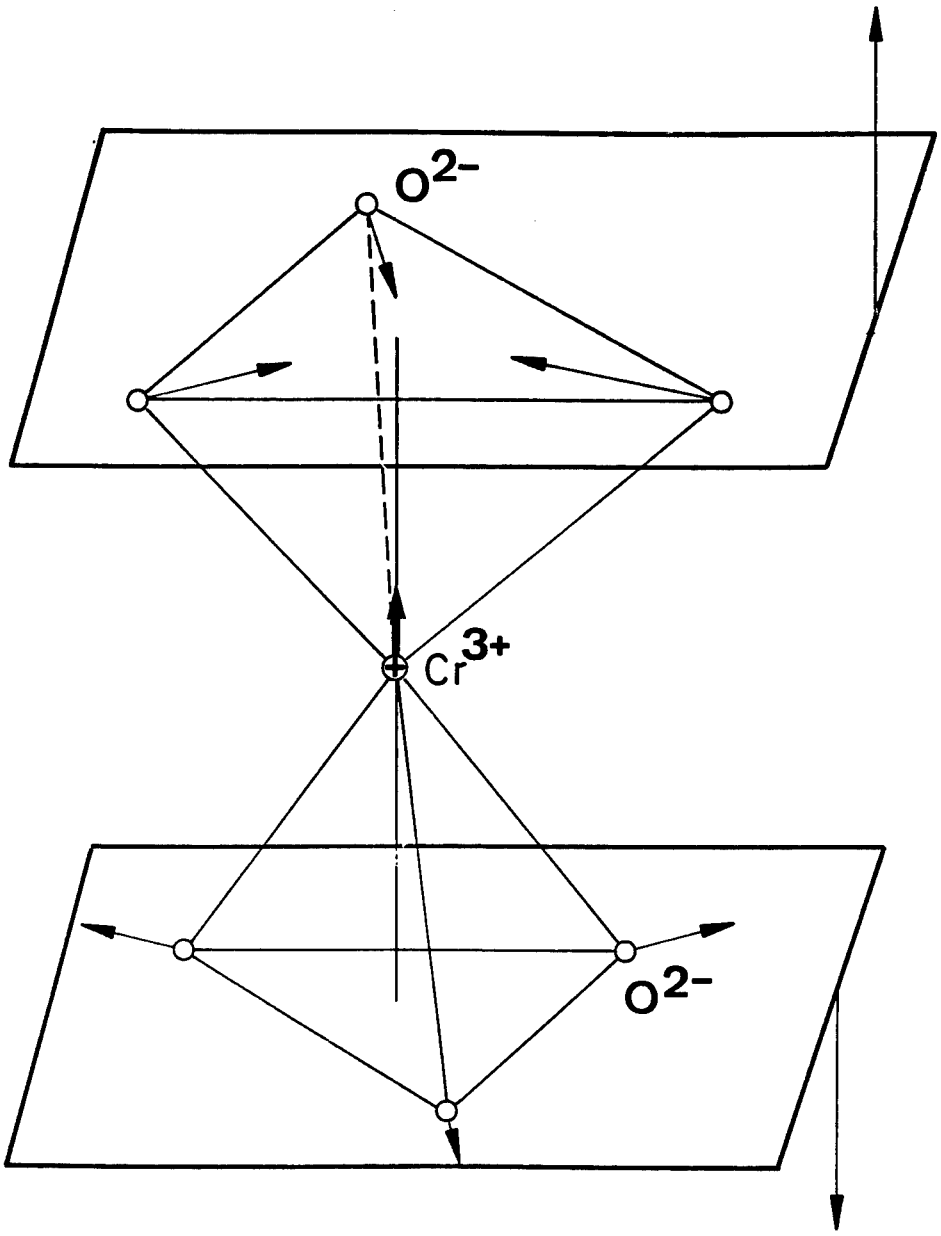

FIGURE 1 The CrO_6:α-Al_2O_3 cluster configuration according to PAIRPOT calculations.

(CCIPs) following an Electron Gas Model procedure developed in our laboratory.[6] The quality of these CCIPs is then examined by computing the equilibrium parameters of the perfect crystal with the pairwise simulation scheme implemented in the PAIRPOT code.[7]

Concerning the cluster-in-the-lattice calculations, both PAIRPOT and aiPI are again used to minimize the effective energy of clusters of increasing size. In this type of calculation, PAIRPOT is shown to be a very efficient tool that helps to design the more accurate and time consuming quantum-mechanical calculations.

3 RESULTS AND DISCUSSION

The most interesting results for the perfect crystals are collected in Table I. Both, α-Al_2O_3 and Cr_2O_3, have the same unit cell definition. Lattice parameters are greater for the Cr_2O_3 crystal in correspondence with a greater ionic radius for the transition metal than for the Al^{3+} ion. The theoretical data are qualitatively in agreement with the observed values, both in the aiPI and PAIRPOT calculations, and the aiPI values are also in quantitative good agreement with the experiments.

Table I
Unit cell parameters for α-Al_2O_3 and Cr_2O_3.

	$\alpha - Al_2O_3$			Cr_2O_3		
	PAIRPOT	aiPI	Ref.8	PAIRPOT	aiPI	Ref.8
a(A)	4.394	4.770	4.761	5.122	5.292	4.961
c(A)	12.003	12.952	12.995	13.706	13.736	13.599
x_o	0.3084	0.2999	0.3061	0.3048	0.2945	
z_{Al}	0.3558	0.3576	0.3522	0.585	0.3593	

In Table II, we include the two shortest calculated Cr^{3+}-O^{2-} distances (d1 and d2) in the ruby crystal. The results from PAIRPOT, where the five coordinates specified before are left free in the minimization of the effective energy of the cluster $(CrO_6)^{9-}$:α-Al_2O_3, are completely reasonable in the sense that d1 and d2 lie in between the metal-oxide distances obtained for both perfect crystals. The 3-dimensional configuration around Cr^{3+} is depicted in Figure 1, where the arrows show the displacements of the Cr^{3+} and its six nearest neighbors. In the aiPI calculations, although the cluster size is the same as in PAIRPOT, the set of free parameters does not yet contain the **x** coordinates of the two triangles of oxygens, and that fact might explain the slight movement of the seven ions in the clusters and the low values found for the Cr^{3+}-O^{2-} distance.

Table II
Shortest metal-oxide distances (d1 and d2) in α-Al_2O_3 and Cr_2O_3.

	α-Al_2O_3			Cr^{3+}:α-Al_2O_3			Cr_2O_3		
	PAIRPOT	aiPI	Ref.8	PAIRPOT	aiPI	Exp.	PAIRPOT	aiPI	Ref.8
d1(A)	1.690	1.842	1.856	1.747	1.826	1.80[a] 1.95[b]	1.955	2.034	1.97
d2(A)	1.857	1.997	1.970	1.965	1.923	2.06[a] 2.04[b]	2.156	2.164	2.02

a—Ref. 1(a), b—Ref. 4.

ACKNOWLEDGEMENTS

Financial support from the Spanish DGICYT, Project No. PB93–0327, is gratefully acknowledged.

REFERENCES

1. (a) V. G. Tsirelson, M. Y. Antipin, R. G. Gerr, R. P. Ozerov, and Y. T. Struchkov, *Phys. Status Solidi* **A87**, 425 (1985); (b) S. C. Moss and R. E. Newtrham, Z. Krist. **120**, 359 (1963).
2. N. Laurence, E. C. McIrvine, and J. Lambe, *J. Phys. Chem.* Solids **23**, 515 (1962).
3. D. S. McClure, *J. Chem, Phys.* **36**, 2757 (1962).
4. S. Emura, H. Maeda, *Rev. Sci. Instrum.* **65**, 1 (1994).
5. V. Luaña, M. Flórez, and L. Pueyo, *J. Chem. Phys.* **99**, 7970 (1993).
6. E. Francisco, J. M. Recio, M. A. Blanco, A. Martín Pendás, and L. Pueyo, *Phys. Rev.* **B51**, 2703 (1995).
7. A. Martín Pendás (unpublished).
8. *Handbook of Chemistry and Physics*, 60th ed., edited by R. C. Weast (Chemical Rubber Co., Boca Raton, FL, 1979).

Radiation Effects and Defects in Solids, 1995, Vol. 134, pp. 127–131
Reprints available directly from the publisher
Photocopying permitted by license only

© 1995 OPA (Overseas Publishers Association)
Amsterdam B.V. Published under license by
Gordon and Breach Science Publishers SA
Printed in Malaysia

LOCAL RELAXATIONS AND OPTICAL PROPERTIES OF Cr^{3+} IN MgO

D. J. GROH,* R. PANDEY,** and J. M. RECIO***

**Department of Physics, Morningside College, Sioux City, IA 51106; **Department of Physics, Michigan Technological University, Houghton, MI 49931; ***Departamento de Química Física y Analítica, Universidad de Oviedo, 33006-Oviedo, Spain*

Local distortions and optical properties induced by the substitutional Cr^{3+} impurity in the MgO host lattice are computed using the embedded cluster approach implemented in the ICECAP (ionic crystal with electronic cluster, automatic program) code. Our calculations predict inward relations of the six O^{2-} nearest neighbors surrounding the Cr^{3+} ion for both cubic and noncubic (tetragonal and orthorhombic) configurations in MgO. For the cubic configuration, selected low-lying excited states, including the 10 Dq generator $^4T_2$, are calculated at several Cr-O separations. After taking into account lattice relaxations and correlation corrections, the computed 10 Dq value lies 0.19 eV lower than the experimental one.

Key words: embedded cluster, optical transitions, local relaxations, Cr^{3+}:MgO.

1 INTRODUCTION

Chromium doped magnesium oxide ($MgO:Cr^{3+}$) provides a prototypical system where extensive spectroscopic studies have been performed.[1,2] These studies have shown that the impurity Cr^{3+} substituting Mg^{2+} in MgO can have a geometrical arrangement with either cubic or noncubic (due to a nearby cation vacancy) symmetry. However a unified microscopic description of the lattice involving both defects (the impurity and the vacancy) has not been reported up to date. In this contribution, we seek to provide such a description using an embedded quantum cluster method, ICECAP.[3] Specifically, our aim is to investigate (i) the geometrical positions of the ions surrounding Cr^{3+} in the three arrangements (O_h, C_{4v}, and C_{2v}), and (ii) the effects of lattice relaxation and correlation effects on d-d transitions associated with the Cr^{3+} ion.

2 COMPUTATIONAL MODEL

The methodology we use here incorporates electronic structure calculations with classical shell-model treatment of lattice polarization and distortion. This embedded cluster model is referred to as ICECAP.[3] The molecular cluster is formed by the impurity Cr^{3+} and the six nearest-neighbor O^{2-} ions, and is embedded in a lattice environment of Mg^{2+} and O^{2-} ions located at their crystallographic positions of the rocksalt phase with R(Mg-O) = 2.106 A. The cluster ions will be described within the framework of the unrestricted Hartree-Fock approximation (UHF).[6] Correlation energy corrections are determined using second order in the many body perturbation theory (MBPT).[7] The rest of the MgO lattice, where the perturbation due to Cr^{3+} is assumed to be weak, will be simulated by the classical shell-model.

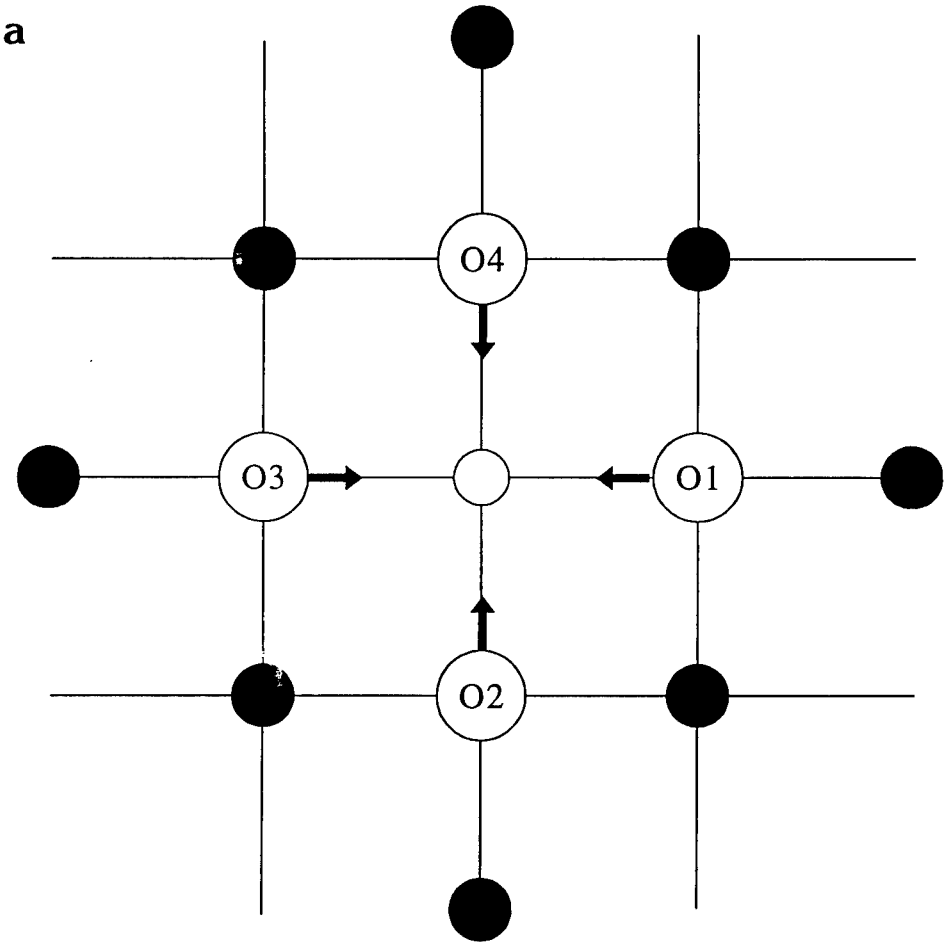

FIGURE 1(a)–(c) Qualitative diagrams of the O^{2-} distortions induced by: (a) a Cr^{3+} impurity, (b) a combined Cr^{3+}–[100]Mg^{2+} vacancy, and (c) a combined Cr^{3+}–[110]Mg^{2+} vacancy in the MgO host lattice. Only the movement of the four O^{2-} ions (O1–O4) in the x-y plane is shown. Black filled and empty circles represent Mg^{2+} and Cr^{3+} ions, respectively, whereas the empty box stands for the vacancy.

3 LOCAL RELAXATIONS

To investigate the local configuration around Cr^{3+} for the O_h, C_{4v}, and C_{2v} symmetries, we investigate clusters of one (Cr^{3+}) and seven ions ($(CrO_6)^{9-}$). In spite of the limited SCF active space, the computed equilibrium configuration shows an excellent agreement with the more expensive calculations involving the octahedral (7-ion) cluster. The effects of the impurity and vacancy on the local environment are qualitatively illustrated in Figure 1(a)–(c). The calculated values for the R(Cr-O) separations are (in angstroms): 2.02 (O_h), 1.92, 2.03 and 2.04 (C_{4v}), and 1.99, 2.04 and 2.06 (C_{2v}).

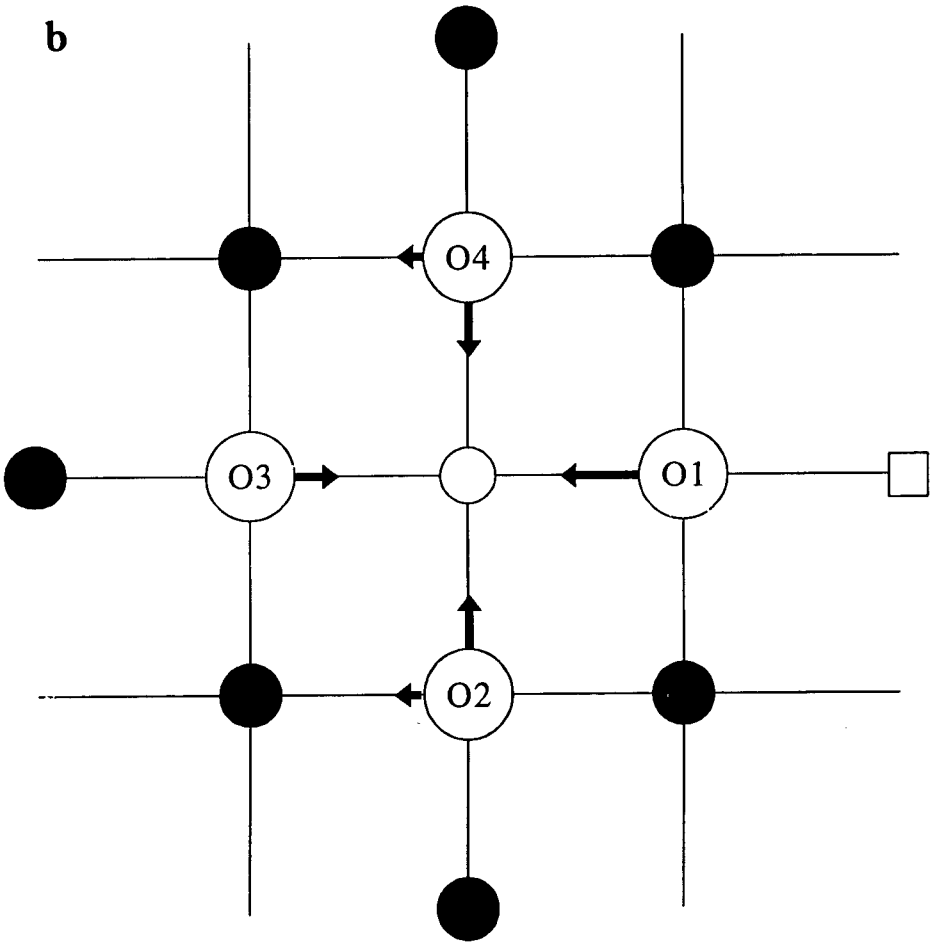

FIGURE 1(b)

The most interesting conclusions emerging from the analysis of our computations can be summarized as follows: (i) Nearest-neighbor ions are attracted by the Cr^{3+} impurity and are repelled by the cation vacancy, being the repulsion greater than the attraction. (ii) The simultaneous effect of the defect complex (Cr^{3+}-vacancy) is lower than the sum of their individual effects. (iii) Our computations are in agreement with the ionic radii expectations[4] for the R(Cr-O) value in the O_h symmetry and with the experimental data reported for the C_{4v} configuration.[5] (iv) The calculated distortions for the three configurations are consistent with each other and lead to a satisfactory global picture of the local geometry of Cr^{3+} centers in MgO.

4 OPTICAL TRANSITIONS

Potential energy surfaces of the t_2^3-$^4A_2$ ground state and the t_2^3-^2E and $t_2^2e^1$-$^4T_2$ excites

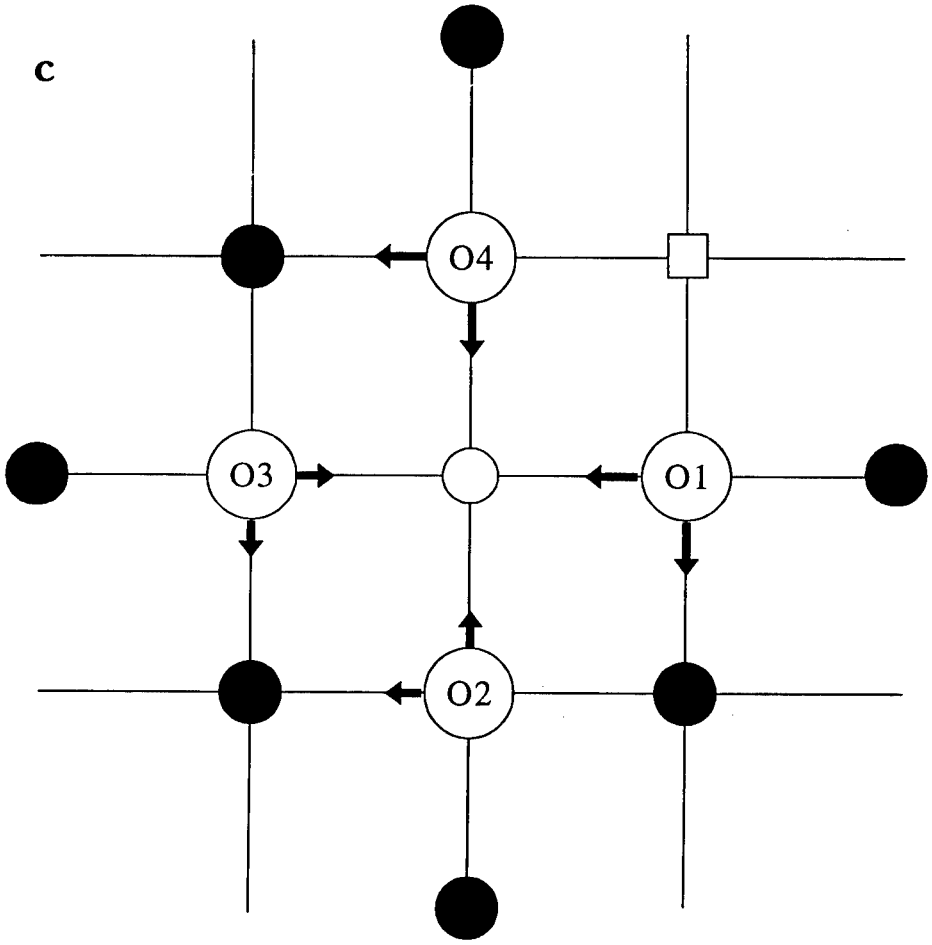

FIGURE 1(c)

states of Cr^{3+} doped MgO have been obtained at the UHF+MBPT level in the cubic configuration. The calculated results allow us to evaluate the 10 Dq parameter, the energy involved in the (t_2^3-$^4A_2 \rightarrow t_2^2e^1$-$^4T_2$ absorption), the R-line phosphorescence (t_2^3-$^2E \rightarrow t_2^3$-$^4A_2$ transition), and the $t_2^2e^1$-$^4T_2 \rightarrow t_2^3$-$^4A_2$ broad fluorescence band. The computation of the three transitions specified above is carried out starting with the calculation of the transition energies in the frozen-lattice configuration, where the Cr-O separation is taken to be the experimental R(Mg-O) value in the host lattice. Here, absorption and fluorescence, obviously, lie at the same energy (1.51 eV at the UHF + MBPT level). When the lattice relaxation is taken into account, absorption and fluorescence lie 0.30 eV and 0.22 eV, respectively, above the corresponding values at the frozen-lattice. For the R-line (phosphorescence) transition, the effect of the lattice relaxation is, however, almost negligible: 1.62 eV and 1.63 eV when the lattice is frozen

and relaxed, respectively.

We now proceed to discuss electron correlation effects on the computation of electronic spectroscopic frequencies. Note that the inclusion of the correlation corrections (MBPT) does not modify significantly the UHF equilibrium configurations. However, after the correlation corrections are taken into account there is an overall better agreement between the computed and observed transition data. As an example, the UHF, UHF+MBPT, and experimental values for the absorption energies show the following progression: 1.74 eV, 1.81 eV and 2.00 eV. In general, the discrepancies obtained with respect to the observed data are less than 10% in the case of our more refined calculation (UHF+MBPT and fully relaxed lattice).

REFERENCES

1. M. B. O'Neill and B. Henderson, *J. Luminescence* **39**, 161 (1988).
2. B. Henderson and J. E. Wertz, *Defects in the Alkaline Earth Oxides* (Taylor & Francis Ltd., London, 1977).
3. J. Vail, R. Pandey, and A. B. Kunz, *Rev. Solid State Science* **5**, 241 (1991).
4. R. Shannon, *Acta Crystallogr.* **A32**, 751 (1976).
5. K. Asakura and Y. Iwasawa, *Materials Chem. Phys.* **18**, 499 (1988).
6. D. Groh, R. Pandey, and J. M. Recio, *Phys. Rev.* **B50**, 14860 (1994).
7. See for example, D. J. Thoules, *The Quantum Mechanics of Many-Body Systems* (2nd edn., Academic Press, New York, 1972), chap. 4.

Radiation Effects and Defects in Solids, 1995, Vol. 134 pp. 133–135
Reprints available directly from the publisher
Photocopying permitted by license only

© 1995 OPA (Overseas Publishers Association)
Amsterdam B.V. Published under license by
Gordon and Breach Science Publishers SA
Printed in Malaysia

ANOMALOUS CHARGE SCREENING IN THE RADIATION-INDUCED RECOMBINATION OF CHARGED DEFECTS IN IONIC SOLIDS

V. N. KUZOVKOV

Department of Theoretical Physics, University of Latvia, 19 Rainis, Riga, Latvia

(Received July 1, 1994)

The cooperative effect is studied in the kinetics of bimolecular A+B→O reactions between charged particles (reactants). Unlike the Debye-Hückel theory, charge screening has an essentially non-equilibrium character. The reaction rate does not approach a steady state, but increases infinitely in time for the asymmetric mobility of reactants (D_A=O, $D_B \neq$O).

Key words: Diffusion-limited reactions; Coulomb interaction; charge screening; many-particle effects; correlation functions.

As is well known [1], irradiation of ionic solids produces both neutral, F-H, and oppositely charged α -I pairs of Frenkel defects. Vacancies (α centers) are immobile up to the room temperatures, whereas interstitial halide ions (I centers) are moble above 20–30 K already. In the case of A+B→O reaction for *neutral* particles *A* and *B* both analytical theories and computer simulation [2–5] have demonstrated a *reduction* of the reaction rate at long times. In the diffusion-controlled regime the result $n(t) \alpha t^{-1}$ generally accepted in formal chemical kinetics [6] is changed for the asymptotic law $n(t) \alpha t^{-d/4}$ (**d** space dimension). Such a delay reaction rate arises due to pattern formation: during reaction a whole volume is divided into domains with distinctive sizes $\xi(t) = \sqrt{Dt}$ (the so-called *diffusion length*); each domain contains predominantly particles *A* or *B* only; that is, similar particles tend to aggregate and thus a well-stirred system is replaced in time by self-organized aggregate structure. If one of partners (reactants) is immobile (say, D_A=O), the reduction in the reaction rate is even larger; $n(t) \alpha t^{-1/2}$ for **d**=3 [4,7]. In this case the spatial distribution of particles *A* is singular [7]: unlike particles B (where local inhomogeneities in their distribution are smoothed on the scale of the length $\xi(t)$, *immobile* particles *A* survive only in rare isolated groups, so we observe something like 'raisins (*A*) in dough (*B*)'.

This results are valid for the reaction between neutral non-interacting particles (F+H→O). If we consider the kinetics of bimolecular recombination between charged particles, α+I→0, the problem of interaction potentials arises [8]. It is known [2] that in the *equilibrium* system of mobile particles their Coulomb interactions are screened, so that the force is $F(r)=-e^2S(r)/r^2$ where $S(r)$ is the *screening factor* such that $S(\infty)$=O (the so-called *normal screening*). *Diffusion-controlled* reaction, α +I→O, allows us to study effect of *non-equilibrium* charge screening (since particles disappear in pairs due to the recombination and move too slowly to be stirred) stenghtened by asymmetric mobilities; $D_1 >> D_\alpha \approx$O. In such a case the screening factor becomes time-dependent [8], $S=S(r,t)$, with $S(\infty,t)=S_0(t) \neq$O (*abnormal screening*). We will demonstrate below that this degenerate situation has unique decay asymptotics, $n(t) \alpha t^{-5/4}$, corresponding to the *accelerated reaction* (in contrast to the above-discussed reaction rate observed for neutral particles).

We start from the equation for the reaction rate $K_o=4\pi DR_{eff}$ where D is the coefficient of the relative diffusion ($D=D_A+D_B$), and the effective reaction radius is described by the Debye equation [6], which reads for the black sphere model (AB pairs disappear when

particles approach each other to within a critical distance r_o) $R_{eff}=r_oL/[1-\exp(-L)]$, where the dimensionless parameter $L=R/r_o$ contains the so-called *Onsager radius*, which is defined as $R=e^2/\epsilon\, k_BT$. The value of the parameter R is defined by a *product* of particle charges; the electroneutrality of a whole system is secured by the conditions, $n=n_A=n_B$, $e=e_A=-e_B$. Note that for $L\gg1$, $K_o \alpha R_{eff} \approx R$ and $K_o \alpha |e_Ae_B|$.

Let us estimate analytically the effect of the non-uniform distribution of immobile particles *A* which, as is shown below, form in time compact aggregates ('raisins') existing on the uniform background of B particles ('dough'). Such A-rich aggregates resembles super-particles with the effective charges $e_{eff}\approx N_Ae_A$ where N_A ($N_A\gg1$) is the number of *A* particles within an aggregate. Therefore, the effective recombination radius is roughly $R_{eff}\approx N_AR$. Making the qualitative estimate, we take into account that diffusive motion of *B* particles destroys small *A*-aggregates, so that at long time t we have the number of aggregates occupying the distinctive volumes $V\approx\epsilon\,(t)^3$. The upper-limit estimate of N_A is a mean number of particles *A* in volume V, i. e. $N_A=n(t)\xi(t)^3$. Substitution of the reaction rate $K(t)\approx4\pi DR_{eff}$, (with $R_{eff}=N_AR$) into the equation

$$\frac{d\,n(t)}{d\,t} = -K(t)n(t)^2 \qquad (1)$$

leads to the asymptotic law sought for: $n(t) \alpha t^{-5/4}$, indicating that the reaction is *accelerated* as compared to the standard result of the chemical kinetic, $n \alpha t^{-1}$. It is easy to see that both K(t) and R_{eff} increase as $K(t) \alpha t^{1/4}$, i. e. as $\to\infty$, there is *no* limiting magnitude! It results in the unusual screening factor $S_o\approx N_A \alpha t^{1/4}$ (concentration decays but a mean number of *A* particles in a cluster *increases* in time), which is very unusual for the standard chemical kinetics [6] and the symmetric case ($D_A\approx D_B$) where $n \alpha t^{-1}$ and $S_o(t)\to O$ [8].

The quantitative analysis of the problem is based on a set of the integrodifferential kinetic equations presented in [8]. We will stress here only some general ideas. A fundamental solution of the Markov process for the A+B→O reaction under study could be presented in a form of the infinite set of coupled equations for the so-called *many-point particle densities* [4, 5]. Single-point densities are nothing but macroscopic concentrations whereas the higher-order densities after extracting the concentration co-factors define a complete set of the *correlation functions*. They give us the statistical information on the relative spatial distribution of reacting particles of both kinds thus defining the *fluctuation spectrum* of the kinetics under study. Mathematical difficulties of the description of the fluctuation spectrum restrict the shortened hierarchy of equations at the level of the *joint correlation functions* for similar and dissimilar particles describing correlations within pairs A–A, B–B and A–B respectively. The approximate treatment of the A+B→O reaction for charged particles inavoidably requires a combination of several approximations: the Kirkwood superposition one for the reaction terms and Debye-Hückel for modification of the drift terms with self-consistent potentials [8].

The screening parameter S(r,t) is shown in [8]. It demonstrates the formation of a *quasi-equilibrium* charge screening ($D_A=D_B$); at any time $S(r,t)\leq O$ and its asymptotic value $S_o(t)$ decays monotonically in time. For $D_A=O$ the screening factor shown here is obviously *nonequilibrium*; its asymptotic value $S_o(t) \alpha t^{1/4}$ increases in time. At low concentrations the values of $S_o(t)$ corresponds to the mean number N_A of particles *A* in their aggregates.

This research has been supported by a grant N LB2000 from the International Science Foundation.

REFERENCES

1. N. Itoh, *Adv. Phys.* **31**, 49 (1982).
2. D. Toussaint and F. Wilczek, *J. Chem. Phys.* **78**, 2642 (1983).

3. Special issue of *J. Stat. Phys.* **65**, N5/6 (1991).
4. V. N. Kuzovkov and E. A. Kotomin, *Rept. Progr. Phys.* **51**, 1479 (1988).
5. E. A. Kotomin and V. N. Kuzovkov, *Rept. Progr. Phys.* **55**, 2079 (1992).
6. H. Eyring, S. H. Lin and S. M. Lin, *Basic Chemical Kinetics* (Wiley, N. Y. 1980).
7. E. Kotomin, V. Kuzovkov, W. Frank and A. Seeger, *J. Phys. A.* **27**, 1453 (1994).
10. V. N. Kuzovkov and E. A. Kotomin, *J. Stat. Phys.* **72**, 127 (1993).

Radiation Effects and Defects in Solids, 1995, Vol. 134, pp. 137–139
Reprints available directly from the publisher
Photocopying permitted by license only

© 1995 OPA (Overseas Publishers Association)
Amsterdam B.V. Published under license by
Gordon and Breach Science Publishers SA
Printed in Malaysia

THE KINETICS OF DEFECT AGGREGATION: A NOVEL LATTICE FORMALISM

V. N. KUZOVKOV

Department of Theoretical Physics, University of Latvia, 19 Rainis, Riga, Latvia

(Received July 1, 1994)

We introduce a stochastic model for the A + B → O reaction on a discrete lattice. The system may include mono- and bimolecular steps (i. e. reaction and diffusion steps). The resulting infinite chain of equations is truncated at a certain level via a modified Kirkwood approximation.

Key words: Master equations; many-point probabilities; correlation functions; Kirkwood superposition approximation.

The kinetics of radiation-induced defect aggregation and, in particular, colloid formation, depends critically on the interaction between defects described potentials $U_{\lambda\lambda}(r)$ where λ is the defect type (interstitial atom or vacancy) [1–5]. Unlike the case of repulsive potential for similar particles (defects), e.g. Coulomb forces, $U_{\lambda\lambda}(r) = e^2/\varepsilon r$ [1, 2] which puts no definite restrictions on the use of continuum approximation, such problems arise in the aggregate (colloid) formation kinetics [5] induced by the *elastic defect attraction*, $U_{\lambda\lambda}(r) = -\alpha/r^3$. In [3–5] this singular potential was cut-off at the interatomic distance, the decay kinetics under study depends also on the particular manner how this cut-off is done.

In this paper, the alternative formalism for the aggregation kinetics is presented which is based on the *discrete lattice* approach and assumes that: (a) all bimolecular processes (diffusion and recombination) are short-range and affect nearest cells only; (b) elastic interaction $E_{\lambda\mu}$ is treated in a *clear-cut approximation* (nearest-neighbour interaction only). The aggregation kinetics is then considered in terms of simple particle densities (concentrations), $C_\lambda(t)$, and the joint (pair) correlation functions $F_{\lambda\mu}(r, t)$.

The reaction takes place on a lattice with coordination number z. Each lattice site is given a lattice vector **l**. The state of the site **l** is represented by the lattice variable σ_l, which may depend on the occupancy number by a particle (defect). Therefore $\sigma_l = \{O,A,B,\ldots\}$ where O represents a vacant site, A a site which is occupied by an A particle and so on.

Monomolecular steps are processes which depend only on a single lattice site. Examples for such steps are the creation of a particle (O → A), its annihilation (A → O) or the particle transformation (A → B). The prominent feature of these steps is the fact that the neighbourhood of the actual site plays no role here. Therefore, these steps can be described by the following equation:

$$\sigma_l \overset{p}{\Rightarrow} \sigma_l' \ , \quad p \equiv P(\sigma_l \to \sigma_l') \tag{1}$$

where p is the transition probability from σ_l to σ_l'.

A more complicated situation of *bimolecular steps* arises if the step depends on *two* lattice sites, **l** and **n**. Examples are reaction process (AB → OO) and diffusion (AO → OA). All these processes can be formulated in terms:

$$\sigma_l\sigma_n \overset{k}{\Rightarrow} \sigma_l'\sigma_n' \ , \quad k \equiv K(\sigma_l\sigma_n \to \sigma_l'\sigma_n')/z. \tag{2}$$

Here we have introduced a factor l/z in order to simplify the equations.

We introduced a probabilities $\rho^{(i)}$ which depend on i lattice sites. For i = 1 we obtain the simple density of particles on the lattice, $C_\lambda = \rho^{(1)}(\sigma_1)$, $\lambda = \sigma_1$. For these density the condition $\sum_\lambda C_\lambda = 1$ holds. The two-point probabilities, $\rho^{(2)}(\sigma_1\sigma_m) = C_\lambda C_\mu F_{\lambda\mu}(\mathbf{r})$, depend on the two states ($\lambda = \sigma_1$, and $\mu = \sigma_m$) respectively and on the coordinate difference $\mathbf{r} = \mathbf{l} - \mathbf{m}$ of the lattice sites (here $F_{\lambda\mu}(\mathbf{r})$ is the *correlation functions*). As $|\mathbf{r}| \to \infty$, the correlations between the particles vanish: $F_{\lambda\mu}(\infty) = 1$. A product $c_\mu = C_\mu F_{\mu\lambda}(\mathbf{r})$ represents the mean density of μ-particles, if the central site is in the state λ. We will use this product later to characterize the different particle phases which appear in this model.

We write down the master equations in the form of infinite set of equations for the many-point probabilities [6, 7].

i) The equation of motion for the one-point probabilities:

$$\frac{dC_\lambda}{dt} = \left.\frac{dC_\lambda}{dt}\right|_{in} - \left.\frac{dC_\lambda}{dt}\right|_{out} = A_\lambda[C,F] - B_\lambda[C,F]C_\lambda \tag{3}$$

where $A_\lambda[C,F]$ and $B_\lambda[C,F]$ are simple positive functions (polynomials) of the densities C and of the correlation functions F, e.g.

$$A_\lambda[C,F] = \left.\frac{dC_\lambda}{dt}\right|_{in} = \sum_{\lambda'} P(\lambda' \to \lambda)C_{\lambda'} + \sum_{\lambda'\nu'} K(\lambda'\nu' \to \lambda\nu)C_{\lambda'}C_{\nu'}F_{\lambda'\nu'}(1)\,. \tag{4}$$

All the correlation functions are taken for $|\mathbf{r}| = 1$ (nearest neighbours).

ii) The equation of motion for the two-point probabilities.

Among the processes which take place on two different lattice sites, **l** and **m**, the following ones are possible:

(1) **l** and **m** are not nearest neighbours on the lattice. (*a*) The state σ_l can be created or annihilated independently of σ_m. Only the neighbourhood of **l** is important. (*b*) The state σ_m can be created or annihilated independently of **l**. Only the neighbourhood of **m** is important.

(2) If **l** and **m** are nearest neighbours on the lattice, additional terms must be taken into account which represent the bimolecular steps. A diagrammatic description for these processes could be introduced:

$$\frac{d\rho^{(2)}(\sigma_l\sigma_m)}{dt} = \blacksquare_{l} \text{ — } \square_{m} + \square_{l} \text{ — } \blacksquare_{m} + \delta_{l,m}\{\blacksquare\blacksquare\}\,. \tag{5}$$

The symbol (□) denotes here the site which plays no role for the determination of the state of the other site. On the site (■) a process takes place. Therefore, the first two terms correspond to the cases (*1a*) and (*1b*) whereas the third term represents the bimolecular step. We must truncate the infinite set of master equations in order to obtain a finite system of non-linear equations. To this end, we use the superposition approximation introduced by Kirkwood [8] (see also [6, 7]). In this approximation the three-point probability is expressed via one- and two-point probabilities.

The equations are solved exactly in a small lattice region, $r = |\mathbf{r}| < r_0$ and their solution is used in calculating the continuous functions which represent the behavior of the system for large distances, $r > r_0$. This formalism has been first tested for a similar problem of the

catalytic surface reaction between adsorbed non-interacting particles ($E_{\lambda\mu}=0$) [6, 7], whereas the general philosophy of lattice models, including particle interactions, $E_{\lambda\mu}\neq 0$, is discussed in [9]. It is demonstrated how the mutual attraction of similar particles results in the formation of pairs of bound interstitial atoms and their larger aggregates. Since even such small aggregates have mobilities much less than single particles, the effective diffusion coefficient is reduced by several orders of magnitude, which stimulates the aggregation process.

This research has been supported by a grant N LB2000 from the International Science Foundation.

REFERENCES

1. V. N. Kuzovkov and E. A. Kotomin, *Physica A* **191**, 172 (1992).
2. V. N. Kuzovkov and E. A. Kotomin, *J. Stat. Phys.* **72**, 172 (1993).
3. V. N. Kuzovkov, in *Defects in Insulating Materials*, ed. O. Kanert and J.-M. Spaeth (World Scientific, Singapore, 1993) p. 795.
4. V. N. Kuzovkov and E. A. Kotomin, *J. Chem. Phys.* **98**, 9107 (1993).
5. V. N. Kuzovkov and E. A. Kotomin, *Physica Scripta* (1994) (to be published).
6. J. Mai, V. N. Kuzovkov and W. von Niessen, *Phys. Rev. A* **203**, 298 (1994).
7. J. Mai, V. N. Kuzovkov and W. von Niessen, *Phys. Rev. E* **48**, 1700 (1994).
8. J. G. Kirkwood, *J. Chem. Phys.* **76**, 479 (1935).
9. J. Mai, V. N. Kuzovkov and W. von Niessen, *Phys. Rev. E* (1994) (to be published).

Radiation Effects and Defects in Solids, 1995, Vol. 134, pp. 141–143
Reprints available directly from the publisher
Photocopying permitted by license only

© 1995 OPA (Overseas Publishers Association)
Amsterdam B.V. Published under license by
Gordon and Breach Science Publishers SA
Printed in Malaysia

ELECTRIC FIELD INDUCED ENERGY SHIFT IN F-CENTRE EMISSION

M. J. PONNAMBALAM

Physics Department, U.W.I., Kingston 7, Jamaica

(Received July 1, 1994)

For the Relaxed Excited States of the F-centre, the simplest vibronic model involves only the Γ_4^- mode in the electron-lattice interaction H_{eL}. In analyzing the perturbation correction due to H_{eL}, Ham and Grevsmühl kept only the linear terms in the coupling constant G and ended up with a positive value for the field-induced shift in the energy of the parallel component in emission $\Delta E_{\|}$—in disagreement with the experiments. In this paper, it is shown that when the perturbation correction terms are kept up to G^2, $\Delta E_{\|}$ is negative.

Key words: Stark effect in F-centre emission.

1 INTRODUCTION

The Stark effect in F-centre emission has been investigated experimentally by Bogan and Fitchen[1] and Ohkura *et al.*[2] On the theoretical side, for the excited states after absorption and relaxation—called the Relaxed Excited States (RES)—static theories were provided at first.[3] Later, several vibronic models were given.[4,5] The simplest one is that of Ham and Grevsmühl[6] (HG) who take into account only the Γ_4^- phonon mode in the electron-lattice interaction. This model has been investigated with a new approach based on the recursion method by Martinelli *et al.*[7] Recently, Ewig *et al.*[8] have studied the detailed electronic distributions of the F-centre in LiF, using a cluster model.

The major drawback of HG's work is that they obtained a positive value for the field-induced shift in the energy of the parallel component ($\Delta E_{\|}$) of the emitted light, in clear disagreement with the experiments. This paper presents a more detailed calculation—on the same basic model of HG—leading to a negative $\Delta E_{\|}$.

2. THEORY

In the presence of an external electric field $\vec{F}$, the F-centre Hamiltonian may be written as

$$H = H_e + H_L + H_{eL} + H_F, \tag{1}$$

where the subscripts e, L, eL and F stand for the electron, lattice, electron-lattice and the electric field respectively. In analyzing H_{eL}, Ham[4] included only the Γ_4^- phonon mode and (comparing the theoretical results with the experiment) showed that the electron-lattice coupling cannot be strong. Accordingly, this paper treats H_{eL} and H_F as perturbations.

In solving the unperturbed Hamiltonian $H_o = H_e + H_L$, the zero of the energy is taken to coincide with the 2s electronic state which is taken to lie at an energy E_{sp} below the 2p electronic state. Thus, the eigenstates of H_o (of interest) are given by the simple product functions 2s $\phi_{\ell mn}$ with energies $(\ell + m + n + 3/2)\,\hbar\omega$ and $p_i\phi_{\ell mn}$ (i = x, y, z) with energies $E_{sp} + (\ell + m + n + 3/2)\,\hbar\omega$. Here, $\phi_{\ell mn}$ is the 3D harmonic oscillator wavefunction.

When H_{eL} is limited to the Γ_4^- mode with frequency ω, distortions Q and the effective mass μ,

$$H_{eL} = G(Q_x\rho_x + Q_y\rho_y + Q_z\rho_z), \tag{2}$$

where, G is the coupling constant and $<2s|\rho_i|p_j> = \delta_{ij}$. Following HG[6], we assume G to be small enough so that

$$E_G = G^2/2\mu\omega^2 \lesssim E_{sp}/4 \tag{3}$$

In the absence of H_{eL} and H_F, the lowest RES (Relaxed Excited State) is 2s ϕ_{000}. In the presence of H_{eL} and $H_F = eFz$ (due to an electric field F along the Z direction), the first order perturbation correction to this wavefunction is given by

$$\psi_1 = b_1[p_x\,\phi_{100} + p_y\,\phi_{010} + p_z\,\phi_{001}] + b_2\,p_z\,\phi_{000}, \tag{4}$$

where
$$b_1 = -G\frac{\sqrt{\hbar/2\mu\omega}}{E_{sp} + \hbar\omega} \;\;\&\;\; b_2 = -<2s\,|\,eFz\,|\,p_z>. \tag{5}$$

The second order correction ψ_2 involves only the 2s electronic state—and hence is not of much interest in Stark effect. The third order correction ψ_3 involves only the p_i (i = x, y, z) electronic states which are important in the Stark effect. For simplicity and due to space limitations, only a part of ψ_3 is given below:

$$\psi_3 = \frac{b_1^2 b_2 E_{sp}(E_{sp} + \hbar\omega)}{\sqrt{2}\hbar\omega\,(E_{sp} + 2\hbar\omega)}\left[p_z\phi_{200} + p_z\phi_{020} + \left\{1 + \frac{2(2E_{sp} + \hbar\omega)}{E_{sp}}\right\}p_z\phi_{002}\right] + \ldots\ldots \tag{6}$$

3 RESULTS AND SUMMARY

When quadratic terms in the coupling constant G are incorporated, the lowest RES is 2s $\phi_{000} + \psi_1 + \psi_2 + \psi_3$. From this state, let us consider the field-induced shift in energy $\Delta E_{\|}$ of the parallel component of emission. When F = 0, there is only one contribution with energy E(0) due to the transition from $p_z\phi_{001}$ to ls ϕ_{001}. When $F \neq 0$, the same transition would have an energy E(F) which is slightly less than E(0) due to the field-induced downward shift of the lowest RES. This would lead to a negative $\Delta E_{\|}$. However, there is a second transition from $p_z\phi_{000}$ to ls ϕ_{000} with the energy $E(F) + \hbar\omega$, since ls ϕ_{000} is below ls ϕ_{001} by $\hbar\omega$. These are the only two contributions when non-linear terms in G are neglected—as done by HG[6]. In this case, combining the above two transition energies with their weighting factors, one finds that $\Delta E_{\|}$ is positive—in disagreement with the experiments.

When quadratic terms in G are taken into account in the lowest RES, Eq (6) shows that there are more contributions to the parallel component of emission—for e.g. from $p_z\,\phi_{002}$ to ls ϕ_{002} with the energy $E(F)—\hbar\omega$, since ls ϕ_{002} is above ls ϕ_{001} by $\hbar\omega$. Further, using Eq. (3), if we put $G^2 \sim E_{sp}\mu\omega^2/2$ and $E_{sp} \gg \hbar\omega$ in Eq. (6), it is seen that the coefficient of $p_z\phi_{002}$ in ψ_3 is as much as 0.9 b_2. This is almost the same as the amount of $p_z\phi_{000}$ in Eq. (4) and hence can compensate for the pull of $p_z\phi_{000}$ and thus leave $\Delta E_{\|}$ negative in agreement with the experiments.

REFERENCES

1. L. D. Bogan and D. B. Fitchen, *Phys. Rev. B* **1**, 4122 (1970).
2. H. Ohkura, K. Imanaka, O. Kamada, Y. Mori and T. Iida, *J. Phys. Soc. Jpn.* **42**, 1942 (1977).

3. M. J. Ponnambalam and J. J. Markham, *J. Phys. Chem. Solids* **47**, 463 (1986).
4. F. S. Ham, *Phys. Rev. B* **8**, 2926 (1973).
5. Y. Kayanuma and Y. Toyozawa, *J. Phys. Soc. Jpn.* **40**, 355 (1976).
6. F. S. Ham and U. Grevsmühl, *Phys. Rev. B* **8**, 2945 (1973).
7. L. Martinelli, G. P. Parravicini and P. L. Soriani, *Phys. Rev. B* **32**, 4106 (1985).
8. C. S. Ewig, J. Tellinghuisen and M. H. Mendenhall, *Chem. Phys. Lett.* **188**, 501 (1992).

Radiation Effects and Defects in Solids, 1995, Vol. 134, pp. 145–146
Reprints available directly from the publisher
Photocopying permitted by license only

© 1995 OPA (Overseas Publishers Association)
Amsterdam B.V. Published under license by
Gordon and Breach Science Publishers SA
Printed in Malaysia

SEMI-EMPIRICAL ANALYSIS OF THE QUANTUM YIELD OF THE THREE CENTER AUGER EFFECT*

A. J. ZAKRZEWSKI

Institute of Physics, Polish Academy of Sciences; Al. Lotnikow 36/42, 02-668 Warsaw, Poland

(Received July 1, 1994)

In this communication we present a simple, semi-empirical model of the three center Auger effect (TCAR). It is based on the dipole approximation of the interaction Hamiltonian. Application of this model to the case of TCAR in ZnS:Fe yields the value of critical distance for the energy transfer about 10 Å.

Key words: nonradiative transitions, deep impurities.

1 INTRODUCTION

One of the important mechanisms of the deactivation of the donor-acceptor pair (DAP) luminescence by deep impurities (such as transition metal centers (TM)) turns out to be the TCAR.[1,2] In this process energy of the recombining DAP is nonradiatively transferred to a nearby TM-related center which is subsequently ionized. Based on the photo-ESR excitation spectra of the isolated iron Fe^{3+} in ZnS:Cu,Fe crystals it was proved, that this mechanisms is an important recombination channel.[1] In this communication we present the semi-empirical model of the TCAR process, which can be used to a simple estimation of its efficiency. Because of large lattice relaxation concomitant with the changes of the charge state of deep center (DC), it was necessary to include in theoretical description of TCAR an electron-phonon interaction. In the following we utilize semiclassical approach developed by Langer[3-7] in his studies on photo-ionization transitions involving deep centers in semiconductors.

1 TCAR IN THE DIPOLE APPROXIMATION

A probability (W) of the energy transfer from DAP to DC is described by the Fermi 'Golden Rule':

$$W = 2\pi/\hbar \, \langle f|H|i\rangle^2 \rho(E) \tag{1}$$

where $|f\rangle$ and $|i\rangle$ denote the wavefunctions of final and initial state, respectively, $\rho(E)$ is a density of final states, and H is the interaction Hamiltonian taken in the form of the screened Coulomb potential with an appropriate value of the dielectric constant ϵ. It is well known, that matrix element of H is a difference of direct and exchange term. According to the conventional approach, the exchange term is usually neglected. Subsequently, following the method of Dexter[6] and Schaffer and Williams,[2] we expand direct electrostatic interaction term into power series of R (i. e. donor-DC distance), with a first term due to dipole-dipole interaction being a dominant term. Thus, interaction Hamiltonian H in the dipole approximation equals to:

$$H = e^2\{r^*r' - 3(r^*R)(r'^*R)/R^2\}/\epsilon R^3 + \ldots \tag{2}$$

*This work was supported by research grant of KBN No. 2 0476 91 01.

where r, r′ denote the coordinate of the elctron bound to DC and donor, respectively. Averaging over all angular orientations of R, one can obtain the following expression for the matrix element for the energy transfer from DAP to DC:

$$<\text{flHli}> = (2/3)^{1/2} M_{DA} M_{DC} / \epsilon R^3 \qquad (3)$$

where M_{DA} denotes the dipole matrix element for radiative de-excitation of the DAP, and M_{DC} is the matrix element for ionization of DC.

Slightly modifying Langer approach which describes the photo-ionization cross sections of the deep centers in semiconductors, we were able to account for the lattice relaxation phenomena accompanying deep center ionization during TCAR transition. Finally, we obtain:

$$W = \text{const} * R^{-6} * \int_{-\beta}^{\infty} dz \exp(-z^2) * (E_{DA} + \Gamma z - E_{opt})^{3/2} * (E_{DA} + \Gamma z)^{-4} \qquad (4)$$

where E_{opt} is the deep center optical ionization energy, E_{DA} is the energy of the recombining DAP, Γ is the broadening parameter defined in[3] and β is defined as: $\beta = (E_{DA} - E_{opt})/\Gamma$.

2 ESTIMATION OF THE TCAR EFFICIENCY IN ZnS:Fe CRYSTALS

The formula (4) derived above can be used for calculating (in the dipole approximation) the critical transfer distance (R_{cr}) in the case of Auger-type energy transfer from DAP to iron center in ZnS. Here, R_{cr} is a such distance R between donor and iron, for which probability of the radiative DAP recombination is equal to the probability of the TCAR recombination. Experimentally determined values of E_{opt} and Γ were taken from the absorption studies of Skowronski and Godlewski.[5] The numerical analysis leads to the critical transfer distance of about 12 ± 1 Å for blue luminescence, and about 8.5 ± 1 Å for green DAP lunimescence. These distances were previously estimated from the analysis of the spectral overlap between photo-luminescence and photo-ionization absorption bands, and were calculated to be 12 Å and 6.3 Å, respectively .[4] Bearing in mind the simplicity of our model there is a satisfying agreement between these two sets of R_{cr} values. On the other hand these values are too small to explain high efficiency of energy transfer from DAP to iron as observed recently in ESR experiments.[8] It means, that in this case dipole approximation is not sufficient. Because contribution of higher terms in the power expansion (2) i.e. dipole-quadrupole, quadrupole-quadrupole terms etc. turns out to be relatively small, in the further analysis exchange interaction has to be included.

REFERENCES

1. A. Zakrzewski and M. Godlewski, *Phys. Rev.* **B34**, 8993 (1986).
2. J. Schaffer and F. Williams, *Phys. Stat. Sol.* **38**, 657 (1970).
3. U. Piekara, J. M. Langer, B. Krukowska-Fulde, *Solid St. Commun*, **23**, 583 (1977).
4. M. Godlewski, A. Zakrzewski and M. Z. Cieplak, *Material Science Forum* ***10–12***, 487 (1986).
5. M. Skowronski and M. Godlewski, *J. Phys. C: Solid State Phys.* **17**, 2901 (1984).
6. D. L. Dexter, *J. Chem. Phys.* **21**, 836 (1952).
7. J. M. Langer, *Proc. Int. Conf. Semiconductors Kyoto 1980 J. Phys. Soc. Japan* **49**, suppl A. 207.
8. A. J. Zakrzewski, to be published.

Radiation Effects and Defects in Solids, 1995, Vol. 134, pp. 147–152
Reprints available directly from the publisher
Photocopying permitted by license only

© 1995 OPA (Overseas Publishers Association)
Amsterdam B.V. Published under license by
Gordon and Breach Science Publishers SA
Printed in Malaysia

ON THE ERROR IN THE ACTIVATION ENERGY OBTAINED BY THE INITIAL RISE METHOD FOR THERMALLY STIMULATED PROCESSES IN DIELECTRICS

ANTÔNIO E. DO NASCIMENTO,† PIOTR TRZESNIAK,‡ MÁRIO E. G. VALERIO† and JOSÉ F. DE LIMA†

†*Universidade Federal de Sergipe, 49.071-970 Aracaju—SE—Brazil e-mail: Mvalerio@brufse.bitnet;* ‡*Escola Federal de Engenharia de Itajubá,37.500-000, Itajubá, MG, Brazil*

TL glow curves were computer simulated for Randall-Wilkins, Garlick-Gibson, May-Patridge and Adirovitch models in a range of activation energies (0.1 to 2.0 eV) which were afterwards recovered by the initial rise method. The systematic error of the recovered energies is always the same independent of the energy used in the simulated curves. It was found that there is no dependence of the error onto the heating rate and there is a dependence of error curves on the models used in computer simulated TL emission. A correction factor can be plotted against the percentage of the peak maxima used in the initial rise for each model and we could apply it even if more than 50% of the ascending part of the glow peak has to be considered.

Key words: Thermoluminescence, simulated glow curves, initial rise method, activation energy, correction factor.

1 INTRODUCTION

Almost all the thermally activated processes that may happen in the dielectrics are described by the same functions. The final expressions are tentatively associated with microscopic phenomena that take place during the process. In the case of Thermoluminescence many different phenomenological models have been used to describe the intensity of light emitted by previously irradiated samples during heating. The basic assumption for all these models is that charge carriers can be trapped in metastable levels and, upon raising the temperature, the recombination process occurs causing the emission of light. The general appearance of the curve of emitted light vs. temperature is a peak whose intensity, shape, and position depend on some parameters describing the process. The most important parameters to be determined are the trap depth (E), which is the activation energy required to liberate the trapped electrons or holes, and the frequency factor (s). One of the main features of the simplest models is that when the temperature is much lower than that of the maximum intensities, the activation energy can be obtained by a plot of ln I vs. 1/T. This is known as the initial rise method. This method, that was originally suggested by Garlick-Gibson,[2] assumes that for temperatures much lower than the temperature of the peak (T_m) the TL intensity can be approximated by:

$$I(T) \approx \exp\left(-\frac{E}{kT}\right) \tag{1}$$

It is easy to see that equation 1 is valid for the first order Randall-Wilkins,[1] second order Garlik-Gibson[2] and arbitrary order May-Patridge[3] models but, for the more general Adirovitch[4,5] theory, it is not clear. In this work, the TL glow curves were computer simulated for all these models in a range of activation energies which were then recovered by the initial rise method. The aim of the work is to obtain the error involved in the

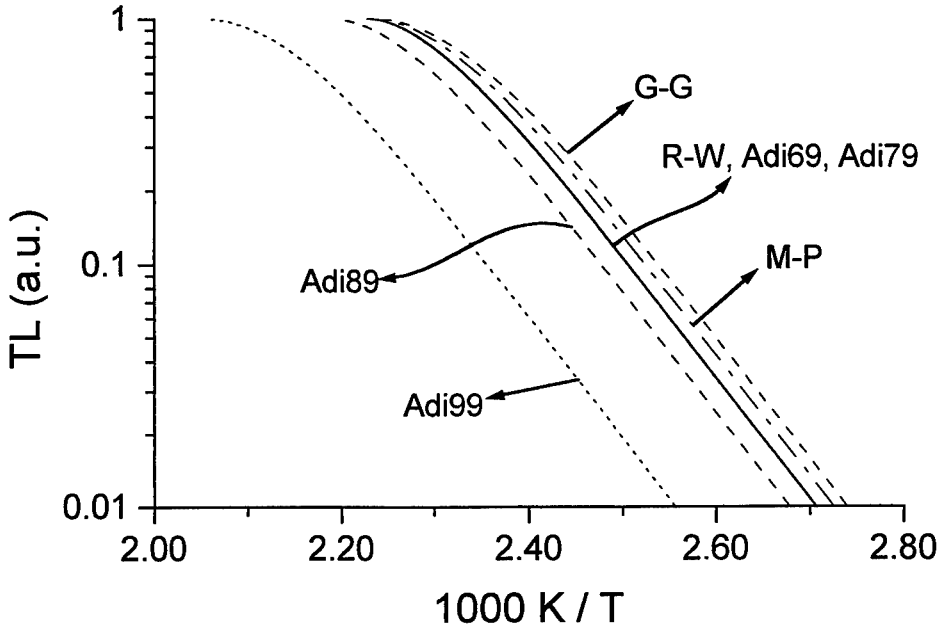

FIGURE 1 Initial rise plot for the computed TL glow curves with the Randall-Wilkins (R-W), Garlick-Gibson (G-G), May-Patridge (M-P) and Adirovitch models. For the Adirovitch model the retrapping parameter $A_n = 10^{-9}$ cm^3/s is fixed and the recombination constant A_m assumes the values 10^{-9} (Adi99), 10^{-8} (Adi89), 10^{-7}(Adi79) and 10^{-6} cm^3/s (Adi69).

determination of the activation energies using the initial rise method and to establish a procedure to correct the values found.

2 METHODOLOGY

The mathematical treatments were based on the final expressions that describe the TL intensity vs. temperature. The first order kinetic glow curves were simulated from the equation:

$$I(T) = n_o s.\ \exp(-E/kT).\exp\left(-\frac{s}{\beta}\int_{To}^{T}\exp(-E/kT')dT'\right) \qquad (2)$$

which was originally proposed by Randall-Wilkins[1]. The general order kinetic expression is:

$$I(T) = n_o s.\ \exp(-E/kT).\left[\frac{(b-1)s}{\beta}\int_{To}^{T}\exp(-E/kT')dT' + 1\right]^{\frac{-b}{b-1}} \qquad (3)$$

which reduces to the Garlick-Gibson model when $b = 2$ and to the May-Patridge when $b = 1.5$. To solve the integration that appears in these expressions we used the approximation suggested by Jenkins.[6]

We used a fourth-order Runge-Kutta routine with adaptive step size control to simulate

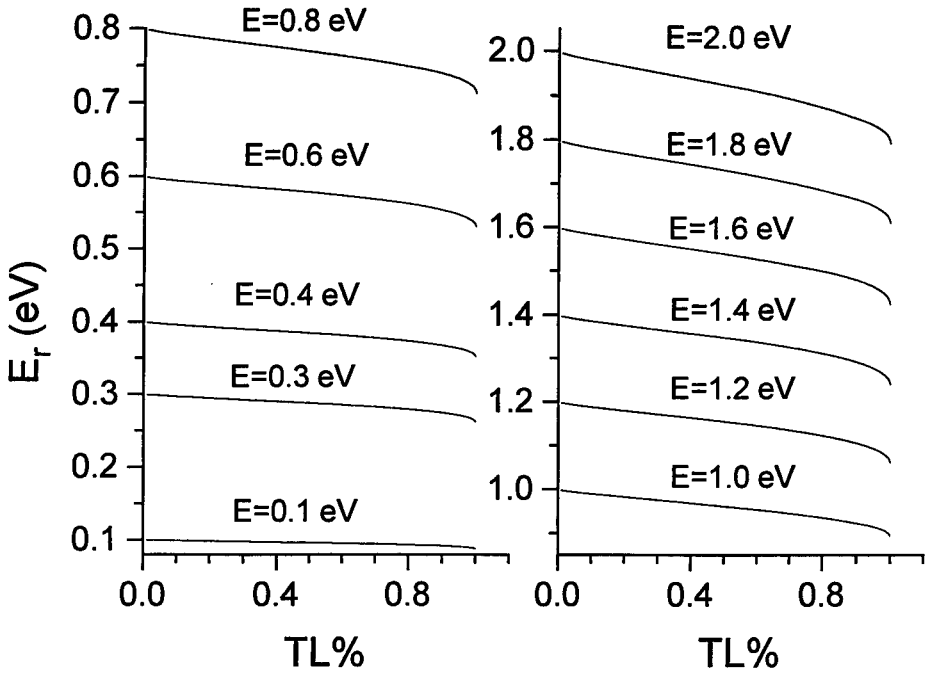

FIGURE 2 Recovered Energies (E_r), obtained from least square fittings to the initial rises of the simulated curves for the Adirovitch model with Am = 10^{-6} cm^3/s, as a function of the percentage of the peak maxima (TL%) for different values of E.

the TL glow curves of the Adirovitch model which is represented by the following equations:

$$\begin{cases} \dfrac{dn_c}{dt} = n.p - n_c(N-n)A_n - n_c.m.A_m \\ \dfrac{dn}{dt} = n_c.(N-n)A_n - n.p \\ \dfrac{dm}{dt} = -n_c.m.A_m \end{cases} \tag{4}$$

where n_c is the concentration of electrons in the conduction band, n is the concentration of electrons in the traps, N is the total concentration of traps with depth E below the conduction band, m is the concentration of holes in the recombination centers, p is the probability of thermal release of the electrons from the traps, A_m is the probability of the recombination of the electrons with the holes and A_n is the probability of the electrons being retrapped.

The activation energies E of the simulated curves were within the range 0.1 to 2.0 eV, the pre-exponential factor s was set as $10^{10}s^{-1}$for all the curves and the heating rates β were varied from 0.5 to 5 K/s. For the Adirovitch model, the retrapping parameter A_n was 10^{-9} cm^3/s while the recombination factor A_m was in the range 10^{-9} to 10^{-6} cm^3/s, the

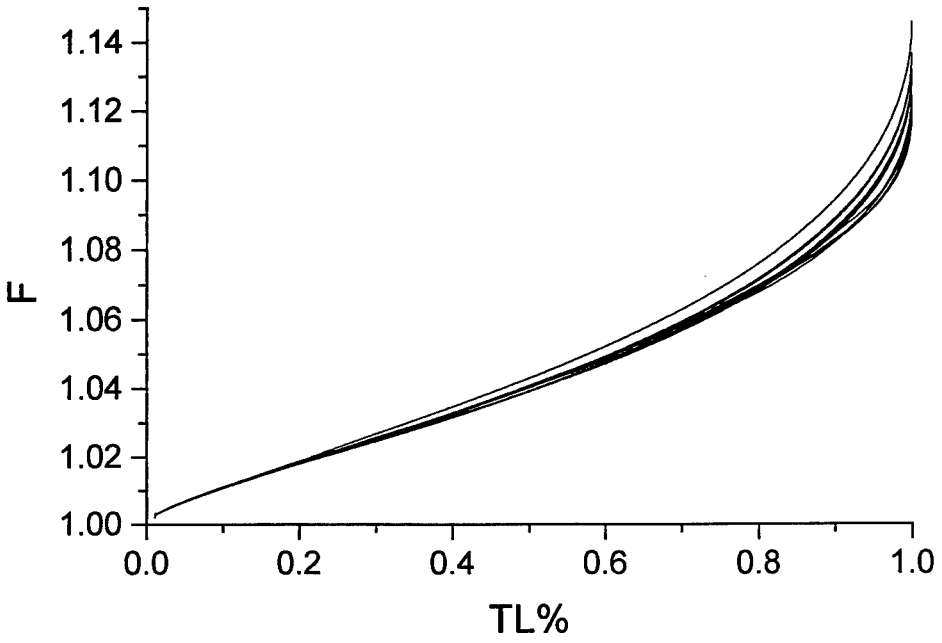

FIGURE 3 Correction factor F as a function of the percentage of the peak maxima (TL%), for the Adirovitch model with Am = 10^{-6} cm^3/s, with different energies E from 0.1 to 2.0 eV.

initial concentration of electrons and holes in traps were both 10^9 cm^{-3}, the initial concentration of electrons in the conduction band was zero, and the total concentration of electron traps N was 10^{10} cm^{-3}.

3 RESULTS AND DISCUSSION

Figure 1 shows the plot of ln I vs. 1/T for the TL glow curves simulated from the Randall-Wilkins, Garlick-Gibson (b = 2), May-Patridge (b = 1.5) and Adirovitch models with the same value of activation energy (E = 1 eV). For each energy in the range from 0.1 to 2.0 eV we plotted curves similar to figure 1. Using a least square fit we recovered the energy (E_r) of each curve in each model as a function of the percentage of the maximum intensity of the peak (TL%) varying from 1% to 100% of the respective maxima. A typical result of this procedure is shown in Figure 2 for the Adirovitch model.

We observed that the recovered energies (E_r) are always smaller than the actual energy (E) and that this difference increases with the percentage of the peak maxima.

The E_r versus TL% curves are independent of E for Randall-Wilkins, Garlick-Gibson and May-Patridge models and they are almost independent of E for all the Adirovitch models. This result suggests that we can define a factor $F = E/E_r$ to correct experimental values of activation energies that is obtained by the initial rise method.

With the values of the recovered energies (E_r) for all above given models and values of E, we plot F against the percentage of the peak maxima and study the effect of varying both, the considered model and the initial energy E, on this correction factor F.

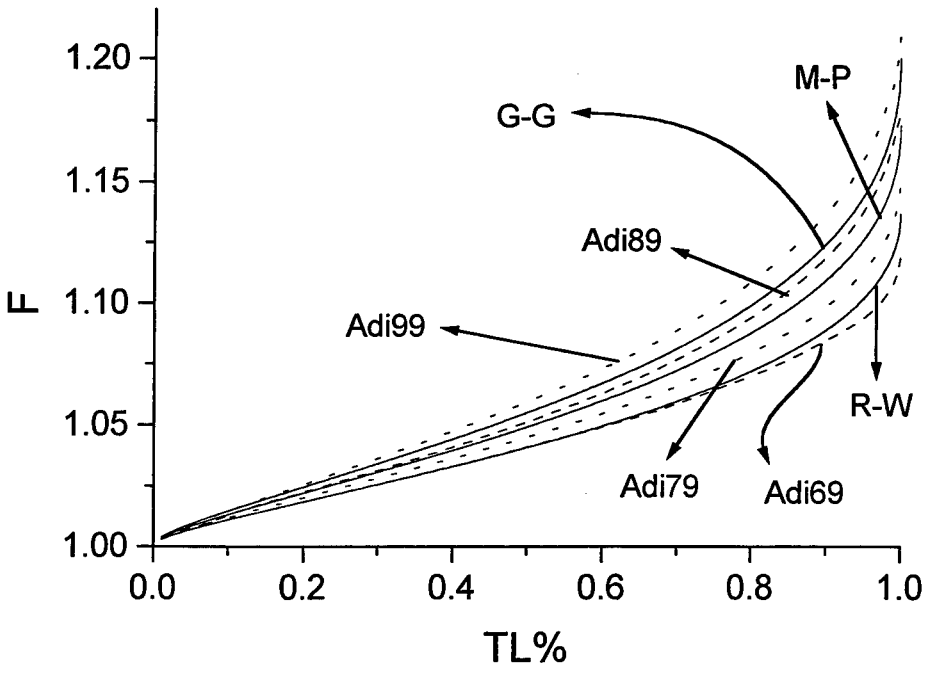

FIGURE 4 Correction factor F as a function of the percentage of the peak maxima (TL%) for the Randall-Wilkins (R-W), Garlick-Gibson (G-G), May-Patridge (M-P) models, and Adirovitch model with $A_m = 10^{-9}$(Adi99), 10^{-8} (Adi89), 10^{-7}(Adi79) and 10^{-6} cm^3/s (Adi69). Only the curves with E = 1.0 eV are shown for reasons of clarity.

Figure 3 shows F plotted against TL% for the Adirovitch model ($A_m = 10^{-6}$ cm^3/s and $A_n = 10^{-9}$ cm^3/s) with different energies E in the range 0.1 to 2.0 eV. As it can be seen, the values of E in this range caused only slight modifications in the F curves.

Fixing now the initial energy E and varying the model used to compute the F factor as a function of the peak maxima (Figure 4), we find that the difference in the factor F from one model to the others is about only 2% when we used 50% of the peak maxima.

We also investigated the influence of different heating rates β in the F × TL% curves for all models and we found that β does not modify the shape of these curves.

4 CONCLUSIONS

Studying the recovered energies obtained by the initial rise method from computer simulated TL glow curves with Randall-Wilkins, Garlick-Gibson, May-Patridge and Adirovitch models, it was possible to define an F-factor that can be used to correct the recovered energy (E_r) when different percentages of the TL peak maxima are considered. One of the main features of this correction F-factor is that it is independent of both the initial energy (E) employed to simulate the glow curves and the heating rate (β). The dependence of F-factor on the model is found to be very weak. As an example if we consider the initial rise until 50% of the peak maxima, the F-factor varies from 1.04 to 1.06, a difference of only 2%.

From all these results we can conclude that for practical use it is possible to correct the experimental values of activation energies obtained by the initial rise method even if more than 50% of TL peak has to be considered by use of a standard F factor.

REFERENCES

1. J. T. Randall and M. H. Wilkins, *Proc. Roy. Soc. (London)* **A184**, 366 (1945).
2. G. F. J. Garlick and A. F. Gibson, *Proc. Phys. Soc.* **60**, 574 (1948).
3. C. E. May and J. A. Patridge, *J. Chem. Phys.* **40**, 1401 (1964).
4. E. I. Adirovitch. *J. Phys. Rad.* **17**, 507 (1956).
5. A. Halperin and A. A. Braner, *Phys. Rev.* **117**, 408 (1960).
6. T. R. Jenkins. *J. Comput Phys.* **29**, 302 (1978).

Radiation Effects and Defects in Solids, 1995, Vol. 134, pp. 153–156
Reprints available directly from the publisher
Photocopying permitted by license only

© 1995 OPA (Overseas Publishers Association)
Amsterdam B.V. Published under license by
Gordon and Breach Science Publishers SA
Printed in Malaysia

ab initio MOLECULAR-CLUSTER MODELING OF A PARAMAGNETIC EXCESS-ELECTRON VACANCY CENTER IN PARATELLURITE

D. P. MADACSI* and K. RAKSÁNY‡

**Department of Physics and Institute of Materials Science, University of Connecticut, Avery Point, Groton, CT 06340, USA; ‡Research Laboratory for Crystal Physics Hungarian Academy of Sciences, Budapest, 1112 Budaörsi Ut 45, Hungary*

An excess-electron point defect associated with an oxygen vacancy as observed in paratellurite has been modeled and studied using the *ab initio* RHF-SCF molecular orbital method of the Many ELectron Description (MELD) program package. Open-shell electronic structure calculations for obtaining spin densities were performed on molecular clusters $Te_2O_6H_6$ having paratellurite geometry and terminated by hydrogen-like atoms with optimized nuclear charges and O-H distances. Hyperfine and superhyperfine matrix elements were calculated based on the spin densities of the *ab initio* results, and the effects of spin delocalization, second-order perturbation magnetic contributions, extended CI calculations, double-zeta quality basis functions and defect-centered basis functions on these parameters were investigated. While specific results in excellent agreement with EPR measurements were obtained and strongly support the proposed defect model, inability to obtain overall agreement with experiment via a single calculation is suggestive of limitations resulting from cluster size as well as basis set quality and size.

1 INTRODUCTION

ab initio LCAO MO calculations were carried out on clusters containing two Te atoms and their respective coordination spheres, to calculate hyperfine and superhyperfine parameters and investigate their dependence on the electronic structure of the cluster. In order to obtain a crystal-like potential and to ensure a suitable bonding character for the lone pairs of the outermost oxygens, hydrogen-like terminators were applied to the cluster, with nuclear charges and bond distances optimized to equalize gross atomic Mulliken populations on the oxygens.[1] Coordination spheres consisting of four oxygen atoms together with the corresponding terminators were used for each Te atom in the cluster. With few exceptions, Te and O atoms were located at crystalline sites. Calculations were carried out on the 'dimer' containing two tellurium atoms with their coordination spheres and terminators of composition $Te_2O_6H_6$ with an oxygen vacancy at the site of the shared oxygen and with an excess electron.

2 METHOD

Molecular orbital electronic structure calculations were carried out using the *ab initio* open-shell restricted Hartree-Fock LCGO MO SCF-CI MELDF program package of the Quantum Chemistry Program Exchange.[2] Basis sets included a [1s, 1p](3s, 3p) pseudo basis[3] extended by a TeO_2-energy optimized d polarization function ($\zeta = 0.016$)[4] for Te, an STO-3G basis set for O and terminator H atoms,[5] and polarization s, p($\zeta = 0.028$)+ diffuse s ($\zeta = 0.001$) for the vacancy. Hyperfine and superhyperfine eigenvalues were calculated using the pseudo spin orbitals and pseudo spin densities of MELD as input data, and an ample Gaussian atomic basis set, Te:(23s, 19p, 13d).[6]

3 RESULTS AND DISCUSSION

Results of all calculations together with experimental hyperfine parameters[7] are summarized in Table I, with the unique details of each calculation given in the notes (1)–(10). Previous hyperfine parameter calculations for the dimer[1] have shown a satisfactory agreement with experiment in terms of average magnitudes, but the relative magnitudes of the parameters were not well-reflected in the calculated values. This is due to the predominant p character of the spin orbital resulting in uniaxial anisotropic values, as calculated in (2).

Table I
Hyperfine and superhyperfine tensor components (in $10^{-4}cm^{-1}$) and eigenvector directions (in degrees, measured with respect to the local Te site coordinate system). Unique details of calculations are given in notes (1)–(10)

	Energy	Hyperfine Components					Eigenvector Directions				
Note		A_{ISO}	A_{XX}	A_{YY}	A_{ZZ}	ϕ_X	θ_X	ϕ_Y	θ_Y	ϕ_Z	θ_Z
EXPT.[7]		634.7	−39.6	−101.7	141.3	89	75	−2	−88	84	15
(1)	−462.133	71.4	−62.5	−62.6	125.2	73	−42	−12	86	81	48
(2)	−462.190	298.8	−60.4	−60.4	120.8	−64	58	15	−73	81	37
(3)	−462.184	53.3	−65.8	−65.9	131.7	72	−43	−13	85	81	48
(4)	−462.221	51.8	−78.8	−78.9	157.7	73	−43	−12	86	82	47
(5)	−462.133	52.0	−62.5	−62.6	125.1	24	−59	−44	57	82	48
(6)	−462.207	85.8	−66.4	−63.6	130.0	−82	42	−2	−81	80	49
(7)	−462.184	53.3	−65.8	−65.9	131.7	72	−43	−13	85	81	48
(8)	−462.116	350.6	−3.1	−3.0	6.2	74	−75	−15	89	78	14
(9)	−461.939	656.4	−58.0	−58.1	116.1	−16	82	65	−42	81	48
(10)	−239.322	4.7	−63.8	−65.3	129.0	15	11	6	78	83	85
	Energy	Superhyperfine Components					Eigenvector Directions				
EXPT[7]		82.5	−4.3	−9.3	13.6	–	–	–	–	–	–
(1)	−462.133	56.0	−0.38	−0.43	0.81	−9	65	−86	−65	42	−37
(2)	−462.190	62.5	−0.30	−0.35	0.64	1	81	−87	−75	62	−16
(3)	−462.184	35.7	−0.42	−0.52	0.94	−17	53	−88	−67	26	−46
(4)	−462.221	49.8	−0.63	−0.74	1.37	−27	41	87	71	11	−56
(6)	−462.207	25.5	−0.15	−0.79	0.94	−37	40	−83	−60	21	−66
(8)	−462.116	0.9	−0.01	−0.02	0.03	−30	14	−79	−81	12	−80
(9)	−461.939	8.9	−0.34	−0.32	0.66	−7	76	−88	−61	60	−33
(10)	−239.322	91.2	−1.28	−1.31	2.59	−27	86	70	29	60	61

(1) no extra AO's centered on vacancy site
(2) as (1), with Te relaxed nearly along the C_2 axis
(3) energy optimized ssp AO's centered in the vacancy site
(4) as (3), extended with double zeta Te 5p orbitals
(5) as (1), using spin orbital amplitudes centered on atoms in the first coordination sphere
(6) as (3), using CI densities after a CI calculation with all singles, doubles and triples in the −5(occupied)/+3(optimized virtual) active space (18996 configurations)
(7) as (3), with second order perturbation results based on 50 singles (s) with the one-electron spin—nuclear spin interaction operator (A):<0 |A| s><s |A| 0>/($E_s - E_o$)
(8) as (1), with modified contracted Te 5d orbitals (2/3*zeta(Te 5p))
(9) as (1), augmenting the energy-optimized diffuse d orbital[4] with a primitive of $\zeta = 0.5$
(10) TeO_4H_4 monomer with an additional Te substituting for an O; Te–Te: 2.56 Å, as in Te_2; Te–H: 1.56 Å as in TeH_2

3.1 *Total Energy*

The energy values in Table I confirm the significance of the basis set. The lowest energy is obtained by the double zeta Te-1s, 2p-(3s, 5p) calculation (4), which is followed by the energy of the CI calculation (6). An interesting result is that the use of diffuse and

polarization s and p orbitals on the vacancy in (3) results in a 0.052 a.u. stabilization, nearly equivalent to that obtained for geometry relaxation (2).[1] However, using only s orbitals centered on the vacancy yielded almost the same energy as $(1)^1$, indicative of directional effects between the Te atom and vacancy. Constraining contracted d orbitals into the basis set in (8) and (9) resulted in energetic destabilization of the cluster.

3.2 *Hyperfine Interactions*

The isotropic hyperfine values in Table I fall into two groups, the low values of (1), (3)–(7), (10) and the high values of (2), (8) and (9). A value in excellent agreement with experiment was calculated in (9) by augmenting the energy-optimized diffuse d orbital[4] with a primitive of $\zeta = 0.5$, and the best agreement with experimental eigenvector directions was calculated in (8) with modified contracted Te 5d orbitals. In general s amplitudes were found to affect isotropic values to a greater degree than the same amount of p and d amplitudes affect the anisotropic values. Thus relatively high isotropic values can originate from calculationally uncertain low s amplitudes. The increase in s amplitudes can be traced back to the displacement of Te 5s orbitals into the virtual and open shell space.

The calculated principal A_{zz} values of the anisotropic matrix agree fairly well with the experimental value, with the best result attained with optimized vacancy-centered orbitals in (3). The only calculation which overestimates experimental values is (4) which may be attributed to the competitive displacement of Te 5d orbitals from the doubly occupied space. The relatively low values for (2) can be explained in terms of a nuclear configuration better suited to the formation of spd hybrids. The extremely low values for (8) are the direct consequence of the oxygen hole character of the corresponding spin orbital. This is the single example here of such a state being produced by modification of the basis centered on the Te atom.

A significant disagreement between theory and experiment is the small differences between the calculated A_{xx} and A_{yy} values. This uniaxial behavior of the eigenvalues is derivable from the low Te 5d participation in the spin orbital. Attempts to modify the d basis on Te tend to decrease the d spin population. Only CI calculations (6) and the inclusion of a vicinal Te atom, a second Te replacing an O in a TeO_4H_4 monomer cluster in (10), lead to some triaxial character.

3.3 *Superhyperfine Interactions*

While isotropic superhyperfine values generally are in good agreement with experiment, anisotropic values generally are underestimated by an order of magnitude, a general feature of these calculations emphasizing the isotropic character of the spin density at nuclei having the lesser spin amplitude. The decrease in the isotropic value with modified d orbital in (8) and (9), and the improved anisotropic values for the monomer calculation in (10) suggest the need for a larger molecular cluster in modeling this defect.

4 CONCLUSIONS

The excess-electron vacancy center model in paratellurite is supported by *ab initio* open-shell RHF-SCF calculations. However, while specific results in excellent agreement with EPR measurements were obtained by including vacancy-centered orbitals, improving the quality of the Te basis set, and modifying the Te d orbital, limitations attributed to cluster

size and basis set were observed in an inability to obtain overall agreement with experimental results via a single calculation. A pentamer cluster with vacancy, $Te_5O_{15}H_{12}$, would retain the C_2 symmetry of the defect, and suggests itself for further computational modeling and investigation of this defect. However, the increased computational time due to the number of atoms in this cluster may restrict the use of modified orbitals and improved quality basis sets.

REFERENCES

1. G. Corradi, R. H. Bartram, A. R. Rossi, J. Janszky, *J. Phys. Chem. Solids*, **48**, 675 (1987).
2. E. R. Davidson, *QCPE 23*, Program No. 580 (1991).
3. W. R. Wadt, P. J. Hay, *J. Chem. Phys.* **82**, 284 (1984).
4. J. Janszky, R. H. Bartram, A. R. Rossi, G. Corradi, *Chem. Phys Lett.* **24**, 26 (1986).
5. W. J. Hehre, R. F. Stewart, J. A. Pople, *J. Chem. Phys.* **51**, 2657 (1969).
6. S. Huzinaga, M. Klobukowski, *Theochem*, **167**, 1–210 (1988).
7. A. Watterich, R. H. Bartram, O. R. Gilliam, L. A. Kappers, G. J. Edwards, I. Foldvari, R. Voszka, *Phys. Rev.* **B32**, 2533 (1985).

Radiation Effects and Defects in Solids, 1995, Vol. 134, pp. 157–159
Reprints available directly from the publisher
Photocopying permitted by license only

© 1995 OPA (Overseas Publishers Association)
Amsterdam B.V. Published under license by
Gordon and Breach Science Publishers SA
Printed in Malaysia

POINT DEFECT MODELLING AND TRANSPORT PROCESSES IN AgBr

RADHA D. BANHATTI and Y. V. G. S. MURTI

Department of Physics, Indian Institute of Technology, Madras, India

We have modelled cationic Frenkel defects, Schottky defects and bound vacancy pairs in AgBr according to the recently introduced EPPI model. Our findings suggest a significant role for Schottky defects in the excess high temperature conductivity and also an important role for bound vacancy pairs in anion self-diffusion.

Key words: AgBr, point defects, formation enthalpies, defect modelling, ionic conductivity and diffusion.

1 MOTIVATION

The charge and mass transport in AgBr reveal a number of curious features[1] such as excess high temperature conductivity, varied behaviour in respect of diffusion of different monovalent impurities, curvature in the Arrhenius plot of anion self-diffusion and occurrence of premelting.[2] Previous analyses of experimental data ignored any possible role of Schottky defects, while in all atomistic calculations, the focus had been on refining potentials with the polarization treatments restricted to the dipolar approximation.

Based on a critical examination[3] of the various data on the electronic and lattice properties, we conclude that van der Waals (vdW) interactions are strong in AgBr (Table I). The short range interatomic potential used is a two-body potential which adequately represents overlap and dispersion forces.[4] The polarizabilities are determined according to the MPPI model.[5] We see that anion (a) and cation (c) polarizabilities are large even in the crystal environment (Table I). This clearly points to the need for a model to account for the strong deformations that prevail around a defect in the highly polarizable AgBr crystal. The Extended Polarizable Point Ion (EPPI) model[6] has been formulated to examine the effect of induced quadrupolar deformations.

Table I
vdW parameters (C_{ij} in eV A^6) and polarizabilities (α_i in A^3)

C_{cc}	C_{ca}	C_{aa}	α_c	α_a	α_d
148.23	148.78	318.92	1.125	4.172	1.638

2 EPPI MODEL

Within the Mott-Littleton (ML) scheme,[7] it is customary to divide the crystal into two regions. Region 1, in the EPPI model consists of the defect and its nearest neighbours. Region 2 is the rest of the crystal, whose displacements and dipole moments are assigned as in the ML scheme. The displacements and induced dipole (p_i) and quadrupole (Q_{ij}) moments of Region 1 are determined by explicit energy minimization. For the vacancy and interstitial defect environments, Region 1 ions have residual site symmetries of C_{4v} and C_{3v} respectively. This leads to axial symmetry of the Q tensor with only one independent

component such as $Q_{z'z'}$ where z′ is the symmetry axis.[6] We solve for the dipole and quadrupole moments simultaneously. The first region polarization energy consists of two parts: the dipole energy (W_p^1) and the quadrupole energy (W_q^1) given by

$$W_p^1 = -\frac{1}{2}\sum_n \vec{p} \cdot \vec{F}_m; \quad W_q^1 = -\frac{1}{2}\sum_n (1/6) \sum_{ij} Q_{ij} F_{m,ij}$$

where n means summation over the ions of Region 1. $F_{m,ij}$ is the ij component of the field gradient tensor due to monopoles.

3 RESULTS AND DISCUSSION

The extension to the quadrupole model is found to be meaningful and significant for silver halides. The contribution to the defect formation energy is between 0.8 eV and 1.0 eV for Schottky and Frenkel defects. From Table II we also see that the gap between formation enthalpies for cation Frenkel defects and Schottky defects is much less ($\approx$ 0.5 eV). This suggests that there is an imperative need for a fresh look at the conductivity anomaly at high temperatures, treating the Schottky defects more seriously. This view finds support in the work of Andreoni and Tosi.[2]

Table II
Defect Formation Enthalpies (h in eV)

Model	W_{av}	W_{cv}	W_{ci}	h_S	h_F	h_{vp}
MPPI	6.08	5.04	−2.70	2.47	2.34	1.26
EPPI	5.95	4.55	−3.21	1.85	1.34	0.70

W_{av}, W_{cv}, W_{ci}—energy for creation of anion & cation vacancies,
—and cation interstitials respectively.

We see from Table III that for the vacancy defect, the polarization contribution ($W_p^1 + W_q^1$) dominates so that the equilibrium displacement s_a of Region 1 ions in the EPPI model is inwards. In the case of the interstitial defect, short range interactions ($W_{sr}^{rep}, W_{sr}^{vdw}$) prevail, with the Region 1 ions relaxing outwards (s_c, s_a) so as to avoid overlap between them. Inclusion of quadrupolar effects does not significantly affect these relaxations. This shows that in AgBr, interstitial defects are stabilized by vdW forces and vacancy defects by the total polarization.

The average experimental values of h_F and h_S for AgBr are 1.21 eV and 1.70 eV respectively. A better agreement of our results with experimental values will result if one were to consider the quadrupolar polarizability of Br^- ion in AgBr to be closer to its free ion value.

Though the other theoretical works obtain a lower value of h_F, the thrust of those calculations is on the potential models; we discuss in detail, the virtues and limitations of such an approach elsewhere.[9] It may be pointed out that the experimental quantification of h_F is based on a rigorous analysis of conductivity data (which ignores possible contributions from Scottky defects) and there is no corresponding independent analysis of the self-diffusion data.

The vacancy pair enthalpy h_{vp} lies between 0.7–1.26 eV (Table II). The EPPI value includes a rough estimate of the quadrupole contribution. This confirms that vacancy pairs have a larger role to play in anion self-diffusion. The activation energy for the single vacancy is much larger than for the pair. This together with the low value of h_{vp} suggests

that the migration enthalpy of the vacancy pair is likely to be lower. One has here a probable explanation for the observed anomalous diffusion in AgBr.[8]

It is interesting to note that in AgBr, three kinds of lattice disorder—cationic Frenkel defects, Schottky defects and vacancy pairs all play a significant role resulting in the richness and complexity of transport processes.

Table III
Details of Results

	Cation Interstitial		Cation Vacancy	
	MPPI	EPPI	MPPI	EPPI
s_c	0.06	0.06	–	–
s_a	0.02	0.02	0.01	−0.03
W_{sr}^{vdw}	0.93	0.93	−0.10	0.28
W_{sr}^{rep}	−1.20	−1.20	0.24	−0.65
$W_p^{sr} + W_q^l$	−1.65	−2.16	−1.48	−2.74
E_D	−2.70	−3.21	5.04	4.55

s_c and s_a are fractional displacements of Region 1; energy terms are in eV.

ACKNOWLEDGEMENT

The first author (RDB) appreciates the financial support extended by the Council of Scientific and Industrial Research (CSIR), India during the course of this work.

REFERENCES

1. A. L. Laskar in *Superionic Conductors and Solid Electrolytes*, eds. A. L. Laskar and S. Chandra (Academic Press, London, 1989) pp. 265.
2. W. Andreoni and M. P. Tosi, *Solid State Ionics*, **11** (1983) 49.
3. Radha D. Banhatti in *Role of Induced Quadrupoles in Modeling Intrinsic Point Defects of AgCl and AgBr*, Ph. D. thesis, Indian Institute of Technology, Madras, India (1993).
4. R. D. Banhatti, Y. V. G. S. Murti and A. L. Laskar, *phys. stat. sol. (b)* **164** (1991) 357 (Set III potential model).
5. Y. V. G. S. Murti and Radha D. Banhatti, *Proc. International Conference in Insulating Materials*, eds. O. Kanert and J. M. Spaeth (World Scientific Pub. Ltd., Singapore, 1993) p. 198.
6. Radha D. Banhatti and Y. V. G. S. Murti, *Phys. Rev.* **B48** (1993) 6839.
7. N. F. Mott and M. J. Littleton, *Trans. Faraday Soc.* **34**(1938) 485.
8. R. J. Friauf, *J. de Physique*, **38** (1977) 1077.
9. Radha D. Banhatti and Y. V. G. S. Murti, in preparation.

Radiation Effects and Defects in Solids, 1995, Vol. 134, pp. 161–164
Reprints available directly from the publisher
Photocopying permitted by license only

© 1995 OPA (Overseas Publishers Association)
Amsterdam B.V. Published under license by
Gordon and Breach Science Publishers SA
Printed in Malaysia

COMPUTER SIMULATION OF URANIUM OXIDE PHASES

ROBERT A. JACKSON[1], JAMES E. HUNTINGTON[1] and RICHARD G. J. BALL[2]

[1]*Department of Chemistry, Keele University, Keele, Staffs ST5 5BG, UK.;* [2]*AEA Technology, Harwell Laboratory, Oxon OX11 ORA, UK.*

(Received July 1, 1994)

Results are presented of computer simulation studies of some uranium oxide phases, using two contrasting methods to calculate defect parameters. The first is based on the Mott-Littleton approach, which assumes defects to be in infinite dilution in an otherwise perfect lattice, and the second allows finite defect concentrations to be modelled, using a supercell approach. Two groups of uranium oxide compounds are studied; firstly the mixed oxide reactor fuel $(U,Pu)O_2$, where lattice and defect properties are obtained as a function of Pu concentration, and secondly the alkaline earth metal uranates M_3UO_6, where the calculation of a complete set of structural data and defect parameters is described, and the dominant mode of intrinsic disorder proposed.

Key words: Computer Simulation, Supercell, Reactor Fuel, Uranates.

1 INTRODUCTION

The many phases of uranium oxide are of considerable importance due to the use of the parent compound, UO_2, as a nuclear fuel, which leads to the formation of other phases as by-products. For reasons ranging from safety issues to the sheer number of such compounds, there is considerable motivation for studying their properties by computer simulation. Some of the the previous computational work in this area has looked at UO_2 in detail,[1,2] the behaviour of fission gas,[3,4] U_3O_8,[5] and the alkali metal uranates[6]. This paper uses a supercell method to model the mixed oxide fuel $(U,Pu)O_2$, and calculates lattice and point defect properties of alkaline earth uranates.

2 THEORY AND COMPUTATION

The computer modelling of ionic and semi-ionic materials is well-established, and will only be described briefly here. Calculation of perfect lattice and defect properties is considered separately.

2.1 *Perfect Lattice Properties*

The procedure used here is lattice energy minimisation, where the properties are calculated from a structure relaxed to its lattice energy minimum.

2.2 *Defect Properties*

Two methods are used to calculate these; which is the more suitable depends on defect concentration. For point defects, a method which assumes infinite dilution is appropriate, i. e. the Mott-Littleton 2-region strategy, which is fully documented elsewhere.[7]

However, where there is a finite defect concentration a method which allows defects to interact is more appropriate, and the supercell method[8] falls into this category, in which a

large unit cell is used, into which the defects are introduced explicitly. The subsequent procedure is as for lattice energy minimisation. An advantage of this method is that lattice properties can be calculate, e. g. as a function of defect concentration.

3 PROCEDURE AND RESULTS

(i) (U,Pu)O_2 There are three possibilities: stoichiometric, hypostoichiometric (deficient of oxygen), and hyperstoichiometric (with oxygen excess). Since little experimental data is available for the latter case, this paper will concentrate on the stoichiometric and hypostoichiometric systems, where comparison is possible.

In each case, the system is simulated using a $3 \times 3 \times 3$ supercell. In the stoichiometric case, $(U_{1-y}\,Pu_y)O_2$, the Pu content is varied from y = 0 to y = 1, and three distribution schemes are considered: a random distribution, a centred distribution and a side ordered one. Figure 1 shows the substitution energy per PU ion plotted versus Pu content, and it is seen that the distribution scheme does not affect the result, which agrees with earlier work which assumed a random distribution would apply. Figure 2 shows the variation of lattice parameter with Pu content, compared with experimental values.

For the hypostoichiometric system, $(U_{1-y}\,Pu_y)O_{2-x}$, the Pu is assumed to be in the form of Pu^{3+} ions,compensated by O^{2-} vacancies. The Pu concentration, y, and the degree of non-stoichiometry, x, are variables, and three ordering schemes are investigated. The first is a random distribution of ions and vacancies, and the second and third are clusters involving respectively one and two Pu^{3+} ions bound to nearest neighbour O^{2-} vacancies. It turns out that the cluster involving two Pu^{3+} ions has the lowest energy, suggesting that it is most likely to be formed. As a further test, the lattice parameter is calculated as a function of x for each scheme; Figure 3 shows the comparison with experiment, and the scheme involving two Pu^{3+} ions is closest, confirming that this is most likely to be formed. It is therefore concluded that in the hypostoichiometric case, the observed disorder is likely to be clusters of this type.

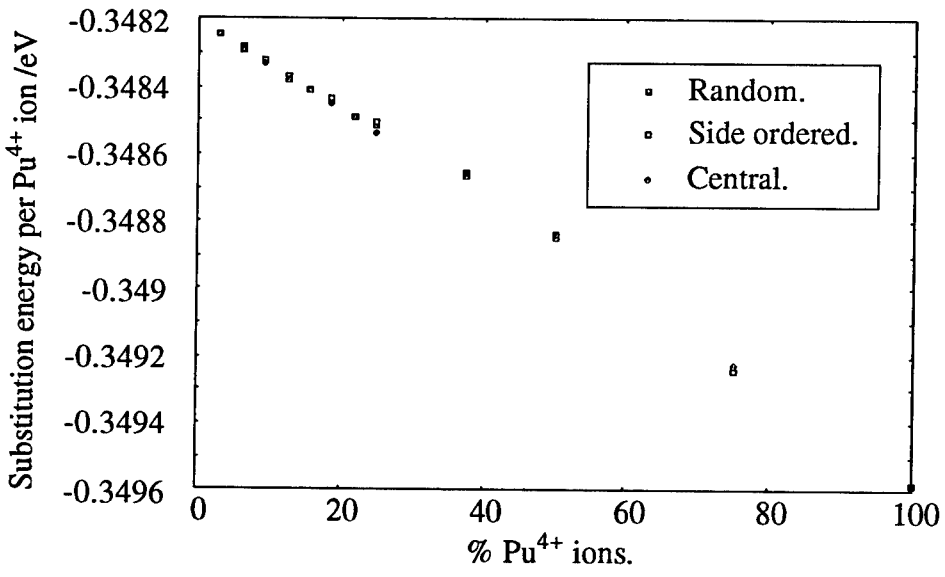

FIGURE 1 Substitution energy per Pu^{4+} cation against Pu concentration.

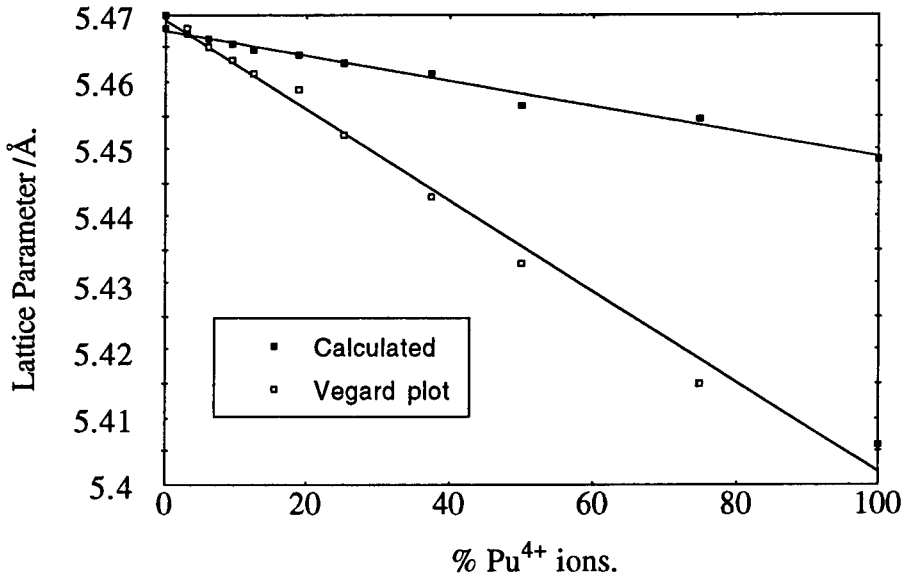

FIGURE 2 Variation of lattice parameter with Pu concentration.

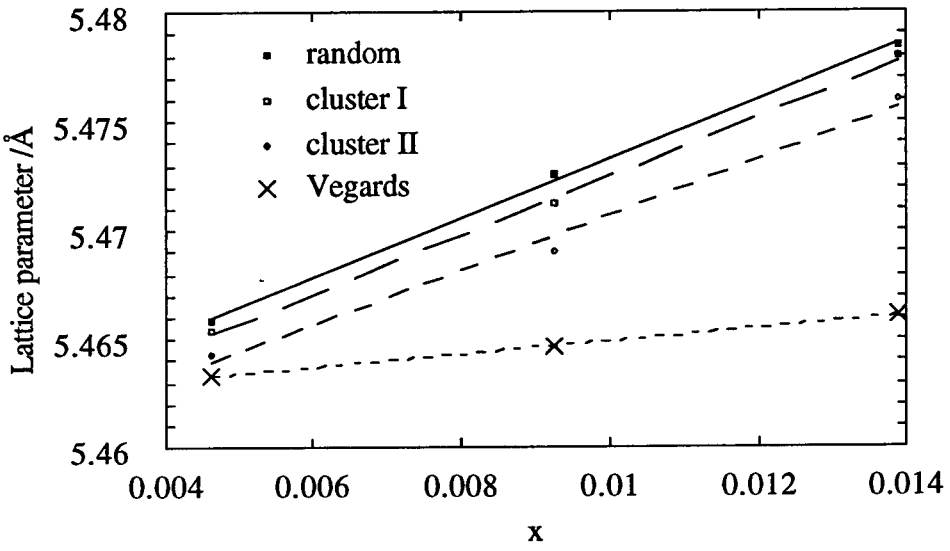

FIGURE 3 Variation of lattice parameter with degree of non-stoichiometry x, for different defect distributions in $(U_{1-y}Pu_y)O_{2-x}$ with 5.5% Pu.

(ii) Alkaline Earth Metal Uranates The compounds M_3UO_6, where M is an alkaline earth cation, are of importance as they are formed by reaction of fission products with nuclear fuel. They have also been recognised as having potential applications in materials chemistry as catalytic materials and electrodes.

The compounds considered here are those with M = Mg, Ca, Sr and Ba. It can be seen that if all the possible combinations of M are considered, this leads to a large number of

compounds. If M is replaced by A,B,C to allow for different combinations then there are compounds of type A_3UO_6, A_2BUO_6, and $ABCUO_6$ for all the elements listed above. Experimental structural information is only available for a small number of these compounds. The aim of this study was therefore to use lattice energy minimisation to calculate the structures and lattice properties of all the possible compounds, and then to go on to look at their defect chemistry.

The structures are mainly orthorhombic, but with a slight distortion in the β angle from 90°. Elastic and dielectric constants are also calculated, although as yet there are no experimental determinations of these quantities for comparison. Space does not permit tabulation of this information in the present paper, but it will be included in a future publication.[9]

A full survey of the defect chemistry has also been carried out for all compounds. This includes calculation of all possible vacancy and interstitial energies for each compound, and their combination to give the various Frenkel and Schottky energies. These calculations were carried out using Mott-Littleton procedures. The predicted intrinsic disorder varies from one group of compounds to another, but for most, pseudo-Schottky behaviour is predicted (formation of cation and oxygen vacancies), with the exception of the Mg_2BUO_6 series, where cation Frenkel disorder is predicted. Full details will be given in a future publication.[9]

REFERENCES

1. C. R. A. Catlow, *Proc. R. Soc.* **353** 533 (1977).
2. R. A. Jackson, A. D. Murray, J. H. Harding and C. R. A. Catlow, *Phil. Mag.* **53** 27 (1986).
3. R. A. Jackson and C. R. A. Catlow, *J. Nucl. Mater.* **127** 161 (1985).
4. R. G. J. Ball and R. W. Grimes, *Phil. Mag. A* ***66*** 473 (1991).
5. R. G. J. Ball and P. J. Dickens, *J. Mater. Chem.* ***1*** 105 (1991).
6. R. G. J. Ball and P. J. Dickens, *J. Mater. Chem.* ***1*** 415 (1991).
7. C. R. A. Catlow, *J. Chem. Soc. Far. Trans. II* ***85*** 335 (1989).
8. R. A. Jackson, J. E. Huntington and R. G. J. Ball, *J. Mater, Chem.* ***1*** 1079 (1991).
9. J. E. Huntington, R. A. Jackson and R. G. J. Ball, *in preparation.*

Radiation Effects and Defects in Solids, 1995, Vol. 134, pp. 165-169
Reprints available directly from the publisher
Photocopying permitted by license only

© 1995 OPA (Overseas Publishers Association)
Amsterdam B.V. Published under license by
Gordon and Breach Science Publishers SA
Printed in Malaysia

SHELL MODEL AND EMBEDDED CLUSTER CALCULATIONS OF HOLE BIPOLARONS IN $BaTiO_3$

H. DONNERBERG and A. BIRKHOLZ

University of Osnabrück, FB Physik, D-49069 Osnabrück

Classical shell-model- as well as embedded-cluster-type calculations are employed in order to supply theoretical arguments in favour of hole bipolarons in $BaTiO_3$. In particular the embedded cluster modelling studies, which explicitly include the local electronic defect structure, suggest the importance of lattice relaxation and electron correlation terms in order to stabilize diamagnetic O_2^{2-} molecules (bipolarons) in the material. Our simulations show that hole bipolarons are predominantly bound at Ti-site acceptor defects.

Key words: Hole bipolarons, $BaTiO_3$, shell model, embedded cluster calculations.

1 INTRODUCTION

Oxides ABO_3 with perovskite structure are highly promising materials for optical applications. In general there is a marked correspondence between the defect structure and the relevant properties of the oxide.

Recently hole bipolarons possibly trapped at suitable acceptor-type defects have been speculated to exist in the photorefractive material $BaTiO_3$.[1] It has been found that light-induced charge-transfer reactions must involve defect-centers which are invisible in photo electron spin resonance (Photo-ESR) experiments. In order to explain these results, holes which are created in the valence band during illumination were assumed to become pairwise bound in form of molecular O_2^{2-} aggregates. Similar to isoelectronic F_2 molecules such oxygen complexes should possess a diamagnetic ground state, thus being insensitive to ESR. Nearby acceptor defects can be expected to aid the required hole localization.

We present corresponding computer simulations of these trapped hole bipolarons which are based on shell model calculations and additional embedded cluster investigations.

2 METHODS AND RESULTS

2.1 *Shell Model Calculations*

Within a classical shell model approach[2] each ion is represented by a massive core to which a shell is harmonically bound. Pair potentials are specified between different ionic components. The minimization of the lattice energy by independent variation of core and shell co-ordinates yields the equilibrium configuration of the perfect and the defective lattice. For details of solid state computer simulations we refer to the monograph edited by Catlow and Mackrodt.[3] All potential parameters appropriate for $BaTiO_3$ and for impurity-oxygen interactions have been taken from the extensive work of Lewis and Catlow.[4] In addition we employed an O^--O^- pair potential to represent the attractive covalent interaction between the respective O^- hole species.[5] This potential has been generated by simulations of selftrapped holes in corundum based on the INDO approximation. These V_k-type defects may be considered as negatively ionized hole bipolarons, the derived pair potential is therefore assumed to model hole bipolarons in $BaTiO_3$ as well.

In table I we summarize our calculated results of hole bipolaron formation close to Ti-

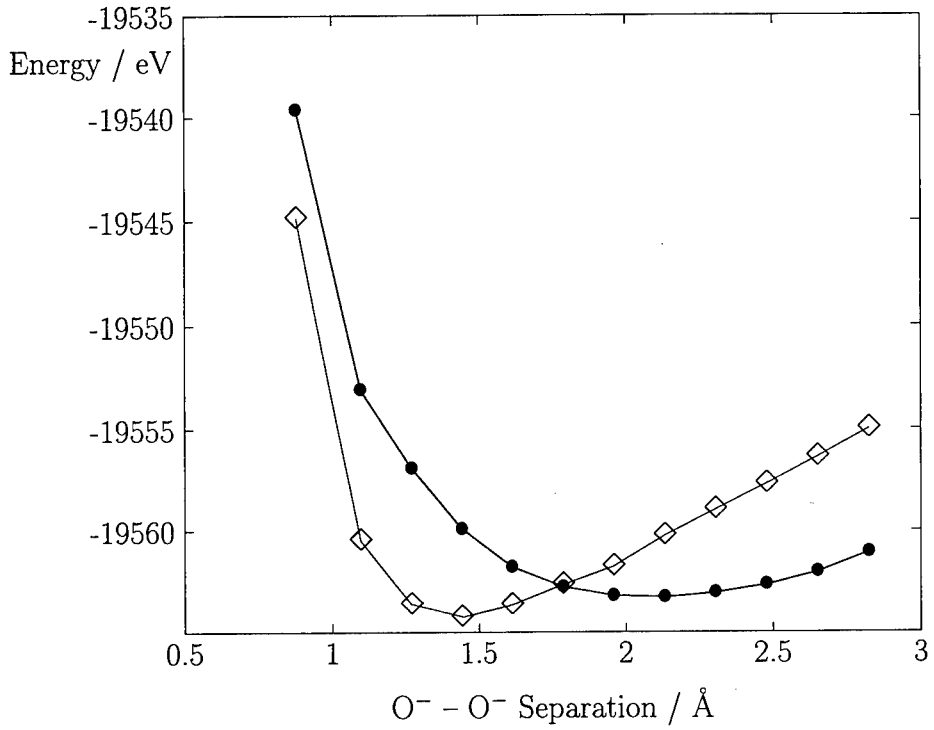

FIGURE 1 Dependence of the bipolaron singlet (◇) and triplet (•) spin states as a function of the O^--O^- separation within HF-theory. Lattice relaxation is included.

site and Ba-site acceptor defects.

Table I
Hole bipolaron formation at Ti-site and Ba-site acceptor defects in $BaTiO_3$.

acceptor defect	bipolaronic bond length / Å	binding energy (eV) of bipolarons to acceptor-type defects
Al_{Ti}^{3+}	1.24	−1.88
Cr_{Ti}^{3+}	1.23	−0.61
Mg_{Ti}^{2+}	1.24	−1.80
Fe_{Ti}^{2+}	1.22	−0.87
V_{Ti}	1.19	−1.63
Li_{Ba}^{+}	1.21	−0.42
Na_{Ba}^{+}	1.23	+0.03
K_{Ba}^{+}	2.70	+0.80
V_{Ba}	2.57	+0.94

Bipolarons may be interpreted as a tightly bound molecules with fixed bond length around 1.2 Å. This calculated bond length is in qualitative agreement with the known bond length ~1.4 Å of isoelectronic free F_2 molecules.[6] Three different binding energies can be

distinguished. The first describes the bonding of bipolarons to acceptor-type defects (see table I), whereas the second and third measure the affinity of the first and the second hole, respectively, to an acceptor. Table II shows hole ionization energies (negative binding energies) for a number of acceptor defects. The 1. hole ionization energy corresponds to the dissociation of molecular bipolarons. Resulting from covalency between the O^- ions this energy is in all cases greater than the 2. hole ionization energy (negative-U behaviour). The 2. ionization energy characterizes single hole trapping.

Table II
Hole ionization energies of trapped hole bipolarons in $BaTiO_3$.

acceptor-type defect	1. hole ionization energy (eV)	2. hole ionization energy (eV)
Ti_{Ti}^{4+} (isolated bipolaron)	1.25	0
Al_{Ti}^{3+}	2.27	0.85
Cr_{Ti}^{3+}	1.29	0.57
Mg_{Ti}^{2+}	2.19	0.82
Fe_{Ti}^{2+}	1.70	0.42
Li_{Ba}^{+}	1.59	0.08
Na_{Ba}^{+}	1.16	0.06

The binding of hole bipolarons to Ba-site acceptor-type defects is generally unfavourable, except to small Li ions (however, a binding to sodium ions cannot be fully ruled out on the basis of the present simulations). The trapping of bipolarons at large Ba-site acceptor defects is in particular unfavourable, because a proper formation of molecules with bond lengths around 1.2 Å is inhibited. K^+ ions but also barium vacancies provide corresponding examples (see table I).

The existence of bipolarons is not only based on the additional covalent interaction, lattice relaxation aids their formation as well. This could be shown by simulating two holes located on neighbouring oxygen ions without any covalent interaction. The holes are bound to each other corresponding to an energy gain of 0.2 eV and to a bond length of 2.69 Å which is slightly less than the perfect lattice separation of 2.80 Å.

2.2 *Embedded Cluster Calculations*

The aforementioned shell model based simulations are useful in order to get an overview of the underlying physics. However, further embedded cluster calculations involving the local electronic defect structure are necessary to correctly model the explicit hole-hole interaction as well as to infer the appropriate spin state of hole bipolarons. Preliminary embedded cluster calculations have been performed in order to extend the shell model simulations in the case of Ti-site acceptors. In particular we have considered a Mg^{2+} acceptor impurity cation. The central defect cluster consisting of 19 ions besides the O_2^{2-} bipolaron is described by means of effective core potentials[7] implemented on the outer Ba- and Ti-cations and by a MO-ansatz for the central acceptor-oxygen complex MgO_6. Gaussian-type basis functions with split-valence (SV) quality have been employed for magnesium[8] and its oxygen ligands;[9] the basis set was further augmented by polarizing *d*-functions. The *ab initio* level of these calculations corresponds to the unrestricted Hartree-Fock (UHF) approximation. In addition, preliminary simulations have been performed including electronic correlation contributions. These calculations were restricted to single and double electronic excitations (SDCI) out of the oxygen 2*p* valence

shell with reference to the respective HF-states. On the basis of perturbation theory the 10,000 energetically most important configurations have been chosen for a diagonalization of the CI-Hamiltonian-matrix.

Two geometrical hole-acceptor configurations have been considered: the bipolaron with two holes on neighbouring oxygen ions trapped at a magnesium impurity and a linear complex O^--Mg^{2+}_{Ti}-O^-. These defects have been investigated under various conditions:

- Hartree-Fock (HF) treatment of the quantum defect cluster employing a rigid crystal lattice with ions on their perfect lattice positions. Only the O^- partners were allowed to relax.
- HF description of the cluster including complete lattice relaxation.
- The equilibrium lattice of the previous step has been used in further investigations using a SDCI description of the central defect cluster.

Figure 1 displays the energies of the singlet and triplet state of the hole bipolaron complex employing full lattice relaxation and the HF-approximation.

The bipolaron bond length corresponds to 1.4 Å, thus being in good agreement with our shell model based simulations. The most favourable electronic state is a diamagnetic singlet state. Increasing the bond length drops the triplet state below the singlet state. The reason for this behaviour, which deviates from corrresponding results for isolated F_2 molecules, is based on electronic interactions between the O^- ions and crystal ions in the neighbourhood. In particular the triplet-bipolaron takes advantage of this interaction because of its antisymmetrical molecular charge distribution. In any case, the equilibrium singlet state is 2 eV below the lowest triplet state. However, within the HF-approximation the linear (triplet-) configuration is ~ 0.5 eV more favourable than the alternative bipolaron. Thus, in the HF-approximation the simulated bipolaron is only metastable. Our results indicate that neither lattice relaxation nor electronic correlation alone is sufficient in order to favour the bipolaron state against the linear hole-acceptor configuration. It is found that both mechanisms must be operative in order to obtain a bipolaron-type groundstate. In this case the singlet state of the bipolaron is 1.65 eV lower in energy than the linear complex in its most favourable triplet state. Anticipating at this stage the shell model based result that the linear configuration is only slightly bound, the above quoted 1.65 eV roughly measure the bipolaron dissociation energy. From Table II a corrresponding shell-model-value of 2.2 eV is inferred, which is in satisfactory agreement with this estimate. Future work aims to rexamine the energy dependence of the respective bipolaron states as a function of the O^--O^- separation by consistent inclusion of electronic correlation.

In summary, our present calculations support Photo-ESR based speculations favouring diamagnetic hole bipolarons in $BaTiO_3$. Lattice relaxation as well as electronic correlation are important in order to stabilize these defect species.

This work is supported by the DFG through SFB 225.

REFERENCES

1. E. Possenriede, P. Jacobs, H. Kröe, O. F. Schirmer, *Appl. Phys.* **A55**, 73 (1992).
2. B. G. Dick and A. W. Overhauser, *Phys. Rev.* **112** (1958) 90.
3. C. R. A. Catlow and W. C. Mackrodt (eds) *Computer Simulation of Solids*, Lecture Notes in Physics, Vol 166, (Springer Verlag, Berlin, 1982).
4. G. V. Lewis and C. R. A. Catlow, *J. Phys. Chem. Solids* **47** (1986) 89.
5. P. W. Jacobs and E. A. Kotomin, *J. Phys.: Condens. Matter* **4**, 7531 (1992).
6. G. Herzberg, *Molecular spectra and molecular structure*, Vol. I, (Van Nostrand Reinhold Company, New

York, Cincinnati, Toronto, London, Melbourne 1950).
7. W. R. Hay and P. J. Wadt, *J. Chem. Phys.* **82**, 270–310 (1985).
8. M. S. Gordon *et al.*, *J. Am. Chem. Soc.* **104**, 2797 (1982).
9. T. H. Dunning and P. J. Hay, in *Methods of Electronic Structure Theory*, H. F. Schaefer (III) (Ed.) (Plenum Press, New York 1977), Chap. 1, pp. 1–27.

Radiation Effects and Defects in Solids, 1995, Vol. 134, pp. 171–174
Reprints available directly from the publisher
Photocopying permitted by license only

© 1995 OPA (Overseas Publishers Association)
Amsterdam B.V. Published under license by
Gordon and Breach Science Publishers SA
Printed in Malaysia

ATOMISTIC LATTICE SIMULATIONS OF DOPANT MIGRATION IN PLANAR-AND HELICAL-CHAIN CONDUCTIVE POLYMERS

J. CORISH, D. A. MORTON-BLAKE, KALYANI VELURI and F. BÉNIÈRE*

*Chemistry Dept., Trinity College, Dublin 2, Ireland; *Laboratoire de Sciences des Matériaux, Université de Rennes, Rennes, France*

The lowest-energy lattices of polypyrrole and polythiophene in their planar conformations derived by atomistic lattice simulation agree with the results of diffraction studies on undoped polythiophene. When doped, the structures become layer lattices, the dopant ions occupying intercalation sites. A defect-lattice method to investigate the migration of Cl^- and BF_4^- gives energy barriers 0.5–2.3 eV. The stabilisation of single chains and lattices of helical polythiophene requires olefinic character in the inter-ring bond. The 'interleaving' of the strands of adjacent chains requires the dopant ions to occupy sites in the axial region of the helical cavity, along which their migration is expected to be rapid.

1 METHOD OF CALCULATION

The simulation method embodied in the lattice simulation codes of **CASCADE**[1] uses a force field of *atomistic potentials* to calculate the lattice energy of a proposed structure. Following the 'two-region strategy' method of treating defect lattices,[2] the motion of a dopant ion is considered by monitoring the **defect energy** during an ion's migration between two vacant sites. At all stages of the migration the lattice is permitted to relax around the defect.

2 RESULTS

2.1 *Perfect Lattice' Simulations*[3]

The energy minimisation procedure in **CASCADE** was used to optimise various proposed structures of the undoped lattices. For polythiophene the *two* lowest-energy structures agree with results of two different diffraction studies,[4,5] suggesting bimorphism. Doping polypyrrole and polythiophene with Cl^-, ClO_4^- or BF_4^- changes the structures by forming **layer lattices**, the dopant ions occupying intercalation-like sites between the chains.

2.2 *Dopant-Ion Migration*

The energy profile (Figure 1) shows that during its 'jump' between a pair of equivalent vacancies in polypyrrole, the ion encounters a broad barrier, defining an activation energy of 2.2 eV. The shape is that of a shallow crater, the crests of which originate in the passage of the BF_4^- ion between pairs of H atoms on different chains.

For the migration of the ion Cl^- in polythiophene, the energy profile is a smooth barrier (0.9 eV) associated with the entry of the ion into a high-energy 'cavity region' between the chains. In polypyrrole, the centre of a similar 'cavity region' constitutes a secondary stable site for the ion, resulting in a double barrier with overall energy 2.3 eV (Figure 2).

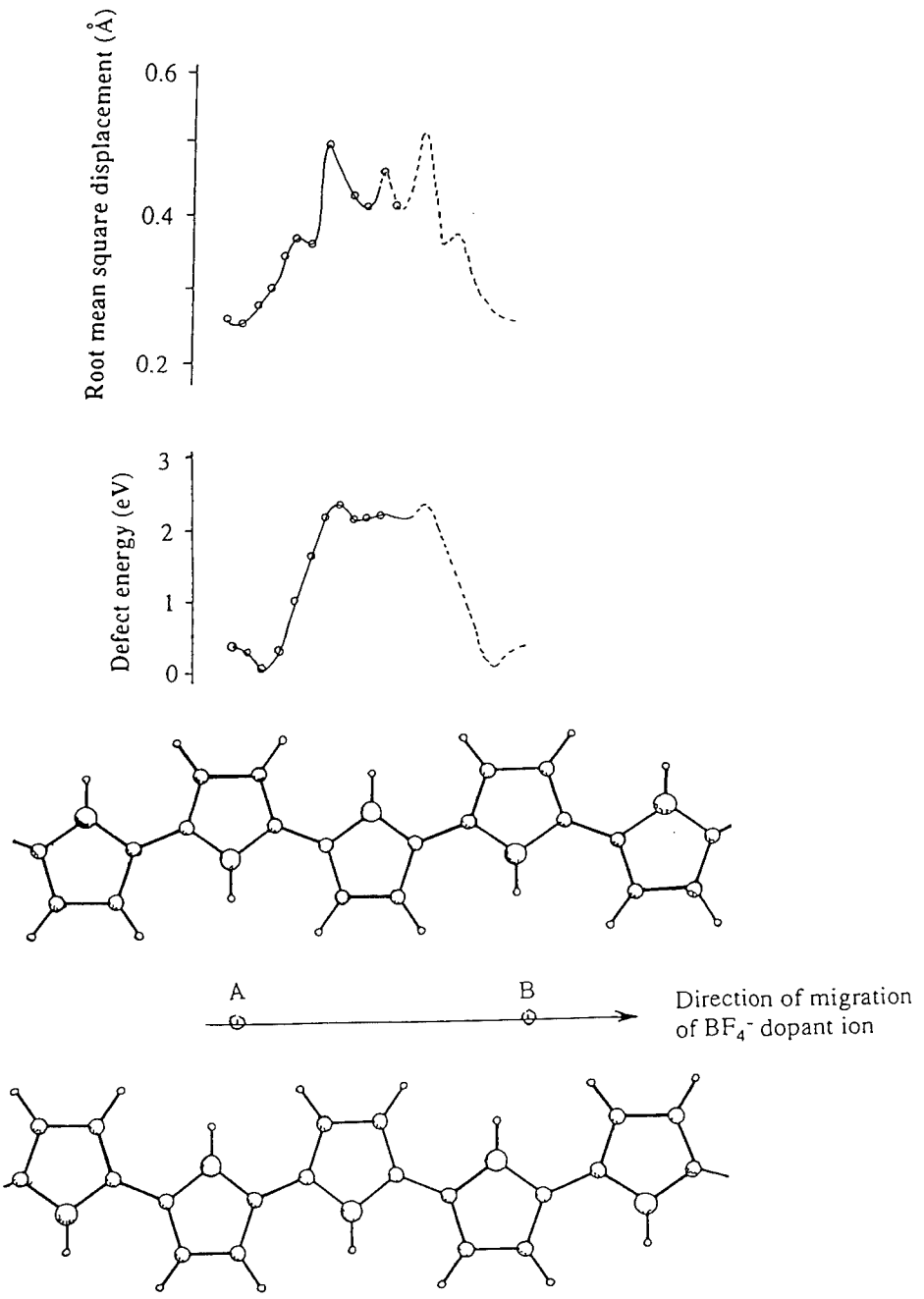

FIGURE 1 Stages in the migration of BF_4^- between two vacancy sites showing (*upper curve*) the extent of the distortion of the host lattice and (*lower curve*) the energy profile for the jump. The position of the BF_4^- ion between adjacent chains is illustrated at the bottom of the Figure, and shows that the energy barrier is caused by the passage of the dopant past a pair of $-CH-CH-$ segments on both chains.

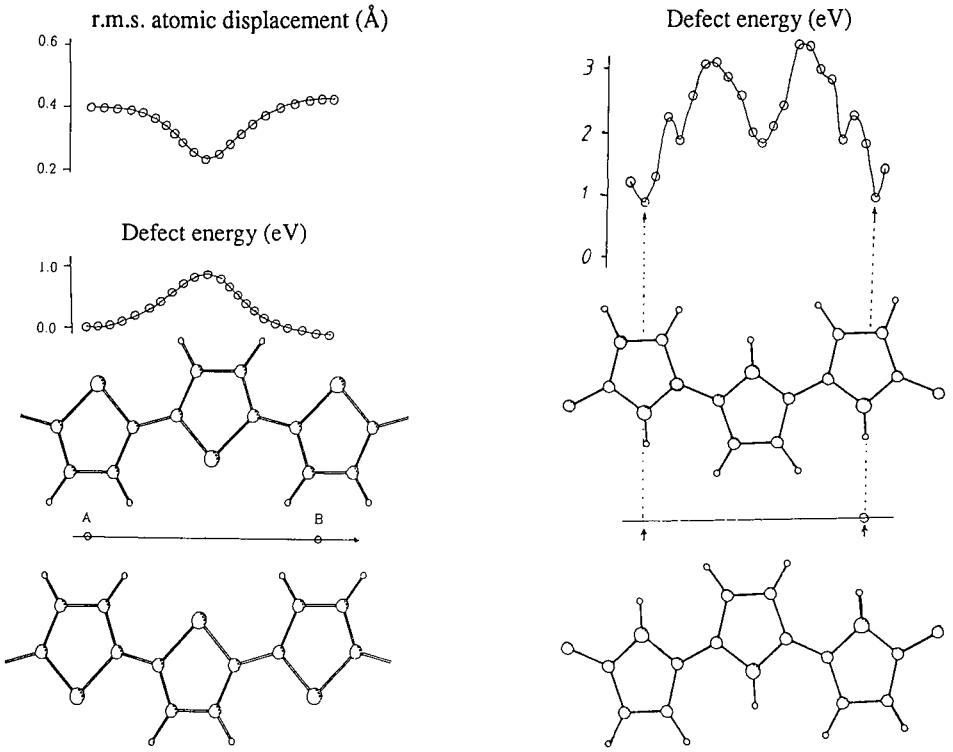

FIGURE 2 The energy profile for the migration of the Cl^- dopant ion between two vacency sites in (*left*) polythiophene and (*right*) polypyrrole. The Cl^- ion experiences the 'cavity region' of polythiophene as one of high energy, but the imino H atoms on polypyrrole present a narrow energy well to the ion at the centre of the corresponding region.

2.3 *Helical Polythiophene*

Unless the inter-ring bond has very low π character, the lattice energy shows that a *single chain* of polythiophene has two stable states.[6] In its lowest energy state the polymer assumes an all-*anti* conformation, slightly higher than which is a nearly all-*syn* helix. The interconversion of these structures is hindered by an energy barrier of $\sim$ 100 kJ (mol ring)$^{-1}$. A full relaxation of the chain produced a structure with a pitch of 7.2 Å and a width of 17.9 Å. The values from scanning tunnelling microscopy are respectively 8 and 18 Å.[7]

The *3-dimensional* lattice was taken to possess the hexagonal symmetry found by the diffraction studies of Garnier *et al.*[8] on polythiophene doped with $CF_3SO_3^-$, in which each chain is surrounded by six identical chains. Figure 3, which presents the structures of the unit cell and of the chains when the lattice is allowed to relax fully, shows that neighbouring chains partially 'interleave'. An important consequence of this is that there is space for the dopant ions only in the helical cavity of the chains, which has a diameter of 11 Å.

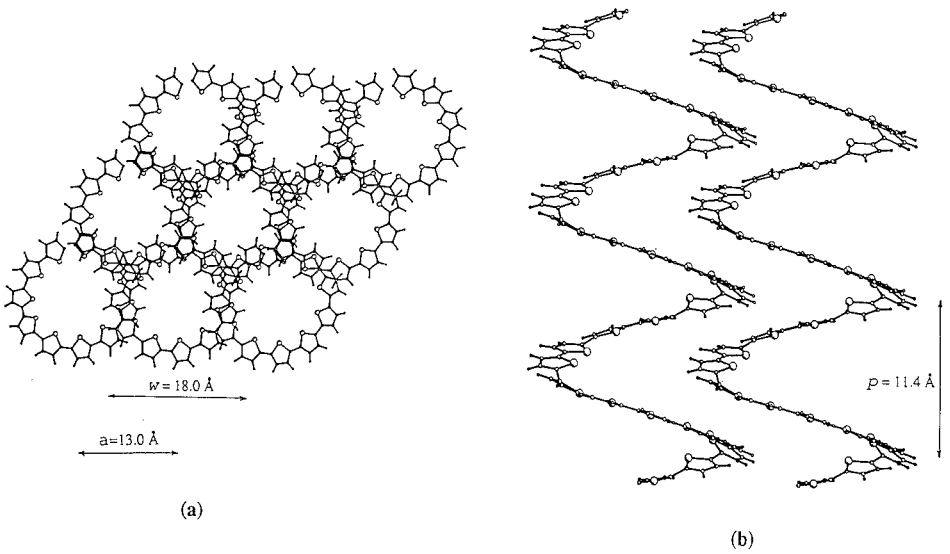

(a) (b)

FIGURE 3 A hexagonal lattice of helical chains of polythiophene, viewed (*a*) along and (*b*) normal to their axes. Notice the partial 'interleaving' of the helices.

2.4 *Dopant Mobility in Helical Polythiophene*

Results of a series of calculations of the relative energies of structures in which the BF_4^- ion was placed at various points in channels within the helical chains reveal an *almost constant energy path through the channel.* However, rather than following a linear path, the BF_4^- ion is at times diverted by 1.5 Å from the channel axis.

The almost featureless lowest-energy pathway for the BF_4^- ion indicates a high mobility of the dopant ion in the channels formed by the helical polymer.

REFERENCES

1. M. Leslie, Daresbury Laboratory Report DL/SCI/TMB36T (1984); CASCADE Program release MK12 (4-body version), February 1989.
2. N. F. Mott and M. J. Littleton, *Trans. Faraday Soc.* **34**, 485 (1938); A. B. Lidiard and M. J. Norgett, *Computational Solid State Physics*, Eds. F. Herman, N. W. Dalton and T. R. Koehler (Plenum, New York 1972), p. 385.
3. For full details see J. Corish, D. A. Morton-Blake, K. Veluri and F. Bénière, *J. Mol. Struct. (Theochem)*, **283**, 121 (1993).
4. Z. Mo, K. -B. Lee, Y. B. Moon, M. Kobayashi, A. J. Heeger and F. Wudl, *Macromolecules* **18**, 1972 (1985).
5. S. Brückner and W. Porzio, *Makromol. Chem.* **189**, 961 (1988).
6. J. Corish, D. A. Morton-Blake and F. Bénière Molecular Simulation (in press).
7. R. Yang, D. F. Evans, L. Christensen and W. A. Hendrickson, *J. Phys. Chem.* **94**, 6117 (1990).
8. F. Garnier, G. Tourillon, J. Y. Barraud and H. Dexpert, *J. Mat. Science* **20**, 2687 (1985); G. Tourillon and F. Garnier, *Mol. Cryst. Liq. Cryst.* **118**, 221 (1985).

Radiation Effects and Defects in Solids, 1995, Vol. 134, pp.175–177
Reprints available directly from the publisher
Photocopying permitted by license only

© 1995 OPA (Overseas Publishers Association)
Amsterdam B.V. Published under license by
Gordon and Breach Science Publishers SA
Printed in Malaysia

OPTICAL PROPERTIES OF Cr^{3+} AND Ni^{2+} IONS IN MgO, $LiNbO_3$ AND LMA

F. MICHEL-CALENDINI

Laboratoire de Physique Université de Bourgogne, BP 138, Batiment Mirande, 21004 DIJON CEDEX (France)

(Received July 1, 1994)

The electronic structures of Co^{2+} and Ni^{2+} ions are obtained by the molecular orbital LCGTO-LSD method. Electrostatic matrix calculations are performed for d^3 and d^8 configurations. Theoretical optical data are discussed in function of the impurity site location in the crystal cell.

Key words: Electronic structures, crystal field spectra, 3d ions.

1 INTRODUCTION

It is well known the 3d ions doping oxides may create local distortions in the crystal host; in particular, different substitutional sites have been observed in $LaMgA1_{11}O_{19}$ (LMA) or $LiNbO_3$ crystals from optical and/or EPR experiments. The aim of the present work is to obtain the ligand field multiplets of Cr^{3+} and Ni^{2+} ions in these oxides from a cluster approach. These calculations, based on the local spin density theory (LSD),[1] are carried out with the LCGTO deMon code.[2] Electrostatic matrix calculations are performed for d^3 and d^8 configurations in cubic and axially distorted crystal fields (CF) with parameters drawn from the eigenvalues and eigenvectors relevant to 3d levels in the molecular orbital diagrams as it was described earlier for some d^3 and d^5 ions.[3,4] The theoretical ligand-field multiplets are compared to the optical emission/absorption spectra of the oxides doped either with Ni^{2+} [5,6,7] or Cr^{3+} [8,9] .This enables one to check the validity of the model on the well identified MgO case and to discuss the possible subtitutional sites of the 3d ions in $LiNbO_3$ and LMA crystals.

2 PRINCIPLES OF TERM ENERGY CALCULATIONS

Molecular orbital calculations are carried out on MO_6 clusters involving the metal atom M(Ni or Cr) and the oxygen octahedron surrounding the substituted site. The cluster symmetries are: O_h (MgO), D_{3d}(LMA: 2a site), C_{3v}(LMA: 4f site, $LiNbO_3$: Li or Nb sites). The eventual local structure changes due to doping are neglected, excepted for $LiNbO_3$. In this latter, the relaxed positions of 3d ions along the c axis from the initial Li or Nb positions predicted by LGGTO calculations[11] are considered in the present work. A scheme of 3d monoelectronic eigenvalues implied in crystal-field calculations is shown in Figure 1. In a trigonally distorted crystal field V_t, the octahedral t_{2g} and e_g levels are scrambled according to [10]:

$$<e_g,2e|V_t|e_g,2e> = 6Dq + 7/3D\tau \quad <t_{2g}, le|V_t|t_{2g}, le> = -4Dq + D\sigma+2/3D\tau$$
$$<t_{2g}, all|Vt|t_{2g}, a_1> = -4Dq - 2D\sigma - 6D\tau \quad <t_{2g}, le|V_t|e_g, 2e> = \sqrt{2}D\sigma-5\sqrt{2}/3D\tau$$

The CF parameters Dq, $D\sigma$ and $D\tau$ are calculated from total energy differences between ground (GS) and excited (ES) configurations : $a_{1\uparrow}^1 1e_\uparrow^2 2e_\uparrow^2 a_{1\downarrow}^1 1e_\downarrow^2$(GS) and

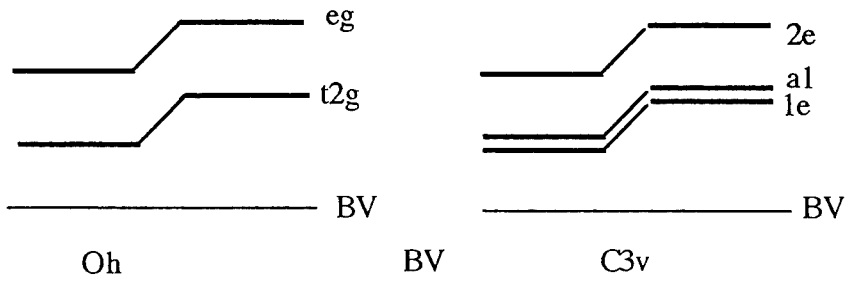

FIGURE 1 Monoelectronic 3d eigenvalues (in O_h and C_{3v} symmetries; VB in the valence band edge of the oxide.

TABLE I
Optical data (cm^{-1}) for Ni^{2+} in MgO, LMA and $LiNbO_3$ (a: this work).

Crystal	MgO[a]	MgO[8]	LMA(4f)[a]	LMA[5]	$LiNgO_3$(Li)[a]	$LiNbO_3$[4]
CF parameters						
Dq	755	831	1 131	1 010	862	815
$D\sigma$	0	0	0	0	250	360
$D\tau$		0			−60	−30
B	799	850	799	795	779	779
C	3198	3 435	3 198	3 100	3 198	3 198
ζ3d	644	650	644		644	
Optical spectra						
$^3T_2$	7 238	8 001	10 806	7 700	8 109(π)	7 810(π)
	7 997	8 751	11 720	10 000	8 592(σ)	7 970(σ)
^1E	11 902	13 005	12 696		12 188	12 120
$^3T_1$	11 775	12 981	17 078	18 182	14 799(π)	13 330(π)
	13 755	14 907	18 310		13 622(σ)	12 990(σ)
$^1T_2$	19 302	21 099	23 403		20 749(π)	19 420(π)
					20 402(σ)	20 450(σ)
$^1A_1$	20 301		21 458	23 809	19 775	20 620
$^3T_1$	22 049	23 882	28 182	27 027	22 805(π)	22 220(π)
	22 661	24 486	28 449		20 072(σ)	23 260(σ)

$a_{1\uparrow}{}^1 1e_\uparrow{}^2 2e_\uparrow{}^2 1e_\downarrow{}^2 2e_\downarrow{}^1$(ES) for Ni^{2+};$a_{1\uparrow}{}^1 1e_\uparrow{}^2$(GS) and $1e_\uparrow{}^2 2e_\uparrow{}^1$(ES) for Cr^{3+}. A second relation is given by the eigenvalue difference between 1e and a_1 down (Ni^{2+}) or up (Cr^{3+}) spin levels. A covalency degree of 0.997 between 1e and 2e orbitals provides the third equation. Spin orbit coupling constant s_{3d} are calculated from relativistic MS LSD calculations on CrO_6^{-9} and NiO_6^{-10} clusters; the B and C parameters are calculated from MS LSD results for Cr^{3+} and taken from reference 3 for Ni^{2+}. Electrostatic matrix calculations are performed in the intermediate CF scheme.

3 RESULTS AND DISCUSSIONS

Calculated term energies are reported in table 1 for Ni^{2+} and table 2 for Cr^{3+}. The extreme values are reported for each band. Available experimental results are given too. For Ni^{2+}, it exist a quite good agreement between LCGTO and experimental terms. For the two sites (cubic 2a and antiprism 4f) of LMA, the Dq values are very close and only terms relevant to the 4f site are supplied. Ni^{2+} appears to substitute the Li site with a relaxation along the c axis in $LiNbO_3$. There exists a relative agreement between calculated and observed

TABLE II
Optical data (cm^{-1}) for Cr^{3+} in MgO, LMA, $LiNbO_3$. (B = 800 cm^{-1}, C = 2986 cm^{-1}, ζ_{3d} = 300cm^{-1}, $^4A_2$ is the reference level, a:this work).

Crystal	MgO[a]	LMA(4f)[a]	LMA(2a)[a]	LMA[8]	$LiNbO_3$(Nb)[a]	$LiNbO_3$(Li)[a]	$LiNbO_3$[9]
Parameter sets							
Dq	1297	1744	1863		1878	1145	1530
$D\sigma$	0	293	269		453	375	
$D\tau$	0	–68	–94		–183	–55	
Optical spectra							
$^4T_2$	12856	17386	18156	17094	18009	11007	15314
	13039	17732	18411		18250	11441	
^2E	14634	14687	14727	14407(4f)	14677	14460	13822
		14702	14727	14512(2a)	14690	14504	13780
$^2T_1$	15304	15335	15353	14870	15232	15021	
	15440	15603	15624		15666	15418	
$^4T_1$	19693	25054	25833	23923	25434	17295	20853
	20037	25697	26612		26891	18306	

absorption bands in LMA:Cr^{3+}, and the 3d ion does not seem to perturb appreciably the local structure around the 2a or 4f sites. The case of $LiNbO_3$:Cr^{3+} is less obvious. Indeed, three Cr sites have been evidenced by their R lines $LiNbO_3$:Cr^{3+} and $LiNbO_3$:Mg:Cr^{3+}, ascribed to Nb, Li and a new site (see ref. 9 and references herein). The present calculations at relaxed Nb or Li sites do not give a correct agreement between observed and calculated spectra. Dq CF strength is overestimated for Nb site while the Li one is underestimated. Taking into account that LCGTO calculations appear reliable in the other cases, it is think that the chromium ions doping $LiNbO_3$, affect the immediate oxygen octahedron, which contracts in the Nb neighbourhood and dilates in the Li case due to charge effects.

REFERENCES

1. D. R. Salahub, in *Applied Quantum Chemistry*, ed by V. H. Smith, H. F. Schaefer and K. Morokuma (Reidel, Dordrecht, 1986) p. 185.
2. R. G. Parr, and W. Yang, *Density functional theory of atoms and Molecules*, Oxford University Press, New York (1989).
3. F. Michel-Calendini and C. Daul, *Ferroelectrics* **125**, 277 (1992).
4. K. Bellafrouh, C. Daul and F. Michel-Calendini, *New Journal of Chem*, **16**, 1123 (1992).
5. L. Arizmendi, J. M. Cabrera and F. Agullo-Lopez, *Ferroelectrics*, **26**, 823 (1980).
6. T. Benyattou, R. Moncorge, J. M. Bretteau and F. Auzel, *Crys. Latt. Def. and Amorph. Mat.*, **15**, 157 (1987).
7. R. Moncorge and T. Benyattou, *Phys. Rev.* **B37**, 9186 (1988).
8. C. Borel, C. Wyon, J. J. Aubert, H. Manaa and R. Moncorge, *J. of Luminescene,* **55**, *95* (1993).
9. E. Camarillo, J. Tocho, I. Vergara, E. Diegez, J. Garcia-Sole and F. Jaque, *Phys. Rev.* **B45**, 4600 (1992).
10. C. J. Ballhausen, *Introduction to ligand field theory*, MacGraw Hill, New-York (1956).
11. F. Michel-Calendini and H. Chermette, *Ferroelectrics*, to appear.

Radiation Effects and Defects in Solids, 1995, Vol. 134, pp. 179–183
Reprints available directly from the publisher
Photocopying permitted by license only

© 1995 OPA (Overseas Publishers Association)
Amsterdam B.V. Published under license by
Gordon and Breach Science Publishers SA
Printed in Malaysia

SIMULATION OF OXYGEN VACANCIES AT THE Si–SiO_2 INTERFACE

S. CARNIATO, G. BOUREAU* and J. HARDING**

**Laboratoire de Chimie Physique Université Pierre et Marie Curie (Paris VI) 75231 Paris Cédex 05 France; **Theretical Studies Dept AEA Industrial Technology Harwell Laboratory Didcot Oxon OXII ORA United Kingdom*

(Received July 1, 1994)

The Si(001)/SiO_2 (tridymite) interface has been simulated using a Monte-Carlo method. It has been shown that in this way reasonable values of angles and interatomic distances are obtained. The oxygen defect formation energy dependence with different vacancy sites has been studied. Because of coulombic interactions, the formation of vacancies is much easier in the vicinity of the interface.

Key words: Monte-Carlo, interface, silicon, oxidation, vacancy.

1 INTRODUCTION.

The Si/SiO_2 interface has been widely studied for several years because of its rôle in MOS technology.[1] We have recently built a model[2] able to reproduce the essential features of the Si(100)/SiO_2 interface. Let the major assumptions of the model be recalled:

—Following the analysis of Ourmazd *et al.*[3] and of Ohdomari et al[4], a tridymite layer has been considered to describe the silica side.

—A classical simulation of the Si(001)/SiO_2 interface using a monte carlo procedure has been used.

—Different semi-empirical potentials have been used: The many body potential proposed by Tersoff[5] which has been fitted to a large number of silicon polytypes and adjusted to reproduce the elastic properties of silicon is probably the best potential to use for Si. This potential has advantages for the problem here, since the silicon coordination (pentagonal ring in the initial step) at the interface is unlikely to be perfect throughout. Because the interfacial stresses, the choice of the Strixrude[6] covalent potential to simulate the interactions crossing the Si/SiO_2 interface seems reasonable. It behaves well under pressure and predicts the quartz/coesite transition. This potential has another interesting feature: It exits in two versions: One without electrostatic interaction and one with explicit electrostatic interactions. Of course, the parameters are not the same. In this way, it possible to use this potential for thin interface regions, which would be more problematic for more sophisticated potentials incorporating electrostatic interactions.

—1800 atoms have been allowed to relax.

—An infinite sample of silicon has been considered but only three ranges of SiO_2 tetrahedron have been considered. In other words, we consider a free surface of silica with H atoms to keep the sample electrically neutral.

The aim of the present work is to compare results concerning the defect formation energy of various oxygen vacancy sites in silica near the interface. It has been known for some time[7] that these vacancies play an essential rôle in the oxidation of silicon. Such studies may be found for pure silica (see for instance the study of Sulimov[8] *et al.* but are scarce for the interface.

2 THEORETICAL BACKGROUND

The structural model draws schematically in Figure 1 has been proposed by Ourmazd *et al.*[4] Lattice spacings of tridymite are compressed to match those of the Si substrate. The orientational relationship between the Si substrate and the tridymite satisfied the following

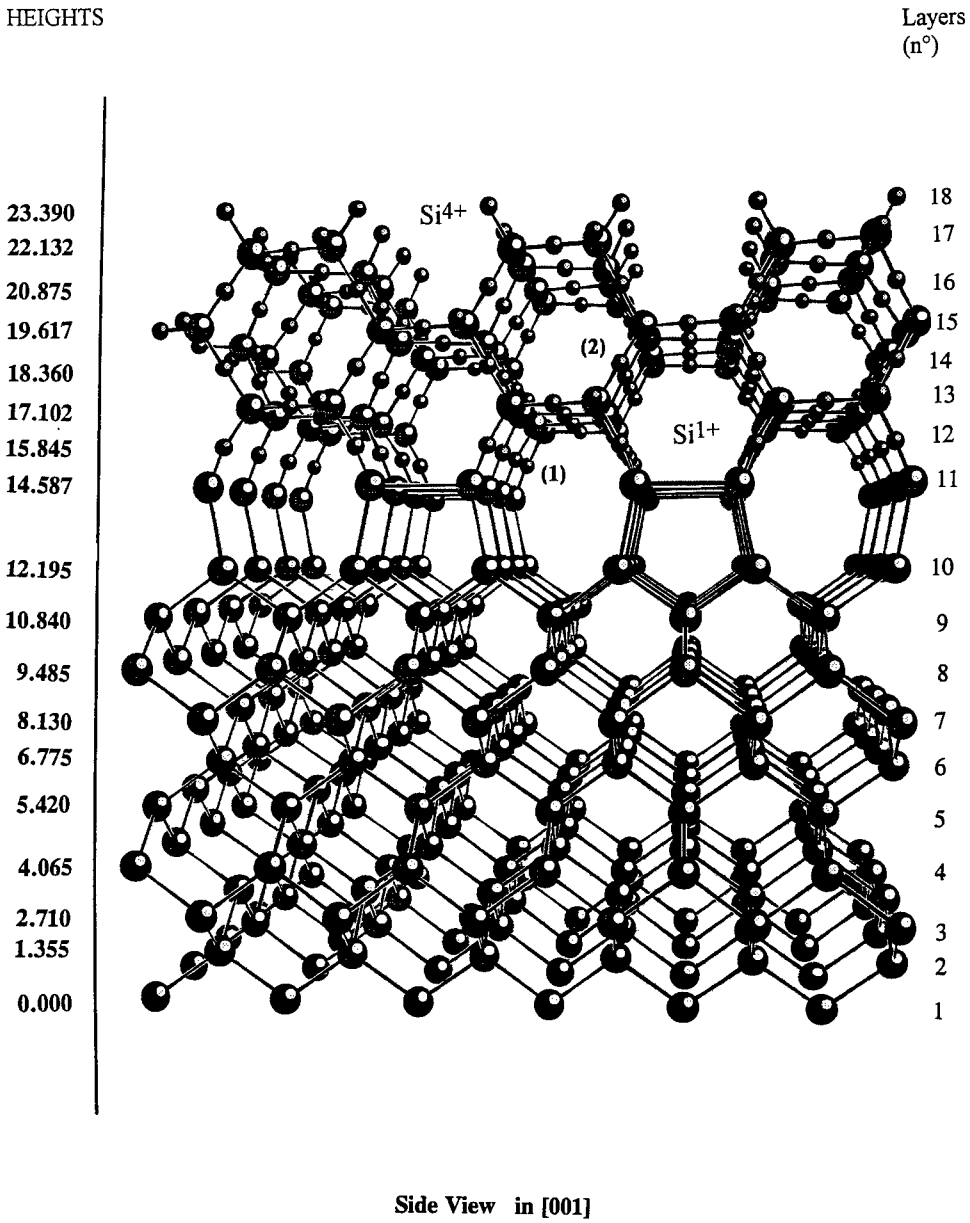

FIGURE 1 Atomic arrangement in the epitaxial tridymite grown over the (001) Si before relaxation: side view. Large and small full circles represent Si and O atoms, respectively. Numbers on the left (right) vertical axis denote heights (Å) from the bottom of the Si substrate. Layers are numbered on the right vertical axis.

conditions: the tridimyte lies with the [001] lattice vector parallel to the interface and the [110] direction in the silicon and the [010] direction parallel to the [001] direction of the silicon. The Si surface lattice vector 1/2[110] is 3.8 Å while the parallel (compressed) tridymite lattice vector [001] is 7.6 Å in length. Each substrate silicon atom at the interface bonds to one oxygen atom presented by the tridymite, and half the interfacial Si dangling bonds are considered to be saturated by Si–Si dimerization. Five membered silicon rings are so needed to connect the two phases because of the topology of the coordination, which help to spread the stress over a wider volume. In its simplest form, this atomically abrupt interface model discussed so far give only Si^+ as intermediate oxidation states. Only one of the two broken bonds of the Si surface atom is connected to SiO_2. The other is presumed either to pair up with a neighbouring Si atom like in a 2*1 structure, like on a clean (100) surface, or also be saturated by forming Si–O–Si bridges.

The cell used in this simulation is five lattice parameters (38.83 Å) long in [100] and [010] directions of the silicon, which allows to handle 100 atoms per plane. The sample was made semi-infinite in the [100] and [010] directions by imposing periodic boundary conditions. Different radius cutoff have been used: Following Tersoff[5], it has been fixed at 3.0 Å for the silicon bulk, 3.50 Å for the Si–Si distance in silica, 1.85Å for Si–O (the largest distance found in the literature), 2.90 Å for O–O. The coulomb cutoff sum for each ion is truncated outside a sphere of side equal to half box length and centered on the ion. For spherical truncation, the truncated potential is given by

$$u_{ij}(r) = u_{ij}(r) - u_{ij}(R_{cut}) \text{ for } r < R_{cut}$$
$$= 0 \qquad \text{for } r > R_{cut}$$

That is the potential is truncated to zero beyond a certain cutoff distance R_{cut} and is shifted for distances shorter than R_{cut}. Then, coulomb energy is decreased uniformely so that coulomb energy is equal to zero at cutoff distance, to avoid a charge collapse around the spherical cutoff. This procedure has been shown to be acceptable as long as large enough cells are used and if electrostatic interactions are not too large[9]. The coulombic charges on Si atoms are directly determined from the oxidation state (0 to 4+), or in other words, to the number of oxygen atoms bonding to a Si atom. One keep in mind that these symbols refer to the oxidation state, not the actual charge transfer, because SiO_2 is not completely ionic system. For oxygen atoms, eventuality of one threefold overcoordinated oxygen O_3 is suggested, and so the charge 2+ is equally distributed over the Si neighbours, by preserving the charge neutrality of the system.

In order to ensure equilibrium, simulation has been performed at 2000 Kelvin. The amplitude of the displacement is chosen such that the ratio of accepted moves is about 40%. In order to ensure that equilibrium 400000 iteration steps have been performed.

At the end or the simulation, the system has been slowly cooled down up to 1600 K. An oxygen atom was removed at two different types of oxygen sites and formation energy defect have been calculated.

3 RESULTS AND DISCUSSION

In Table I we have reported the altitudes of all the layers in the initial configuration such as defined in the previous section before allowing random displacements but after a collective motion of the planes aimed to get the 109.47° angle for SiO_2 tetrahedrons. This is obtained by a compression of silica. The 'initial' atomic configuration in the near interface region has been compared with the values of the 'frozen' model. The average d(Si–O) in silica is about 1.38 Å, i. e. much lower than that for crystalline SiO_2 which is about 1.62 Å. So it is not unexpected that these distances increase strongly during the simulation.

TABLE I
Altitudes, average nearest Si–O (O–Si) distances and distribution of Si (0) atoms in terms of the number of their neighbouring oxygen (silicon) atoms before relaxation.

Layer n°	Initial Altitude(Å)	Nearest neighbouring distances (Å)				%Si^0	%Si^1	%Si^2	%Si^3	%Si^4	Angle
		Si–O_1	Si–O_2	Si–O_3	Si–O_4						
10	12.35	3.56	5.06	5.10	5.26	100.0	0.0	0.0	0.0	0.0	—
11	14.78	1.22	3.17	3.30	3.40	0.0	100.0	0.0	0.0	0.0	—
13	17.02	1.38	1.38	1.38	1.48	0.0	0.0	0.0	0.0	100.0	109.47
15	19.27	1.38	1.38	1.38	1.48	0.0	0.0	0.0	0.0	100.0	109.47
17	21.52	1.38	1.38	1.38	1.48	0.0	0.0	0.0	0.0	100.0	109.47
		O–Si_1	O–Si_2	O–Si_3		%O^1	%O^2	%O^3			
12	15.90	1.22	1.38	3.46		0.0	100.0	0.0			159.00
13	17.02	1.42	1.42	3.23		0.0	100.0	0.0			180.00
14	18.15	1.38	1.38	3.40		0.0	100.0	0.0			180.00
15	19.27	1.42	1.42	3.50		0.0	100.0	0.0			180.00
16	20.40	1.38	1.38	3.46		0.0	100.0	0.0			180.00
17	21.52	1.42	1.42	3.50		0.0	100.0	0.0			180.00
18	22.64	1.42	1.42	3.50		100.0	0.0	0.0			—

After 400 000 iteration steps, the average O–Si–O angles are about 109° which is close to that for bulk SiO_2. The presence of the five membered silicon ring configuration after relaxation is direct evidence that the crystallinity in the vicinity of the interface is quite kept. The Si–O–Si angles are about 143° for the O atoms near the interface and 137° for the O atoms near the surface. For the Si–O–Si, the former is close to, but the latter is much smaller to the one generally observed in the bulk of 144°–150°. The rather close calculated value obtained for the Si–O–Si angles near the interface shows the important role of the large amount of free volume in the interfacial region in the unrelaxed structure which acts as a buffer during the simulation and help to relieve the stresses at the interface. Nevertheless this free volume does never disappear. The system manage to reach Si–O distances of about 1.60 Å.

In the vicinity of silicon (site 1 on Figure 1) the vacency formation energy at 1600 Kelvin is only 9 ev while this value is increased to 13 ev for oxygen sites far from silicon (site 2 on Figure 1). This effect is not observed if the purely covalent version of the Stixrude potential is used. This author has found that both potentials provide similar resultsfor phase stability. In the present case, a significant difference has been found for the study of interfaces. In our opinion, the electrostatic interactions play a major rôle in the understanding of defect formation. A study of the rôle of image charges is under way.

It is noteworthy that the Si–Si distance strongly increases (from 3.01 Å to 3.15 Å). This behaviour typical from ionic compounds has been experimentally observed in some non-stoichiometric oxides.[10]

ACKNOWLEDGEMENTS

The authors would like to thank Drs Dufour Rochet and Roulet for many helpful discussions and useful discussions.

REFERENCES

1. See for examples; S. M. Sze, *Physics of Semiconductor Devices, 2nd ed.* (Wiley, New York, 1981); The Physics of SiO_2 and its interfaces, edited by S. T. Pantelides (Pergamon, New York, 1978); The Physics and Chemistry of SiO_2 and the Si–SiO_2 Interface, edited by C. Robert Helms and Bruce E. Deal (Plenum Press, 1988, 1993).
2. S. Carniato, G. Boureau and J. Harding, submitted.
3. A. Ourmadz, D. W. Taylor, J. A. Rentschler and J. Bevk, *Phys. Rev.* Lett. **5**, 213 (1987).
4. I. Ohdomari, H. Akatsu, Y. Yamakoshi and K. Kishimoto, *J. Appl. Phys.* **62**, 3751 (1987).
5. J. Tersoff, Phys. Rev. **B38**, 9902 (1988).
6. L. Stixrude and M. S. T. Bukowinski, *Phys. Chem. Minerals* **16**, 199 (1988).
7. F. J. Himpsel, F. R. McFeely, A. Taieb-Ibrahimi, J. A. Yarmoff and G. Hollinger, *Phys. Rev.* **B38**, 6084 (1988)
8. V. B. Sulimov, C. Pisani, F. Cora and V. O. Sokolov, *Solid State Commun.* **90**, 511 (1994) [see references therein].
9. P. Linse and H. C. Andersen, *J. Chem. Phys.*, **85**, 3027 (1986).
10. B. Touzelin, *J. Nucl. Mat.*, **101**, 92 (1981).

Radiation Effects and Defects in Solids, 1995, Vol. 134, pp. 185–188
Reprints available directly from the publisher
Photocopying permitted by license only

© 1995 OPA (Overseas Publishers Association)
Amsterdam B.V. Published under license by
Gordon and Breach Science Publishers SA
Printed in Malaysia

WHY IS 10Dq SO USEFUL FOR MEASURING CHANGES OF THE IMPURITY-LIGAND DISTANCE?

M. T. BARRIUSO,‡ J. A. ARAMBURU* and M. MORENO*

**DCITTYM. Facultad de Ciencias. Universidad de Cantabria. 39005 Santander, Spain;*
‡Dpto. Física Moderna. Facultad de Ciencias. Universidad de Cantabria. 39005 Santander, Spain

The microscopic origin of the strong dependence displayed by the cubic field splitting parameter, 10Dq, on the metal-ligand distance in transition metal complexes is explored within a realistic molecular orbital framework. Taking as a guide the case of the $CrF_6^{3-}O_h$ complex it is shown that though the admixture of $2s(F^-)$ orbitals in the antibonding eg $*(\sim 3z^2 - r^2; x^2 - y^2)$ orbital is very small $[(N_e\lambda_s)^2 \cong 5\%]$ it is the main responsible of the law $10Dq \propto R^{-n}$ with n close to five. By contrast the admixture of $2p(F^-)$ orbitals though more important $[(N_e\lambda_{p\sigma})^2 \cong 16\%]$ is shown to be no relevant as regards the R dependence of 10Dq. Thus this analysis demonstrates that the R dependence of 10Dq is ultimately related to that displayed by the isotropic superhyperfine constant for O_h complexes with unpaired σ-electrons.

Key words: Impurity levels; Ligand field; CrF_6^{3-}; Xα method; Extended Hückel method.

1 INTRODUCTION

The cubic field splitting parameter, 10Dq, is a fundamental quantity for understanding the optical properties associated to d-impurities placed in insulator lattices. Apart from determining the number and positions of the so called $d \rightarrow d$ transitions it has been shown that 10Dq is very sensitive to changes of the metal-ligand distance, R, 10Dq being proportional to R^{-n} where n is close to five.[1–6] This important property has been used to measure the variations of the metal-ligand distance R induced by hydrostatic or chemical pressures applied upon the transition metal complex embedded in a host lattice.[2] Furthermore, the dependence of 10Dq upon R greatly determines the Huang-Rhys factor $S(a_{1g})$ and the corresponding contribution to the Stokes shift [called $\Delta E_s(a_{1g})$] associated to the symmetric mode of the complex.

Having in mind all these facts the microscopic origin of the significant dependence of 10Dq upon R appears as an attractive point deserving investigation. In fact, though the well known crystal-field scheme gives $n = 5$ this has to be viewed as a fortuitous circumstance because crystal-field theory produces 10Dq values much smaller than experimental ones.

Within a Molecular Orbital (MO) description[7] of the MX_6 complex (M = d − ion, X = ligand) 10Dq is related to the *different chemical bonding* existing for $e_g^*(\sim x^2 - y^2; 3z^2 - r^2)$ and $t_{2g}^*(\sim xy; xz; yz)$ electrons. To be more specific, the wavefunctions for the antibonding $|e_g^*>$ and $|t_{2g}^*>$ orbitals can be briefly written as

$$\begin{aligned} |e_g^* > &= N_e\{|d(e_g) > -\lambda_{p\sigma}|\chi_{p\sigma} > -\lambda_s|\chi_s >\} \\ |t_{2g}^* > &= N_t\{|d(t_{2g}) > -\lambda_{p\pi}|\chi_{p\pi} >\} \end{aligned} \tag{1}$$

Here $|\chi_{p\sigma}>$ and $|\chi_s>$ are suitable LCAOs involving the $n_L p_\sigma$ and $n_L s$ valence orbitals of ligands. In the case of $|t_{2g}^*>$ an d-orbital like $|\, d(xy) >$ cannot be mixed with any LCAO involving $n_L s$ orbitals of ligands. Therefore, within this view 10Dq is related to the

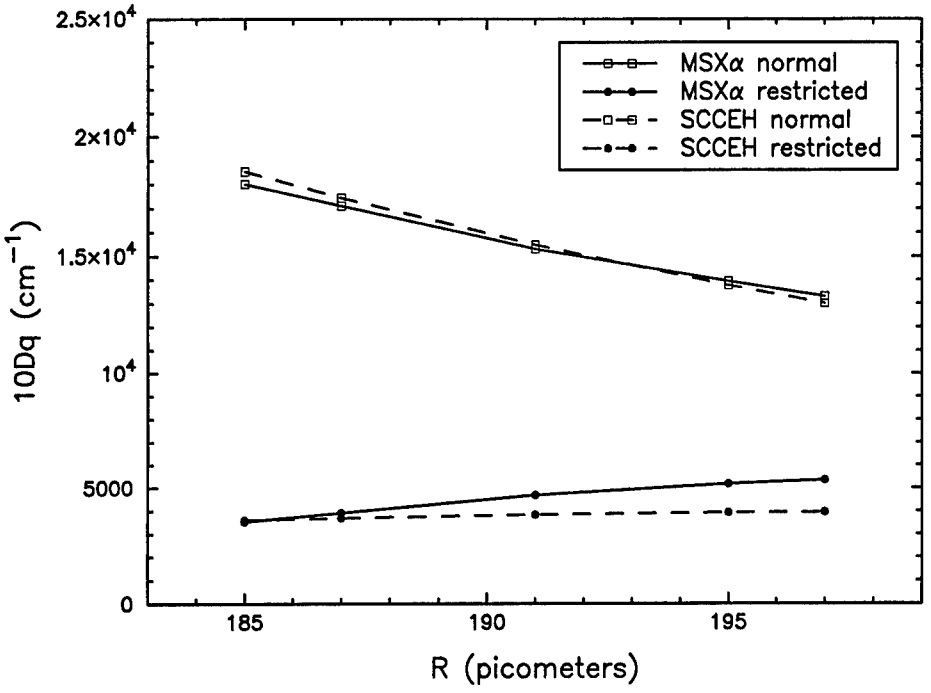

FIGURE 1 R dependence of 10Dq for the CrF_6^{3-} complex, derived from MS-Xα and SCCEH methods in normal and restricted calculations.

quantities $[(N_e\lambda_{p\sigma})^2 - (N_t\lambda_{p\pi})^2]$ and $(N_e\lambda_s)^2$ which also appear in the microscopic interpretation of the superhyperfine tensor.

The main goal of this work is to show that though $(N_e\lambda_{p\sigma})^2 \gg (N_e\lambda_s)^2$ for halide ligands the R dependence displayed by 10Dq is related to the strong dependence of $(N_e\lambda_s)^2$ upon R. Such a dependence is in turn reflected by the isotropic superhyperfine constant, A_s, provided there are unpaired σ-electrons in the ground state.[8]

For clarifying these ideas we have taken the $CrF_6^{3-}O_h$ complex as a *guide* and performed electronic structure calculations as a function of R using two different MO methods: the Self-Consistent Charge Extended Hückel (SCCEH)[9,8] and the Multiple Scattering Xα (MS-Xα).[10,8] Furthermore for both methods we have carried out two types of calculations. In a *normal* calculation the valence 2s and 2p orbitals for F^- have been included, as usually, within the basis set while in the so-called *restricted* calculation the 2s orbitals of F^- have been suppressed from the basis set and thus $\lambda_s = 0$.

For analysing the R dependence of any quantity, Q, in the *neighbourhood* of $R_c = r_M + r_X$ (where r_M and r_X are the ionic radii of metal and ligand, respectively) we have written

$$Q(R) = A\, R^{-nq} \tag{1}$$

In particular the exponents corresponding to 10Dq, $(N_e\lambda_{p\sigma})^2$, $(N_t\lambda_{p\pi})^2$ and $(N_e\lambda_s)^2$ (denoted as n, n_σ, n_π and n_s, respectively) have been derived from the calculations.

2 RESULTS AND DISCUSSION

The main results of the calculations are depicted in Figure 1 and Table I. It can be seen that in a normal calculation both MS-Xα and SCCEH methods lead to $10Dq \propto R^{-n}$ in the vicinity of $R_c = 1.9$ Å. The SCCEH ($n = 5.5$) and MS-Xα ($n = 4.8$) values are not far from $n = 4.6$ estimated by Dolan *et al.*[5] The suppression of the $2s(F^-)$ orbitals in both calculations gives rise however to the destruction of the strong dependence of 10Dq upon R. Even in the case of the restricted MS-Xα calculation, the exponent n becomes negative. At the same time the suppression of $2s(F^-)$ orbitals decreases the 10Dq value itself for a given distance. By contrast other quantities like $(N_e\lambda_{p\sigma})^2$, $(N_t\lambda_{p\pi})^2$, the value of charge transfer transitions and their R dependence are practically unaffected. Therefore, the present results demonstrate that the $2s(F^-)$ admixture in the wavefunction of $|e_g^*>$ though very small $[(N_e\lambda_s)^2 \cong 5\%]$ is *microscopically responsible* for the law $10Dq \propto R^{-n}$ (n being close to five) observed experimentally for CrF_6^{3-} as well as for other complexes in ionic lattices. Theoretical results similar to the present one are reached for other complexes involving cations like Mn^{2+}, Ni^+, etc.

Table I

Calculated values of 10Dq (in cm^{-1}), $(N_e\lambda_s)^2$, $(N_e\lambda_{p\sigma})^2$ and $(N_t\lambda_{p\pi})^2$ (in %) for CrF_6^{3-} at R = 191 pm in normal and restricted (excluding 2s ligand orbitals calculations). Writing $10Dq \propto R^{-n}$, $(N_e\lambda_s)^2 \propto R^{-n_s}$, $(N_e\lambda_{p\sigma})^2 \propto R^{-n_\sigma}$ and $(N_t\lambda_{p\pi})^2 \propto R^{-n_\pi}$ the exponent n, n_s, n_σ and n_π are also given. First and second rows report MS-Xα and SCCEH results, respectively.

	Normal	Restricted
10Dq	15310	4680
	15480	3830
n	4.81	−6.66
	5.51	−1.44
$(N_e\lambda_s)^2$	7.18	–
	4.60	–
n_s	5.43	–
	7.00	–
$(N_e\lambda_{p\sigma})^2$	17.89	19.01
	15.51	17.89
n_σ	−0.53	−1.50
	−0.85	−0.60
$(N_t\lambda_{p\pi})^2$	9.49	9.86
	11.82	11.69
n_π	1.53	1.35
	0.49	0.85

An explanation of the present conclusion which is certainly amazing is given in Ref. 11. For an ionic system 10Dq can be approximately written, following the perturbation scheme by Löwdin[12] as follows:

$$10Dq = (\varepsilon_d - \varepsilon_p)[(N_e\lambda_{p\sigma})^2 - (N_t\lambda_{p\pi})^2] + (\varepsilon_d - \varepsilon_s)(N_e\lambda_s)^2 \quad (3)$$

where ε_d, ε_p and ε_s are the energies associated to 3d, 2p and 2s levels before chemical bonding is taken into account. As for CrF_6^{3-} $\varepsilon_d - \varepsilon_p \cong 7$ eV and $\varepsilon_d - \varepsilon_s \cong 22$ eV the

contribution arising from the 2s quasi-core levels can be as important as that from the 2p levels. Furthermore, eq. (3) points out that the R dependence of 10Dq is in fact *related* to the very strong R dependence of $(N_e\lambda_s)^2$ which is experimentally well observed for O_h complexes involving Mn^{2+} or Fe^{3+} as well as for D_{4h} systems involving d^9 ions[8].

ACKNOWLEDGEMENTS

This work has been supported by the CICYT under project No. PB92-0505.

REFERENCES

1. H. Drickamer, *J. Chem. Phys.* **47**, 1880 (1967).
2. F. Rodríguez and M. Moreno, *J. Chem. Phys.* **84**, 692 (1986).
3. V. Luaña, M. Bermejo, M. Florez, J. M. Recio and L. Pueyo, *J. Chem. Phys.* **90**, 6409 (1989).
4. S. J. Duclos, Y. K. Vohra and A. L. Kappers and R. H. Ruoff, *Phys. Rev.* B **41**, 5372 (1990).
5. J. F. Dolan, A. G. Rinzler, L. A. Kappers and R. H. Bartram, *J. Phys. Chem. Solids* **53**, 905 (1992).
6. M. Moreno, M. T. Barriuso and J. A. Aramburu, *J. Phys. Condens. Matter* **4**, 9481 (1992).
7. S. Sugano, Y. Tanabe and H. Kamimura 'Multiplets of Transition-Metal Ions in Crystals'. Academic Press (New York) 1970.
8. M. Moreno, M. T. Barriuso and J. A. Aramburu, *Appl. Magn. Reson.* **3**, 283 (1992).
9. J. H. Ammeter, A. B. Burgi, J. C. Thibeault and R. Hoffmann, *J. Am. Chem. Soc* **100**, 3686 (1978).
10. K. H. Johnson, *Adv. Quantum Chem.* **7**, 143 (1973).
11. M. Moreno, M. T. Barriuso and J. A. Aramburu, *Int. J. Quant. Chem.* **52**, 829 (1994).
12. P. O. Löwdin, *J. Chem. Phys.* **19**, 1396 (1951).

Radiation Effects and Defects in Solids, 1995, Vol. 134, pp. 189–192
Reprints available directly from the publisher
Photocopying permitted by license only

© 1995 OPA (Overseas Publishers Association)
Amsterdam B.V. Published under license by
Gordon and Breach Science Publishers SA
Printed in Malaysia

THE JAHN-TELLER EFFECT IN THE EXCITED STATES OF MnF_6^{4-} AND CrF_6^{3-} COMPLEXES

J. A. ARAMBURU,* M. T. BARRIUSO♯ and M. MORENO*

**DCITTYM. Facultad de Ciencias, Universidad de Cantabria, 39005 Santander, Spain;*
♯Dpto. Física Moderna, Facultad de Ciencias, Universidad de Cantabria, 39005 Santander, Spain

The coupling coefficient, V_E, with the Jahn-Teller mode, E_g, for the first excitations of MnF_6^{4-} and CrF_6^{3-} complexes has been investigated through Molecular Orbital calculations for different values of the tetragonal Q_θ coordinate. The present analysis reveals that the stable geometry for the first excited state of $MnF_6^{4-}(^4T_1)$ and $CrF_6^{3-}(^4T_2)$ is that of an elongated and compressed octahedron respectively. The calculated values for MnF_6^{4-} at the equilibrium distance (R = 212 pm) of $RbMnF_3$ are close to the experimental value $V_E = 65$ cm^{-1}/pm. As a salient feature it is shown that $V_E \propto R^{-p}$ (p being close to six) and thus it exhibits the *same* dependence as the coupling coefficient, V_A, with the symmetric mode. Finally, the present analysis predicts an increase of the Stokes shift upon increasing R *provided* the Gruneisen constant is higher than two. It thus explains recent experimental data on Mn^{2+}-doped fluoroperovskites.

Key words: Jahn-Teller effect; MnF_6^{4-}; CrF_6^{3-}; Xα calculations; Extended Huckel calculations.

1 INTRODUCTION

The first excited state of luminescent cations (like Cr^{3+}, V^{2+} or Mn^{2+}) in O_h symmetry is a triplet state. Thus optical parameters (like the Stokes shift, Huang-Rhys factors or bandwidth) associated to the first transition are mainly determined by the coupling to the Jahn-Teller mode E_g as well as to the symmetric mode A_{1g}. The effective hamiltonian describing the linear electron-phonon coupling *within* the orbital triplet state (measured with respect to the ground state) can simply be written as follows[1]

$$H_{eff} = V_A Q_A I + V_E(\Gamma_\theta Q_\theta + \Gamma_\varepsilon Q_\varepsilon) \tag{1}$$

where I is the 3×3 identity matrix, V_A and V_E the electron-fonon coupling coefficients for A_{1g} and E_g modes, respectively, and Γ_θ and Γ_ε are given by

$$\Gamma_\theta = \begin{pmatrix} 1/2 & 0 & 0 \\ 0 & 1/2 & 0 \\ 0 & 0 & -1 \end{pmatrix} \qquad \Gamma_\varepsilon = \begin{pmatrix} -\sqrt{3}/2 & 0 & 0 \\ 0 & \sqrt{3}/2 & 0 \\ 0 & 0 & 0 \end{pmatrix} \tag{2}$$

If R is the metal-ligand distance for an O_h symmetry a value $Q_\theta \neq 0$ depicts an *instantaneous* tetragonal symmetry giving rise to two different distances, called R_{ax} and R_{eq}, such as $(R_{ax} + 2R_{eq}) = 3R$ and $Q_\theta = -(12)^{1/2}(R_{eq} - R)$.

An understanding of the associated Huang-Rhys factors, S_A and S_E, the Stokes shift, ΔE_s, and their dependence upon hydrostatic and chemical pressures thus requires to investigate about the microscopic origin of V_E and V_A and their dependence upon the metal-ligand distance R. As regards V_A it has been shown[2] that it is essentially determined by d10Dq/dR as the Racah parameters B and C, for a system like MnF_6^{4-}, are nearly independent upon R.[3]

The present work is devoted to explore the microscopic origin of V_E, taking as a guide the cases of the MnF_6^{4-} and CrF_6^{3-} complexes. Main goals of the present work are the following:

1) To relate V_E to the energy changes undergone by the one-electron levels produced by a tetragonal distortion depicted by Q_θ.
2) To calculate V_E and S_E for MnF_6^{4-} and CrF_6^{3-} using Molecular Orbital (MO) methods and to compare it to available experimental results.
3) To explore the dependence of V_E and S_E upon R. This point is particularly attractive as recent results[4] on the Stokes shift for Mn^{2+}-doped fluoroperovskites reveal that ΔE_s increases upon increasing R, ΔE_s being proportional to $R^{-5.3}$.

For achieving all these goals we have performed MS-Xα and Self-Consistent Charge Extended Hückel (SCCEH) calculations for different values of the Q_θ coordinate and also of R in order to derive $V_E(R)$.

2 RESULTS

The ground state wavefunction of the MnF_6^{4-} complex can be briefly written as[1]

$$|^6A_1 >= |\overset{+}{xy}\ \overset{+}{xz}\ \overset{+}{yz}\ 3z^2-\overset{+}{r^2}\ x^2-\overset{+}{y^2}| \tag{3}$$

where an spin-orbital like $|\overset{+}{xy}>$ actually means a MO transforming like xy with spin up. When $Q_\theta \neq 0$ an instantaneous tetragonal distortion occurs and $^4T_1$ state gives rise to a singlet state ($^4T_1(z)$) and to a doublet state [$^4T_1(x)$;$^4T_1(y)$]. The expression for the wave function $|^4T_1(z)>$ is given by[1]

$$|^4T_1(z) > |\overset{+}{xy}\ \overset{+}{xy}\ \overset{+}{xz}\ \overset{+}{yz}\ 3z^2-\overset{+}{r^2}| \tag{4}$$

thus, taking into account eq. (1), V_E is just given by

$$V_E = -(\partial/\partial Q_\theta)[\varepsilon(xy) - \varepsilon(x^2 - y^2)] \tag{5}$$

which in view of the center of the gravity theorem can be expressed as follows

$$V_E = (1/2)(\partial/\partial Q_\theta)[\Delta_e - (4/3)\Delta_t] \tag{6}$$

where $\Delta_e = \varepsilon(x^2 - y^2) - \varepsilon(3z^2 - r^2)$ and $\Delta_t = \varepsilon(xy) - \varepsilon(xz)$ are the splittings produced by the tetragonal distortion upon e_g and t_{2g} one-electron levels, respectively.

In the case of the $^4T_2$ state of d^3 ions in O_h symmetry a similar treatment to the preceding one can be carried out, the results being

$$V_E = -(\partial/\partial Q_\theta)[(1/2)\Delta_e - (2/3)\Delta_t] \tag{7}$$

Therefore, as normally $\Delta_t < \Delta_e$ and $\Delta_e>0$ when $Q_\theta>0$, it appears that V_E would be *positive* for the $^4T_1$ state of MnF_6^{4-} but negative for the $^4T_2$ state of CrF_6^{3-}. In other words, the equilibrium situations for both cases would correspond to an elongated and compressed octahedra, respectively.

As regards the $^4T_1$ state of MnF_6^{4-} Table I collects the numerical values of V_E calculated for different Mn^{2+}-F^- distances, R. It is worth noting that the SCCEH value ($V_E = 61.6\ cm^{-1}/pm$) and the MS-Xα one ($V_E = 46.2\ cm^{-1}/pm$) calculated for $R = 213$ pm are not far from $V_E = 65.5\ cm^{-1}/pm$ measured in $RbMnF_3$ and $V_E = 52\ cm^{-1}/pm$ calculated by Nikiforov *et al.*[5] At variance with these results we have verified that for this case crystal-field theory leads to $V_E = 12\ cm^{-1}/pm$. This important underestimation is very similar to that undergone by V_A.

A salient feature emerging from Table I concerns the dependence of V_E upon R. Both calculations support that in the vicinity of $R_O = 213$ pm, $V_E = K R^{-n_E}$ where $n_E = 5.9$ and 6.5 from SCCEH and MS-Xα calculations, respectively. Therefore, both calculations indicate that for MnF_6^{4-} V_A and V_E exhibit the *same dependence* upon R. This has important consequences on the R dependence followed by the Stokes shift, ΔE_s. At high temperatures (where the influence of odd phonon absorption and emission processes upon ΔE_s is not important) ΔE_s can be written as

$$\Delta E_s = \Delta E_s(A) + \Delta E_s(E)$$

$$\Delta E_s(A) = (1/2M_L)(V_A/\omega_A)^2 \tag{8}$$

$$\Delta E_s(E) = (1/2M_L)(V_E/\omega_E)^2$$

where M_L is the ligand mass. Therefore, if *both* V_A and V_E are proportional to R^{-p} and assume that the two *stretching* frequencies ω_A and ω_E follow the Gruneisen law

$$\Delta\omega/\omega = -3\gamma(\Delta R/R) \tag{9}$$

with the same γ coefficient, then ΔE_s will be proportional $R^{2(3\gamma-p)}$.

Table I

Calculated values (in cm^{-1}/pm) of the coupling coefficients V_E and V_A between the $^4T_1$ electronic state and the E_g and A_{1g} modes, respectively, corresponding to the MnF_6^{4-} complex, for three values of the metal-ligand distance R (in pm). First and second rows report MX-Xα and SCCEH results, respectively. Assuming $|V_A| \propto R^{-n_A}$ and $|V_E| \propto R^{-n_E}$ it is found $n_A = 6.3$, $n_E = 5.9$ from MS-Xα values and $n_A = 7.0$, $n_E = 6.1$ from SCCEH ones.

R	V_A	V_E
206	−89	57.4
	−108	75.2
213	−70	46.2
	−85	61.6
220	−59	39.0
	−68	50.2

As the γ value calculated for the ground state of MnF_6^{4-} and VF_6^{4-} are equal to[3,6] $\gamma = 2.3$ and 2.9, respectively, it can expected that ΔE_s in MnF_6^{4-} increases upon increasing R as it is observed indeed.[4] More precisely if p = 5.7 as measured experimentally[7] for V_A the dependence $\Delta E_s \propto R^{5.3}$ observed experimentally would be compatible with $\gamma = 2.8$ which is a reasonable figure.

In the case of CrF_6^{3-} the calculated values for R = 191 pm are equal to $V_E = -107$ cm^{-1}/pm and -130 cm^{-1}/pm for MS-Xα and SCEEH calculations, respectively. Such values of $|V_E|$ are smaller than the corresponding $|V_A|$ values (140 and 182 cm^{-1}/pm, respectively). The contribution $\Delta E_s(E)$ to the Stokes shift is calculated to be equal to 950 cm^{-1} and 1360 cm^{-1} from MS-Xα and SCEEH values, respectively, using $\hbar\omega_E = 468$ cm^{-1} measured[8] in $Rb_2KGaF_6:Cr^{3+}$. The present values (which are to be compared with $\Delta E_s(E) = 930$ cm^{-1} calculated by Woods *et al.*[9] for $K_2NaScF_6:Cr^{3+}$) stress that $\Delta E_s(E)$ is about 40% of the experimental[9] Stokes shift $\Delta E_s = 2650$ cm^{-1} which is thus dominated by $\Delta E_s(A)$.

It is worth noting that the present SCEEH and MS-Xα calculations both give rise to

reasonable figures for the first $F^- \rightarrow Cr^{3+}$ charge transfer transition of CrF_6^{3-} observed[10] at 8.0–8.7 eV for the $Na_3In_2Li_3F_{12}:Cr^{3+}$ system, while the ab initio results by Woods *et al.*[9] place the mainly ligand levels *above* the mainly d-levels. This point likely related to an underestimation of the electronic affinity of F^- is discussed in Ref. 11.

Table II
Idem than Table I, for the CrF_6^{3-} complex. Then, it is found $n_A = 5.4$, $n_E = 5.1$ from the MS-Xα values and $n_A = 6.6$, $n_E = 6.6$ from the SCCEH ones.

R	V_A	V_E
185	−166	−120
	−225	−160
191	−140	−107
	−182	−130
195	−125	−91
	−159	−113

ACKNOWLEDGEMENTS

This work has been supported by the CICYT under project No. PB92-0505.

REFERENCES

1. E. I. Solomon and D. S. McClure, *Phys. Rev.* **B9**, 4690 (1974).
2. M. Moreno, M. T. Barriuso and J. A. Aramburu, *J. Phys. Condens. Matter* **4**, 9481 (1992).
3. V. Luaña, M. Bermejo, M. Florez, J. M. Recio and L. Pueyo, *J. Chem. Phys.* **90**, 6409 (1989).
4. C. Marco de Lucas, F. Rodríguez and M. Moreno. *Phys. Rev.* **B50**, 2760, (1994).
5. A. E. Nikiforov, S. Y. Shaskin and A. I. Krotkii, *Phys. Status Solidi b* **98**, 289 (1980).
6. N. W. Winter and R. M. Pitzer, *J. Chem. Phys.* **89**, 446 (1986).
7. F. Rodríguez and M. Moreno, *J. Chem. Phys.* **84**, 692 (1986).
8. C. Marco de Lucas, F. Rodríguez, J. M. Dance, M. Moreno and A. Tressaud, *J. Lumin.* **48–9**, 835 (1991).
9. A. M. Woods, R. S. Sinkovits, J. C. Charpie, W. L. Huang, R. H. Bartram and A. R. Rossi, *J. Phys. Chem. Solids* **54**, 543 (1993).
10. D. de Viry, M. Casalboni and M. Palumno, *Sol. St. Comm.* **76**, 1051 (1990).
11. R. Valiente, J. A. Aramburu, M. T. Barriuso and M. Moreno, *J. Phys. Condens, Matter* **6**, 4515 (1994).

Radiation Effects and Defects in Solids, 1995, Vol. 134, pp. 193–196
Reprints available directly from the publisher
Photocopying permitted by license only

© 1995 OPA (Overseas Publishers Association)
Amsterdam B.V. Published under license by
Gordon and Breach Science Publishers SA
Printed in Malaysia

ENERGETICS OF THE RbF + CaF_2 → $RbCaF_3$ SOLID STATE REACTION: A FIRST-PRINCIPLES STUDY

M. FLÓREZ, J. M. RECIO, A. MARTÍN PENDÁS, E. FRANCISCO and V. LUAÑA

Departamento de Química Física y Analítica. Universidad de Oviedo. E–33006, Oviedo, España

(Received July 1, 1994)

In this contribution, we report the preliminary results of a theoretical calculation of relevant thermodynamic magnitudes involved in the RbF+CaF_2 → $RbCaF_3$ solid state reaction. We combine pairwise and quantum-mechanical simulations to determine the static equations of state for the three crystals involved in this heterogeneous reaction. Then, we compute the standard enthalpy and volume of the reaction ($\Delta H°$, $\Delta V°$) and the dependence of ΔH and ΔV with pressure. Finally, the influence of crystal polymorphism in these magnitudes is examined.

Key words: solid-solid reaction, ab initio calculation, interionic potentials, RbF, CaF_2, $RbCaF_3$.

1 INTRODUCTION

The continuous development of efficient and accurate simulation techniques able to investigate the response of solid materials at different pressure (p) and temperature (T) conditions bring us the opportunity of carrying out theoretical studies covering the thermodynamic and kinetic aspects of solid-solid reactions. For instance, such investigations have been already performed to explore the chemical equilibrium of the cation distributions in simple spinels[1] or the mechanism of structural solid-solid phase transitions.[2]

It is our aim in this contribution to analyze the influence of several polymorphs in the thermodynamics of a simple solid state reaction, the formation of the $RbCaF_3$ perovskite from CaF_2 and RbF. Specifically, our work is directed to determine the volume and enthalpy of the reaction and their change with hydrostatic pressure.

2 SIMULATION TECHNIQUES

Our first-principles approach combines quantum-mechanical *ab initio* Perturbed Ion (aiPI) calculations,[3] and pairwise simulations (PAIRPOT).[4] The aiPI method involves ion-in-the-lattice Hartree-Fock-Roothaan calculations using high quality STOs basis sets. The correlation energy is estimated by means of the Clementi's Coulomb-Hartree-Fock method.[5] Besides, the aiPI method provides a partition of the total energy into ionic and interionic contributions, which is used to generate crystal-adapted pair potentials. These potentials are introduced in the PAIRPOT code to compute the 0 K molar Gibbs energy of a given lattice. In this way, PAIRPOT is used as a helping tool for the more time consuming quantum-mechanical aiPI calculations.

3 THE RbF, CaF_2, AND $RbCaF_3$ CRYSTALS

The equilibrium lattice parameters (a_e), bulk moduli (B_0), and cohesive energies (E_{latt}) for RbF in the cubic B1 and B2 phases, CaF_2 in the cubic (C1) and orthorhombic (C23) phases,

TABLE I
Cohesive properties for the crystalline polymorphs studied in this work. First row aiPI results. Second row experimental data.

	RbF(B1)	RbF(B2)	CaF_2(C1)	CaF_2(C23)	$RbCaF_3$
a_e(Å)	5.518	3.299	5.445	7.015, 5.859, 3.540	4.493
	5.63		5.444	7.15, 5.63, 3.49	4.4484
B_0(GPa)	24.25	34	82	83	46
	26.7–30.1		84.7–90.2		50.4
E_{latt}	–192.5	–193.2	–631.6	–629.5	–820.3
(kcal/mol)	–188.7		–626.7		

and $RbCaF_3$, in the cubic (perovskite) phase are collected in Table I. Our calculations show that at 0 T and p the B2 phase of RbF is the most stable polymorph, whereas for CaF_2 is the C1 phase. Nevertheless, as the C23 structure has also been shown to exist metastable at ambient conditions in the laboratory,[6] we will also report results using this polymorph as a reactive. The overall comparison with the experimental data is very satisfactory and provides a reliable starting point to infer thermodynamic properties for the formation reaction of $RbCaF_3$.

Concerning the equation of state (EOS) of the reactants, the usual V/V_0 versus p diagram is plotted in Figure 1. It is observed that the hardness of the crystalline polymorphs decrease

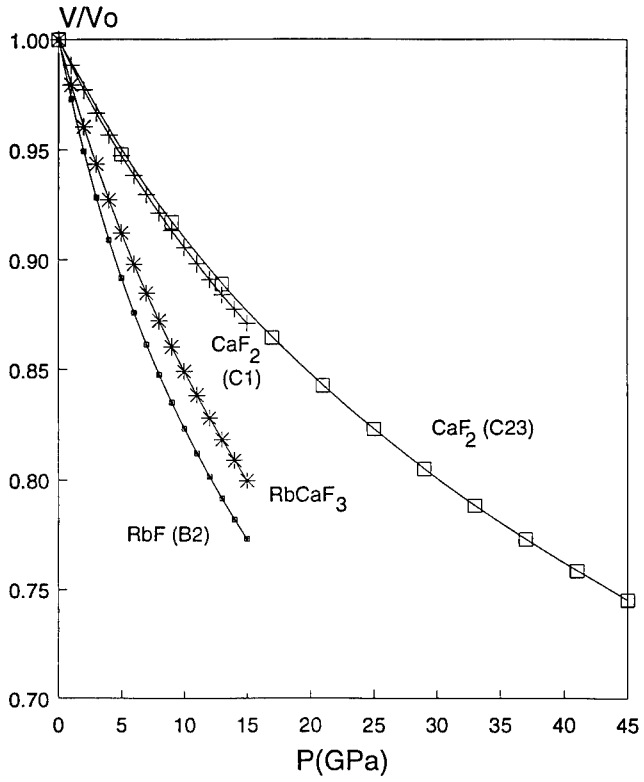

FIGURE 1 Equations of state for RbF(B2), CaF_2(C1), CaF_2(C23) and $RbCaF_3$ (perovskite).

following the sequence $CaF_2(C23) \approx CaF_2(C1) > RbCaF_3 > RbF(B2)$, in concordance with the corresponding values for B_0.

4 THE $RbF + CaF_2 \rightarrow RbCaF_3$ REACTION

From the tabulated data above, we have computed the standard enthalpy and volume ($\Delta H°$, $\Delta V°$) of this solid state reaction. In the case of CaF_2 (C1), $\Delta H° = 4.45$ kcal/mol and $\Delta V° = 14.45$ Å^3, whereas if the CaF_2(C23) is involved, we obtain $\Delta H° = 2.39$ kcal/mol and $\Delta V° = 18.43$ Å^3. It is generally assumed that for solid-solid reactions $\Delta G°(298\ K) \approx \Delta H°(298\ K) \approx \Delta H°(0\ K)$. We therefore conclude that, according to our calculations, this reaction is not thermodynamically favoured at ambient conditions.

We have also explored the pressure variation of ΔH (see Figure 2) and ΔV depending whether CaF_2 is in the C1 or in C23 phase. $\Delta V(p)$ curves are continuous decreasing functions with similar slopes for the two polymorphs. Concerning $\Delta H(p)$ curves, they are increasing functions of p, and show a crossing point at about 4 GPa, which is the predicted pressure for the C1 $\rightarrow$ C23 transition in CaF_2.

Financial support from the Spanish DGICYT, Projects Nos. PB90–795 and PB93-0327, is gratefully acknowledged.

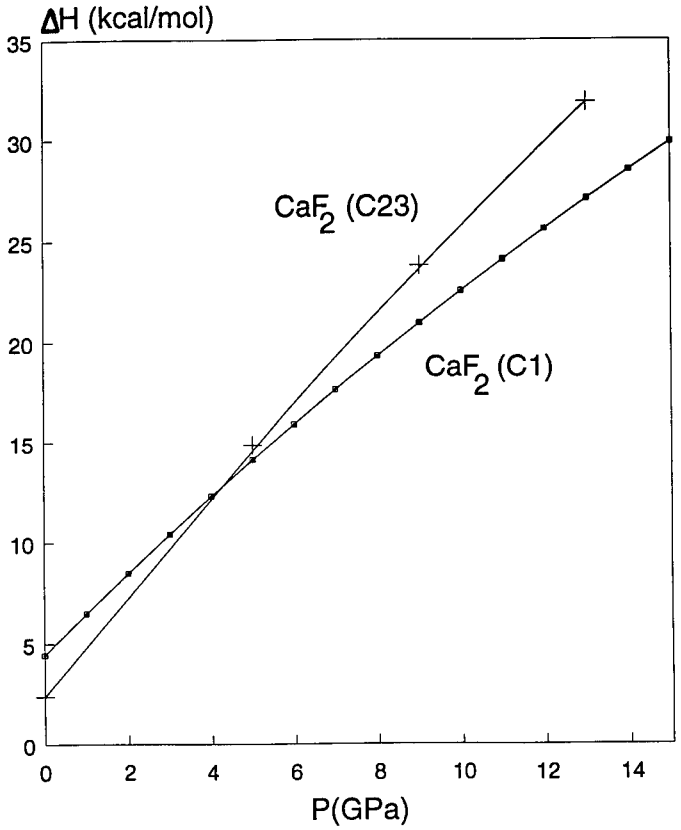

FIGURE 2 Pressure dependence of ΔH for the $RbF(B2) + CaF_2(C1,C23) \rightarrow RbCaF_3$ reaction.

REFERENCES

1. A. Navrotsky and O. J. Keppla, *J. Inorg. nucl. Chem.* **29**, 2701 (1967).
2. A. Martín Pendás, V. Luaña, J. M. Recio, M. Flórez, E. Francisco, M. A. Blanco, and L. N. Kantorovich, *Phys. Rev.* **B 49**, 3066 (1994).
3. V. Luaña and L. Pueyo, *Phys. Rev.* **B 41**, 3800 (1990); V. Luaña, A. Martín Pendás, J. M. Recio, E. Francisco, and M. Bermejo, *Comput. Phys. Commun.* **77**, 107 (1993).
4. A. Martín Pendás (unpublished).
5. S. J. Chakravorty and E. Clementi, *Phys. Rev.* **A 39**, 2290 (1989), and references therein.
6. L. Gerward, J. S. Olsen, S. Steenstrup, M. Malinowski, S. Asbrink, and A. Waskowska, *J. Appl. Cryst.* **25**, 578 (1992).

Radiation Effects and Defects in Solids, 1995, Vol. 134, pp. 197–200
Reprints available directly from the publisher
Photocopying permitted by license only

© 1995 OPA (Overseas Publishers Association)
Amsterdam B.V. Published under license by
Gordon and Breach Science Publishers SA
Printed in Malaysia

EFFECTS OF A QUANTUM CRYSTAL POTENTIAL ON THE DERIVATION OF ELECTRON GAS INTERIONIC ENERGIES

E. FRANCISCO, J. M. RECIO, M. A. BLANCO, A. MARTÍN PENDÁS and L. PUEYO

Departamento de Química Física y Analítica, Facultad de Química, Universidad de Oviedo, 33006–Oviedo, Spain

Taking the NaCl crystal as a test example, we analyze the performance of the Electron Gas model of Gordon and Kim with ionic electron densities obtained from the localized quantum-mechanical descriptions of the ions embedded in a quantum crystal potential. We also rationalize the potential answers of rigid and relaxed interionic potentials in terms of the charge densities used in their derivation.

Key words: Localized quantum mechanical methods, electron gas model, interionic potentials, ionic crystals.

1 INTRODUCTION

One of the best known methods of generating interatomic potentials (IP's) is the Electron Gas Model (EGM) of Gordon and Kim.[1] This model computes the IP's using density functionals of the ionic electron densities (IED's). Although these IED's can be approximated by their gas-phase values, improved versions of the method include an approximated crystal potential (CP) in the ionic calculation. However, as far as we know, no attempt has been made up to date to develop EGM IP's from quantum mechanical (*QM*) crystalline IED's that were self-consistent with the crystal potential they generate. It is our aim in this work to investigate this issue in a particular test example: the NaCl crystal.

2 QUANTUM MECHANICAL DESCRIPTIONS OF THE IED'S

To obtain the *QM* descriptions of the ions, we have used the *ab initio* Perturbed Ion (*ai*PI) model, that is described elsewere.[2–3] The minimization of the total crystal energy required by this localized Hartree-Fock approach provides a set of crystal-like atomic wavefunctions that respond self-consistently to the nearly exact crystal potential. This potential (*QM* in the following) includes the Madelung contribution, a coulombic correction due to the non-punctual character of the ions, a non-local exchange potential, and a projection operator that tends to procure the atom-crystal orthogonality. We have also performed calculations using other three CP's, labelled *Class*, *Watson*, and *Local*. The *Class* and *Local* CP's are formed only by the point charge part and the local part (point charge plus coulombic repulsion) of the most accurate *QM* CP, respectively, and the *Watson* CP, that is the crudest one, corresponds to approximate the *Class* CP by a Watson sphere.

In Figure 1 we plot the ionic radius for Na^+ and Cl^- *versus* the lattice parameter **a** of the NaCl crystal (B1 phase) as computed with the four different crystalline models. The Na^+ ionic radius hardly suffers any change with **a** and is always essentially equal to the free-ion value, regardless the CP used. On the contrary, the Cl^- ionic radius is highly dependent on the CP. The *QM* CP yields a contraction of the anionic IED that is much greater than the obtained with the *Class* and *Watson* CP's. On the contrary, the *Local* CP turns to yield a pronounced expansion of the Cl^- IED.

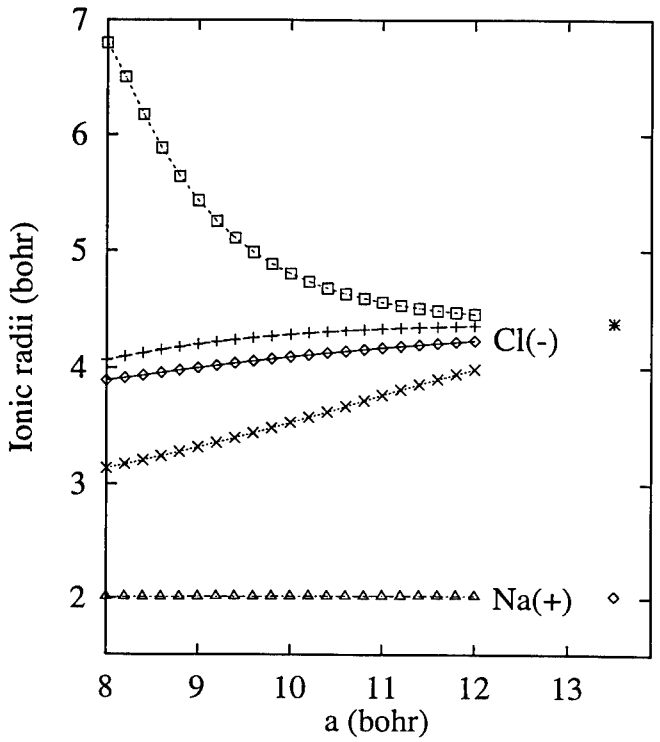

FIGURE 1 Radii of the spheres containing 99% of the electron density of Na^+ and Cl^- *versus* the lattice parameter **a** in NaCl (B1 phase). Symbols stand for the following crystal potentials: *Class* (plus), *Watson* (diamonds), *Local* (squares), and *QM* (crosses (Cl^-) and triangles (Na^+)). Free ion values are indicated by an asterisk (Cl^-) and a doted diamond (Na^+).

The effect of the four crystal models on the IED's can also be quantitatively measured by means of the self energy of the Cl^- ion ($E^{Cl^-}_{self}$), plotted in Figure 2. The *Class* model yields values that are very small and slightly increase when **a** decreases. The *Watson* CP emphasizes again the effect of the *Class* CP, whereas the *Local* CP gives values of $E^{Cl^-}_{self}$ that increase very sharply with decreasing **a**'s. Finally, the *QM* CP produces values of $E^{Cl^-}_{self}$ much greater than the two point charge crystal models.

3 RESULTS IN THE TEST EXAMPLE AND CONCLUSIONS

Once the IED's are available, the pairwise part of the IP's is computed by the usual expressions of the EGM.[1] Along with these pairwise interionic energies, a term containing the self-energy of the ions as a function of **a** has been taken into account to confer a relaxed attribute to the IP's.

We have computed the equilibrium lattice parameter $\mathbf{a}_e$, the cohesive energy $E_{coh}(\mathbf{a}_e)$, and the equation of state (EOS) of the NaCl crystal using three types of crystal consistent IP's (CCIP's), labeled CCIP(ρ^0), CCIP(ρ^e), and CCIP(ρ). The CCIP's (ρ^0) and CCIP's (ρ^e) are rigid and use as frozen IED's the free ion and the *ai*PI equilibrium geometry (a_e = 10.58 bohr) solutions, respectively. Contrarily, the CCIP's (ρ) are relaxed, as the IED's used in their derivation are the different *ai*PI solutions corresponding to different crystal

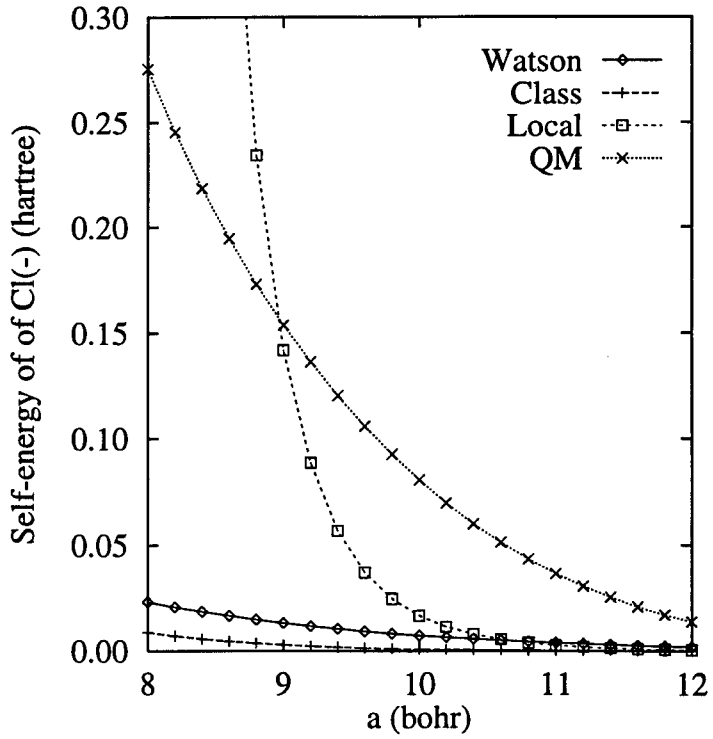

FIGURE 2 Self-energy of Cl^- *versus* the lattice parameter **a** according to several crystal potential models. The energy of the free ion is taken as zero.

geometries. Our results are gathered in Table I. From the analysis of these and other data not presented here we conclude that the pairwise repulsive interactions computed with the energy density functionals are overestimated with respect to the *QM* result provided by the *ai*PI method. In Section 2 we remarked that the many-body energy was underestimated in the *Class* and *Watson* calculations with respect to the *QM* result. This opposite behaviour is a plausible explanation to some of the good results previously obtained within the EGM approach.

Our main conclusions are: 1) Only a precise description of the quantum contributions to the crystal potential can account for the global contraction of the anionic IED and the increase of its self energy upon crystal formation. 2) The change of these two properties

TABLE I
Static properties of NaCl (B1 phase) at zero temperature and pressure obtained in several calculations.

	a_e(bohr)	$-E_{coh}$(kcal/mol)	B_0(GPa)	B_o
CCIP(ρ^0)	11.33	173.2	23.3	5.61
CCIP(ρ^c)	10.72	186.1	30.5	5.56
CCIP(ρ)	11.06	185.5	26.2	4.55
*ai*PI	10.58	189.6	28.9	4.75
Other EGM results	10.65, 10.66	184.0, 183.8	29.0, 28.1	—
Exptal.	10.66	185.3	28.5	4.88

with **a** is captured to a small fraction of its total value with a classical lattice. 3) There exists an overestimation of the pairwise repulsive energy as calculated with the EGM. A cancellation effect may appear if we combine these pairwise interactions with deformation energies of IED's computed using approximate CP's.

Financial support from the Spanish Dirección General de Investigación Científica y Tecnológica (DGICYT), Projects Nos. PB90–795 and PB93-0327, is acknowledged.

REFERENCES

1. R. G. Gordon and Y. S. Kim. J. *Chem. Phys.* **56,** 3122 (1972).
2. V. Luaña and L. Pueyo, *Phys. Rev.* **B 41**, 3800 (1990).
3. V. Luaña, A. Martín Pendás, J. M. Recio, E. Francisco, and M. Bermejo, *Comput. Phys. Commun.* **77**, 107 (1993).

Radiation Effects and Defects in Solids, 1995, Vol. 134, pp. 201–203
Reprints available directly from the publisher
Photocopying permitted by license only

© 1995 OPA (Overseas Publishers Association)
Amsterdam B.V. Published under license by
Gordon and Breach Science Publishers SA
Printed in Malaysia

STABILITY OF B1 AND B2 PHASES FROM ELECTRONIC DENSITY TOPOLOGY CONSIDERATIONS

A. MARTÍN PENDÁS, J. M. RECIO, M. FLÓREZ, M. A. BLANCO and E. FRANCISCO

Departamento de Química Física y Analítica, Facultad de Química, Universidad de Oviedo, 33006-Oviedo, Spain

It is preliminary reported how the consideration of the topology of the electronic density of B1 and B2 phases of alkali halides, obtained *via* quantum mechanical simulation, makes it possible to connect the stability or metastability of the lattices with geometrical factors. The latter turn out to validate the classical ionic model and some of the most controversial critics posed against it over the years.

Key words: Localized Quantum Mechanical Methods, Atoms in Molecules, Ionic Crystals, Phase Transitions.

1 INTRODUCTION

A very wide theoretical framework has been recently proposed[1] for the *ab initio* investigation of the mechanism of the pressure induced B1-B2 transition. In that work, restricted to alkali halides but with results of otherwise general applicability, we showed how if a continuous path on a high dimensional space connecting the two phases is assumed, it is possible to construct a hierarchy of models of increasing complexity and precision for the study of the static and dynamic features of the phase transition process. As a result of this investigation, a clear picture of the extreme role that symmetry plays in the establishment of the topology of the energetic hypersurface both at the B1 and B2 configurations and along the transition path has emerged. It was also conjectured there about the interest of examining the connection between the topologies of the energy surface and of the electronic density according to Bader's theory.[2] It is the purpose of this work to briefly show, for the first time in a solid material, that the relation actually exists and that, in this way, it is possible to recover the empirical ionic model.

2 METHOD AND MODELING

In order to obtain the *ab initio* energetic and electronic density surfaces we have employed the *ab initio* perturbed ion method,[3] a first principles approach for the elucidation of the electronic structure of weakly overlapping solids. Based upon the Theory of Electronic Separability,[4] it solves the Hartree-Fock equations of the crystal in a localized Fock space. As a result of the procedure, local and global properties are obtained from which it is easy to recover both energetic and electronic quantities. Its main advantages over other available schemes lie on its computational flexibility and speed. In this way, it is made feasible to examine multidimensional energy hypersurfaces in a workable amount of computer time. As for the modeling of the phase transition is concerned, and following the considerations found in Ref. 1, a suitable set of variables defining the transition configuration space is formed by the rhombohedral cell angle, α, and lattice spacing, **a**, of the primitive B1 and B2 crystallographic cells. These endpoint structures are constrained

to $\alpha = 60°$ and $\alpha = 90°$, respectively. The transition paths are then obtained by constructing the minimum Gibbs potential paths connecting the B1 and B2 points. After the analysis of their properties, an appropriate reaction coordinate is found to be the α angle. The complete characterization of the topology of the electronic density along the transition path is in progress and will be presented elsewhere.

3 STABILITY AND ELECTRONIC DENSITY TOPOLOGY

In the study of the properties of the Gibbs transition path in the series of the alkali halides, we have found three different topologies in the zero pressure energy profiles at the B1 and B2 configurations: a maximum (M), a minimum (m), and a quasi saddle situation (s). Table I shows this information.[5]

Table I
Energetic topological properties of the 20 alkali halides at the B1 and B2 theoretical equilibrium configurations. Each system is labelled with a two character code plus, possibly, a star. The first two characters refer to the B1 and B2 phases, respectively. 'm', 'M' and 's' stand for minimum, maximum and saddle (see text). The star implies a system that is more stable in the B2 phase than in the B1 one.

	F	Cl	Br	I
Li	mM	mM	mM	mM
Na	mm	ms	ms	mM
K	mm	mm	mm	ms
Rb	mm*	mm*	mm*	mm
Cs	mm*	mm*	mm*	mm*

One of the most important outcomes associated to this fact[5] is the discovery of a direct relation between the topology of the energetic surface at the endpoint configurations and the fulfilment of a number of interphase universal relations among thermodynamic and kinetic magnitudes: the alkali halides can be separated into different classes composed by systems described by two equal symbols in Table I. Only those crystals belonging to the same class show universal relations. For the joint consideration of these facts together with the electronic density structure, the location of the critical points of the latter becomes essential. Let us remind the reader, that in a molecular (solid) system, the properties of these points are directly coupled to the nature of bonding through Bader's analysis. Only three non-degenerated critical points, excluding the positions of the nuclei, have been found in the ionic materials so far investigated: the bond point $(3,-1)$, displays two orthogonal directions in which the electronic density is a maximum plus other in which it is a minimum; the ring point $(3,+1)$, with two minima and one maximum directions; and the cage point $(3,3)$, a threefold local minimum. Many of the critical points have been found to be symmetry dependent and to follow nicely our intuitive knowledge on the formation of molecular rings and cage clusters. Some surprises have arisen, nevertheless. As an example, and as the B1 phases are concerned, the coordination indexes change from 6–18 (cation-anion) to 18–6 as the cation gets larger, showing the great importance of second neighbor cation-cation bonding in the stabilization of the B2 phase. If **topological radii** are defined (as distances between the nucleus of interest and its first neighbor bond points), geometrical inference recovers its lost place in the theory of ionic solids. Another interesting example, a crystal stable in the B1 phase becomes metastable or even more stable in the B2 structure when the classical ionic radii ratio, written in terms of topological radii, gets greater than the classical packing ratio, 0.732. When the ratio is smaller than that value, the anion must distort from sphericity in order to accommodate itself into the lattice.

That requires a great energetic demand in the case of small, hard repulsive cations.

We have also found that only the B2 phase of CsF may be considered as a lattice of cations whose holes are filled by anions. In all the other crystals, second neighbor anion interactions contribute with a bond critical point or, in the less favourable systems, with a ring critical point to the bond graph.

Another topic that has been many times pointed out over the years (see Ref. 6) evince that, in some sense, it is the heavy cations group of the alkali halides the one which shows a typical hard sphere, point charge interaction behavior. This enforces the view that the cations are the main responsibles for repulsive interactions. Our calculations reveal that in the very heavy systems, like CsI, with a large, classically polarizable cation, there is not an important energetic cost in the distortion of the electronic density from the spherical geometry. In this way, the electrons fill quite comfortably empty lattice positions, transforming the ion into something more similar to a sticky sphere than to a hard core. The very slight distortion of the electronic cloud that is usually needed to satisfy the geometric constraints of the crystal in these cases are, then, satisfied at very low energetic cost. As a demonstration of these statements, we will only show here, for brevity, the evolution of the ratio of the lattice parameters of the B1 and B2 phases with the system investigated. It is very easy to find that, assuming only point charge interactions between constant radii spheres, the B2 phase becomes more stable than the B1 one when $a_{B_2}/a_{B_1} < 0.8236$, and that both lattices have identical nearest neighbor distances when $a_{B_2}/a_{B_1} = \sqrt{2/3} \sim 0.816$. We can see from Table II that the ideal situation is almost exclusively exhibited by the cesium salts.

Table II
a_{B_2}/a_{B_1} ratio for the 20 alkali halides at their theoretically computed equilibrium geometries.

	F	Cl	Br	I
Li	0.878	R0.893	0.889	0.887
Na	0.840	0.868	0.861	0.866
K	0.853	0.845	0.845	0.853
Rb	0.854	0.833	0.831	0.839
Cs	0,824	0.827	0.834	0.831

ACKNOWLEDGEMENTS

Financial support from the Spanish Dirección General de Investigación Científica y Tecnológica (DGICYT), Project No. PB93–0327, is greatly acknowledged.

REFERENCES

1. A. Martín Pendás, V. Luaña, J. M. Recio, M. Flórez, E. Francisco, M. A. Blanco, and L. N. Kantorovich, *Phys. Rev* **B49**, 3066 (1994).
2. R. F. W. Bader, *Atoms in Molecules* (Oxford University Press, Oxford, 1990).
3. V. Luaña, A. Martín Pendás, J. M. Recio, E. Francisco, and M. Bermejo, *Comput. Phys. Commun.* **77**, 107 (1993).
4. R. McWeeny, *Proc. R. Soc, London, Ser.* **A253**, 242 (1959).
5. A. Martín Pendás, unpublished.
6. I. M. Boswarva, *J. Phys. Chem. Solids*, **42**, 487 (1981).

Radiation Effects and Defects in Solids, 1995, Vol. 134, pp. 205–208
Reprints available directly from the publisher
Photocopying permitted by license only

© 1995 OPA (Overseas Publishers Association)
Amsterdam B.V. Published under license by
Gordon and Breach Science Publishers SA
Printed in Malaysia

PHYSICAL PROPERTIES OF THE GROUND STATE OF A TUNNELLING PARTICLE IN A PHONON FIELD IN THE INTERMEDIATE COUPLING REGIME

G. BENIVEGNA, A. MESSINA and E. PALADINO

Istituto di Fisica dell'Università di Palermo, Via Archirafi 36, 90123 Palermo, Italy

We present some characteristic properties of the ground state of a two-level system linearly coupled to a phonon field. Such properties are valid over the whole range of the parameters appearing in the Hamiltonian of the system. The knowledge of these exact results provides a physical basis for an accurate variational determination of the ground state. A physical picture of the self-trapping transition is discussed in terms of particle-field correlations. Our treatment is based on operator methods combining symmetry considerations with some general properties of the lowest energy state.

Key words: ground state, tunnelling particle, self-trapping transition.

The Hamiltonian model

$$H = \sum_{i=1}^{N} \hbar\omega_i \alpha_i^{\dagger}\alpha_i + \sum_{i=1}^{N} \varepsilon_i(\alpha_i + \alpha_i^{\dagger})\sigma_x + 1/2\ \hbar\omega_0\sigma_z \qquad (1)$$

plays a fundamental role to understand the physics of a wide variety of phenomena. In condensed matter physics it is known as spin-boson model.[1] In cavity quantum electrodynamics it represents a generalization of the Jaynes-Cummings model.[2] Generally speaking, we may say that the Hamiltonian model (1) offers a good conceptual starting point to simulate the effects of the environment on the dynamics of a 'small object'.[1,3] In this paper we present some characteristic properties of the ground state of a tunnelling particle linearly coupled to a phonon field. Our approach exploits appropriate operator techniques combining symmetry arguments with general properties of the lowest energy state. It is possible to verify[4] that the canonical transformation which changes the sign of α_i, $\alpha_i^{\dagger}$, σ_x, σ_y, leaving σ_z unmodified, is a symmetry transformation of H. This fact makes legitimate the classification of its eigenstates according to the eigenvalues $+1$ and -1 of the excitation number parity operator G. This implies the possibility of obtaining an exact decoupling of the localized degrees of freedom from those relative to the field. Our first result is a rigorous proof that, for any N and without any restriction on the coupling regime, there always exists a ground state of (1) which is also an eigenstate of G with eigenvalue $+1$. In addition we may show that the lowest energy eigenvalue is a monotonically decreasing negative function of the coupling strength. Let's denote by $|g\rangle$ a ground state of H. We may prove that over the whole range of the characteristic parameters appearing in the Hamiltonian and for any N, results $\langle g|\sigma_z|g\rangle < 0$ and $\langle g|(\alpha_i+\alpha_i^{\dagger})\sigma_x|g\rangle < 0$. The physical meaning of the first inequality is self-evident. To appreciate the physical content of the second inequality we note that the operator $\alpha_i+\alpha_i^{\dagger}$ is proportional to the operator associated with the elastic force acting on the i-th oscillator. Considering the expression of its acceleration operator we may furthermore deduce that σ_x is proportional to the operator associated to the force that the two-level system exerts on the same oscillator. Thus we may interpreter the second inequality saying that in the ground state the two forces on a given oscillator are strongly correlated and have opposite directions. Using a technique yielding to other exact relations among the quantum covariances of appropriate operators, some interesting aspects of the mode-mode and spin-field

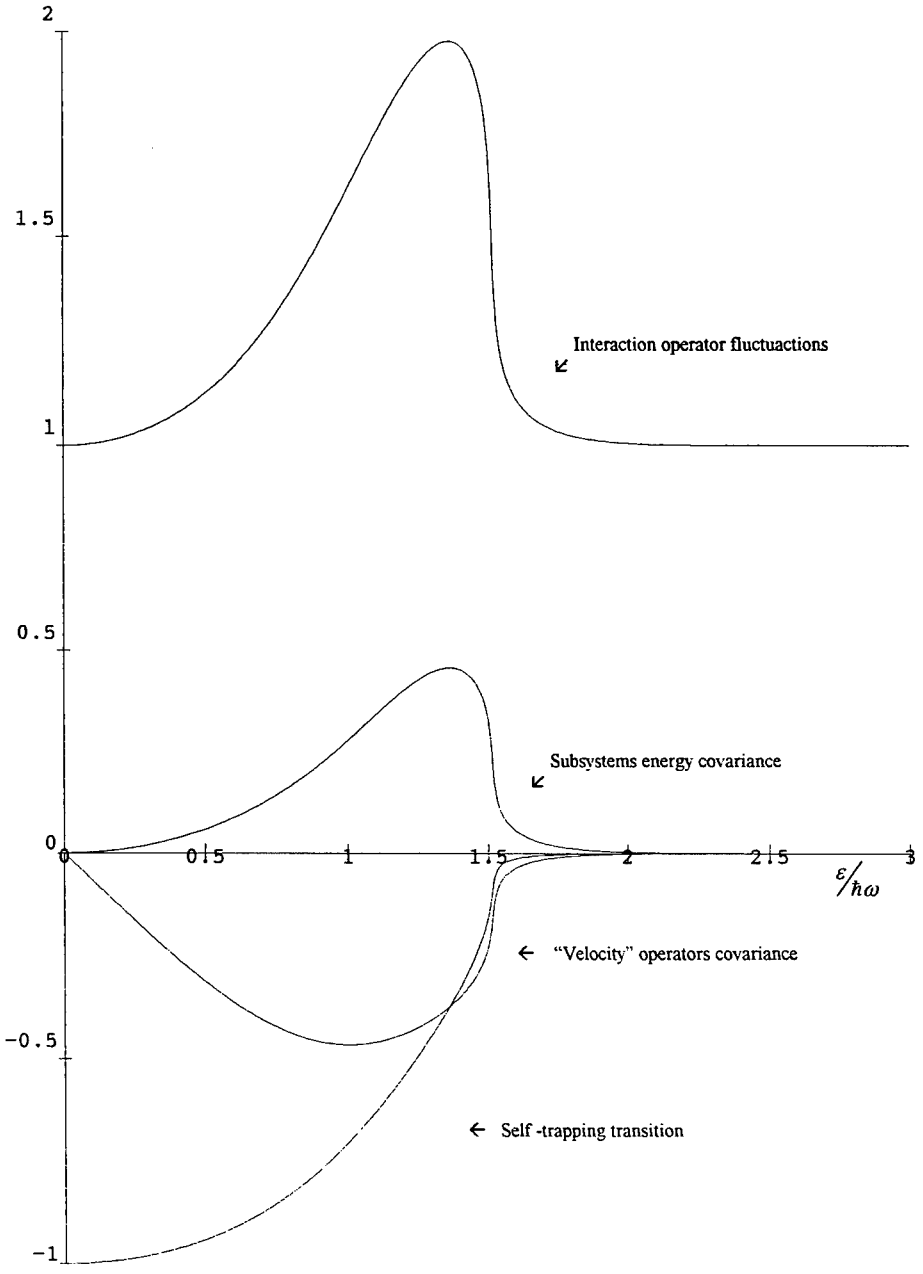

FIGURE 1 Representation of the physical quantities indicated as functions of the adimensional coupling strength $\varepsilon/\hbar\omega$ and for $\omega_0 = 2\omega$.

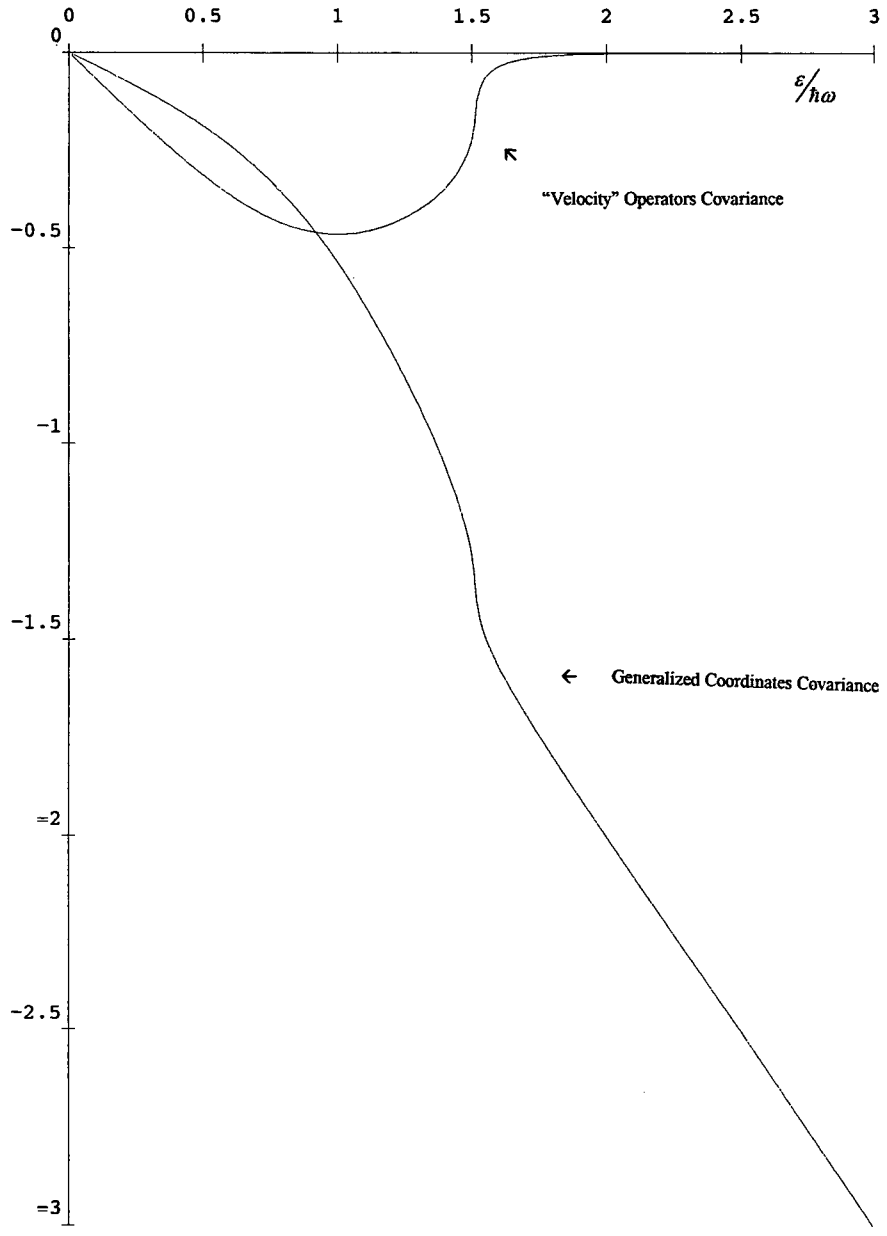

FIGURE 2 Representation of the physical quantities indicated as functions of the adimensional coupling strength $\varepsilon/\hbar\omega$ and for $\omega_0 = 2\omega$.

correlations are also investigated. The knowledge of these exact results provides a physical basis for an accurate variational determination of the ground state. For N = 1 we introduce the following set of normalized trial states containing γ and η as real variational parameters:

$$| \phi(\gamma,\eta)\rangle = \exp[i\,\pi/2\,(\sigma_x - 1)\alpha^\dagger\alpha]\,\exp[\gamma/2(\alpha^{\dagger 2} - \alpha^2)]\,\exp[\eta(\alpha^\dagger - \alpha)]\,|\,0\,;-\rangle \quad (2)$$

We are able to solve the variational problem showing that the ground state differs from the exact one for perturbative contributions. This circumstance makes legitimate the calculation of the mean value of operators other than the Hamiltonian. Our results are represented in Figure (1) as functions of the coupling strength and for $\omega_o = 2\omega$. The 'self-trapping transitions' curve gives the variation of the mean value of σ_z with $\varepsilon/\hbar\omega$. This plot exhibits a drastic but continuous change in an interval of values of $\varepsilon/\hbar\omega$ which may be considered conceptually coincident with the region of intermediate coupling. In the same range, the variance of the interaction energy in units of ε^2 and the covariance between $\alpha^\dagger\alpha$ and σ_z display a simultaneous maximum. A possible physical meaning of such a behaviour is that the two subsystems manifest, in the intermediate coupling region, a relatively larger ability of influencing one another. Thus the covariance between the time derivatives of their respective generalized coordinates should reach a maximum for the same value of the coupling strength. The negative of the covariance between the operators $i(\alpha^\dagger\text{-}\alpha)$ and σ_y, proportional to the respective 'velocity' operators, represented in Figure (1), yields a confirmation of this 'dynamical' point of view. This curve, in fact, shows a minimum in the region of intermediate coupling, followed once more by a rapid variation. Grasping the common features of the four plots, we suggest the following physical picture for the passage between the two extreme coupling regimes. The transition from the weak coupling condition to the strong coupling regime is characterized by the onset of a competition between two different types of atom-field correlations. In fact, when the covariance between the two adimensional velocities is comparable with the covariance between the two coordinates (see Figure (2)), a high nonlinear feedback appears. Such effect reduces the tunnelling parameter of the particle quenching, therefore, the mutual 'dynamical' influence between the subsystems. This point of view provides a new characterization of the 'equilibrium' conditions existing in the lowest energy state of a tunnelling particle coupled to its environment under intermediate coupling conditions. We have extended our approach to the multimode case (N > 1) reaching qualitatively similar physical conclusions. We point out that the ideas presented in this paper can be applied to a wide variety of problems and, in particular, to paraelectric and paraelastic systems.[5]

REFERENCES

1. A. J. Leggett *et al.*, *Rev. Mod. Phys.* **59**, 1 (1987).
2. B. W. Shore and P. L. Knight, *J. Mod. opt.* **40**, 1195 (1993).
3. A. Amann, *J. Chem. Phys.* **96**, 1317 (1992); R. Silbey and R. A. Harris, *J. Chem. Phys.* **93**, 7062 (1989); W. Zwerger, *Z. phys.* **B53**, 53 (1983).
4. G. Benivegna and A. Messina, *Phys. Rev.* **A53**, 3313 (1987).
5. X. Wang and F. Bridges, *Phys. Rev.* **B46**, 5122 (1992); T. Kranjc, *J. Phys.* **C20**, 3663 (1987).

2 DEFECTS IN OXIDES

Radiation Effects and Defects in Solids, 1995, Vol. 134, pp. 209–211
Reprints available directly from the publisher
Photocopying permitted by license only

© 1995 OPA (Overseas Publishers Association)
Amsterdam B.V. Published under license by
Gordon and Breach Science Publishers SA
Printed in Malaysia

MICROSTRUCTURE OF SINGLE-CRYSTAL SILLENITE FIBERS

V. V. PROKOFIEV*, J. P. ANDREETA*, C. J. DE LIMA*, M. R. B. ANDREETA*, A. C. HERNANDES *, J. F. CARVALHO*, A. A. KAMSHILIN*, T. JÄÄSKELÄINEN*

**University of Joensuu, Department of Physics, P.O. Box 111, SF-80101, Joensuu, Finland. FAX: +358 73 1513290. E-mail: VICPROK@JOYL.JOENSUU.FI.;*
Universidade de São Paulo, Instituto de Física e Química de São Carlos, Departamento de Física e Ciência dos Materiais, 13560 São Carlos–SP, Brazil

(Received July 1, 1994)

Single-crystal fibers of $Bi_{12}SiO_{20}$ and $Bi_{12}TiO_{20}$ up to 90 mm in length with diameters of 200–1200 μm have been pulled along the <001> and <011> crystallographic axis by the LHPG method. The powder X-ray diffraction and the electron-probe microanalysis have been used for characterization of the as-grown fibers. Microstructure of the sillenite fibres has been studied by the chemical etching method. The dislocations, inclusions and striations have been found to be the main imperfections in the as-grown fibers. The dislocation density has been estimated on the ground of the etching pits using optical and electronic microscopy and compared with that evaluated by the Tsivinskii's relation. The conditions of formation of microdefects are discussed in relation with the growth conditions, morphology and chemical composition of the as-grown fibers.

Key words: single-crystal fibers, microstructure, $Bi_{12}SiO_{20}$, $Bi_{12}TiO_{20}$.

1 INTRODUCTION

Sillenites ($Bi_{12}GeO_{20}$, $Bi_{12}SiO_{20}$, $Bi_{12}TiO_{20}$, etc.) are perspective materials in optical information processing.[1] Single-crystal fibers of sillenites have many advantages over bulk crystals, however, they should meet the higher requirements of structural perfection because the existence of the various defects causes the optical losses and decreases the damage threshold, limiting the practical applications of the as-grown fibers. In this report we present first results of the studies of microstructure of the sillenite fibers grown by the Laser-Heated Pedestal Growth (LHPG) method.

2 EXPERIMENTAL

The single-crystal fibers of $Bi_{12}SiO_{20}$ and $Bi_{12}TiO_{20}$ with diameters of 200–1200 μm have been pulled along the <001> and <011> crystallographic axis from the previously grown single crystal source rods of BSO and BTO by the LHPG method.[2] The powder X-ray diffraction and the electron-probe microanalysis have been used for characterization of the as-grown fibers. The microstructure of the sillenite fibers has been studied by the chemical etching method. The natural facets of BSO and BTO fibers and the faces cut perpendicular to the pulling axis have been etched in 1 min at 20°C in 1*M* solution of bromine (Br_2) in ethanol C_2H_5OH. The dislocation density has been estimated on the ground of the etching pits using optical and electronic microscopy.

3 DISCUSSION

The stable growth of the fiber with a constant diameter requires that the length of the molten zone (L), the meniscus angle (θ) and the laser power (Q) be kept constant.[3] The thermal stresses induced by very high temperature gradients are the main source of dislocations in the fiber. According,[4] the density of dislocations (N_d), calculated in terms of the axial temperature gradient, dimensions of the transverse fiber cross-section and the elastic properties of the material, is equal to about 1.10^5 pits/cm^2. This value is in a good agreement with that estimated by the chemical etching method (5.10^5 pits/cm^2).

It is necessary to note other causes of the formation of imperfections in the fibers. In the calculations of the temperature gradients we assumed that a growing fiber has a smooth, uniform cylindrical geometry. However, large facets were present in all sillenite fibers

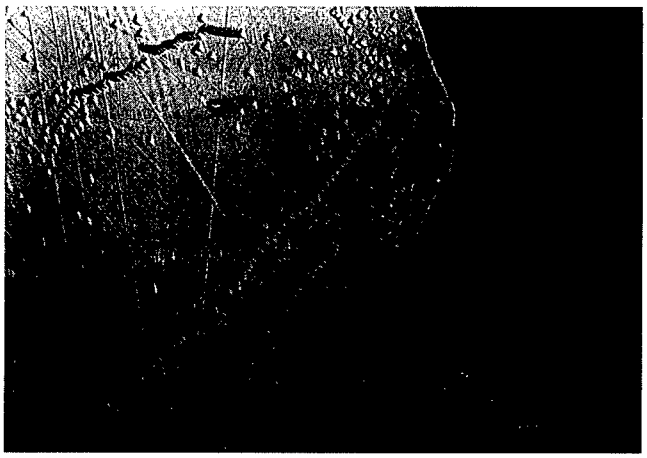

FIGURE 1 Dislocation etch-pit pattern of the $Bi_{12}TiO_{20}$ single crystal fiber near the natural facet. Pulling axis <011>.

FIGURE 2 Inclusions of the foreign phases in the $Bi_{12}TiO_{20}$ fiber pulled along <011> axis.

pulled along both <011> and <001> crystallographic axes. These facets are induced to the growth anisotropy and are also the source of additional strains and, therefore, dislocations. The strains due to the facets are appreciable compared with the breaking strain of the BSO crystal.[5] The typical pattern of etching pits near the natural facet of a BTO fiber pulled along <011> axis is shown in Figure 1. Each of the crystallographic facets requires a different meniscus angle for diameter stability. Therefore, the careful diameter maintenance in the cause of the faceting fiber growth becomes quite difficult. Any instabilities in the laser power Q as well as in the pulling V_f and feeding V_s rates produce periodical and/or random fluctuations in the growth rate and the fiber diameter and consequently are also the cause of the formation of striations and other additional imperfections in the fiber. Figure 2 shows the foreign inclusions in the end part of BTO fiber. According to data of electron-probe microanalysis, the concentration of Bi_2O_3 in these inclusions is higher than in defect-free regions of the fiber. Evaporation of bismuth oxide from the surface of the molten zone generates the formation of stoichiometric defects in the growing fibers. All these reasons must be considered at the growth of sillenite fibers by the LHPG method.

REFERENCES

1. 'Photorefractive materials and their applications I', (*Topics in Applied Physics*, **61**), ed. by P. Günter and J. P. Huignard, Springer-Verlag, 1988.
2. V. V. Prokofiev, J. P. Andreeta, C. J.de Lima, M. R. B. Andreeta, A. C. Hernandes, J. F. Carvalho, A. A. Kamshilin, T. Jääskeläinen, *J. of Crystal Growth* **137**, 528 (1994).
3. R. S. Feigelson, *J. Crystal Growth* **79**, 669 (1986).
4. V. V. Prokofiev, J. P. Andreeta, C. J. de Lima, M. R. B. Andreeta, A. C. Hernandes, J. F. Carvalho, A. A. Kamshilin, T. Jääskeläinen, Report C-V/P11 on the EMRS'94 Spring Meeting, 24–27 May 1994, Strasbourg, France.
5. J. C. Brice, *J. Crystal Growth* **42**, 427 (1977).

Radiation Effects and Defects in Solids, 1995, Vol. 134, pp. 213–217
Reprints available directly from the publisher
Photocopying permitted by license only

© 1995 OPA (Overseas Publishers Association)
Amsterdam B.V. Published under license by
Gordon and Breach Science Publishers SA
Printed in Malaysia

OH VIBRATIONAL MODES IN SILLENITES

P. BENEVENTI,[1] R. CAPELLETTI,[1] L. KOVÁCS,[2] Á. PÉTER,[2] and F. UGOZZOLI[3]

[1]Department of Physics, University of Parma, Viale delle Scienze, 43100 Parma, Italy; [2]Research Laboratory for Crystal Physics, Hungarian Academy of Sciences, 1112 Budapest, Budaörsi út 45, Hungary; [3]Institute of General and Inorganic Chemistry, University of Parma, Viale delle Scienze, 43100 Parma, Italy

(Received July 1, 1994)

High resolution (0.05 cm^{-1}) FTIR spectroscopy in the temperature range 9–320 K is applied to study the OH and OD stretching modes in BSO, BGO, BTO and mixed BSO-BGO sillenite crystals. A model is proposed for the OH-defect responsible for the main line. The anharmonic effects are analyzed in the framework of the Morse model and compared to those reported for OH-defects in insulating materials. The temperature dependence of the line position and width fits to a weak phonon coupling model and gives the frequency of the coupled phonons.

Key words: OH vibration, FTIR spectroscopy, sillenites, impurities phonon-coupling.

1 INTRODUCTION

Many oxides, as BGO, BSO, and BTO, crystallize in the b. c. c. sillenite structure and are described by the general formula $Bi_{12}MeO_{20}$ (with Me = Ge, Si, and Ti). The photorefractive effect exhibited by such materials makes them attractive for applications in the field of optoelectronics.[1] Since crystals are grown in air, OH is expected to enter the matrix. Moreover hydrogen impurities are good candidates as being responsible for the thermal fixing of the holographic gratings,[1] as in the case of $LiNbO_3$: therefore it is worthwhile to study the properties of defects induced by OH-impurities in sillenites. High resolution (0.05 cm^{-1}) FTIR spectroscopy in the temperature range 9–320 K was used to show that the narrow line absorption spectra, monitored in the wavenumber ranges 3400–3600 cm^{-1} and 2500–2600 cm^{-1}, in as grown and in deuterated samples of BGO, BSO, mixed xBGO·(1–x)BSO, and BTO single crystals, are due to the stretching modes of OH and OD impurities. The stretching frequencies were analyzed in the framework of the Morse anharmonic oscillator and the results were compared to those reported for OH-related defects in other oxides and alkali halides.[2] The temperature dependence of the line position and width was studied in order to determine the phonon coupling of the hydroxyl ion.

2 EXPERIMENTAL DETAILS

BSO, BGO and mixed BSO-BGO crystals were grown in air by the balance controlled Czochralski method. The incongruently melting BTO crystals were grown from solution by the top seeding technique .[3] In the mixed $(1-x)$ BSO·xBGO crystals the nominal fraction x was 0.25, 0.5, and 0.75, however the actual fraction in the crystal was different, as stressed by lattice constant measurements[3] and chemical analysis performed by means of the ICP emission spectroscopy. The sample thickness was in the range 0.4–40 mm. The isotopic substitution of H with D was obtained by heating the samples at ~800 °C in dry O_2 flowing through D_2O.

The optical absorption measurements were performed by means of 1) a Bomem DA8 FTIR spectrophotometer in the range 7000–200 cm^{-1}, with a resolution as good as

0.04 cm^{-1}, and 2) a Varian 2390 spectrophotometer in the range 3300–5 × 10^4 cm^{-1}. The spectra were recorded in the range 9–320 K, by assembling the sample in a 21SC model Cryodine Cryocooler of CTI-Cryogenics.

3 RESULTS AND DISCUSSION

The spectra of as grown BSO, BGO, and BTO, measured at 9K in the range 3420–3520 cm^{-1}, are compared in Figure 1. A few narrow lines appear in BGO (curves b and c) and in BTO (curves d and e), while only one in BSO (curve a). The lines broaden and shift towards shorter wavenumbers by increasing the temperature: the line labeled with M in Figure 1 (henceforward defined as the main line) exhibits practically the same temperature shift in the three different matrices, as shown in Figure 2 (full symbols). The fact that the lines appear in a wavenumber range typical for the OH stretching and the samples are grown in air suggests that they are due to the presence of OH. Such an attribution is supported by the line shift to the region 2500–2600 cm^{-1} as a consequence of the isotopic substitution of D for H. The line position in deuterated samples is that expected (within 2 ÷ 3%) on the basis of the hydroxyl reduced mass change.[3] Moreover a very weak line is detected in a thick BSO sample at 3432.09 cm^{-1} which can be regarded as the isotopic

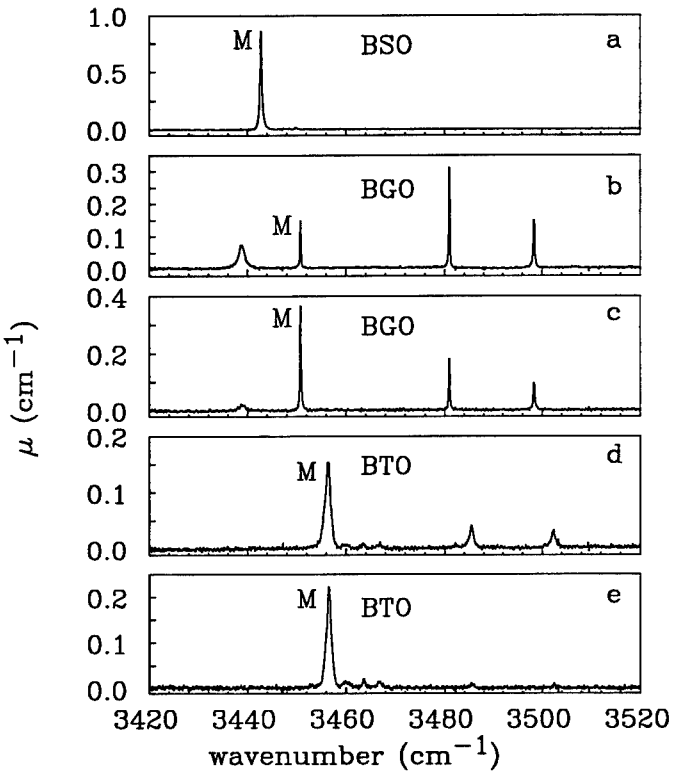

FIGURE 1 High resolution (0.05 cm^{-1}) optical absorption spectra of BSO (curve a), BGO (curves b and c), and BTO (curves d and e) measured at 9 K. The two curves for BGO and BTO are related to samples cut from different ingots. The label **M** indicates the main line.

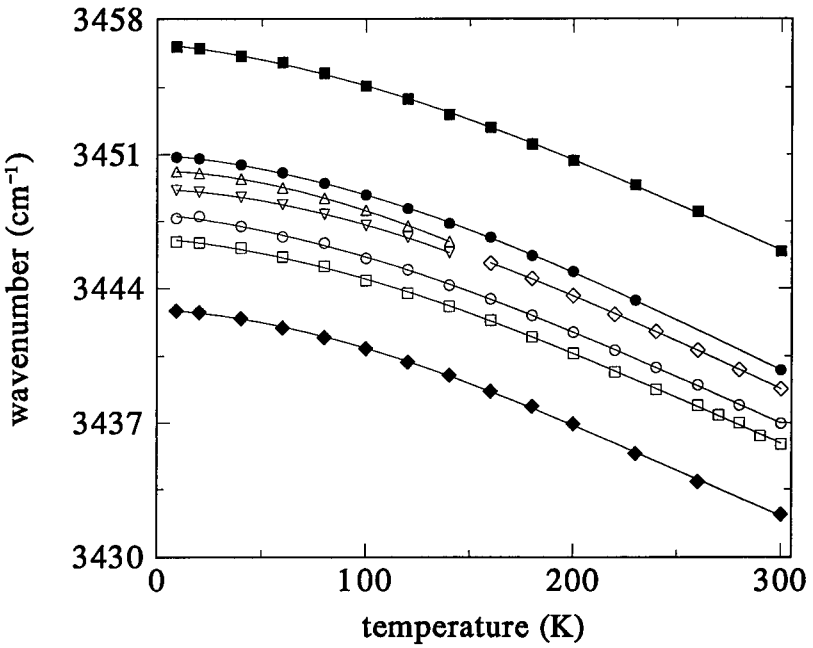

FIGURE 2 Temperature dependence of the main line position in BSO (full diamonds), BGO (full circles), BTO (full squares) and in mixed xBGO·(1–x)BSO (open symbols). The nominal fraction x is as follows: $x = 0.25$ (open circles), $x = 0.5$ (open squares) and $x = 0.75$ (open diamonds and triangles to show the line splitting at low temperatures). The actual fraction x is 0.63, 0.48, and 0.75 respectively.

replica of the main line at 3442.84, induced by the presence of ^{18}O (natural abundance $\sim 2 \times 10^{-3}$).

In mixed $(1 - x)$ BSO·xBGO crystals by increasing x the position of the main line shifts smoothly from that in BSO to that in BGO and shows practically the same temperature dependence as BSO and BGO (see Figure 2). It should be remarked that even at 9 K the main line in mixed samples is broad and for $x = 0.75$ splits into two components, which merge by increasing the temperature (see Figure 2). A linear relationship holds between the main line position ν_M and the x fraction as measured from the chemical analysis of Ge and Si (Figure 3a). Such a trend makes it possible 1) to determine from ν_M the actual composition of mixed crystals grown in air, which doesn't necessarily coincide with the nominal one, and 2) to account for the splitting observed at $x = 0.75$ as due to the coexistence of two phases. ν_M showed also a linear dependence on the lattice constant.[3] These features suggest that the main line is due to the same OH-related defect in BSO, BGO, BTO and mixed BSO-BGO and its position is sensitive to the nature of Me.

A possible model for the defect is an OH substituting one of the four oxygens at the corners of the tetrahedron around the Me, the charge compensation being accomplished by a Bi-antisite. This last (a Bi^{3+} located at the Me^{4+} site) charge-compensated by a hole, is assumed to be responsible for the shoulder, which overlaps the onset of the fundamental absorption edge in undoped BSO, BGO, and BTO samples.[1,4] In the present case the H^+ of the hydroxyl ion could play the same role as the hole. Therefore we looked for a possible correlation between the absorption coefficient μ_{sh} of the shoulder (at 2.9 eV) and the OH content c_{OH} in BSO, BGO and mixed BSO-BGO systems. c_{OH} was determined from the area under the main line,[3] μ_{sh} was found indeed roughly proportional to c_{OH}, see Figure 3b, supporting the hypothesis that Bi-antisites are involved in defects responsible for the main line.

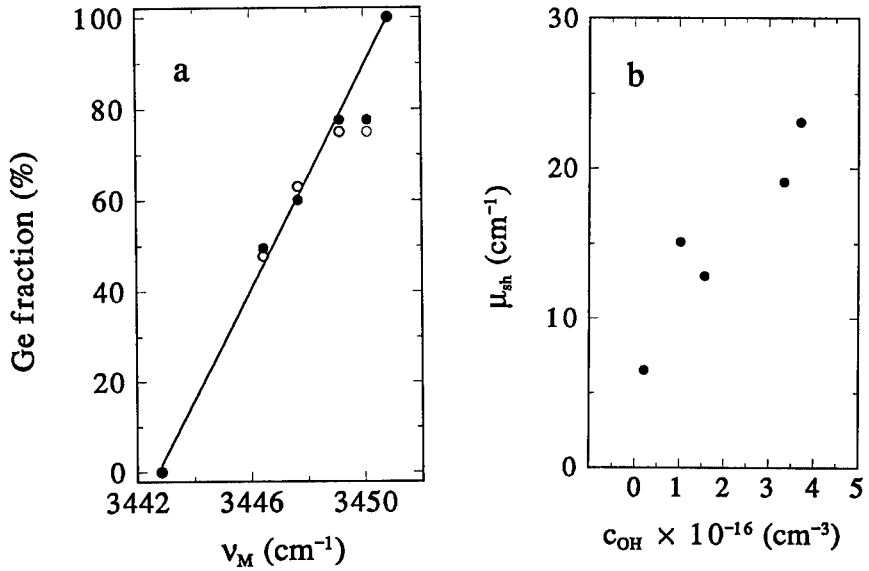

FIGURE 3 Correlation between OH stretching parameters, chemical composition and 'blue' absorption in mixed xBGO·(1–x)BSO sillenites. a) Plot of the Ge fraction vs the main line position ν_M at 9 K as obtained directly from the Ge chemical analysis (full circles) and as a complement to 1, starting from the chemical analysis of Si (open circles). The double ν_M value for the Ge fraction = 0.75 is related to the main line splitting displayed in Figure 2. b) Plot of the absorption coefficient μ_{sh} of the shoulder (measured at 2.9 eV at 300 K) vs the OH concentration c_{OH} estimated from the area under the main line (at 300 K).

In addition to the main line, other lines are present in BGO and BTO spectra, see Figure 1. Their relative amplitude depends on the ingot from which the sample has been cut, compare curves b and c (BGO) and curves d and e (BTO). This rules out that the additional lines are due to different transitions between energy levels of the same defect. Some of the lines shift as a consequence of the substitutions of D for H: therefore they should be associated to defects in which H is involved, possibly complexes of OH with unwanted impurities already present in the reagent powders.

In BSO a weak overtone of the main line was detected: in this way the whole set of the Morse parameters was evaluated. The anharmonicity parameter x_{em} = 0.02532 and the binding energy D_e = 4.417 eV were found comparable with those of the free OH molecule, of OH in $LiNbO_3$, and in alkali halides.[2,3] If the dipole moment is a linear function of the O-H separation, x_{em} should equal the ratio of the transition probability for the first overtone to that of the fundamental, which can be evaluated from the ratio between the areas under the two corresponding lines:[2] such a value was ~3.23×10^{-3}, i.e. different from that quoted above and obtained from the position of fundamental and overtone. This suggests that electrical anharmonicity effects are present as well. In the case of BGO and BTO x_{em} could be evaluated only from the isotopic replica of the main line, by assuming for OH the model of free diatomic molecule: again the values found were comparable with those of OH centers in other compounds.

The lines are very narrow in the unmixed crystals (0.15–1.44 cm^{-1} at 9 K) and broader in the mixed ones. The lineshape is Lorentzian for the former, suggesting a homogeneous broadening, and is described by a Voigt profile in the latter, suggesting that an inhomogeneous broadening is induced by a random distribution of Ge and Si on the Me sites. The phonon coupling of the stretching modes observed was studied by analyzing the

detailed temperature dependence of the line position (see Figure 2) and width. A fitting of our data according to a weak coupling model[5] was quite satisfactory. The frequencies of coupled phonons were found in the range $122 \div 135$ cm^{-1} for all the systems investigated (included the mixed ones) in good agreement with those obtained by reflectance, Raman scattering measurements and theoretical calculations.[6]

ACKNOWLEDGEMENTS

One of the authors (L. K.) undertook this work with the support of the ICTP Programme for Training and Research in Italian Laboratories, Trieste, Italy. Financial support from the National Fund of Hungary (OTKA T4420) is acknowledged.

REFERENCES

1. L. Arizmendi, J. M. Cabrera, and F. Agulló-López, *Intern. J. Optoelectr.* **7**, 149 (1992).
2. W. B. Fowler, R. Capelletti, and E. Colombi, *Phys. Rev.* **B 44**, 2961 (1991).
3. P. Beneventi, R. Capelletti, L. Kovács, Á. Péter, A. M. Lanfredi Manotti, and F. Ugozzoli, *J. Physics: Cond. Matter.* **6**, 6329 (1994) and quoted references.
4. H. J. Reyher, U. Hellwig, and O. Thiemann, *Phys. Rev.* **B 47** 5638 (1993).
5. P. Dumas, Y. J. Chabal, and G. S. Higashi, *Phys. Rev. Lett.* **65**, 1124 (1990).
6. W. Wojdowski, *Phys. Stat. Sol.* (b) **130**, 121 (1985) and quoted references.

Radiation Effects and Defects in Solids, 1995, Vol. 134, pp. 219–222
Reprints available directly from the publisher
Photocopying permitted by license only

© 1995 OPA (Overseas Publishers Association)
Amsterdam B.V. Published under license by
Gordon and Breach Science Publishers SA
Printed in Malaysia

ON THE SUBSTITUTION SITE OF Cr AND Fe IN $LiNbO_3$: AN EXAFS STUDY

G. CORRADI[1,2,3], A.V. CHADWICK[2], A. R. WEST[4], K. CRUICKSHANK[4] and M. PAUL[4]

[1]*Research Laboratory for Crystal Physics, Hungarian Academy of Sciences, P.O. Box 132, H-1502 Budapest, Hungary;* [2]*Chemical Laboratory, University of Kent, Canterbury, Kent CT2 7NH, United Kingdom;* [3]*Universität Osnabrück, Fb. Physik, D-49069 Osnabrück, Germany;* [4]*Department of Chemistry, University of Aberdeen, Aberdeen AB9 2VE, United Kingdom*

(Received July 1, 1994)

K-edge EXAFS spectra of 5 molar% Cr or Fe have been observed in $LiNbO_3$ and also in Mg co-doped samples. The results in congruent $LiNbO_3$ can be interpreted in terms of a relaxed Li substitution model, however, in the case of Cr, the formation of pairs occupying Li and Nb sites seems also to be important. In stoichiometric or Mg-containing samples Fe is partly displaced to the Nb site while for Cr the dominating process seems to be the formation of aggregates with the participation of Mg.

Key words: crystal defects, impurity centres, transition elements, lithium niobate, EXAFS.

1 INTRODUCTION

Dopants and Impurities in lithium niobate play decisive roles in most applications of $LiNbO_3$ systems e.g. Fe in photorefractive and Cr in prospective laser devices. The first decisive argument in the long-standing dispute on the substitution site of Fe in $LiNbO_3$ has come recently from extended X-ray absorption fine structure (EXAFS) measurements.[1–3] Presently the Fe dopant in essentially congruent $LiNbO_3$, for concentrations up to a few percent, is known to substitute predominantly for Li. There are indications to different behaviour in Mg co-doped[4,5] or essentially stoichiometric[6] $LiNbO_3$.

For the Cr dopant no EXAFS data have been reported. The dispute remains unsettled, however, for Mg co-doped crystals the coexistence of two substitution sites[7–9] and for Cr concentrations above 1% the formation of self-compensating Cr-Cr pairs[10] have been reported. Most interpretations and model calculations suffer from the neglect of both local relaxation and associations with other defects.

In this paper we have undertaken systematic EXAFS measurements in congruent and stoichiometric $LiNbO_3$, single doped with Cr^{3+} or Fe^{3+} and also in materials double doped with Mg+Cr or Mg+Fe, in order to obtain direct information on the substitution sites, local relaxations and possible associations.

2 EXPERIMENTAL AND COMPUTATIONAL DETAILS

Sintered powder samples were prepared from high-purity Johnson-Matthey and Merck materials. The Li:Nb composition ratio was either congruent or stoichiometric with dopant levels of 5 mol% Cr or Fe. A series of 5% Mg co-doped samples was also prepared together with some congruent samples co-doped with up to 15% Mg. K-edge EXAFS spectra were taken at station 7.1 of the Daresbury Synchrotron Facility. For a better signal/noise ratio transmission was measured for Fe and fluorescence for Cr. The Daresbury suite of programs

using Hedin-Lundquist exchange potentials was used for deriving structural parameters including ligand distances.

3 RESULTS FOR $LiNbO_3$: CR AND $LiNbO_3$:Fe

The Fourier transform of the EXAFS spectrum measured at the Cr edge in congruent $LiNbO_3$ doped with 5% Cr is shown in Fig 1. The analysis has been carried out using the following model sites for Cr^{3+}, allowing large relaxations for the Cr^{3+} ion and the first few neighbour shells:

a) the Li site, where a closest Nb neighbour may be missing or replaced by another Cr,
b) the Nb site, where a closest Li neighbour may be replaced by Nb or Cr.

The oxygen octahedrons containing the Cr^{3+} in various models may be undistinguishable due to relaxation. The essential difference from the point of view of EXAFS is the number of close Nb neighbours in the models, 4 or 3 Nb's in model a), and 0 or 1 in model b), all at roughly 3.07 Å. The difference between the models is further increased by three more Nb's at appr. 3.35 Å and two more triplets of oxygens within 3.5 Å in model a), all of which are absent in model b).

The close Li neighbours appearing instead in model b) are much weaker at backscattering X-rays than Nb and O.

The analysis is in favor of Li substitution. The large Fourier amplitudes measured between 2.8 and 3.5 Å cannot be explained assuming only Li neighbours in this range. The ligand distances obtained are given in Table I and indicate a strong relaxation of the oxygen octahedron with a shift of the Cr towards a central position. The relaxations also correspond to the charge misfit.

The fit can be improved if the accidental coincidence of the distances of the four close Nb neighbours (one on the C_3 axis and three in off-axis positions) is allowed to be lifted. The resulting small distance, 2.95 Å, for the on-axis Nb seems again to correspond to a relaxation of the Cr^{3+} ion towards a central position by at least 0.12 Å from the Li site.

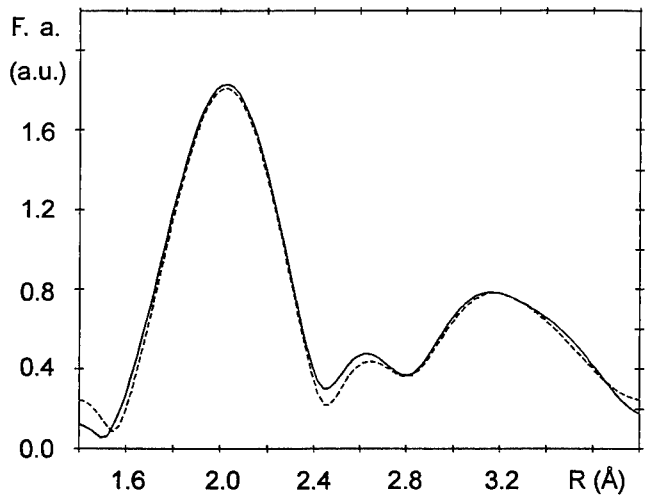

FIGURE 1 Fourier transform of the K edge EXAFS spectrum of 5% Cr in congruent $LiNbO_3$. The dashed line was calculated using the data for the 4Nb variant of the Li substitution model in Table I.

TABLE I
Best fit values for dopant-ligand distances (in Å) in congruent $LiNbO_3$: Cr compared to cation-ligand distances in perfect $LiNbO_3$

Shells around Li	**3 O**	**3 O**	**1 Nb + 3 Nb**	**3 O**	**3 Nb**	**3 O**
Perfect $LiNbO_3$	2.050	2.271	3.07	3.28	3.35	3.41
Cr_{Li}	2.033		3.22	~3.27	3.38	~3.37
models	2.033		2.95 3.19	~3.30	3.34	~3.32

However, as the fitting procedure is unsensitive to small (±1) changes of the number of ligands in a given ligand shell, the presence of a considerable minority of Cr on Nb site, which would contribute to the first oxygen peak but only weakly to the rest of the spectrum, cannot be excluded.

The data for $LiNbO_3$: Fe confirm the Li substitution model[1–3] and indicate some relaxation of the Fe towards a central position, though less than for Cr. Due to the larger relative amplitude of the peak near 3.3 Å in the Fourier spectrum (which is mainly due to Nb ligands), the portion substituting on Nb site must be considerably less than in the Cr case.

4 RESULTS FOR Mg CO-DOPED AND STOICHIOMETRIC $LiNbO_3$

The spectra in both $LiNbO_3$:Mg:Cr and $LiNbO_3$:Mg:Fe are dramatically changed compared to samples without Mg. The qualitative differences become larger for increasing Mg concentrations and cannot be described by the simple Li or Nb substitution models with any reasonable relaxations.

The most important change for $LiNbO_3$:Mg:Cr is an increase of the relative amplitude of the peak near 3.2 Å (see Fig. 2). This indicates that upon Mg codoping Cr is increasingly associated with strongly X-backscattering near cation neighbours, which may be e. g. Mg instead of Li, or more Cr and/or Nb neighbours. A possible fit with a Cr–Mg aggregate is shown in Figure 2.

In the case of $LiNbO_3$:Mg:Fe the peak near 3.3 Å strongly decreases upon Mg co-doping as compared to the oxygen peaks, indicating that increasing numbers of Fe are associated with less effectively backscattering neighbours just outside their oxygen octahendrons. This may be the effect of Fe_{Nb}, since Fe_{Li}–Mg_{Nb} associates are unexpected for other reasons[11] (lower indices refer to substitution sites).

A Li:Nb composition ratio of 1:1 instead of the congruent one resulted in relatively small changes for $LiNbO_3$:Cr and $LiNbO_3$:Mg:Cr. For Fe, stoichiometry caused more conspicuous effects similar to those caused by an additional 5% of Mg. In the case of Fe this may be understood assuming that both stoichiometry and Mg eliminate the intrinsic defect structure stabilizing Fe_{Li} and thus lead to increasing numbers of Fe_{Nb}. For Cr, charge compensation at the 5% dopant level is apparently less determined by intrinsic defects but can be strongly affected by Mg co-doping. A reasonable explanation for this situation can be that a considerable part of Cr is paired or aggregated even in single doped congruent samples, and Mg is a competitive partner for Cr to form paires and aggregates.

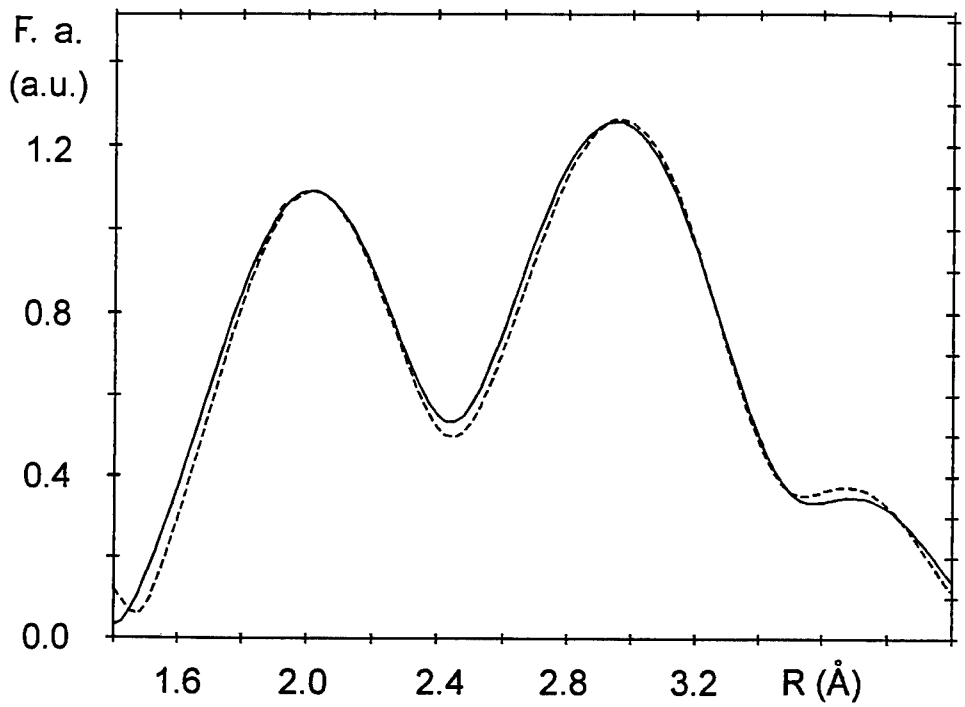

FIGURE 2 Fourier spectrum for 5% Cr in congruent $LiNbO_3$ co-doped with 10% Mg. The dashed line is a fit for a possible Cr–Mg aggregate containing, in addition to oxygens, 2±1 magnesiums and 2±1 niobiums at distances in the range 2.74–2.86 Å from the Cr.

ACKNOWLEDGEMENTS

The authors benefited from a Daresbury project for the measurements. One of the authors (G. C.) was also supported by a PHARE ACCORD Fellowship (H9112–0055). Support from the National Scientific and Research Fund of Hungary (OTKAT4110 AND T4367) is also acknowledged.

REFERENCES

1. C. R. A. Catlow, A. V. Chadwick, M. Cole and S. M. Tomlinson, *Rad. Eff. Defects. Solids* **119–121**, 565 (1991).
2. T. S. Bush, C. R. A. Catlow, A. V. Chadwick, M. Cole, R. M. Geatches, G. N. Greaves and S. M. Tomlinson, *J. Mater. Chem.* **2**, 309 (1992).
3. C. Prieto and C. Zaldo, *Sol. State Commun.* **83**, 819 (1992).
4. A. Böker, H. Donnerberg, O. F. Schirmer, and Feng Xiqi, *J. Phys. Condens. Matter* **2**, 6865 (1990).
5. Feng Huixian, Wen Jinke, Wang Huafu, Han Shiying, and Xu Yunxia, *J. Phys. Chem. Solids* **51**, 397 (1990).
6. G. I. Malovichko, V. G. Grachev, O. F. Schirmer and B. Faust, *J. Phys.: Cond. Matter* **5**, 3971 (1993).
7. G. Corradi, H. Söthe, J.-M. Spaeth, and K. Polgár, *J. Phys. Condens. Matter* **3**, 1901 (1991).
8. E. Camarillo, J. Tocho, I. Vergara, E. Díeguez, J. Carcía Solé, and F. Jaque, *Phys. Rev.* **B45**, 4600 (1992).
9. F. Jaque, J. Garcia-Sole, E. Camarillo and F. J. Lopez, H. Murrieta and J. Hernandez, *Phys. Rev.* **B47**, 5432 (1993).
10. V. G. Grachev, G. Malovichko and V. V. Troitskii, *Fiz. Tverd. Tela* **29**, 607 (1987) Engl. transl. *Sov. Phys. Solid State* **29**, 349 (1987).
11. H. Donnerberg, S. M. Tomlinson, and C. R. A. Catlow, and O. F. Schirmer, *Phys. Rev.* B **44**, 4877 (1991).

Radiation Effects and Defects in Solids, 1995, Vol. 134, pp. 223–228
Reprints available directly from the publisher
Photocopying permitted by license only

© 1995 OPA (Overseas Publishers Association)
Amsterdam B.V. Published under license by
Gordon and Breach Science Publishers SA
Printed in Malaysia

MAGNETIC BISTABILITY AND MEMORY OF CONDUCTION ELECTRONS RELEASED FROM OXYGEN VACANCIES IN GALLIUM OXIDE

D. GOURIER, L. BINET and E. AUBAY

Laboratoire de Chimie Appliquée de l'Etat Solide (URA 1466 CNRS), Ecole Nationale Supérieure de Chimie de Paris, 11, rue Pierre et Marie Curie, 75231 Paris cedex 05 France

Conduction electrons released from oxygen vacancies in gallium oxide exhibit an electron spin resonance (CESR) line with pronounced hysteresis when the magnetic field is swept upward and backward. This memory effect is due to the existence of a bistable nuclear field induced by dynamic nuclear polarization of gallium nuclei. It is shown that this bistability is the consequence of the one-dimensional (1D) character of the band structure of gallium oxide, with the conduction band formed almost exclusively from 4s orbitals of gallium in octahedral sites, forming isolated double chains aligned along the **b**-axis.

Key words: Bistable Conduction Electron Spin Resonance, Gallium oxide, Oxygen vacancies, band structure.

1 INTRODUCTION

Gallium oxide β-Ga_2O_3 is normally an insulating material with a gap of about 4.8 eV. However, single crystals are in general slightly oxygen-deficient, and the resulting doubly compensated oxygen vacancies (F centers) form shallow donors with ionization energy $E_d \approx 0.03-0.04$ eV.[1] Conduction electrons released from these shallow donors exhibit a very narrow CESR line (peak-to-peak linewidth $\Delta B \approx 0.04$ mT). Upon partial saturation, the CESR line exhibits a strong Overhauser shift to low magnetic fields[2] produced by dynamic nuclear polarization (DNP) of gallium nuclei by the Overhauser effect.[3] The most striking feature is that the partially saturated CESR line shows a pronounced hysteresis upon sweeping upward and backward the magnetic field.[2,4] An example is shown in Figure 1. This hysteresis is observable in full temperature range from 4 to 300 K. We have demonstrated that this phenomenon is due to a bistable nuclear polarization, which means that two different stable values of the nuclear field exist for given values of the external control parameters, namely the magnetic field, the microwave frequency and the microwave field. This is the simplest example of bistability with memory effect for a transition within a two-level system (the two levels being the spin states of conduction electrons).

It is however evident that this phenomenon supposes an intimate relation with the electronic structure of β-Ga_2O_3, since such bistability has not yet been observed for other conducting materials. In this paper we show how the conditions required for the occurence of a bistable hysteresis of CESR are met in gallium oxide, from consideration of its band structure.

2 CONDITIONS FOR BISTABLE HYSTERESIS OF CESR

The resonance condition for free electron spins in a conduction band is given by:

$$h\nu = g\beta(B_0 + B_n) \tag{1}$$

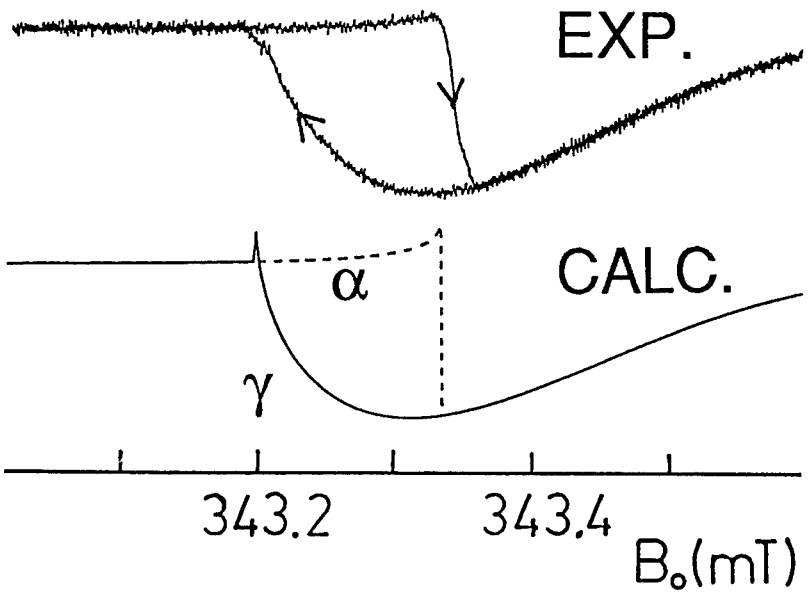

FIGURE 1 Example of experimental (top) and calculated (bottom) bistable magnetic resonance of conduction electrons in a β-Ga_2O_3 single crystal at 150 K and at microwave power $P = 80$ mW (microwave field $B_1 = 0.04$ mT).

where B_0 and B_n are respectively the external magnetic field and the internal field produced by the nuclear polarization. B_n is insignificant at thermal equilibrium at high temperatures ($B_n < 10^{-3}$ mT for $B_0 = 340$ mT). Overhauser[3] has shown that saturation of the CESR line can produce polarization of the nuclear spins which results in a considerable increase of B_n, with a shift of the CESR line known as the Overhauser shift. In β-Ga_2O_3, B_n can reach the value of 0.4 mT at 150K.[4] Since the DNP is obtained from saturation of the CESR line, a complete expression of B_n can only be obtained from a combination of the Overhauser equation for nuclear polarization and of the Bloch equation for saturation:[4,5]

$$B_n = (\Delta B_{o\nu})_{max} \frac{\gamma^2 T_1 T_2 B_1^2}{1 + \gamma^2 T_2^2 (B_n + B_0 - h\nu/g\beta)^2 + \gamma^2 T_1 T_2 B_1^2} \tag{2}$$

where B_1 is the amplitude of the microwave field and $(\Delta B_{o\nu})_{\max}$ is the Overhauser shift of the CESR at maximum saturation (equality of spin state populations). Equation (2) means that B_n is a function of itself, $B_n = f(B_n)$. Figure 2 shows the variation of B_n versus the external field B_0 for β-Ga_2O_3 at different microwave field values. Under sufficiently strong saturation, B_n exhibits an S-shaped curve versus B_0, typical of bistable systems. The two accessible states α and γ are obtained respectively for upward and downward variations of

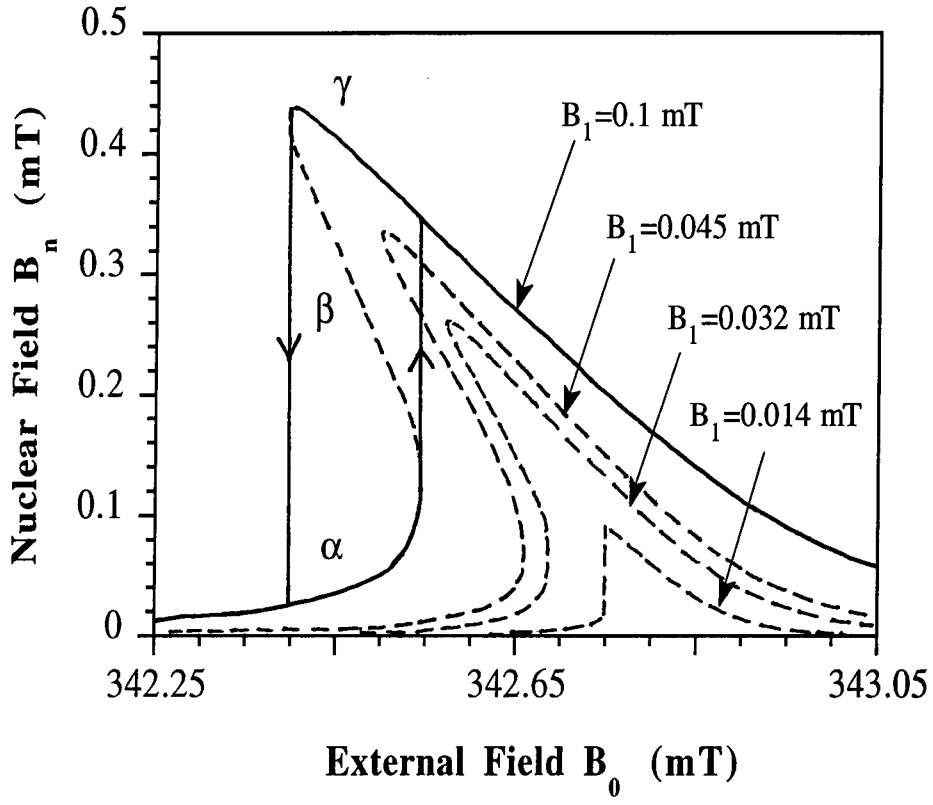

FIGURE 2 Variation of the nuclear field B_n versus the external field B_0 in β-Ga_2O_3 for different values of the microwave field B_1. In bistable regime B_n exhibits two stable states α and γ separated by an unstable state β.

B_0. Substituted in expression (1), this bistability of B_n is responsible for the hysteresis of the CESR line position. With values of T_1 and T_2 usually encountered in conducting materials, equation (2) has only one solution for B_n, and the nuclear field is thus monostable (no hysteresis for the CESR line). However it accepts three solutions if the following condition is satisfied:[6]

$$\frac{I(I+1)NA}{kT} > 6\sqrt{3}\frac{\Delta B}{B_0} \tag{3}$$

where N is the average number of nuclei interacting with each electron spin, A being the isotropic hyperfine interaction with each nucleus. Expression (3) shows that most compounds may exhibit bistability at sufficiently low temperatures and sufficiently high field B_0. This seems to be actually the case for AsGa.[7] However, under moderate

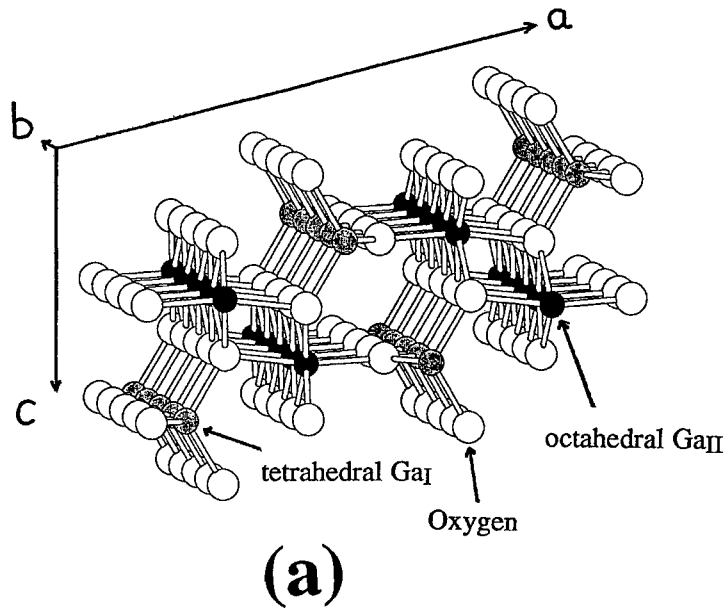

(a)

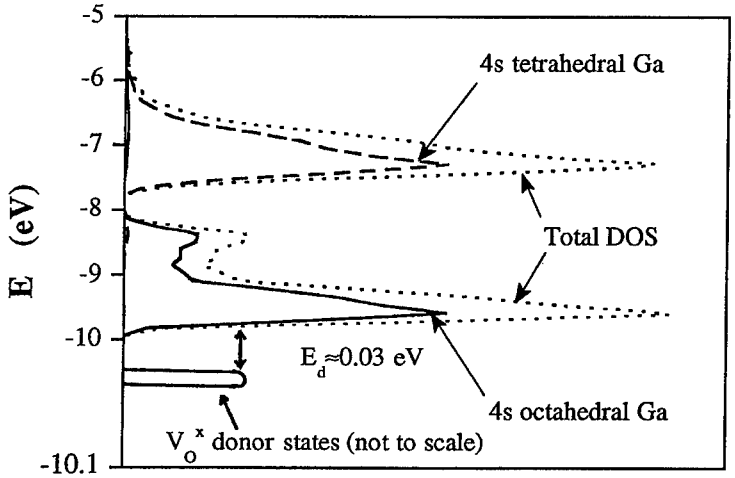

(b)

FIGURE 3 a) Structure of β-Ga_2O_3. b) Density of states (DOS) of the conduction band. Dotted lines: total DOS; dashed line: projected DOS on 4s Ga_I atomic orbitals; full line: projected DOS on 4s Ga_{II} atomic orbitals.

conditions of B_0 (about 340 mT at X band) and temperature (close to RT), inequality (3) is satisfied only if the CESR linewidth ΔB is sufficiently small (-i.e-if T_1 and T_2 are sufficiently long) and if the hyperfine interaction NA is sufficiently high. We show that the peculiar electronic structure of β-Ga_2O_3 makes these two conditions possible.

3 RELATION BETWEEN CESR BISTABILITY AND THE ELECTRON BAND STRUCTURE OF GALLIUM OXIDE

Figure 3 shows the crystallographic structure of β-Ga_2O_3 and the portion of its electronic structure corresponding to the conduction band. The former may be described as an assembly of double chains of octahedral gallium (Ga_{II}) surrounded by six tetrahedral chains (Ga_I), oriented along the crystallographic axis **b**. The band structure was calculated in the crystalline extension of the extended Hückel method. The results show that the conduction band, principally made of 4s orbitals of gallium ions ($\approx 60\%$), is split into two secondary bands. The 4s gallium contribution to the lower sub-band is only due to octahedral Ga_{II} ions, while tetrahedral Ga_I contribute only to the upper sub-band. The other contributions to the conduction band are mainly due to oxygen 2p orbitals. This anisotropic band structure clearly implies that the conduction electrons released from oxygen vacancies move along the octahedral chains, and thus exhibit a quasi one-dimensional behavior, which has an important consequence for the electron spin relaxation time. Assuming an Elliott-Yafet mechanism for the spin relaxation, one obtains:

$$T_1 = T_2 \approx a \frac{|t_{//}|^2}{|t_\perp|^2} \frac{\tau_r}{(\Delta g)^2} \tag{4}$$

where $\tau_r \approx 10^{-14}$ s is the characteristic time for the electronic motion, Δg is the g-shift, a is a constant of the order of unity, and $t_{//}$ and $t_\perp$ are respectively the longitudinal and the transverse transfer integrals. Band structure calculation gives $|t_{//}|^2/|t_\perp|^2 \approx 2 \times 10^5$, which leads to $T_1 \approx T_2 \approx 10^{-6}$ s, while an isotropic band structure would give $T_1 \approx T_2 \approx 10^{-11}$ s. The experimental value for β-Ga_2O_3 is[4] $T_1 \approx T_2 \approx 0.2 \times 10^{-6}$ s, in satisfactory agreement with the calculated one. Moreover, the important gallium 4s contribution to the conduction band edge is responsible for the strong nuclear field induced by DNP. The theoretical hyperfine interaction NA deduced from the orbital composition of the conduction band edge is $NA \approx 5700$ MHz, which is comparable with the experimental value $(NA)\exp = 3020$ MHz. It should be noted that the latter is a lower limit since the apparent hyperfine interaction is reduced if the DNP mechanism is not fully efficient. Comparison of the calculated and experimental values shows that the efficiency of DNP in β-Ga_2O_3 is about 50%, which is a reasonable value. If we report the calculated values of T_1,T_2(proportional to ΔB^{-1}) and NA in expression (3), it can be seen that the inequality is verified, implying a bistable hysteresis for the CESR of β-Ga_2O_3.

4 CONCLUSION

The existence of a bistable hysteresis of the magnetic resonance of conduction electron spins in β-Ga_2O_3, observed even at room temperature, is the direct consequence of the electron band structure of this compound. The latter implies that conduction electrons, which are released from oxygen vacancies acting as shallow donors, move along double

chains of gallium 4s orbitals. The 1D and 4s characters of the conduction band are the primary causes of the bistable nuclear field. It is thus expected that many other compounds are liable to exhibit a bistable CESR.

REFERENCES

1. M. R. Lorenz, J. F. Woods and R. J. Gambino, *J. Phys. Chem. Solids.* **28**, 403 (1967).
2. E. Aubay and D. Gourier, *J. Phys. Chem.* **96**, 5513 (1992).
3. A. Overhauser, *Phys. Rev.* **92**, 411 (1953).
4. E. Aubay and D. Gourier, *Phys. Rev. B.* **47**, 15023 (1993).
5. J. I. Kaplan, *Phys. Rev.* **99**, 1322 (1955).
6. E. Aubay and D. Gourier, *Solid State Commun.* **85**, 821 (1993).
7. M. Dobers, K. v. Klitzing, J. Shneider, G. Weimann and K. Ploog, *Phys. Rev. Lett.* **61**, 1650 (1988).

Radiation Effects and Defects in Solids, 1995, Vol. 134, pp. 229–232
Reprints available directly from the publisher
Photocopying permitted by license only

© 1995 OPA (Overseas Publishers Association)
Amsterdam B.V. Published under license by
Gordon and Breach Science Publishers SA
Printed in Malaysia

SECOND HARMONIC GENERATION AND THERMALLY STIMULATED DEPOLARIZATION CURRENT INVESTIGATION OF $K_{1-x}Li_xTaO_3$

P. VOIGT, S. KAPPHAN, L. OLIVEIRA* and MAXIMO SIU LI*

*FB Physik, University of Osnabrück, D–49069 Osnabrück, Germany; *Dept. de Fisica, USP, Sao Carlos, SP 13560, Brazil*

(Received July 1, 1994)

In the incipient ferroelectric $KTaO_3$ small substitutional Li-ions are known to induce dipolar microgregions due to their off-center dipole moment. A sensitive method to observe the appearance of non-inversion symmetric regions in $K_{1-x}Li_xTaO_3$ is based upon monitoring the second harmonic intensity (SHG) of Nd: YAG laser light. At low temperatures a considerable SHG intensity (calibrated with respect to $LiNbO_3$) is observed with a characteristic temperature-, field- and Li-concentration dependence. The time and temperature dependence of the electric field induced SHG intensity change shows an Arrhenius-like behavior with fast and slow relaxation processes. For concentrations larger that $x \approx 0.02$ the slow relaxation process with an activation energy of $E_A \approx 86$ meV has been interpreted as a reorientation of mainly antiparallel ferroelectric domains. Measurements of the thermally stimulated depolarization current (TSDC), performed after removing the bias field at LHe-temperature, yield for a $x = 0.028$ sample a broad current peak with a maximum at ≈ 60 K. A good fit to the experimental data can be reached for a distribution of relaxing dipoles according to a Havriliak-Negami model with a mean activation energy $\Delta A = 178$ meV. The difference in activation energies will be discussed in terms of different reorientation processes.

Key words: Solid-solid phase transition, $K_{1-x}Li_xTaO_3$, second harmonic generation, thermally stimulated depolarization current.

1 INTRODUCTION

Nominally pure $KTaO_3$ is an incipient ferroelectric, inversion symmetric cubic perovskite. Addition of small substitutional Li-ions is known to induce local polarization in $KTaO_3$ due to the off-center displacement of the Li.[1] The impurity induced low temperature phase transition in $K_{1-x}Li_xTaO_3$ is still controversially discussed either as a ferroelectric transition or in terms of a dipole glass behavior.[2]

Within this work we present time and temperature dependent SHG experiments which reveal many details of the polarization build-up or decay in $K_{1-x}Li_xTaO_3$. Measurements of the thermally stimulated depolarization current (TSDC) give additional information about the dynamics of the phase transition.

2 EXPERIMENTAL PROCEDURE

The $K_{1-x}Li_xTaO_3$ crystals were either grown by H. Hesse ($x = 0.008, 0.016, 0.028$ and 0.043) in the crystal growth laboratory of the University of Osnabrück[3] or by D. Rytz[4] at the University of Lausanne ($x = 0.022$, 0.036 and 0.063). Details of the crystal growth have been reported elsewhere.[3]

A Nd:YAG laser with a peak power of ≈ 10 kW, a pulse width of ≈ 100 nsec (FWHM) and a repetition rate of 1 kHz as fundamental beam is focussed to the sample by a lens with a long focal length ($f_1 = 160$ mm) and the SHG intensity is calibrated with respect to $LiNbO_3$.

The SHG dynamics was investigated by measuring the temporal change of the SHG intensity after switching on and subsequently off of an applied electric field (parallel <100> direction) at constant temperature in the phase transition region. The experimental setup used, is described in more detail in reference.[3,5] The thermally stimulated depolarization current (TSDC) was measured after removing the applied bias field at LHe-temperature. The experimental setup is described in reference.[6]

3 RESULTS AND DISCUSSION

The temperature dependence of the SHG intensity for concentrations $x \leq 0.016$ shows a very gradual increase with decreasing temperature and practically no thermal hysteresis. However, for concentrations $x \geq 0.022$ the SHG intensity reveals a step-like increase at the phase transition and a clearly expressed thermal hysteresis.[7,8,3]

The SHG-Intensity $S_{zzz}(E = 0)$ at zero applied electric field strongly increases with Li-concentration. With applied electric field we find an increase of the SHG intensity $S_{zzz}(E)$ with increasing fields E up to a concentration dependent saturation field E_{sat}. The SHG intensity ratios S^{max}_{zzz} $(E = 0)/S^{max}_{zzz}(E = E_{sat})$ decrease from 250 for $x = 0.008$ to 1 for $x = 0.063$.[8,5] The concentration dependence of the largest value of the field induced SHG intensity $S^{max}_{zzz}(E = E_{sat})$ shows a maximum around $x \approx 0.03$.[5] Corresponding field-induced birefringence ratios $\Delta n^{max}(E)/\Delta n^{max}(0)$[9,10] are more than one order of magnitude smaller. Therefore our SHG intensity results have been interpreted mainly in terms of the reorientation of antiparallel dipolar regions, which are not distinguishable in birefringence measurements. The SHG results yield[5] an estimation of the mean size of dipolar regions $\xi_d(E = 0)$ at $T \leq 20$ K extending from 12 nm ($x = 0.008$) to ≥ 2800 nm ($x = 0.063$).

The appearance of lateral scattering peaks for $x \geq 0.022$ in the spatial distribution of the SHG intensity additionally indicates the existence of antiparallel domains with mean size $\xi_d \geq 0.1$ μm in this concentration range.[5,11]

The variation of S_{zzz} with the polarization direction of the Nd:YAG laser light at low temperature (with $E = 0$) shows an angular periodicity pointing to dipolar regions with tetragonal symmetry. These regions are oriented at an angle of 90° to each other. The ratio of the SHG tensor components[3,5] in all cases turn out to be $(d_{33}/d_{31})^2 = 6.3 \pm 0.6$ and $(d_{31}/d_{15})^2 \approx 1$.

Two examples of the time dependent SHG experiments are shown in Figure 1 for concentrations $x = 0.008$ and 0.022. Plotting the data in a semilogarithmic scale one recognizes for small Li-concentrations ($x \leq 0.016$) a behavior which can be described by a superposition of two exponential processes with time constants τ_1 and τ_2. The time constant τ_1 of the fast process is smaller than that of our instrumentation, and the process can therefore not to be resolved. But the amplitude A of this process can be determined from the intersection with the **abscissa** at $t = 0$ of the straight line in Figure 1A, which is describing the slow process (with amplitude $1 - A$). The amplitude A of the fast process τ_1 vanishes at the phase transition[5] and can therefore be interpreted as the reorientation of weakly correlated Li-ions.

The slow process has been measured in detail in its temperature dependence (Figure 2) and turned out to be Arrhenius-like $\tau_2(T) = \tau_0 \exp(E_A/k_BT)$ with an activation energy E_A increasing with concentration x ($E_A = 170$ K for $x = 0.008$, $E_A = 810$ K for $x = 0.016$ and $E_A = 1000$ K for $x = 0.022$ and $x = 0.036$). For the two highest doped samples the field-induced change of the SHG intensity becomes very small ($x = 0.043$) or vanishes completely ($x = 0.063$) and therefore no values for E_A and the attempt frequency τ_0 could be determined. Comparing the τ_2 process with the τ_1 process and the dielectric results for the Li-reorientation[12,13] this process can be interpreted as the reorientation of strongly correlated Li-ions.

The temperature dependence of the thermally stimulated depolarization current (TSDC), performed after removing the bias field at LHe-temperature, is shown for a

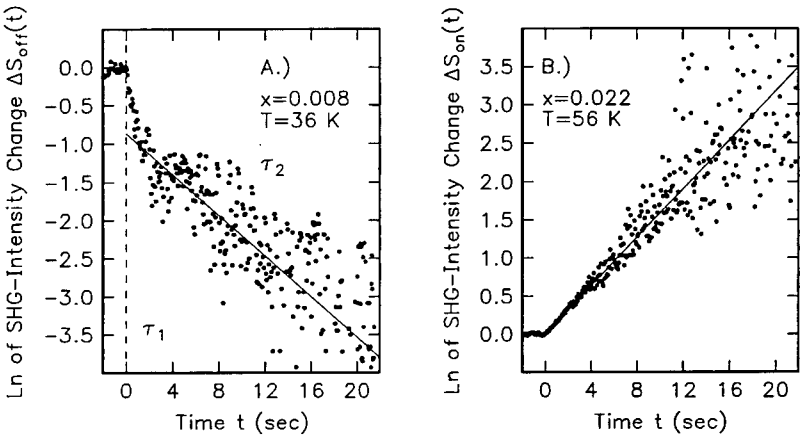

FIGURE 1 A.) Time dependence of the integral SHG intensity in $K_{1-x}Li_xTaO_3$ after fast switching off ($E \rightarrow 0$) of an electric field $E = 200$ kV/m > E_{sat} at T = 36 K for $x = 0.008$. Intensity is plotted in a logarithmic scale. The dashed line indicates the fast process with τ_1 and amplitude $A = 0.58$ and the solid line the slow process with τ_2 = 7.5 sec and amplitude 1–A = 0.42. B.) Time dependence of the integral SHG intensity in $K_{1-x}Li_xTaO_3$ after fast switching on ($0 \rightarrow E$) of an electric field $E = 200$ kV/m > E_{sat} at $T = 56$ K for $x = 0.022$. Intensity is plotted in a logarithmic scale. The solid line is the slow process with $\tau_2 = 6.3$ sec. The scattering of the data appears to be connected with both, probing a particular volume of the sample with the laser beam and domain boundaries passing through the laser beam focus.

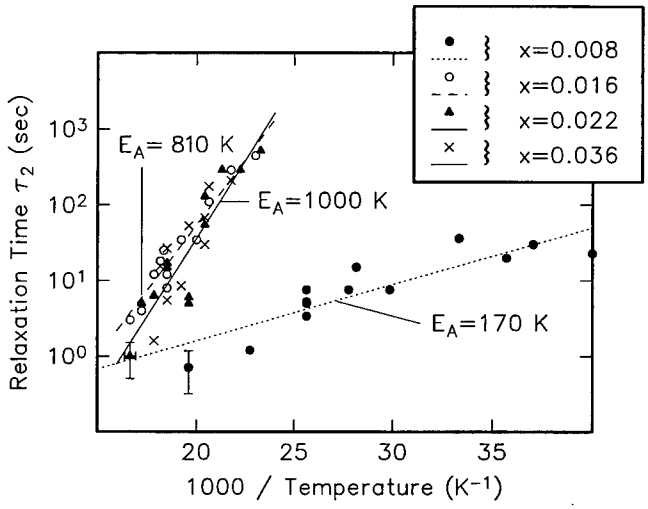

FIGURE 2 Temperature dependence of the relaxation time τ_2 of the slow process in $K_{1-x}Li_xTaO_3$ for $x = 0.008$, 0.016, 0.022 and 0.036 for an applied electric field $E = 200$ kV/m > E_{sat}.

concentration $x = 0.028$ in Figure 3. A broad current peak is obtained with a maximum at ≈ 60 K. A good fit to the experimental data can be reached for a distribution of relaxing dipoles according to a Havriliak-Negami model[14] with a mean activation energy ΔA = 178 meV. The value of ΔA is about two times larger than the E_A value of the SHG experiments in this concentration range. Possible explanations may be that the TSDC experiment is more sensitive to the reorientation of larger, e.g. 90°-domains or that the

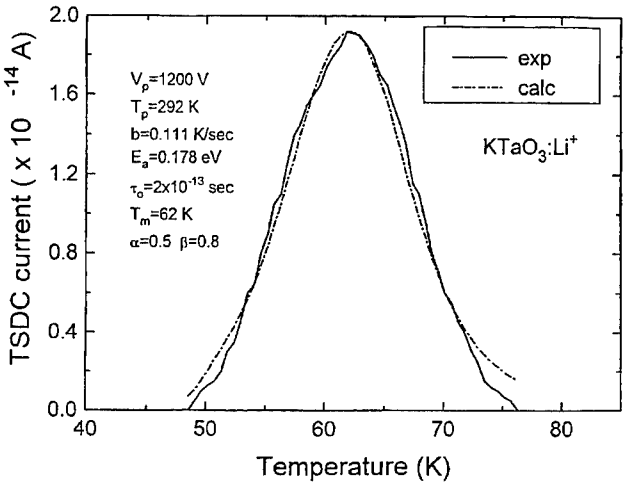

FIGURE 3 Temperature dependence of the thermally stimulated depolarization current (TSDC) for a $K_{1-x}Li_xTaO_3$ sample with $x = 0.028$. The experimental data are presented as solid line. The dashed line represents a fit according to a Havriliak-Negami model[14] with the fit parameters indicated. The thickness of the sample is about 3 mm.

above Havriliak-Negami distribution does not take into account the spontaneous polarization due to long range dipolar interaction.

The nature of the phase transition in $K_{1-x}Li_xTaO_3$ appears to be dominated by the temperature dependence of two dynamic processes associated with the Li-ions in a statistical distribution. For $x \leq 0.016$ the transition is dipole glass-like, mainly characterized by the slowing down of the reorientation of weakly correlated Li-ions. For $x \geq 0.022$ the transition is dominated by the reorientation of strongly correlated Li-ions.

ACKNOWLEDGEMENTS

This work was supported by the Deutsche Forschungsgemeinschaft (Graduiertenkolleg "Mikrostruktur Oxidischer Kristalle" und SFB 225). We are grateful to D.Rytz and H. Hesse for providing samples of $K_{1-x}Li_xTaO_3$ crystals.

REFERENCES

1. Y. Yacoby and A. Linz, *Phys. Rev.* **B9**, 2723 (1974).
2. U. T. Höchli, K. Knorr, and A. Loidl, *Adv. Phys.* **39**, 405 (1990).
3. P. Voigt, H. Hesse, and S. Kapphan, (G. Schmidt and G. Sorge, Ed.), *Proceed. 20th Spring Conf. Ferroelectr., Güntersberge (1992)*, 24, FB Physik Univ. Halle-Wittenberg, Germany (1992).
4. J. J. van der Klink and D. Rytz, *J. Cryst. Growth* **56**, 673 (1982).
5. P. Voigt and S. Kapphan, *J. Phys. Chem. Solids*, Vol. **55,** No. 9, 853-869 (1994)
6. M. Siu Li, M. de Souza, and S. E. Kapphan, *Phys. Stat. Sol.* **112**, 685 (1982).
7. P. Voigt, K. Betzler, N. Schmidt, and S. Kapphan, *Ferroelectrics* **106**, 149 (1990).
8. P. Voigt and S. Kapphan, *Ferroelectrics* **124**, 243 (1991).
9. W. Kleemann, S. Kütz, and D. Rytz, *Europhys. Lett.* **4**, 239 (1987).
10. W. Kleemann, S. Kütz, F. J. Schäfer, and D. Rytz, *Phys. Rev.* **B37**, 5856 (1988).
11. P. Voigt and S. Kapphan, Proceed. IMF 8 Gaithersburg, USA (1993), to be publ. in *Ferroelectrics* (1994).
12. U. T. Höchli and M. Maglione, J. Phys.: Condens. *Matter* **1**, 2241 (1989).
13. F. Wickenhöfer, W. Kleemann, and D. Rytz, *Ferroelectrics* **124**, 237 (1991).
14. J. Vanderschueren and J. Gasiot, (P. Bräunlich, Ed.), *Thermally Stimulated Relaxation in Solids*, 135, Springer, Heidelberg (1979).

Radiation Effects and Defects in Solids, 1995, Vol. 134, pp. 233–237
Reprints available directly from the publisher
Photocopying permitted by license only

© 1995 OPA (Overseas Publishers Association)
Amsterdam B.V. Published under license by
Gordon and Breach Science Publishers SA
Printed in Malaysia

INFLUENCE OF YTTRIUM AND OF THE OXYGEN PRESSURE ON α ALUMINA MICROSTRUCTURE. RELATION WITH MECHANICAL PROPERTIES

M. K. LOUDJANI, C. HAUT and S. PARISOT

Laboratoire de Métallurgie Structurale, CNRS URA 1107, Univ. Paris Sud, 91405 Orsay

The influence of yttrium doping on the alumina microstructure is correlated to the Y amount and to the oxygen pressure. A low oxygen pressure promotes the solubility of yttrium in the bulk, its segregation in grain boundaries and increases the alumina toughness. Moreover alumina grain growth is limited either by garnet precipitation or by yttrium segregation along boundaries.

Key words: α-alumina, yttrium doping, microstructure, toughness, oxygen pressure.

1 INTRODUCTION

The objective of this work is to point out the mechanisms by which yttrium can modify the polycrystalline α alumina microstructure and toughness according to the doping element amount and to the oxygen pressure. Such a study was mainly performed by scanning electron microscopy (SEM, equiped with an Energy Dispersive X-ray Spectrometry) associated to image analyses and by indentation.

2 MATERIAL ELABORATION AND EXPERIMENTAL PROCEDURE

Mixed powders doped with 1%, 0.1% and 0.03% mol Y_2O_3 were prepared by a wet mixing in an yttrium nitride solution [1]. The sintering was performed under an uniaxial load of 45 MPa at 1550°C, in vacuum, in a graphite crucible at a pO_2 equal to $\approx 10^{-13}$ atm [2] (by P. Carry, E. P. F. Lausanne). Sintered samples were heat-treated at either 1650°C or 1400°C, in air or in a reducing atmosphere (in graphite crucible) for times varying between 15 mn to 72 h, then cooled at $\approx 20°/mn$. The microstructural observations by SEM and the following image analyses were performed on the surface of the samples by back-scattered electrons. Electronic images were transformed in binary images, transferred and treated on a computer. It was verified that the microstructure at the surface was similar to that in the core of the samples (fracture observations).

The toughness measurements [3–6] were made with a Vickers diamond indenter, the toughness (K) is defined by: $\boxed{K = 0.014\left(\frac{E}{H_v}\right)^{1/2}\frac{P}{c^{3/2}}}$, with (2c) the radial crack length, suppress P the applied load (m = 1 kg), E the Young modulus of alumina ($E \approx 400$ MPa) and Hv the hardness.

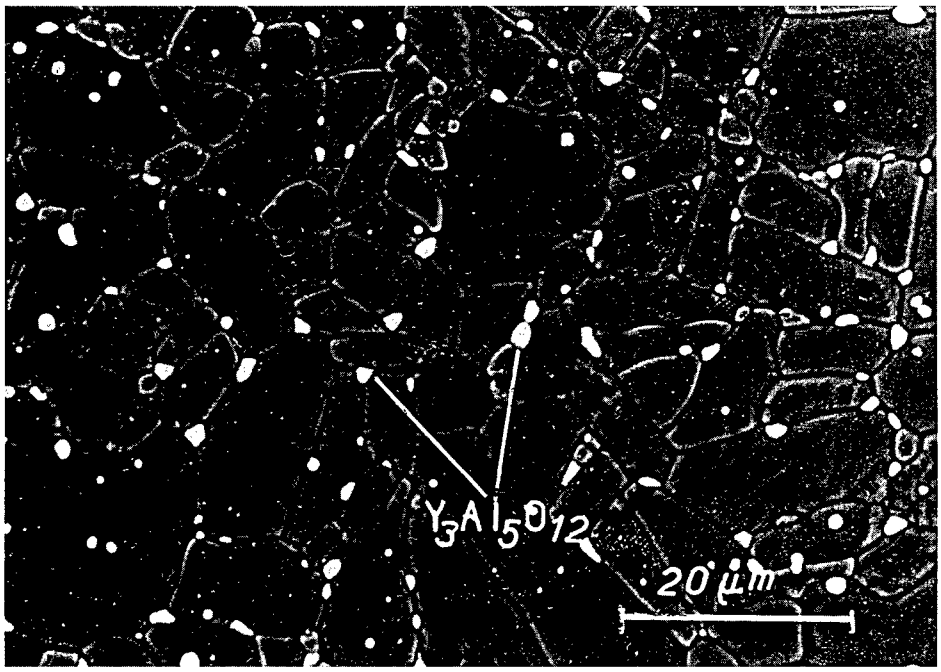

FIGURE 1 Microstructure of alumina doped samples heat-treated for 24 hours at 1650°C. White particules consist in $Y_3Al_5O_{12}$ (arrow), average size: 1.8–2.6 μm
FIGURE 1(a) 1% mol. Y_2O_3 doped sample treated in air atmosphere.

3 RESULTS

3.1 *SEM observations*

3.1.1 *Samples heat-treated in air* (Figure 1a): In case of the highly doped sample (1% mol. Y_2O_3), the grain size and the distribution of the second phase $Y_3Al_5O_{12}$ are homogeneous as previously analysed by STEM [7–8]. Abnormal grain growth is not observed when it is the case on the sample doped with 0.03% mol. Y_2O_3(Figure 1b). Image analyses performed with a population of about 1300 grains indicate that the grain size is bimodal: a lot of grains have a diameter included between 1 et 5 μm and the diameter of the other grain population can reach 140 μm. Moreover, on all samples, whatever the doping amount, $Y_3Al_5O_{12}$ precipitates are observed at the surface, and, the longer the heat-treatment duration, the greater the amount of the garnet precipitates at the surface. In the case of highly doped samples, the grain growth is limited by the precipitation of the $Y_3Al_5O_{12}$ phase along alumina grain boundaries.

3.1.2 *Samples heat-treated in CO/CO_2*: for the sample doped with 0.03% mol. Y_2O_3, it is then observed (Figure 1c) that the grain size is fairly homogeneous when compared to the same sample treated in air (Figure lb). Most of the grains have a size included between 4 et 15 μm. Besides, the amount of $Y_3Al_5O_{12}$ precipitates at the surface is much smaller than for the same sample treated in air. These observations are similar to those performed on as-sintered samples.

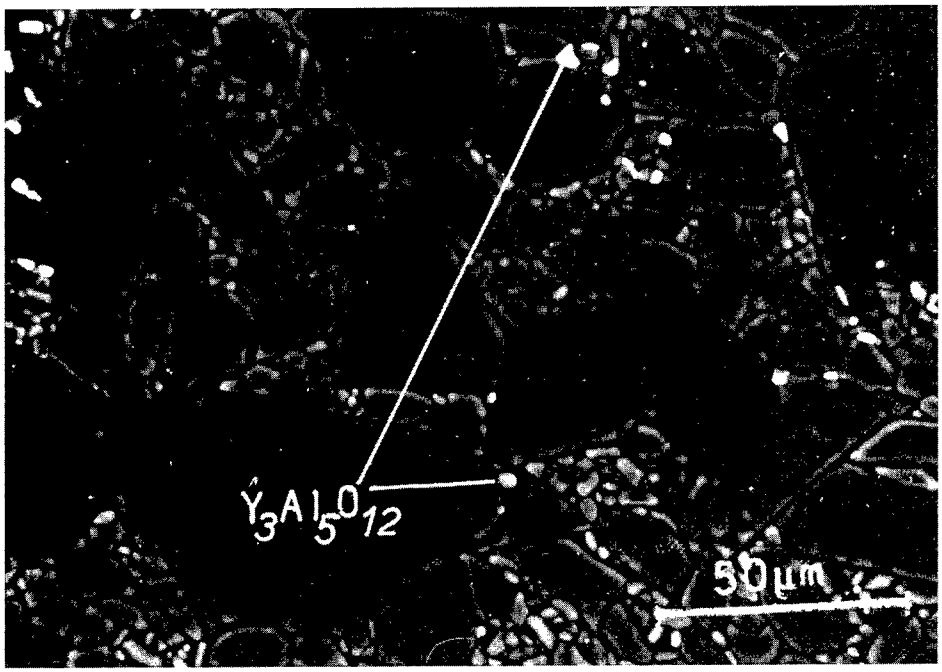

FIGURE 1(b) 0.03% mol. Y_2O_3 doped sample treated in air atmosphere.

3.2 *Toughness Measurements by Indentation*

The variation of the toughness on as sintered samples, i.e. treated in a low oxygen pressure, versus the yttrium amount is shown in Figure 2. As usually observed with ceramics, a great scattering in the values appears and the average value for each sample was also plotted (dashed line). Then, a slight increase of the toughness is obtained for the sample doped with 0.03% mol. Y_2O_3 whatever the heat treatment (as sintered, treated in air).

4 DISCUSSION AND CONCLUSION

In order to explain the effects of the oxygen pressure and of the yttrium doping on the alumina microstructure, it is necessary to come back to previous results. By STEM on thin foils of as sintered alumina doped with 0.03% mol. Y_2O_3 [7–8], it was shown that yttrium segregates along grain boundaries with an average relative concentration equal to $\frac{c_{gb}}{c_B} \approx 50$ (c_B and c_{gb} being the average atomic yttrium concentration in the bulk and along grain boundaries respectively). In this case, $Y_3Al_5O_{12}$ precipitates are observed neither in the bulk nor in grain boundaries.

Besides, EXAFS analyses of the local disorder around yttrium in the alumina lattice [7–9] have shown that, due to the great size of yttrium ions compared to that of aluminum ions, yttrium ions in solid solution (on the cationic sub-lattice) induce distorsions in the anionic sub-lattice: it generates oxygen vacancies as first neighbouring and oxygen

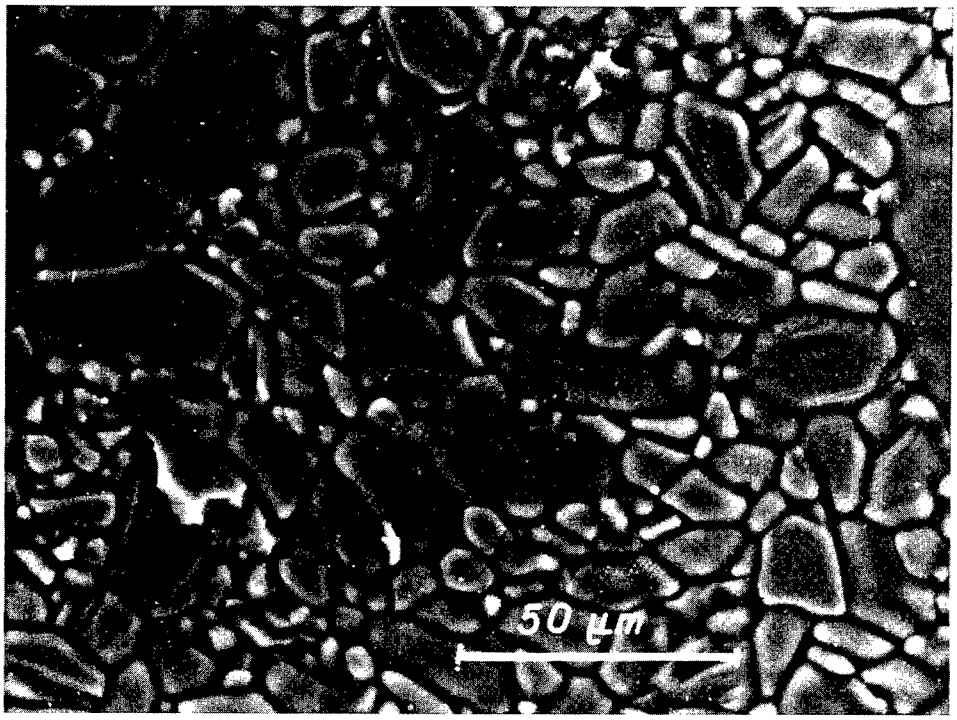

FIGURE 1(c) 0.03% mol. Y_2O_3 doped sample treated in carbon graphite crucible.

interstitials in a second shell, which means that defect complexes are created as it follows: $3O_O^x + 2Y_{Al}^x \leftrightarrow (2Y_{Al}^x + mV_O^{\bullet\bullet} + n\,O_i'')^{2(m-n)\bullet} + \frac{3-n}{2}O_2 + 2(m-n)e'$ with $m > n$ and $m \leq 3$ [7–9]. Such a reaction is promoted at low oxygen pressure as, in this case, the predominant defect is the oxygen vacancy ($V_O^{\bullet\bullet}$) (with $[V_O^{\bullet\bullet}] \propto (p_{O_2})^{-1/6}$). After an heat-treatment in air, STEM analyses did not allow to detect any yttrium neither in the bulk nor along grain boundaries. This indicates that, in air, the yttrium enrichment towards the alumina outer surface is mainly due to the oxygen chemical potential gradient defect between the core of the material and its surface. The driving force is given by $F_C \propto kT\frac{\Delta C}{C}$ [10]. Another driving force could be related to a temperature gradient [11, 12], induced during cooling between the outer surface and the core, which would be given by: $F_T \propto -\Delta H_f \frac{\Delta T}{T}$. In our case, the yttrogarnet enrichment at the outer surface is mainly due to an equilibrium segregation phenomenon. Thus, it appears that yttrium solubility in alumina (in the bulk and along grain boundaries) increases when the oxygen pressure decreases. The alumina grain growth is limited by the yttrium segregation along grain boundaries (or the garnet precipitation for the highly doped material). Toughness measurements indicate that yttrium in solid solution associated to defect complexes $(Y_{Al}^x + m\,V_O^{\bullet\bullet} + n\,O_i'')^{2(m-n)\bullet}$ or segregated along grain boundaries slightly increase the alumina toughness when compared to materials for which yttrium is precipitated as a garnet $Y_3Al_5O_{12}$ phase (highly doped alumina or heat-treatment in air).

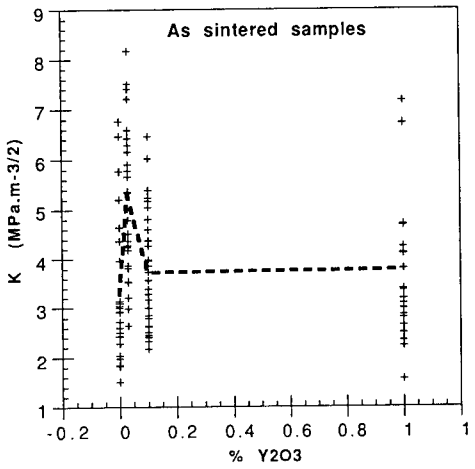

FIGURE 2 Toughness measurements on undoped and Y_2O_3 doped as sintered aluminas.

ACKNOWLEDGEMENT

The authors are indebted to A. M. Huntz and P. Carry for fruitful discussion and to P. Carry for providing hot sintered materials.

REFERENCES

1. M. K. Loudjani, B. Lesage, A. M. Huntz, *L'Industrie Céramique*, n°801, 53 (1986).
2. J. D. Fridez, *Thèse de doctorat*, E. P. F. Lausanne (1986).
3. A. G. Evans and E. A. Charles, *J. Am. Ceram. Soc.* **59**, (1976), 7.
4. B. R. Lawn and A. G. Evans, *J. Am. Ceram. Soc.* **63**, N°9–10, (1980), 574.
5. R. F. Cook and G. M. Pharr, *J. Am. Ceram. Soc.* **73** [4] (1990) 787.
6. P. Laval and E. Felder, *Mat. et Téch*, N° 1–2–3, (1993) 93.
7. M. K. Loudjani, A. M. Huntz, R. Cortès, *J. of Material Science* **28** (1993) 6466.
8. M. K. Loudjani, *Thèse d'Etat es-Sciences Orsay* (1992) France.
9. M. K. Loudjani, R. Cortès, *J. Eur. Ceram. Soc.* **14** (1994) 67.
10. W. C. Mackrodt, *Adv. in Ceramics*, Vol. 23, 247, (1987).
11. G. Petot-Ervas, C. Petot, *J. Phys. Chem. Solids*, Vol. **51**, 901, (1990).
12. D. Bouchet, F. Dupau, S. Korinek, *Mic. Mic. Mic*, N°4, **561**, (1993).

Radiation Effects and Defects in Solids, 1995, Vol. 134, pp. 239–242
Reprints available directly from the publisher
Photocopying permitted by license only

© 1995 OPA (Overseas Publishers Association)
Amsterdam B.V. Published under license by
Gordon and Breach Science Publishers SA
Printed in Malaysia

THE GIGANTIC IONS OF CHROMIUM IN RUBY

V. I. FLEROV* and A. V. FLEROV**

**Nuclear Research Center, Latvian Academy of Sciences, Salaspils-1, LV-2169 Latvia; **Institute of Physics, Latvian Academy of Sciences, Salaspils-l, LV-2169 Latvia*

The experimental data on photoconductivity, X-ray luminescence, thermoluminescence, and optical absorption of corundum single crystals doped with chromium testify to the existence of gigantic ions of chromium in corundum lattice.

Key words: gigantic ions, photoconductivity, thermoluminescence, X-ray luminescence, optical absorption, ruby.

1 INTRODUCTION

Experimental data on photoconductivity of ruby crystals, 1.) the unexpected low (unexponential) concentration dependence of transverse photocurrent $j_\perp$ in external field $\mathbf{E}\perp\mathbf{C}$[1], 2.) very high speed of photoinduced charge transfer $1/\tau \geq 10^5$ s^{-1} and its independence on temperature up to 180 K[2], allowed Prof. Vikhnin to make the assumption about existence of an unusual state of chromium ions, named Big Radius State (BRS),[3] in ruby crystals.

Experimental results on X-ray luminescence, thermoluminescence (TL) and optical absorption confirm this assumption.

1.1 *Luminescence*

X-ray luminescence spectra of sapphire crystals contain a wide composite band in UV-region extended from 5 to 3 eV and band in red region that is due to chromium ions, which always is present as impurity in sapphire crystals (Figure l). The increase of chromium contents up to sufficiently low concentration of about 0.01 weight % sharply changes the appearance of luminescence spectrum. The intensity of chromium band increases and UV-band disappears completely, and it is not induced even under irradiation by high-energetic electrons (5 MeV) and in a high-current accelerator of electrons at electron energy 300 keV at current 1000 A in impulse (Figure 1).

1.2 *Thermoluminescence*

The heating of sapphire crystal (irradiated at room temperature) from 300 to 700 K **arises** from 4 to 7 TL glow peaks, depending on crystal quality. The most high-temperature TL glow peak at 630 K is due to chromium impurity. It should be emphasized, that TL glow curves appear to have a strong dependence on crystal origin. It varies for crystals grown in different redox atmosphere[4] and depends on growth technique more than on quality of used charge.[5,6]

The most **intense** TL is observed from crystals grown by Verneuils method.[5,6] Ruby crystals are usually grown by Verneuils method, therefore they have characteristics of a large TL spectrum. However, the intensity of non-chromium, low-temperature TL peaks decreases **as** the increase of chromium concentration. Only one high-temperature TL peak caused by chromium remains in the laser crystal (concentration 0.034 % Cr), as is shown

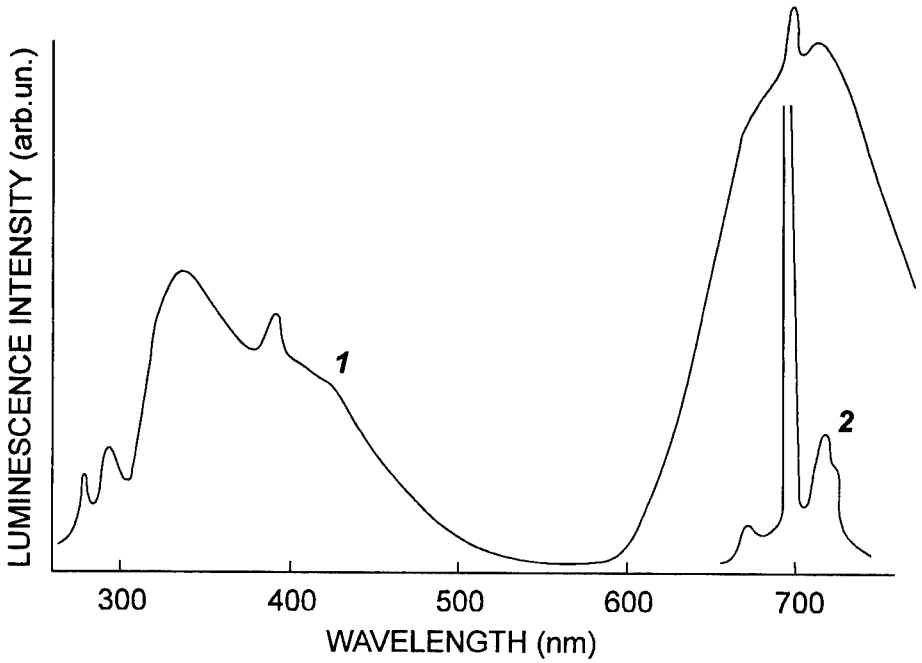

FIGURE 1 X-luminescence spectra of sapphire (1) and ruby (2) crystals.

in Figure 2. This TL peak, contrary to all known peaks[4,7] shifts to low temperatures approximately on 50–80 K as the dose increases. The peak intensity has an extreme nature with Cr concentration. The highest peak occurs at 0.02% Cr then decreases to zero at 0.2% Cr.[8,9]

1.3 *Optical Absorption*

Irradiation of ruby crystals creates Cr^{2+} and Cr^{4+} centers that cause the appearance of additional absorption, which spectrum, after irradiation of the crystal with high-energy electrons at a fluency of 10^{13} cm^{-2}, generally coincides with that reported in ref.[10,11] Absorption bands at 468 nm (2.64 eV) and 230 nm (5.4 eV) are ascribed to Cr^{2+} ions.[12] All bands are saturated at dose 10^5 Gy and are totally annealed at temperature 700 K.

It is worth noting for the aim of our work the behavior of additional absorption of crystals with different chromium concentration. Bessonova *et al.*[8] have shown the dependence of absorption coefficient under X-ray irradiation on chromium concentration, that has an extreme nature with maximum at 0.04 weight %.

In the same paper, the dependence of absorption coefficient at 2.65 eV of photon energy, during and after X-ray irradiation, is shown for crystals with concentration 0.005 and 0.115 weight %. In the first case, the coloration remains constant for an indefinitely long time after irradiation termination and in the second one, the crystal is decolored rapidly. The additional absorption does not appear totally at chromium concentration 0.2 weight %, which is similar to TL response at such concentration.

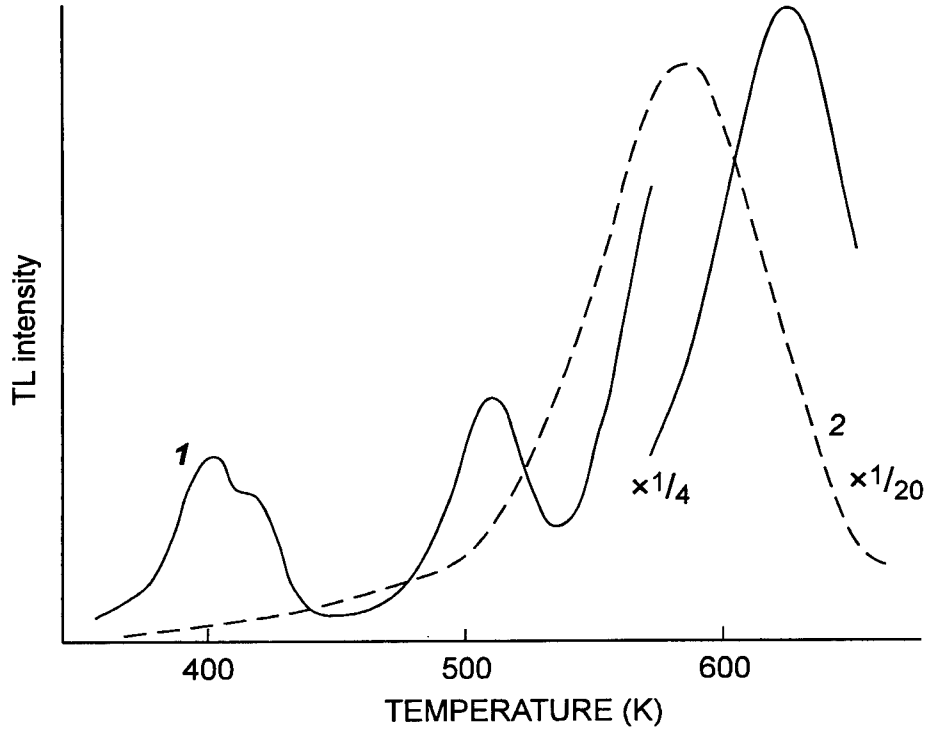

FIGURE 2 TL glow curves for corundum crystals with 0.001 weight % Cr (1) and 0.034 weight % Cr subjected to 1 min irradiation in electron accelerator.

2 DISCUSSION

All experimental data mentioned above can be explained most naturally by the existence of a chromium ion state with a big capture radius of charge carriers.

A sufficiently low concentration, chromium ions **trap** all free charge carriers **induced** under irradiation. Therefore, all recombination processes with the emission of light occur only with chromium ions, that is why we observe only a red emission of chromium ions. This does not occur with other impurities. At the presence Ti, Sc, Mg, Mn, and other impurities in a crystal with the concentration of about 0.1 weight %, i.e. at least on the order of magnitude greater than in the case of chromium, the intrinsic emission of impurity ions appear, as well as the emission intrinsic to undoped corundum, and the chromium emission in the red region of the spectrum and the structural defects in the uv-region remain.

This phenomenon becomes most apparent in the experiment reported by Bessonova and Akulenok.[13] The chromium impurity at different concentrations has been introduced into corundum crystal that contained 0.05 weight % Ti. It is known that titanium ions are responsible for blue luminescence with the maximum at 2.9 eV.[14] The blue luminescence is almost suppressed already at chromium concentration 0.01 weight %, i.e., much less than titanium concentration.

From the point of view of a big radius state of chromium ions, the experimental results on TL and optical absorption are explained by the most organically way.

A part of free charge carriers captured by chromium ions increases, and those which are trapped by other defects decreases as chromium concentration increases. At certain sufficiently low chromium concentration, chromium ions overlap all volume of crystal and TL glow peaks caused by other defects disappear.

The big radius chromium ions created during irradiation can move through crystal by hopping at chromium concentration 0.1 weight %, and can meet a chromium ion of contrary charge and recombine with them. The additional absorption decreases after irradiation termination, and for some time, disappears totally. At concentration 0.2 weight % Cr, the recombination already occurs very intensively during irradiation process and additional absorption does not appear and it concerns also to TL response absence at such concentration of chromium.

The wave functions overlapping of both BRS and Cr^{3+} ions have no place in crystal with small Cr concentration so the hopping diffusion is suppressed and additional absorption remains for a long time.

Thus, under irradiation of ruby crystal with ionizing radiation the uncommon big chromium ions are created that can relax in basic state or move through the lattice by a hopping diffusion for a sufficiently long lifetime.

Preliminary estimations of BRS radius have a value of approximately 5.0 nm, i.e., the BRS size is two orders of magnitude greater than Bohr radius.

This state has probably a positive charge with respect to the lattice.

REFERENCES

1. A. A. Kaplyanskii, S. A. Basun, S. P. Feofilov, *J. Luminescence* **38**, 120 (1987).
2. S. A. Basun, A. A. Kaplyanskii, S. P. Feofilov, *Sol. St. Physics* **29**, 1284 (1987).
3. V. S. Vikhnin, *Sol. St. Physics* **1, No 11**, 149 (1989).
4. G. P. Summers, *Rad. Prot. Dos.* **8**, 69 (1984).
5. V. I. Flerov, A. V. Flerov. In: *10th Int. Con. in Sol. St. Dosimetry Washington, July 1992, p. 52.*
6. V. I. Flerov and A. V. Flerov, *Kristallografiya* **38**, 222 (1993).
7. V. I. Flerov and A. V. Flerov, *Optika I spektroskopiya* **73**, 542 (1992).
8. T. S. Bessonova. M. P. Stanislavskii, V. I. Tumanov, V. Ya. Haimov-Malkov, *J. prikladnoi spektroskopii* **27**, 238 (1977).
9. T. I. Voicenya, V. T. Gricina, A. V. Sicora, *Ukrainskii fizicheskii j.* **32**, 1042 (1987).
10. T. S. Bessonova, M. P. Stanislavskii, V. I. Tumanov, V. Ya. Haimov-Malkov, *Optika i spectroskopiya* **37**, 701 (1974).
11. N. A. Kulagin, O. T. Sviridov, *J. Phys.* **C17**, 4539 (1984).
12. N. Maruyama, Y. Matsuda, *J. Phys. Soc. Jap.* **19**, 1096 (1964).
13. T. S. Bessonova, E. M. Akulenok, *J. prikladnoi spektroskopii* **43**, 471 (1985).
14. A. Lupei, V. Lupei, C. Ionescu *et al.*, *Optics Communications* **59**, 36 (1986).

Radiation Effects and Defects in Solids, 1995, Vol. 134, pp. 243–245
Reprints available directly from the publisher
Photocopying permitted by license only

© 1995 OPA (Overseas Publishers Association)
Amsterdam B.V. Published under license by
Gordon and Breach Science Publishers SA
Printed in Malaysia

THE SHORT LIFE-TIME DEFECT FORMATION IN α- Al_2O_3 UNDER THE SYNCHROTRON RADIATION

V. V. HARUTUNYAN[a], A. N. BELSKY[b], V. A. GEVORKYON[a], V. V. MIKHAILIN[b], G. N. YERITSIAN[a]

[a]*Yerevan Physics Institute, Alikhanian Brs. 2, Yerevan, Armenia;* [b]*Moscow State University, 117234, Moscow, Russia*

(Received July 1, 1994)

The luminescence excitation spectra of α-Al_2O_3 were measured in the spectral range from 400 to 640 nm.

Immediate luminescence spectra are superposition of different spectral regions with the centre of gravity on the wavelengths 450, 480, 550 nm and intensive region with maximum at 620 nm.

The obtained spectra were analized and several assumptions are proposed for explanation the nature of short life-time structural defect formation in α-Al_2O_3 under SR irradiation.

Charge carriers absorption accompanied by their luminescence is observed in α-Al_2O_3 exposed to a beam of KeV electrons (with an energy less than the threshold energy of E_d ~ 0.45 MeV) with heavy current and picosecond pulses.[1,2]

The present report considers the study of the nature of short life-time defect formation in α-Al_2O_3 under picosecond X-ray SR.

The study of α-Al_2O_3 luminescence spectral characteristics is carried out on the SR channel of VEPP-3 storage ring. The corundum crystals grown by the horizontally oriented crystallization method are excited by a SR 'white' beam in the energy region from 0.124 to 124 KeV with T = 100 ps pulses.

The kinetics of the rising and decay of SR luminescence (SRL) is shown in Figure 1 where one can see a compound character of the luminescence spectrum. At first a weak

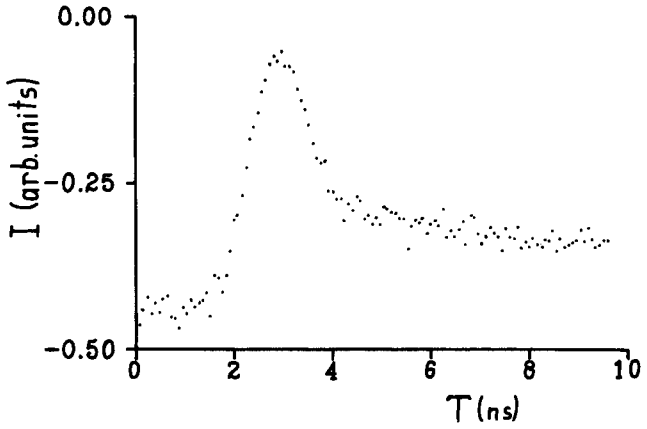

FIGURE 1 Luminescence excitation in α-Al_2O_3 using the SR.

part is observed which is either the 'tail' of the exciting impulse or the ultrafast component with a duration of less than 0.5 ns. Further, one can observe an intensive increase of SRL, this being in a good agreement with the law of $n = n_o.\ (1-\exp(-t/\tau_1))$, where $\tau_1 = 0.4$ ns. After that the intensity falls down according to $n = n_o.\ \exp(-t/\tau_2)$, where $\tau_2 = 1.2$ ns and long time luminescence ($\tau_3 > 6$ ns) occurs.

As shown in Figure 2a, the spectrum of SRL consists of a clearly observed maximum of 620 nm, a wide-band range with its centre of gravity at 550 nm and an intensive luminescence at the blue and ultraviolet regions. Besides, weakly expressed regions of 475, 500 and 500–530 nm are revealed in the spectrum.

In $\tau = 41$ ns the immediate spectrum is changed, i.e. the band of 472 nm almost disappears and the wide-band maximum is relaxed. After a time interval of 82 ns one can see a maximum only at 620 nm and in the region with the centre of gravity at 400 nm, what has been observed by us at 77 K (zero phonon line at 395 nm with phonon reiterations).

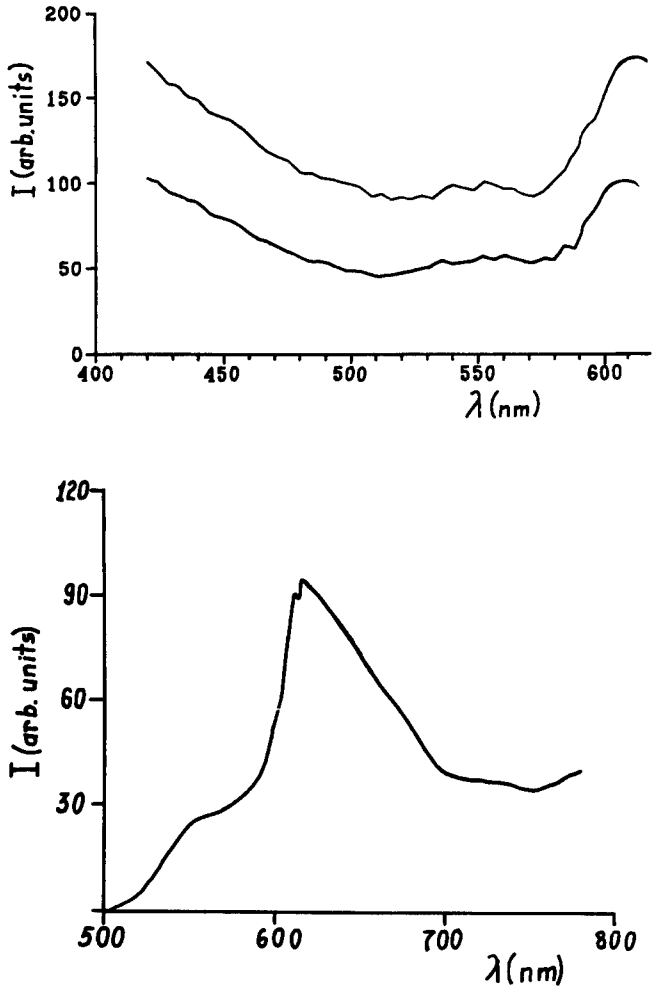

FIGURE 2 a) The kinetics of the decay of immediate luminescence spectra in α-Al_2O_3. b) The photoluminescence spectrum of α-Al_2O_3 irradiated by electrons with dose 3×10^{18} e/cm^2 ($\lambda_{exc} = 450$ nm).

It should be noted that in the photoluminescence spectrum the bands of 550 and 620 nm appear at continuous irradiation by 50 MeV electrons and 2 MeV neutrons (Fig. 2b), as well as at a pulsed SR excitation.

We offer the following mechanisms to interprete the results obtained:

1. the SR quanta intensively induce free thermal carriers such as electrons and holes from the depth of the zone. It is known that the thermal electron's life time is about 10^{-11}–10^{-10}s[2] what is two orders of magnitude less than the observed time of decay (Fig. 1). As far as the exponential decay law is characterized as a first-order kinetics, the number of the carriers with like sign, thermalized off the zone is much smaller because of different location of the conduction band minimum and the valence band maximum.[2]
2. another channel of carriers localization can be the growth defects, point F–, F^+–, F^{2+}–, V-centres[3] and [Al_iF]-type complex centres. These centres capture the carriers and disturb their balance.
3. at irradiation with SR quanta of KeV energies, there can take place an underthreshold defect formation in α-Al_2O_3. The hypothesis of Indenbom,[4] i.e. 'radiation shaking', can be successfully applied to the theory of defect formation in α-Al_2O_3. We assume that the high-intensity SR irradiation leads to elastic wave formation due to interaction of SR quanta with the corundum lattice. As a result of the elastic wave reflection from the atom sites and their meeting with the forward wave, a standing-wave-type interference occurs, which is able to kick out the ions from the sites, forming the short-lived excited Frenkel pairs. The life-time of these pairs depend on the impurity concentration and growth defects.

REFERENCES

1. R. G. Deich, *Fiz. Tverd. Tela (Russia)* **30**, 25 (1988).
2. E. D. Aluker, V. V. Gavrilov, A. M. Sytdikov, S. A. Chernov, *Fiz. Tverd. Tela (Russia)* **29**, 1470 (1987).
3. R. R. Atabekyan, R. K. Ezoyan, V. A. Gevorkyan and V. L. Vinetsky, *Cryst. Latt. Def. and Amorph.* **14**, 155 (1987).
4. V. M. Indenbom. *Pisma v ZTF (Russia)* **5**, 489 (1979).

Radiation Effects and Defects in Solids, 1995, Vol. 134, pp. 247–249
Reprints available directly from the publisher
Photocopying permitted by license only

© 1995 OPA (Overseas Publishers Association)
Amsterdam B.V. Published under license by
Gordon and Breach Science Publishers SA
Printed in Malaysia

THERMAL DEPOLARIZATION SPECTROSCOPY FOR PROBING THE CONTRIBUTION OF $CaCO_3$ TO THE DIELECTRIC RELAXATION OF DOLOMITE ($CaMg(CO_3)_2$)

A. N. PAPATHANASSIOU, J. GRAMMATIKAKIS, V. KATSIKA
and A. B. VASSILIKOU-DOVA

University of Athens, Dept. of Physics, Section of Solid State Physics Panepistimiopolis, GR15784, Zografos, Athens, Greece

The Ionic Thermocurrent (ITC) technique probes a relaxation mechanism in both polycrystalline and monocrystal dolomite, at 189 K. Dielectric characterization shows that it is dipolar and is probably related to the defect structure of the calcium sublattice.

1 INTRODUCTION

The knowledge of the physical properties of carbonates can extend their industrial applications and uses.[1] Dolomite ($CaMg(CO_3)_2$) is a mixed ionic material proper for studying the dielectric relaxation in relation to the end members relaxation. In the present work, the Thermal Depolarization (TD) or Ionic Thermocurrent technique (ITC) is used as a probing method for deeper insight of ionic relaxation.

2 EXPERIMENTAL DETAILS

Polycrystalline dolomite from Greece and monocrystals from Oberdorf, Austria were studied. The chemical analysis results for the polycrystals are: Loss on ignition: 46.91%, SiO_2:0.20%, Al_2O_3:0.12%, Fe_2O_3:0.04, CaO:30.51%, MgO:21.81%. Information about the monocrystals have previously been reported.[2] Additional atomic absorption analysis for the impurity content of polycrystals gave: Mn^{2+}:0.02%wt, Sr^{2+}:0.02%wt and for the monocrystals Sr^{2+}:0.02%wt. Details about the ITC apparatus used has been given elsewhere.[3]

3 RESULTS AND DISCUSSION

An intense peak (Figure la) of the low temperature thermal depolarization spectra of polycrystal dolomite maximizes at $T_M = 189$ K. The peak positioned around 140 K is related to the Mg^{2+} sublattice, because it is also detected in $MgCO_3$ (the results will appear in a forthcoming paper) while it is completely absent in $CaCO_3$.[4] The 189 K band is insensitive to the electrode material used (platinuum, bronze, teflon, silver paste, graphite) and to the sample thickness, by keeping E_P the same. The results strongly indicate the dipolar character of the mechanism. Annealing at 400°C for 30 min and subsequent quench to room temperature results in a decrease of the peak amplitude (Figure la). The mechanism is also insensitive to mechanical treatment (bending) of the sample. Peak cleaning[3] isolates the dominant mechanism with parameters: $E = 0.53$ eV,

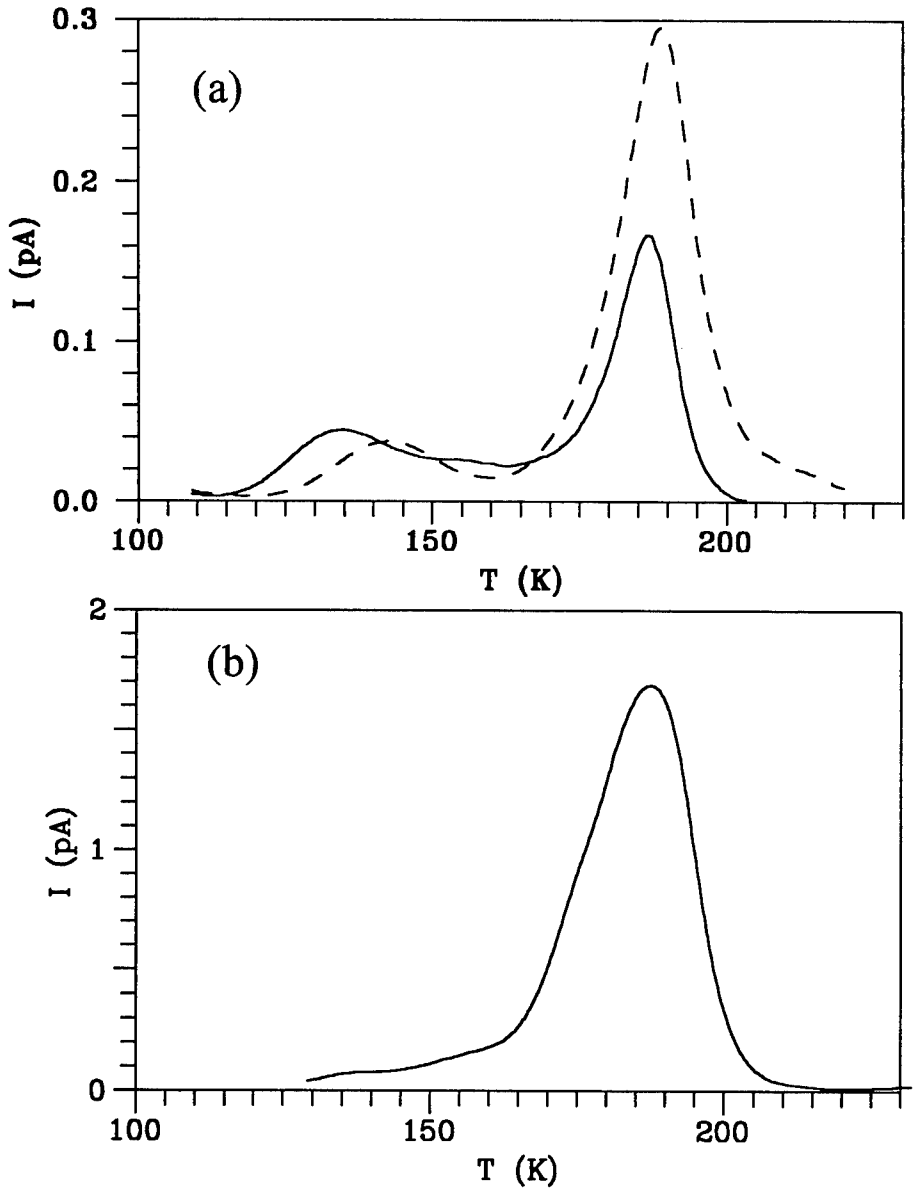

FIGURE 1(a) ITC of as received (dashed line) and thermally treated at 400°C for 30 min (solid line) polycrystalline dolomite. In both cases the sample was polarized at $T_p = 200$ K. The heating rate was 3 K/min. (b) Isolation of the 189 K band in monocrystal dolomite by polarizing at $T_p = 180$ K for a too short period of time ($t_p = 1-2$ sec).

$\tau_o = 1.22 \times 10^{-11}$ sec. By partial heating[3] we get $E = 0.5-0.62$ eV. In monocrystal dolomite we have also isolated a peak located at $T_M = 189$ K as well (Figure lb). Due to neighbourhooding overlap, we evaluated by partial heating[3] the activation energy to be $E = 0.5-0.75$ eV. The above mentioned dispersion is also detected in calcite ($CaCO_3$)[4] while, in our preliminary experiments, is absent in $MgCO_3$. Consequently, it involves the relaxation of the defect structure of the calcium sublattice. The dipolar characteristics and the thermal treatment probably indicate the existence of impurity–vacancy complexes. By comparison of the impurity content of all carbonates studies we speculate that the defect dipoles come from Ca^{2+} substitution by Al^{3+}. The distribution of Sr^{2+} to interstitial[5] or Ca^{2+} lattice sites in relation to the lattice constant of carbonates may also favour the creation of defect dipoles. A previous[4] explanation for the rotation of distorted CO_3^{2-} tetrahedra is rejected as it should stimulate the same band also in $MgCO_3$.

REFERENCES

1. A. Baysar and J. L. Kuester, *IEEE Trans. Microware Theory and Techniques*, **40**, 2108 (1992).
2. H. Effenberger, K. Mereiter and J. Zemmann, *Z. Kristallogr* **156**, 233 (1981).
3. A. N. Papathanassiou, J. Grammatikakis and N. Bogris, *Phys. Rev.* **B48**, 17715 (1992).
4. N. Bogris, J. Grammatikakis, A. N. Papathanassiou and A. Vassilikouova, *Proceedings of the XII International Conference on Defects in Insulating Materials, Germany, 1992*, p. 804, ed. O. Kanert and J.-M. Spaeth, World Scientific (1993).
5. R. J. Reeder, *Reviews in Mineralogy, vol. ll: Carbonates: Mineralogy and Chemistry*, pp. 267, Mineralogical Society of America (1983).

Radiation Effects and Defects in Solids, 1995, Vol. 134, pp. 251–255
Reprints available directly from the publisher
Photocopying permitted by license only

© 1995 OPA (Overseas Publishers Association)
Amsterdam B.V. Published under license by
Gordon and Breach Science Publishers SA
Printed in Malaysia

DEFECTS AND FEATURES OF ION-ELECTRON PROCESSES IN GARNETS

A. E. NOSENKO and V. N. SHEVCHUK

Depart. of Physics, Lviv University, 50 Dragomanov Str., 290005 Lviv, Ukraine

The results of the electroconductivity investigations, the thermal polarization and the depolarization currents of some gallium garnet monocrystals are considered. Models of the transport processes realized during heating from 80 to 1200 K are proposed. Major point defects are cation and anion vacancies and their aggregates in different charge states. The *p*-type of conductivity is connected with O^--type centres.

Key words: electroconductivity, polarization, thermally stimulated depolarization, gallium garnet, point defect, electret state.

1 INTRODUCTION

Application of rare-earth (RE) gallium garnet (GG) or its perspective in quantum electronics result in considerable quantity of publications on impurity centres spectroscopy. However fundamental defects are insufficiently studied and their nature is being discussed. We carry out the phenomenological consideration of most probable equilibrium point defects in respect to the physico-chemical crystal growth conditions, the structural features, the deviation from stoichiometry and local charge compensation for the scheme: a). Cation (V_c) and anion (V_o) vacancies in different charge states. b). Vacancies couple (dipole centres), in particular, the interrelation $V_c - V_o$ (dipolons). c). Cations in 'strange' cation positions. Vacancies V_{Ga} and V_o prevail. Concentration of the V_{Ga} dominate. The $V_c - V_o$ dipolons are effective centres of holes (*p*) occupation due to incomplete charge compensation of the V_c by V_o. The concentration of electronic defects (*p, e*) are minor from ionic. The holes prevail.

Such defects I) cause considerable number of local levels in forbidden gap,[1] II) determine localization and movement delocalizating of charge carriers (type and mechanism of electroconductivity, polarization effects etc),[1,2] III) modify photosensitivity and mechanism of selective *f*-photoconductivity of REGG[3,4] which is realized for RE-ions *f*-bands absorption in 200 ÷ 400 nm region, IV) cause the lattice parameters variation,[5] V) forme additional absorption spectra[6] etc.

2 EXPERIMENTAL METHODS

The investigated garnet monocrystals $R_3Ga_5O_{12}$ (R-RE-ions) and isostructural $Ca_3Ga_2Ge_3O_{12}$ (CaGGG) were grown by Czochralsky method. The currents of electroconductivity, of thermally stimulated polarization (TSP) I_{TSP} and thermally stimulated depolarization (TSD) I_{TSD} thermal- and photoelectret states (TES and PES) are analyzed. The details of investigation are traditional and are described in.[1,4] The mechanism of polarization from space-charge (SC) and dipolar (D) positions was established for TSP and TSD spectra using the method of variation of polarization conditions (applied voltage U_p, temperature T_p, time τ_p and wavelength of excitation light λ_p in PES case, too). The determination and calculation of the relaxation parameters are carried out in accordance with known theories.[7] The thickness of samples is 0.5 mm, the

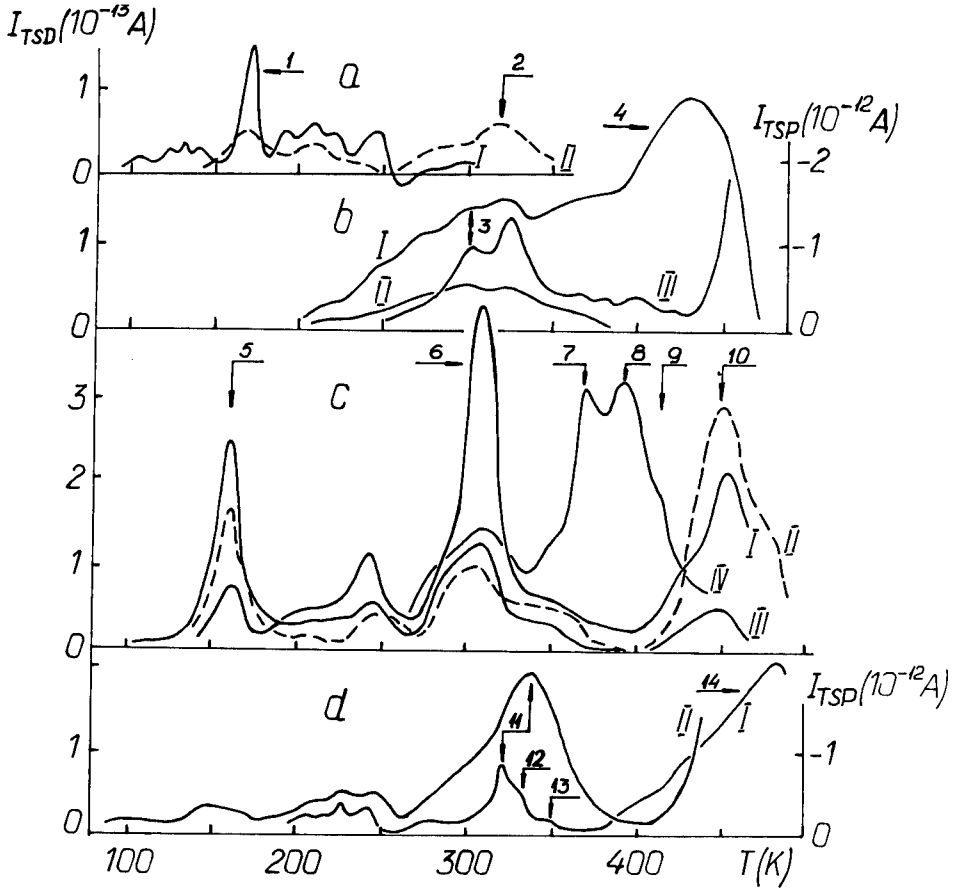

FIGURE 1 The typical spectra of thermally stimulated currents in NdGG (a) (T_p=90 K, U_p = 400 V, τ_p = 300 s); SmGG (b) (I T_p = 380 K; II T_p = 300 K; I, II U_p = 400V; I, II τ_p = 120s; III U_p = 200V); GdGG (c) (I, II T_p = 90 K; III - 300; IV - 390. IIλ_p = 275 nm. U_p = 400 V, τ_p = 60 s) and CaGGG (d) (I T_p = 400 K, I U_p = 400 V, I τ_p=200 s; II U_p = 30 V). The PES is formed at λ_p = 290 ÷ 400 nm and blocking electrodes. The curves Ia, Ic, IIc, IIIc are corresponding to TSD of PES; IIa, Ib IIb, IVc, Id - TSD of TES; IIIb, IId are TSP spectra.

heating velocity is 0.15 K/s.

3 ELECTRICAL CONDUCTIVITY

Electrical conductivity σ of REGG and CaGGG was measured in the temperature range T = 300 – 1200 K in vacuum (I) and air (II) atmosphere. The dependence σ(T) is approximated by law $\sigma \sim exp(-E_a/kT)$, here k is Boltzman's constant. The parameter E_a are shown in the Table I. The value of forbidden gaps E_g width are presented also here.

4 TSD SPECTRA

The typical TSD curves of some garnets are displayed in Figure 1. The basic relaxation

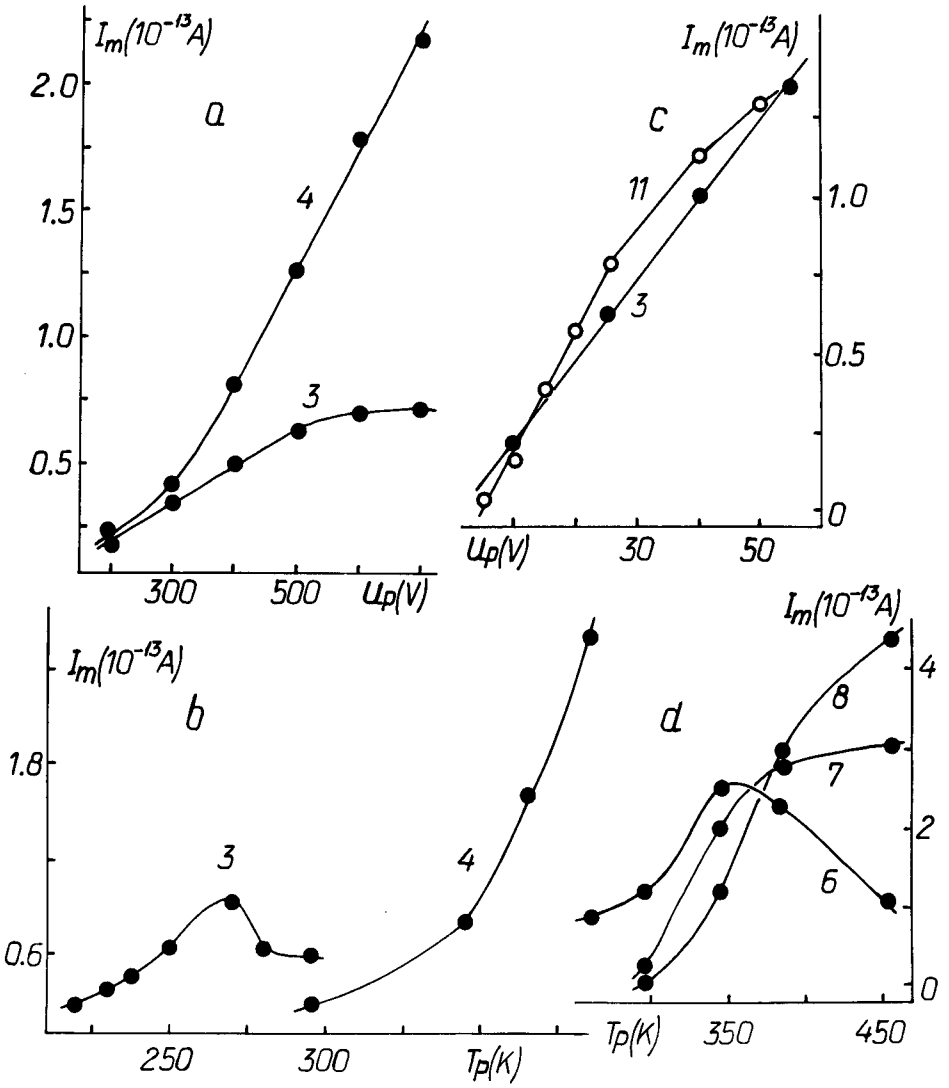

FIGURE 2 The intensity of corresponding to Figure 1 peaks vs polarizational conditions (U_p and T_p) in SmGG (a, b, 3c), GdGG (d) and CaGGG (11c).
The curves 3c and 11c corresponding to TSP peaks, in other cases—TSD peaks.

processes investigation results conditioned by SC and D-orientation effects are shown in Table. II. Dipolar TSD peaks for dipolons $V_c - V_o$ are connected. The excitation (hole is captured by such centres) at 200 ÷ 400 nm light irradiation (Figure 1c) in external electrical field even at $T << T_m$ of corresponding TSD peak, stimulates the reorientation and induces the dipolar polarization. In particular, the features of electronic structures of each crystal result in the difference of corresponding TSD spectra of TES and PES. The TSD peak N1 is inducted by thermal and optical excitation. The elementary simetrical

peak N5 is observed only in TSD of PES case. In the CaGGG, owing to absence of photoconductivity, the PES is no formed.

Table I
Data of the investigation of the conductivity of some REGG, pure CaGGG and Cr^{3+}, Nd^{3+} (0.02 at.%) doped CaGGG crystals.

Crystal	E_g (eV)	$\sigma(10^{-15}$ Ohm^{-1}cm^{-1}) T(K)	I	II	T(K)	E_α (eV) I	II
NdGG	4.9	300	0.062		430 ÷ 500	1.77	
SmGG	5.2	300	0.061		430 ÷ 500	1.92	
GdGG	5.4	300	0.044	0.12	430 ÷ 500	1.80	
		470	91	550			
CaGGG	5.5	300	0.1	40	300 ÷ 350	1.23	
		450	470	5500	350 ÷ 500	1.58	
		1200		2×10^{10}	470 ÷ 1200		1.09
CaGGG:Cr		300	4.6	2000	300 ÷ 350		0.12
		450	660	8040	390 ÷ 450		0.25
					450 ÷ 500		0.53
					500 ÷ 570		1.14
CaGGG:Nd		1000	8×10^8	870 ÷ 1200		1.09	

Table 2
Temperatures T_m of the TSD maxima, energies of activation E_t concentration of some electrical active centres M_o and their frequency factor ω_o for garnet crystals. Numeration of peaks corresponds to Figure 1.

Crystal	Peak number	T_m(K)	E_t (eV)	M_o (10^6 Cm^{-3})	ω_o (10^6s^{-1})	Nature of peak
NdGG	1	171	0.33	0.61	0.2	SC
	2	320	0.80	0.39	7.5	D
SmGG	3	306	0.56	0.62	2.1	D
	4	420	2.00			SC
GdGG	5	161	0.23	1.95	0.15	SC
	6	312	0.57	2.08	11.0	D
	7	370	0.64	2.25	2.8	SC
	8	390	0.67	2.85	2.3	SC
	9	412	0.71	1.50	8.1	SC
	10	450	0.78		2.4	SC
CaGGG	11	320	1.00	78000	92000	D
	12	335	1.02	38400		D
	13	350	1.04	20000		D
	14	480	1.10			SC

The results of polarization condition influence on intensity (I_m) of some distinguische TSD or TSP peaks Figure 2 are presented.

5 CONCLUSIONS

The simplified evolution picture of the ion-electronic processes in REGG and in CaGGG due to the temperature change at 80 ÷ 500 K range in conformity with the experimental results are described corresponding to the several stages. 1). The *p*-localization on corresponding defects (T < 160 K). 2). The possibility of individual *p*- or *e*-hops in boundaries of the complete anion (cation). Correlational *p*- *(e)*-hops from site to site are prevailing. We give preference to O^--type centres (T < 300 K). 3). Reorientation of the

dipolons because of more mobile component transference ($T \simeq 320$ K). Dipoles of impurity ion-vacancy type are not considered. 4). Ionic processes are active. Mass *p(e)*-migration. The σ is sharply rising ($T > 400$ K).

Analogical appearance TSD curves of PES (formation O^- centres, the same quantity TSD peaks etc) at variable λ_p and also $\lambda_p = 275$ nm (*f*-transition of Gd^{3+} in case of GdGG) confirms the conception that the *f*-photoconductivity mechanism[8] demands the inclusion of electronic shel of ligands (in particular, 2p-states of oxygen) together with excitation R^{3+}-ions states.

REFERENCES

1. A. E. Nosenko, V. N. Shevchuk *et al.* , *Fiz. tverd. tela.* **29** (1987) 620.
2. A. E. Nosenko, V. N. Shevchuk, *Ukr. fiz. zhurn.* **30** (1985) 1546.
3. A. E. Nosenko, V. N. Shevchuk, *Proc. Intern. conf. Phys. in Ukraine. Kiev*, 22–27 June 1993. *Solid State Phys.* p. 159–162.
4. A. E. Nosenko, V. N. Shevchuk. Zhurn. tekhn. fiz. **63** (1993) 69.
5. G. M. Kuzmicheva, B. V. Muchin *et al. Neorgan. material.* **29** (1993) 89.
6. Ya. O. Dovgiy, I. V. Kityk *et al.*, *Fiz. tverd. tela.* **35** (1993) 290.
7. Yu. A. Gorochovatsky and H. A. Bordovsky, *Thermally activational current spectroscopy of high-resistance semiconductors and dielectrics.* Nauka, Moskov, 1991.
8. A. E. Nosenko, V. N. Shevchuk, *Proc. yuvileinoi konf. IEF-93.* Uzhgorod 29–30 veresnya 1993. Sekciya A. p. 35–39.

Radiation Effects and Defects in Solids, 1995, Vol. 134, pp. 257–260
Reprints available directly from the publisher
Photocopying permitted by license only

© 1995 OPA (Overseas Publishers Association)
Amsterdam B.V. Published under license by
Gordon and Breach Science Publishers SA
Printed in Malaysia

DIELECTRIC RESPONSE OF NATURAL ZEOLITE (STILBITE) SINGLE CRYSTALS

J. M. KALOGERAS and A. VASSILIKOU-DOVA

University of Athens, Department of Physics, Section of Solid State Physics, Panepistimiopolis, 157 84 Zografos, Athens, Greece

The dielectric properties of single crystals of the natural zeolite stilbite were studied employing two complementary methods; the Thermally Stimulated Depolarization Currents (TSDC) technique applied over the temperature range 77–300 K and the Dielectric Relaxation Spectroscopy (DRS) method with frequency measurements over the range 5 mHz–1 GHz. A distinct contribution to the dielectric relaxation response of the mineral arises from the activated hopping of Na^+ counterions between vacant interstitial sites, and is described by both TSDC and dielectric measurements.

Key words: Zeolites, Stilbite, Depolarization Currents, Dielectric Relaxation.

1 INTRODUCTION

Zeolites constitute a prominent category of high surface area inorganic solids with natural and synthetic members extensively used in research and industry.[1] Their three-dimensional network of interconnected large molecular cavities contains a variety of extraframework cationic species; which counterbalance the net negative charge of the framework, and posses a considerable freedom of movement. Moreover, they have the remarkable ability to retain within the structural cavities, water molecules up to 30% by weight. In the stilbite lattice two principal cation sites exist. The first, at the centre of the main channel parallel to a-axis, is fully occupied by Ca^{2+} cations, each of which is surrounded by $8H_2O$ molecules. A second Na^+-binding site of low occupancy is again in the main channel but nearer to the lattice, so that Na^+ is coordinated with lattice oxygens and 4 water molecules.

2 EXPERIMENTAL

All the investigated samples were transparent colourless crystals (Poona, India) of typical dimensions $7 \times 7 \times 1$ mm.[3] The chemical analysis resulted in the formula: $K_{0.05}Na_{0.861}Ca_{3.97}Fe_{0.03}Al_{8.28}Si_{27.55}O_{72} \cdot 30H_2O$. Details for the sample pretreatment procedures, basic aspects of the theoretical background of the TSDC and DRS methods, and the experimental apparatus used have been given elsewhere.[2]

3 RESULTS AND DISCUSSION

For natural stilbite single crystals, two thermocurrent bands (B and C in Figure 1) emerge in the intermediate temperature range of the TSDC spectra. The dipolar origin of band B is supported by (i) its positional stability around 210 K in all TSDC runs, and (ii) the consistent behaviour in experiments with use of the thermal sampling (TS) method[2] or with blocking electrode configurations (Figure 1). The decrease in the band amplitude in the MISM and MISIM electrode configurations is not inconsistent with a dipolar interpretation[3] and is related with a decrease of the internal electric field, partially by the

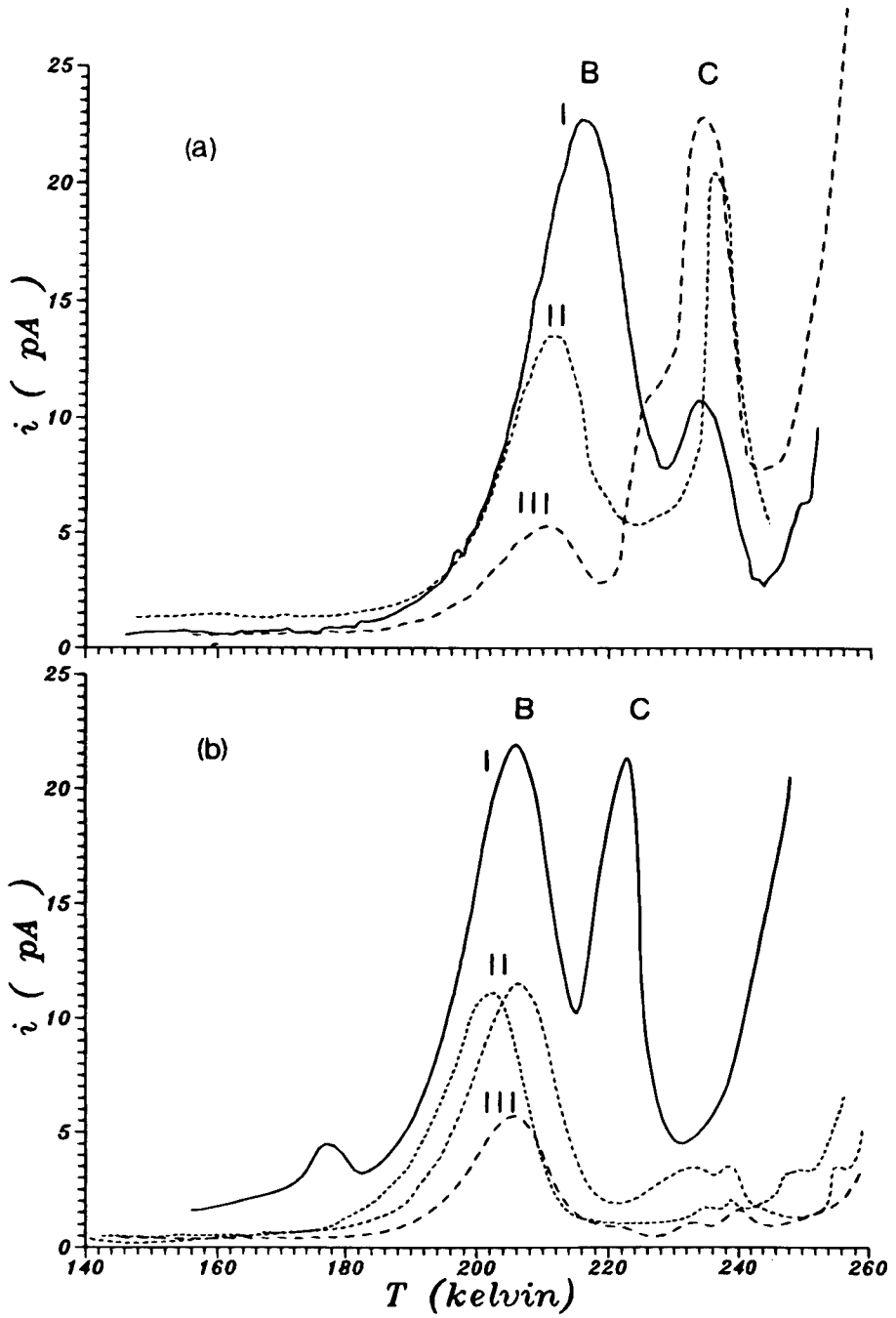

FIGURE 1 Representative plots of the effect on the (140–260) K thermocurrent range from the interposition between the electrodes and the sample of thin insulating teflon films. Curves I, II and III correspond to the MSM, MISM and MISIM electrode configurations [M: electrode material (platinum), S: sample and I: insulating film]. The plots given here (a and b) for different samples, but also recorded in TSDC runs with the same sample, stress the inconsistent behaviour of band C and its differences with band B.

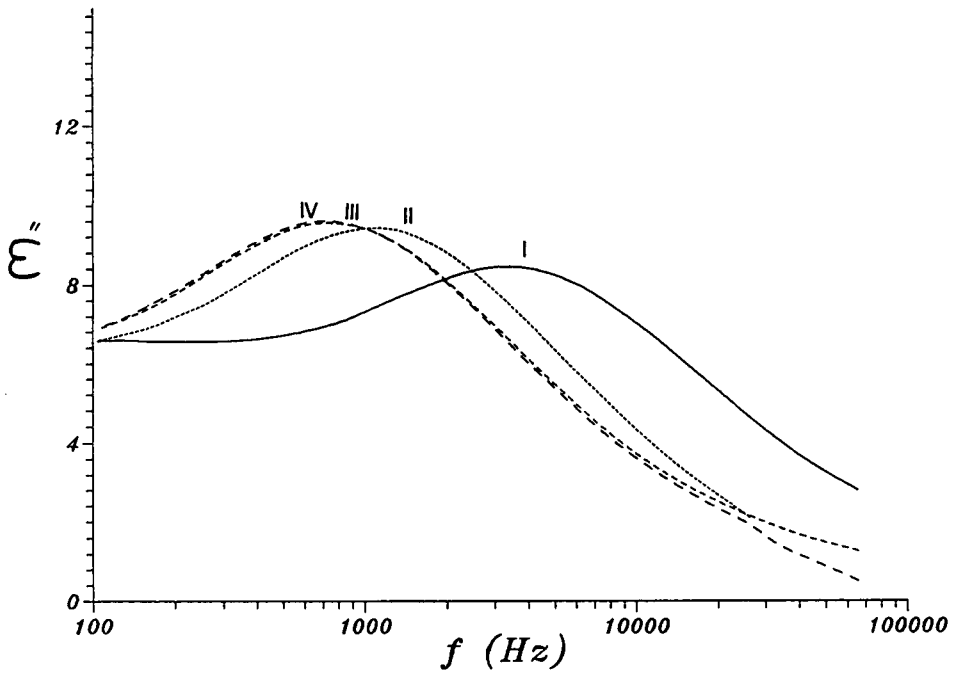

FIGURE 2 Variation of the kHz dispersion for stilbite single crystal. The dielectric relaxation spectra were obtained at 343 K, in vacuum and employing blocking FEP electrodes. Absorption I was recorded after 2 hours under vacuum conditions, and II, III and IV for 1, 2 and 3 days respectively.

formation of charged layers on the sample-electrode surface contact. Applying an Arrhenius type equation for the relaxation time $[\tau(T) = \tau_o exp(W/kT)]$ the mean values of the distributed dipolar relaxation parameters were found to be $W = 0.55$ eV and $\tau_0 = 2.49 \times 10^{-12}$ sec. The relaxation parameters have derived from Arrhenius plots ($ln\tau$ *vs* $1/T$) and a measure of the distribution width has been given from the analysis of the partial TSDC curves obtained with the TS technique.[2] The energy barrier value (W) shows consistency when compared with those from formulae using band shape parameters.[2]

For the dielectric dispersion centred at a frequency of 0.2 kHz at room temperature the relaxation parameters were found to be $W = 0.59$ eV and $\tau_0 = 0.1 \times 10^{-12}$ sec. Our interpretation of this kHz dispersion as a cationic jump relaxation is being supported by investigations in other zeolitic systems, which designate this region as the primary cations relaxation frequency band.[4–6] Several factors indicate that both the relaxational peak B and the kHz dielectric dispersion shown in Figure 2 can be attributed to the same cation diffusion mechanism over potential energy barriers involving interstitial Na^+ ions and the vacant Na^+-binding sites. As cationic relaxations in zeolites occur between well defined extraframework sites, migration necessitates the presence of vacant host sites. This is not the case for the $Ca^{2+}(H_2O)_x$ ($x \cong 8$, coordination number) complexes which fully occupy their sites. Cation-cation repulsions and steric hindrance effects might prevent jumps of the $Ca^{2+}(H_2O)_y$ ($y \leq 8$, hydration number[7]) complexes at Na^+ sites. Thus a jumping process of the highly mobile sodium cations appears as a more plausible attribution. The correlation of the bands is supported by (a) the good agreement between the sets of the

dielectric relaxation parameters obtained, (b) the directly related dipolar relaxation strengths ($\Delta\epsilon$) calculated for both processes (being 20.8 ± 3.6 for band B and 23.5 ± 3.9 for the DRS dispersion), and (c) interrelated calculations of the equivalent critical frequencies (f_c) and thermocurrent maximum temperatures (T_M).[2] Similar ion-jumping relaxation processes encountered in the dielectric literature of zeolitic structures have been manipulated as resembling to the rotational relaxation of counterion-anionic charged lattice dipoles.[8]

The thermal curves of stilbite show three main water losses (DTG and DTA peaks), the smallest one being at 343 K.[9] The magnitude of the kHz dispersion with the sample under vacuum conditions increases only within the first two days and appears insensitive for longer times of evacuation. This could suggest that the gradual desorption of H_2O molecules, at 343 K, is completed within the second day. Higher temperature heating has been avoided in order to prevent structural damages.[9] The lowering of the critical frequencies (f_c) might be related with an increase in W, in the concept of the polar water molecules reducing, as an electrostatic shield, the cation attraction from the anionic lattice field. By varying the crystal water content we introduce a modification of the factor $N_t f(1+f)$ which determines the dispersion strength, where N_t is the trap concentration and f is the probability of their occupancy by an ion. The dielectric response of the zeolite materials significantly alters in the presence of an absorbate,[3–5,10] and in the stilbite case, the desorption of water molecules occupying cation jumping sites apparently increases mechanism's efficiency (Figure 2).

The interpretation of band C, positioned at around 228 K, is rather impossible by virtue of the current results. Arrhenius plots for band C resulted in single curves (in series of experiments), and derived relaxation parameters were concentrated around two distinct sets, (0.85 eV, 10^{-17} sec) and (1.55 eV, 10^{-35} sec). The bands shape and relaxation parameters variations could imply the presence of two different mechanisms which appear independently among the series of different TSDC runs and/or samples. However, the second peculiar set of parameters can not be interpreted in the present stage.

4 CONCLUSIONS

In the dielectric spectra of natural stilbite contribute several processes related to the mobility of the various extraframework species.[2] The thermally (TSDC) and electric field (DRS) induced short range hopping of the interstitial sodium ions, gives rise to a 'dipolar' relaxation process with distributed relaxation parameters, and relaxation times (τ) affected by the desorption of small H_2O amounts from the structural cavities.

REFERENCES

1. J. M. Thomas, *Zeolite Facts, Figure, Future*, pp. 3 (P. A. Jacobs and R. A. Van Santen, Elsevier, Amsterdam 1989); M. S. Spencer, *Crit. Rep. Appl. Chem.* **12**, 65 (1985).
2. J. M. Kalogeras, E. Vitoyianni, A. Vassilikou-Dova and S. Bone, *J. Phys. Chem. Solids* **55**, 545 (1994).
3. P. Pissis and D. Daoukaki-Diamanti, *J. Phys. Chem. Solids* **54**, 701 (1993).
4. B. Morris, *J. Phys. Chem. Solids* **30**, 73, 89, 113 (1969).
5. G. Jones, *J. Phys. Chem. Solids* **37**, 887 (1976); *J. Chem. Soc. Faraday Trans.* **1** 71, 2085 (1975).
6. T. Ohgushi and S. Sato, *J. Solid State Chem.* **87**, 95 (1990).
7. O'M Bockris J. and Saluja P. P. S., *J. Phys. Chem.* **76**, 2140 (1972).
8. R. A. Schoonheydt, *J. Physique* **C6–216**, 41(1980).
9. G. Gottardi and E. Galli, *Natural Zeolites*, pp. 284–300, Springer, Berlin (1985).
10. R. A. Schoonheydt, W. Wilde and F. Velge, *J. Phys. Chem.* **80**, 511 (1976).

Radiation Effects and Defects in Solids, 1995, Vol. 134, pp. 261–264
Reprints available directly from the publisher
Photocopying permitted by license only

© 1995 OPA (Overseas Publishers Association)
Amsterdam B.V. Published under license by
Gordon and Breach Science Publishers SA
Printed in Malaysia

EPR SPECTRA OF Cr^{3+} IONS IN $LiNbO_3$:ZnO AND $LiNbO_3$:CaO

D. BRAVO, A. MARTÍN,† M. VODA‡ and F. J. LÓPEZ

Dpto. Física de Materiales, C-IV, Universidad Autónoma de Madrid, E-28049 Madrid, Spain; †Dpto. Física e Instalaciones ETSAM-UPM, Avda. Juan de Herrera 4, E-28040 Madrid, Spain; ‡Inst. of Physics and Technology of Materials, Bucharest-Magurele, P.O. Box MG-7, Romania

The electron paramagnetic resonance spectra of Cr^{3+} in $LiNbO_3$ co-doped with ZnO or CaO ($\approx$ 6%) have been studied. Both impurities give rise to the same effect as that observed in MgO-doped samples: a strong diminution of the anisotropic (axial) spectrum reported for $LiNbO_3$:Cr and the appearance of an intense and isotropic line. The origin of this line in the co-doped samples is discussed.

Key words: $LiNbO_3$, EPR, Cr.

1 INTRODUCTION

$LiNbO_3$ is an important non-linear material for applications in optical devices. Various of these applications are related to dopant ions (transition-metal or rare-earth). Therefore, knowledge on the location of these impurities in the $LiNbO_3$ lattice is important to understand the properties of this material. On the other hand, $LiNbO_3$ is commonly doped with MgO ($\sim$ 6%) to inhibit photoinduced damage that takes place through the so-called photorefractive effect. It is believed that Mg ions occupy the anti-site positions (Nb^{5+} ions in Li^+-sites) reducing the anti-site concentration in congruent $LiNbO_3$. Recently, the location of Cr^{3+} ions has been studied in $LiNbO_3$:MgO by electron paramagnetic resonance (EPR) and ENDOR[1,2] as well as optical spectroscopy.[3,4] The EPR of these samples shows the same axial spectrum as for $LiNbO_3$ crystals, although of much lower intensity, in addition to a new isotropic spectrum.[1,2] This spectrum has been attributed to Cr ions at the Nb-site (hereafter denoted as $Cr^{3+}(Nb^{5+})$) perturbed by some nearby Mg^{2+} ion.[1–4] By contrast, the axial EPR spectrum observed in $LiNbO_3$:Cr is assigned to Cr ions at the Li-site[1] (denoted as $Cr^{3+}(Li^+)$). The optical studies in crystals containing MgO show a red shift in the $^4A_2 \rightarrow {}^4T_1$ absorption band,[1] as well as three different groups of R lines attributed to $Cr^{3+}(Nb^{5+})$, $Cr^{3+}(Li^+)$ (regular lattice sites) and $Cr^{3+}(Nb^{5+})$ perturbed by Mg^{2+} ions.[3,4] In order to make a consistent interpretation of the results from both techniques, it has been proposed[5] that most Cr ions are forming $Cr^{3+}(Nb^{5+})$-$Cr^{3+}(Li^+)$ pairs which are EPR silent due to an antiferromagnetic coupling and that a small fraction of Cr^{3+}(Li) is diluted in the host. This small part of non-paired Cr ions being solely responsible for the axial EPR spectrum.

It has been recently ascertained that other ions such as Sc[6] or Zn[7] play a role analogous to Mg avoiding the photorefractive effect. On the other hand, the optical spectroscopy studies of ZnO-doped $LiNbO_3$:Cr crystals,[8] reveal that ZnO produces the same effect as MgO. Thus, it is interesting to ascertain whether other impurities make the EPR spectrum behave in the same way as Mg does. In this work, we have studied the EPR spectra of Cr^{3+} in $LiNbO_3$ crystals containing ($\sim$ 6%) ZnO or CaO attempting to observe signals from $Cr^{3+}(Nb^{5+})$ perturbed by Zn^{2+} or Ca^{2+} ions, respectively. In both cases, the EPR results are similar to those obtained for the Mg-doped crystals. A weak axial spectrum

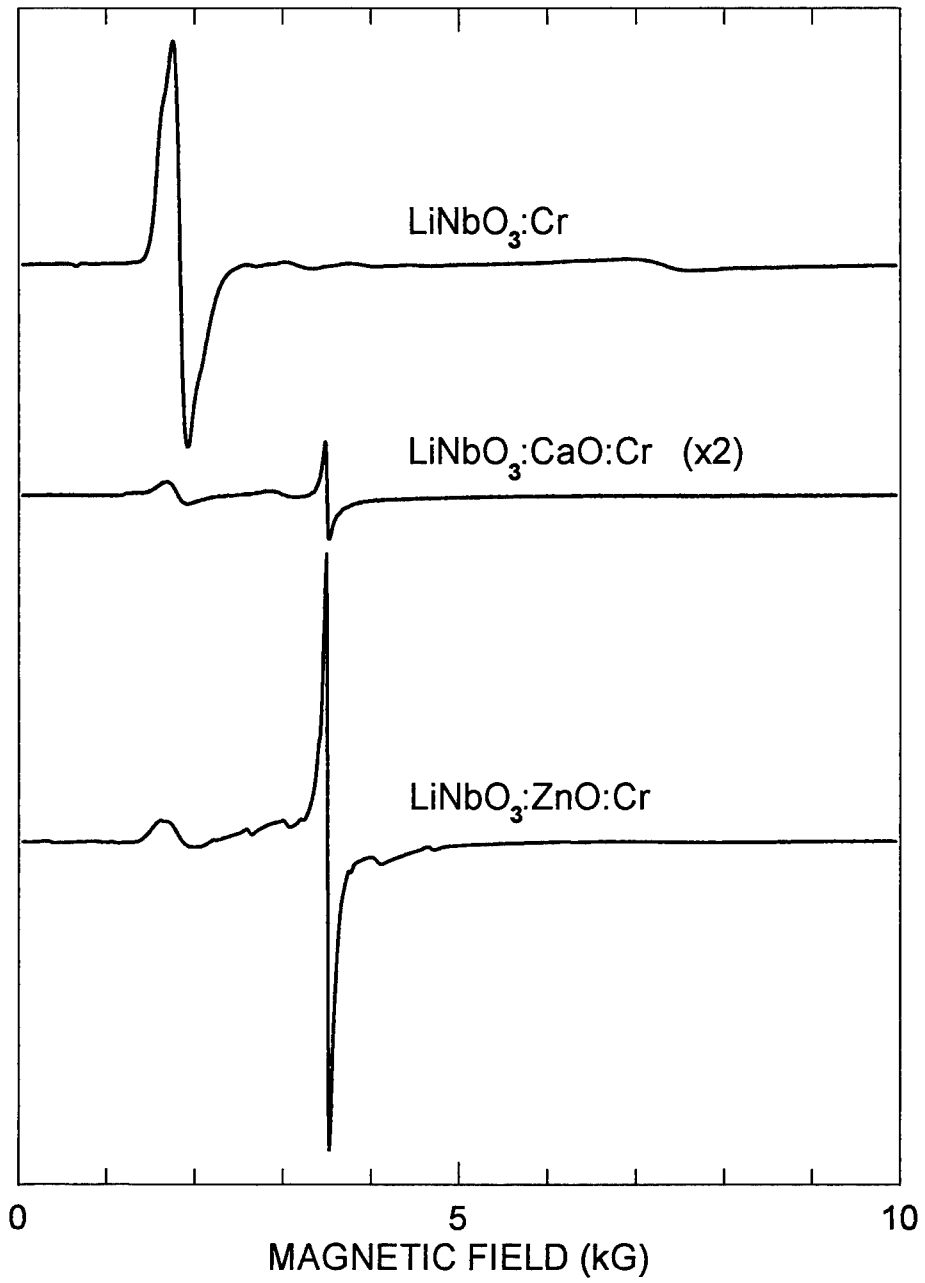

FIGURE 1 EPR spectra, measured at RT, of $LiNbO_3$:Cr, $LiNbO_3$:CaO:Cr and $LiNbO_3$:ZnO:Cr. In all cases the magnetic field is perpendicular to the *c*-axis.

corresponding to $Cr^{3+}(Li^+)$ together with an intense and isotropic single line ($g = 1.973 \pm 0.003$) were observed. These results are discussed and compared with those for the Mg-doped samples.

2 EXPERIMENTAL DETAILS

Congruent $LiNbO_3$ crystals were grown by the Czochralski technique in our laboratory from grade I Johnson-Matthey powder. The concentrations of dopants (molar fraction in the melt) were 6% for Zn or Ca ions, and 0.5% for the Cr ion. The blocks show a color distribution: greenish at the top and pink at the bottom. The results for these crystals and for the Mg-doped samples, have shown that the pink region of blocks contains the higher concentration of Mg, Zn or Ca in each case. Therefore, samples taken from the pink part were used for our studies. The $LiNbO_3$:Ca, Cr crystal presents an inhomogeneous aspect with some inclusions. However, the x-ray diffraction patterns, as well as the EPR spectra confirm that samples are monocrystalline. The samples were oriented by x-ray diffraction and cut with their faces parallel and perpendicular to the c-axis.

The EPR spectra were obtained with a Bruker ESP 300 E spectrometer in the X band with 100 kHz field modulation frequency at room temperature (RT). Accurate values of the resonance magnetic fields and microwave frequencies were measured with a Bruker NMR gaussmeter (model ER 035M) and a Hewlett-Packard frequency meter (model 5342A), respectively.

3 EXPERIMENTAL RESULTS AND DISCUSSION

Figure 1 shows the EPR spectra, measured at RT with the magnetic field perpendicular to the c-axis, of Cr^{3+} in $LiNbO_3$ as well as $LiNbO_3$ containing ($\sim$ 6%) ZnO or CaO. The single-doped sample only shows the anisotropic spectrum with axial symmetry attributed to $Cr^{3+}(Li^+)$.[1] In the double-doped samples, the anisotropic spectrum is very weak as compared to the single doped sample. Moreover, the samples co-doped with Zn or Ca present also a strong isotropic line with $g = 1.973$. This line coincides, within the experimental error, with that reported for the Mg-doped samples.[2] In that case, it has been proposed that the isotropic spectrum is due to Cr^{3+} substituting for Nb^{5+} being perturbed by Mg^{2+} ions.[1,2] It is interesting to note that the symmetry of this center is not cubic. However, it has been shown[2] that if the Cr^{3+} impurity experiences a small shift (0.12 Å) along the c axis with respect to the host ion, the calculated value of the D ($3B_2^0$) parameter in the spin-Hamiltonian becomes zero, thus producing an isotropic line in the EPR spectrum.

The coincidence of results for the three impurities (Mg, Zn and Ca) is a surprising fact if one accepts that the isotropic spectrum is related to $Cr^{3+}(Nb^{5+})$ perturbed by the corresponding divalent ion. In fact, the perturbation produced by the divalent ion should be somewhat different as a consequence of the different ionic radii values. Thus, as the isotropic line is the same in the three cases, it must be concluded that the perturbation is very weak and it does not reveal itself in the EPR spectrum. Alternatively, one can consider that the Cr^{3+} responsible for the isotropic line is not perturbed by any divalent impurity in its neighborhood. In this case, the isotropic line would be due to the *intrinsic* $Cr^{3+}(Nb^{5+})$ center. This center would have an energy minimum when Cr^{3+} is shifted from the Nb^{5+} lattice position, giving $D = 0$. The ENDOR studies performed in Mg-doped samples,[1] show that the two nearest Li^+ neighbors are present. Unfortunately, this result

does not elucidate between both possibilities.

ACKNOWLEDGMENTS

This work has been partially supported by Comisión Interministerial de Ciencia y Tecnología (CICyT) under project MAT92-0163.

REFERENCES

1. G. Corradi, H. Söthe, J.-M. Spaeth and K. Polgár, *J. Phys.: Condensed Matter* **3**, 1901 (1991).
2. A. Martín, F. J. López and F. Agulló-López, *J. Phys.: Condensed Matter* **4**, 4847 (1992).
3. E. Camarillo, J. Tocho, I. Vergara, E. Diéguez, J. García Solé and F. Jaque, *Phys. Rev.* **B45**, 4600 (1992).
4. U. Caldiño G., J. García Solé and F. Jaque, *Opt. Materials* **2**, 157 (1993).
5. F. Jaque, J. García Solé, E. Camarillo, F. J. López, H. Murrieta S. and J. Hernández A., *Phys. Rev.* **B47**, 5432 (1993).
6. J. K. Yamamoto, K. Kitamura, N. Iyi, S. Kimura, Y. Furukawa and M. Sato, *Appl. Phys. Lett.* **61**, 2156 (1992).
7. T. R. Volk, V. I. Pryalkin and N. M. Rubinina, *Optics Lett.* **15**, 996 (1990).
8. M. Voda, U. Caldiño G., J. García Solé and F. Jaque, *Ferroelectrics* (in press).

Radiation Effects and Defects in Solids, 1995, Vol. 134, pp. 265–272
Reprints available directly from the publisher
Photocopying permitted by license only

© 1995 OPA (Overseas Publishers Association)
Amsterdam B.V. Published under license by
Gordon and Breach Science Publishers SA
Printed in Malaysia

TUNNELING AFTERGLOW AND POINT DEFECTS IN FELDSPARS

R. VISOCEKAS and A. ZINK

LUAP, Université Denis Diderot (Paris 7), case 7087
2 Place Jussieu, 75251 PARIS Cedex 05, France

The recent development of the infrared stimulated luminescence (OSL) of feldspars enhanced their importance for geological dating in the last 100 000 years. Unfortunately this application is hindered by the phenomenon of anomalous fading of their thermoluminescence (TL) and OSL, attributed to tunnel effect between (D-A) pairs. In the case of feldspars, this fading is very frequent and so far unpredictable.

A systematic comparative study of the tunnel effect in afterglow of irradiated feldspars has been made on a collection of some well caracterised 32 different samples of feldspar crystals. All of them display a low temperature afterglow due to tunnel effect in a gaussian near-infrared band centered on 710 nm. It is attributed to Fe^{3+} ions involved with the so-called phenomenon of 'Al-Si order-disorder' in occupation of sites in the feldspar lattice. This effect is known classically in mineralogy and crystallography of feldspars, but had not been related to tunnel luminescence so far.

This tunnel afterglow constitutes an easy criterion of TL datability of feldspars.

Key words: Thermoluminescence. feldspars. Point defects. Order-disorder. Tunnel effect. Anomalous fading.

1 INTRODUCTION: DATING FELDSPARS BY TL

Feldspars cannot be introduced as a new family of materials. But investigation of their thermoluminescence led us to the observation of unusual phenomena, which call for new models of point defects, quite different from F or V-like vacancy or interstitial defects.

1.1 *Feldspar Structure*

Feldspars are among the most common materials of the earth's crust.

As crystals, they may be thought of as silica (made up of SiO_4 tetraedra linked by their corners), where a given fraction of Si^{4+} atoms are substituted by Al^{3+} in the centers ('T' sites) of tetraedra. The corresponding unbalance of charge is compensated by atoms, Na^+, K^+ or Ca^{2+} which enter the lattice in interstitial positions. Alkali feldspars are compensated by Na-K mixtures, with a 25% Al/Si ratio, which leads to formulas from $KAlSi_3O_8$ to $NaAlSi_3O_8$. Plagioclases are compensated by Na-Ca mixtures, and the Al/Si ratio may reach 50%, with formulas up to $CaAl_2Si_2O_8$. When one adds to these variable possible compositions the various framework and crystal systems feldspars derive from their composition and from their history, a unique very extensive family of materials results. Feldspars have been extensively studied in mineralogy, from early XIXth century to now, and most of their characteristics are well known.

1.2 *Point Defects in Feldspars*

In one domain the knowledge is more limited, it is the domain of point defects, much less studied in feldspars than in alkali halides or II-VI compounds. The luminescent or electrical properties of feldspars were not worthy of great attention, and their crystal structure, involving at least four different types of atoms, are challenging for theoreticians.

1.3 *Dating by Thermoluminescence (TL) And Anomalous Fading*

Recently, starting in the 1960's, the TL of feldspars was investigated for dating purposes, e.g. in lava flows. This TL was shown to display a good intensity, but appeared to be blighted by the phenomenon of loss of stored charges by the effect of 'anomalous fading', characterized in the course of such studies. First observed with samples of lunar origin, but further observed in most feldspars in the 1970's, anomalous fading was attributed to the tunnel recombination of electron-hole pairs trapped after the ionizing irradiation. Only a few feldspars were observe not to fade, hence to be datable, mostly microclines from very old formations in Scandinavia.

In the 1980's, a better knowledge of optical bleaching and the related effects of optically stimulated luminescence (OSL and IRSL) led to new applications of afterglow for dating quaternary sediments. And reappraisals were made of anomalous fading in feldspars when dated with these new OSL and IRSL methods. An extensive work was done recently[1] consisting in detailed scanning of fading of some 24 different well defined samples of feldspars from mineralogical collections. It turned out that anomalous fading was also prevalent in these samples as it was in classical TL.

The aim of the present investigation was to observe whether these samples displaying fading of TL did display as well tunnel recombination emission proposed theoretically to account for that fading. Tunnel recombination emission is quite characteristically not thermally stimulated, and may be observed at temperatures much lower than the temperature of the initial irradiation. This is in strong contrast with TL. Typically, following a room temperature irradiation, tunnel afterglow is observed down to 77 K without reduction. Second, the kinetics of this afterglow are like (1/t) (t being the time), in contrast with phosphorescences which vary usually like ($1/t^2$) or exponentially. This tunnel emission involves the same traps and radiative centers as the TL generated by the initial irradiation: it displays the same emission spectra as TL and disappears after TL emptying of traps. These observations were done already before on one sample of labradorite.[2]

2 EXPERIMENTAL

2.1 *Samples*

The 24 samples which had been investigated for fading[1] were put at our disposal, plus some others dated microclines from Finland,[3] plus several other samples not studied previously obtained from various mineralogical museums, 32 in all, mostly under single crystal form. The composition of these feldspars was monitored by X-ray luminescence with a SEM.

One aim was first to scan a set of feldspars as representative as possible of the diversity of that family. This being done, the investigation was more detailed with alkali feldpars of the sanidine type, originating from volcanic areas (Chaine des Puys, France; Eifel, Germany) and microclines from Finland (Helsinki region).

2.2 *Equipment and Methods*

It was basically the same as was used previously.[2] The basical process of study is:

- First step, irradiate the sample with a beta Sr-Y source with some 250 Gy.
- 2nd: Starting the recording of light intensity, take the sample down to 77 K.
- 3rd: Stay at 77 K one hour or so, to monitor the expected tunnel emission, if any.

- 4th: Increase the temperature linearly (10 K/min) to 500°C, to observe the TL proper.

The emission is monitored with a RCA 31034 photomultiplier, which has an extended flat spectral response from 250 to 890 nm (unusual in TL dosimetry where IR thermal radiation is to be avoided). Using filters on a carousel, mostly a Schott low pass OG 590 filter, the spectral sensitivity range is divided in two domains:

- one from 250 nm to 590 nm, wide domain loosely termed hereafter 'blue' spectral region. It is the range of sensitivity scanned with conventionnal TL dosimetry equipment.
- the other domain, from 590 to 890 nm, is termed here 'red-IR'. This range is not used conventionnally.

3 OBSERVATIONS

3.1 *Tunnel afterglow*

Following the procedure outlined above, the most outstanding observation made (shown on Figure 1) is a very intense afterglow at lower temperatures down to LNT, with all the criteria of tunnel recombination. We observed it already before in the study of one feldspar,[2] but this time it is observed with all feldspars under study. The very few exceptions are with samples with no fading reported.[1] The relative intensity of tunnel afterglow appears to be in proportion with the rate of fading reported.

We do not know reports of systematic investigations for tunneling afterglows since our study[2] was published. Personnally, we did several studies on luminescent materials others

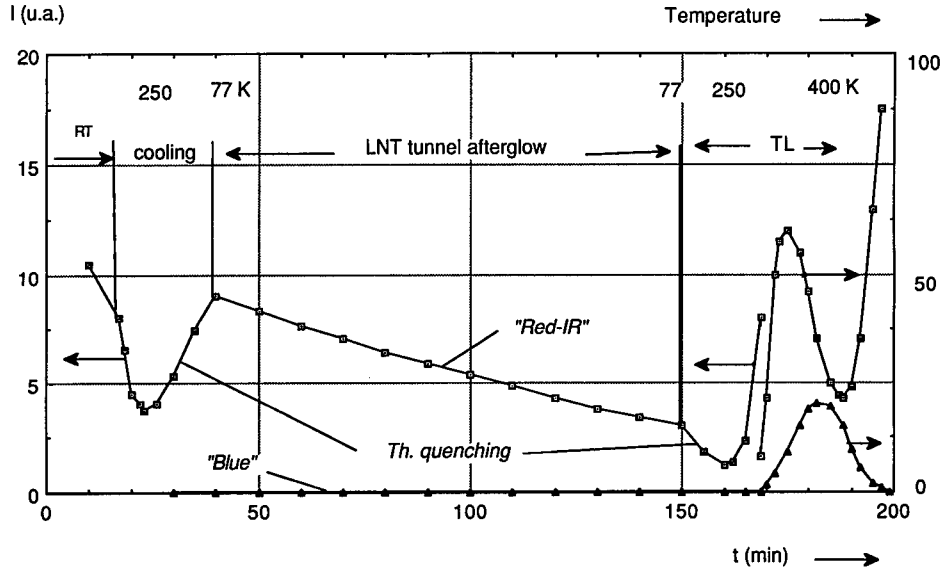

FIGURE 1 Intensity of light vs time starting from end of irradiation in a process of investigation of tunnel afterglow in an average feldspar. On higher scale is the programmed temperature. Showing the low temperature tunnel afterglow, the thermal quenching of luminescence, the TL proper, in the two ranges 250 to 590 nm ('blue') and 590 to 900 nm ('red-IR').

than feldspars which display tunnel afterglow as well. But the intensity and generality of this effect in feldspars appears quite remarkable to us.

3.1.1 *Emission spectrum* Another unique feature of the tunneling afterglows thus observed is that their emission spectra are wholly in the infrared. More detailed spectral studies show in every case the same narrow spectrum, with a gaussian shape, centered on 710 nm (14 000 cm^{-1}), with a mean width 0.3 eV (1900 cm^{-1}).

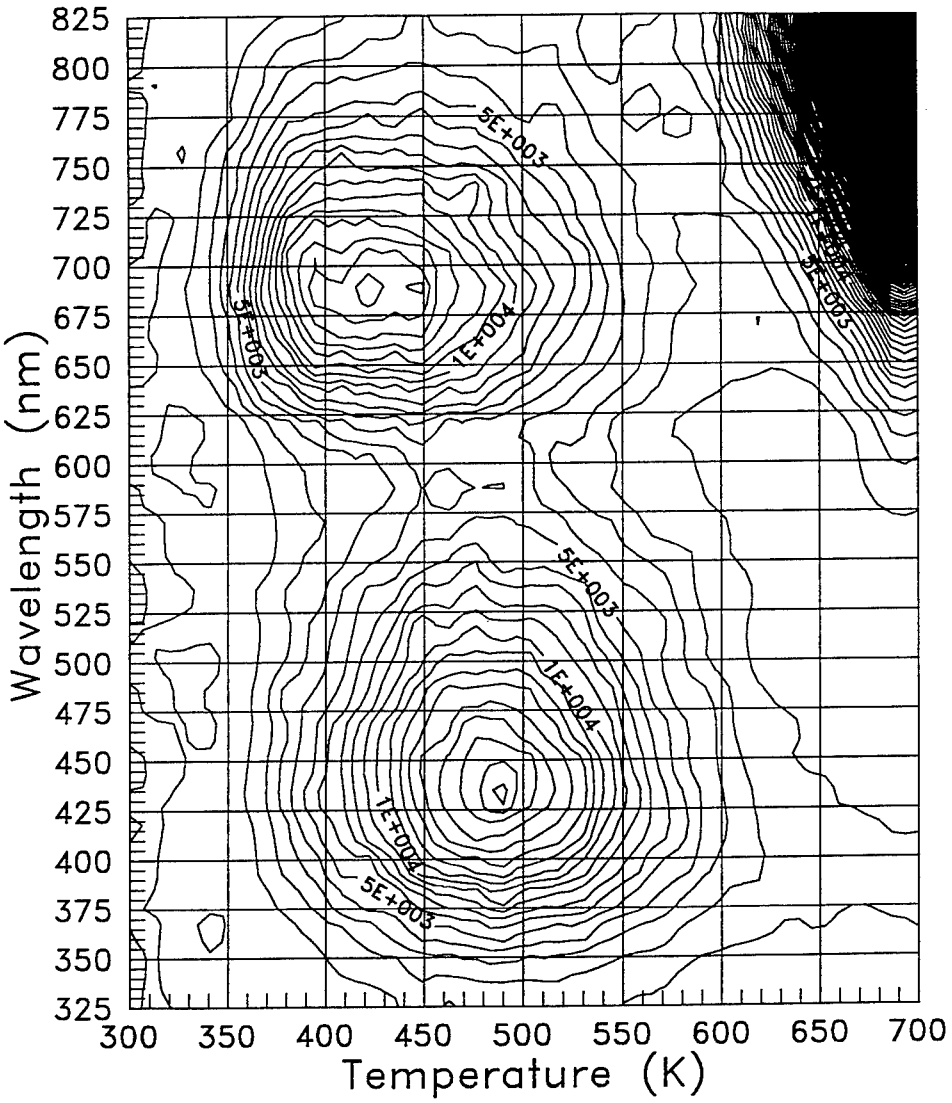

FIGURE 2 3D representation of TL of a sanidine from Puy de Sancy, showing the two distinct TL emission bands, 'blue' and 'infrared', separated spectrally around 590 nm, and with different peak temperatures. At the top right is seen the thermal emisson. (By A.J.J. Bos, Delft University of Technology).

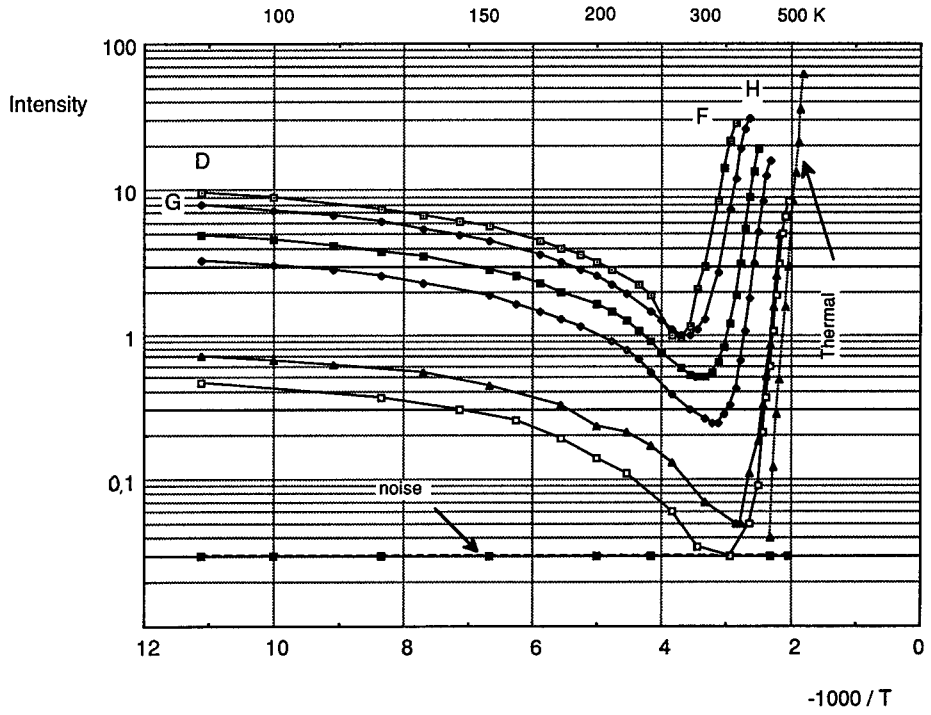

FIGURE 3 Intensity vs (1/T) in a 6 cycles fractional heating process for a sanidine (start in D). Showing for following cycles lower and lower intensities, first in tunnel afterglows with a thermal quenching effect, followed by the initial rises of TL. Activation energies are 0.50; 0.66; 0.72; 0.78; 0.82; 0.90; (and 1.4 eV for thermal emission).

3.1.2 *Thermal quenching* One more unique feature is the 'thermal quenching' visible on Figure 1, as temperature is lowered, then raised, resulting in a decrease of luminescence by a ratio like 10 between 77 K and 300 K.

3.2. TL proper

When the temperature is eventually raised above RT, TL proper shows up in the 'blue' range (as defined above) as shown in Figure 1. It is identified with the TL reported up to now in the many studies dealing with feldspars. But TL shows up as well in the 'red-IR' range, quite often more intense than in the 'blue' range, with a spectral maximum around 700 nm, and with different glow peak. In that range, observation is possible only up to 500 K, due to thermal radiation.

3.2.1 *'Blue' and 'infrared' TL emissions* All this TL emission is not one single glow peak with a wide spectrum emission band but two well separated peaks as had been hinted before.[4] This is better shown in Figure 2 using the facilities of a 3D TL equipment:[5] the resolution both in temperature and in wavelength shows that there are actually two well separated emission bands. More precisely, from sample to sample, the 'blue' band, may vary in size and emission spectrum, as reported in the litterature. The 'IR' band (which was

at best partly detected up to now) appears as more stable in intensity and spectrum.

3.2.2 *Analysis of the 'infrared' TL emission by fractional heating* It must be asked whether the LNT afterglow just observed in infrared is not due to thermal emptying of shallow traps instead of tunneling. Besides, glow peaks in both bands appear as very wide in temperature, they should correspond to multiple trap depths or activation energies as was shown for the blue band.[4] This was not known for the infrared TL.
To characterize the traps responsible for this infrared TL, experiments of fractional heating were led with the same equipment. They are shown on Figure 3 which displays vs temperature the intensity of TL of a sanidine ($(K, Na)AlSi_3O_8$) from the Eifel region through a filter OG 590.

As shown on Figure 1, the experiment is started at point D, until the exponential initial rise portion of the TL ends (point F). Then the heating program is reversed, the temperature is brought down to LNT (point G) and, without further irradiation, a new cycle of heating is started, dealing with deeper traps, and again reversed in point H, end of initial rise etc. In the present case, after 6 cycles, all the TL traps are emptied and thermal radiation alone shows.

Several observations are made:

- At the beginning of every cycle, just after the lower upturn of temperature, the tunnel afterglow is clearly observed, bent down by the 'thermal quenching' effect described above. This afterglow is observed on beginning of all the cycles always in the same proportion to following TL as long as there is TL left. This shows that tunneling is equally related with shallow and deeper traps.
- The initial rise part of the curves gives activation energies distribution of 'infrared' traps from 0.50 eV to 0.90 eV (at 470 K, higher obtainable value due to thermal radiation), which are quite usual values, with a continuous distribution of values.[6]

4 DISCUSSION

Some conclusions may be derived from the above observations. They take also into account results we published elsewhere,[6] studies quoted hereafter and a great number of other studies impossible to quote here.

TL Trap Distribution It has been reported that the 'blue' TL does not correspond to a single glow peak, not even to separate glow peaks, but rather to a continuous distribution of activation energies E. It is seen above that we have the same situation with the infrared band. The values above proposed for E (Figure 3) are only some 25% lower than values already reported for the 'blue' emission. They correspond to thermally stable traps. Hence their fading is anomalous as well.

4.1 *Infrared Emission Band and Fe^{3+}*

This infrared emission band had been partly observed previously, it has been lately measured in toto.[5,6] It was attributed to various causes, among these to the impurity Fe^{3+}.[4,7]

We observed the excitation spectra of that infrared emission on this feldspar and others. They showed excellent agreement with excitation spectra of Fe^{3+} published elsewhere.[7] The thermal quenching of luminescence observed (in Figure 3) and reported above is another well known characteristic of Fe^{3+} luminescence.[8]

One objection was raised by the observation that this infrared emission appears systematically in all feldspars with comparable intensities, while as a rule, luminescence due to impurities vary in proportion with the content in phosphors.

An explanation brought by geochemistry is that, due to the process of genesis of feldspars, there is a rather constant saturating content of Fe^{3+} in feldspars. It is substituted to Al^{3+} on 1% to 4% of T sites of silica tetrahedra.[9] Thus the distance between Fe atoms is of the order of 3 or 4 lattice cells at most, which is rather short. We are past saturation of iron as far as luminescence effects are concerned. Hence, the stable ubiquitous presence of infrared emission due to Fe^{3+} may be understood, as well as vicinity effects like tunnel recombination.

It may be concluded that Fe^{3+} is the source of infrared emission.

4.2 *Fading in feldspars, tunneling and crystal disorder*

From our experiments it is concluded that the phenomenon of anomalous fading so generalized in feldspars is strictly related with tunnelling infrared radiative recombination of trapped opposite charges competing with the regular thermal eviction of charges from traps. Tunnelling derives from presence of many pairs of donor-acceptor (D-A) sites with various short separations.

4.3 *Crystal 'disorder'*

Here it must be reminded that feldspars have a crystallographic characteristic unknown in simpler crystal lattices: it is the common occurrence of lattice 'disorder', known since 1934. Disorder does not consist in proper 'defects' like vacancies or interstitials in alkali halides, but random distributions of the Al atoms substituted for Si without vacancies. 'Younger' feldspars, like sanidines from recent volcanic lavas solidify in 'disordered' states, while 'ordered' states, more stable, call actually for very long times to be obtained by a solid state transformation. It is observed only in feldspars from very old geological formations.

4.4 *Disorder and charge traps*

Such states of crystal disorder, where a great proportion of trivalent atoms like Al^{3+} exchange their sites with tetravalent atoms like Si^{4+} create a great density of local 'charge defects'. This has been known by mineralogists since a long time.

We propose that such crystal defects act actually like classical defects, behaving as donors and acceptors which can trap opposite charges. Hence they are prone to tunnel recombination. Considering the high proportion of these defects, many have short separations and it is understandable why feldspars have an important TL and fade anomalously more than other known phosphors.

This view explains the experimental fact that the few 'non fading' feldspars, which could be dated, are microclines with an 'ordered' lattice where the proportion of these charge defects is much smaller.

Such new types of point defects originating from ion exchanges has been proposed very recently[10] to explain the observed wide, continuous distribution of activation energy in TL

of aluminosilicates (as seen on Figure 3). Our observations and analyses of tunnel afterglows bring strong vindication to this model.

4.5 *Fe^{3+} and Crystal Disorder*

We have reached two apparently unrelated conclusions from our study of the infrared emission: first, that it is due to disorder effects in the lattice because it shows outstanding tunnel kinetics, second, that it is due to Fe^{3+} because it is infrared.

These two conclusions may be brought together, by considering as follows that Fe^{3+} atoms in feldspars are, so to say, the centers of disorder. The limit in the content of Fe^{3+} derives from the big radius of that ion, some 0.064 nm vs some 0,050 nm for Al^{3+} and 0.41 for Si^{4+} which he substitutes. In other words, iron atoms bring in an additional crystal strain and generate charge defects. When on top of that, there is a situation of lattice disorder, that is of charge defects with random separations, all the conditions are met for intense infrared radiative tunnel recombinations.

Many questions are raised concerning the 'blue' band. It is spectrally independent from the 'infrared' one, and yet there is the fact that tunneling at lower temperatures, which empties traps resulting into infrared light only, results in preferential fading of the blue emission. No clear relation appears so far.

5 CONCLUSIONS

At the practical point of view of dating, the low temperature tunneling infrared emission we observe appears as a good criterion of the presence and intensity of fading, that is of the possibility of dating a feldspar by thermoluminescence.

A new type of point defect is proposed, directly related with order/disorder effects in crystal structure of feldspars and involving Fe^{3+} impurities substitutional for Al^{3+} to account for this infrared tunnel recombination.

ACKNOWLEDGMENTS

We thank A. J. J. Bos (Delft University of Technology), Ph. Blanc (UPMC, Paris), N. A. Spooner (LRAHA, U. of Oxford, now in A.N.U. Canberra, Aus.), G. Hutt (Inst. of Geology, Tallinn, Est.), I. Tale and his colleagues (Inst. of Solid State Ph., U. of Latvia, Riga), H. Jungner (U. of Helsinki), G. Walker (UMIST, Manchester, GB); Collection de Minéralogie, (UPMC) and Musée de l'ENSMines (Paris) for advice or direct contributions to this study.

REFERENCES

1. N. A. Spooner, *Radiat. Meas.* **23** (2/3) 625 (1994).
2. R. Visocekas, *Nucl. Tracks* **10**, 4–6, 521 (1985).
3. G. Hutt, H. Jungner, R. Kujansuu, M. Saarnisto, *J. of Quat. Sc.* **8 (2)** 125 (1993).
4. Y. Kirsh and P. D. Townsend, *Nucl. Tracks Radiat. Meas.* **14 (1/2)** 43 (1988).
5. A. J. J. Bos, T. M. Piters and P. J. Ypma *Radiat. Meas.* **23 (2/3)** 349 (1994).
6. R. Visocekas, N. A. Spooner, A. Zink and P. Blanc *Radiat. Meas.* **23 (2/3)** 377 (1994).
7. D. J. Telfer and G. Walker, *Modern Geology* **6**, 199 (1978).
8. W. B. White, *et al. American Mineralogist* **71**, 1415 (1986).
9. Ivan Petrov, S. S. Hafner, *American Mineralogist* **73**, 97 (1988).
10. P. Brovetto, *et al. Nuovo Cimento* **D15**, 1017 (1993).

Radiation Effects and Defects in Solids, 1995, Vol. 134, pp. 273–275
Reprints available directly from the publisher
Photocopying permitted by license only

© 1995 OPA (Overseas Publishers Association)
Amsterdam B.V. Published under license by
Gordon and Breach Science Publishers SA
Printed in Malaysia

EVIDENCE FOR SCHOTTKY BARRIER FORMATION DUE TO HOLE CENTERS IN Al_2O_3:Mg AND MgO:Li WITH METAL CONTACTS

R. VILA[1] and M. JIMÉNEZ DE CASTRO[2]

[1]*CIEMAT, Instituto de Investigación Básica, Av. Complutense 22,28040 Madrid, Spain;*
[2]*CSIC, Instituto de Ciencia de Materiales, Serrano 113, 28006 Madrid, Spain*

(Received July 1, 1994)

Thermally stimulated polarization (TSP) measurements in quenched Al_2O_3:Mg and MgO:Li are presented. A parallel behavior between the quenching-induced hole centers and the TSP spectra in both materials has been observed. The evolution of the main peak in each spectrum with the thermal annealings, the applied voltage and the sample thickness shows the existence of a Schottky barrier for holes at the metallic electrode-sample contacts. The current-voltage characteristics at room temperature also support this conclusion.

Key words: Thermally stimulated polarization oxides, hole centers, Schottky barriers.

1 INTRODUCTION

It is well known that oxidizing quenching from temperatures above 1200 K induces in Al_2O_3:Mg and MgO:Li hole centers, namely $[Mg]^\circ$ and $[Li]^\circ$ centers, respectively, which are stable above room temperature.[1,2] The electrical properties (conduction and polarization) of these doped oxides are determined by the thermally activated ionization of these centers.[3–5] The materials may then be regarded as wide-band-gap type p semiconductors, the Fermi level lying near the valence band. They have therefore a very high work function and hence, any metal used as electrode on their surfaces will form a Schottky barrier for holes. Blocking contacts in metal-insulator-metal systems give rise to thermally stimulated polarization (TSP) and depolarization (TSD) processes when thermally activated electric charge release occurs. They appear as a result of relaxations of the depletion region near one of the electrodes (the anodic one when the carriers are holes). These processes have been extensively studied by Simmons and coworkers.[6] This paper is devoted to show that our TSP results in Al_2O_3:Mg and MgO:Li single crystals are in very good agreement with Simmons' theory, giving thus experimental evidence about Schottky barrier formation in these materials for any of the metals used for electrodes (either pressed indium foils or evaporated platinum, gold or aluminum).

2 RESULTS AND DISCUSSION

When Al_2O_3:Mg and MgO:Li are subjected to thermal quenching in oxidizing atmosphere, $[Mg]^\circ$ and $[Li]^\circ$ centers, respectively, are created, and TSP spectra appear. Typical TSP spectra are plotted in Figure1. They are very similar to the TSD ones.[4,5] A main peak at about 265 K in Al_2O_3:Mg and 255 K in MgO:Li (these temperatures are treatment-dependent), together with another one around room temperature are clearly seen. The experimental data presented in this paper correspond to the main peak in each case.

A pulsed thermal annealing experiment reveals that the hole center optical absorption band and the TSP spectrum vanish together in both materials.[4,5] This indicates that $[Mg]^\circ$

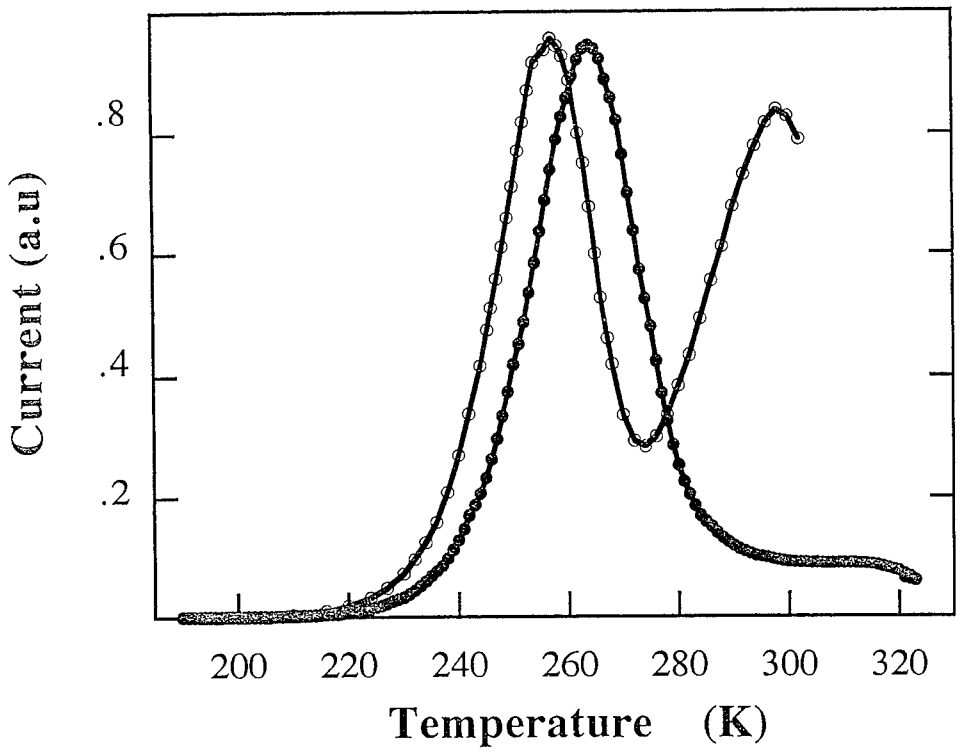

FIGURE 1 Normalized TSP spectra of quenched Al_2O_3:Mg (●) and MgO:Li (○). Applied voltage: 25 V.

and $[Li]^o$ centers are closely related to the TSP processes. The values for the total polarization (P_o), calculated from the TSP areas, are too much large to ascribe the TSP processes to dipolar reorientations involving Mg or Li ions. Therefore the TSP peaks has to be related to limited electric charge conduction processes, the electric carriers being holes released from $[Mg]^o$ or $[Li]^o$ centers.

The P_o values depend almost linearly on the square root of the applied voltage (V_p) for both materials, as it can be seen in Figure 2. On the other hand, P_o/E_p, where $E_p = V_p/d$ is the applied field, is linearly dependent on the sample thickness d. These two very important observations disregard the TSP processes in both materials to be related to Maxwell-Wagner polarization of impurity-rich regions embedded in the insulator matrix, as it was proposed for the TSD of MgO:Li.[3] Instead they agree with the predictions of Simmons' theory for TSP processes in metal-insulator-metal systems with blocking electrodes.[6] Other experimental results obtained in this work supporting this model are the dependences of the peak temperatures (T_m) with V_p (T_m decreases with increasing V_p) and with d (T_m increases with increasing d). Also the hysteresis effects in the total polarization with respect to V_p found here are explained by the above mentioned theory.

The current-voltage curves of Al_2O_3:Mg at room temperature are strongly non-linear. They can be well fitted to a combination of two terms: One of them, which represents the behavior at low voltages, can be explained by both the thermoionic (Richardson-Schottky) and thermoionic-field emission equations and is consistent with the formation of a Schottky barrier at the sample surface.[7] The second term, which dominates at high voltages, is proportional to V^2/d^3; this is the Mott-Gurney equation for a space-charge limited conduction

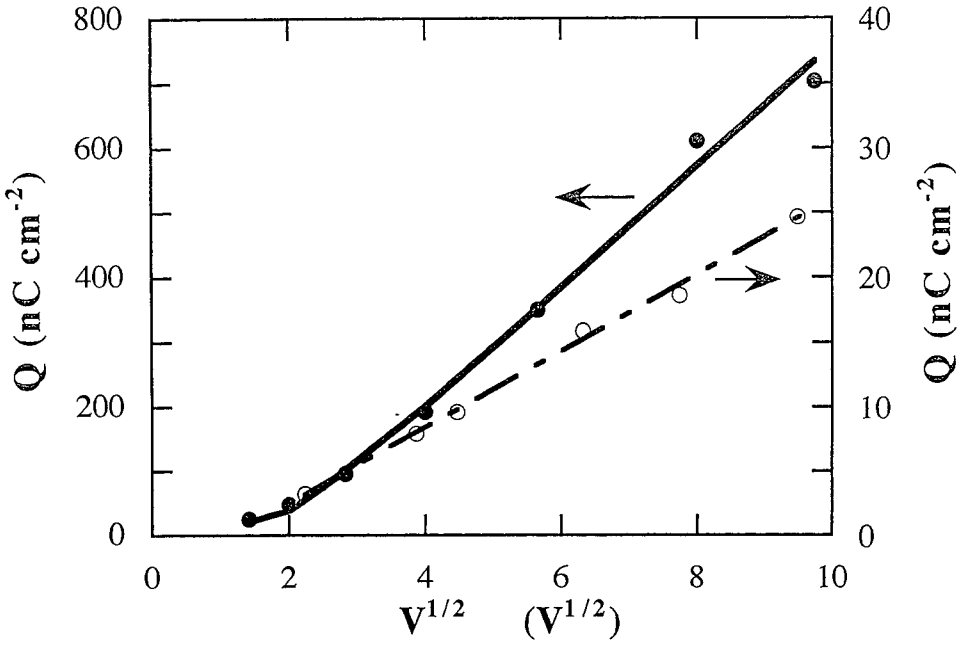

FIGURE 2 Dependence of the main TSP peak area on the applied voltage for Al_2O_3:Mg(●) and MgO:Li(○). Samples have been quenched from 1300 °C.

process.[8] The overall behavior of the I–V curves shows the occurrence of an electrode-limited to bulk-limited transition, which has been observed in other systems with blocking contacts.[9] Highly non-linear I–V curves are known in MgO:Li,[3] but have not been analyzed.

In conclusion, the TSP results as well as the I–V curves show the formation of Schottky barriers at the electrode- sample contact due to the presence of hole centers in the crystals. The large polarization values are related to changes in the anodic depletion region width caused by thermally stimulated hole release and subsequent drift under the applied electric field. This could explain TSP-TSD processes in a wide range of doped oxides.

REFERENCES

1. H. A. Wang, C. H. Lee, F. A. Kröger and R. T. Cox, *Phys. Rev.* **B 27**, 3821 (1983).
2. Y. Chen, H. T. Tohver, J, Narayan and M. M. Abraham, *Phys. Rev.* **B 16**, 5535 (1977).
3. J. H. Crawford, in *Structure and Properties of MgO and Al_2O_3 Ceramics* (Adv. in Ceramics, vol 10), ed. by W. D. Kingery (The American Ceramic Soc., Ohio, 1984), pp. 21–24.
4. R. Vila and M. Jiménez de Castro, *Phys. Rev.* **B 49**, 1969 (1994).
5. R. Vila, A. Ibarra, M. Jiménez de Castro and D. F. Mariani, *Solid State Commun.* **90**, 61 (1994).
6. J. G. Simmons and G. W. Taylor, *Phys. Rev.* **B 6**, 4804 (1972).
7. E. H. Rhoderick and R. H. Williams, *Metal-Semiconductors Contacts* (Clarendon Press, Oxford, 1988), 2nd ed., Chap. 3, pp. 124–132.
8. N. F. Mott and R. W. Gurney, *Electronic Processes in Ionic Crystals* (Dover, New York, 1964), 2nd ed., Chap. 5, p. 172.
9. J. G. Simmons, *Phys. Rev.* **166**, 912 (1968).

Radiation Effects and Defects in Solids, 1995, Vol. 134, pp. 277–281
Reprints available directly from the publisher
Photocopying permitted by license only

© 1995 OPA (Overseas Publishers Association)
Amsterdam B.V. Published under license by
Gordon and Breach Science Publishers SA
Printed in Malaysia

NUCLEAR MAGNETIC RESONANCE AND ELECTRICAL CONDUCTIVITY IN SINGLE-CRYSTALLINE PARATELLURITE

J. WEGENER, O. KANERT, R. KÜCHLER and A. WATTERICH*

*Inst. of Physics, University of Dortmund, 44221 Dortmund, Germany; *Research Lab. f. Crystal Physics, Budapest, Hungary*

^{125}Te nuclear spin relaxation (NSR) and electrical conducvitiy measurements were performed on single-crystalline paratellurite (α-TeO_2) between room temperature and the melting point (1007K) at various oxygen partial pressures. A defect model is developed which fits the experimental data. The model involves ionic oxgyen interstitials (O_i''), doubly charged oxygen vacancies ($V_O^{\bullet\bullet}$) and charge-compensating electron holes ($h^{\bullet}$). The pressure dependence suggests that the NSR rate is induced by the motion of $V_O^{\bullet\bullet}$ while the conductivity is due to diffusion of $h^{\bullet}$. Further, the chemical diffusion coefficient is shown to be caused by ambipolar diffusion of O_i'' and $h^{\bullet}$.

Key words: Oxides, defects, nuclear spin relaxation, conductivity, diffusion.

1 INTRODUCTION

Paratellurite (α-TeO_2) is an insulator (gap energy about 4.3 eV) which crystallizes in the space group $P4_12_12$. As shown earlier,[1] the ^{125}Te NMR spectrum consists of four lines according to four magnetically non-equivalent Te lattice sites in the tetragonal unit cell. To our knowledge only two investigations have been carried out in the past on the diffusion properties of α-TeO_2.[2,3] Both studies deal with the temperature dependence of the electrical conductivity at elevated temperatures. Here we present a defect model which is able to explain consistently both the temperature dependence and the oxygen partial pressure (p_{O_2}) dependence of electrical conductivity and the motion induced ^{125}Te NSR rate observed in pure single-crystalline α-TeO_2.

2 EXPERIMENTAL RESULTS

In order to investigate the diffusional properties of oxygen-induced defects in paratellurite we have performed two types of experiments. (i) Temperature dependence of the ^{125}Te NSR rate T_1^{-1} and conductivity σ under constant p_{O_2}-pressures; (ii) time response of T_1^{-1} and σ after a sudden change of p_{O_2} at constant temperatures (see Figures 1–4). As shown earlier, the observed NSR rate T_1^{-1} (Figure 1) consists of a phonon-induced contribution $T_1^{-1}|_{Ph}$, and a diffusion-induced contribution $T_1^{-1}|_{Diff}$, which becomes significant at elevated temperatures:[1]

$$T_1^{-1} = T_1^{-1}|_{Ph} + T_1^{-1}|_{Diff} = aT^2 + b\exp(-E_{NMR}/kT) \tag{1}$$

Analysis of the NSR data leads to the relation

$$T_1^{-1}|_{Diff} \propto \omega^2 p_{O_2}^{-1/6} \exp(-3.0\ eV/kT) \tag{1a}$$

which is consistent with the following mechanism: The NSR rate is induced by the diffusion of vacancies of concentration $\{V\}$ and hopping rate $\Gamma_V \propto \exp(-H_m/kT)$ via CS-fluctuations

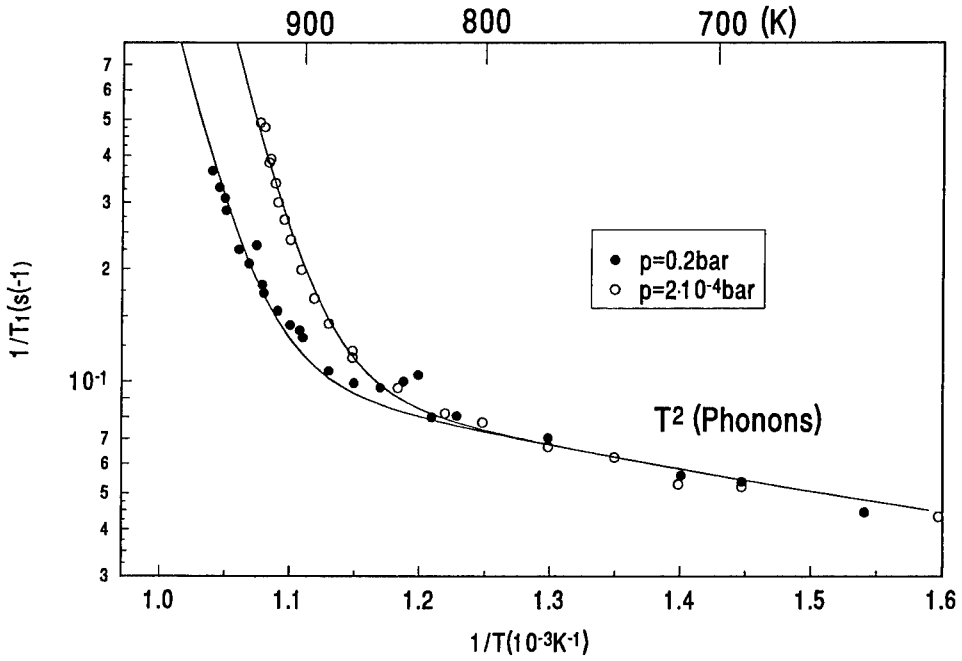

FIGURE 1 ^{125}Te NSR-rate T_1^{-1} vs inverse temperature for two different p_{O_2}-pressures.

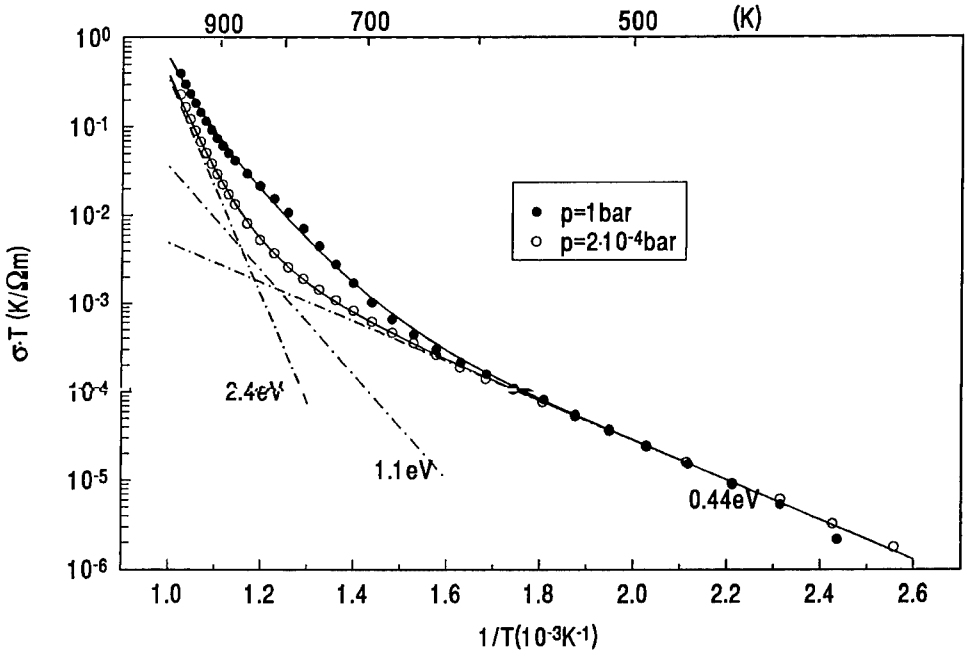

FIGURE 2 Arrhenius plot of conductivity σT at two different p_{O_2}-pressures.

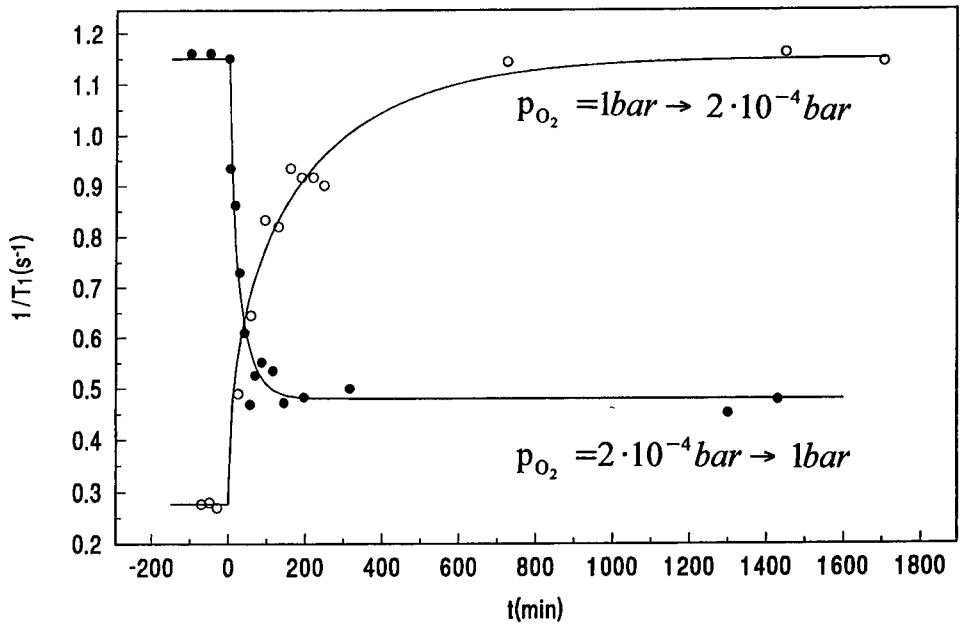

FIGURE 3 Time response of T_1^{-1} of ^{125}Te after a sudden change of p_{O_2}.

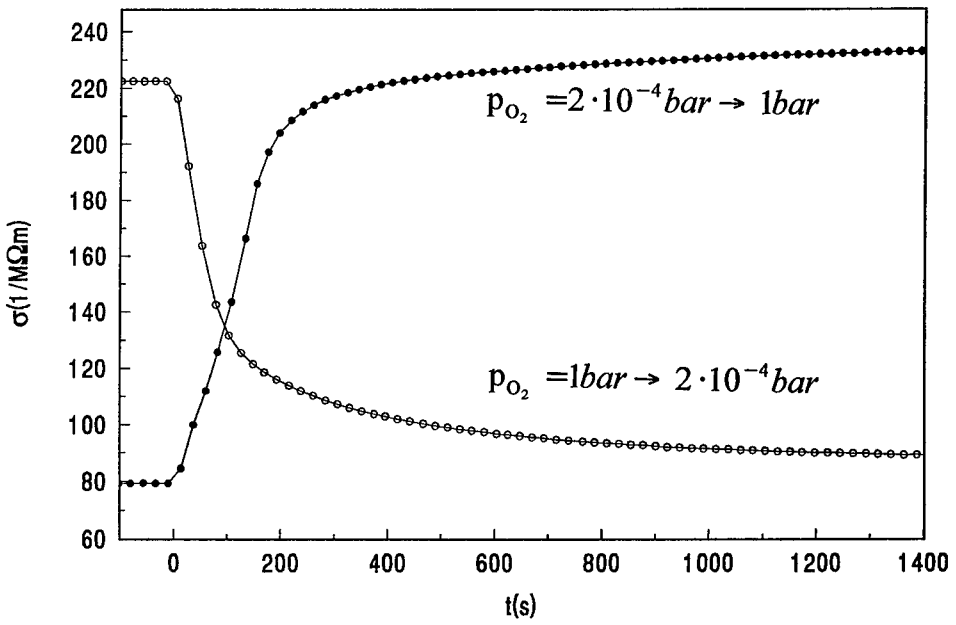

FIGURE 4 Time response of conductivity σ after a sudden change of p_{O_2}.

occuring when a vacancy encouters a ^{125}Te probe nucleus. Then assuming $\Gamma_V >$ Larmor frequency ω, the standard relations of diffusion-induced NSR[4] lead to:

$$T_1^{-1}|_{Diff} \propto \omega^2 \{V\} \Gamma^{-1}{}_V \tag{2}$$

Comparing Eq. (1a) and Eq. (2) leads to $\{V\} \propto p_{O_2}^{-1/6}$.

The observed temperature and p_{O_2}-dependence of the conductivity (Figure 2) can be related to three thermally activated processes according to

$$\sigma T = \sum_{i=1}^{3} a_i(p_{O_2}) \exp(-E_i/kT) \tag{3}$$

with the following activation energies: $E_1 = 0.44 \pm 0.02$ eV, $E_2 = 1.1 \pm 0.1$ eV, $E_3 = 2.4 \pm 0.2$ eV. The first and third contribution are found to be independent of p_{O_2}, while the second contribution depends on p_{O_2}:$a_2 \propto p_{O_2}^{-1/6}$. Following Hartmann,[3] we assume that the first contribution is due to the migration of impurity-controlled (i.e. extrinsic) vacancies ($E_1 = H_m$), whereas the magnitude of E_3 indicates an electronic mechanism for the third contribution ($E_3 \equiv 1/2E_{gap}$). The defect model presented in the next section demonstrates that the second contribution can be related to the motion of electron holes $h^\bullet$.

The observed time evolution of T_1^{-1} (Figure 3) and σ (Figure 4) are opposite with respect to the sign of the p_{O_2}-change in accord with the observed pressure dependence of the two observables shown in Figures (1,2). Further, the corresponding time constants are equal for σ(t) when raising (oxidation) or lowering (reduction) p_{O_2} other than the time constants of the response function of T_1^{-1}.

3 DEFECT MODEL

A model of dilute, noninteracting point defects is developed for TeO_2 considering that the self-diffusion of Te is observed to be extremely low up to the melting point ($D(950K) \leq 10^{-15}$ cm^2/s), i.e. Te does not take part in internal defect-chemical reactions. Hence, only the reactions of oxygen have to be taken into account. Oxygen gas is supposed to be solved as ionic oxygen at interstitial sites under formation of electron holes:

$$\frac{1}{2}O_2(g) \leftrightarrow O_i'' + 2h^\bullet \tag{4}$$

The corresponding law of mass action (LMA) is given by

$$p_{O_2}^{-1/2}\{O_i''\}\{h^\bullet\}^2 \propto \exp\left(-\frac{H_s}{kT}\right) \tag{4a}$$

where H_s denotes the enthalpy of the solution process. Further, oxygen Frenkel pairs, consisting of O_i'' and $V_O^{\bullet\bullet}$, are formed according to

$$O_O \leftrightarrow O_i'' + V_O^{\bullet\bullet} \tag{5}$$

where O_O denotes a regular oxygen on an anion site. The LMA of this Frenkel reaction is

$$\{O_i''\}\{V_O^{\bullet\bullet}\} \propto \exp\left(-\frac{H_F}{kT}\right) \tag{5a}$$

with H_F being the enthalpy of pair formation. Charge neutrality requires

$$2\{O_i''\} + \{e'\} = 2\{V_O^{\bullet\bullet}\} + \{h^{\bullet}\} \tag{6}$$

Assuming $\{O_i''\} \gg \{V_O^{\bullet\bullet}\}$, one obtains from eqs. (4–6)

$$\{h^{\bullet}\} \propto p_{O_2}^{1/6} \exp\left(-\frac{\frac{1}{3}H_S}{kT}\right) \qquad \{V_O^{\bullet\bullet}\} \propto p_{O_2}^{-1/6} \exp\left(-\frac{H_F - \frac{1}{3}H_S}{kT}\right) \tag{7a, b}$$

for the concentration of the holes and vacancies.

The observed pressure dependence of the conductivity part σ_2 is in accord with Eq. (7a). Hence, we conclude that $\sigma \propto \{h^{\bullet}\}$ and therefore $H_s = 3E_2 = 3.3 \pm 0.3$ eV. Further, the measured pressure dependence of T_1^{-1} (Eq.(1a)) agrees to that predicted in Eq.(7b), indicating that the relaxation process is caused by the motion of the minority carriers $V_O^{\bullet\bullet}$. Comparison of Eqs. (1a, 2, 7b) yields $H_F = E_{NMR} + 1/3H_S + H_m \approx 4.5$ eV for the formation of the oxygen frenkel pairs (Eq.(5)), using $H_m = E_1 = 0.44$ eV and $E_{NMR} = 3$ eV.

The time response of σ presented in Figure 4 is determined by the evolution of the local concentration of the predominant carriers (O_i'', $h^{\bullet}$) in space and time according to Fick's second law, where D^C is the chemical diffusion coefficient. Solutions of this equation are symmetric with respect to the sign of the p_{O_2} change, as measured in the experiments (Figure 4). On the contrary, the corresponding evolution of the local concentration of the minority carriers $V_O^{\bullet\bullet}$ responsible for the measured transient of T_1^{-1} (Figure 3) is controlled by the local concentration of the O_i'' via eq. (5a). The solid lines in Figures (3,4) result from solutions of Fick's second law using appropriate boundary conditions and a uniform value of $(1 \pm 0.3).10^{-5}$ cm^2/s for the diffusion coefficient D^C(950K).

ACKNOWLEDGEMENTS

The authors would like to thank Prof. Schmalzried for helpful discussion. The work was financially supported by the Deutsche Forschungsgemeinschaft.

REFERENCES

1. J. Wegener, R. Küchler, O. Kanert and A. Watterich *Proc. XII Int. Conf. on Def. in Insulating Mat.* (World Scientific, Singapore, 1993), Vol. 2, p. 715.
2. H. Jain and A. S. Nowick *Phys. Stat. Sol.* (a) **67**, 701 (1981).
3. E. Hartmann and L. Kovacs *Phys. Stat Sol* (*a*) **74**, 59 (1982).
4. O. Kanert *Phys. Report* **91**, 183 (1982).

Radiation Effects and Defects in Solids, 1995, Vol. 134, pp. 283–286
Reprints available directly from the publisher
Photocopying permitted by license only

© 1995 OPA (Overseas Publishers Association)
Amsterdam B.V. Published under license by
Gordon and Breach Science Publishers SA
Printed in Malaysia

VIBRATION + LIBRATION ABSORPTION BANDS OF OH CENTRES IN $LiNbO_3$

A. GRÖNE and S. KAPPHAN

FB Physik, University of Osnabrück, D–49069 Osnabrück, Germany

Hydrogen centres in the bulk of stoichiometric (VTE) $LiNbO_3$ exhibit a sharp absorption band of the OH(OD) stretching vibration near 3466 (2562) cm^{-1}. In congruent $LiNbO_3$ the OH band ($\bar{\nu}_{max}$ = 3484cm^{-1}) is rather broad (FWHM ~30 cm^{-1}) and for the high proton concentration layers in proton exchanged $LiNbO_3$:PE the broad absorption band (FWHM ~30 cm^{-1}) is shifted to about 3507 cm^{-1}. For all the above bands which are completely polarized perpendicular $\vec{z}$ weak high energy sidebands have been found, shifted by about 950 cm^{-1} for OH and 700 cm^{-1} for OD with respect to the position of the stretching vibration. The intensity of these sidebands and their spectral form is found to be proportional to the stretching vibration, respectively to the concentration of the H(D) centres. These sidebands are identified as libration + vibration combination bands and display the polarization dependence ($I_{\parallel}/I_{\perp} \approx 0.5$ for OH with respect to $\vec{z}$) of a three-dimensional oscillator. The libration + vibration combination bands have also been detected as sidebands to higher vibrational transitions in proton (deuteron) exchanged $LiNbO_3$:PE(DE).

Key words: OH defect centers, vibration + libration absorption bands, $LiNbO_3$.

1 INTRODUCTION

Hydrogen centres in $LiNbO_3$ have been shown to be very mobile[1] and influence many properties important for technical applications. For instance the laser optical damage,[2,3] the thermal fixing of volume phase holograms,[4] the production of wave guiding layers by proton implantation[5] or proton exchange,[6] the properties of TIPE waveguides[7,8] and the phase matching temperature for optical second harmonic generation of Nd:YAG laser light[9] have been reported to be modified by protons. The presence of hydrogen in $LiNbO_3$ is revealed by a characteristic OH stretching vibration near 3500 cm^{-1}. For the discussion of the protonic mobility in TiO_2 an additional librational motion as an attempt frequency has been calculated.[10] Experimental evidence for the librational mode of OH centres has not been found so far, neither in TiO_2 nor in $LiNbO_3$ or any other ABO_3 crystals. However a librational mode of $OH^-(OD^-)$ molecules in alkali halide crystals is well known.[11] This prompted us to start an intensive search for the librational motion and eventual combination bands of libration + vibration in order to clarify this important parameter for the model discussion of OH defects and their protonic mobility. In particular the identification of the libration+vibration combination band in $LiNbO_3$ is the topic of this paper. We present evidence from the concentration and the polarization dependence for the identification of weak sidebands of the OH stretching vibration as the sought after libration + vibration combination bands.

2 EXPERIMENTAL

For the investigations of the OH/OD absorption bands in the bulk of stoichiometric $LiNbO_3$ we use congruent $LiNbO_3$ which has been treated by the vapour transport equilibration (VTE) technique[12,13,14] in our own laboratory.

To raise the hydrogen concentration in the bulk of $LiNbO_3$ the method of field supported proton diffusion was employed.[2,15]

Proton as well as deuteron exchanged (PE/DE) $LiNbO_3$ layers have been produced by immersion of thin samples (d = 0.5–0.7 mm) in benzoic acid melt buffered by 0.5 mol % lithium benzoate at T_{PE} = 244°C for ~10 hours[6,16] and then in deuterated benzoic acid for ~10 hours at the same temperature T_{PE} = 244°C to get nearly equal optical densities for the OH and the OD stretching vibration, respectively.

The infrared absorption spectra were obtained with a Fourier-IR-Spectrometer (Bruker 113 Cv) in the range from 2400 cm^{-1}–7900 cm^{-1} with a resolution up to 0.05 cm^{-1}.

3 RESULTS

The spectra of OH and OD centres in a proton and deuteron exchanged sample of $LiNbO_3$ at room temperature are shown in Figure 1. Besides the well known stretching vibration, weak sidebands at 3278 cm^{-1} for OD and at 4444 cm^{-1} for OH are observed. These sidebands and their properties will be discussed in congruent, in stoichiometric (VTE) and in proton (deuteron) exchanged $LiNbO_3$:PE(DE) in the following chapters.

Figure 2 shows a detailed comparison of the band shape of the main OH stretching vibration $\bar{\upsilon}_{01}$ near 3500 cm^{-1} and the weak sidebands $\bar{\upsilon}_{vib_{01}+lib}$ near 4450 cm^{-1}. The similarities in the band shape and relative position is evident for all three samples. Similar sidebands $\bar{\upsilon}_{vib_{02}+lib}$ are also observed with the next higher vibrational transitions $\bar{\upsilon}_{02}$ in proton(deuteron) exchanged $LiNbO_3$:PE(DE). The positions of these absorption bands are given in Table I.

A main argument for the identification of these bands comes from the concentration dependence which shows a direct correlation with the intensity of the main stretching vibration $\bar{\upsilon}_{01}$. In Figure 3 the constant ratios of the integrated absorption intensity of the fundamental $\bar{\upsilon}_{01}$ and the sidebands $\bar{\upsilon}_{vib_{01}+lib}$ is plotted versus concentration (proportional to the absorption coefficient). The same holds for the OD centres in these crystals. The constant ratio over one order of magnitude in concentration strongly supports the interpretation of the sidebands as belonging to the OH/OD vibrational properties. We therefore take it as

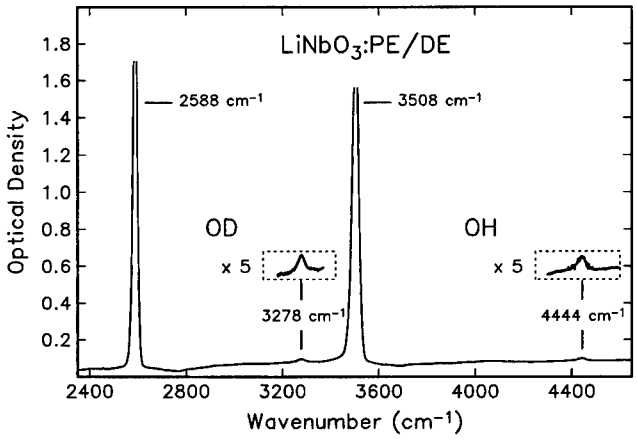

FIGURE 1 OH and OD stretching vibration ($\bar{\upsilon}_{01,OH}$ = 3508 cm^{-1} and $\bar{\upsilon}_{01,OD}$ = 2588 cm^{-1}) and OH and OD libration + vibration combination bands ($\bar{\upsilon}_{vib_{01}+lib,OH}$ = 4444 cm^{-1} and $\bar{\upsilon}_{vib_{01}+lib,OD}$ = 3278 cm^{-1}) in proton (PE) and deuteron exchanged (DE) $LiNbO_3$ at RT (in the dashed boxes the spectra of the librational sidebands are enlarged by a factor 5). The optical densities of the OH and OD stretching vibration bands are so high in this case that it is not possible to resolve them exactly. Therefore they are vertically limited. The spectra are recorded unpolarized for a z-cut crystal ($\vec{k}_{Light} \parallel \vec{z}$).

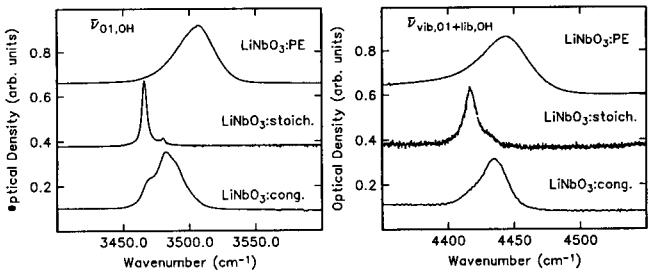

FIGURE 2 OH stretching vibration $\bar{\nu}_{01,OH}$ (left) and libration + vibration combination band $\bar{\nu}_{vib_{01}+lib,OH}$,(right) in different $LiNbO_3$ crystals at RT: in proton exchanged $LiNbO_3$:PE, in the bulk of nearly stoichiometric (VTE) $LiNbO_3$: stoich. and in the bulk of congruent $LiNbO_3$:cong. ($\vec{E}_{Light} \perp \vec{z} \perp \vec{k}_{Light}$). The spectra are shifted vertically for better viewing.

TABLE I

Observed wavenumbers of the peaks of the absorption maxima of the OH and OD stretching vibrations ($\bar{\nu}_{01}$) and of the libration + vibration combinations bands ($\bar{\nu}_{vib_{on}+lib}$) at RT.

$LiNbO_3$	$\bar{\nu}_{01,OH}$ (cm^{-1})	$\bar{\nu}_{01,OD}$ (cm^{-1})	$\bar{\nu}_{vib_{01}+lib,OH}$ (cm^{-1})	$\bar{\nu}_{vib_{01}+lib,OD}$ (cm^{-1})	$\bar{\nu}_{vib_{02}+lib,OH}$ (cm^{-1})	$\bar{\nu}_{vib_{02}+lib,OD}$ (cm^{-1})
PE/DE	3508 ± 2	2588 ± 2	4444 ± 2	3278 ± 2	7738 ± 4	5767 ± 4
cong.	3484 ± 2	2574 ± 2	4436 ± 2	3274 ± 2		
stoich.	3465.9 ± 0.2	2561.9 ± 0.1	4417 ± 1	3271 ± 1		

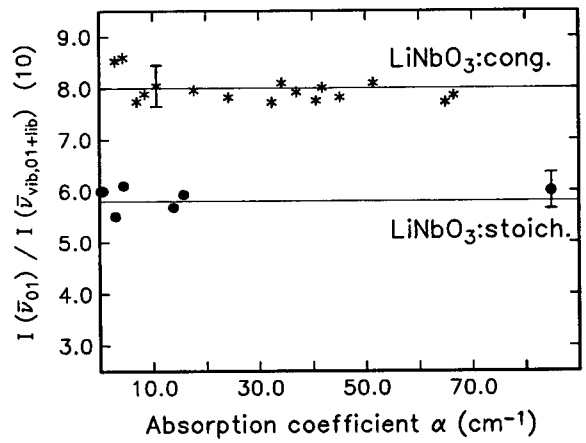

FIGURE 3 Ratio of the integrated absorption intensities $I_{01}/I_{vib_{01}+lib}$ of the OH vibration band $\bar{\nu}_{01}$ and the OH libration + vibration combination band $\bar{\nu}_{vib_{01}+lib}$ in the bulk of congruent $LiNbO_3$ (*) and in the bulk of nearly stoichiometric (VTE) $LiNbO_3$ (•). The horizontal lines are guides for the eye.

evidence for a librational motion of the OH/OD centres which appears as a combination of libration + vibration in these sidebands. These sidebands are shifted by about 950 cm^{-1} for OH and by about 700 cm^{-1} for OD with respect to the position of the main stretching vibration $\bar{\nu}_{01}$. These shifts should therefore correspond (with minor corrections due to the excited vibrational state) to the frequencies of the OH/OD librations in these host lattices. The ratio of the librational sideband splitting, i.e. the difference between the wavenumbers of the libration+vibration combination band and the wavenumber of the streching vibration, for OH and OD is in accord with the ratio of the reduced mass of the OH/OD oscillator $\dfrac{\bar{\nu}_{vib_{0n}+lib} - \bar{\nu}_{0n}(\mathrm{OH})}{\bar{\nu}_{vib_{0n}+lib} - \bar{\nu}_{0n}(\mathrm{OD})} \approx \sqrt{\dfrac{\mu_m, \mathrm{OD}}{\mu_m, \mathrm{OH}}}$.

Further evidence for the librational character of the sidebands can be obtained from the polarization properties of these transitions. Whereas the OH/OD stretching vibration in all cases has been observed to be completely polarized perpendicular to the polar z-axis in $LiNbO_3$, the libration is expected to display a three-dimensional character. Indeed the absorption of the combination bands yields for polarized light ratios of the integrated absorption intensities of $I_{\parallel}/I_{\perp} \approx 0.55 \pm 0.05$ for OH with respect to $\vec{z}$. This indicates a strong component of the librational transition moment which occurs parallel to the z-axis as well and supports the three-dimensional character of the librational motion. The fact that the absorption parallel and perpendicular to the z-axis appears at the same spectral position points to a potential for the libration which is the same in both directions (parallel and perpendicular $\vec{z}$). For the interpretation of the mobility of the protons in $LiNbO_3$ with the libration as an attempt frequency this would lead to an isotropic activation energy E_A which indeed has been observed in $LiNbO_3$ for OH/OD centres.[1] These properties and the existence of a librational motion will advance the model discussion of the OH centres in $LiNbO_3$.

This work was supported by the DFG (SFB 225).

REFERENCES

1. S. Klauer, M. Wöhlecke, and S. Kapphan, *Phys. Rev. B* **45**, 2786 (1992).
2. R. G. Smith, D.B. Fraser, R. T. Denton, and T. C. Rich, *J. Appl. Phys.* **39**(10), 4600 (1968).
3. J. L. Jackel, D. H. Olson, and A. M. Glass, *J. Appl. Phys.* **52**(7), 4855 (1981).
4. D. L. Staebler and J. J. Amodei, *Ferroelectrics* **3**(13), 107 (1971).
5. P. Moretti, P. Thevenard, K. Wirl, P. Hertel, H. Hesse, E. Krätzig and G. Godefroy, *Ferroelectrics* **128**, 13 (1992).
6. J. L. Jackel, C. E. Rice, and J. J. Veselka, *Appl. Phys. Lett.* **41**(7), 607 (1982).
7. J. L. Jackel, A. M. Glass, G. E. Peterson, C. E. Rice, D. H. Olson, and J. J. Veselka, *J. Appl. Phys.* **55**(1), 269 (1984).
8. A. L. Dawar, S. M. Al-Shukri, R. M. De La Rue, A. C. G. Nutt, and G. Stewart, *Opt. Commun.* **61**(2), 100 (1987).
9. N. Schmidt, K. Betzler, M. Grabs, S. Kapphan, and F. Klose, *J. Appl. Phys.* **65**, 1253 (1989).
10. J. B. Bates, J. C. Wang, and R. A. Perkins, *Phys. Rev.* **19**(8), 4130 (1979).
11. M. V. Klein, B. Wedding, and M. A. Levine, *Phys. Rev.* **180**(3), 902 (1969).
12. R. L. Holman, Ed. H. Polmour and R. F. Davidsin, *Processing of Crystalline Ceramics (Mat. Sci. Res.)* **11**, 343 (1978).
13. Y. S. Luh, M. M. Fejer, R. L. Byer, and R. S. Feigelson, *J. Cryst. Growth* **85**,264 (1987).
14. P. F. Bordui, R. G. Norwood, D. H. Jundt, and M. M. Fejer, *J. Appl. Phys.* **71**(2), 875 (1992).
15. A. Förster, S. Kapphan, and M. Wöhlecke, *Phys. Stat. Sol.* (b) **143**, 755 (1987).
16. S. Kapphan and A. Breitkopf, *Phys. Stat. Sol.* (a) **133**, 159 (1992).

Radiation Effects and Defects in Solids, 1995, Vol. 134, pp. 287–291
Reprints available directly from the publisher
Photocopying permitted by license only

© 1995 OPA (Overseas Publishers Association)
Amsterdam B.V. Published under license by
Gordon and Breach Science Publishers SA
Printed in Malaysia

OH^- ABSORPTION IN $Bi_4Si_3O_{12}$ SINGLE CRYSTALS

L. KOVÁCS*, P. BENEVENTI •, R. CAPELLETTI•

**Research Laboratory for Crystal Physics—Hungarian Academy of Sciences—1112 Budapest, Budaörsi út 45—Hungary; • Department of Physics—University of Parma—Viale delle Scienze, 43100 Parma—Italy*

(Received July 1, 1994)

High resolution FTIR absorption spectroscopy has been used to study the vibrational modes of hydroxyl ions incorporated into $Bi_4Si_3O_{12}$ crystals. The single narrow absorption band observed at 3570.92 cm^{-1} at 9 K has been attributed to the fundamental stretching mode of the OH^- ion. The first overtone of the OH^- vibration and the fundamental OD^- transition in deuterated crystal have also been measured. The model of the anharmonic oscillator in the Morse potential has been applied to interpret the spectra observed. The phonon coupling of the OH^- vibration has been studied by analyzing the temperature dependence of the OH^- absorption line position and width.

Key words: $Bi_4Si_3O_{12}$ crystal, OH^- vibration, FTIR spectroscopy.

1 INTRODUCTION

Bismuth germanate ($Bi_4Ge_3O_{12}$) single crystals of the eulytite structure (with $I\bar{4}3d$ cubic space group) are commonly used as scintillators because of their efficient luminescence properties. Their defect structure is widely studied by using various spectroscopical methods: recently the presence of hydroxyl ions detected by the infrared absorption technique has been reported.[1,2] A set of lines around 3400–3500 cm^{-1} attributed to localized OH^- vibrations was detected in hydrothermally grown $Bi_4Ge_3O_{12}$,[1] while in crystals grown by the Czochralski method only one relatively narrow band (~5 cm^{-1} at 9 K) was found at ~3385 cm^{-1}.[2]

Much less is known about the orthosilicate eulytite ($Bi_4Si_3O_{12}$) itself. Although the infrared absorption spectra of $Bi_4Si_3O_{12}$ in the 400–4000 cm^{-1} wavenumber range have already been measured,[3] no signal attributable to OH^- vibration has been observed.

The present paper fits in the series of our studies on the vibrational properties of hydroxyl ions in crystals based on bismuth oxide (e.g. $Bi_{12}MeO_{20}$ sillenite, $Bi_4Me_3O_{12}$ eulytite with Me = Ge, Si).[2,4] The presence of OH^- in these crystals grown from the melt in air atmosphere seems to be a general phenomenon, its incorporation and vibrational properties are, however, strongly influenced by the crystal and defect structure.

2 EXPERIMENTAL

The $Bi_4Si_3O_{12}$ crystal was grown in air by the diameter controlled Czochralski method using high purity Bi_2O_3 and SiO_2 raw materials. An 18 mm long sample perpendicular to the growth axis was cut and polished to detect the OH^- signal expected. OD^- absorption was measured on the same sample after the isotopic substitution of H with D obtained by heating the sample at ~800 °C for 4 hours in O_2 gas flowing through heavy water (D_2O).

The high resolution (0.05 cm^{-1}) spectra were measured by a Bomem DA8 FTIR spectrophotometer in the 9–300 K temperature range using a 21SC model cryostat of CTI-Cryogenics.

3 RESULTS AND DISCUSSION

Only one narrow absorption band was detected in the 3300–3600 cm^{-1} wavenumber range typical for OH^- vibrations in oxide crystals. The position and halfwidth (full width at half maximum) of the line at 9 K are 3570.92 cm^{-1} and 0.45 cm^{-1}, respectively. By increasing the temperature the intensity of the band decreased, the halfwidth increased and the position shifted to lower wavenumbers (Figure 1). The integrated intensity remained constant in the whole temperature range between 9–300 K. The concentration of OH^- estimated from the integrated intensity and calibrations for other oxides[5,6] is about $3 \div 8 \times 10^{15}$ cm^{-3}.

In order to ascertain that hydrogen is involved in the defect responsible for the above line the sample was kept at 800 °C in D_2O vapour atmosphere. After the treatment the absorption at 3570.92 cm^{-1} decreased and a new band at 2637.6 cm^{-1} appeared as it can be seen on the inset of Figure 2. (The strong and wide overlapping bands between 2550–2800 cm^{-1} belong to the three-phonon transitions of the SiO_4 tetrahedral vibrations.[3]) The ratio between the positions of the 3570.92 and 2637.6 cm^{-1} bands (R = 1.354) is nearly equal to the square root of the ratio of the reduced masses of free OD and OH molecules (R_f = 1.374) confirming the assumption that the lines belong to OH^- and OD^- vibrations, respectively. The difference between the ratios mentioned above reveals the anharmonicity of the oscillator. Due to the anharmonicity overtone transition was expected and indeed found at 6970.7 cm^{-1}. Applying the model of the anharmonic oscillator in the Morse potential[4] the anharmonicity parameter, x_e was determined both from the wavenumber of the overtone and from that of the OD^- vibration assuming free OH/OD molecules (see Table I). The small difference between the two x_e values shows that the free OH molecule model can be regarded as a good approximation. The values calculated are in agreement with those

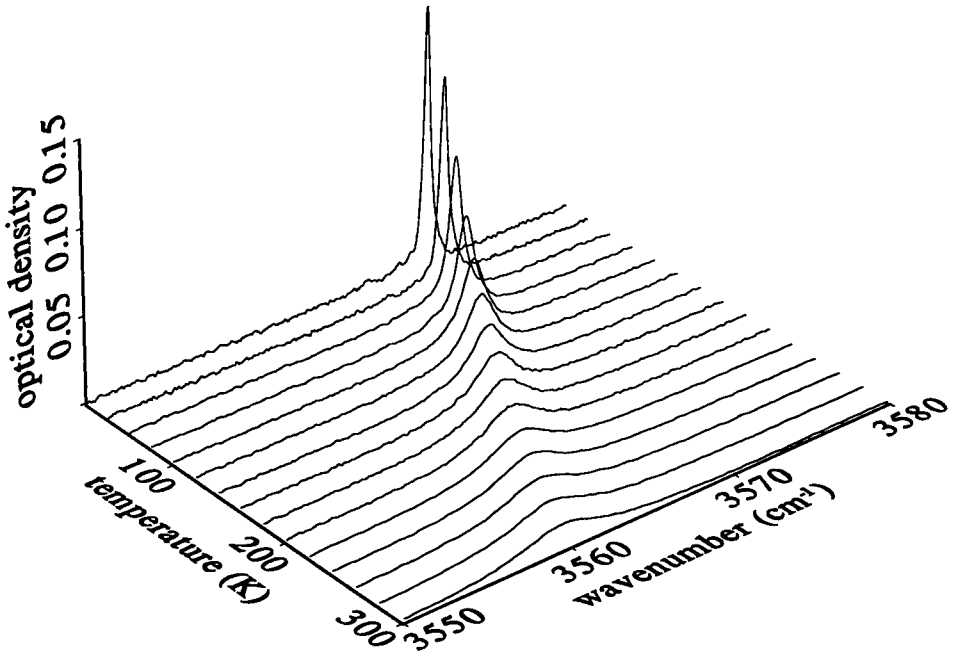

FIGURE 1 Temperature dependence of the OH^- absorption band in $Bi_4Si_3O_{12}$ crystals measured by high resolution FTIR spectroscopy in the 20–300 K temperature range.

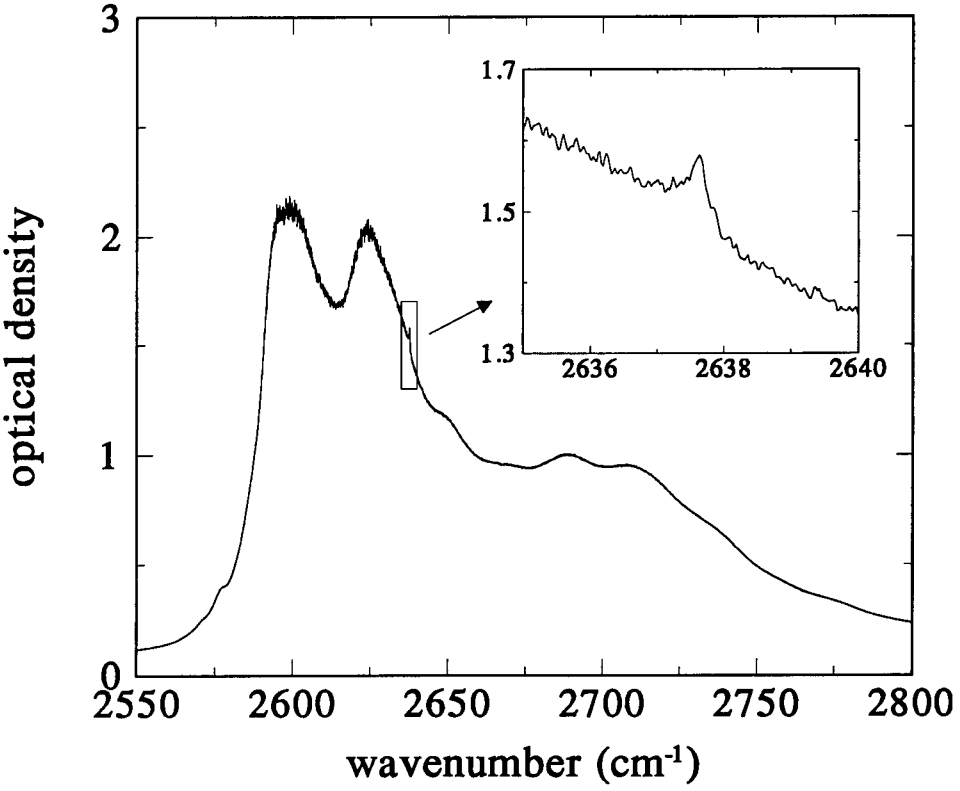

FIGURE 2 FTIR spectrum of the $Bi_4Si_3O_{12}$ crystal in the range of the three-phonon absorption measured at 9 K. The inset shows the OD^- absorption band in the sample treated in heavy water.

TABLE I
Hydroxyl absorption band parameters in $Bi_4Si_3O_{12}$ crystals measured at 9 K, and the anharmonicity parameter, x_e calculated by applying the model of the Morse potential [4] (ΔG is the position, W is the halfwidth of the absorption bands).

	ΔG (cm^{-1})	W (cm^{-1})	x_e
$OH_{0\to1}$	3570.92	0.45	
$OH_{0\to2}$	6970.70	1.04	0.0229
$OD_{0\to1}$	2637.60	0.35	0.0255

reported for OH^- -related defects in other oxides and in alkali halides providing further confirmation that the 3570.92 cm^{-1} band observed belongs to the stretching mode of the hydroxyl ion.

The phonon coupling of the OH^- vibration has also been studied by analyzing the detailed temperature dependence of the line position and width (Figure 3). Assuming a single phonon coupling model[7] the phonon frequency ω_0, the width γ, and the coupling constant $\delta\omega$ can be determined using equations (13) and (14) of ref. 4. The solid lines shown in Figure 3 represent the fitted curves in the 9–100 K temperature range. The parameters obtained are

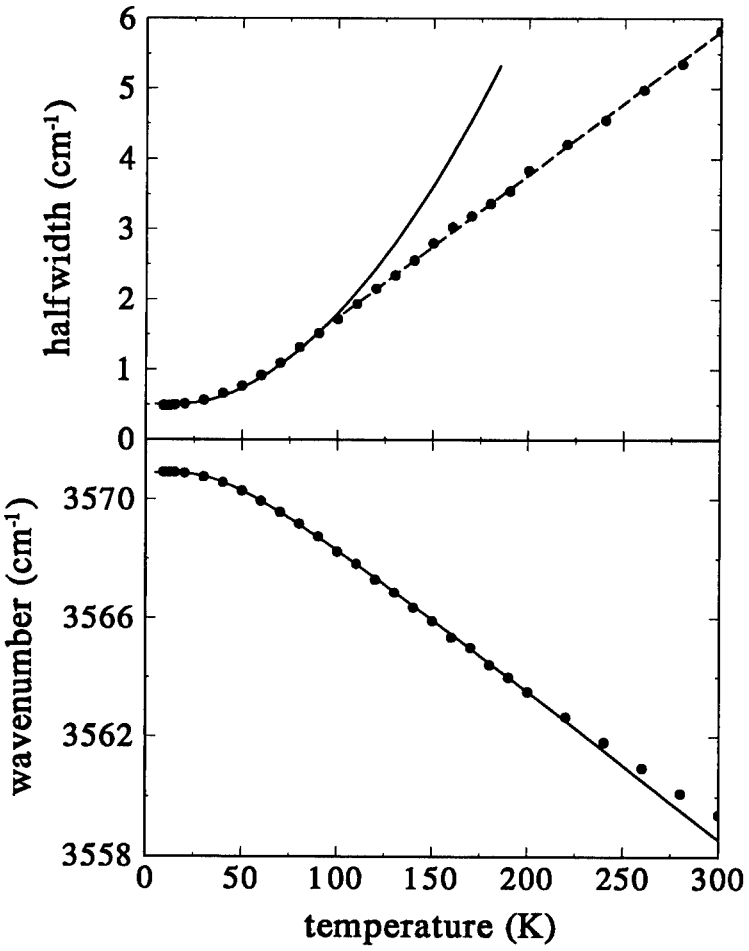

FIGURE 3 Temperature dependence of the width (upper part) and position (lower part) of the OH^- absorption band. The solid lines represent the fitted curves of the weak phonon coupling model.

$\omega_0 \approx 83\ cm^{-1}$, $\gamma \approx 35\ cm^{-1}$, and $\delta\omega \approx -6\ cm^{-1}$. The frequency of the coupled phonon is close to a phonon line measured by Raman scattering method ($\omega_R \approx 94\ cm^{-1}$).[8] Although the OH^- absorption lineshape was found to be Lorentzian in the whole 9–300 K temperature range as it is expected in the model and the $|\delta\omega| << \gamma$ assumption for the weak coupling is roughly fulfilled, a relatively good fit could only be obtained up to 100 K. Above 100 K the temperature dependence of the halfwidth became linear (dashed line in the upper part of Figure 3) instead of the exponential behaviour as expected and found e.g. in the case of BSO, BGO, BTO sillenites.[4]

A well established model for the OH^- defect cannot be concluded from our data. From the general charge compensation role of the hydroxyl ion and from the similarities of the sillenite BSO and eulityte $Bi_4Si_3O_{12}$ structures one may assume that the OH^- ion replaces oxygen sitting near an antisite tetrahedrally coordinated Bi_{Si}^{3+} ion.

ACKNOWLEDGEMENTS

One of the authors (L.K.) undertook this work with the support of the ICTP Programme for Training and Research in Italian Laboratories, Trieste, Italy. Financial support from the National Science Fund of Hungary (OTKA T4420) is acknowledged.

REFERENCES

1. A. V. Khomich, V. F. Kargin, Yu. F. Kargin, E. M. Kozhbakhteev, A. V. Dubovskii, A. A. Marin, P. I. Perov, and V. M. Skorikov, *Inorg. Mater.* **26**, 742 (1990).
2. L. Kovács, R. Capelletti, *Proc. ICDIM'92, World Scientific*, Vol. 2, p. 1194 (1993).
3. A. V. Khomich, Yu. F. Kargin, P. I. Perov, and V. M. Skorikov, *Inorg. Mater.* **26**, 1456 (1990).
4. P. Beneventi, R. Capelletti, L. Kovács, Á. Péter, A. M. Lanfredi Manotti, and F. Ugozzoli, *J. Phys.: Condens. Matter*, **6**, 6329 (1994).
5. M. S. Paterson, *Bull. Mineral*, **105**, 20 (1982).
6. S. Klauer, M. Wöhlecke, and S. Kapphan, *Phys. Rev. B*, **45**, 2786 (1992).
7. P. Dumas, Y. J. Chabal, and G. S. Higashi, *Phys. Rev. Lett.*, **65**, 1124 (1990).
8. P. Beneventi, D. Bersani, P. P. Lottici, L. Kovács, *Solid State Commun.* **93**, 143 (1995)

Radiation Effects and Defects in Solids, 1995, Vol. 134, pp. 293–297
Reprints available directly from the publisher
Photocopying permitted by license only

© 1995 OPA (Overseas Publishers Association)
Amsterdam B.V. Published under license by
Gordon and Breach Science Publishers SA
Printed in Malaysia

ANHARMONIC EFFECTS ON LATTICE VIBRATION MODES OF SILLENITES

P. BENEVENTI,[1] R. CAPELLETTI,[1] and L. KOVÁCS[2]

[1]*Department of Physics, University of Parma, Viale delle Scienze, 43100 Parma, Italy;*
[2]*Research Laboratory for Crystal Physics, Hungarian Academy of Sciences, 1112 Budapest, Budaörsi út 45, Hungary*

(Received July 1, 1994)

High resolution FTIR absorption spectroscopy in the 600–3500 cm^{-1} wavenumber and 9–300 K temperature ranges was applied to study multi-phonon transitions of the tetrahedral unit modes in BSO, BGO, BTO and mixed BSO-BGO sillenite crystals. Up to four-phonon (overtones of the F mode and combination of F and A modes) transitions were detected in BGO, BSO, and BTO and up to three- in the mixed crystals. The F mode anharmonicity, evaluated in the framework of the Morse oscillator model, was in the range 0.0024–0.0056. Fine structures due to Si-isotopes were observed in BSO. The two- and three-phonon transitions in the mixed crystals were well described by a two-mode behaviour.

Key words: vibrational modes, FTIR spectroscopy, sillenites, multi-phonon transitions.

1 INTRODUCTION

BGO, BSO and BTO belong to sillenites with the general formula $Bi_{12}MeO_{20}$ (with Me = Ge, Si and Ti). They are large gap semiconductors and show many interesting properties (e.g. the photorefractive effect) which can be exploited for advanced technological applications.

The vibrational spectra of sillenites have already been studied by means of infrared (IR) reflectivity,[1] Raman spectroscopy measurements,[2] and theoretical calculations.[1] In the wavenumber region $\nu < 600$ cm^{-1} the vibrational frequencies differ slightly in the different matrices and are attributed to the vibrational modes of Bi and O in Bi_3O_4 and Bi_3O units. For 600 $cm^{-1} < \nu < 850$ cm^{-1} the reflectivity and Raman peaks are characteristic of a given matrix and have been attributed to the asymmetric F and symmetric A stretching modes in the MeO_4 tetrahedral unit. Two- and three-phonon transitions related to the tetrahedral unit modes have been detected by optical absorption measurements performed mainly at room temperature.[3–5] In the present paper we have applied high resolution FTIR absorption spectroscopy in the 600–3500 cm^{-1} wavenumber and 9–300 K temperature ranges to study the overtone and combination transitions of the tetrahedral unit modes (up to four phonons) in BGO, BSO, BTO crystals, in order to evaluate the anharmonicity contributions. The analysis was extended to mixed BSO-BGO systems in which the two-mode behaviour[6] gives a satisfactory description even for the two- and three-phonon transitions.

2 EXPERIMENTAL DETAILS

BSO, BGO and mixed BSO-BGO crystals were grown in air by the balance controlled Czochralski technique. The incongruently melting BTO crystals were grown from solution by the top seeding technique.[7] In the mixed crystals $(1-x)$BSO·xBGO the nominal x fraction was 0.25, 0.5 and 0.75. Oriented samples were cut in shape of parallelepipeds and the (100) faces were polished. The cross section was ~1 cm^2 and the thickness was in the range 0.4–24

mm. Chips of sillenite single crystals were finely ground and mixed with KBr powders in the weight ratio 1:100 to obtain pellets used to measure the IR spectra in the high absorption coefficient region.

The optical absorption measurements were performed by means of a Bomem DA8 FTIR spectrophotometer operating in the range 4000–200 cm^{-1}, with a resolution as good as 0.04 cm^{-1}. The spectra were recorded in the range 9–300 K, by assembling the sample in a 21SC model Cryodine Cryocooler of CTI-Cryogenics.

3 RESULTS AND DISCUSSION

The main features of the BSO absorption spectrum measured at 9 K in the range 600–3500 cm^{-1} are summarized in Figure 1. A single line appears at $\nu_F = 830$ cm^{-1} which is attributed to an asymmetric F stretching mode of the MeO_4 tetrahedral unit.[1] Two strong lines, accompanied by a few weaker ones, are detected at wavenumbers which are roughly n times ν_F (with $n = 2, 3, 4$). A magnified presentation of the spectra is given in Figure 2. The amplitude of the lines decreases drastically by increasing n, as can be guessed by comparing the magnification factors and the thicknesses d of the samples, used for detecting each n-order spectrum, see Figure 1. The absorption for $n = 1$ could be measured only on a pellet where the BSO equivalent thickness is drastically reduced, thanks to the dilution into KBr. Similar results were obtained for BGO (with $\nu_F = 680$ cm^{-1}) and BTO (with $\nu_F = 666.5$ cm^{-1}), although the spectra do not show the fine structure displayed by BSO. By increasing the temperature from 9 to 300 K, no remarkable shift of the main lines is observed, but most of the weaker lines and the fine structure are lost: for example of the 10 lines displayed at 9 K in BSO (see Figure 2 for $n = 2$) only 3 are detected at 300 K.

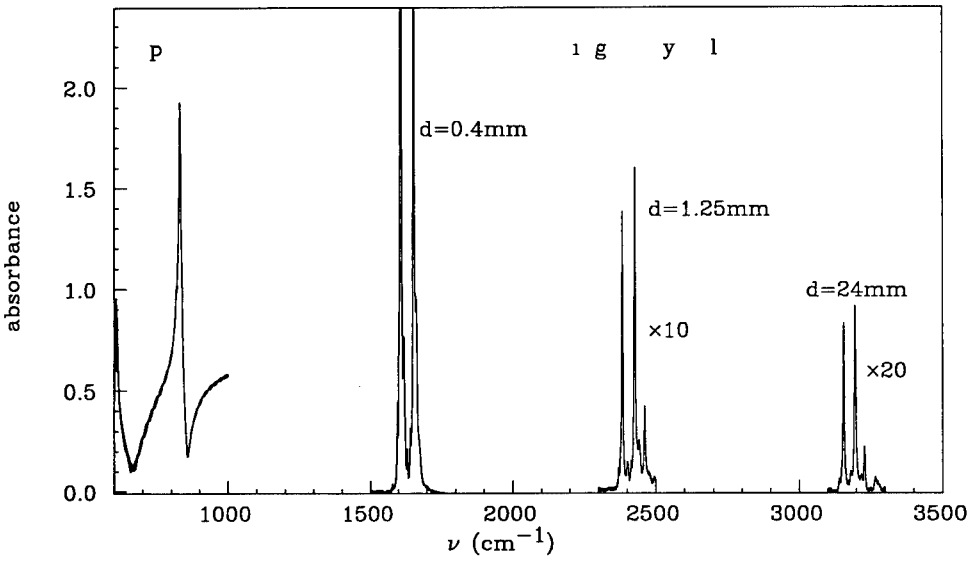

FIGURE 1 Optical absorption spectra measured at 9 K in the range 600–3500 cm^{-1} of BSO crystals. The short wavenumber side spectrum was measured on a KBr + BSO pellet, due to the high absorption coefficient of BSO. The spectra in the other regions were measured on massive samples, whose thickness d is indicated. ν_F is the frequency of the short wavenumber peak. The spectra in the region at $3\nu_F$ and $4\nu_F$ are magnified by a factor 10 and 20 respectively.

Most of the structures shown by the infrared spectra of sillenites can be understood by considering 1) absorptions due to combination modes, i. e. one or more F modes (IR active) + one or more A modes (IR inactive) are contemporaneously excited; 2) absorptions due to overtone transitions of the F mode; 3) isotopic effects, which are particularly relevant in the case of BSO, since in addition to the most abundant ^{28}Si (92.2%) there are also ^{29}Si and ^{30}Si present in natural abundances of 4.7% and 3.1% respectively. By following the above criteria most of the lines were assigned as summarized in Figure 2. For $n = 1$ the shoulders at short wavenumbers can be attributed to the isotopic replica due to ^{29}Si and ^{30}Si of the main peak at 830 cm^{-1} due to the most abundant ^{28}Si, in agreement with the Raman spectroscopy results.[2] The two strong lines observed for $n = 2, 3, 4$ are due to ($l \times F + m \times A$) combination modes ($l = 1, 2$; $m = 1, 2, 3$) and to overtone of the F mode ($n = 2$), while the minor structures are due to overtones (for $n = 3, 4$) and to combination ($n = 4$). In the case of $n = 2$ the isotopic effects are also clearly detectable, as indicated in Figure 2. The same approach was used to interpret the results for BGO and BTO: in these cases, however, the fine structure due to Si-isotopes is missing and only a broadening of the lines is observed. The presence of the F mode overtones up to $n = 4$ suggests that anharmonic effects occur in the asymmetric stretching of the MeO_4 tetrahedron. Therefore, as a first approach, we fitted the observed transition wavenumbers (for $n = 1, 2, 3, 4$) in BSO, BGO, and BTO to those ΔG_{n0} predicted in the framework of the Morse anharmonic oscillator model.[7] One has:

$$\Delta G_{n0}/n = \omega_e[1 - x_e(n + 1)] \tag{1}$$

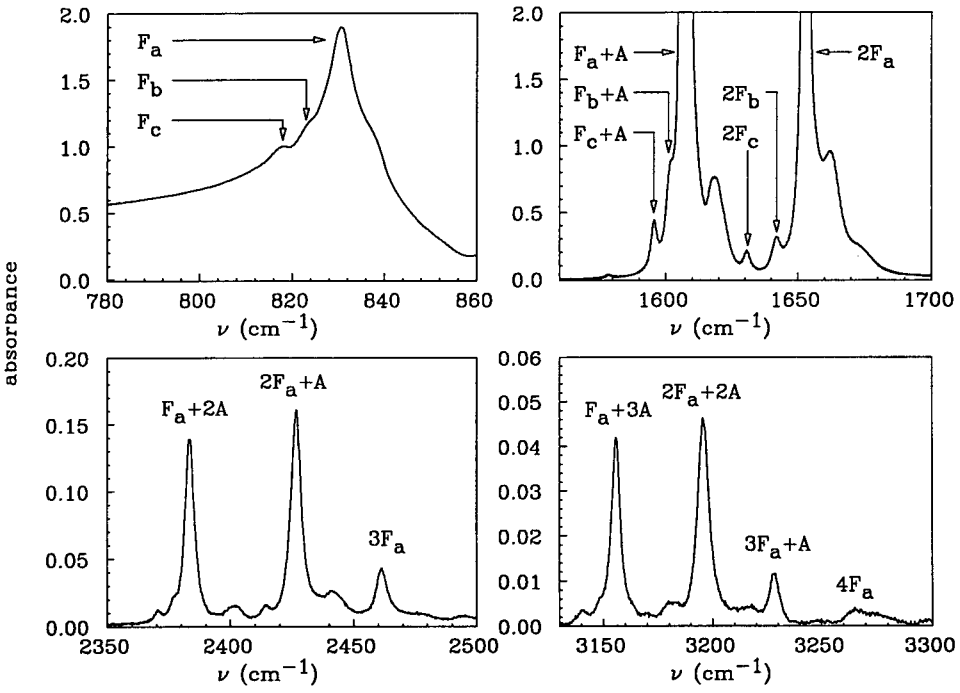

FIGURE 2 Optical absorption spectra measured at 9K of BSO crystals in the region at ν_F (top left), at $2\nu_F$ (top right), at $3\nu_F$ (bottom left), and at $4\nu_F$ (bottom right). The assignment of the most of the lines is shown as overtones of the F modes and as combinations of F and A modes. F_a, F_b, and F_c are the F mode absorptions related to different isotopes, ^{28}Si, ^{29}Si, and ^{30}Si respectively.

where ω_e, x_e and n are the oscillator frequency, the anharmonicity parameter, and the vibrational quantum number, respectively. According to (1) a plot of $\Delta G_{n0}/n$ vs. n should give a straight line, from the slope of which one can evaluate x_e. This relationship was indeed fulfilled for all the F modes detected (up to $n = 4$) in BSO, BGO, and BTO: the values of x_e were 0.0056, 0.0039, and 0.0024, respectively. It turns out that the tetrahedron asymmetric F stretching can be satisfactorily described by the Morse model, which has been proposed originally for a simple free diatomic molecule. This confirms the hypothesis according to which the measured frequencies in BGO and BSO ($n = 1$) fit quite well the highest of the normal-mode frequencies of GeO_4 and SiO_4 molecular groups.[1] The anharmonicity of the tetrahedral vibration is smaller than that ($x_e \sim 2.7 \times 10^{-2}$) reported for the localized mode induced by OH^- in the same matrices.[7]

A similar analysis has been extended to the mixed $Bi_{12}Ge_xSi_{1-x}O_{20}$ crystals. The overtone spectra (detected up to $n = 3$) typical of BGO and BSO were both present, as well as the combination of A and F modes. Their amplitude scales with x and $(1 - x)$, respectively, and their separation decreases slightly by increasing the deviation from the extreme compositions. The shift of each line with respect to the position observed in the crystal of extreme composition, i. e. $x = 0$, or $x = 1$, was found to be a linear function of x or $(1 - x)$, respectively, as is shown in Figure 3 for the region of $n = 3$. Such a linearity is observed

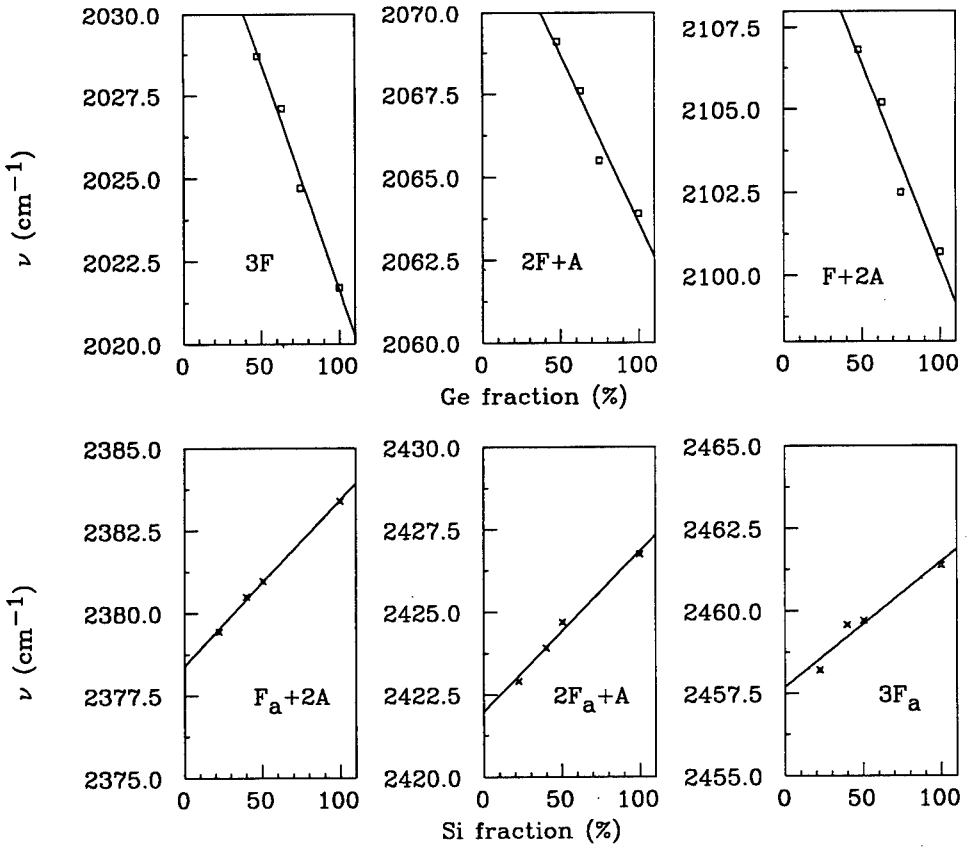

FIGURE 3 Shift of the lines, measured at 9 K, in the region at $3\nu_F$ in mixed BSO-BGO crystals as a function of the Ge and Si fraction.

only if the x value are those obtained from the chemical analysis of Si and Ge performed on the samples investigated, and not the nominal ones (in the melt). The position and the amplitude of the lines stress that the MeO_4 tetrahedron stretching modes in BSO-BGO mixed crystals are well described by a two-mode behaviour,[6] not only for the fundamental transitions but also for the overtones and the combination transitions (at least up to $n = 3$).

REFERENCES

1. W. Wojdowski, T. Lukasiewicz, W. Nazarewicz, J. Żmija, *Phys. Stat. Sol. (b)* **94**, 649 (1979).
2. M. V. Belousov, E. I. Leonov, and A. G. Shcherbakov, *Sov. Phys. Solid State* **28**, 336 (1986).
3. M. V. Belousov, E. I. Leonov, V. D. Petrikov, and A. G. Shcherbakov, *Sov. Phys. Solid State* **30**, 226 (1988).
4. A. V. Khomich, M. G. Ermakov, P. I. Perov, and V. V. Kucha, *Zhurnal Prikladnoi Spektroskopii* **40**, 387 (1982).
5. A. V. Khomich, Yu. F. Kargin, P. I. Perov, and V. M. Skorikov, *Inorg. Mater.* **26**, 1635 (1990).
6. L. Genzel, T. P. Martin, and C. H. Perry, *Phys. Stat. Sol (b)* **62**, 83 (1974).
7. P. Beneventi, R. Capelletti, L. Kovács, A. Péter, A. M. Lanfredi Manotti, and F. Ugozzoli, **6,** 6329 (1994) *J. Physics: Cond. Matter.*

Radiation Effects and Defects in Solids, 1995, Vol. 134, pp. 299–302
Reprints available directly from the publisher
Photocopying permitted by license only

© 1995 OPA (Overseas Publishers Association)
Amsterdam B.V. Published under license by
Gordon and Breach Science Publishers SA
Printed in Malaysia

ON THE DIELECTRIC RELAXATIONS IN CRYSTALLINE INSULATORS AND AMORPHOUS SYSTEMS

E. LAREDO, M. ALDANA and A. BELLO

Physics Department, Universidad Simón Bolívar, Apartado 89000, Caracas 1081, Venezuela

(Received July 1, 1994)

The Direct Signal Analysis is applied here to the decomposition of the whole TSDC peak in elementary curves with temperature dependencies for the relaxation times either Arrhenius or Vogel-Fulcher in crystalline (SrF_2:Gd^{3+} or La^{3+}) or amorphous materials (Bisphenol A Polycarbonate). The energy histogram obtained after fitting the complex peak gives the profile of the energy distributions; Lorentzian distributions were found for the simple dipolar peaks and small clusters in crystalline materials, whereas for the β-band in PCBA, the distributions are Gaussian. The high temperature spectrum corresponds for both materials to very narrow distributions both for the Maxwell Wagner polarization originated high temperature peak in SrF_2 or for the glass rubber transition in PCBA. Vogel-Fulcher relaxation times had to be used in the latter case.

Key words: Thermally stimulated depolarization currents, dielectric relaxations, fluorites, polycarbonate, glass transition, Vogel-Fulcher relaxation time.

1 INTRODUCTION

Thermally Stimulated Depolarization Currents (TSDC or ITC) technique is the most sensitive technique for the study of the dielectric relaxations of a material that contains polarizable entities such as the impurity-interstitial fluorine dipoles in fluorite crystals doped with trivalent rare earths[1] or the orientable molecular segments with net dipolar moment in amorphous materials.[2,3] In highly doped crystals or in amorphous materials the spectrum is made of broad bands which are the sum of different processes which occur over strongly overlapping temperature regions. We propose a new method[4] based on the idea of the Direct Signal Analysis (DSA) recently introduced by Cost.[5] The advantage of this procedure upon the usual ones, where the energy or τ_0 are assumed to be distributed, is that no a priori guess has to be made on the analytical expression of the distribution function, or even on the number of overlapping relaxations whose sum is represented by the recorded current.

2 DIRECT SIGNAL ANALYSIS

A computer program was written to analyze complex TSDC relaxations, i.e. the complex curve is thought as the composition of N curves whose characteristic energies are equally spaced in a given energy window. The expression for the current density $J_D(T)$ when the temperature is raised with a linear rate, b, is now written as a sum of N elementary TSDC curves, each of them characterized by E_i, $\tau_i(T_j)$ and by a contribution to the total polarization, P_{0i}:

$$J_D(T_j) = \sum_{i=1}^{N} \frac{P_{0i}}{\tau_i(T_j)} \exp\left[-\frac{1}{b}\int_{T_0}^{T_j} \frac{dT'}{\tau_i(T')}\right], \quad (j = 1, m), \quad (N \leq m)$$

The experimental trace can now be fitted by solving either the above linear set of equations if τ_0 is not a parameter of the fitting, or non linear least squares procedure if the N τ_{0i} are included in the parameters to be adjusted. The initial parameters are the threshold and the width of the energy window divided in N adjacent intervals or energy bins, the τ_{0i} which may be identical or distributed, and the N starting values for P_{0i}, which form a square box distribution, i.e. all the bins are initially contributing equally to the total polarization of the sample. The computer program based on the Levenberg-Marquardt algorithm will return an energy histogram whose height is the adjusted contribution of each energy bin to the polarization, together with the best fitted value for the corresponding τ_{0i}. The program was successfully tested with computer generated curves with an increasing degree of complexity.

The Arrhenius temperature dependence for the relaxation time $\tau(T) = \tau_0 \exp(E/kT)$, has been successfully used in the case of dipolar relaxations in crystalline solids where the Debye model has been shown to be valid. In the case of polymers or glass forming materials, the low temperature relaxations can still be described by an Arrhenius law for the relaxation time. The relaxations which occur at temperatures above the glass-transition temperature, T_g, are best described by a Vogel-Fulcher temperature dependence, $\tau(T) = \tau'_0 \exp[E'/k(T - T_0)]$, where T_0 is the temperature at which the relaxation is frozen. When using this expression for the relaxation times in our program, T_0 was included among the parameters to be fitted.

3 EXPERIMENTS AND RESULTS

The crystalline samples chosen here were SrF_2 disk shaped single crystals doped with La^{3+} (0.5% in molar fraction) or with Gd^{3+} (2% in molar fraction) provided by Optovac Inc.. The amorphous material is a sample of Polycarbonate of Bisphenol A, PCBA, (4,4′ Isopropylidene Diphenol) grown from pellets from Bayer, Makrolon 3203, with 2% of crystallinity obtained by exposures to acetone vapors. The heating rate is approximately 0.1 Ks^{-1} for all the peaks shown in this work. The polarizing temperatures were chosen at the maximum of the peaks under study.

The TSDC spectra of the solid solutions of the form $Sr_{1-x}Gd_xF_{2+x}$ consist of at least four relaxations below room temperature and a high temperature complex peak. In Figure 1 the

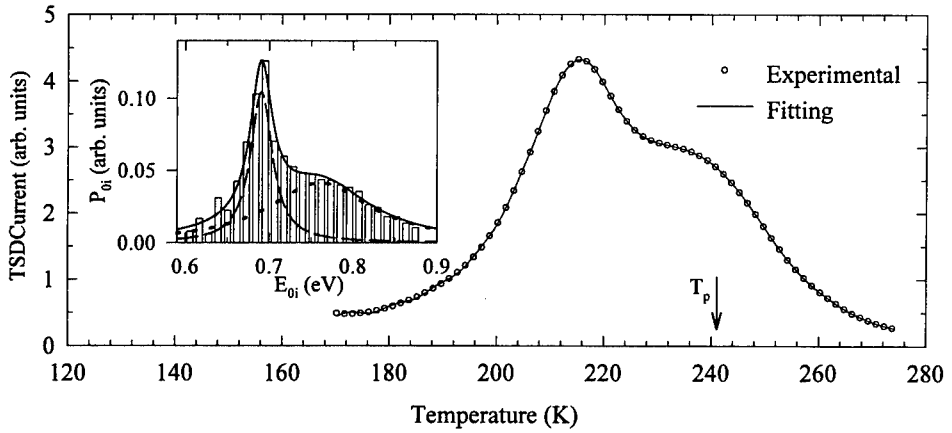

FIGURE 1 TSDC relaxation for a $Sr_{0.98}Gd_{0.02}F_{2.02}$ crystal, nnn and cluster associated dipolar relaxation. Energy histogram resulting from the Direct Signal Analysis is represented in the insert, interrupted lines are Lorentzian distributions and the continuous line their sum.

most intense band for $Sr_{0.98}Gd_{0.02}F_{2.02}$ shows a maximum at 210 K which is attributed to the next nearest neighbor $Gd^{3+} - F_i^-$ dipole and another at 237 K which is due to the reorientation of a larger polarizable cluster. The result of the DSA fitting is represented by a continuous line and it can be seen that the agreement is excellent. In the insert of Figure 1 the energy histogram resulting from the DSAnalysis is shown. The τ_{0i} values are almost constant and equal to 5×10^{-15} s for most of the energy bins. The energy histogram can now be fitted by the composition of two Lorentzian energy distributions respectively represented by interrupted and dotted lines in the insert. This fitting with Lorentzian distributions is obtained here for the first time in the analysis of the profile of TSDC peaks. For this highly doped crystal it shows that the dipole-dipole interaction is responsible for the peaks broadening.

The High Temperature peak for $Sr_{0.995}La_{0.005}F_{2.005}$, whose anomalous behavior has been reported[6] and explained as a Maxwell-Wagner polarization around the dislocations of the crystal, was also fitted and Arrhenius relaxation times were used. The energy histogram found here is very close to a box shape ranging from 1.25 to 1.30 eV, with a single $\tau_0 = 1.5 \times 10^{-15}$ s.

In the case of amorphous materials such as the PCBA with 8% of crystallinity, the TSDC spectrum consists of a β-band for the secondary relaxation at low temperatures which could be decomposed after the DSA fitting into four components each of them with Gaussian energy distributions and which are attributed to the local motions in the amorphous zones involving either the methyl groups or the carbonate groups, restricted or not by the adjacent phenyl groups.

In Figure 2 the high temperature TSDC spectra given by the PCBA sample is shown and again the continuous line is the result of the DSA procedure. The predominant peak is the α transition at 421 K which is the dielectric manifestation of the glass-rubber transition observed by Differential Scanning Calorimetry at $T_g = 418$ K. A second relaxation is observed at 444 K which has been attributed to the space charge relaxation. The sum of squares residual, χ^2, could only reach acceptable values, i.e. less than 10^{-8}, if the relaxation time was supposed to follow a Vogel-Fulcher temperature dependence. An additional parameter, T_0, had then to be included in the fitting. The energy histogram is shown in the insert of Figure 2 and is remarkable for the sharpness of the zone corresponding to the T_g peak which is concentrated in .02 eV. The corresponding distribution in τ_0 shows clearly the existence of 3 relaxation mechanisms, with an almost constant value for the T_g transition, 0.9×10^{-15} s.

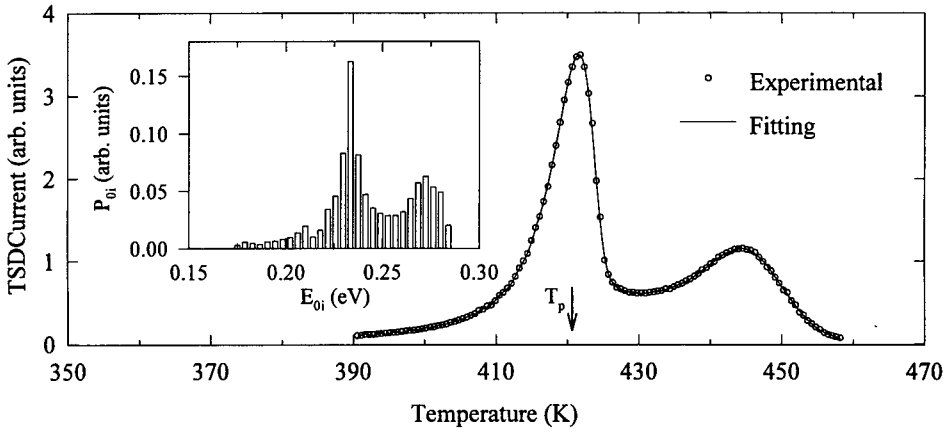

FIGURE 2 HT TSDC spectrum of Polycarbonate of Bisphenol A, Glass-Transition Relaxation and Space Charge Peak. Energy histogram resulting from the Direct Signal Analysis is represented in the insert.

The value found for T_0 is 349.3 K. The Vogel-Fulcher equation is related to the free volume theory where the free volume fraction trapped in the material has an expansion coefficient α_f for temperatures above T_0. This expansion coefficient is $\alpha_f = k/E'$ which for the central energy bin of our distribution will give a value of 3.8×10^{-4} K^{-1}. The fractional free volume calculated at T_g as $\nu_f = \alpha_f\ (T_g - T_o)$ was found equal to 2.7% which is most reasonable for this kind of material. The highest temperature peak reported here corresponds to the relaxation of the space charge blocked at the electrodes as it depends strongly on the nature of the contacts with the metallic plates.

4 CONCLUSIONS

We have shown the validity of the Direct Signal Analysis to decompose the complex TSDC curve in its elementary components when it is applied to crystalline and amorphous materials. In the case of the fluorite crystals we have been able to show that the dipoles in a highly doped crystal present a Lorentzian energy distribution which is the expected result if the dipole-dipole interaction is the main cause of the broadening of the TSDC peak. For amorphous polycarbonate the secondary relaxations are broadened due to Gaussian energy distributions accompanied by a variation in the τ_0 values corresponding to each energy bin. As to the relaxation related to the glass transition temperature is has been shown that the TSDC curve can only be decomposed if the free volume concept for the relaxation times is used and then a very sharp distribution is found. The Maxwell Wagner relaxation in SrF_2, due to the interfacial polarization around the dislocations, also gives a narrow distribution, in this case box-shaped

ACKNOWLEDGMENTS

The authors gratefully acknowledge financial support from the Consejo Nacional de Investigaciones Cientifícas y Tecnológicas (Programa de Nuevas Tecnologías Proyecto NM–012).

REFERENCES

1. N. Suarez, M. Diaz, A. Bello and E. Laredo, *Defects in Insulating Materials*, O. Kanert and J. M. Spaeth eds, (World Scientific, London, 1993), p. 810.
2. E. Laredo, M. Aldana, N. Suarez, A. Bello and M. Diaz, *Mat. Eng.* **4**, 237 (1993).
3. A. Bernès, D. Chatain and C. Lacabanne, *Polymer* **33**, 4682 (1992).
4. M. Aldana, E. Laredo, A. Bello and N. Suarez, *J. Polymer Sc.: Polym. Phys.*, **32**, 2197 (1994).
5. J. R. Cost, *J. Appl. Phys.* **54**, 2137 (1983).
6. N. Suarez, E. Laredo, F. Lorenzo, A. Bello and M. Puma, *Solid State Ionics* **37**, 103 (1990).

Radiation Effects and Defects in Solids, 1995, Vol. 134, pp. 303–305
Reprints available directly from the publisher
Photocopying permitted by license only

© 1995 OPA (Overseas Publishers Association)
Amsterdam B.V. Published under license by
Gordon and Breach Science Publishers SA
Printed in Malaysia

LATTICE DEFECTS IN BERYLLIUM OXIDE

I. N. ANTSIGIN and A. V. KRUZHALOV

Ural State Technical University, Ekaterinburg, Russia

(Reveiced July 1, 1994)

Classification, brief description of structure as well as paramagnetic and optical properties of point defects found to date in beryllium oxide crystals are presented.

The data on paramagnetic and optical properties of point defects in beryllium oxide crystals are considered in this paper. An attempt has been made for the first time to create a comprehensive picture of the already known defects in BeO. We classify the defects by the following features:

—defects in cation and anion sublattice;
—proper and impurity defects:
—growth defects and radiation-induced defects;
—point and complex defects.

V-type defects are hole-trapped centers based on cation vacancies.[1] They are formed during crystal growth (which is non-stoichiometric in cation sublattice) and under neutron irradiation. The difference above the mechanisms of defect formation appears itself in annealing—a) in the first case thermoactivated hole delocalization takes place b) in the second case there occurs an annihilation of interstitial-vacancy cation pairs.

Impurity defects B^{2+}, Al^{2+}, Zn^{+} centers are substitutional ions in the cation site trapping the electron at X-irradiation.[2,3,4] The [Li]o center has a different structure—the hole is trapped as the oxygen ions nearest to Li impurity.[5] No impurity centers in the anion sublattice were found.

The proper defects in the anion sublattice are formed only under neutron irradiation. F,F^{+} centers are anion vacancies in different charge states.[6,7]

Complex defects appear in BeO crystal upon thermal treatment of neutron-irradiated samples. We have studied the P^{-} center (which is an anion-cation divacancy trapping the electron)[4] and complex hole defects transforming their structure and changing the luminescent properties in the process of annealing.[8]

The optical and paramagnetic characteristics of the centers, their structure and schemes of destroy are listed in the Table.

TABLE

Defect type	Electron Spin Resonance	
	parameters	measurement conditions
$V^- = V_c h^+$	isotropic g = 2.0117	300 K, X-band
$V^o = V_c 2h^+$	g_{xx} = 2.0107, g_{vv} = 2.0154 g_{zz} = 2.0075, S = 1 D = –103.7mT, E = –20mT	10 K, X-band
$V_B = V_c h^+ - B^{3+}$ I—'axial' II—'unaxial'	$g_{\|}$ = 2.0026, $g_{\perp}$ = 2.0155 $g_{\|}$ = 2.0026, $g_{\perp}$ = 2.0164	300 K, X-band
$[Li]^o = Li^+ h^+$	$g_{\|}$ = 2.0023, $g_{\perp}$ = 2.0153 HFS:^{7}Li(I = 3/2; 92.6%) $A_{\|}$ = 1.37, $A_{\perp}$ =9.5 MHz	300 K, X-band
$B^{2+} = B^{3+} e^-$	$g_{\|}$ = 2.0035, $g_{\perp}$ = 2.0044 HFS:^{11}B(I = 3/2; 80.4%) $A_{\|}$ = 343, $A_{\perp}$ = 214.6 MHz	300 K, X-band
$B^{2+} = B^{3+} e^-$ octohedrical interstitial site	$g_{\|}$ = 2.0023, $g_{\perp}$ = 2.0028 HFS:^{11}B(I = 3/2; 80.4%) $A_{\|}$ = 821, $A_{\perp}$ = 714.8 MHz	77 K, X-band
$Al^{2+} = Al^{3+} e^-$	$g_{\|}$ = 2.003 $g_{\perp}$ = 2.004 HFS:^{27}A1(I = 5/2; 100%) $A_{\|}$ = 583.1, $A_{\perp}$ = 495 MHz	300 K, X-band
$Zn^+ = Zn^{2+} e^-$	isotropic g = 2.0008 HFS:^{67}Zn(I = 5/2, 4.11%) $A_{\|}$ = 901 MHz	77 K, X-band
$F^+ = Vae^-$	isotropic g = 2.0030 sHFS:4*^{9}Be(I = 3/2, 100%) $A_{\|}$ = 11.2 MHz	300 K, X-band
$F = V_a 2e^-$	ground state—S = 0	
$P^- = V_a V_c e^-$	isotropic g = 2.0026 sHFS:3*^{9}Be(I = 3/2, 100%) $A_{\|}$ = 25.2 MHz	300 K, X-band
C = complex (V-type)		
I	isotropic g = 2.0150	300 K, X-band
II	not found	
III	isotropic g = 2.0096	

TABLE

Optical properties		Temperature and destroy mechanism	Creation condition
adsorption, eV	lumines.(excite), eV		
4.0, 2.1	not found	620 K, $V^- \rightarrow V_c + h^+$	growth, n-irradiation
not found	not found	550 K, $V^0 \rightarrow V^- + h^+$	growth, n-irradiation
3.85 2.1	not found	680 K, $V_B \rightarrow VB^- + h^+$	growth, X-ray
3.65, 2.1	not found	450 K $[Li]^0 \rightarrow Li^+ + h^+$	growth, X-ray
not found	not found	540 K $B^{2+} \rightarrow B^{3+} + e^-$	growth, X-ray
not found	not found	>90 K, $Bi^{2+} \rightarrow Bi^{3+} + e^-$	growth, X-ray
not found	not found	580 K, $Al^{2+} \rightarrow Al^{3+} + e^-$	growth, X-ray
not found	not found	310 K, $Zn^+ \rightarrow Zn^{2+} + e^-$	growth, X-ray
5.4	3.9(5.4)	>900 K	n-irradiation
6.6	5.0, 3.4(6.0)	>900 K	n-irradiation
not found	not found	>900 K, ionic processes	n-irradiation, 700 K annealing
not found	1.97(3.5)	>650 K	n-irradiation, annealing —
4.05	2.12(4.2)	>800 K	400–650 K
not found	2.03(3.8,4.7)	>1100 K	700–1100 K

REFERENCES

1. B. Maffeo, A. Herve. *Phys. Rev.* **B 13**, 1940 (1976).
2. A. R. Reinberg. *J. Chem. Phys.* **41**, 850 (1964).
3. R. C. DuVarney, A. K. Garrison, S. B. Harem. *Phys. Stat. Sol.* **B 45**, 259 (1977).
4. I. N. Antsigin, A. V. Kruzhalov *et al. Hyperfine Interaction.* **60**, 881 (1990).
5. R. C. DuVarney, A. K. Garrison. *Phys. Stat. Sol.* **A. 42**, 609 (1977).
6. A. K. Garrison, R. C. DuVarney. *Phys. Rev.* **B. 7**, 4686 (1973).
7. S. V. Gorbunov, A. V. Kruzhalov *et al. Phys. Stat. Sol.* **B. 141**, 293 (1987).
8. I. N. Antsigin, S. V. Gorbunov. *Proc. Int. Symp. LUMDETR'91*, (Riga, Latvia, 1991).

Radiation Effects and Defects in Solids, 1995, Vol. 134, pp. 307–309
Reprints available directly from the publisher
Photocopying permitted by license only

© 1995 OPA (Overseas Publishers Association)
Amsterdam B.V. Published under license by
Gordon and Breach Science Publishers SA
Printed in Malaysia

EFFECTS OF THE MICROINDENTATION, X-IRRADIATION AND ANNEALING ON THE F-CENTRE-LIKE DEFECTS PRODUCTION IN MgO

T. A. NAZAROVA and M. V. NAZAROV

Technical University of Moldova, 277012, Kishinev, Moldova

Local cathodoluminescence analysis have been applied to defects recognition in indented MgO crystals. Influence of X-irradiation and annealing on the kind and concentration of F-centre-like defects was established.

Key words: cathodoluminescence, microindentation, defects, annealing, irradiation, MgO.

1 INTRODUCTION

Of the many problems which still remain unanswered, the more fundamental aspect concerns the production and behavior of point defects. This paper presents a brief account of experiments designed to clarify the effects of external influences on the defects production of MgO. Cathodoluminescence (CL) modes (total, monochromatic and pointal) in the scanning electron microscope (SEM) in conjunction with computer graphic were used for this purpose.

2 EXPERIMENTAL DETAILS

To create different dislocation structures, Vickers diamond pyramid indentations were made on (100) MgO at P = 2 N. The irradiation was made by a soft X-rays during 70 h. The annealing temperature had been increased from 20°C to 907°C during 6 h. and decreased with a rate $\Delta T/\Delta t = 20°C/h$. Three series of the indented regions: nonirradiated, subsequently X-irradiated and annealed were under study. CL examinations were performed in 'JSM-50A' commercial SEM at T = 80 K.

3 EFFECTS OF THE EXTERNAL INFLUENCE ON THE DEFECTS PRODUCTION

3.1 *Study of The Microindentation*

In nondeformed region CL spectra contain two weak broad partial bands of equal intensity at 3 and 2.4 eV, referred to as F^+- and F-luminescence.[1] In dislocation zone created by the microindentation we have observed five peaks. The most intensive peaks appear to be in UV zone ($\lambda = 350$ nm and $\lambda = 375$ nm) and are not perceived by the eye. We have visualized their total CL intensity distribution using CL mapping. The peak at 350 nm has been interpreted with a surface origin of F-centre (F_s)[2]. Partial bands at 375 and 475 nm have been attributed to F_2- and F_2^+-centres.[3] Their composite distribution, visualized by CL mapping, is shown in Figure 1a. Our experiments revealed, that a very high density of dislocation loops gliding under microindentation induce an enhancement of the F_2- and F_s-centres concentrations relative to that of the F_2^+.

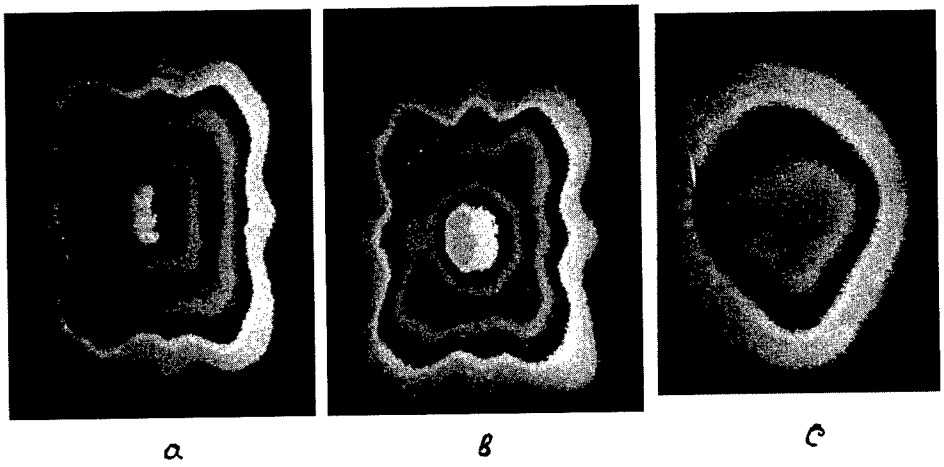

FIGURE 1 Total CL intensity maps: a) nonirradiated MgO; b) X-irradiated; (c) annealed. U = 40 kV. Horizontal field width = 100 μm.

3.2 *Study of the X-Iirradiation Effect*

Total CL map from the indented and subsequently X-irradiated MgO (Figure 1b) shows that irradiation leads to insignificant spreading of zones, rich of defects and to increasing of CL intensity from the whole zone of plastic deformation. Analogous maps, obtained at the monochromatic (375 and 475 nm) CL show that, subsequent X-irradiation leads mainly to enhancement of the F_2-centre concentration.

3.3 *Study of the Annealing Effect*

The map of total CL from the indented and annealed MgO (Figure 1c) cardinally differs from the other ones. Local spectrum in Figure 2 shows, that after the annealing a peak position of UV emission is completely shifted to 350 nm. We have revealed, that subsequent annealing stimulates the enhancement of partial densities of the F_2- and especially of the F_s-centres and annihilation of some part of the $F^+{}_2$-centres, created by the microindentation.

4 CONCLUSIONS

The composite density of all kinds of F-center-like defects in MgO reaches maximum in the dislocation zone around the indentation crater. Subsequent annealing induces an annihilation of the defects in this zone. However, in zone of the indentation crater the partial density of F_s- and, especially, of F_2-center are prevailed over the F_2^+ one. The partial density of F_2-center increases due to the X-irradiation and decreases due to the annealing; however, only the partial density F_s becomes dominant after annealing.

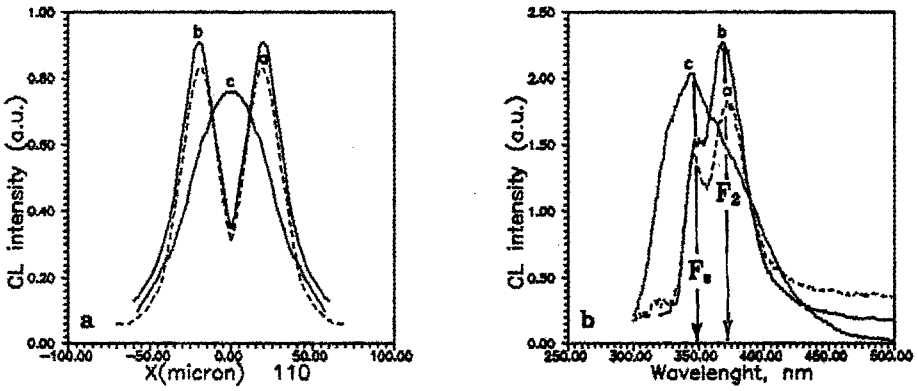

FIGURE 2 CL intensity profiles for nonirradiated (a), X-irradiated (b) and annealed (c) samples along <110> crystallographic direction and local CL spectra in the centres of indentation for these samples.

REFERENCES

1. G. H. Rosenblatt *et al. Phys Rev* **B39**, 14, 10309 (1989).
2. H. Namba and Y. Murata, *J Phys Soc Jpn*, **53**, 5, 1888 (1984).
3. J. M. Bolton, B. Henderson, D. O' Connell. Solid State Commun. **38**, 287 (1981).

Radiation Effects and Defects in Solids, 1995, Vol. 134, pp. 311–313
Reprints available directly from the publisher
Photocopying permitted by license only

© 1995 OPA (Overseas Publishers Association)
Amsterdam B.V. Published under license by
Gordon and Breach Science Publishers SA
Printed in Malaysia

OPTICALLY STIMULATED LUMINESCENCE IN ANION-DEFECTIVE CARBON DOPED α-Al_2O_3 CRYSTALS

N. KRISTIANPOLLER* and L. OSTER**

**School of Physics and Astronomy, Tel-Aviv University, 69978, Israel; **Physics Department, Ben Gurion University, Beer Sheva, 84105, Israel*

Optically stimulated luminescence (OSL) was studied in C-doped α-Al_2O_3 crystals, which had previously been exposed to X or β irradiations. The OSL was excited by monochromatic UV light in 200–300 nm region. Emission maxima appeared at 330 nm and 410 nm which are attributed to F^+ and F-luminescence respectively. This is supported by measurements of excitation spectra, which showed maxima at 260 and 215 nm. Results were compared to those obtained by measurements of the X-luminescence and phototransferred thermoluminescence in the same samples as well as in pure α-Al_2O_3 crystals. Effects of previous irradiations and of thermal treatment on the OSL intensities were also investigated.

Key words: luminescence, defects, aluminum oxide.

Optically stimulated luminescence (OSL) and its applications to dosimetry and dating have recently been studied in quartz and various other insulating materials.[1,2] In this method the samples are exposed to ionizing radiation and subsequently illuminated by light of wavelengths, which can not directly excite luminescence in an unirradiated crystal. These wavelengths can, however, cause the stimulation and transfer of carriers, trapped by previous exposure to ionizing radiation at the site of existing defects or impurities.

In the present work the excitation and emission of the OSL and its dependence on the irradiation history and on thermal pretreatment were studied in α-Al_2O_3:C crystals.

The C-doped α-Al_2O_3 crystals were grown by M. Akselrod and V. Kortov at the Urals Polytechnical Institute.[3] Nominally pure α-Al_2O_3 crystals were grown by Insaco Inc.

The OSL was excited by monochromatic near UV light in α-Al_2O_3:C crystals which had previously been exposed to X or β-radiations. The OSL emission spectra showed two maxima at $\sim$ 330 and 410 nm (Figure 1, curves a and b). The 410 nm maximum also appeared in the luminescence, emitted during X-irradiation (XL) of the same samples (Figure 1, curve c). After X-irradiation phosphorescence was observed at 330 and 410 nm (Figure 1, curve d); its decay time was of the order of 100 sec. For comparison also emission spectra of the thermoluminescence (TL) and phototransferred TL (PTTL) of the C-doped samples as well as the TL and XL of the above-mentioned nominally pure α-Al_2O_3 crystals were measured. The TL and PTTL of α-Al_2O_3 crystals showed the same 410 nm emission band. In the nominally pure samples the 330 nm and a strong narrow 700 nm band appeared.[4] Emission band at 330 and 410 nm have previously been ascribed to F^+ and F center luminescence of pure α-Al_2O_3 crystals.[5] The 700 nm emission band is apparently due to casual Cr^{3+} impurities.

Previous investigations have shown that luminescence as well as TL can be excited in fresh untreated α-Al_2O_3crystals only by wavelengths shorter than 145 nm.[4] UV light of longer wavelengths can cause in samples, which have previously been exposed to ionizing radiation, the stimulation or transfer of trapped carriers. The OSL emission at 330 and 410 nm recorded in the present work is attributed to the following process. During exposure to ionizing radiation electrons may be trapped at oxygen vacancies and F as well as F^+ centers are formed; by subsequent illumination with near UV light the trapped electrons can be stimulated to an excited level of these centers and the characteristic F and

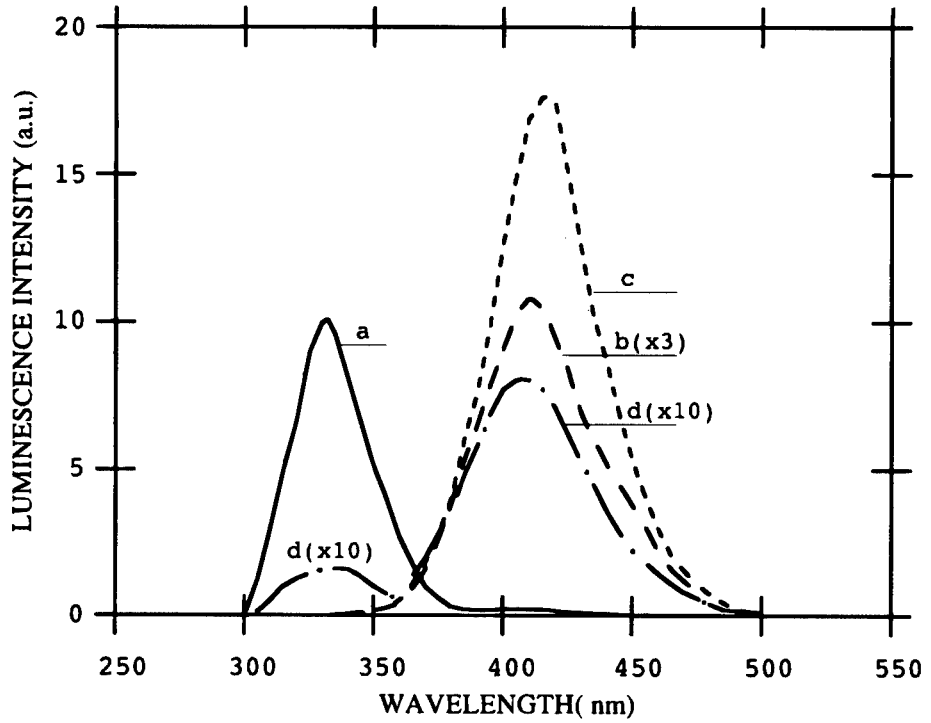

FIGURE 1 Emission spectra in α-Al_2O_3:C at RT of: (a) the OSL excited by 260 nm; (b) the OSL excited by 215 nm; (c) the XL; (d) the phosphorescence.

F^+ luminescence is emitted during radiative decay. This is supported by the present measurements of the OSL excitation spectra. The 410 nm emission band showed an excitation maximum at 215 nm, which is located on the long-wavelength tail of the F-absorption band, while the 330 nm OSL emission band had an excitation maximum at 260 nm, which coincides with the peak of the F^+ absorption (Figure 2). It has recently been reported, that the PTTL of these crystals also has excitation maxima at ~ 220 nm and at 260 nm.[6] The finding, that the same emission bands and the same excitation maxima appear in the OSL and PTTL indicates that analogous processes are involved in both cases.

Heating of the irradiated samples to 300°C caused a decrease in the 410 nm emission intensity. Heating to ~ 500°C caused a further decrease in the intensity of the F-emission, and a notable increase in F^+-emission of 330 nm, indicating a F to F^+ conversion; the electron released from the F center is probably captured by an impurity atom. Heating to ~ 950°C and slow recooling to RT caused a slight increase in both emission bands, while fast recooling to RT caused mainly an increase in the F^+-emission. The increase in the F and F^+ luminescence after the heating to 950°C may be due to a thermal ionization of the impurity and transfer of electrons to existing anion vacancies.

The finding that the OSL as well as the PTTL and XL of the C-doped α-Al_2O_3 crystals is dominated by the F and F^+ center emission while in the nominally pure α-Al_2O_3 crystals the Cr^{3+} emission band near 700 nm is dominant, fits the statement of Akselrod

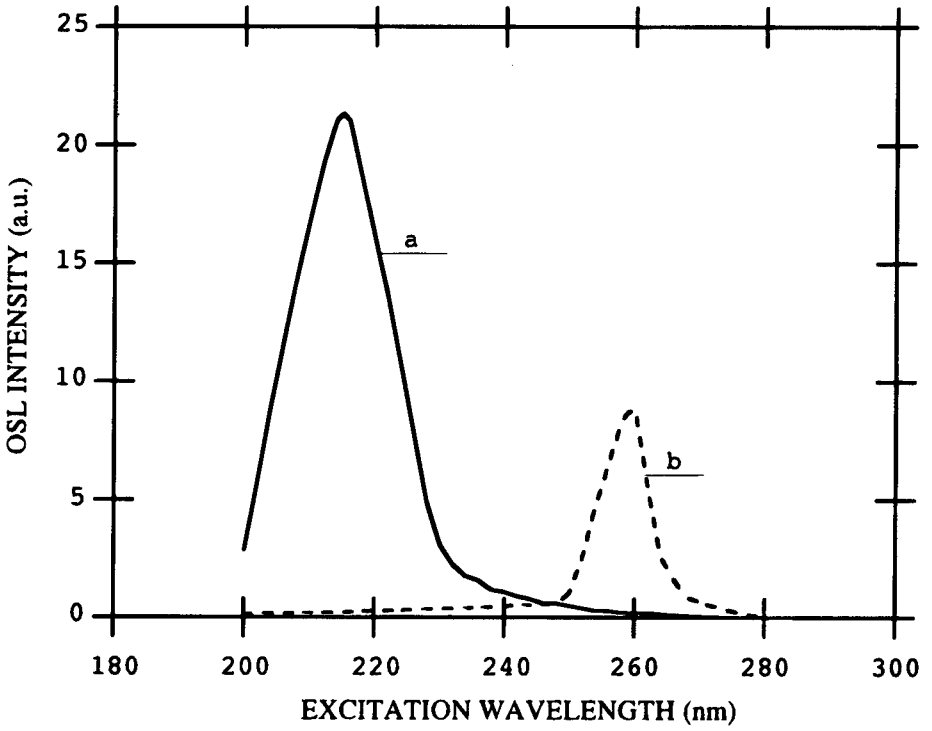

FIGURE 2 Excitation spectra of: (a) the 410 nm OSL band; (b) the 330 nm OSL band in α-Al_2O_3:C.

et al.[3] regarding the high concentration of oxygen vacancies in the C-doped crystal and their decisive role in the luminescence properties of this material.

REFERENCES

1. D. J. Huntley, D. J. Godfrey-Smith and M. L. W. Thewalt. *Nature* **313**, 105 (1985).
2. A. S. Wintle. *Radial. Prot. Dosim.*, **47**, 627 (1993).
3. M. S. Akselrod, V. S. Kortov, D. J. Kravetsky and V. I. Gotlib. *Radiat. Prot. Dosim.* **32**, 15 (1990).6
4. N. Kristianpoller and A. Rehavi. *J. Physique* **37**, C7–212 (1976).
5. T. J. Turner and J. H. Crawford. *Phys. Rev.* **B13**, 1735 (1976).
6. L. Oster, D. Weiss and N. Kristianpoller. *J. Phys. D; Appl. Phys.* **27**, 1732 (1994).

Radiation Effects and Defects in Solids, 1995, Vol. 134, pp. 315–319
Reprints available directly from the publisher
Photocopying permitted by license only

© 1995 OPA (Overseas Publishers Association)
Amsterdam B.V. Published under license by
Gordon and Breach Science Publishers SA
Printed in Malaysia

THERMALLY STIMULATED DEPOLARIZATION CURRENTS IN NATURAL BERYL

CARLOS VIANNA and ANA REGINA BLAK*

Instituto de Física, Departamento de Física Nuclear, Universidade de São Paulo, Caixa Postal 66318, CEP 05389-970, São Paulo, SP, Brasil.

Thermally Stimulated Depolarization Current (TSDC) spectra of untreated pink, green and blue beryl samples show a single peak centered at 200 K, unaffected by heat and linearly dependent on the polarization field, a typical behaviour of defects with a dipolar origin. When the samples are thermally treated above 1000 K in air two new peaks appear at 170 K and 220 K. Above 1200 K water is removed from the channels of the beryl, the Fe^{3+} is reduced into Fe^{2+} and the formation of iron dipoles is then enhanced, giving rise to the observable bands. An increase in the peak height of the 170 K and the 220 K bands is observed when the samples are ultraviolet (UV) illuminated after the heat treatments. UV illumination of the samples leads to the photodissociation of hydroxyls followed by the displacement of the hydrogen to isolated sites, thereby contributing to the formation of iron dipoles.

Key words: morganite, aquamarine, dipoles, thermally stimulated depolarization currents.

1 INTRODUCTION

This report describes Thermally Stimulated Depolarization Currents (TSDC) in pink (morganite), blue and green (aquamarine) beryl samples from 150 K up to 250 K before and after heat treatments (HT) and ultraviolet (UV) illumination. Natural beryl occurs in transparent, good-quality crystals of high perfection. Their growth-defect configuration is of great interest with respect to their crystal growth and mineralogy.

Beryl is a ring cyclosilicate having the chemical formula of $\mathbf{Be_3Al_2Si_6O_{18}}$. The silicate rings lie one above the other along the C_6 axis in such a way as to form long channels of quite large dimensions that can shelter a large variety of impurities such as alkalis, transition metals, OH^- ions and molecules of CO_2, CH_4 and H_2O.[1] The water molecules can assume two orientations in the channel. Type I water has its H-H vector parallel to c and type II has its H-H vector perpendicular to c and always lies near an alkali cation. Individual water molecules can hop between the two orientations.[1,2]

Optical Absorption (OA), Mössbauer spectra and Electron Paramagnetic Resonance (EPR) spectra have been studied in detail by several workers referred to in a previous paper.[3] The Thermoluminescence (TL) emission of different samples of beryl has been studied by Singha and Gartia[4] and Blak and McKeever.[5]

The TSDC technique allows the study of the behaviour of defects of dipolar origin and also the nature of aggregation of dipoles. Natural crystals present a great variety of impurities exhibiting TSDC bands. Many Brazilian beryl crystals were examined in order to investigate dipole defects. A study of the role played by hydrogen in the TSDC of pink and colourless beryl samples has already been published.[6] This work complements the results obtained for green and blue types and explains the general behaviour of dipole defects in beryl.

*The participation in the conference was supported by Fundação de Amparo à Pesquisa do Estado de São Paulo (FAPESP).

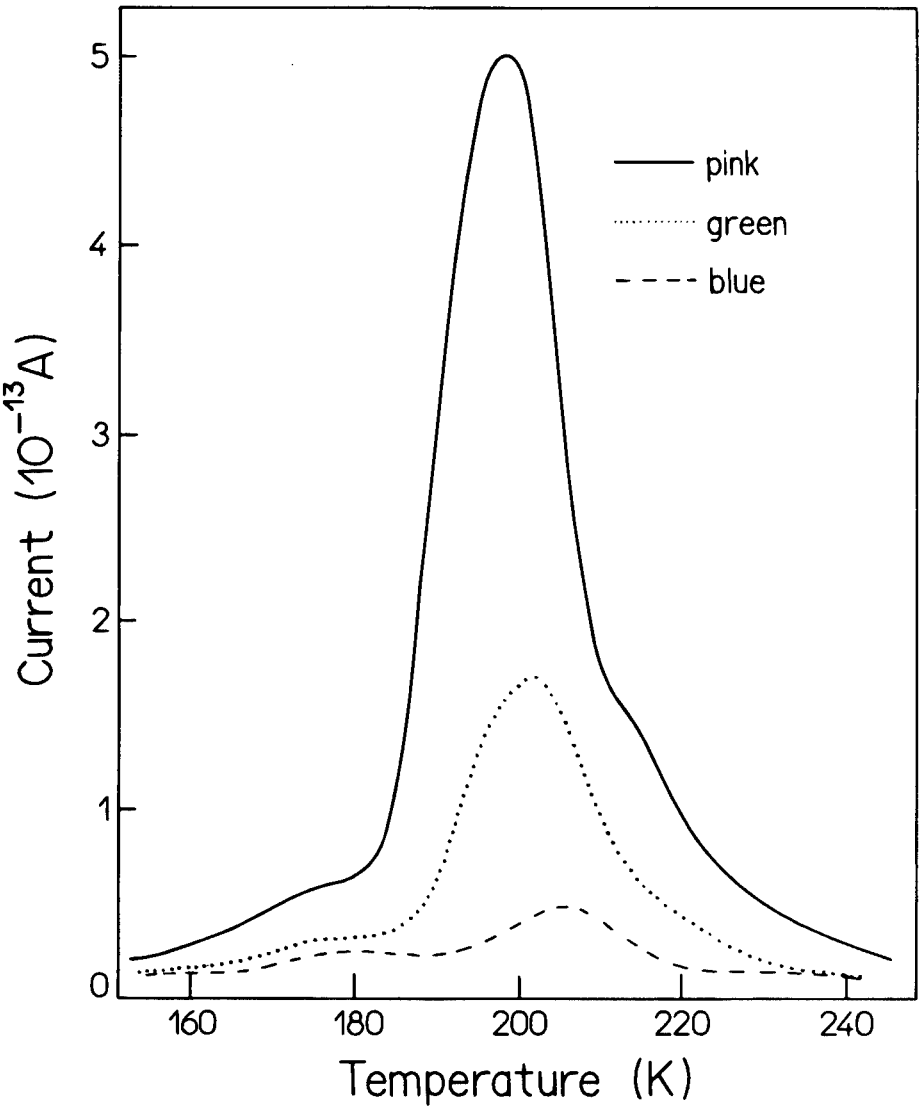

FIGURE 1 TSDC spectra of pink (——), green (...) and blue (- - -) beryl samples without any thermal treatment.

2 EXPERIMENTAL

Natural beryl samples were obtained from several sources, including commercial dealers, private collections and various individuals. Plane sections 0.3 to 1.0 mm thick were cut and polished. Infrared (IR) spectra were recorded with a Jasco IR-700 spectrophotometer for the range 400–4000 cm^{-1} For the TSDC measurements, the samples were polarized

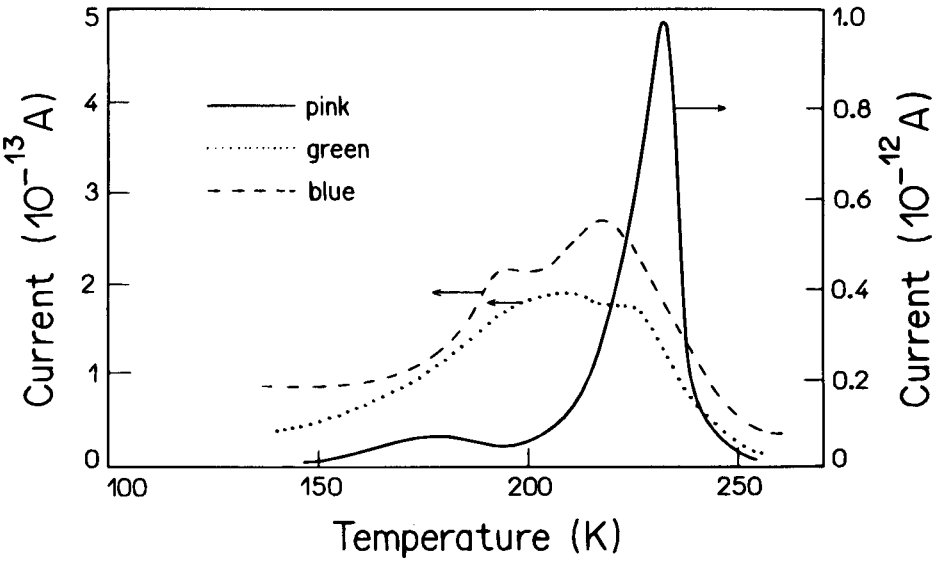

FIGURE 2 TSDC spectra of pink (——), green (...) and blue (- - -) beryl samples after HT of 1000 K for 60 minutes.

from 77 K to 230 K by an up to 30 kV/cm electric field. The depolarization currents were detected by a Keithley 617 electrometer connected to an AT microcomputer. In Table I, a quantitative analysis of some of the impurities (transition metals) in beryl obtained by neutron activation analysis and X-ray fluorescence analysis is presented.

Table I
Transition metals in beryl (in ppm)

Sample	Fe	Mn	Cr	V	Na	Cs
Goshenite	263±8	60±9	79±9	112±9	5717±21	6400±700
Pink	408±8	201±9	132±9	42±13	7488±27	11500±1500
Pale Blue	4100±200	28±9	80±9	85±9	216±2	
Pale Green	6600±300	27±9	82±9	35±9	5665±20	

3 RESULTS AND DISCUSSION

The TSDC spectra of untreated samples of pink, blue and green beryl show a prominent single peak centered at 200 K which is not affected by heat, linearly dependent on the polarizing field and related to Mn^{2+} ions occupying the aluminium sites near alkali ions in the channels.[6] In Figure 1, the spectra of samples without any treatment are shown. The 200 K band in the morganite (pink) samples is very high in comparison to the aquamarines (blue and green). This band becomes imperceptible behind other peaks when the crystals are thermally treated above 1000 K in air. For a heat treatment of 1000 K for 60 minutes the spectra are shown in Figure 2. Two bands become prominent at 170 K and 220 K,

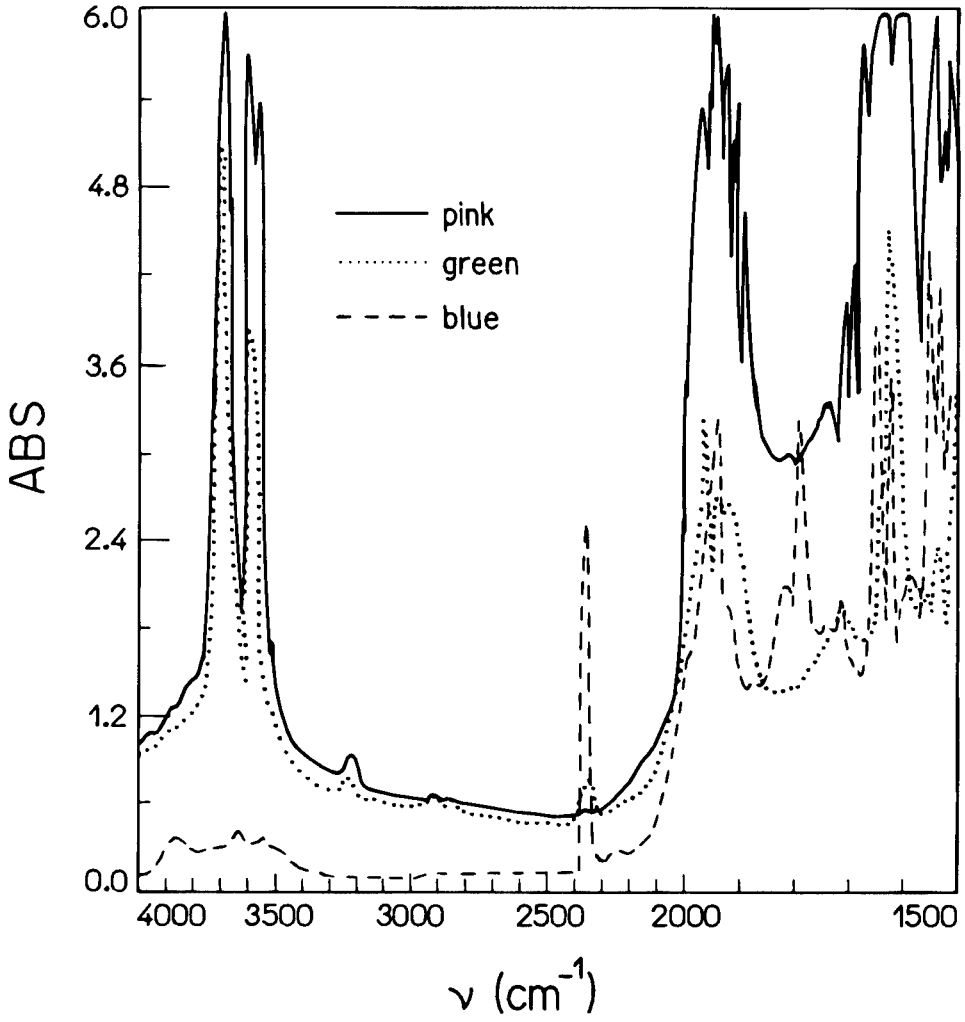

FIGURE 3 IR spectra of pink (——), green (...) and blue (- - -) beryl samples.

masking the previous 200 K band. The intensity of the peak at 220 K becomes very high for the morganite. The peak is linearly dependent on the polarization field, behaviour of defects with dipolar origin. Blue and green samples could not support the heat above 1200 K in air. For thermal treatments above 1000 K, a difference was observed between the blue and the green samples. For the blue samples the 220 K band became prominent and the 170 K almost disappeared. For the green samples the 170 K band increases. In blue aquamarines, Fe^{3+} replaces Al^{3+} at octahedral sites.[7] In green aquamarines, most of the Fe^{3+} is in the channels.[3] Thermal treatment reduces Fe^{3+} to Fe^{2+} in both cases and thereby contributes to the formation of iron dipoles. These results indicate therefore that the 170 K peak is related to the dipole formed with iron in the channel and that the 220 K peak is

related to the iron at an aluminium site. In both cases the presence of alkali ions is related to the formation of dipoles. For thermal treatment of morganite up to 1300 K a change of relative height of the two Fe^{2+} bands is observed, confirming the competition between the two different sites of the iron. Above 1200 K, water is removed from the channels leaving the alkali ions free to move, and thus favouring the increase of the TSDC bands. In Figure 3 the Infrared (IR) spectra reveal that the amount of water varies from sample to sample. The blue aquamarine is poor in water molecules and the morganite has a very high amount of water molecules, mainly of type II. From Table I it is seen that the morganite samples present more alkali ions than the other types of beryl. The alkali ions are in fact responsible for the formation of the dipoles in the pink beryl in spite of the lesser iron content.

UV illumination of the samples produces the photodissociation of OH^- ions, leaving hydrogens free to contribute to the formation of iron dipoles.

REFERENCES

1. D. L. Wood and K. Nassau, *J. Chem. Phys.* **47**, 2220 (1968).
2. D. S. Goldman, G. R. Rossman, and K. M. Parkin, *Phys. Chem. Minerals* **3**, 225 (1978).
3. A. R. Blak, S. Isotani and S. Watanabe, *Phys. Chem. Minerals* **8**, 161 (1982).
4. R. Singha and R. K. Gartia, *Phys. stat. sol.* **(a) 87**, 305 (1985).
5. A. R. Blak and S. W. S. McKeever, *Radiat. Prot. Dosim.* **47**, 95 (1993).
6. C. A. P. Vianna, M. E. G. Valério and A. R. Blak, *Radiation Eff. Def. Solids*, **119–121**, 603 (1991).
7. M. Dvir and W. Low, *Phys. Rev.* **119**, 1587 (1960).

Radiation Effects and Defects in Solids, 1995, Vol. 134, pp. 321–324
Reprints available directly from the publisher
Photocopying permitted by license only

© 1995 OPA (Overseas Publishers Association)
Amsterdam B.V. Published under license by
Gordon and Breach Science Publishers SA
Printed in Malaysia

CRYSTAL STRUCTURE PERFECTION AND DOMAIN STRUCTURE REVEALING IN EPITAXIAL FERROELECTRIC THIN FILMS

V. A. ALYOSHIN, E. V. SVIRIDOV, I. N. ZAKHARCHENKO
and V. P. DUDKEVICH

Institute of Physics, Rostov-on-Don, Russia

The deposition of epitaxial ferroelectric films with optically-perfect surface and interface is shown to be possible. (Ba, Sr)TiO_3/(001)MgO epitaxial films are c-domain and slightly self-polarized. The contrast of domain boundary revealing in the films becomes worse as the crystal structure perfection decreased. The role of film microvolumes with zero spontaneous deformation arising upon influence of microstrains is discussed.

Key words: ferroelectrics, thin film, domain structure.

1 INTRODUCTION AND PROCEDURE

Ferroelectric film surface and interface qualities and domain structure peculiarities are of importance for film applications.[1] Evolution of the film surface and cross-section relief was studied by the electron microscopy replica method. The fact of epitaxy and the type of domain texture were established by XRD analysis. Film crystal structure perfection was estimated by the value of microstrains $\Delta c/c$ obtained from XRD data.

2 RESULTS AND DISCUSSION

Epitaxial growth of (Ba, Sr)TiO_3/(001)MgO rf-sputtered films could be realized by means of 3-dimensional nucleation and layer-by-layer growth at the expense of variation of oxygen pressure P and substrate temperature T.[2] Corresponding surface relief and interface quality variations are displayed on Figure 1. The deposition of mirror-smooth films with pore-free interface was shown to be possible (Figure 1.2).

We succeded in growth of mirror-smooth epitaxial films with different crystal structure perfection. According to the XRD data the films with microstrain values $\Delta c/c$ less than tetragonality of the bulk material $c/a-1 = 0.010$ had c-axis of crystal lattice normal to the film surface due to the thermoelastic compressive stresses. The distortion of film crystal lattice with $\Delta c/c$ comparable with the $c/a-1$ value and, thus, the type of domain texture could not be established by XRD methods.

As the positive sides of c-domains are etched faster than negative ones forming more rough surfaces,[3] the character of film chemical etching made it possible to reveal the film domain structure peculiarities. The most perfect films after etching displayed 180° c-domain structure and possessed partial self-polarization: positive sides of the domains occupied the smaller area on the film surface (Figure 2.1). As film perfection decreased the visible sizes and concentration of positive domains decreased (self-polarization increased) and the contrast of domain boundaries etching became worse (Figure 2.2). The further decrease of the structural perfection resulted in the ceasing of the domain boundary

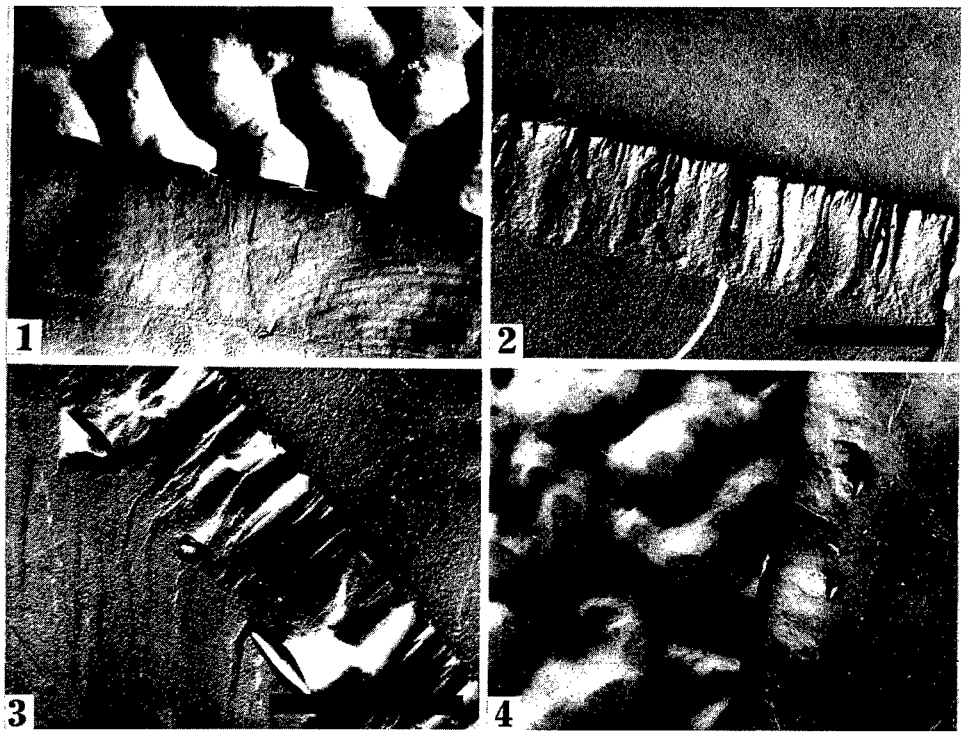

FIGURE 1 Surface and cross-section relief of the BST epitaxial films grown by 3-dimensional (1, 4) and layer-by-layer (2, 3) growth. The working gas pressure P and substrate temperature T are: P = 60 Pa, T = 650°C (1); 80 Pa, 825°C (2); 80 Pa, 875°C (3); and 100 Pa, 925°C (4). At the P-T-high-value deposition conditions the pores in the film-substrate interface are formed (3, 4). Bar—1 um.

revealing on the film surface: films with $\Delta c/c = 0.006$ seemed to be completely self-polarized with the spontaneous polarization vector directed to the substrate ('minus-single-domain', Figure 2.3) whereas the most defect films after chemical etching looked like plus-single-domain (Figure 2.4).

The study of film cross-sections after chemical etching allowed to establish that: i) near the film cleavage surface the rearrangement of the domain structure (c-to-a domain switching) due to tensile stresses arising upon cleaving occured (Figure 3.1, 3.2). ii) the domains in the films which looked like minus-single-domain did exist (Figure 3.2). and iii) no domain structure could be revealed even on the cleavage surface of the most defect films (Figure 3.3).

The results obtained from the film cross-section observations allowed to assume the specific surface layer existence. After removal of this layer by polishing etching the 180° c-domains on the surface of the 'minus-single-domain' films appeared. The removal of the surface layer led to the decrease in the degree of self-polarization in the more perfect films as well. The most defect films did not demonstrate domains neither before nor after removal of the surface layer. However, according to the dielectric measurements these films possessed ferroelectric properties.

As microstrains are the mean value of local variations of lattice interplanar distances

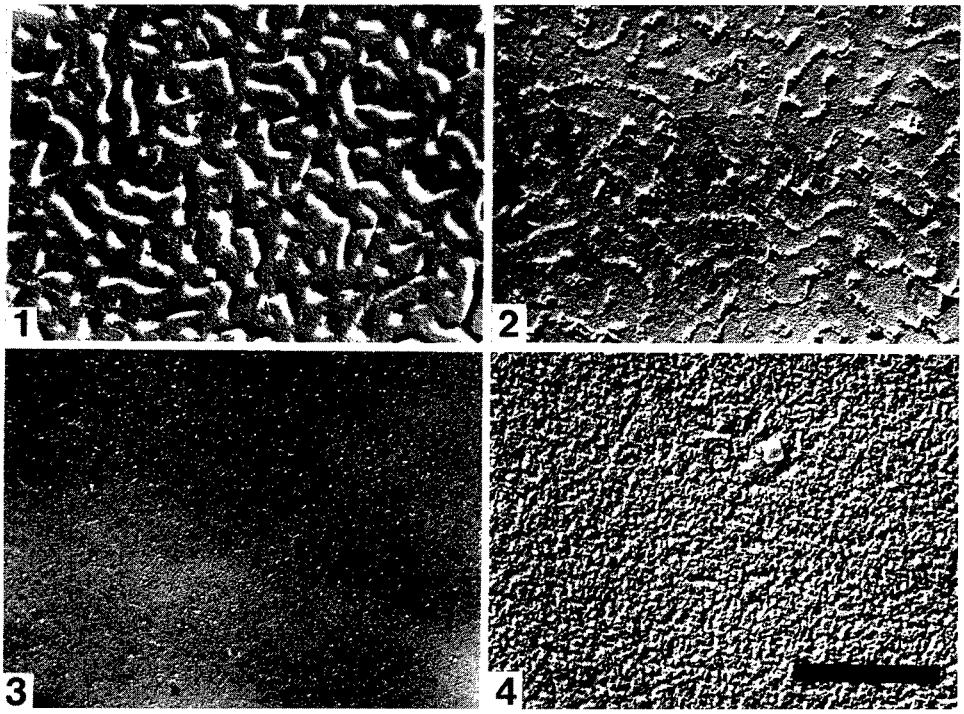

FIGURE 2 Surface relief of the BST epitaxial films after chemical etching. Microstrain values are: $\Delta c/c = 0.001$ (1), 0.003 (2), 0.006 (3), and 0.010 (4). Bar—1 um.

they are equivalent to the local variations in unit-cell spontaneous deformation c/a-1. Therefore the most defect films may contain the areas with resulting zero unit-cell deformation and, thus, zero polarization. We suppose that just these areas play the role of the 180° domain boundaries that means the 'spreading' of the domain boundaries and make impossible to reveal them by etching. The observed data on the decreasing the degree of film self-polarization after removal of the surface layer seemed to indicate the presence of the space charge in this layer, probably due to its nonstoichiometry.

REFERENCES

1. S. L. Swartz, *IEEE Trans. Elec. Insul.* **25 (5)**, 935 (1990).
2. Z. Surowiak, Y. Nikitin, S. Biryukov, Y. Golovko, V. Mukhortov and V. Dudkevich, *Thin Solid Films.* **208**, 76 (1992).
3. W. J. Merz, *J. Appl. Phys.* **25 (10)**, 1346 (1954).

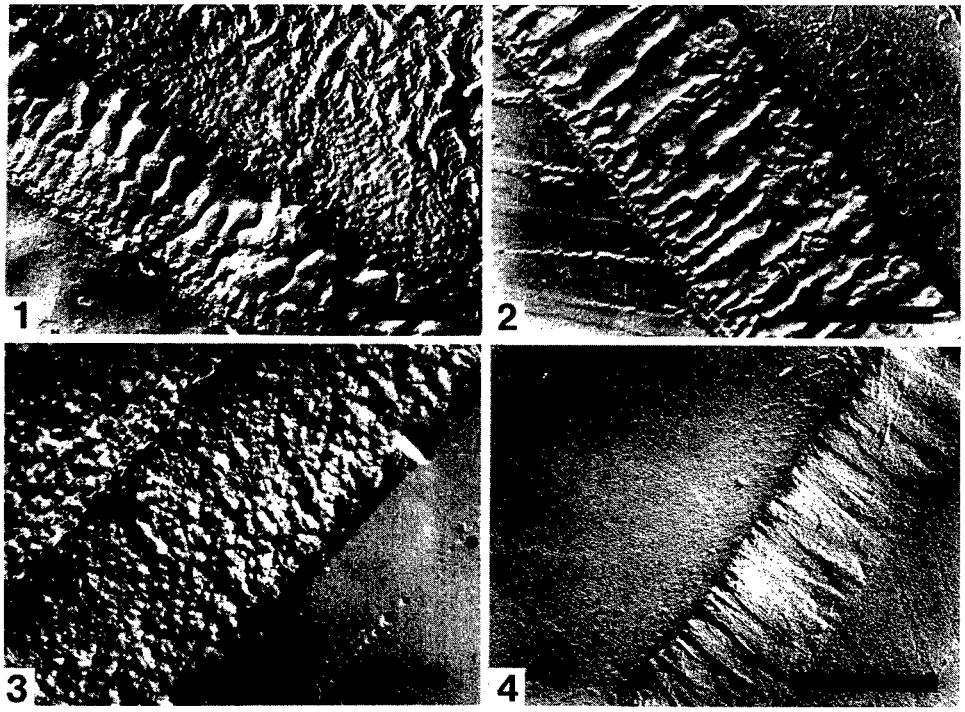

FIGURE 3 Surface and cross-section relief of the BST epitaxial films prior to (4) and after (1–3) chemical etching. Microstrain values are: $\Delta c/c = 0.001$ (1), 0.005 (2), and 0.010 (3, 4). Bar—1 um.

Radiation Effects and Defects in Solids, 1995, Vol. 134, pp. 325–328
Reprints available directly from the publisher
Photocopying permitted by license only

© 1995 OPA (Overseas Publishers Association)
Amsterdam B.V. Published under license by
Gordon and Breach Science Publishers SA
Printed in Malaysia

THE EFFECT OF LOCAL ORDERING IN A SYSTEM OF DEFECTS IN WEAKLY DOPED $KTaO_3$: DIELECTRIC ANOMALIES AND THEIR ORIGIN

V. TREPAKOV,[†] F. SMUTNÝ,[‡] V. VIKHNIN,[†] V. BURSIAN,[†] L. SOCHAVA,[†] L. JASTRABÍK[‡] and P. SYRNIKOV[†]

[†]*A. F. Ioffe Phys.-Techn. Institute, 194 021 St. Petersburg;* [‡]*Institute of Physics, Ac. Sci. of the Czech Rep., Praha 8*

The temperature-frequency behaviour of the permittivity $\varepsilon'(T, f)$ and $tg\delta(T, f)$ (20–300 K, 120 Hz–9 MHz), EPR, optical absorption and luminescence of $KTaO_3$ single crystals, pure and with Li 0.1; Cr 0.02; Cu 3; Fe 1; Li 0.1 + Cr 0.1, and Li 0.1 + Cr 0.1 + Cu 0.02 wt.%, were studied. Below 70 K, in all the doped samples, dielectric dispersion occurs, with $tg\delta(T)$ maxima obeying Arrhenius law. This is associated with a local ordering in dipole-dipole clusters (which contain reorienting defects of various kind) with correlations due to interactions via the TO-soft mode.

Key words: doped incipient ferroelectrics, dipolar collective effects.

1 INTRODUCTION

In ABO_3 incipient ferroelectrics, an indirect dipole–lattice–dipole interaction via the soft TO-mode (DTOII) leads to collective ordering effects in a system of randomly substituted relaxing polar defects, to unusual precursor effects, and to phase transformations.[1–4] Even undoped $KTaO_3$ reveals temperature-size dependent microregions with broken symmetry of unclear origin. In this work, the dielectric spectra, supplemented by optical absorption, photoluminescence (0.2–0.8 μm) and EPR (9.2 GHz) spectra, for both nominally pure and weakly doped $KTaO_3$ were studied.

Pure $KTaO_3$ reveals no unusual behaviour of $\varepsilon'(T, \omega)$ and $tg\delta(T, \omega)$, nor does it reveal any EPR and optical defects spectra. But all the weakly doped samples show a low-temperature dispersion of Arrhenius type, with the positions of $tg\delta$ maxima on the temperature axis nearly independent of the type of impurity introduced (see Figures 1–2). For all the samples, the activation energy Δ and the attempt frequency ω_0 ranged within 960–1065 K and $2.1 \times 10^{13} - 1.4 \times 10^{14} s^{-1}$, respectively, (Figure 3) which is typical for Li^+ off-centers in $KTaO_3$. We associate this strikingly similar relaxation with a local ordering of defects of various types in dipole-dipole clusters, where correlations originate as a consequence of the DTOII. We attribute this to: (*i*) the presence of several types of reorienting dipolar defects in all the doped crystals; (*ii*) a low local symmetry of these defects in the lattice (this enhances the local field considerably, and increases the DTOII) and to low frequencies of the TO-mode at low temperatures (this increases the DTOII too); (*iii*) and, (this point is principal) to high activation energies of reorientational jumping of actual defects, and a considerable mutual difference in the magnitude of their preexponential factors. Thus, the relaxation rates of various dipolar defect pairs (or clusters) are close to each other in magnitude and the critical slowing down of resulting cooperative relaxation rate in various clusters appears in the same (sufficiently narrow) temperature range:

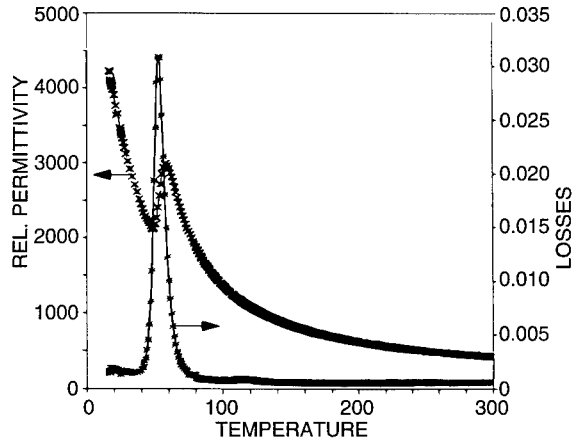

FIGURE 1 $KTaO_3$: Li 0.1 + Cr 0.1 + Cu 0.02 wt.%. The permittivity and losses at 20 kHz. Taken on cooling at a rate of -18 mKs^{-1}.

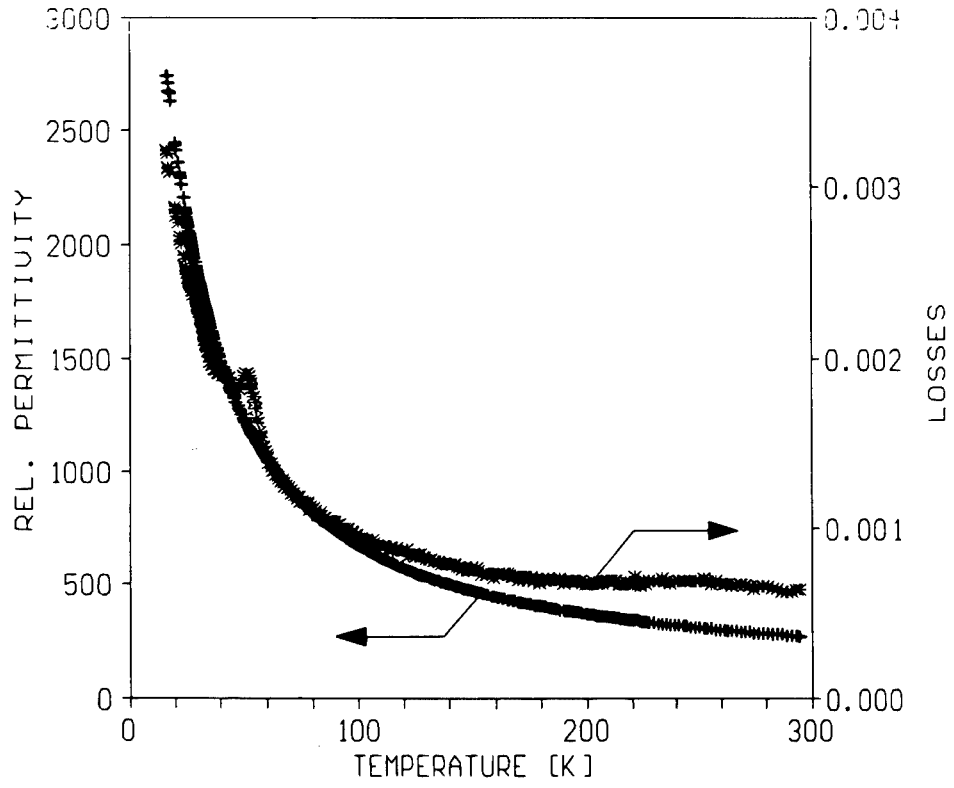

FIGURE 2 $KTaO_3$:Cu 3 wt.% (in the batch). The permittivity and losses at 20 kHz. Taken on cooling at a rate of -18 mKs^{-1}.

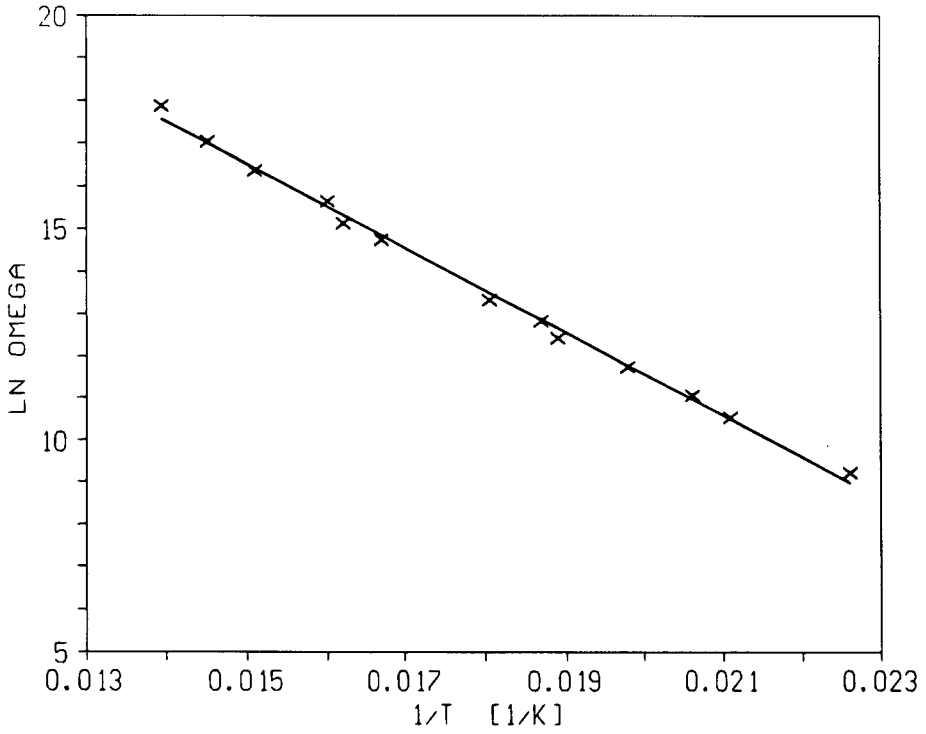

FIGURE 3 $KTaO_3$:Cr 0.01 wt.%. Arrhenius behaviour of the losses maxima (crosses) for f = 1592Hz−9 MHz. Solid line: least-squares fit of $f_0 = 6.25 \times 10^{12}$ Hz and = 986 K.

$$T_0 \cong \frac{\Delta_1 + \Delta_2}{-\ln(J^2 \tau_1^0 \tau_2^0)},$$

where J is the amplitude of DTOII and $1/\tau_n^0$ is the hopping pre-exponential factor for paired defects. Our data can be interpreted as follows: Li^+ present in a low concentration, is the leading participant of the pairing process in all the doped crystals, and other centers (having comparably low values of τ_i^0 and Δ_i) form pairs with it. Due to a rapid (exponential) rise of $1/\tau(T)$ for the 'leading' dipole with large τ^0 and Δ, the temperature behaviour of dielectric dispersion in various crystals shows a high degree of conformance. Our EPR and optical data detected the following centers with reorienting electric dipole and quadrupole moments or a reorienting elastic moment, which can participate in pair interaction: Fe^{2+}, $Fe^{3+}-O^-$ exchanging pairs, axial bipolaron $O^- - Fe^{3+} - O^-$ ($KTaO_3$:Fe); axial $Cu^{2+} - V_0$ ($KTaO_3$:Cu and $KTaO_3$:Li + Cr+ Cu); $Ta^{3+} - V_0$ ($KTaO_3$:Cu, $KTaO_3$:Li + Cr+ Cu and $KTaO_3$:Cr).

ACKNOWLEDGEMENTS

This work was supported in part by Russian Acad. Fundamental Res. Grant N94-02-06292-a. The dielectric measurements were supported by grant No. 202/95/1393 of the Grant Agency of the Czech Republic.

REFERENCES

1. V. S. Vikhnin and Y. B Borkovskaya, *FTT* **20**, 3603 (1978).
2. B. V. Vugmeister and M. D. Glinchuk, *ZhETF* **89**, 947 (1980).
3. U. T. Höchli *et al.*, *Adv. in Phys.* **39**, 405 (1990).
4. W. Kleemann, *Int. J. of Mod. Phys. B* **7**, 2469 (1993).

Radiation Effects and Defects in Solids, 1995, Vol. 134, pp. 329–332
Reprints available directly from the publisher
Photocopying permitted by license only

© 1995 OPA (Overseas Publishers Association)
Amsterdam B.V. Published under license by
Gordon and Breach Science Publishers SA
Printed in Malaysia

A CATION VACANCY CENTER IN CRYSTALLINE Al_2O_3

BRUCE D. EVANS[1] and LAURENCE S. CAIN[2]

[1]*United Solar Technologies, Inc., 10914 S. E. 26th Street, Bellevue, WA 98004;*
[2]*Department of Physics, Davidson College, Davidson, NC 28036*

(Received July 1, 1994)

Two experiments delineate the nature of the broad, weak, 3-eV absorption band in Al_2O_3: (1) anion self-implants clearly establish its association with aluminum vacancies, and (2) optical properties of this V-type center are exemplified after hole transfer from Ti^{+4} impurities. These properties confirm a previous theoretical description.

Key words: Defects, Ti^{+4}, holes, alumina, ion-implantation, photobleaching.

Optical and transport properties of many insulators are strongly influenced by the presence of lattice defects, including impurities and vacancies. The concentration of vacancies and interstitials is dependent upon sample thermo-chemical history; the concentrations of these two are intimately interrelated by the necessity to maintain macroscopic charge neutrality. The introduction of host ions by self-ion-implantation alters the stoichiometry, as well as introduces large numbers of Frenkel-type defects on both sublattices due to elastic collisions by the incident ion. Material properties within the spatial range (0.1–3 mμ) of energetic ions (30 keV–3 MeV) can be significantly altered.

For example, ion implantation of aluminum upsets local stoichiometry in favor of anion vacancies, which, when decorated with electrons, result in F-type centers as evidenced by well-known ultra-violet optical absorptions and a blue photoluminescence.[1] In a complementary manner, the first experiment, self-implantation by 200-keV oxygen ions suppresses the formation of anion vacancies, as shown in Figure 1. However, closer examination revealed a broad, weak absorption band centered near 3 eV, shown in the insert. This band was obtained by subtracting a background component (dashed line), which is a Tauc-like absorption associated with lattice disorder of the form $\alpha^{1/2} \propto \lambda^{-1}$. The 3-eV band has been associated with a hole trapped on an oxygen ion adjacent to an aluminum vacancy, a V-type center.[2] Bartram *et al.* have presented a theory of these trapped hole centers.[3] The V-band is broader in the present example than that from ionizing radiation exposures alone, due to perturbations from the high local damage level, >1 dpa, accompanying implantation. This result clearly associates the 3-eV band with Al^{+3} vacancies.

In experiment two, with a much lower vacancy concentration, V-type center details are revealed evaluating the relation between an aliovalent impurity and charge compensating Al^{+3} vacancies. Ti^{+4} impurities are often present in Al_2O_3, as evidenced by a nearly-ubiquitous, anisotropic absorption band at 5.4 eV.[4] This charge transfer transition leaves a hole on an oxygen 2p orbital, O^-, and an electron on a nearby titanium, Ti^{+3}. As-received Czochralski-grown, undoped sapphire, with a post-growth heat treatment in a mildly oxidizing atmosphere, after exposure to uv-irradiation (~230 nm), revealed an absorption band near 3 eV, shown in Figure 2. Concomitantly, the absorption shoulder at 5.4 eV significantly decreased, indicating a reduction in the Ti^{+4} population. Therefore, under uv irradiation, holes were transfered from Ti^{+4} to existing cation vacancies, which were originally formed during the oxidizing anneal to charge compensate for trace Ti^{+4}.

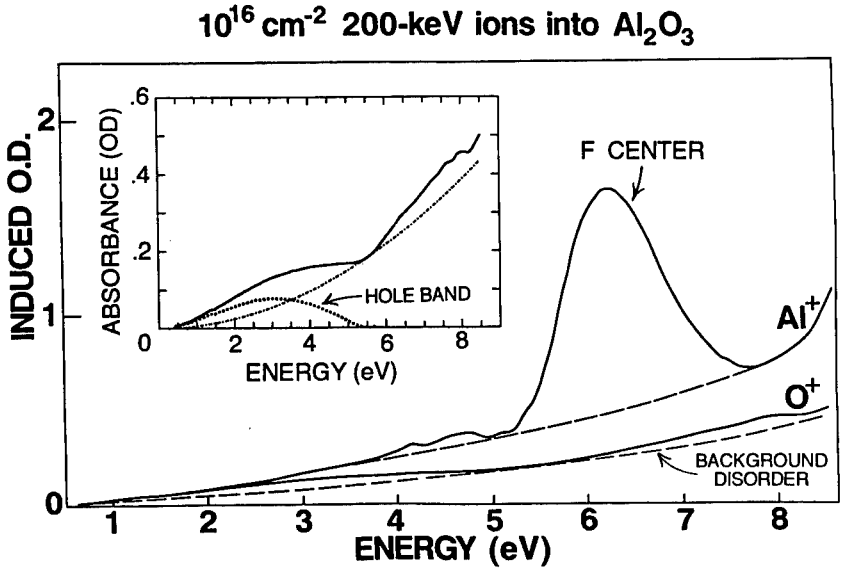

FIGURE 1 Absorption induced in Al_2O_3 by self-implant of 200-keV ions to 1×10^{16} cm^{-2}. The dashed curve represents background absorption. The insert shows oxygen-implant absorption on an expanded scale. Here the dashed curve represents the V-type band after background (dot-dash) subtraction.

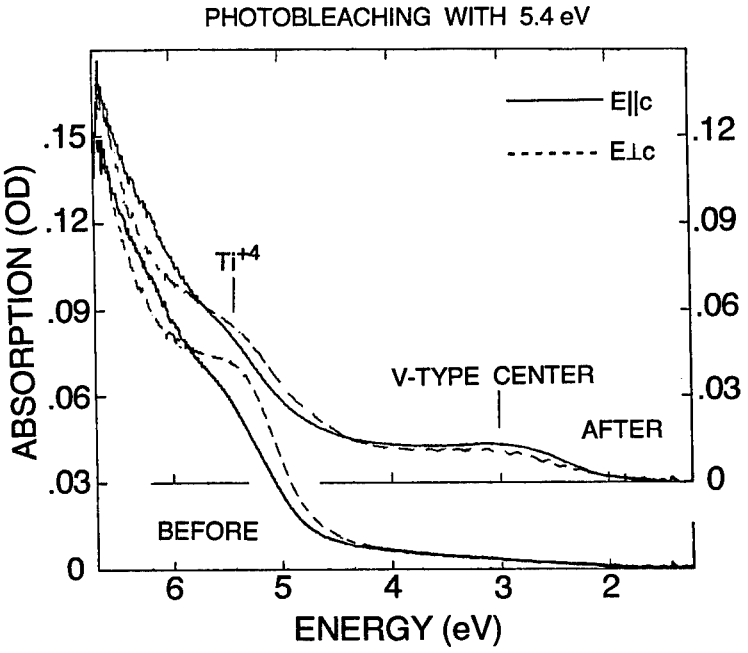

FIGURE 2 (a) Polarized absorption at 300 K of as-received, undoped, single crystal α-Al_2O_3, 0.89 mm thick. (b) The same sample after a 20-minute exposure to 230-nm radiation at 300 K. E||c solid curve; E⊥c, dashed curve. Note, the absorption at 1.24 eV has been set to zero for convenience.

Figure 2 is analyzed for V-type center concentration and oscillator strength. With $\sigma_\perp = 28 \times 10^{-18}$ cm^2,[4] and $\alpha = 0.78$ cm^{-1} from Figure 2(a), $N = \alpha/\sigma = 2.8 \times 10^{16}$ cm^{-3} = 0.4 appm Ti^{+4} per host cation. Assuming one empty aluminum vacancy charge compensates for three Ti^{+4}, and assuming the presence of no other significant compensating species, $[V_{Al}'''] = 1/3[Ti^{+4}] = 9.2 \times 10^{15}$ cm^{-3}. Furthermore, from the intensity of the observed V-type band, the oscillator strength, f, is estimated from Smakula's expression.[5] With $\alpha_\parallel \approx 0.24$ cm^{-1} at 3 eV, and halfwidth $\Delta E \approx 1$ eV, then $Nf = 5.8 \times 10^{15}\ \alpha\ \Delta E = 1.4 \times 10^{15}$ cm^{-3}. This, together with the above value for $[V_{Al}''']$, yields f = 0.15, a reasonable value. The oscillator strength for the analogous V-type center in MgO, based on epr and optical techniques, is 0.1.[5]

Figure 3 shows, in more detail, the uv-radiation-induced polarized spectrum, post-irradiation minus pre-irradiation. There are two salient features. The V-type band is anisotropic with $\alpha_\parallel > \alpha_\perp$. Second, the V-type band appears to be a composite of two bands, 3.0 ± .1 eV and 4.8 ± .1 eV. Both these qualitative features were predicted in the analysis by Bartram *et al.*[3] Their calculation showed the normal lattice crystal field splitting the upper state, ^{2}PE, yielding two possible transitions from the ^{2}PA ground state. Further, because of two possible bond lengths and two inequivalent orientations, four transitions result. In one, when the vacancy site and O^- share the same molecule along a 1.97 Å bond, transitions were predicted at 2.40 and 4.59 eV. These are in fact close to the two transitions shown in Figure 3. If the vacancy and O^- ion straddled neighboring molecules, along a 1.86 Å bond, transitions at 1.29 and 3.40 eV were predicted. A superposition of these four transitions was foreseen to yield a broad composite absorption band, as observed.

In summary, oxygen self-implants have shown that the weak, ~3-eV absorption band in Al_2O_3 is associated with positive charge trapped near an aluminum vacancy. Photobleaching

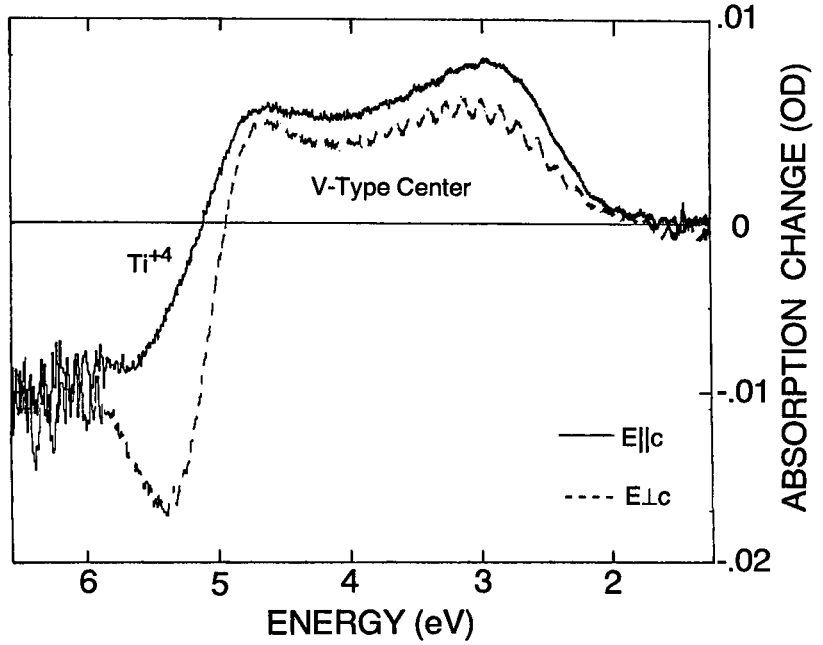

FIGURE 3 UV-radiation induced change in absorption of sample shown in Figure 2. E||c solid; E⊥c, dashed curve. Oscillations on the dashed curve are an instrumental artifact.

the 5.4-eV Ti^{+4} charge transfer band decorates an aluminum vacancy with a hole trapped on a neighboring oxygen. The oscillator strength for the V-type band has been estimated to be 0.15. Band position, composite nature, and anisotropy predicted by Bartram *et al.* have been confirmed.

REFERENCES

1. B. D. Evans, H. D. Hendricks, F. D. Bazzarre, and J. M. Bunch, *Ion Implantation in Semiconductors*, 1976 (Plenum, New York, 1977), pp. 265–274.
2. T. J. Turner and J. H. Crawford, Jr., *Solid State Comm.* **17**, 167 (1975).
3. R. H. Bartram, C. E. Swenberg and J. T. Fournier, *Phys. Rev.* **I39**, 941 (1965).
4. B. D. Evans, *J. Luminescence*, **55**, 6079 (1994).
5. E. Sonder and W. A. Sibley, in *Point Defects in Solids: Vol. 1,* eds., J. H. Crawford, Jr, and L. M. Slifkin (Plenum, New York, 1972), Chaps. 4, pp. 267, 269; A. E. Hughes and B. Henderson, ibid., Chap. 7, pp. 445.

3 COLOUR CENTERS

Radiation Effects and Defects in Solids, 1995, Vol. 134, pp. 333–336
Reprints available directly from the publisher
Photocopying permitted by license only

© 1995 OPA (Overseas Publishers Association)
Amsterdam B.V. Published under license by
Gordon and Breach Science Publishers SA
Printed in Malaysia

OPTICAL SPECTRA OF Cu^{2+} IONS IN LiF CRYSTALS

A. SCACCO[1], C. MARASCA[1], U. M. GRASSANO[2] and N. ZEMA[3]

[1]Dipartimento di Fisica, Universitá La Sapienza P.le A. Moro 2, 00185 Roma, Italy; [2]Dipartimento di Fisica, Universitá di Roma Tor Vergata, Via della Ricerca Scientifica 1, 00133 Roma, Italy; [3]Istituto di Struttura della Materia, C. N. R., Via E. Fermi 38, 00044 Frascati, Italy

Optical absorption and luminescence of Cu^{2+} ions in LiF are measured in the UV and VUV spectral regions. Absorption peaks are identified at 133 and 145 nm, in good agreement with predictions of a model valid for LiCl:Cu^{2+} and LiBr:Cu^{2+}. Three emission bands, excited with different efficiencies in the two absorptions, are revealed at 270, 320 and 360 nm.

Key words: VUV Spectroscopy, Single Crystals, LiF:Cu^{2+}

1 INTRODUCTION

Information on the optical behaviour of Cu^{2+} ions in crystals of alkali halides is rather poor: absorption spectra were measured only in a few Cu^{2+}-doped systems [1,2], and photoluminescence was never observed. Due to the relatively high energy value of the fundamental absorption of LiF (about 105 nm), absorption bands of Cu^{2+} impurities are expected at shorter wavelengths with respect to other alkali halides. For this reason, spectroscopic studies in LiF:Cu^{2+} have been carried out in the vacuum ultraviolet region, by taking advantage of the Synchrotron radiation at the ADONE storage ring in Frascati, Italy. Crystals used in the experiments were home grown by the Kyropoulos method and doped with 0.6 mole % of CuF_2 in the melt. According to recent detailed studies on the incorporation of copper impurities in alkali fluorides,[3] LiF crystals cannot be appreciably doped with Cu^{+} ions because of the pronounced instability of CuF at the melting point (1113 K) of LiF and its complete transformation into Cu and CuF_2. This means that the known coexistence of both Cu^{2+} and Cu^{+} species, possible in alkali chlorides, cannot occur in LiF doped with CuF_2, where the only impurity is given by Cu^{2+} ions.

2 ABSORPTION SPECTRA

Figure 1 shows the absorption spectra, measured at various temperatures in the spectral region 130–300 nm, of a LiF:Cu^{2+} crystal. Evident absorption bands are observed at 133, 145, 200 and 280 nm, and less pronounced peaks are found at 170 and 230 nm. Previous investigations showed that nominally undoped LiF crystals generally exhibit absorptions at 170, 200, 230 and 280 nm, which are attributed to metal impurities (Mg, Ti) or to oxygen-related defects accidentally contained in the starting LiF powder.[4–7] From these known data, it seems at first evident, in spite of a not very high quality of the sample, that doping with Cu^{2+} ions causes the appearance of the new absorptions at 133 and 145 nm. Their temperature dependence is quite different with respect to that of the other absorption bands: with increasing temperature, the new bands are strongly depressed, whereas the other bands show negligible changes, as previously reported.[7] A preliminary conclusion is that the 133 and 145 nm absorptions are not caused by oxygen-related defects, and therefore they can be assigned to the absorption of Cu^{2+} ions in LiF.

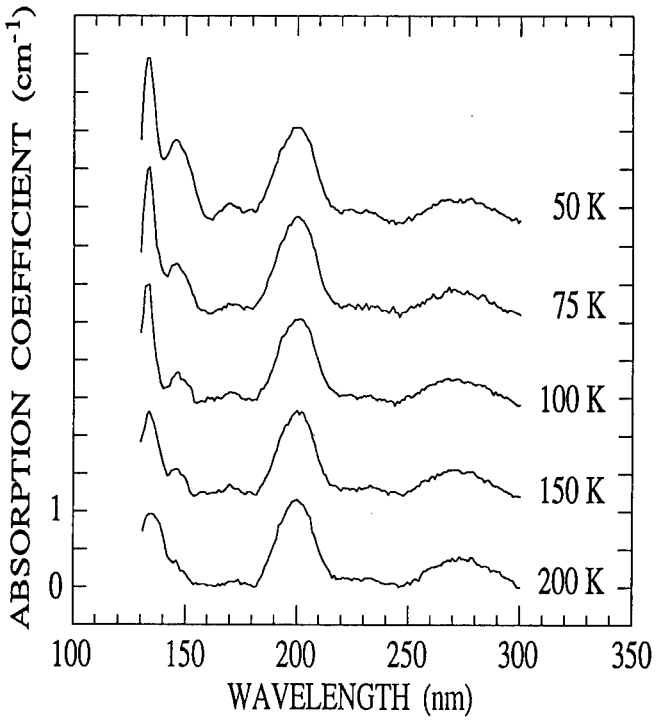

FIGURE 1 Absorption spectra at various temperatures of a LiF:Cu^{2+} crystal (0.6 mole % of dopant in the melt)

3 EMISSION SPECTRA

Luminescence excited at 135 nm and 145 nm, namely in the range of the Cu^{2+} absorption in LiF, is shown in Figure 2. Under optical pumping at 135 nm, the emission spectrum consists of a composite band peaking at about 320 nm and overlapping a weaker band at about 410 nm. Excitation at 145 nm causes a more complex emission spectrum, formed by three overlapping bands at about 270, 340 and 410 nm. Both spectra have been computer resolved into gaussian components, peaking at 300, 340 and 410 nm under 133 nm excitation, and at 270, 340 and 410 nm under 145 nm excitation. Such experimental results can be interpreted recalling that in undoped LiF crystals a typical emission at 410 nm is observed under excitation in the whole range between 130 and 280 nm. Such a luminescence is commonly assigned to oxygen-related defects responsible for the absorption bands at 170, 200 and 280 nm. As a consequence, it seems reasonable to attribute the other emissions between 250 and 370 nm to Cu^{2+} defects. The excitation spectra of the luminescence are shown in Figure 3. Excitation of the emissions at 270 and 330 nm (the latter not shown) are coincident and show a main peak at 133 nm, with a weak contribution of the 145 nm absorption. The luminescence at 365 nm is effectively excited in both 133 and 145 nm bands, but some excitation is also present in the 200 and 280 nm absorptions because of the overlap with the 410 nm luminescence.

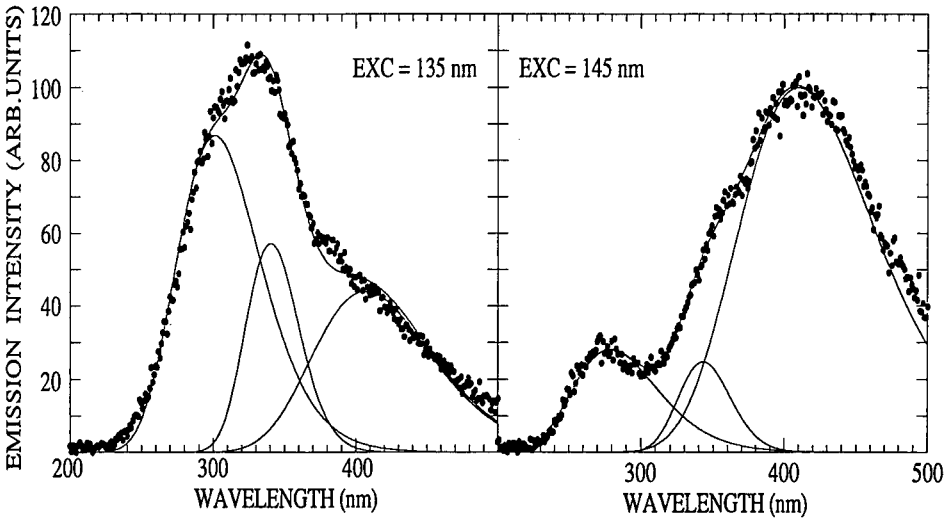

FIGURE 2 Emission spectra at 13 K of LiF:Cu^{2+} under two VUV excitations.

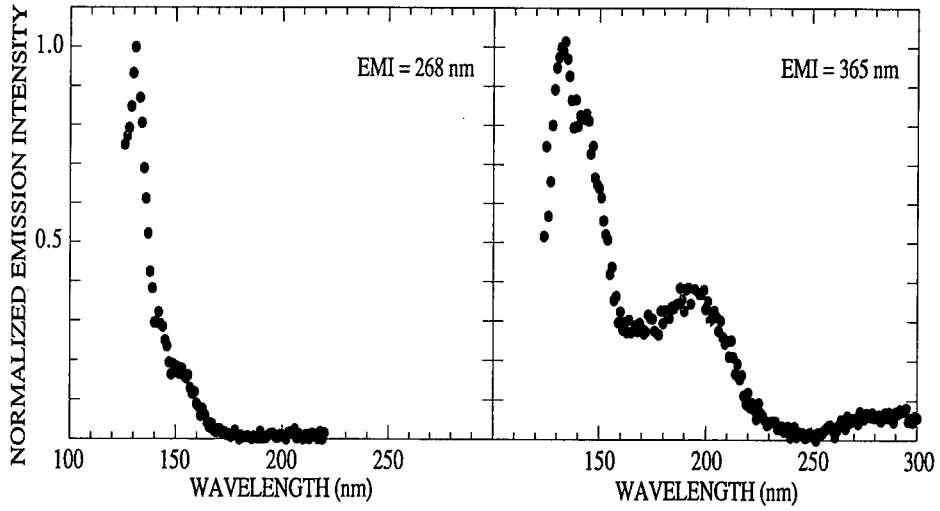

FIGURE 3. Excitation spectra at low temperature for the emission bands of LiF:Cu^{2+}.

4 CONCLUSIONS

The above preliminary experiments, to be confirmed by forthcoming measurements on crystals free of unwanted impurities, show that the absorption of Cu^{2+} impurities in LiF consists of two bands, peaking at 133 and 145 nm, the former producing luminescence at 300 and 340 nm, and the latter giving rise to emission at 270 and 340 nm. The absorption spectrum can be explained by analogy with the known data for Cu^{2+} ions in LiCl and LiBr.

In these systems, a model has been proposed[2] suggesting transitions of the octahedral molecular ion $(CuX_6)^{4-}$ from the ground state ^2E_g to the excited states $^2T_{1u}\sigma$ and $^2T_{1u}\pi$ for the higher energy and the lower energy bands, respectively. The very good agreement of both peak positions at 133 and 145 nm in LiF:Cu^{2+} with those predicted by the Mollwo-Ivey law clearly shows the validity of such a model for LiF as well. The lack of any information concerning photoluminescence of Cu^{2+} ions in other alkali halides makes it difficult to identify the deexcitation mechanisms responsible for the emission bands. A detailed study with this aim is in progress.

REFERENCES

1. E. Kratzig, T. Timusk and W. Martienssen, *phys. stat. sol.* **10**, 709 (1965).
2. S. Hirako and R. Onaka, *J. Phys. Soc. Japan* **50**, 1637 (1981).
3. D. S. McClure and S.C. Weaver, *J. Phys. Chem. Solids* **52**, 81 (1991).
4. E. W. Claffy, *phys. stat. sol.* **22**, 71 (1967).
5. M. R. Mayhugh, *J. Appl. Phys.* **41**, 4776 (1970).
6. E. Radzhabov, *phys. stat. sol. (b) 123*, **K79** (1984).
7. A. Scacco, C. Marasca, U. M. Grassano, R. Capelletti, S. Prato and N. Zema, J. Phys.: Condens. Matter 6, 7813 (1994).

Radiation Effects and Defects in Solids, 1995, Vol. 134, pp. 337–339
Reprints available directly from the publisher
Photocopying permitted by license only

© 1995 OPA (Overseas Publishers Association)
Amsterdam B.V. Published under license by
Gordon and Breach Science Publishers SA
Printed in Malaysia

NATURE OF UNCOMMON NUCLEAR SPIN RELAXATION IN NaCl WITH HIGH CONCENTRATION OF REORIENTING OH– IMPURITIES AT LOW TEMPERATURES

O. KANERT, M. BACKENS, M. FRICKE, S. KAPPHAN*, R. KÜCHLER and V. S. VIKHNIN**

*Institute of Physics, University of Dortmund, Germany; *University of Osnabrück, Germany; **A. F. Ioffe Physical Technical Institute, Saint-Petersburg, Russia*

The unusual features of low temperature nuclear spin relaxation in NaCl with high concentration of reorienting OH– impurities, with its primarily uncommon temperature and electric field dependencies, are explained in the framework of a model based on cooperative OH– dipole relaxation with taking into account the role of critical dipole-dipole clusters.

Key words: nuclear spin relaxation, reorienting impurities, dipole-dipole interaction, critical dependencies, clusters.

1 INTRODUCTION

The method of nuclear spin-lattice relaxation is informative not only from the hand of spin-phonon interaction and spin dynamic investigations. It is shown in[1] that this method is effective for study of motion connected with internal degrees of freedom of impurities, like reorienting degrees of freedom as in the case of OH– dipole impurities in NaCl.

The present work is devoted to experimental and theoretical studies of the uncommon behavior of nuclear spin relaxation in NaCl with high concentration of reorienting OH– impurities. This case is specially interesting due to possibility of cooperative effects. Although the first experimental results in this direction were obtained by us earlier[2,3] the elucidation of the nature of this phenomenon needed new direct experiments for verification of actual theoretical models.

In this work we have performed such experiments. This is the investigation of the influence of external electric field E on nuclear spin lattice relaxation in the case of interest. The E-field effect produces a strong change in the state of OH– dipoles and may be used for a check of theoretical models based on cooperative behavior of impurity dipole system. Besides this, we perform the theoretical consideration and develop the model which explained the main results of experiment.

2 EXPERIMENTAL RESULTS

The ^{23}Na nuclear spin relaxation (NSR) rate $1/T_1$ in NaCl containing different amounts of reorienting OH– impurities (with concentration n = 40 ppm, 130 ppm, 160 ppm, 420 ppm, 700 ppm, 1200 ppm and 1350 ppm) has been measured between 0.4 K and 300 K at three different Larmor frequencies (16 MHz, 27 MHz and 48 MHz).

For high n (for the $n \geq 130$ ppm) and at low temperatures (below 10 K), the uncommon behavior of $1/T_1$ was discovered. There are nearly temperature independent $1/T_1$ values

below 3 K and for n up to 700 ppm, and temperature dependence of $1/T_1$ with a maximum at 3 K for highest concentrations (1200 ppm and 1350 ppm).

Besides this, a logarithmic low of NSR rate decrease with external electric field increase was observed in the region of high OH– concentrations and low temperatures: $1/T_1 \sim \ln(E)^{-1}$.

3 MODEL OF PHENOMENON

The idea of the explanation of these NSR rate anomalies is based on the effect of dipole-dipole interaction in the system of reorienting OH– impurities. The dipole-dipole clusters with critical relaxation dynamics near the temperature of local dipole ordering T_{loc} (critical clusters) appear due to spatial OH– distribution. There is a critical decrease of dipole reorientation rate $1/\tau$ in critical clusters resulting in corresponding increase of NSR rate $1/T_1$ and in changing of its temperature dependence:

$$1/\tau = AT(T - T_{loc}). \tag{1}$$

In (1) we assume that the single dipole reorientational process at low temperatures is a single-phonon induced tunneling (the A is proportional to the square of tunneling matrix element).

The next important step is taking into account the distribution of T_{loc} with parameters which are depended on dipole concentration and electric field. The shape of this distribution $F[T_{loc}]$ changes with concentration variation. For a small number of critical clusters (when the main part of reorienting dipoles belongs to para-phase regions), or vice versa for high concentration of reorienting dipoles (with ordered clusters or microdomain regions existence), the shape of $F[T_{loc}]$ is Lorentzian with shifted center of the distribution:

$$F[T_{loc}] = B\alpha[(T_{loc} - T(0))^2 + \alpha^2]^{-1} \tag{2}$$

where the center of distribution T(0) and its width α are proportional to n, and B is a normalization parameter. Let us consider now the important intermediate case when the essential part of reorienting dipoles belongs to critical clusters but the number of ordered clusters or microdomains is small. Here we have to deal with a long range dipole-correlated system. The dipole-dipole interaction is strongly changed due to additional dipole-dipole correlation via critical clusters with high polarizability. It should be noted that a percolation in the system of critical clusters under consideration corresponds to dipole glass phase. The $F[T_{loc}]$in long range dipole-correlated system may be adopted as a rectangle-type dependence:

$$F[T_{loc}] = (T_{loc(max)} - T_{loc(min)})^{-1}, T_{loc(min)} < T_{loc} < T_{loc(max)}$$

$$F[T_{loc}] = 0, \qquad T_{loc} < T_{loc(min)}, T_{loc(max)} < T_{loc}. \tag{3}$$

where $T_{loc(min)}$ is determined by average static field of non-reorienting defects. We may consider the spin-relaxation process as a result of two steps for the actual case of the fast spin-spin relaxation $1/T_2 \gg 1/T_1$: (i) spin diffusion to fast relaxing centers which are the nuclei near the reorienting OH–dipoles, and (ii) spin-dipole relaxation of these fast relaxing centers. If the bottleneck is the second step the expression for $1/T_1$ is as follows:

$$1/T_1 = n\Omega^2 < \tau[1 + (\omega\tau)^2]^{-1} + 4\tau[1 + (2\omega\tau)^2]^{-1} > \tag{4}$$

where Ω^2 is mean square of quadrupole interaction of the nuclei near the reorienting centers, τ corresponds to (1), and $< \ldots >$ is averaging on T_{loc} with distribution function $F[T_{loc}]$ (in accordance with (2), (3) in the limits under consideration). If an external electric field E is larger than average static field of non-reorienting defects the minimum value of T_{loc} is equal to

$$T_{loc(min)} = pE/k \tag{5}$$

where p is electric dipole moment of OH– impurity. The expression (5) is caused by E-field suppressing of cooperative behavior for values of internal dipole electric fields which are less than E.

This model gives the possibility to explain the main features of experiment on a quantitative level. In particular, for the $kT \ll pE$ and on the basis of (3), which is actual for $T = 2$ K, $n = 700$ ppm and $E \geq 20$ kV/cm as on the experiment, we received from (1), (4) and (5) the following expression:

$$1/T_1 \sim \ln[kT_{loc(max)}/pE] \tag{6}$$

with well agreement with experiment.

ACKNOWLEDGEMENT

This work was supported by the Deutsche Forschungsgemeinschaft (German-Russian Project 436 RUS 113/39 OS 1994) and Russian Fund of Fundamental Investigations (Project 94-02-06292-a).

REFERENCES

1. O. Kanert, *Phys. Reports* **91**, 183 (1982).
2. M. Backens, M. Fricke, R. Küchler, O. Kanert, S. Kapphan. *Rad. Eff. and Def. in Solids* **119–121**, 657 (1991).
3. M. Backens, M. Fricke, R. Küchler, O. Kanert, S. Kapphan, V. Vikhnin. *Proc. of the XII International Conference on Defects in Insulating Materials*, Nordkirchen, Germany, August 16–22 1992 (Word Scientific, Singapore-New Jersey-London-Hong Kong, 1993), ed. by O. Kanert, J.-M. Spaeth, Vol. 2, pp. 798–800.

Radiation Effects and Defects in Solids, 1995, Vol. 134, pp. 341–344
Reprints available directly from the publisher
Photocopying permitted by license only

© 1995 OPA (Overseas Publishers Association)
Amsterdam B.V. Published under license by
Gordon and Breach Science Publishers SA
Printed in Malaysia

RELAXATION AND IR SPECTROSCOPIC PROPERTIES OF THE CN^- STRETCHING MODE IN SILVER HALIDES

C. E. MUNGAN*, U. HAPPEK*, W. VON DER OSTEN**, and A. J. SIEVERS*

*L.A.S.S.P and M.S.C., Cornell University, Ithaca, N.Y. 14853-2501 (USA)
**Fachbereich Physik, Universität-GH, 33095 Paderborn (Germany)

The relaxation times of the CN^- stretching mode in AgCl and AgBr at 1.7 K are found to be a few hundred microseconds. These times are shorter by more than two orders of magnitude than those for CN^- in most alkali halides. High frequency local modes discovered in the silver halides are suggested to act as fast relaxation channels causing this difference. Reexamination of CN^- doped sodium halides also reveals a local mode clearing up the previously found short times in these materials, too. An energy gap law fits all data.

Key words: Silver halides, CN^- impurity molecule, vibrational absorption and luminescence, lifetime of CN^- stretching mode, vibrational relaxation mechanism.

1 INTRODUCTION

CN^- molecular ions substituted at anion sites in alkali halides have been widely used as a model system to explore the effect of an ionic crystal matrix on properties of the impurity molecule. As to the vibrational spectra of the cyanide, the occurrence of infrared luminescence due to deexcitation of the CN^- stretching mode[1] allows to determine relaxation times and to investigate the possible relaxation mechanisms which were not cleared up satisfactorily until now. At low temperature, for the majority of the alkali halide crystals the stretching mode is long-lived with lifetimes close to radiative ($\tau_{rad} \simeq 50$ ms)[2] in striking contrast with CN^- in the sodium halides. Here the decay times are a few hundred microseconds, i.e. shorter by more than two orders of magnitude.

In seeking to understand this remarkable difference and explore the nature of the nonradiative decay channels we have investigated cyanide doped into the silver halides AgCl and AgBr[3]. Like alkali halides, these materials are ionic but with a considerable degree of covalent bonding. It originates from the presence of the Ag 4d-electrons which also can be expected to have a marked influence on the impurity-lattice interaction and, hence, vibrational relaxation behaviour.

2 EXPERIMENTAL RESULTS

Like in alkali halides, we observed in AgCl and AgBr vibrational luminescence around the fundamental CN^- stretchmode frequency but with relaxation times as short as in NaCl and NaBr[1,3]. Using tunable infrared laser pulses with 6 ns duration and pumping either the sideband of the fundamental ($v = 0 \rightarrow 1$) or the weak overtone-absorption ($v = 0 \rightarrow 2$) the time dependence of the $v = 1 \rightarrow 0$ and $v = 2 \rightarrow 1$ intensities was measured exploiting that the transitions are shifted relative to each other by 26 cm^{-1} due to anharmonicity. For CN^- concentrations ≤ 0.5 mol%, the decay curves were single exponential giving at 1.7 K lifetimes of 150 (370) μs for $v = 1 \rightarrow 0$ and 80 (170) μs for $v = 2 \rightarrow 1$ in AgCl (AgBr), respectively. These times differ by nearly three orders of magnitude from those found in the potassium, rubidium, and cesium halides[1] where the long times are ascribed to the fact

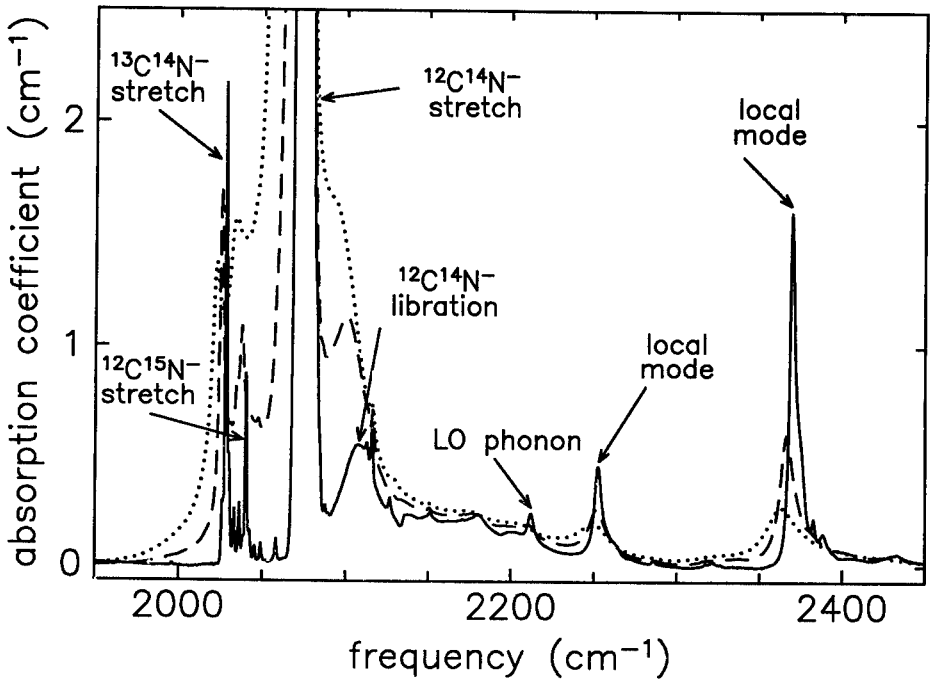

FIGURE 1 Infrared absorption of AgBr + 1 mol% AgCN (nominally) at 1.7 K (solid line), 85 K (dashed) and 150 K (dotted) showing the CN^- stretch mode and coupled sideband spectra.

that the nonradiative processes, which can be fast compared with the radiative decay, would require a large number of phonons to match the vibrational energy and thus are unlikely.

In order to explain the short times found for the silver halides and reveal the type of coupling modes we measured the vibrational sideband spectra of the main $^{12}C^{14}N^-$ line (at 2070 and 2071 cm^{-1} in AgCl and AgBr; Figure 1) employing Fourier-transform spectroscopy. Most important, besides the interaction with librational modes (at $\approx$ 40 cm^{-1}) and the lattice phonons, we discovered two unusual intense modes at 207 (182) cm^{-1} and 317 (299) cm^{-1} for CN^- in AgCl (AgBr). These modes also absorb directly in the far-infrared suggesting dipole transitions as origin. The excitation spectra of the CN^- vibrational luminescence measured by tuning the laser across each of the sidebands (Figure 2) nicely reproduce the absorption. It indicates that they are localized excitations of the cyanide, which transfer their energy into the pure stretching mode excitations. Additional support for this interpretation comes from the isotope shift of the sidebands in $^{13}C^{15}N^-$ doped AgBr (at 176 and 290 cm^{-1}) which is in agreement with the prediction by the simple oscillator model. In the silver halides, these localized modes obviously represent an efficient nonradiative decay channel for the cyanide vibration, of lower order than the phonons. Acting as accepting modes they are the reason for the reduced relaxation times that we find.

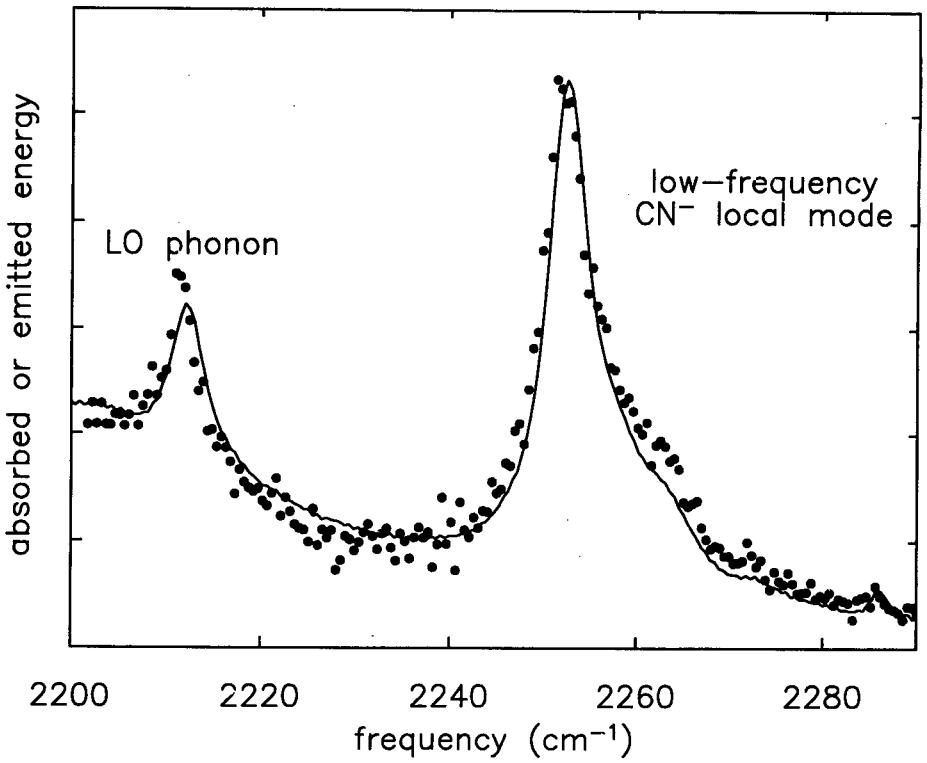

FIGURE 2 Excitation spectrum of the CN^- stretchmode luminescence at 1.7 K (points) measured across part of the CN^- sideband in Figure 1. Solid line: absorption.

3 CONCLUSIONS

Supposing that the CN^- stretchmode in the silver and alkali halides each decays into the highest-frequency (localized or lattice phonon) mode available, an energy gap law[4] can be fitted to all decay times as function of the number N of accepting modes (Figure 3). This scheme suggests the existence of cyanide local modes also for NaCl and NaBr to account for their short CN^- relaxation times, and in fact we found these modes. Physically, the local modes are caused by a sufficiently strong interatomic potential in the neighborhood of the impurity. Obviously, in the sodium halides the potential must be qualitatively different from that in the other halide crystals as reflected by the $\langle 100 \rangle$ orientation of the cyanide in NaCl and NaBr in contrast to the usual $\langle 111 \rangle$ orientation in the other fcc alkali halides. It is worthwhile noting that a $\langle 100 \rangle$ orientation has been conjectured as most likely in the silver halides, too.[5] In that case the $2\sigma_z$- and $2\pi_{xy}$-orbitals of the cyanide would strongly overlap with the d-electron wavefunctions of the surrounding host lattice silver ions presumably being the origin of the strong high energy local modes.

ACKNOWLEDGEMENT

This work is supported by NSF-DMR-9312381 and ARO-DAAL03-92-G-0369. One of us (W.v.d.O.) wishes to thank the Deutsche Forschungsgemeinschaft and the Cornell M.S.C. for financial assistance.

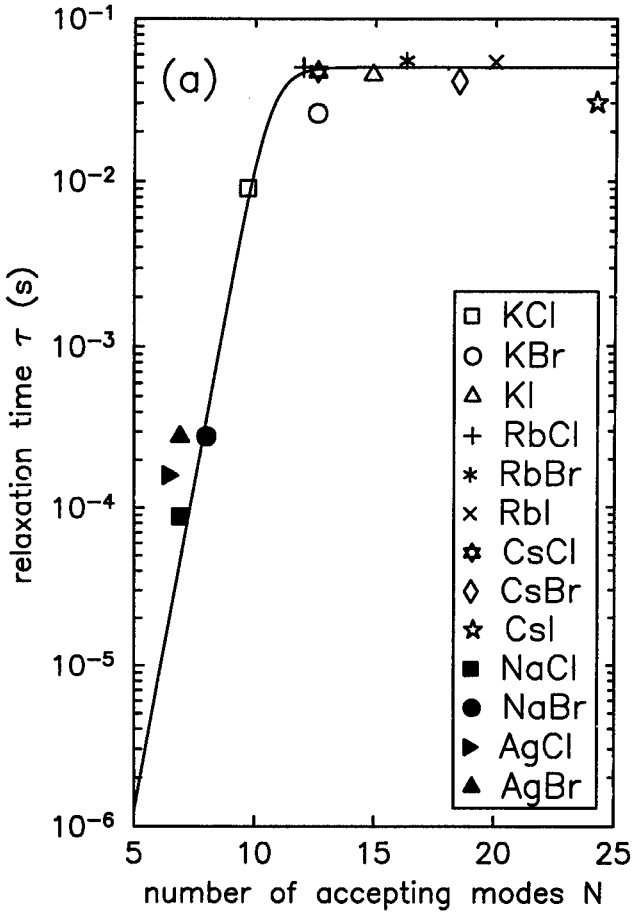

FIGURE 3 $CN^-(v = 1 \rightarrow 0)$ stretchmode relaxation times at 1.7 K vs. number of accepting modes in various host crystals as shown. The alkali halide data are taken from Ref. 1; the solid line is a fit by an energy gap law and using $\tau_{rad} = 50$ *ms* (for details see Ref. 3).

REFERENCES

1. F. Luty, *Cryst. Latt. Def. and Amorph. Mat.* **12**, 343 (1985).
2. K. P. Koch, Y. Yang, and F. Luty, *Phys. Rev.* **B29**, 5840 (1984).
3. U. Happek, C. E. Mungan, W. von der Osten and A.J. Sievers, *Phys. Rev. Lett.* **72**, 3903 (1994).
4. A. Nitzan, S. Mukamel, and J. Jortner, *J. Chem. Phys.* **63**, 200 (1975).
5. D. Samiec, Diplomarbeit, Universität Paderborn (1990).

Radiation Effects and Defects in Solids, 1995, Vol. 134, pp. 345–348
Reprints available directly from the publisher
Photocopying permitted by license only

© 1995 OPA (Overseas Publishers Association)
Amsterdam B.V. Published under license by
Gordon and Breach Science Publishers SA
Printed in Malaysia

TIME-RESOLVED PICOSECOND SPECTROSCOPY OF THE RESONANT SECONDARY RADIATION OF *F* CENTERS IN KCl

N. AKIYAMA, F. NAKAHARA and H. OHKURA

Department of Electronic Engineering, Okayama University of Science, 1–1 Ridai-cho, Okayama 700, Japan

The linear polarization (P_{HL}) of hot luminescence (**HL**) composing of the resonant secondary radiation of the *F* centers has been measured using a time-resolved picosecond spectroscopy over the whole Stokes wavenumber Ω range. The P_{HL} holds constant value of about 40% until the onset of ordinary luminescence (**OL**), from where it decreases to vanishingly small with decrease of Ω. This implies that the optically excited *F* center relaxes down along the 2p-like adiabatic potential energy surface (**APES**) trough, and transits to the 2s-like APES trough to form the relaxed excited state (RES). The lattice relaxation time and the dynamical transition time are ultra fast estimated to be less than 15 psec.

1 INTRODUCTION

De-excitation processes (**DEP**) of the optically excited *F* centers have been studied qualitatively with special interest for many years. Hizhnyakov and Tehver[1] in 1968 and Toyozawa[2] in 1976 derived general theory of DEP of optically excited state. Amongst all, the optically excited *F* center is a typical one electron system coupled strongly with phonons in condensed matters. The DEP of the *F* center is represented as the resonant secondary radiation (**RSR**) process which occurs resonants Raman scattering (**RRS**), hot luminescence (**HL**), and ordinary luminescence (**OL**) successively over the whole Stokes range as a function of Ω.

In 1982, Mori, Hattori, and Ohkura[3] firstly observed the RSR spectrum and its linear polarization P_{HL} of the *F* centers over the Stokes range, after resonant excitation. Excitation light was from a cw Ar^+ ion laser which was associated with a dye laser to vary Ω for the excitation. Most outstanding information obtained from their experimental results are (1) HL is decreased to vanishingly small value with decrease of Ω. (2) The P_{HL} holds constant value of about 40% over the wide range of Ω, but it finally reduces to zero nearly at the onset range of OL. They explained these results based on the concept of the RSR. The lattice relaxation time τ_l is estimated to be as 3×10^{-13} sec by adopting classical damping oscillator model. The quantum theory has been developed by Muramatsu and Nasu,[4] and Kayanuma.[5] From theoretical interpretation of experimental data, they estimated the same amount of τ_l mentioned above.

In 1987, Nakamura *et al.*[6] carried out a time-resolved picosecond spectroscopy measurement for the RSR of the *F* centers. They have found the same HL spectrum as in Ref. 3. One thing very different is that the P_{HL} spectrum is independent of Ω nearly by the onset of the OL band. A merit of the time-resolved method is to facilitate the resolution of HL and OL. However, for this purpose, one should choose the repetition rate (**rps**) of laser pulse to be less than the inverse of the radiative lifetime τ_r of the relaxed excited state (**RES**) of the F center (τ_r=0.67 μsec for KCl). Otherwise, the OL from the many numbers of preceding excitation could be admixed into the HL decay signal. The rps of 80 MHz adopted in Ref. 6 would not satisfy this condition. In a previous article,[7] we tried to reduce the rps to 0.38 MHz. In the present work, we finally reduced it to 253.3 kHz. With this

reduction, we could find that P_{HL} is decreased to vanishingly small value in the onset Ω range of the OL band. With this information obtained, we have proposed a refined model of de-excitation of the F centers which will be discussed later.

2 EXPERIMENTAL APPARATUS AND RESULTS

The laser light pulse used for optical excitation in the present picosecond time-resolved measurement has a width of at most 8 psec which is generated using a cavity dumped dye laser pumped with a mode-locked YAG laser (Coherent Antares 7220, 702, & 76-s). RSR signals are detected by a photon counting method with a streak camera (Hamamatsu Streak Scope C4334, with time resolution of about 15 psec). The rps of laser pulse was 253.3 kHz.

Transient shape of time-resolved RSR observed is relevant to Ω for the observation. In the Ω range from the multi-phonon RRS to 13 200 cm^{-1}, the shapes of HL and excitation laser pulse are confirmed to be exactly the same. This implies that the de-excitation occurs as a dropping down motion of excited packet in the 2p adiabatic potential energy surface (APES) trough with τ_1 which is indistinguishably fast in comparison with the laser light pulse. We estimated that it is less than 15 psec being the detection limit of our apparatus. In the Ω range below 14 000 cm^{-1} nearly at the onset range of OL, apparent rise time of RSR shows a slightly time lag from that of the excitation laser pulse. The deconvolution technique is adopted to separate HL from instantaneous line shape of RSR. Thus-separated I_{OL}, and I_{HL} are plotted in Figure 1 with dotted lines and closed inverse triangles as a function of Ω.

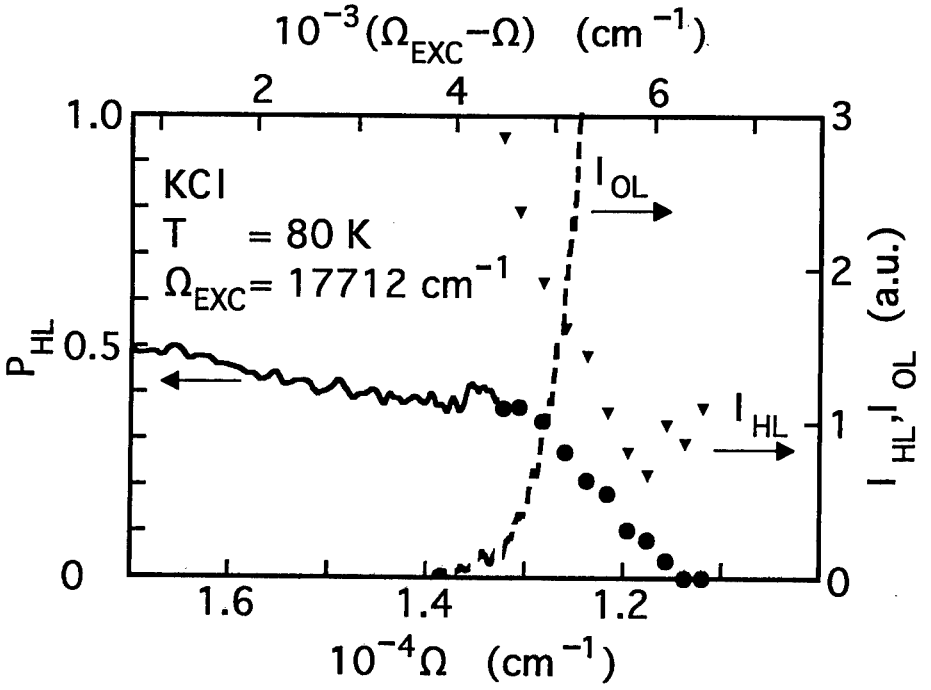

FIGURE 1 Summary of results by means of a time-resolved picosecond spectroscopy of the F centers in KCl at 80 K. The P_{HL} is plotted with solid lines (closed circulars are for the P_{HL} in the OL range). I_{HL} and I_{OL} are with closed inverse triangles and dotted lines versus Ω.

Then, the P_{HL} are calculated in this low Ω range: They are plotted with closed circles in Figure 1. The P_{HL} spectrum is clearly decreased to vanishingly small value in the OL range with decrease of Ω. On the contrary, P_{HL} calculated at the range above 13 200 cm^{-1} is plotted with solid lines in Figure 1, which shows nearly constant value of about 40%. The decrease of P_{HL} in the OL range is the first observation with using the picosecond spectroscopy.

It is also confirmed that the delay time of onset of OL is estimated to be less than the detection limit of 15 psec. This time may correspond to dynamical transition time from the 2p APES trough to the 2s APES trough by way of Landau-Zener mechanism.[8] Thus-transferred electron would be thermalized in the 2s APES to form the RES to emit OL, thereafter ceasing the optical cycle of the *F* center.

3 CONCLUSION

With the information obtained from the present work, we may propose a de-excitation mechanism of the optically excited *F* centers with references to Figure 2 in which the APES are plotted as a function of interaction coordinates Q. De-excitation occurs along the 2p-like APES trough immediately after the resonant excitation. When it reached nearly at

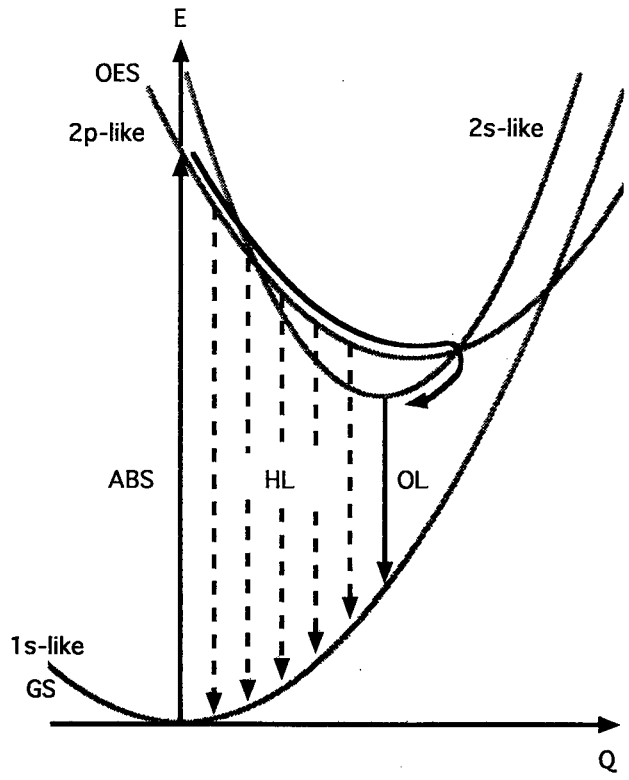

FIGURE 2. APES for the ground (GS) and optically excited states (OES) of the F center are plotted as a function of the interaction coordinates Q. Optical pumping process (absorption, de-excitation path, and OL) are shown with solid lines. HL is shown with broken lines.

the bottom of the 2p APES trough, it could undergo the dynamical transition to the 2s APES trough. The lattice relaxation time and the dynamical transition time to the 2s-like APES trough are ultra short of less than 15 psec which is less than the limit of our apparatus.

Finally, we should mention the electronic structure of the Franck-Condon state (**FCS**) that had been determined by Grassano *et al.*[9] from the Stark effect of the FCS. They concluded that the 2s-like state lies slightly above 2p-like state in the FCS. Thus, one may expect that the level crossing of the 2s and 2p APES troughs could occur during the lattice relaxation. However, the present results would not show such an evidence. This implies that, in the first stage of de-excitation, the speed of excited phonon packet is so high that it would relax non-adiabatically without suffering from the presence of the 2s APES trough.

ACKNOWLEDGEMENT

We are much obliged to Professor Y. Kayanuma, Tohoku University, and Professor S. Muramatsu, Utsunomiya University, for their heartful cooperation to proceed this problem.

REFERENCES

1. V. Hizhnyakov and I. Tehver, *Phys. Status. Solidi* **21**, 673 (1967).
2. Y. Toyozawa, *J. Phys. Soc. Jpn.* **41**, 400 (1976).
3. Y. Mori, R. Hattori, and H. Ohkura, *J. Phys. Soc. Jpn.* **51**, 2713 (1982).
4. S. Muramatsu and K. Nasu, *J. Phys.* **C18**, *3729 (1985)*.
5. Y. Kayanuma, *J. Phys. Soc. Jpn.* **57**, 292 (1988).
6. A. Nakamura, T. Sano, Y. Kondo, and M. Hirai, *J. Phys. Soc. Jpn.* **56**, 1603 (1987).
7. N. Akiyama and H. Ohkura, *J. Lumin.* **60 & 61**, 713 (1994).
8. Y. Kayanuma, *J. Phys. Soc. Jpn.* **53**, 108 (1984).
9. U. M. Grassano, G. Margaritondo, and R. Rosei: *Phys. Rev.* **2B**, 3319 (1970).

Radiation Effects and Defects in Solids, 1995, Vol. 134, pp. 349–352
Reprints available directly from the publisher
Photocopying permitted by license only

© 1995 OPA (Overseas Publishers Association)
Amsterdam B.V. Published under license by
Gordon and Breach Science Publishers SA
Printed in Malaysia

FOUR-WAVE PHASE CONJUGATION WITH F_3^+ COLOR CENTERS IN LiF

T. TSUBOI* and H. E. GU**

**Faculty of Engineering, Kyoto Sangyo University, Kyoto 603, Japan; **Physics Department, Tianjin University, Tianjin 30072, China*

F_3^+ color centers in LiF crystals have been demonstrated to generate a phase-conjugate 460 nm wave. It is shown that the generation is caused by the saturation of optical absorption due to the non-radiative electron transitions between the singlet and metastable triplet levels in F_3^+ centers.

Key words: phase conjugation, F_3^+ color centers.

Color centers in alkali halide crystals have attracted growing interest because of important applications to tunable solid-state lasers, Q switching of Nd:YAG lasers, and optical phase conjugation. Optical phase conjugation is a technique for reversing both the direction of propagation and the phase of an incoming light wave. Generation of the phase conjugate wave by color centers has been demonstrated using the F_2, F_2^+ and F_2^- centers in LiF crystals.[1–3] In the present paper, we show the phase conjugation with F_3^+ color centers in LiF and explain why F_3^+ can generate the phase conjugate wave.

When an LiF crystal was irradiated with Co^{60}-rays at room temperature (RT), F, F_2, F_3^+ and F_3 color centers were mostly created. After the crystal was cooled to 77 K and illuminated by a N_2 laser beam, they were converted to F^+, F_2^+ and F_3^+, respectively. When this crystal was warmed to RT again, the F^+ centers became mobile in the lattice to form F_3^+ by combining with F_2, while the F_2^+ centers form F_3^+ by combining with F. In this way we obtained a colored LiF crystal containing rich F_3^+ centers of $2 \times 10^{17}/cm^3$.

The observation of the phase conjugate wave was made by the degenerate four-wave mixing method using an experimental setup shown in Figure 1. As a pump source we used pulsed 460 nm light emitted from a coumarin-460 dye laser. The angle between the forward pump light (E_1) and the probe light (E_p) was 3.4°. The phase conjugate wave E_c was incident on a 50% beam-splitter M_5. The generation of a phase conjugate wave was confirmed as follows. Firstly, the spot size of the E_c beam which entered the photo-detector D was the same size as the probe light beam. Secondly, when the forward pump beam was cut off, no signal was detected. This indicates the spot is the phase conjugate wave.

The observed phase conjugation reflectivity R is plotted in Figure 2 against the power of the probe beam. The reflectivity has a maximum of 0.1% at the probe beam power of approximately 1.5 mJ. This value corresponds to a power density of 0.86 MW/cm^2 since we used a 460 nm laser beam with a radius of 0.37 cm and with a pulse width of 4 ns as the probe beam.

The F_3^+ center consists of three adjacent negative-ion vacancies forming an equilateral triangle in a (111) plane with two trapped electrons in cubic alkali halide crystals.[4] The F_3^+ centers in LiF produce an emission band with a peak at 528 nm by excitation in the 458 nm absorption band.[5] The ground state of the F_3^+ center is $^1A_1$ and the low-lying excited states are $^3E_1$, ^1E, and $^3A_2$ in order of increasing energy.[6] The 458 nm absorption band is caused by the $^1A_1 \rightarrow {}^1E$ dipole transition.

The electrons excited to the ^1E level are relaxed to the relaxed excited state $^1E^*$ nonradiatively. Then the electrons make a transition to the non-relaxed ground state $^1A_1{}^*$

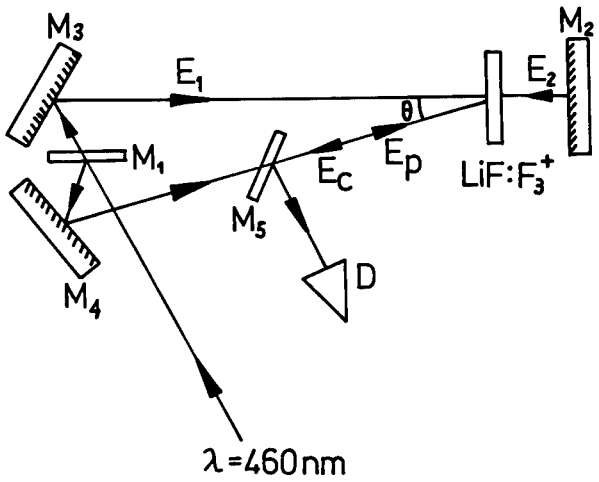

FIGURE 1 Optical arrangement for the phase conjugation experiment with an LiF:F_3^+ crystal. E_1: forward pump beam, E_2: backward pump beam, E_p: probe beam, E_c: phase conjugate beam, M_1, M_5: beam splitter, D: photo-detector, M_2, M_3, M_4: mirror.

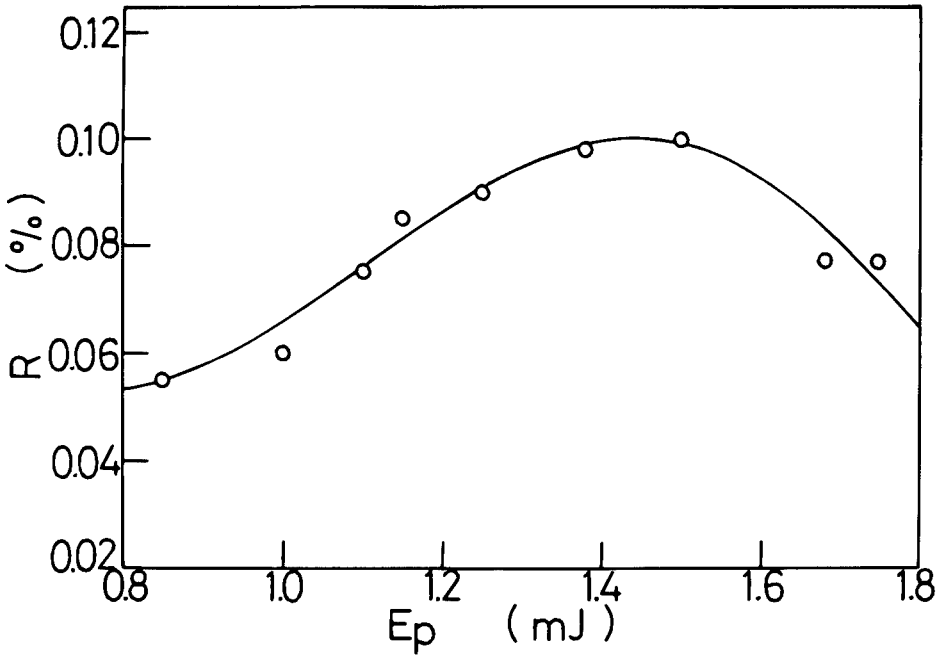

FIGURE 2 Reflectivity (R) of the phase conjugate wave plotted against the power (E_p) of the probe beam.

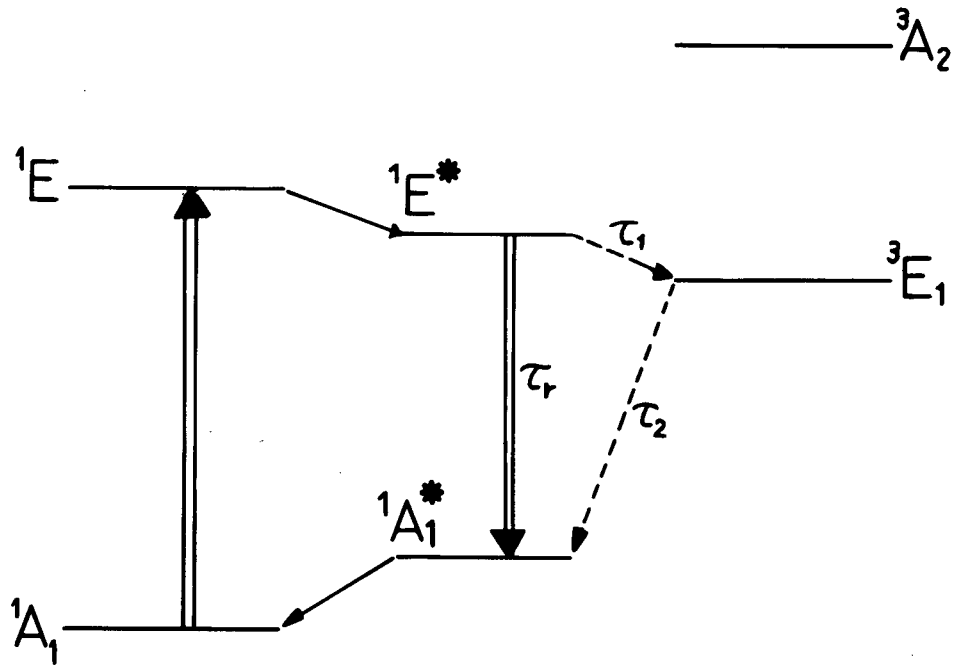

FIGURE 3 Energy level diagram (schematic) of F_3^+ center and the optical cycle of absorption and luminescence.

giving rise to the 528 nm emission, while some electrons in the $^1E^*$ level are moved to the nearby $^3E_1$ level nonradiatively (Figure 3). The characteristic time of radiationless transition (RT) from the $^1E_1^*$ to $^3E_1$ level is $\tau = 0.5$ s (see Figure 3),[7] while the characteristic time of RT from the $^3E_1$to $^1A_1^*$ level is $\tau_2 = 5$ s.[7] Such a long RT characteristic time creates a population inversion between the $^3E_1$ and $^1A_1$ levels with increasing the pump power, resulting in the saturation of the absorption.

A saturated absorption was certainly observed for the F_3^+ centers: the saturation power density was about 1 MW/cm^2. This value is close to the saturation value for the reflectivity R. Therefore it is suggested that the phase conjugation is caused by the nonlinear saturation of absorption in LiF:F_3^+. This suggestion is confirmed to be reasonable as follows.

The F_3^+ centers in LiF crystal have been used as a green roomemperature-stable color center laser.[8] For the stable lasing, the colored LiF crystal was pumped by a pulsed coumarin-460 dye laser with a low repetition rate of 1.2 Hz.[8] Unlike the case of lasing, in phase conjugation we used the dye laser with a repetition rate of 10 Hz. Such a high repetition rate induces a saturated absorption in the F_3^+ centers since a high population in the $^3E_1$ level is achieved by the slow relaxation time from the metastable $^3E_1$ level into the $^1A_1^*$ level. This gives rise to optically induced refractive-index gratings in LiF:F_3^+ crystal by the interference of the forward and probe beams. As a result, the phase conjugate wave is generated by a diffraction of the backward beam at the grating.

In conclusion, we observed a generation of 460 nm phase-conjugate wave using LiF:F_3^+ crystals and we confirmed the generation is caused by the saturation of F_3^+ absorption due to the long singlet-triplet radiationless transition time.

REFERENCES

1. T. T. Basiev, Yu. K. Voron'ko, P. G. Zverev, S. B. Mirov and A. M. Prokhorov, *Sov. Tech. Phys. Lett.* **8**, 658 (1983).
2. S. C. Rand, *J. Physique Coll. C7, Suppl.* **10**, 46, 507 (1985).
3. T. Zhang, L. F. Wan and Y. F. Ruan, *Chinese Phys. Lett.* **2**, 369 (1985).
4. R. M. Macfarlane, A. Z. Genack and R. G. Brewer, *Phys. Rev.* **B17**, 2821 (1978).
5. J. Nahum and D. A. Wiegand, *Phys. Rev.* **154**, 817 (1967); J. Nahum, *Phys. Rev.* **158**, 814 (1967).
6. L. F. Stiles and B. D. Fitchen, *Phys. Rev. Lett.* **17**, 689 (1966).
7. S. Paciornik, R. A. Nunes, J. P. von der Weld, L. C. Scavarda do Carmot and V. S. Kalinov, *J. Phys. D: Appl. Phys.* **24**, 1811 (1991).
8. T. Tsuboi and H. E. Gu, *Appl. Optics* **33**, *982 (1994)*.

Radiation Effects and Defects in Solids, 1995, Vol. 134, pp. 353–356
Reprints available directly from the publisher
Photocopying permitted by license only

© 1995 OPA (Overseas Publishers Association)
Amsterdam B.V. Published under license by
Gordon and Breach Science Publishers S.A
Printed in Malaysia

CU^+ AND OH^- PAIRS DEFECTS INTERACTION IN NaF CRYSTALS

J. L. FABRIS, M. MÜLLER, A. C. HERNANDES, M. SIU-LI and S. KAPPHAN*

*Instituto de Física de São Carlos — USP, São Carlos — SP, Brazil; *FB Physik, Universität Osnabrück, 49069 Osnabrück, Germany*

The presence of Cu^+ in OH^- doped NaF crystal results in several new infrared absorption bands with ~ 0.2 cm^- halfwidth at 100 K, and their relative intensities are strongly impurity concentration dependent. Their assignments are not evident and are mostly attributed to different vibrational internal modes of the molecular OH^- perturbed by neighboring Cu^+ ions.[1] We report the results of the temperature dependence of several OH^- sidebands around the 3737.8 cm^{-1} 'free' OH^- stretching mode. The temperature dependence reveals a different behaviour from already known OH^- quasi free rotor in several cesium halides.[2] For the temperature range from 100 to 300 K, the free OH^- halfwidth shows a T^2 behaviour. While for three chosen absorption sidebands are determined to be $T^{1.6}$, $T^{1.8}$ and $T^{2.5}$. The lack of observable thermally stimulated depolarization current and electric field induced dichroism[3] indicates that the OH^- is frozen-in, so it is also the same with the OH^-–Cu^+ pairs.

Key words: Alkali halides. NaF. OH^-/Cu^+ impurities.

It is well known that molecular OH^- ions and positive divalent metal (Me^{2+}), can interact in alkali halides and fluorides[4] host crystals. These interaction results from an OH^-/Me^{2+} defect formation, where a charge compensating cation vacancy is required to reach a local charge compensation. The formations of these defects change the stretching vibrational mode absorption band of the OH^- ions, resulting in new infrared sidebands as well as altered shapes of the stretching vibration band.

We have reported recently the existence of an interaction effect between Cu^+ ions and OH^- molecular ions in NaF single crystals, where charge compensating vacancies' effects are not necessary. From the interaction results a more complex infrared line spectrum around 3700 cm^{-1} shifted to the low energy side to the 'free' OH^- stretching mode[1]. It was also observed some changes in the ultraviolet Cu^+ electronic transition as compared with 'free' Cu^+ ions in the same host.[1]

Two different types of NaF:Cu^+:OH^- samples were used, one where the Cu^+ was diffused after the crystal was grown, and the other where the Cu^+ is introduced during the melt of the crystal growth.

A color center laser spectrophotometer (CCLS) was used to obtain the infrared absorption spectra. The resolution of the CCLS was 0.186 cm^{-1} for the interval range of 3520 to 3900 cm^{-1}.

The coupling effect between Cu^+ ions and molecular OH^- ions in the studied NaF crystals, produce a set of 15 new absorption lines,[1] assigned form A to O. These lines, among 3560 to 3710 cm^{-1}, are shifted to the low energy side of the free OH^- 3737.8 cm^{-1} absorption in NaF at 100 K. This energy shift is due to the change in the anharmonic parameter of the OH^- well potential due to its interaction with a neighboring Cu^+ ion.

To unveil the degree of doping homogeneity between both samples, we scanned the absorption intensity of selected new lines at different depths of the sample. This is shown in the inset of Figure 1, with a length L of 3.5 mm. Figure 1(a) shows the plot of several scans for the selected 'K', 'M' and 'O' lines, which are respectively at 3600.2, 3592.8 and 3572.0 cm^{-1}. As it is observed the absorption intensity, for each of the lines, changes with the depth of the sample, that indicates an inhomogeneous distribution of the impurities. The same experimental measurement setup was used to analyze the second type of

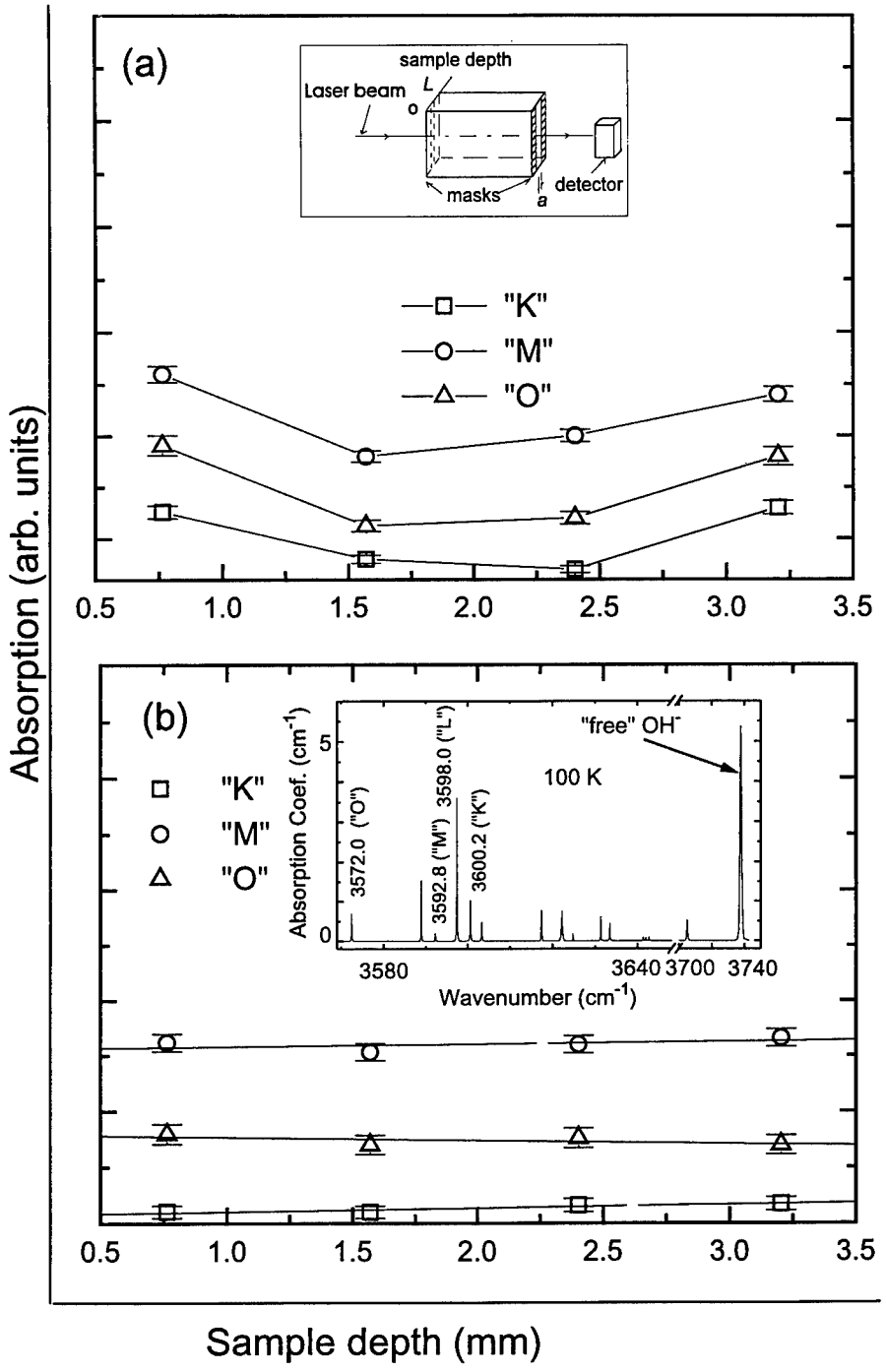

FIGURE 1 Absorption strength distribution from lines 'K', 'M' and 'O' at different depths of the sample. (a) For thermally diffused Cu^+ doped sample. (b) For copper doped in the melt during the crystal growth. The insets show the sample setup for OH^-/Cu^+ depth profile and the infrared absorption measurement at 100 K.

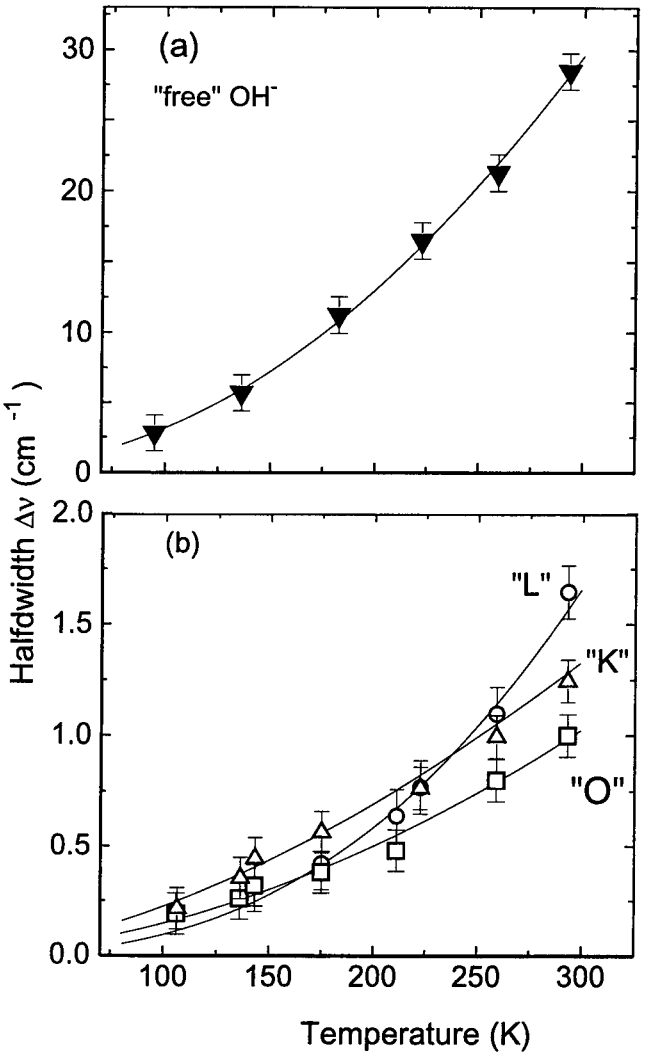

FIGURE 2 Halfwidth temperature dependence of more intense absorption bands in $NaF:Cu^+:OH^-$: (a) Free OH^- at 3737.8 cm^{-1}. (b) 'O' line at 3572.0 cm^{-1}. 'K' line at 3600.2 cm^{-1}. 'L' line at 3598.0 cm^{-1}.

samples. The results for the distribution of impurities are shown in figure 1(b), where it is also shown the IR absorption measurement. In this case a rather good distribution homogeneity throughout the depth of the sample is observed. In spite of the different concentration profile for the two samples, the new set of spectral lines is the same.

It is likely well known that the OH^- molecule behaves as a quasi free rotor in several studied cesium halides,[5] and this mechanism would provides a $\Delta\nu \approx T^{1/2}$. For $kT \ll V_0$ case, the molecules realize oscillatory movements, and the vibrational spectra consist of an intense Q branch. The reorientation between the equivalent oriented direction is limited to tunnelling processes.[5] The molecular OH^- impurity absorption linewidth shows temperature dependence and different functional behaviour, and it depends on whether

it is in a free or coupled state with Cu^+. Figure 2 shows several plots of these behaviors in the NaF crystal. Figure 2(a) is for the free OH^-, and Figure 2(b) the lines 'O', 'K' and 'L' are from the coupled OH^-–Cu^+ pair.

For the case of single OH^- doped NaF crystal, the absorption linewidth of the stretching mode at 3737.8 cm^{-1} shows a T^2 temperature dependence in the 90 to 300 K range. This indicates the behaviour can not be compared with a $T^{1/2}$ quasi free rotor case. The strong change to T^2 behaviour indicates that the molecule is more hindered to rotate, allowing to induce that the molecule is suffering a more permanent alignment in the lattice. To verify the non existence of classical reorientation process for the OH^- in $NaF:Cu^+:OH^-$, the samples were submitted to thermally stimulated depolarization current (TSDC) experiments. Effectively no depolarization current was detected. Since the TSDC technique works only for classical dipole system, there are two possibilities for the OH^- behaviour, as it would be for the free as also for the coupled case:

- Permanent oriented frozen-in OH^- dipole due to high potential barrier between the multiequivalent oriented directions.
- The existence of reorientation processes by tunnelling between the multiequivalent oriented directions.

Moreover, earlier results of electric field induced dichroism studies[6] in $NaF:OH^-$ revealed no observable effect, even using electric fields as high as 10^5 V/cm. That means that a tunnelling process would be unlikely to occur, which together with our TSDC results it can be concluded the OH^- is permanently frozen-in.

ACKNOWLEDGMENTS

We acknowledge Mr. J. Frigo for growing some of the crystals and Mr. E. Cardoso for preparing the thermal diffusion cell. The present work received the support from DFG/SFB 225 (Germany) and from several Brazilian agencies: Fapesp, Finep, CNPq and Capes.

REFERENCES

1. J. L. Fabris, M. Müller, A. C. Hernandes and M. Siu-Li. *Rad. Eff. and Def. Sol.* (accepted).
2. M. Krantz and F. Lüty, *Phys. Rev.* **B37**, 7038 (1988).
3. S. Kapphan, J. Koppitz, *Int. Conf. on Def. in Insul. Crystals* (Gattlinburg, USA) 228, (1977).
4. R. Capelleti, E. Colombi, R. Fieschi, A. Gainotti, *Rad. Eff. and Def. Sol.* **119–121**, 319 (1991).
5. M. Krantz, F. Lüty, *Phys. Rev.* **B37**, 7038 (1988).
6. S. Kapphan, J. Koppitz, *Proc. of the Int. Conf. on Def. in Insul. Cryst.* (Gattlingburg, USA) 228 (1977).

Radiation Effects and Defects in Solids, 1995, Vol. 134, pp. 357–360
Reprints available directly from the publisher
Photocopying permitted by license only

© 1995 OPA (Overseas Publishers Association)
Amsterdam B.V. Publihsed under license by
Gordon and Breach Science Publishers S.A
Printed in Malaysia.

CU^+ HIGH DOPING EFFECTS IN KCl AND KBr FILMS

L. OLIVEIRA, *C. M. G. S. CRUZ, M. A. P. SILVA AND M. SIU-LI

Instituto de Física de São Carlos—USP, P.O.Box 369, 13560, São Carlos – S.P., Brazil.

Highly Cu^+ doped KCl and KBr polycrystalline films were investigated in the range of 10^{20}–10^{21} cm^{-3} Cu^+ concentration. Several techniques were used to obtain the optical and structural properties, as optical absorption and transmittance, electronic microscopy (SEM), X-ray diffraction and ellipsometry. The Cu^+ off-center effect is still present in the films, as determined by optical and thermally stimulated depolarization current measurements (TSDC). The films were obtained by thermal evaporation, and the corresponding doping Cu-halide is introduced in the same evaporating crucible. Samples with diverse concentrations, ranging from nominal 1 to 10% mole, were prepared. The increase of Cu^+ concentration results in an improved cyrstallynity of the grains, with higher density and a better transmittance of the film above 350 nm. Optical application as UV filter device can be considered.

Key words: Alkali halides, polycrystalline films, optical properties, impurities.

Several reported works on Cu^+, as an impurity in alkali halides, have concluded that it can be found sitting in either an on-center or off-center position.[1] Independent of such an on- or off-center substitutional position, the Cu^+ ion shows an UV absorption band, due to its $3d^{10}$–$3d^9 4s$ transition. This transition becomes possible in both situations by lattice dynamic effect (on-center) or by static effect (off-center). The present work reports strong differences observed between single crystal samples, grown by the Kyropoulos-Czochralski method, and polycrystalline film samples. For the same nominal doping concentration, for example 1%CuCl mole, it is found different concentrations in both kinds of samples: 10^{18} cm^{-3} in the single crystal and 10^{21} cm^{-3} in the film. This fact yields to different optical properties. So, a more detailed investigation of the films has been done through electron microscopy (SEM), X-ray diffraction, optical absorption and transmittance, ellipsometry and TSDC.

The samples were produced by thermal evaporation process of KCl(Br) and x%CuCl(Br) mole ($1 < x < 10$), on diverse room temperature substrates: sapphire, quartz and copper foil. The morphologic observations are substrate type independent. It was used a pressure of 10^{-6} torr in the evaporating chamber, and under this pressure an estimated growing rate of 9 nm/s (13 nm/s) for KCl(KBr) films were used.

In Figure 1 it is shown the obtained SEM images, together with their respective X-ray diffractions and optical transmittance measurements for KCl:Cu^+ polycrystalline films, for 1, 5 and 10%CuCl mole doping. As the doping concentration is increased it is observed a distinguished increase in grain density. Similarly, the X-ray diffraction measurements reveal the grains prefer to grow along the ⟨100⟩ direction. The X-ray diffractions also show a decreasing behavior of the linewidths. Comparison between obtained X-ray diffraction results in KBr and KBr:Cu^+ polycrystalline films reveal a 30% narrower linewidth for KBr:Cu^+. Both X-ray diffraction results suggest that the Cu^+ is an active element for improving the crystallynity of the grains. The obtained lattice parameter was 6.295 Å for

*On leave from Centro Federal de Educação Tecnológica de Paraná, Brazil.

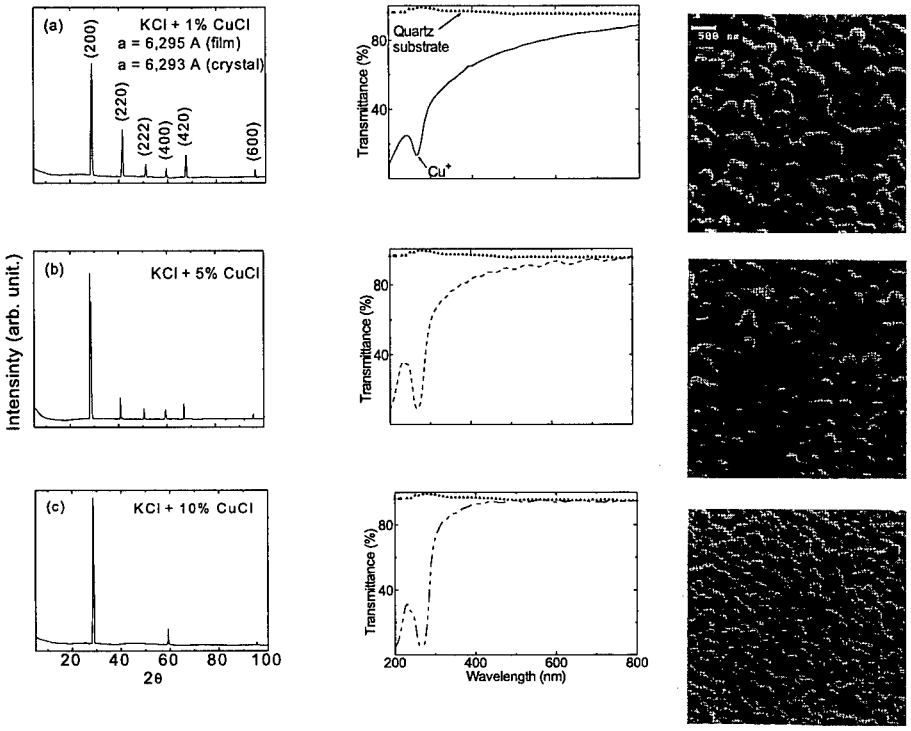

FIGURE 1 SEM images, X-ray diffraction and optical transmittance measurements observed in KCl:Cu^+ films at different nominal concentrations of 1, 5 and 10% CuCl mole.

KCl:Cu^+ and 6.601 Å for KBr:Cu^+, these values are close to the one found in usual crystallographic references. It is observed from the respective optical transmittance spectra, shown in the same Figure 1, that there is an improvement in the transmittance above 350 nm. The band observed at 266 nm (278 nm) for KCl(KBr) is attributed to the Cu^+ impurity, that remains in the same position in spite of increasing the doping concentration, but the width at half height also decrease. These observations are completely different from the one observed with single crystal samples. It was found, for instance, a 10^3 time larger absorption coefficient in the film than in the single crystal for the case of a nominal 1%CuCl doping. Usually for the same nominal concentration in single crystals, it is found a $10^{18}\,cm^{-3}$ concentration, with a broad halfwidth of 48 nm at 274 nm, as shown in Figure 2(a). After a thermal treatment at 600°C for 5 minutes and quenched to room temperature, the absorption band appears narrower with 35 nm

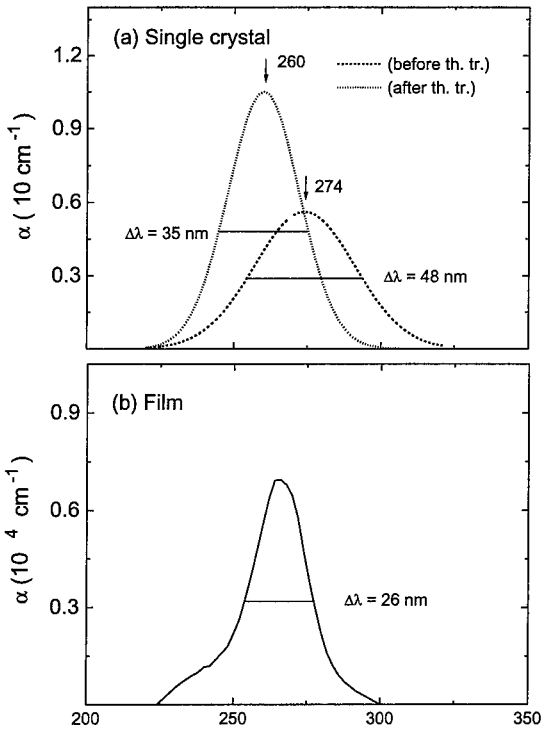

FIGURE 2 (a) Optical absorption measurement of KCl + 1%CuCl single crystal (– – –) before thermal annealing and (- - - - -) after thermal annealing at 600° C for 5 minutes and quenched to room temperature. (b) Room temperature optical absorption measurement of KCl + 1% CuCl polycrystalline film.

bandwidth and shifted to 260 nm. This suggests also the existence of agglomerates that can be diluted after a thermal treatment. The results obtained for the film samples show a narrower bandwidth of 26 nm and a much larger absorption constant, as can be observed from Figure 2(b). This result also confirms that the degree of crystallynity is better in the film grains.

Since the Cu^+ was determined to be in a substitutional off-center position in single crystals, we tried to look for the same profile in the films. The integrated absorption band was determined to be temperature independent, which is a fact for the off-center behavior. We also determined the Cu^+ oscillator strength by using the Smakula's formula and the concentration obtained by EDX, yielding a value of 0.034, which is very close to the value observed in single crystal. The TSDC measurements show the existence of an electric dipole system on behalf of the Cu^+ off-center effect. This is shown in Figure 3, where we can observe a typical TSDC scan of KCl + 1%CuCl film of 3 μm thickness. The peak position is at 49 K, obtained with a heating rate of 0.052 K/s. Three different fitting models were used, and the best one was obtained with the distribution function of Havriliak-Negami. A mean activation energy of 147 meV and a time constant of 2×10^{-14}s were obtained.

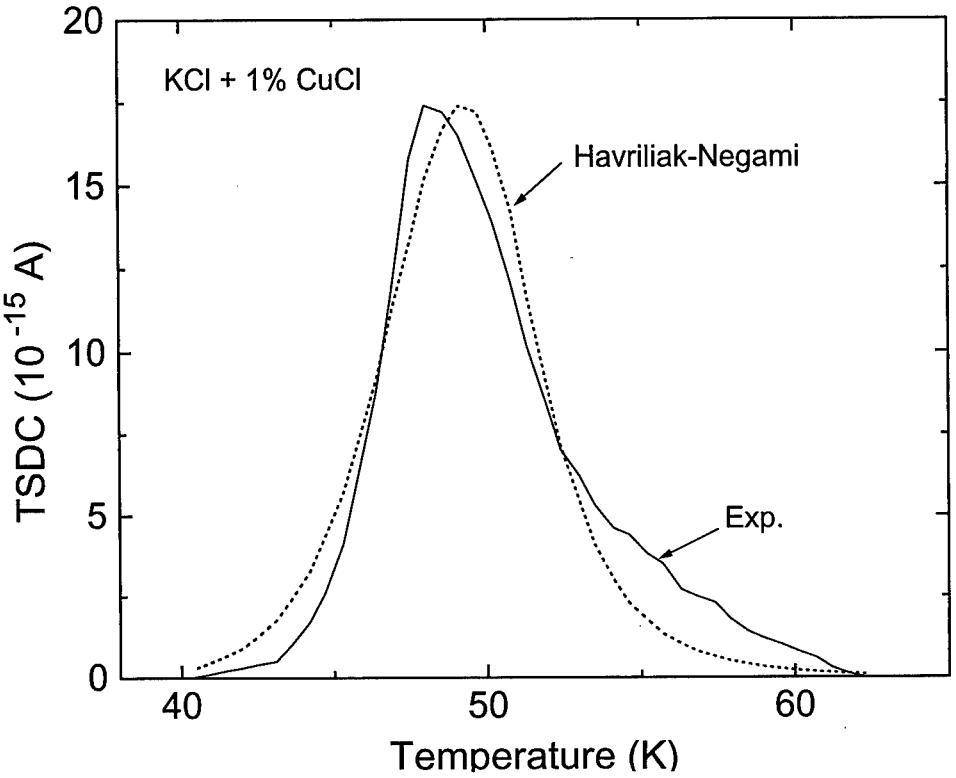

FIGURE 3 TSDC measurement of KCl + 1%CuCl film, the solid curve represents the experimental result, and the dashed curve is the fitted curve obtained through the Havriliak-Negami distribution model.

ACKNOWLEDGEMENT

We acknowledge Prof. M. Aegerter for the SEM and EDX results and several Brazilian agencies: Fapesp, Finep, CNPq and Capes.

REFERENCES

1. D. S. McClure and S. C. Weaver, *J. Phys. Chem. Solids* **52**, 709 (1991).

Radiation Effects and Defects in Solids, 1995, Vol. 134, pp. 361–366
Reprints available directly from the publisher
Photocopying permitted by license only

© 1995 OPA (Overseas Publishers Association)
Amsterdam B.V. Published under license by
Gordon and Breach Science Publishers SA
Printed in Malaysia

RADIATION INDUCED COLOUR CENTRES IN CERIUM FLUORIDE

E. APOSTOL, I. DAFINEI, GH. MITROAICA, T. TANASE and V. TOPA

I.F.T.M. I.F.A. Bucuresti Romania; E. AUFFRAY, P. LECOQ CERN Geneve, Switzerland; M. SCHNEEGANS LAPP Annecy, France

Radiation induced colour centres in CeF_3 crystals have been studied by spectroscopic techniques using eight crystals produced with various degrees of purity by different manufacturers in slightly different growing conditions. The crystals were irradiated at liquid nitrogen temperature with electrons of 7 MeV at doses of 10^4 to $3 \cdot 10^6$ rad. Absorption spectra ranging between 250 and 750 nm recorded at irradiation temperature are quite different from one producer to another, regarding both the values of absorption coefficient ($17\ cm^{-1} - 5\ cm^{-1}$) and the number and form of the absorption bands. Step-by-step annealing up to room temperature produces new absorption bands. In the range of 200–240 K, three well resolved bands appear as in the case of crystals irradiated at room temperature.

Key words: CeF_3, radiation damage, colour centres, annealing.

1 INTRODUCTION

As was shown by the Crystal Clear Collaboration at CERN, the irradiation of CeF_3 crystals with γ-rays at room temperature induced the formation of colour centres in which the fluorine vacancies can play an important role.[1–3] It has been found that there are (even in the same, long crystal of CeF_3 at both ends) two kinds of colour centres illustrated by two different absorption spectra. The majority of the crystals have shown three bands peaking at 340, 380, and 450 nm, while others exhibited only two bands peaking at 320 and 500 nm. It is also very important to investigate colour centres induced by irradiation at low temperature as was recently made by Halliburton and Edwards[4] because such centres created at low temperature can give important information also about the defects induced by irradiation at room temperature.

In this paper we report some selected results of our studies concerning the formation, stability and conversion of colour centres. The crystals were irradiated by electron beam at 85 K and annealed at higher temperature afterwards. The aims of this paper are:

- to obtain a higher concentration of colour centres than at room temperature irradiation;
- to compare different crystals (undoped and doped), supplied by four producers (OPTOVAC, KARL KORTH, PRECIOSA- TURNOV, CRISMATEC), from the point of view of radiation damage;
- to study the formation of colour centres versus radiation dose;
- to study using the step-by-step annealing, the kinetics of destruction, formation and conversion of the colour centres produced at low temperature;

2 EXPERIMENTAL

All samples were irradiated with a 7 MeV electron beam at the Linear Accelerator Facility of the Institute of Atomic Physics in Bucharest at dose rates ranging from $0.1 \cdot 10^3$ to $1.6 \cdot 10^3$ rad/sec, at 85 K.

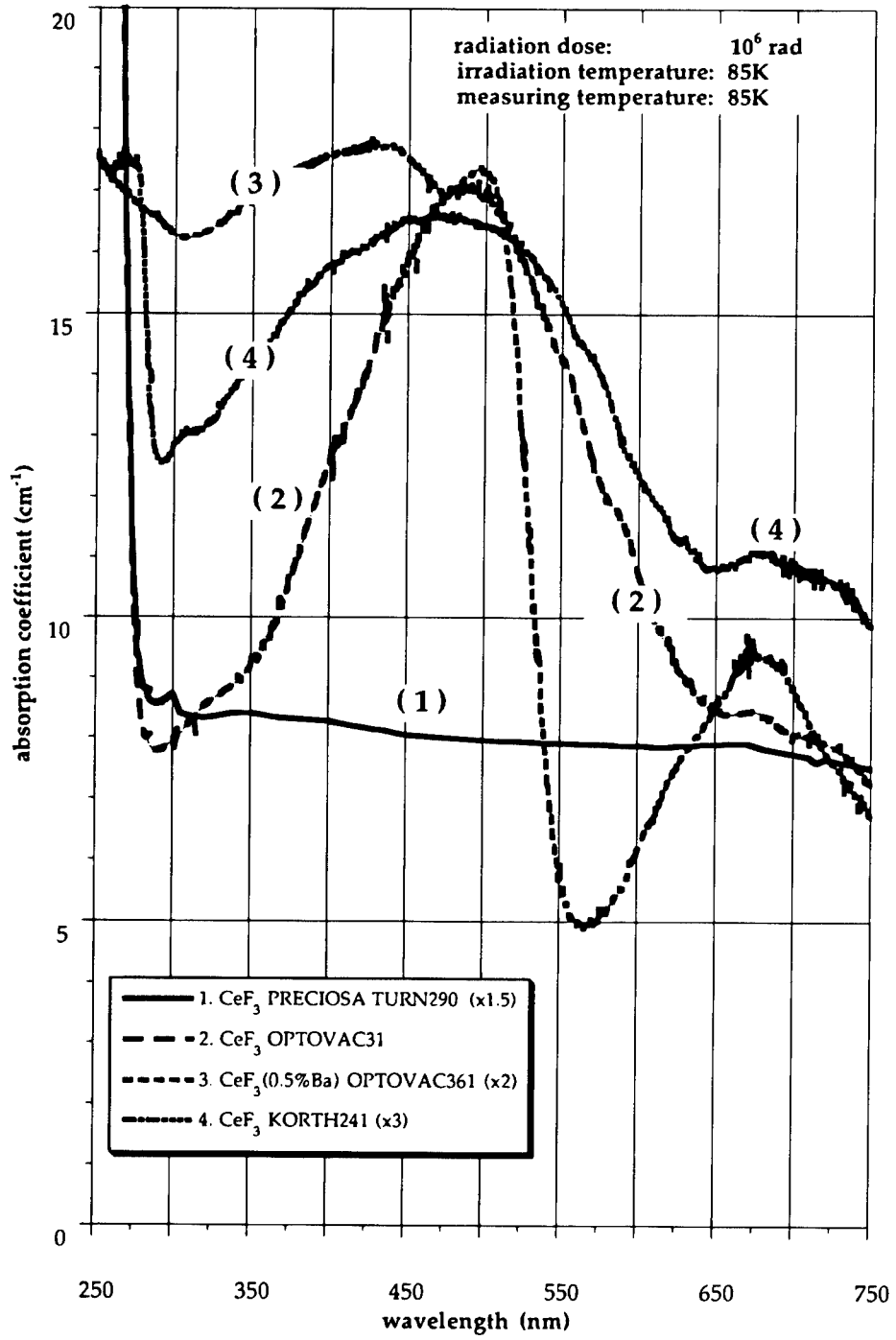

FIGURE 1 Optical absorption spectra of electron irradiated CeF_3 crystals from four producers.

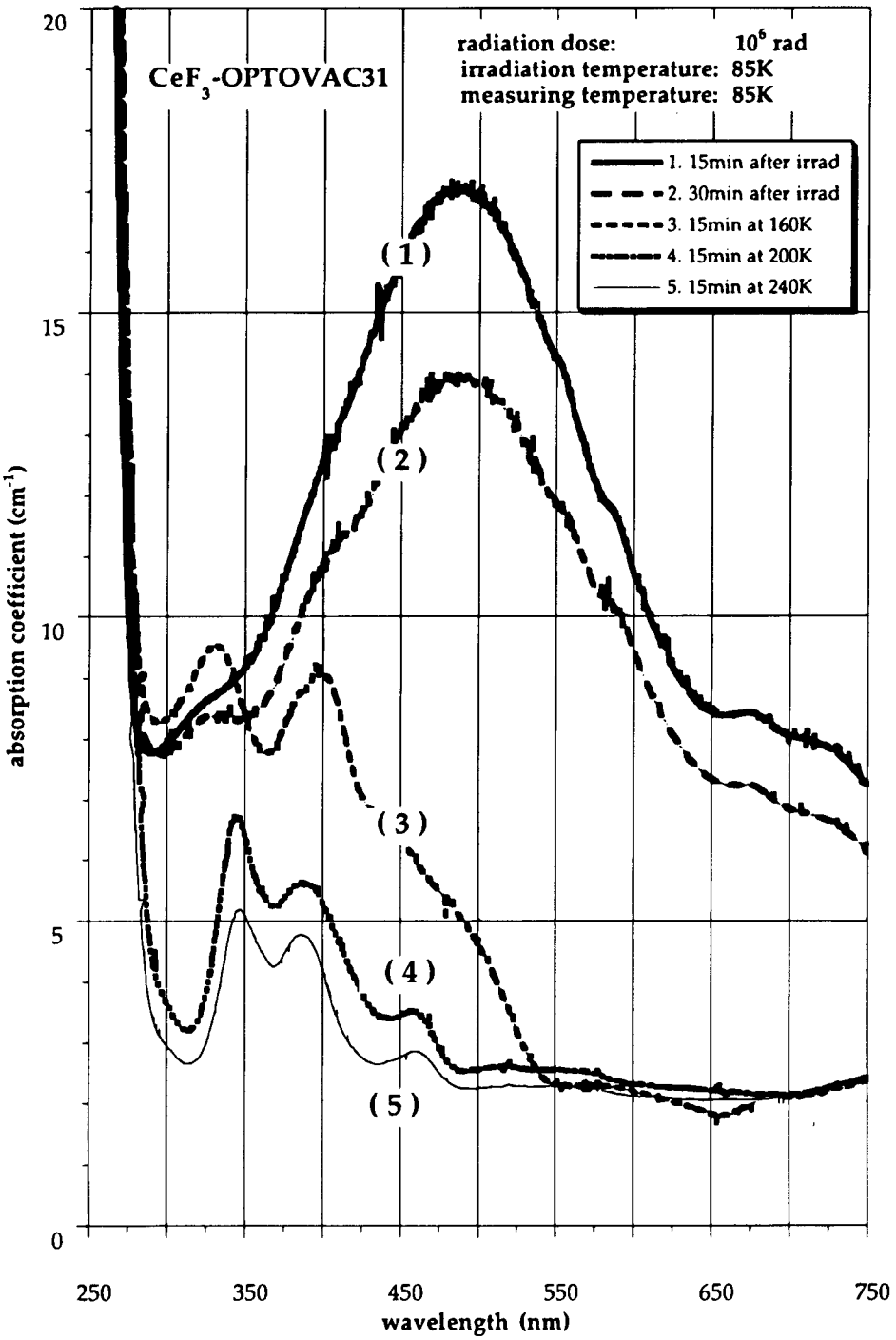

FIGURE 2 Optical absorption spectra of electron irradiated CeF_3 crystal submited to thermal annealing.

The sample was fixed on a cooled finger of a metallic cryostat with four CaF_2 windows, two of them used for electron irradiation and another two for absorption spectra measurements. These spectra have been recorded with a Carry 17D spectrophotometer linked with a PC computer where the data were stored and analyzed. The samples that we used were not oriented.

3 EXPERIMENTAL RESULTS

At the highest dose used ($3 \cdot 10^6$ rad) the samples become opaque in the spectral range 250–800 nm. At this dose, it seems that a saturation occurs and we have not observed (keeping the crystal at liquid nitrogen temperature) even after 6 hours, any recovery in time. The annealing at room temperature leads to the disappearance of the additional absorption spectra induced by radiation. Nevertheless, three very weak bands in the 300–470 nm region, remain like those in γ-irradiated crystals at room temperature.[3] At the dose $1 \cdot 10^6$ rad structured absorption spectra were measured with a very large height and half-width peaking at 500 nm and similar band peaking at about 700 nm, quite like to the ones reported by Halliburton and Edwards[3] in X-ray irradiated CeF_3 crystals at 20 K. At low doses (10^4 rad), the same absorption bands appear with lower intensity, and at a dose still lower the recovery at liquid nitrogen temperature is faster then for the dose 10^6 rad. The absorption spectra immediately after irradiation (with the same dose 10^6 rad) are very different for crystals made by different producers both in form and intensity of the bands as shown in Figure 1.

Figure 2 shows the change in absorption, 30 min. (curve 2) after irradiation and after annealing at 160 K (curve 3), 200 K and 240 K (curve 4 and 5). It is clear from this figure that even when the crystal is kept at liquid nitrogen temperature, the recovery of two main bands (475 and 700 nm) occurs. At least two new bands are formed, which become well resolved (330 and 400 nm) after annealing at 160 K. At this temperature, the 475 and 700 nm bands disappear almost completely, the annealing about 200 K changes the spectrum once again, and at least three bands peaking at 340, 380, and 450 nm appear that are well-known in crystals irradiated at room temperature. These are slightly shifted in maximum position and half-width in comparison with the bands formed at 160 K. The annealing up to room temperature leads only to a decrease of intensity of these three bands (curves 4 and 5, Figure 2). Among the eight crystals used, we found two crystals (K. KORTH 241 and OPTOVAC 606) which in the last step of annealing (200–300 K) exhibited a different spectrum (see Figure 3, curve 4) from the other six crystals which showed three bands (with different relative intensities) as is illustrated in Figure 3 (curve 2 and 3). It is interesting to point out that by a suitable annealing (temperature and time), it is possible to obtain only the bands at 340 nm and 450 nm. The band at 385 nm is completely suppressed (Figure 3 curve 1).

The main result of the annealing measurements is that there are three steps in colour centre formation : 1st step : near liquid nitrogen temperature (bands at 475 and 700 nm, Figure 2 curves 1 and 2); 2nd step : between 100 and 160 K (bands at 330 and 400 nm, Figure 2 curve 3); 3rd step : between 180–300 K (bands at 340, 380, 450 nm, Figure 2 curves 4 and 5).

4 DISCUSSION AND CONCLUSION

CeF_3 crystals contain cationic and anionic impurities from the raw material or crucible. Besides, the producers add some divalent fluoride (CdF_2, PbF_2 or BaF_2) to improve the

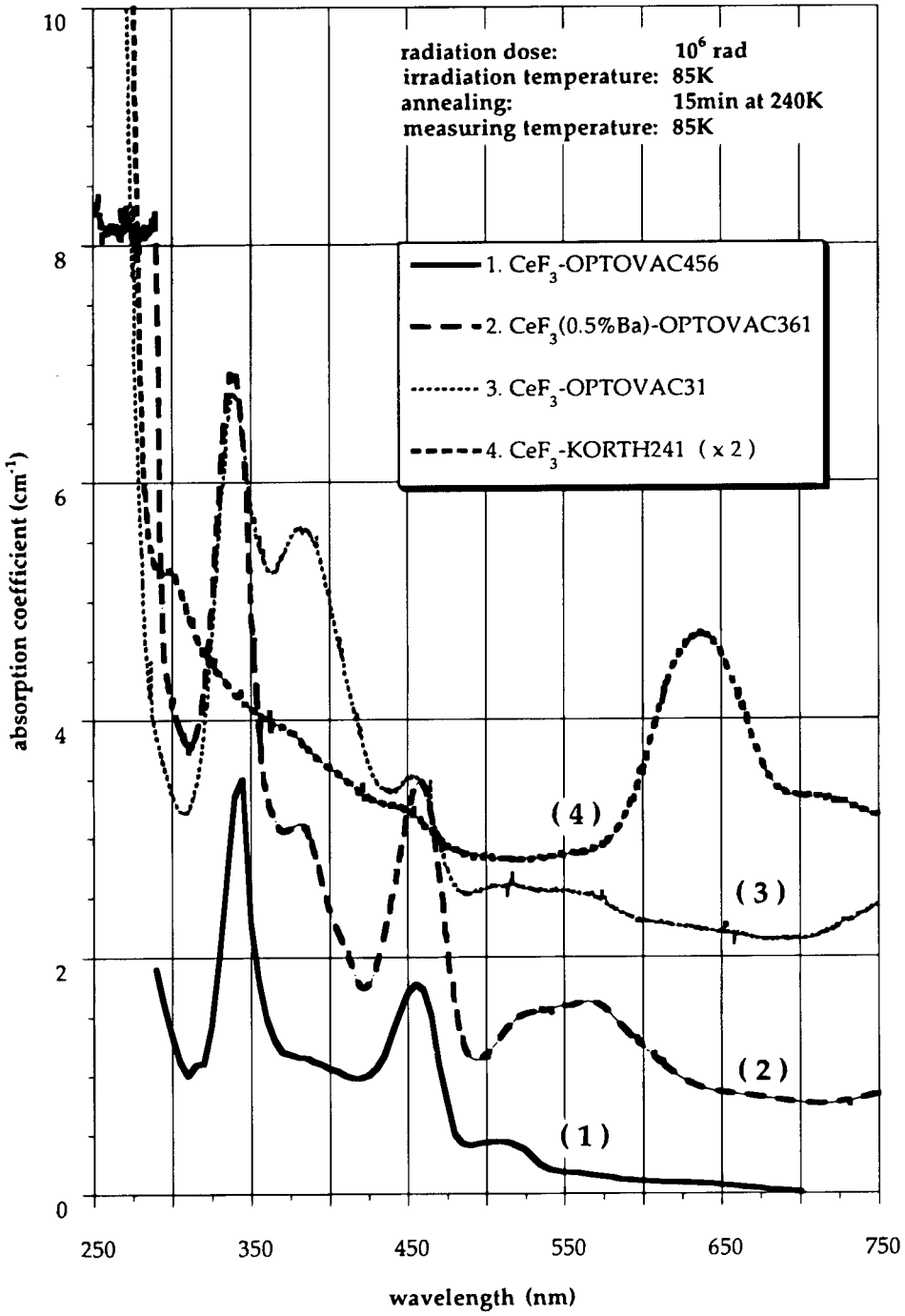

FIGURE 3 Optical absorption spectra of electron irradiated CeF_3 crystals annealed at 240 K.

optical quality of the crystals. Consequently, there are structural point defects, cationic and anionic vacancies for charge compensation, interstitial fluorine ions and several cationic and anionic impurities in the crystals. In these conditions, in irradiated CeF_3 crystals at low temperature, we expect that, besides the classical F, V_K or H centres, various perturbed centres will be formed by a combination of classical colour centres with impurities cations or anions (especially rare-earth and oxygen ions).

Taking into account the results obtained in this paper, the results of Halliburton and Edwards[4] and those of Williams *et al.*,[5] which demonstrated the existence of F centres in CeF_3 by EPR spectra, we tentatively assume that the bands (330 and 400 nm) found in the second annealing step are due to the F like center defect. The two intense bands peaking at 475 and 700 nm can be attributed to V_K or H type centres. The may overlap the absorption bands of the F center detected by EPR in the same range between 20–180 K.[5] The bands formed at 180–300 K (340, 380 and 450 nm) are due to an F center perturbed by rare-earth ions. Favoring this assumption is the surprising similarity of these bands with those obtained in CaF_2 doped with rare-earth ions and irradiated with X-rays.[6] Moreover, the fact that in this annealing step some crystals where found to exhibit an absorption spectrum (curve 4 Figure 3) different from those found in most CeF_3 crystals studied, is also in agreement with our assumption.

REFERENCES

1. D. F. Anderson *et al.*, NIM A332, 373 (1993).
2. I. Dafinei *et al.*, Crystal 2000 Chamonix, Sept. 22–26 1992, pp. 459, *Heavy Scintillators for Scientific and Industrial Applications*, Eds. F. De Notaristefani, P. Lecoq, M. Schneegans, Ed. Frontieres, 1993.
3. E. Auffray *et al.*, *Proceedings of MRS Spring Meeting 94*, San Francisco, April 5–8, 1994.
4. L. E. Halliburton and G. J. Edwards, *Proceedings of MRS Spring Meeting 94*, San Francisco, April 5–8, 1994.
5. R. T. Williams *et al.*, *15th Crystal Clear Collaboration Meeting*, CERN, Geneva, June, 27–28 1994.
6. W. Hayes and D. Staebler, chap 7, in Crystals with the Fluorine structure, Ed. W. Hayes, Clarendon Press Oxford, 1974.

Radiation Effects and Defects in Solids, 1995, Vol. 134, pp. 367–370
Reprints available directly from the publisher
Photocopying permitted by license only

© 1995 OPA (Overseas Publishers Association)
Amsterdam B.V. Published under license by
Gordon and Breach Science Publishers SA
Printed in Malaysia

UP-CONVERSION AND RELAXATION KINETICS AMONG CN^- VIBRATIONAL STATES AFTER SINGLE PULSE 0→1 EXCITATION IN RUBIDIUM-HALIDE-CYANIDE CRYSTALS

H. NAKAGAWA† and F. LÜTY

Physics Department, University of Utah, Salt Lake City, Utah, USA

Vibrational luminescence (VL) spectra and time-dependence of their components have been investigated at 14 K under direct excitation of the fundamental v(0→1) CN^- transition with strong and short pulses from a frequency-doubled CO_2 laser. Up-conversion among CN^- vibrational states were established up the v =13 state, typically, depending on CN^- concentration, excitation density and sample temperature. Time-dependence of the VL-signal shows a variety of aspects relevant to the build-up and relaxation processes for each v-level population after single pulse v(0→1) excitation. The observed VL behaviors are explained in terms of rather fast v-v energy transfer among CN^- vibrational states due to phonon-assisted resonant processes and slow radiative decay processes of each v-level.

Key words CN^-, rubidium halide, cyanide, up-conversion, v-v transfer, vibrational luminescence.

1 INTRODUCTION

With excitation of the fundamental vibrational (v) level of CN^- molecules isolated in alkali halide matrices, strong vibrational luminescence (VL) is observed at $\sim 5\mu$m with long life-times close to the calculated radiative decay time ($\tau \approx 100$ ms). These systems allow us to study the mechanism of migration, trapping, up-conversion and relaxation of photo-excited vibrational energy by observing VL spectra from various slightly anharmonicity-shifted v-levels and time-dependence of each VL component. Studies of this type have been carried out extensively by Dierolf and Lüty[1] using e-v energy transfer from photo-excited F-centers as an indirect pumping source for CN^- v-level excitation, and by Dubost and Charneau[2,3] and Manz *et al.*[4,5] on CO molecules diluted in solid rare gas matrices. In the present study we have performed direct excitation of the fundamental v(0→1) CN^- transition and pursued spectral and time-dependence VL measurements from the v-levels of various CN^- isotopes in Rb-halide-cyanide crystals.

2 EXPERIMENTAL

The crystal sample was mounted on a copper holder in a closed cycle cryostat and cooled down to 14 K. Strong excitation was made with SHG pulse light (200 kW in peak power, 40 ns duration, 1 Hz repetition) of a CO_2-laser from a combination of the laser, a Te crystal for frequency-doubling, a LiF crystal absorbing the fundamental laser light and a focusing CaF_2 lens. Selective excitation was accomplished by tuning the laser wave-length to the fundamental v(0→1) transition. VL was detected in the direction perpendicular to the exciting laser beam with two CaF_2 lenses, a band-pass filter, a monochromator (Aries

† On leave from Fukui University, Fukui910, Japan.

FF250) and an InSb detector. VL-signals were fed into a personal computer through a lock-in amplifier for spectral measurements or a digital storage oscilloscope to obtain the time-dependence.

RESULTS AND DISCUSSION

An example of VL spectra is shown in Figure 1 for RbI:CN^-($x=1\times10^{-2}$; concentration of CN^- in mole fraction), excited at the, v(0→1) absorption band (2063 cm^{-1}). Both first (1st, v = 1) and second (2nd, v = 2) harmonic spectra were measured and are drawn so that their peak positions coincide with each other for transitions from the same initial v-level. It should be noted that the sensitivity of the InSb detector drops rather abruptly below 1850 cm^{-1} in the 1st harmonic spectrum, and that the spectral band-pass of the 2nd harmonic (4 cm^{-1}) spectrum had to be much wider than that of the 1st harmonic (1 cm^{-1}) spectrum. In

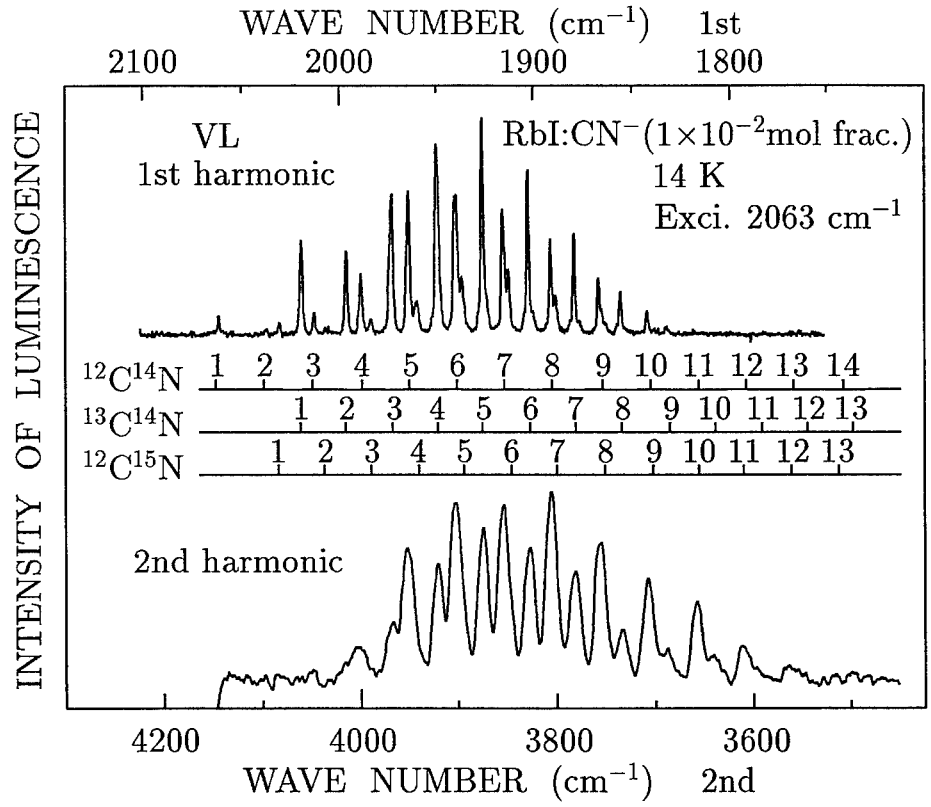

FIGURE 1 First (v = 1) and second (v = 2) vibrational luminescence (VL) spectra of RbI:CN^- ($x=1\times10^{-2}$) obtained at 14 K under selective excitation into the v(0→1) absorption band at 2063 cm^{-1} of $^{12}C\ ^{4}N$ with SHG pulse light from a CO_2 laser. In the middle part are give VL-band energy positions for three isotope systems which are estimated by using absorption data, where the number indicates the initial v-level for each VL-transition. The 1st spectrum is limited above 1800 cm^{-1} owing to the InSb detector sensitivity. The spectral band-pass was set at 1 cm^{-1} for the 1st harmonic and at 4 cm^{-1} for the 2nd harmonic spectrum.

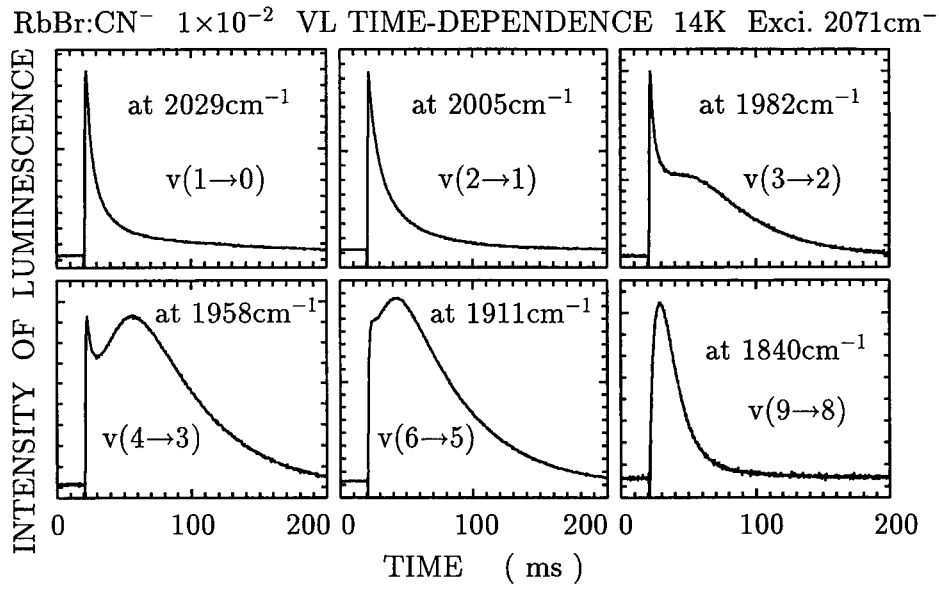

FIGURE 2 Time-dependence of vibrational luminescence (VL) of $^{13}C^{14}N$ in RbBr:CN^- ($x=1\times10^{-2}$) observed at 14 K under selective excitation into the v(0→1) absorption band at 2071 cm^{-1} of $^{12}C^{14}N$ with SHG pulse light of 40 ns duration from a CO_2 laser. The energy of the observed VL is indicated in the figure together with the corresponding v-transition as v(n→n − 1). Initial quick rise of each curve corresponds to the incidence of the exciting lase pulse, which is located at the position of 20 ms on the abscissa in the figure. The complicated behavior in time-dependence is produced by a variety of related processes changing the population of each v-level through trapping, migration, up-conversion and radiative decay of v-energy.

the middle of the figure is given each VL-band position calculated for the three isotope systems by using the absorption data. Correspondence of the spectral peak positions with the calculated ones is excellent except for the unresolved $^{12}C^{15}N$ peaks in the 2nd harmonic spectrum. Since total v-relaxation is finished within repetition time of the exciting laser (1 s), the observed spectrum reflects the time-integrated population for each v-level. It is obvious in the figure that up-conversion of the v-level population is achieved up to v=13 for the abundant $^{12}C^{14}N$ and v=12 for $^{13}C^{14}N$ (see 2nd harmonic) and that trapping and v-v energy transfer in the dilute isotope systems, $^{13}C^{14}N$ (1.1%) and $^{12}C^{15}N$ (0.36%), occur with fairly high efficiency (see 1st harmonic).

Figure 2 represents a typical time-dependence result of VL. The curves in the figure were observed at 14 K for each v-transition v(n→n −1) of $^{13}C^{14}N$ in RbBr:CN^- ($x=1\times10^{-2}$) under excitation in the fundamental v(0→1) absorption band of the abundant $^{12}C^{14}N$. Initial quick rise of each curve corresponds to the incident time of an exciting laser pulse located at the 20 ms position on the abscissa in the figure. The response-time of the detector was set below 0.1 ms. In the case of VL bands between lower v-levels, e.g. v(1→0) and v(2→1), the quick rise of $\tau_{r1} < 0.5$ ms just after the laser shot is followed by a decay in two stages, a fast ($\tau_{d1} \sim 10$ ms) and slow ($\tau_{d2} \sim 100$ ms) one. VL bands between middle v-levels, i.e. v(3→2), v(4→3) and v(6→5), show another rise ($\tau_{r2} \sim 20$ ms) and rather slow decay ($\tau_{d2} = 60 \sim 40$ ms). Upper VL band, v(9→8), has comparatively slow initial rise ($\tau_{r1} \sim 3$ ms) and rather fast decay ($\tau_{d2} \sim 20$ ms). The initial rise time τ_{r1}

represents the time constant to populate each v-level through the v-energy trapping process of $^{13}C^{14}N(v=1)$ from $^{12}C^{14}N(v=1)$ and through the energy up-conversion process from lower to higher v-levels. The observed decay times τ_{d1} and τ_{d2} are produced by escape of v-energy from lower levels by up-conversion and radiative decay, respectively. The radiative decay time should become shorter for upper v-levels. The rise time τ_{r2} is related to the re-population of lower v-levels arising from radiative decay of upper v-levels. The value of τ_{r2} roughly coincides with that of τ_{d2} of the $v(9\rightarrow 8)$ transition.

The resonance energy transfer process due to dipole-dipole interaction is applicable to the energy migration among CN^- molecules of common isotopes. As for the energy trapping and up-conversion, it is necessary to take account of phonon-assisted resonant transfer processes because of the v-energy difference of the rare isotopes from the abundant $^{12}C^{14}N$ ($\sim$43 cm^{-1} for $^{13}C^{14}N$ and $\sim$32 cm^{-1} for $^{12}C^{15}N$), and of the anharmonicity-shift of about 25 cm^{-1} between adjacent v-transition energy in the same molecule. At low temperature, the phonon-emission process dominates advancing the trapping and up-conversion processes. For elevated temperature, the phonon-absorption process would cause de-trapping and downward conversion which act against the expected energy up-conversion. In fact, it was confirmed experimentally that the VL from the upper v-levels disappeared above 40 K and only $v(1\rightarrow 0)$ VL of $^{12}C^{14}N$ was observed.

The final goal of this study is two-fold: (a) to work out a comprehensive kinetics in order to describe the time-dependence of VL as a function of x, excitation density, host variation and temperature, and (b) to test possibilities for v-e transfer of the up-converted v-energy into electronic defect transitions by observing the electronic luminescence. Its success would mean energy conversion form the infrared to visible or ultraviolet region.

This work is supported by NSF grant DMR 92-23230 and ONR grant N-00014-296-0140.

REFERENCES

1. V. Dierolf and F. Lüty, *Reviews of Solid State Sciences* **4**, 479 (1990).
2. H. Dubost and R. Charneau, *Chem. Phys.* **12**, 407 (1976).
3. H. Dubost and R. Charneau, *Chem. Phys.* **41**, 329 (1979).
4. J. Manz, *Chem. Phys. lett.* **51**, 477 (1977).
5. A. Blumen, J. Manz and V.Yakhot, *Chem. Phys.* **26**, 287 (1977).

Radiation Effects and Defects in Solids, 1995, Vol. 134, pp. 371–374
Reprints available directly from the publisher
Photocopying permitted by license only

© 1995 OPA (Overseas Publishers Association)
Amsterdam B.V. Published under license by
Gordon and Breach Science Publishers SA
Printed in Malaysia

THE ESTIMATION OF SIZE OF GIGANTIC IONS OF CHROMIUM IN CORUNDUM LATTICE

V. I. FLEROV*, A. V. FLEROV**, and S. I. FLEROV***

**Nuclear Research Center, Latvian Academy of Sciences, Salaspils-1, LV-2169 Latvia; **Institute of Physics, Latvian Academy of Sciences, Salaspils-1, LV-2169 Latvia; ***REC IAT 'AERCOM', Rezeknes St. 1, Riga, LV-1073 Latvia*

Some TL glow peaks appear in corundum crystals subjected to ionizing irradiation. The highest temperature TL peak at about 600 K, is due to chromium impurity. The non-chromium TL peaks are suppressed at an increase of chromium concentration. They disappear completely at a sufficiently low chromium concentration because of an anomalous big capture cross-section of charge carriers by chromium ions. The free charge carriers capture radius was estimated from dependence of TL intensity of non-chromium TL glow-peaks on the chromium concentration. It was equal to 4.2 nm.

Key words: thermoluminescence, gigantic ions, corundum, ruby.

1 INTRODUCTION

Prof. Vikhnin[1] as a result of experiments on photoconductivity of ruby crystals has proposed the existence of chromium ion's state with a big radius (BRS).

Our results of X-ray luminescence, thermoluminescence (TL), optical absorption of corundum crystals contained impurity of chromium and also an analyses of literature data[2,3] have verified this assumption with a large degree of probability.

The aim of the present work is the determination of the size of this very unusual state. We have used the dependence of TL intensity on chromium concentration in corundum crystals for this purpose.

In nominally pure sapphire crystals from 4 to 7 TL peaks, dependent on the crystal's quality, are observed during heating from 300 to 700 K after irradiation at room temperature.[4] The Verneuil's crystals are characterized with the most intensive TL response. The ruby crystals, as usual, are grown by Verneuil's technique, so they could have the rich TL spectra. However, sometimes we observe the contrary picture. The TL glow curve of corundum crystal with chromium concentration around 10^{-3} weight % is shown in Figure 1. The high-temperature peak at approximately 630 K is due to chromium impurity. The increase of chromium concentration suppresses the intensity of other non-chromium TL peaks and in the laser's crystals at a chromium concentration of the order of 10^{-2} weight % they disappear completely and only one chromium peak remains on the TL glow curve (Figure 1).

The idea of the present work is the following. We have investigated the TL intensity of non-chromium peaks on chromium concentration. The TL intensity in our case is the area under TL glow curve. At a certain chromium concentration the intensity of non-chromium TL peaks is equal to zero, i.e., the chromium ions at such a concentration permeate the complete volume of crystal and capture all free charge carriers arising under irradiation. From the value of this limit concentration we can determine the capture radius of chromium ions for the free charge carriers.

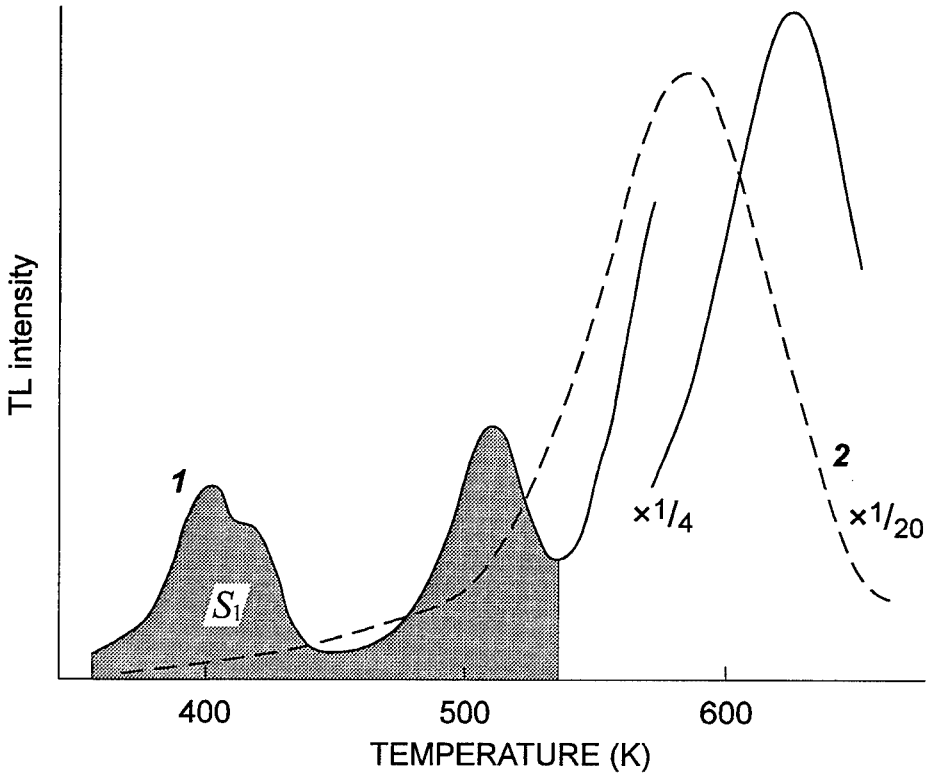

FIGURE 1 TL glow curves for corundum crystals with 0.001 weight % Cr (1) and with 0.034 weight % Cr subjected 1 min irradiation in electron accelerator.

2 EXPERIMENTAL PROCEDURE

The crystals have been irradiated in linear electron accelerator by the same fluency $5 \cdot 10^{13}$ cm^{-2}, that corresponds to a dose of about 10^4 Gy.

Thermoluminescence was detected by FEU-130 (S-5 response). A linear heating rate of 1 K/s was used over the entire temperature range 300–700 K. The weight of specimen did not exceed 20 mg.

We needed for our purpose a set of crystals with different chromium concentrations and especially with sufficiently low concentrations. We had two crystals with good detectable absorption in the U band (2.65 eV) of Cr^{3+} ions at a thickness of 10 mm. We used for concentration determination the formula from ref.[5]:

$$C = a(D_{555} - D_{700})100\%/d,$$

where $a = 2.9 \cdot 10^{-4}$ cm^{-1}, D_{555}, D_{700}—are the optical densities at 555 and 700 nm, correspondingly, and d is the crystal's thickness. The concentrations were equal to $2.1 \cdot 10^{-3}$ and $2.9 \cdot 10^{-3}$ weight %. The other two crystals had good detectable chromium

TL peaks and weak optical absorption. We used the TL method for determination of chromium concentration in the latter crystals. It is known, that at small impurity concentration, the intensity of the proper TL peak is proportional to the impurity concentration. On the basis of two measured crystals we have made a graduation curve, and knowing the TL intensities for other two crystals, we find the chromium concentration in that. They were equal to $1.5 \cdot 10^{-4}$ and $5.0 \cdot 10^{-4}$ weight %.

Optical absorption spectra were taken with a 'Specord M40' spectrophotometer.

3 DISCUSSION AND RESULT

TL intensity (area under the TL glow curve) depends on many factors: defect's concentration, dose, mass of specimen, PMT sensitivity, etc. As is known, all TL peaks are usually saturated at dose 10^3 Gy.[6,7] That is why we irradiated all samples with a larger dose 10^4 Gy in order to exclude its influence on discussed results.

Conditions of all experiments were absolutely identical, and only the mass of specimens and contents of chromium were changed. Therefore, for the TL intensity S we can write

$$S = km = k\rho V,$$

where k is the constant, m is the mass of specimen, ρ is the density of corundum, V is the specimen volume. For TL intensity without chromium peak S_1, i.e. area under TL glow curve in region from 300 to 580 K, as is shown in Figure 1, we can write

$$S_1 = k\rho C_d(V - V_{ch}) = k\rho V C_d(1 - V_{ch}/V),$$

where V_{ch} is the volume overlapped by chromium ions. C_d is the concentration of other defects except chromium impurity. We do not know this concentration that is why we assume that it is equal for all samples. It is not a very rough approximation because all samples were the same origin.

$$S_1/\rho V = S_1/m = S_o,$$

where S_o is the TL intensity reduced to 1 mg, which excludes the influence of the specimen mass on the results. Transform the expression in the brackets

$$V_{ch}/V = N_{ch}/N R_{br}^3/R^3 = C R_{br}^3/R^3$$

where N_{ch} is the number of chromium ions and N is total number of ions in given volume, R_{br} is the radius of BRS of chromium ions, R is the middle radius of ions in corundum lattice, C is chromium concentration in ppm. Therefore:

$$S_o = k\, C_d(1 - C R_{br}^3/R^3).$$

Extrapolation of dependence $S_o = \mathrm{f(C)}$ to abscissa, shown in Figure 2 gives us the value of chromium concentration C_o at which all volume will be overlapped by spheres of influence of chromium ions, so

$$k\, C_d(1 - C_o R_{br}^3/R^3) = 0,$$

and for the radius of BRS of chromium ion we obtain

$$R_{br} = R/C_0^{1/3}.$$

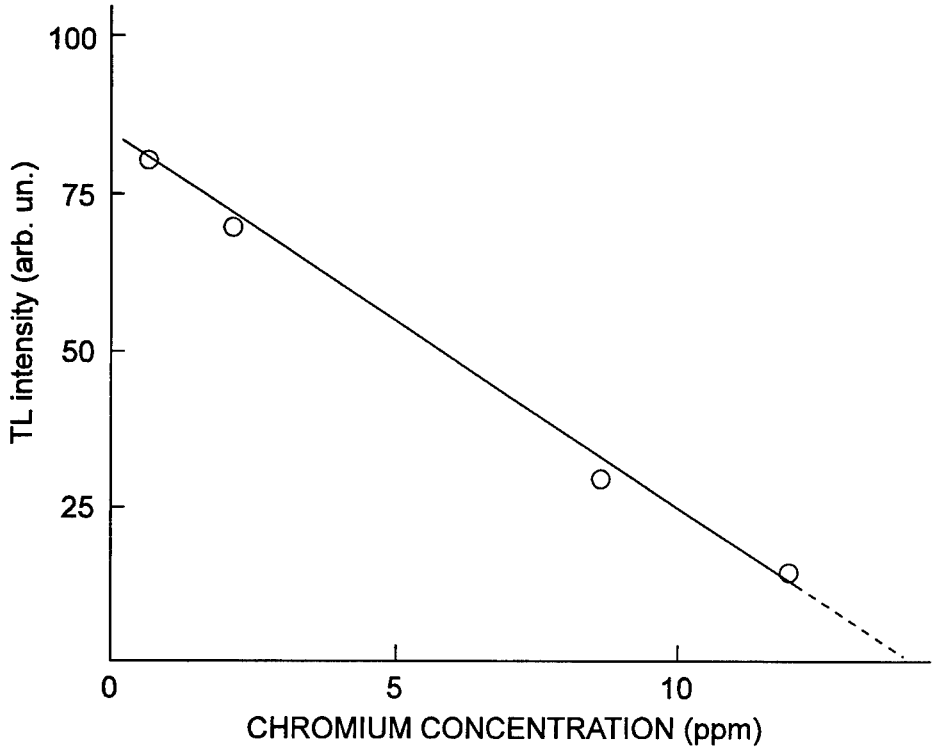

FIGURE 2 Intensity of non-chromium TL glow peaks versus chromium concentration.

The straight line in Figure 2 testifies that our assumption about the concentration of C_d was valid.

As is seen from Figure 2 $C_o = 14$ ppm, so $R_{br} = 42$ R. Since the middle radius of ions in corundum lattice equals to 0.1 nm for radius of BRS we obtain 4.2 nm.

REFERENCES

1. V. S. Vikhnin. *Sol. St. Physics*, **31**, No. 11, 149 (1989).
2. T. S. Bessonova, M. P. Stanislavskii, A. I. Sobko, and V. Ya. Haimov-Malkov. *J. prikladnoi spektroskopii* **27**, 238 (2977).
3. T. S. Bessonova, E. M. Akulenok, *J. prikladnoi spektroskopii* **43**, 471 (1985).
4. V. I. Flerov, A. V. Flerov, V. M. Konyaev at al. *Kristallografiya* **38**, 222 (1993).
5. Methods and devices for control of ruby crystals quality. (S. V. Grum-Grgimailo and M. V. Klassen-Nekludova, Moscow, 1968) p. 51.
6. V. I. Flerov and A. V. Flerov. *Optika I spektroskopiya* **77**, 542 (1992).
7. V. I. Flerov, A. V. Flerov. In: *10th Int. Con., Sol. St. Dosimetry, Washington, July 1992*, p. 52.

Radiation Effects and Defects in Solids, 1995, Vol. 134, pp. 375–378
Reprints available directly from the publisher
Photocopying permitted by license only

© 1995 OPA (Overseas Publishers Association)
Amsterdam B.V. Published under license by
Gordon and Breach Science Publishers SA
Printed in Malaysia

OFF-CENTRE EFFECTS IN THE TRIPLET RELAXED EXCITED STATE OF IMPURITY ns^2 IONS IN ALKALI HALIDES

V. HIZHNYAKOV, K. KALDER, V. KORROVITS, V. NAGIRNYI, A. STOLOVICH, and S. ZAZUBOVICH

Institute of Physics, Estonian Academy of Sciences, Riia 142, EE2400 Tartu, Estonia

An off-centre displacement of an excited ns^2 ion from a crystal lattice site is studied for Ga^+, In^+ and Tl^+ centres in alkali halides at 0.09–5 K by the time-resolved polarization spectroscopy method. A theory is developed, which considers the off-centre effects as a result of the mixing of the impurity ^{3}nsnp and ^{3}npnp excited states by T_{1u} vibrations.

Key words: off-centre impurity, tunnelling, luminescence, decay kinetics, 'Off-centre effects for an excited ns^2 ion'.

Some years ago the manifestations of the off-centre position of an excited impurity ion were discovered by us in the low-temperature decay kinetics of the triplet emission of ns^2-ion-doped alkali halides.[1,2] This effect has now been studied in detail at 0.09–5 K by the method of time-resolved polarization spectroscopy and with the use of magnetic and electric fields for tetragonal (T) and trigonal (X) Jahn-Teller minima of triplet ^{3}nsnp relaxed excited state (RES) of Ga^+, In^+ and Tl^+ centres in various f.c.c. and b.c.c. crystals (Table I). It has been shown that in T minima the off-centre displacement of Ga^+ and In^+ ions exists in all the crystals studied, and in each minimum it occurs in the direction normal to the Jahn-Teller distortion axis.[1–5] In X minima this effect was observed for Ga^+ and In^+ centres in b.c.c. crystals, where X minima are of a higher energy than T ones,[2] but it was not found for the most of f.c.c. crystals, where X minima are the lowest ones. The only f.c.c. crystal, where the off-centre effects were observed in both T and X minima, is KBr:In, where their depths are nearly equal. No off-centre effects were found for Tl^+ ion, where the separation of impurity states is relatively large.

These results are explained in terms of the theory considering the off-centre effects as a result of the mixing of the impurity ^{3}nsnp and ^{3}npnp excited states by odd T_{1u} vibrations (pseudo Jahn-Teller effect).[6] According to this theory, the off-centre distortion takes place if $2\beta^2/k\varepsilon > 1$, where β is the vibronic mixing constant, ε is the energy difference between the mixing states and k is the elastic constant; the displacement of ns^2 ion in tetragonal (or trigonal) minimum occurs in one of the four (or three) directions normal to the tetragonal (or trigonal) Jahn-Teller distortion axis of the centre.

Let us consider this theory in more detail.

As in the nsnp RES spin-orbit interaction is strongly reduced due to the strong Jahn-Teller effect, the triplet ^{3}nsnp states can be vibronically mixed only with other triplet states. The most important in this respect are the nearest one-electron ^{3}ns(n+1)s and ^{3}nsnd states and two-electron ^{3}npnp states. For example, the ^{3}nsnp$_z$ states (z is the direction of tetragonal distortion axis) can be vibronically mixed with ^{3}ns(n+1)s state by Z-odd vibrations of T_{1u} representation (the corresponding vibrational coordinate is Q_z). This mixing can cause an additional distortion along z axis, which contradicts to experimental data. The ^{3}nsnp$_z$ state can be mixed with the ^{3}nsnd$_{z^2}$, ^{3}nsnd$_{zx}$ and ^{3}nsnd$_{zy}$ states as well. The largest mixing is with the ^{3}nsnd$_{z^2}$ state, as it is energetically the nearest one. This

TABLE I

Decay times (τ_{SC}, $\tau_{SC'}$) and light sums (S_{SC}, $S_{SC'}$) of two slow decay components (SC and SC') of the triplet A_T and A_X emission caused by the off-centre position of an excited ns^2 ion.

Crystal	Emission	τ_{SC},ms	$\tau_{SC'}$,ms	$\tau_{SC}/\tau_{SC'}$	$S_{SC'}/S_{SC}$
NaCl:Ga	A_T	3.0	1.4	2.14	0.8
KCl:Ga	A_T	3.6	1.6	2.25	0.9
RbCl:Ga	A_T	4.8	1.75	2.74	0.8
KBr:Ga	A_T	1.6	0.7	2.30	0.8
CsBr:Ga	A_T	1.2	0.5	2.40	~1.0
	A_X	2.4	0.22	11	~1.0
KI:Ga	A_T	1.07	–	–	–
NaCl:In	A_T	1.10	0.81	1.36	0.75
KCl:In	A_T	1.79	1.00	1.80	0.90
RbCl:In	A_T	2.20	1.10	2.10	1.15
KBr:In	A_T	1.60	0.70	2.30	2.50
	A_X	~2.5	~1.2	~2.1	~1.3
RbBr:In	A_T	1.55	0.65	2.40	1.70
CsBr:In	A_T	1.40	0.56	2.50	2.20
	A_X	1.20	0.50	2.40	0.75
KI:In	A_T	0.95	0.35	2.70	2.70
RbI:In	A_T	1.00	0.37	2.70	2.32
KCl:Tl RbCl:Tl CsCl:Tl CsBr:Tl CsI:Tl	no off-centre effects are observed				

mixing is also caused by Z-odd T_{1u} vibrations and may also result in an additional distortion along z axis. Consequently, vibronic mixing of one-electron ^{3}nsnp states with other one-electron excited states cannot cause the odd distortion in the direction normal to the Jahn-Teller distortion axis. The same conclusion holds also for trigonal minima of ^{3}nsnp states; in the last case one should choose the reference frame with z axis directed along an $\langle 111 \rangle$ axis of the crystal.

On the contrary, vibronic mixing of one-electron ^{3}nsnp states with two-electron ^{3}npnp excited states can lead to the distortion perpendicular to the Jahn-Teller distortion axis of the ^{3}nsnp state. Indeed, the considered two-electron excited states can be obtained by excitation of the second ns electron to np state, its spin orientation being conversed. There are three orbital states of this type: $^3np_xnp_y$, $^3np_xnp_z$ and $^3np_ynp_z$ (the triple states $^3(np_x)^2$, $^3(np_y)^2$ and $^3(np_z)^2$ are forbidden by the Pauli principle). The $^3nsnp_z$ states can be mixed with the $^3np_xnp_z$ and $^3np_ynp_z$ states by X-odd and Y-odd T_{1u} vibrations (the corresponding vibrational coordinates are Q_x and Q_y). This mixing can cause an off-centre distortion only in the direction perpendicular to z axis, in agreement with experiment. This conclusion holds both for tetragonal and trigonal minima of the ^{3}nsnp state.

Let us consider the conditions for off-centre distortion. First let us regard the tetragonal minima of the $^3nsnp_z$ states. The APES of the mixed states in the space of the Q_x and Q_y configurational coordinates are determined by the eigenvalues of the vibronic matrix $U = U_0 I + V$, where $U_0 = k(Q_x^2 + Q_y^2)/2$ is the harmonic potential of the Q_x and Q_y vibrations, I is the 3×3 unit matrix,

$$V = \begin{pmatrix} 0 & \beta Q_x & \beta Q_y \\ \beta Q_x & \varepsilon & 0 \\ \beta Q_y & 0 & \varepsilon \end{pmatrix} \quad (1)$$

is the matrix of vibronic mixing in linear (with respect to Q_x and Q_y) approximation, ε is the energy difference between the minimum of the $^3nsnp_z$ state and the APES of the $^3np_{x,y}np_z$ states for $Q_x = Q_y = 0$ and for other nuclear coordinates corresponding to their values in the $^3nsnp_z$ RES. The diagonalization of the matrix V gives the following eigenvalues: $V_{1,3} = \varepsilon/2 \mp (\varepsilon^2/4 + \beta^2 Q^2)^{1/2}$, $V_2 = \varepsilon$, where $Q^2 = Q_x^2 + Q_y^2$. The APES sheet $U_1 = kQ^2/2V_1 = kQ^2/2 + \varepsilon/2 - (\varepsilon^2/4 + \beta^2 Q^2)^{1/2}$ has the deepest minimum. If $\beta^2/k > |\varepsilon|/2$, the minimum is at $Q = Q_0 = (\beta^2/k^2 - \varepsilon^2/4\beta^2)^{1/2} \neq 0$, i.e. the odd distortion normal to z axis takes place. This conclusion holds not only for tetragonal but also for trigonal minima.

In the considered approximation the APES is symmetrical with respect to rotations to an arbitral angle $\varnothing = \arccos(Q_x/Q)$ around z axis. However, the account of higher-order terms in vibronic coupling and anharmonicity removes this orientational degeneracy of the APES. This removal is different for tetragonal and trigonal RES. In tetragonal ^3nsnp RES it comes from quadratic anharmonic potential terms $A(Q_x^4 + Q_y^4 + Q_z^4) + B(Q_x^2Q_y^2 + Q_x^2Q_z^2 + Q_y^2Q_z^2)$ (and also from the third-roder vibronic terms; cubic anharmonic terms are absent in the centres with inversion symmetry). For example, the APES of the tetragonal $^3nsnp_z$ RES transforms into $U_1 + Q^4(A + \overline{B}\sin^2 2\varnothing)$, where $\overline{B} = B/2 - A$ ($Q_z = 0$), and z axis becomes the fourth-order symmetry axis of the considered APES sheet. In trigonal ^3nsnp RES the anharmonic terms mentioned do not remove the orientational degeneracy, but the second order terms in vibronic matrix do. Indeed, with the account of these terms, the vibronic matrix for the $\langle 111 \rangle$ trigonal minimum has the form (1), where Q_x is replaced by $Q_{x'} + \gamma(Q_{y'}^2 - Q_{x'}^2)$ and Q_y by $Q_{y'} + 2Q_{x'}Q_{y'}$ (here and below $Q_{x'} = (Q_x - Q_y)/\sqrt{2}$, $Q_{y'} = (Q_x + Q_y - 2Q_z)/\sqrt{6}$, $Q_{z'} = (Q_x + Q_y + Q_z)/\sqrt{3}$, $Q'^2 = Q_{x'}^2 + Q_{y'}^2$, $\varnothing' = \arccos(Q_{x'}/Q')$, $\gamma\beta$ is the constant of quadratic interaction). This leads to the replacement of Q^2 by $Q'^2(1 - 2\gamma Q \cos 3\varnothing')$. Consequently, the $\langle 111 \rangle$ axis of the crystal becomes the third-order symmetry axis of the trigonal ^3nsnp RES, and the APES sheet obtains three minima.

The important parameters of the considered vibronic mixing are β and ε. The value of ε can be found from the corresponding excited-state absorption spectrum (e.g., for KI:In ε is about 2.9 to 2.6 eV, see[6]). The value of β is not yet known. The existence of an off-centre distortion means that $\beta^2/k > \varepsilon/2 \sim 1.3$–$1.5$ eV. Consequently, $|\beta|$ is of the order of the corresponding vibronic parameters for even vibrational modes.

The wave functions of the two-electron ^3npnp excited states are strongly localized; their localization is noticeably stronger than that of the one-electron $^3ns(n+1)s$ and ^3nsnd excited states. As the wave functions of ^3nsnp states are also strongly localized, the vibronic mixing parameter $|\beta|$ should exceed analogous vibronic mixing parameters of ^3nsnp and $^3ns(n+1)s$, ^3nsnd states. The energy difference between ^3nsnp and $^3ns(n+1)s$ and ^3nsnd states is also larger than the difference ε between ^3nsnp and ^3npnp states. This explains why the vibronic mixing of the ^3nsnp state with two-electron triplet ^3npnp states is the strongest one in the centres studied. The existence of two-electron ^3npnp states has been proved in the experiments on optical dichroism of excited state absorption.[6]

ACKNOWLEDGEMENTS

This work was supported by the Soros Foundation Grants and the Estonian Science Foundation Grants No. 355 and 369.

REFERENCES

1. G. Liidja, V. Nagirnyi, T. Soovik, S. Zazubovich. *Phys. stat. sol. (b)* **152**, 563 (1989).
2. V. Nagirnyi, P. Vaino, S. Zazubovich. *Phys. stat. sol. (b)* **167**, 659 (1991).
3. V. Nagirnyi, A. Stolovich, S. Zazubovich, N. Jaanson. *Phys. stat. sol. (b)* **173**, 743 (1992).
4. K. Kalder, V. Korrovits, V. Nagirnyi, S. Zazubovich. *Phys. stat. sol. (b)* **178**, 391 (1993).
5. K. Kalder, V. Korrovits, V. Nagirnyi, S. Zazubovich, N. Jaanson. *J. Lumin.* **59**, 71 (1994).
6. V. Hizhnyakov, M. Karklinya, V. Nagirnyi, L. Nagli, S. Zazubovich. *Phys. stat. sol. (b)* **162**, K91 (1990).

Radiation Effects and Defects in Solids, 1995, Vol. 134, pp. 379–383
Reprints available directly from the publisher
Photocopying permitted by license only

© 1995 OPA (Overseas Publishers Association)
Amsterdam B.V. Published under license by
Gordon and Breach Science Publishers SA
Printed in Malaysia

ANHARMONICITY EFFECTS AND PHONON COUPLING OF OH-DIVALENT IMPURITY COMPLEXES IN ALKALI HALIDES

P. BENEVENTI,* R. CAPELLETTI,* M. DARRA,* R. FIESCHI,* W. B. FOWLER,** and A. GAINOTTI*

**Department of Physics—University of Parma—Viale delle Scienze, 43100 Parma—Italy;*
***Department of Physics—Lehigh University—Bethlehem, Pennsylvania 18015–3182–USA*

High resolution (0.04 cm^{-1}) FTIR absorption measurements were performed in the range 9–300 K to study the vibrational modes of OH in NaCl:Cd^{++} and NaCl:Ca^{++}. The narrow lines (down to ~ 0.05 cm^{-1} at 9 K) in the range 3550–3600 cm^{-1} were attributed to stretching of OH embedded in Me^{++}-complexes on the basis of isotopic substitutions, thermal treatments, and different Me^{++} contents. The spectra (fundamentals, overtones, and isotopic replicas) were analyzed in the framework of the Morse anharmonic oscillator model, whose parameters were evaluated and compared to those of similar systems. The temperature dependence of the line position and width, described by a single phonon coupling model, made it possible to determine the frequencies of the coupled phonons.

Key words: OH stretching, FTIR spectroscopy, alkali halides, impurities, anharmonicity.

1 INTRODUCTION

OH ions strongly interact with divalent cation impurities (Me^{++}) in alkali halides, giving rise to a variety of complexes, which heavily affect their electrical, optical, and thermal properties. The OH stretching frequency is very sensitive to small changes of the symmetry of Me^{++}-complex in which OH is embedded, as shown by the large number of optical absorption lines detected in the range $3500-3700$ cm^{-1} in Mg-doped LiF and NaF.[1] In such systems the lines are already very narrow at room temperature: this fact suggests a weak coupling of the OH-stretching mode to the lattice. On the contrary in other systems, as NaCl:Ca, Cd, they are broad. Therefore high resolution (0.04 cm^{-1}) FTIR absorption spectroscopy measurements have been performed in the range 9–300 K to study the vibrational modes of OH in NaCl:Cd^{++} and NaCl:Ca^{++}. The aim of the work was 1) to get an insight on the nature of the complexes in which OH is embedded, 2) to detect possible anharmonic effects in the framework of the Morse model for the OH oscillator, 3) to compare the Morse parameters to those obtained for similar systems, and 4) to analyze the phonon coupling of the OH stretching modes.

2 EXPERIMENTAL DETAILS

NaCl single crystals were grown by means of the Kyropoulos method in N_2 atmosphere. The doping with Cd or Ca was obtained by adding to the melt $CdCl_2$ or $CaCl_2$ molar fractions in the range 10^2-10^4 ppm. Dry N_2 flowing in H_2O and/or D_2O was let in the growth apparatus, in order to produce the co-doping with OH and/or OD. The optical absorption measurements were performed by means of 1) a FTIR Bomem DA8 spectrometer in the range $600-7500$ cm^{-1} with a resolution as good as 0.04 cm^{-1} and 2) a Varian 2390 spectrophotometer in the range $9000-10^4$ cm^{-1} with low resolution.

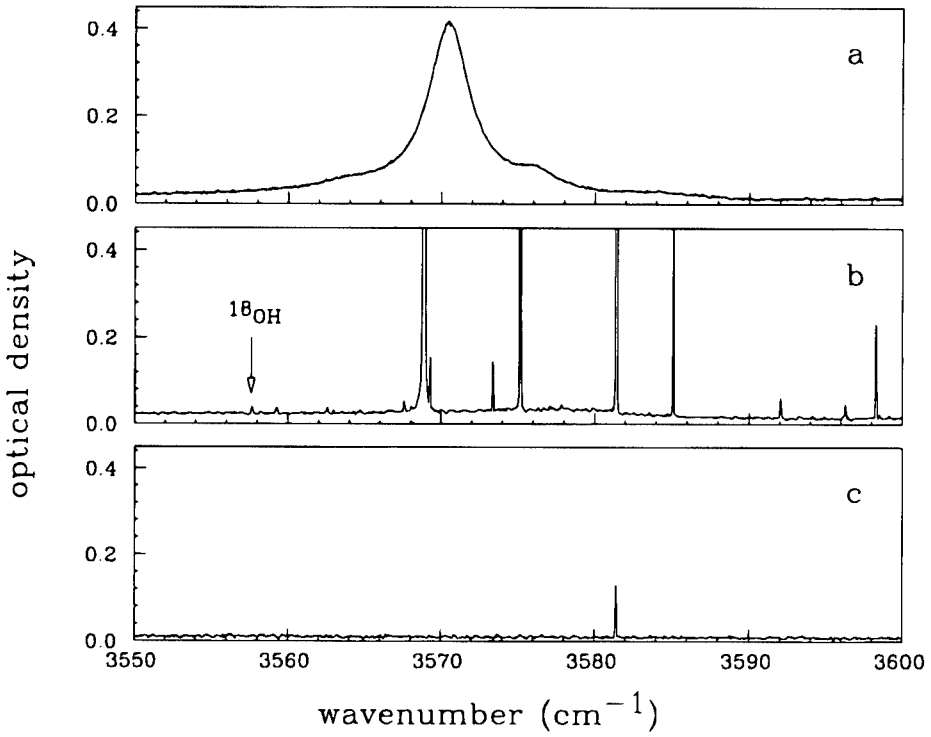

FIGURE 1 High resolution (0.04 cm^{-1}) optical absorption spectra in the OH^- stretching region of NaCl:Cd, OH samples. (a) NaCl:Cd (10^4 ppm): spectrum measured at 300 K (thickness x = 18 mm); (b) same sample as above: spectrum measured at 9 K; (c) nominally pure NaCl sample: spectrum measured at 9 K (x = 28 mm).

The spectra were measured in the range 9−300 K by using a 21SC model Cryodine Cryocooler of CTI-Cryogenics.

3 RESULTS AND DISCUSSION

Figure 1 shows the absorption spectra of NaCl:Cd, OH in the 3550−3600 cm^{-1} range, i.e. in the region typical for the OH^- stretching mode: curve a displays the broad spectrum measured at 300 K, while curve b gives that taken at 9 K. At low T the lines are very narrow ($\sim$ 0.06 cm^{-1}) as , or even more than those detected in LiF and NaF:Mg.[1] Similar spectra have been obtained for NaCl:Ca, OH, OD, see Figure 2, curve a. The presence of OD induces a nice replica of such a spectrum at shorter wavenumbers, see Figure 2, curve b. An additional isotopic effect is displayed by Figure 1b, where the weak line at 3557.6 cm^{-1} is the replica of the strong line at 3568.9 cm^{-1} and is due to ^{18}O, present in natural abundance of 2×10^{-3}, as in the case of NaF and LiF: Mg^2 and of sillenites.[3] These results support the hypothesis that the lines observed are due to hydroxyl ions. The lines of Figures 1 and 2 appear only if NaCl:OH is co-doped with Cd (or Ca). Moreover by changing the Me^{++} concentration in the melt, the relative weight of the lines in the spectra

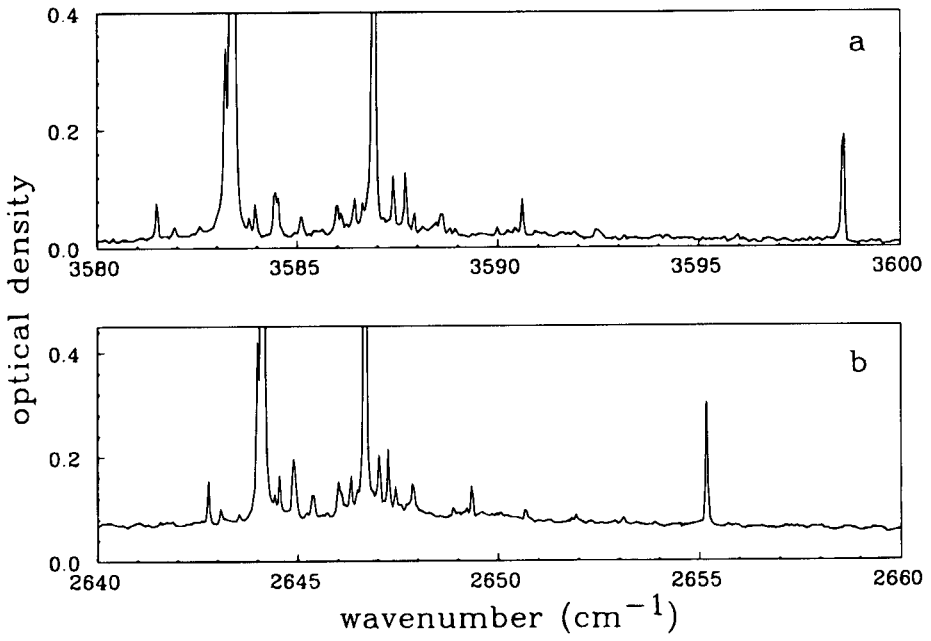

FIGURE 2 High resolution (0.04 cm^{-1}) optical absorption spectra of NaCl:Ca (100 ppm), OH, OD measured at 9 K (x = 10.5 mm). (a) region of OH^- stretching; (b) isotopic replica in the region of OD^- stretching.

changes, confirming that they are due to the OH^- interaction with Me^{++}-related defects. Hints on the nature of defects can be obtained by submitting the samples to proper thermal treatments. In fact, a quenching from 700°C of a thin NaCl:Cd sample induces an increase of the line at 3581 cm^{-1} and a decrease of the other lines, suggesting that the first might be related to OH^- interacting with a simple Cd defect, as the I. V. dipole, while the other lines should be due to OH^- in more complex Cd-defects, as clusters and/or aggregates. This hypothesis is supported by a weak 3581 cm^{-1} line in a nominally pure NaCl, where traces of Cd can be present only as the simplest defects, see Figure 1, curve c.

At wavenumbers which are twice (within 2%) those of the lines displayed in Figures 1 and 2 weak lines have been detected, which can be regarded as due to overtone transitions ($\Delta n = 2$, n being the vibrational quantum number), see Figure 3 (insert at the top left). A very weak band was monitored at \10,192 cm^{-1} (T = 9 K) in a very thick NaCl:Cd sample, which corresponds to $\Delta n = 3$ (the fundamental being at 3568.9 cm^{-1}), see Figure 3 (insert at the bottom right). Lines due to bending modes and to bending+stretching combination modes were detected as well in the 570 - 800 and 4150-4160 cm^{-1} respectively.

The stretching mode spectra (fundamentals, overtones, and isotopic replicas) were analyzed in the framework of the Morse anharmonic oscillator and the related parameters were determined. The anharmonicity parameter x_{em} was ~ 0.023 for Cd-OH defects and ~ 0.022 for the Ca-OH ones. The D_e values, i.e. the binding energy of the OH molecule, were of the order of 40,500 cm^{-1} for the former and of 42,500 for the latter. Such values are comparable to those obtained for Mg-OH defects in LiF and NaF[1] and for the isolated

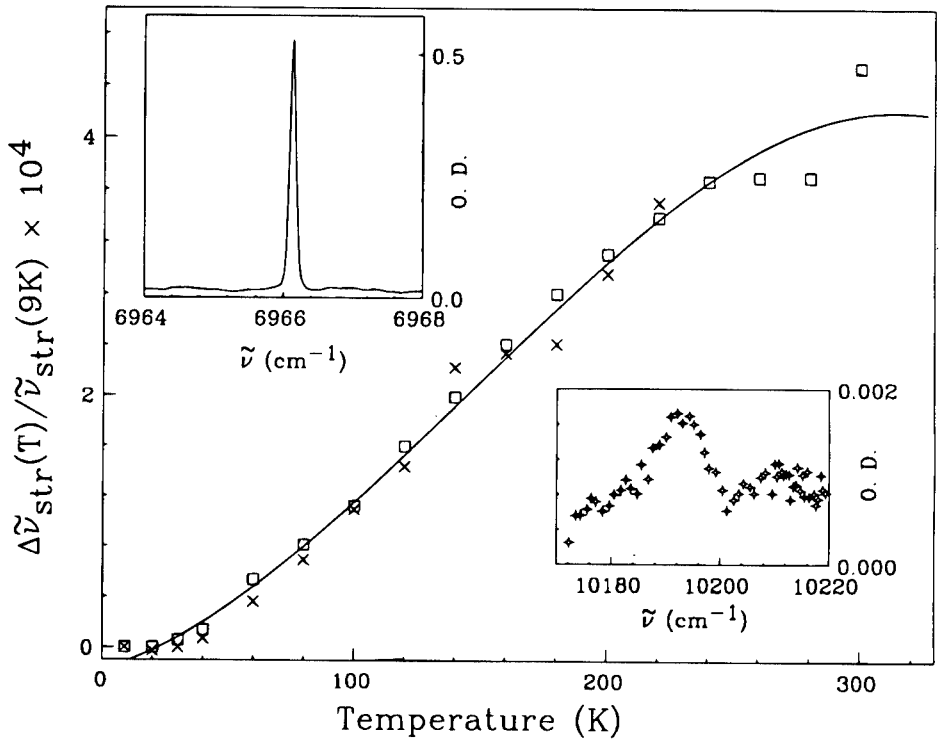

FIGURE 3 Temperature dependence of the normalized line shift, i.e. the ratio between the shift $\Delta\tilde{\nu}_{str}(T)$ at a given temperature T and the line position $\tilde{\nu}_{str}(9\ K)$ measured at 9K, in NaCl:Cd (10^4 ppm), OH sample (x = 18 mm). Open squares are for the fundamental transition line (peaking at 3568.9 cm^{-1} at 9 K, see Figure 1b); crosses are for the related overtone (peaking at 6966.1 cm^{-1} at 9 K, see insert at the top left).
In the insert at top left: high resolution (0.04 cm^{-1}) optical absorption spectrum of the same sample measured at 9 K displaying the overtone transition ($\Delta n = 2$).
In the insert at bottom right: low resolution optical absorption spectrum of a thick (x = 39 mm) NaCl:Cd (10^4 ppm), OH sample, measured at 9 K displaying the overtone transition ($\Delta n = 3$).

OH ion.[4] The 4% difference between the x_{em}'s of Cd-OH and Ca-OH defects is well beyond the experimental error (< 0.3%), and therefore meaningful and appreciable, in fact x_{em} for isolated OH^- changes only within 6% along the whole series of alkali halides.[4] This means that the electronic polarizability (higher for Cd than for Ca) could play a more important role on the anharmonicity than the ion size (practically the same for Cd and Ca). The ratio ρ between the reduced masses of OH and OD embedded in the same complex (ρ being meaningful of the hydroxyl ion coupling to the lattice) was found to lie between 0.5300 and 0.5364, related to the simplified models of the free diatomic molecule and of the molecule strongly coupled to the lattice respectively, again in agreement with the results obtained for Mg-OH defects.[1] If the dipole moment is a linear function of O-H separation, x_{em} should equal the ratio $x_{ee} \equiv I_{0\to2}/I_{0\to1}$ between the oscillator strengths of the first overtone and of the fundamental line. In the present case the two values coincide within the experimental error, excluding electrical anharmonicity contributions, at variance with the results reported for isolated OH.[4]

Since the spectra are heavily affected by temperature (compare curves a and b in

Figure 1), the line positions $\tilde{\nu}_{str}(T)$ and the widths $\Delta W(T)$ were analyzed as a function of the temperature T. By increasing T the lines broaden and shift. A 'red' (i.e. towards lower wavenumbers) shift is observed for Ca-OH complexes, as for isolated OH^- in sillenites,[3] and of Mg-OH complexes in LiF and NaF,[1] while an unusual 'blue' shift is detected for Cd-OH complexes (see Figure 3). In the range 9–300 K the line shift $\Delta\tilde{\nu}_{str}(T)$ is very small for both impurities (less than 1.5 cm^{-1} in NaCl:Cd) and the normalized shift, i.e. $(\Delta\tilde{\nu}_{str}(T)/\tilde{\nu}_{str}(9\ K))$, is practically the same for the fundamental and overtone ($\Delta n = 2$) line (see Figure 3), confirming that both are related to the same center. The lines are very narrow at low T, see Figure 1, and, anyway, more narrow than those due to the isolated OH. A single phonon coupling model,[5] recently successfully applied to describe the shift and broadening of the narrow OH-stretching line in sillenites,[3] was assumed to analyze the temperature dependence of $\tilde{\nu}_{str}$ and ΔW. The lines are well described by a Lorentzian, as predicted by the model. However, in the case of NaCl:Ca, where ΔW is comparable with the apparatus resolution, the lineshape could not be correctly analyzed, at least at low T. Except for such cases, the data fit satisfactorily the model and made it possible to evaluate the frequency $\tilde{\nu}_{ph,OH}$ of the coupled phonon. $\tilde{\nu}_{ph,OH}$ values obtained for the 3583 cm^{-1} Ca-line and for the 3568.9 cm^{-1} Cd-line were 46 ± 15 cm^{-1} and 27 ± 11 cm^{-1}, i.e. a frequency comparable to that of OH^- center of mass mode ($\sim$ 30 cm^{-1}).[6] Both the 'red' and 'blue' shift can be accounted for by the model proposed by Zhang.[7]

REFERENCES

1. R. Capelletti, P. Beneventi, E. Colombi, W. B. Fowler, *Il Nuovo Cimento* **15D**, 415 (1993).
2. R. Capelletti, P. Beneventi, E. Colombi, W. B. Fowler, in *'Defects in Insulating Materials'*, O. Kanert & J.-M. Spaeth eds., *World Scientific*—**1**, 440 (1993).
3. P. Beneventi, R. Capelletti, L. Kovács, Á. Péter, A. M. Lanfredi Manotti, and F. Ugozzoli, *J. Physics: Cond. Matter.* **6**, 6329 (1994).
4. A. Afanasiev, C. P. An, F. Luty, in *'Defects in Insulating Materials'*, O. Kanert & J.-M. Spaeth eds., *World Scientific*—**1**, 551 (1993).
5. P. Dumas, Y. J. Chabal, and G. S. Higashi, *Phys. Rev. Lett.* **65**, 1124 (1990).
6. B. Wedding and M. V. Klein, *Phys. Rev.* **177**, 1274 (1969).
7. Z. Y. Zhang, *Phys. Lett.* **A143**, 413 (1989).

Radiation Effects and Defects in Solids, 1995, Vol. 134, pp. 385–388
Reprints available directly from the publisher
Photocopying permitted by license only

© 1995 OPA (Overseas Publishers Association)
Amsterdam B.V. Published under license by
Gordon and Breach Science Publishers SA
Printed in Malaysia

STRUCTURE AND THERMODYNAMIC BEHAVIOR OF In^{3+}–$2V_{Ag}$ DEFECTS IN AgBr

J. C. AUSTIN, K. J. PRICE, B. K. PATNAIK and M. L. SWANSON

Department of Physics and Astronomy, University of North Carolina, Chapel Hill, NC 27599-3255, USA

We have used perturbed angular correlation (PAC) spectroscopy to study the structure and thermodynamic behavior of point defect complexes containing trivalent indium ions in AgBr. When indium atoms are introduced into AgBr they generally substitute for silver atoms, and two silver vacancies are created compensating the excess charge of each indium atom. The vacancies interact with the indium atoms via the Coulomb force, forming complexes whose structure depends on details of the interionic potentials. PAC allows the structure and populations of these complexes to be probed over a wide range of temperatures via the ^{111}In PAC probe. Our results show that the behavior of these defects is surprisingly intricate, with several structures occurring and transitions occurring among them as the temperature is varied between 50 K and 100 K. Analysis of these transitions provides information on thermodynamic potentials that, together with defect structural information, can provide insight into fundamental properties like interionic potentials. Recent results on AgBr:In are presented and compared with earlier studies of the AgCl:In system.

Key words: (AgBr, AgBr:In, defects, color centers)

1 INTRODUCTION

When an aliovalent impurity is introduced into an ionic material, vacancies are normally formed to offset the excess charge of the impurity. In the silver halides, for example, a divalent ion such as cadmium often substitutes for monovalent silver, resulting in the creation of a silver vacancy. Since this vacancy has relative charge opposite to that of the impurity ion, it can be trapped at either a nearest or a next-nearest site to the impurity ion. The impurity ion's size and the polarizability of the halogen ion, primarily, determine which site is occupied. Trivalent ions require two vacancies for charge compensation, both of which may bind to the impurity, so the opportunity for structures of greater complexity exists. Although defects involving divalent cations have been the subject of considerable research for many years, relatively little work has been done on complexes involving trivalent impurities, as their greater complexity makes their characterization more difficult.

Complexes formed between vacancies and aliovalent impurities are interesting from a technological point of view. These complexes often act as traps of photocarriers in silver halides, and can have significant effects on the performance of photographic films. The photocarrier trapping behavior of a particular complex depends on its charge, the electronic structure of the impurity, and the ionic structure of the complex itself.[1] Trivalent dopants are often used to dope silver halides in practical photographic films.

Perturbed angular correlation (PAC) spectroscopy is able to provide information on the structure of complexes involving trace quantities ($\sim$1 ppb) of the trivalent ion ^{111}In. Because PAC measurements have no fundamental temperature limitation (in contrast to most microscopic techniques that can be used to study defects), they are able to reveal transitions in the structure of defect complexes that could not be observed by other methods.

Previous publications have documented the AgCl:In defect system.[2,3] In the following pages we present a brief summary of recent progress in the characterization of AgBr:In

defects and a comparison to AgCl:In. Space limitations prevent a comprehensive presentation—a more detailed treatment will follow later.[4]

2 EXPERIMENTAL

The local symmetry of the charge distribution around a probe nucleus such as ^{111}In is generally lowered when an impurity atom or intrinsic point defect is trapped. Consequently, an inhomogeneity in the local electric field occurs at the site of the impurity. A nucleus with a quadrupole moment will interact with such electric field gradients (efg's) via the electric quadrupole interaction, lifting the energy degeneracy and causing oscillations in the occupation of the nuclear hyperfine energy levels. These oscillations appear as a precession of the nuclear spin at a frequency equal to $\Delta E/h$, where ΔE is the difference in energy between hyperfine energy levels and h is Plank's constant.

^{111}In, a typical PAC probe isotope, decays via a pair of gamma radiations, the intermediate state having a quadrupole moment of 0.83 barn and a lifetime of 84 nanoseconds. An oriented ensemble of nuclei is selected via the conservation of angular momentum, by detecting the first radiation of the cascade along a particular direction. The precession of the nucleus during the intermediate state is then observed by monitoring the angular distribution of the second radiation as a function of time. This effect is usually displayed by forming a ratio $R(t)$ of the radiation patterns measured at several angles. The theory for this effect is well established and the time-dependence of $R(t)$ can be written in a simple form.[5] Each unique defect structure causes a unique quadrupole interaction and a term $s_0 + \sum_{n=1}^{3} s_n \cos \omega_n t$ in $R(t)$. There is one such term for each unique structure. The strength and symmetry of the quadrupole interaction (described by parameters ν_Q and η, respectively) determine the frequencies ω_n. The coefficients s_n are determined by the symmetry of the interaction and the orientation of the electric field gradient tensor relative to the detectors. The magnitude, symmetry, and orientation of the tensor describing the gradient of the electric field can be deduced by fitting the theoretical equation to experimental data. Because these field gradient arise from asymmetries in the distribution of charge near the probe nucleus, the structure of the complex can often be deduced or inferred.

3 RESULTS

The two materials studied, AgBr and AgCl, have very similar structure and properties. The most important differences are the polarizabilities and sizes of the anions; bromine's ionic radius is larger than chlorine's by about eight percent, and its polarizability is larger by about one third. Slight differences also exist in the polarizability of the silver ion within the two materials. These microscopic differences manifest themselves as differences of a few percent in such bulk properties as melting point, cohesive energy, dielectric constant, and diffusion energies.[6]

Surprisingly, the behavior of In–V_{Ag} defect complexes shows qualitative differences. In AgCl a transition in the structure of In_{Ag}–$2V_{Ag}$ complexes occurs between 120 K and 180 K, centered at about 130 K. Below this temperature two structures occur with approximately equal probability. PAC data show that these defects have the structure shown in Figure 1(a) and (b), both having vacancies at next-nearest silver sites to the indium. Both of these structures nearly vanish above the transition (one completely, the

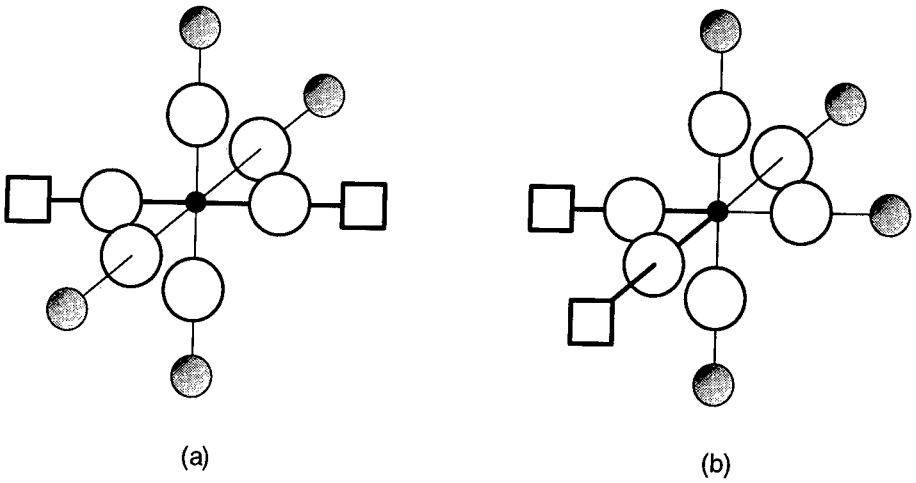

FIGURE 1 The structure of defects involving the trivalent ion of indium in silver chloride and silver bromide. The small filled circles represent indium ions, the large unfilled circles represent halogen ions, the shaded circles represent silver ions, and the squares represent vacant silver sites. The defects shown in the figure both appear in both materials, AgCl and AgBr. In silver chloride both defects occur below the 130 K transition, and vanish, for the most part, above the transition. In AgBr the defects shown in (a) and (b) dominate below and above the 80 K transition, respectively.

other by about 90%) replaced by a new defect whose structure has not yet been determined. This temperature-reversible transition is probably a result of vibrational effects that change the relative stability of two different structures as the temperature is changed. The relative probability for the occurrence of the low and high temperature structures at a certain temperature is given by a ratio of Boltzmann factors in the Gibbs free-energy. Analysis in terms of this formalism provides $\Delta h = 64 \pm 5$ *me*V and $\Delta s = 5.7 \pm 0.5 k_B$ for the enthalpy and entropy differences between the two structures (Ref. 3). The entropy difference reflects both structural and vibrational contributions. No significant change in the structure of defect complexes is seen below about 120 K (Ref. 2), consistent with bulk diffusion parameters.

In *AgBr*, in contrast to AgCl, no significant change is observed in the defect structure between 120 K and 180 K. There is, however, a transition at a much lower temperature (around 80 K), most likely *between* the two structures shown in Figure 1(a) and (b), which in AgCl occur together below the 130 K transition. The structure seen *above* this 80 K transition in AgBr is apparently very similar to that shown in Figure 1(b). The PAC signature is in most respects identical to that seen for this defect in AgCl. The orientation of the main ('zz') axis of the principal axis system of the electric field gradient tensor is the same ($\langle 100 \rangle$) in AgCl and AgBr. The fundamental quadrupole interaction frequency ν_Q is also very similar, smaller in *AgBr* by an amount that scales with the lattice constant cubed, as expected for the quadrupole interaction in an ionic material. But the asymmetry parameter η, which can take on values between zero and one (zero describes a structure with a three-fold symmetry axis) differs dramatically. The asymmetry parameter is very close to zero for the AgCl complex and is very large—approaching 0.5—in AgBr. This profound difference probably arises from different ionic displacements and polarizations in AgCl and AgBr. A detailed analysis of this difference is required and is in progress.

Below 80 K for AgBr, the structure shown in Figure 1(a) seems to dominate, as the PAC signature of the defect commonly seen at this temperature is identical in almost every respect to the corresponding defect in AgCl: size, symmetry and orientation of the efg tensor are the same to within the margin of experimental error. Analyzing this transition in terms of equilibrium thermodynamics allows us precisely to determine differences in thermodynamic parameters between the two structures. This analysis reveals an enthalpy difference of about 30 meV between the two complexes shown in Figure 1, and an entropy difference of between 5 k_B and 6 k_B. The details of this transition are complex and elusive, varying from one sample to another and from run to run within the same sample. The treatment presented here has been abbreviated because of length limitations.

That any structural change should occur at such a low temperature is extraordinary, since a free vacancy in *AgBr* makes approximately six jumps per year at 80 K. Subtle changes in the structure of the low-temperature complex occur at still lower temperatures, as low as 50 K. Free vacancies at this temperature succeed at jumping from site to site only once every 10^{12} years. PAC data suggest that the processes responsible for the 50 K and 80 K transitions are different, since the rates at which the transitions occur at the two temperatures cannot be described by a single Arrhenius relationship. It is likely, then, that the subtle effects seen at the lowest temperatures involve very small adjustments in the positions of the ions (the small indium ion in particular), perhaps between centered and uncentered positions. It is probable that the rearrangement seen at 80 K involves a site-to-site hop, as inferred from our model that the transition is from the structure of Figure 1(a) to that of Figure 1(b). The apparent enhancement in this rate, relative to free-vacancy migration, can perhaps be explained by the extra space left in the lattice when three silver ions are replaced with a single, rather small, indium ion.

ACKNOWLEDGEMENTS

The authors gratefully acknowledge the assistance of: NSF grant DMR-9200295; Mr. Charles Childs who grew the crystals used in these experiments; and Prof. Larry Slifkin for many productive discussions.

REFERENCES

1. R. S. Eachus and Myra T. Olm, *Cryst. Latt. Def. and Amorph. Mat.* **18** (1989) 297.
2. J. C. Austin, *et al., Phys. Rev.* **B42** (1990) 7699.
3. J. C. Austin, *et al., J. Phys.: Condens. Matter* **5** (1993) 8829.
4. J. C. Austin, *et al.*, in press.
5. T. Butz, *Hyperfine Interactions* **52** (1989) 189.
6. Robert J. Friauf, from *The Physics of Latent Image Formation in Silver Halides*, ed., A. Baldereshi, *et al.* (World Scientific, 1984), p. 79.

Radiation Effects and Defects in Solids, 1995, Vol. 134, pp. 389–393
Reprints available directly from the publisher
Photocopying permitted by license only

© 1995 OPA (Overseas Publishers Association)
Amsterdam B.V. Published under license by
Gordon and Breach Science Publishers SA
Printed in Malaysia

COLOR CENTERS IN MIXED CRYSTALS OF ALKALI SILVER HALIDES AND AMMONIUM SILVER HALIDES

T. AWANO and T. MATSUYAMA*

Department of Applied Physics, Tohoku Gakuin University, Tagajo 985, Japan;
**Research Reactor Institute, Kyoto University, Osaka 590-04, Japan*

ESR study was executed on the mixed crystal of rubidium silver iodide and ammonium silver iodide. In $(Rb_{0.9}(NH_4)_{0.1})_2AgI_3$ γ-rayed at 77 K, I_2^- was on the horizontal edge of the iodine tetrahedron that chained by each other in the direction parallel with the *b*-axis of the crystal. I^0 was on one of the iodine ion on the horizontal edge of the iodine tetrahedron and slightly distributed to one of near ammonium ions. Their hyperfine parameters were approximately the same as those in the ammonium silver iodide or alkali silver iodides. I_2^- : $|A_{//}| = 42.0$ mT, $|A_\perp| = 19.5$ mT, $g_{//} = 1.91$, $g_\perp = 2.57$. I^0: $|A_{//}| = 51.0$ mT, $|A_\perp| = 21.0$ mT, $g_{//} = 1.99$, $g_\perp = 2.26$. The I_2^- and I^0 were thermally more stable than those in the each component crystal.

Key words: alkali-ammonium silver halide, self-trapped hole, one center, V_K center, I^0, ESR.

1 INTRODUCTION

γ-ray irradiation induces self-trapped holes (STHs) of the form of I^0 in alkali silver iodides[1] or $(halogen)_2^-$ and $(halogen)^0$ in ammonium silver halides.[2,3] The $(halogen)^0$ is weakly coupled with the nearest alkali metal ion or ammonium ion. It is able to be denoted as RbI^+, KI^+, NH_4I^+ or NH_4Br^+. In the case of alkali halides and ammonium halides, there is no difference in the structure of the STHs. It is interesting to investigate the reason those STHs have different forms in alkali silver halides from ammonium silver halides. In this study, we have investigated the structures of self-trapped holes in the mixed crystal of alkali silver halides and ammonium silver halides. We report the structure of self-trapped holes in $(Rb_{0.9}(NH_4)_{0.1})_2AgI_3$ by ESR measurements in this paper.

The crystal structure of $(Rb_x(NH_4)_{1-x})_2AgI_3$ is shown in Figure 1(c). The structure is orthorhombic and belongs to the space group of D_{2h}^{16}. A unit cell is projected into *a*–*c* plane. Each of the four silver ions in a unit cell is surrounded by an iodide tetrahedron that is chained with next one in the direction parallel with the *b*-axis of the crystal. This crystal structure is the same as that of Rb_2AgI_3 shown in Figure 1(a) or $(NH_4)_2AgI_3$ in Figure 1(b).[4] A part of rubidium ions seems to be substituted by ammonium ions in the $(Rb_x(NH_4)_{1-x})_2AgI_3$ crystal considering from x-ray diffraction analysis. Detail of this analysis will be described elsewhere. Directions d1 and d2 in Figure 1(a) show those of the distribution of I^0. I^0 exists only on two sorts of iodide site I(I) and I(III).[1] Directions d1 and d2 in Figure 1(b) show those of the distribution of X^0 in $(NH_4)_2AgX_3$(X = Br, I). In this crystal, X^0 exists on X(I) and X(II). X_2^- exists on each pair of X^-s in the direction parallel to the *b*-axis of the crystal.

2 EXPERIMENTAL

The mixed crystal of alkali silver iodide and ammonium silver iodide were grown in saturated aqueous solution of a mixture of NH_4I, RbI and AgI. Crystals of sizes of about $5 \times 10 \times 25$ mm^3 were obtained by growth for one week. The concentration ratio of Rb

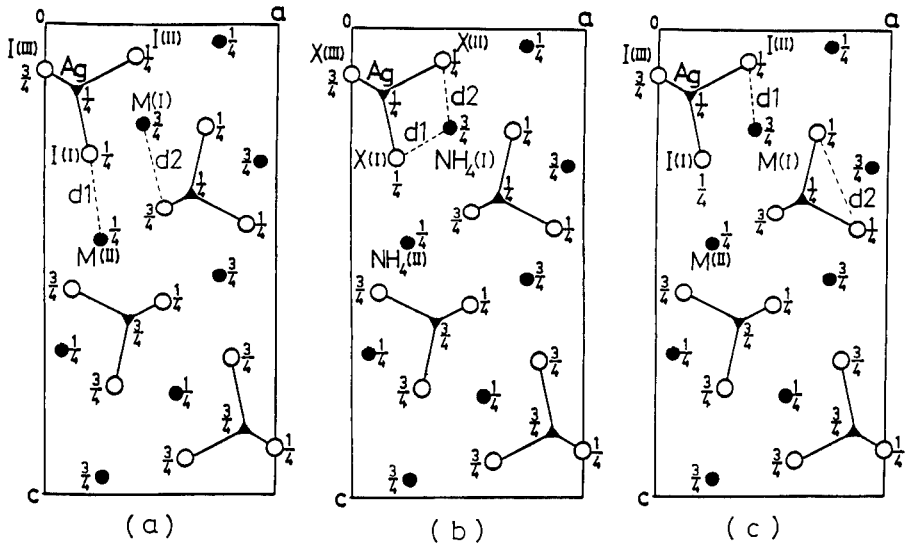

FIGURE 1 Crystal structure of (a) alkali silver iodides, (b) ammonium silver halides and (c) alkali-ammonium silver halides. A unit cell is projected on *a–c* plane. Figures show *b*-coordinates of each ion. 'M' in (a) denotes alkali metal ion. 'X' in (b) denotes halogen ion. 'M' in (c) denotes rubidium or ammonium ion. Directions d1 and d2 are subscribed in the text.

and NH_4 was determined by neutron activation analysis. The dose of γ-ray was about 5×10^7 rad.

3 RESULTS AND DISCUSSIONS

3.1 *Structures of Self-trapped Holes*

Figure 2 shows examples of ESR spectra of $(Rb_{0.9}(NH_4)_{0.1})_2AgI_3$ γ-rayed at 77 K. The measurement temperature was also 77 K. Magnetic field was applied along the *a*-axis of the crystal at the top and along the *c*-axis at the bottom of the Figure 2. Angles in the Figure 2 denote those from the *a*-axis in *a–c* plane. Hyperfine signal of I_2^- was observed clearly at the third figure as shown by 11 vertical lines. Two sets of I_2^- had their uniaxial directions apart 27 degree from the *c*-axis in *a–c* plane, which was concluded from the angular dependence analysis of the peak position of I_2^- signal. These directions almost coincide with those of horizontal edges of iodine tetrahedrons, which is shown as d2 in the Figure 1(c). Hyperfine parameters were; $|A_{//}| = 42.0$ mT, $|A_{\perp}| = 19.5$ mT, $g_{//} = 1.91$, $g_{\perp} = 2.57$. These hyperfine parameters were approximately the same as those in the ammonium silver iodide.[2]

Figure 3 shows examples of ESR spectra when the magnetic field was applied in the *b–c* plane of the crystal. Hyperfine signal of I^0 is clear at the second top figure as shown by 6 vertical lines. Each hyperfine peak was split into three lines that seemed to be the super-hyperfine structure by a nitrogen nucleus. This means that the I^0 is slightly distributed not to a rubidium ion but to an ammonium ion. According to an angular dependence analysis of the peak position of I^0, two sets of I^0 had their slightly distributed directions 40 degree apart from the *c*-axis in the *b–c* plane of the crystal. These directions almost coincide with those between I(II) and M(I) as shown in Figure 1(c) by 'd1'. Hyperfine parameters were;

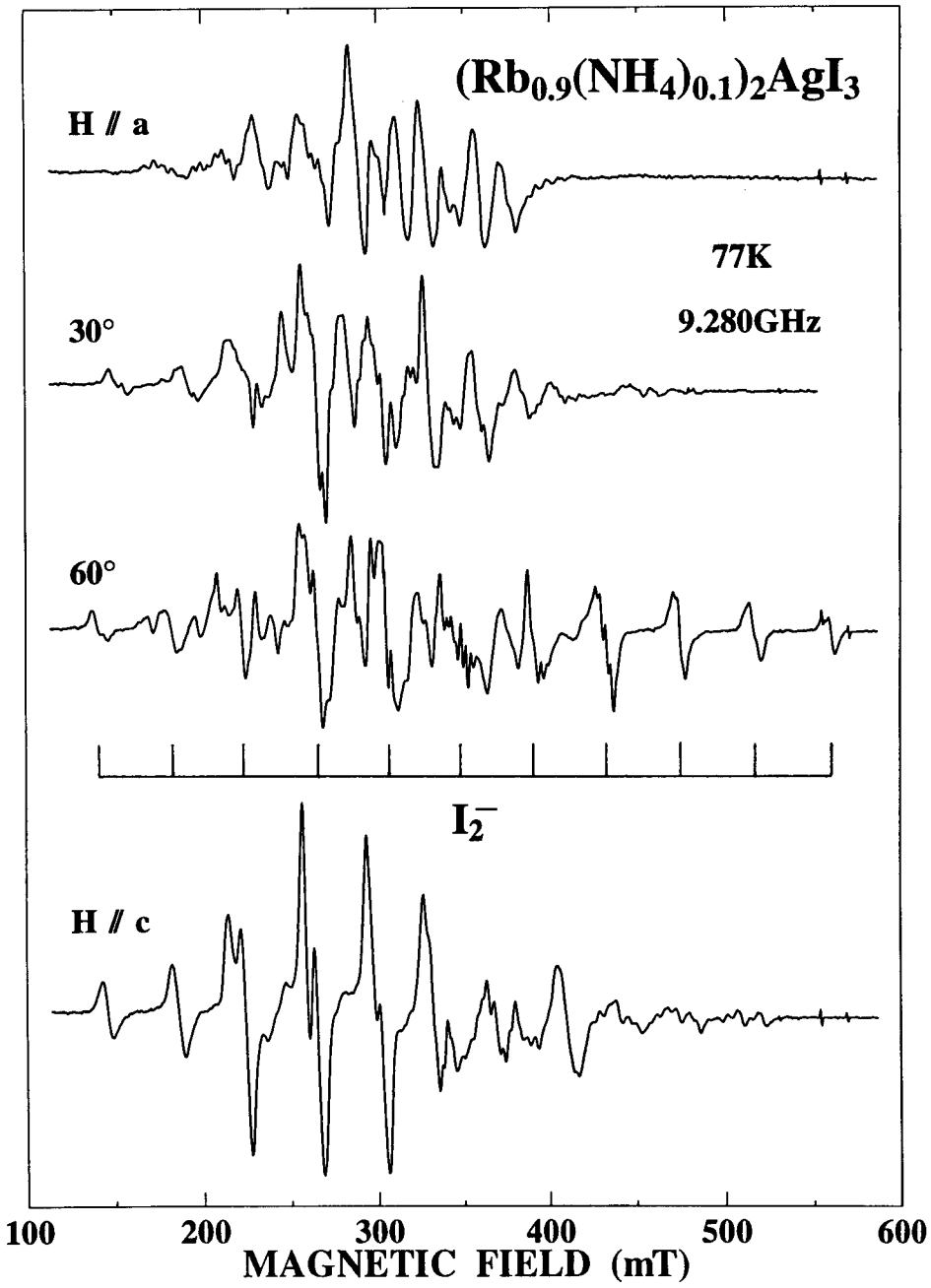

FIGURE 2 ESR spectra of $(Rb_{0.9}(NH_4)_{0.1})_2AgI_3$ γ-rayed at 77 K. Magnetic field was applied in the a–c plane of the crystal.

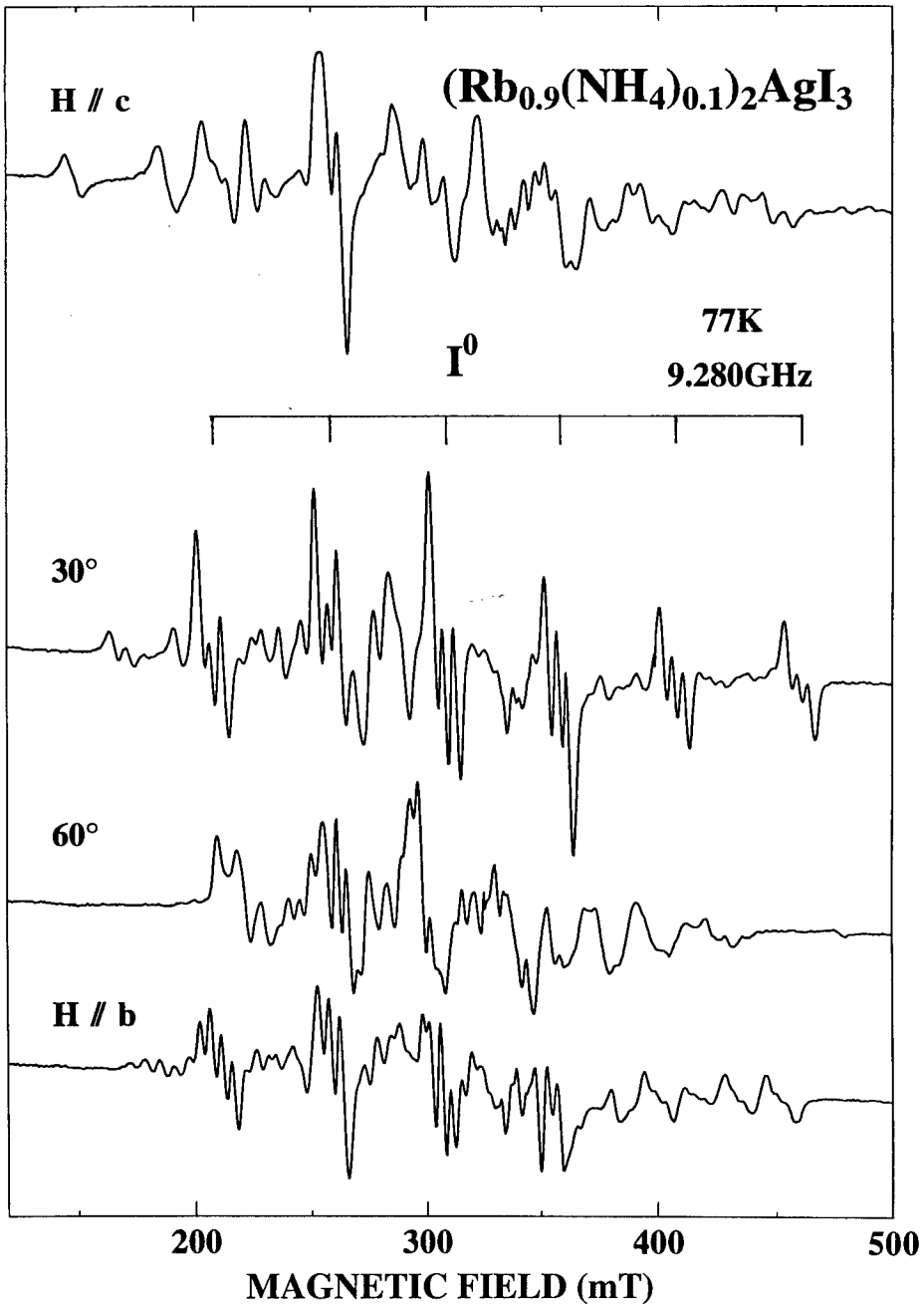

FIGURE 3 ESR spectra of $(Rb_{0.9}(NH_4)_{0.1})_2AgI_3$ γ-rayed at 77 K. Magnetic field was applied in the *b*–*c* plane of the crystal.

$|A_{//}| = 51.0$ mT, $|A_{\perp}| = 21.0$ mT, $g_{//} = 1.99$, $g_{\perp} = 2.26$. These hyperfine parameters were approximately the same as those in the alkali silver iodides[1] or the ammonium silver iodide.[2]

These directions of I^0 and I_2^- are different from those in the alkali silver iodides[1] and the ammonium silver halides.[2,3] I^0 is oriented nearly parallel to the *c*-axis in alkali silver iodides.[1] This direction coincides with the directions of the iodine (I) and (III) to the alkali metal which are drawn as d1 and d2 in the Figure 1(a) by dashed lines. I^0 is oriented in other directions in ammonium silver halides.[2,3] They are almost coincident with the direction from halogen ion (I) or (II) to the ammonium ion (I) in Figure 1(b) as shown by d1 and d2. In the result of this study in $(Rb_{0.9}(NH_4)_{0.1})_2AgI_3$, I^0 exists only in iodine ion (II) and slightly distributes only to NH_4^+(I) in Figure 1(c). The V_K center directs itself parallel to the *b*-axis in the ammonium silver halides.[2,3] This direction is the same as that between two iodine ions on a vertical edge of an iodide tetrahedron chained each other in the direction parallel to the *b*-axis of the crystal. In this result of $(Rb_{0.9}(NH_4)_{0.1})_2AgI_3$, I_2^- is in two iodine ions on the horizontal edge of the iodide tetrahedron.

3.2 *Thermal Decay*

Each of the I_2^- and I^0 in $(Rb_{0.9}(NH_4)_{0.1})_2AgI_3$ crystal decayed at 250 K and 240 K in an annealing process. Comparing with the alkali silver iodides and the ammonium silver iodide, I_2^- and I^0 were stable in the mixed crystal in the annealing process. The $(halogen)^0$ decays at 150 K in the alkali silver iodides and the ammonium silver halides.[1–3] The V_K center decays at 170 K in the ammonium silver halides. The structural conversion of $(halogen)_2^-$ occurs around 200 K in the ammonium silver halides.[2,3] This new V_K center is stable up to 250K and disappears at 280 K. This conversion did not occur in the $(Rb_{0.9}(NH_4)_{0.1})_2AgI_3$ crystal.

4 CONCLUSION

The structures of self-trapped holes induced in the mixed crystal of the alkali silver iodide and the ammonium silver iodide are almost the same as those in each component crystal. Their orientations are, however, different from those in each component crystal. They are thermally stable comparing with those in each component crystal. These facts suggest that small differences of site energies resulted into rather large differences of the stability of the STHs.

ACKNOWLEDGEMENT

This work was executed under the visiting researcher program of the Research Reactor Institute of Kyoto University.

REFERENCES

1. T. Awano, M. Ikezawa, T. Matsuyama and H. Yamaoka, *J. Phys. Soc. Jpn.*, **58**, 2570 (1989).
2. T. Awano, M. Ikezawa, T. Matsuyama and H. Yamaoka, *Defect in Insulating Materials* (World Scientific, Singapore, 1993), vol. 1, pp. 491.
3. T. Awano and T. Matsuyama, Nucl Intrum. Methods, **B 91**, 227 (1994).
4. C. Brinc and H. A. S. Kroese, *Acta Cryst.* **5**, 433 (1951).

Radiation Effects and Defects in Solids, 1995, Vol. 134, pp. 395–399
Reprints available directly from the publisher
Photocopying permitted by license only

© 1995 OPA (Overseas Publishers Association)
Amsterdam B.V. Published under license by
Gordon and Breach Science Publishers SA
Printed in Malaysia

ON F-AGGREGATE CENTRE FORMATION IN KCl CRYSTALS CONTAINING O^{2-}-VACANCY COMPLEXES

P. RAERINNE and P. KETOLAINEN

Väisälä Laboratory, Department of Physics, University of Joensuu, P.O. Box 111, FIN-80101 Joensuu Finland

The formation of F-aggregate colour centres was studied in oxygen-doped KCl crystals. Compared to the undoped crystals, a remarkably enhanced F → M (F_2) conversion and an increase of absorption in the N band region were obtained after white light exposure at RT. An aftergrowth of M absorption after a short (10 s) exposure was also observed.

Key words: Colour centres, F-aggregates, photosensitivity.

1 INTRODUCTION

Oxygen-doped alkali halide crystals containing colour centres are used as active components of tunable lasers. In order to produce laser active $(F_2^+)_H$ centres, e.g. an F_2^+ centre associated with a doubly charged chalcogenide ion, in additively coloured crystals a two step light exposure process has been used. First, a heavily coloured crystal is exposed near RT with F-band light to generate the active units, and second, an exposure at LNT orients the centres in their most stable configuration.[1] Quite recently the authors have produced these centres by using electrolytic coloration of partially doped KCl:KNO_3 crystals.[2]

In all the studies published so far on chalcogenide doped coloured crystals no real attention has been paid to the photosensitivity of the crystals and especially to the formation of different F-aggregate centres. The understanding of these properties was the goal of the present study.

2 EXPERIMENTAL

KCl crystals were grown in Ar atmosphere by the Czochralski method. During the growth the crystal was partially doped by adding small amounts of KNO_3 in the melt, when the crystal had reached a height of ~ 15 mm. This partial doping technique was used to help the electrolytic coloration, because a direct electron injection in the oxygen-doped crystal is very difficult or even impossible to perform.[2]

The KNO_3 doping tends to concentrate into thin and sharp layers which form immediately after the doping addition. Because of that property the doping pills (0.2 mg KNO_3 mixed with KCl powder) were added stepwise into the melt. As a result the topmost part of the crystal bulk was undoped, whereas below it there were several doped layers. The first one of them contained a nominal doping of 5 ppm in the melt (0.2 mg KNO_3 in 40 g KCl) whereas in the others the doping increased gradually towards the bottom of the crystal.

When dropped in the KCl melt the KNO_3 doping immediately decomposes into KNO_2 and O_2. The characteristic peaks of the NO_2^- molecule (at 1385, 1275, and 820 cm^{-1} were

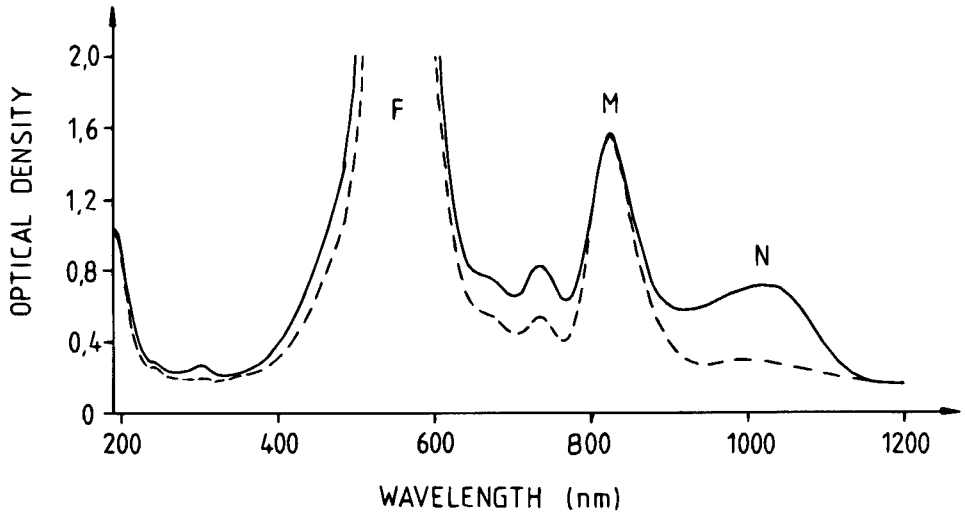

FIGURE 1 Absorbance spectra of coloured KCl/KNO_3 (solid line) and KCl (dashed line) crystal samples (thickness 2 mm) after white light exposure at RT. Exposure times were 110 s for KCl/KNO_3 and 16 min for KCl. The spectra are measured at RT.

observed in IR spectra of heavily doped crystals. The oxygen gas liberated in that process causes some small bubbles in the doped layers.

Crystal rods (20 × 12 × 12 mm) cleaved from the crystallized bulk and containing pure KCl and three or four doped layers were coloured electrolytically by the matrix-cathode technique.[3] When the colour centre diffusion enters the doped layer, each O_2^- ion reacts with three F-centres and accordingly two [O^{2-}- anion vacancy] complexes are formed. This reaction makes the F-centre diffusion slower, and the F-centre concentration higher in the doped layers than in the other parts of the coloured crystal. By that means it was easy to recognize the doped layers in the electrolytically coloured crystal rods. Equal rods were also coloured additively to compare these two methods. In these rods the colour was homogeneous, and the doped layers were found with the help of the electrolytically coloured ones. The obtained F-centre concentration was quite high, varying in the range of $1 - 3 \times 10^{17}$ cm^{-3}.

Samples for the measurements were cleaved from the coloured crystal rods. Each sample (~ 2 mm thick) contained one oxygen-doped layer. For comparison, also one undoped sample was cleaved just next to the first doped layer. The samples were heated at 600°C for 2–3 min and quenched in dark on a copper plate to remove aggregate colour centres before experiments. However, it was not possible to fully remove these aggregates in doped samples.

The samples were exposed with slide projector (unfiltered white light from 150 W tungsten lamp) at different temperatures. The growth of aggregate bands was measured with a spectrophotometer, which was equipped with a liquid-nitrogen cryostat.

3 RESULTS

The oxygen-doped samples showed a remarkably increased photosensitivity compared to the undoped ones. Typically, at room temperature an exposure of 1–2 min led to

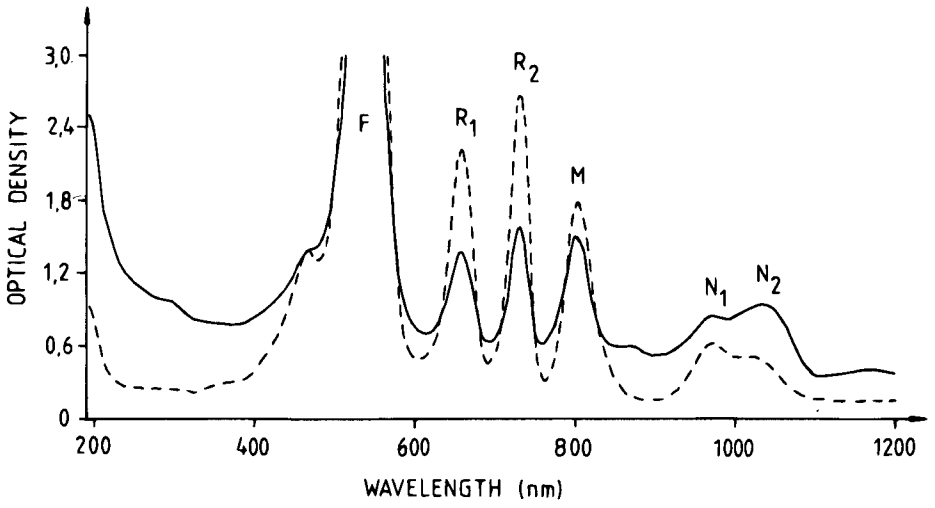

FIGURE 2 Absorbance spectra of coloured KCl/KNO_3 (solid line) and KCl (dashed line) crystal samples (thickness 2 mm) after prolonged white light exposure at RT. Exposure times were 9 min for KCl/KNO_3 and 45 min for KCl. The spectra are measured at LNT.

M(F_2)-band saturation, whereas in undoped KCl ten times longer exposures were needed (Figure 1). Short exposure produced also simultaneously remarkably high absorption in the N band region in doped samples.

A prolonged exposure led to the formation of R (F_3) and N centres. In doped samples the peak wavelengths of all other absorption bands (F, R, M, and N_1) coincide well with those of undoped KCl and with previously known values at LNT.[4] However, the N_2 band has shifted 10 nm (1024 nm → 1034 nm at LNT) towards longer wavelengths in doped samples (Figure 2).

In doped samples, the N-absorption rapidly increases at the beginning of the white light exposure. In the early phase of that process, until the M band has saturated, the ratio of the two N-band heights is like in undoped samples, the N_1 band being higher than N_2. In later phase the N_2 band increases faster, and finally it is higher than the N_1 band. The relative heights of these bands can be changed with different exposures, but the situation obtained is not stable: the N_2 band grows further to some extent also during storage in dark at RT.

Further, in doped samples an aftergrowth of the M (F_2) absorption after a short (10 s) exposure was observed. This aftergrowth process lasted several minutes at RT (Figure 3) and it was also checked below RT, where the phenomenon became weaker and diminished at −10°C. At lower temperatures (below −30°C) the ostensible change in the M absorption (a rapid increase during the exposure and then a decrease to original value) was due to the formation of F′ centres. The broad absorption band of those centres raised the backround absorption of the M band, and gradually diminished after the exposure. This low-temperature behaviour was similar in doped and undoped samples.

The comparison between electrolytically and additively coloured samples showed no difference in this aftergrowth process.

4 DISCUSSION

The experiments show that even a few ppm oxygen doping can remarkably enhance the photosensitivity of coloured KCl crystals. Obviously the enhanced tendency to form

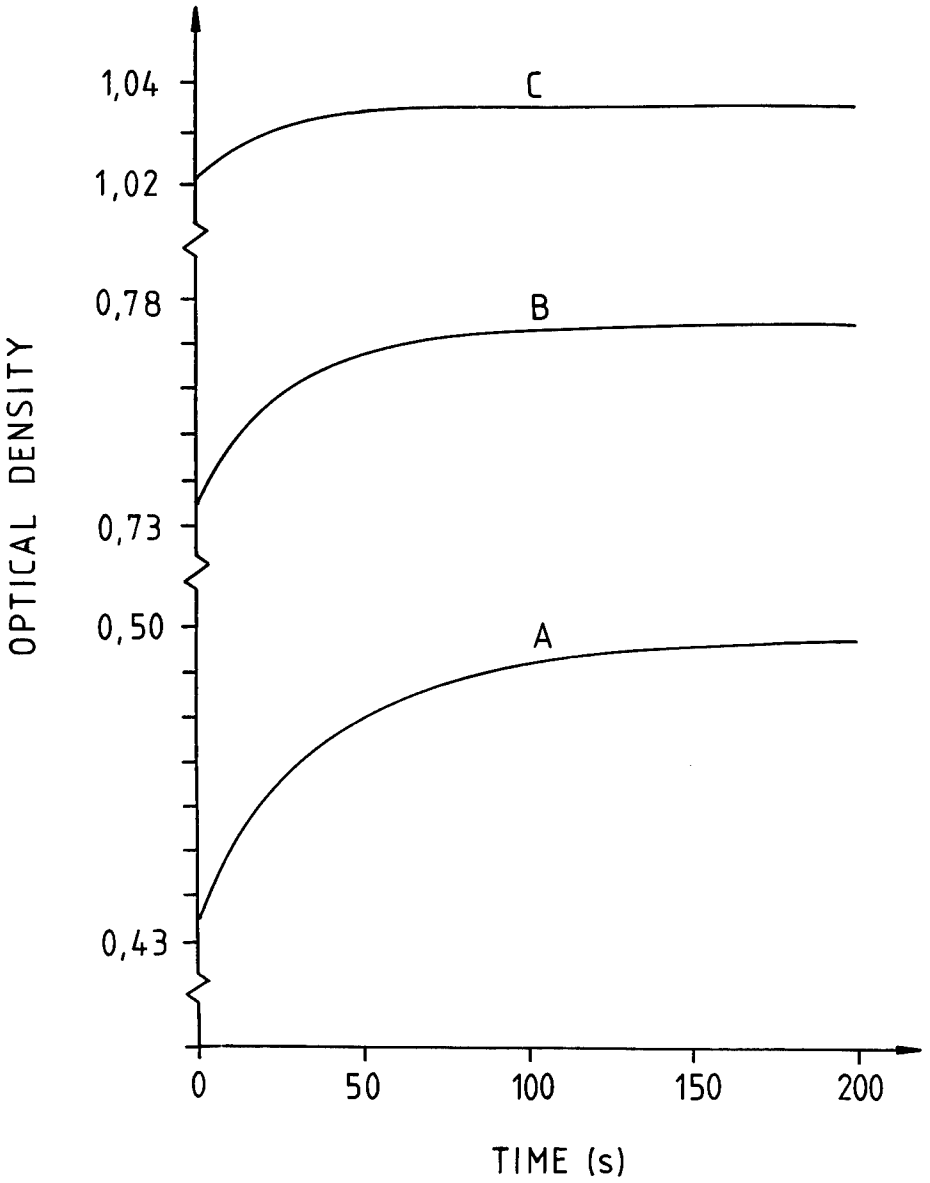

FIGURE 3 Aftergrowth of optical density at 821 nm due to short light exposures in KCl/KNO_3 sample. The timedrive curves A, B and C are measured after successive white light exposures each lasting 10 s.

F-aggregate centres requires a suitable low F-centre concentration compared to the concentration of [O_2^--anion vacancy] complexes. A strongly increased sensitivity was observed in the samples, where the F-concentration was reduced by several thermal treatments: a 10 s exposure was enough to raise the M absorption near to the saturation.

The absorption bands located near 1000 nm need a special attention. The slightly shifted N_2 band in undoped KCl sample (1024 nm; 1019 nm in[4]) is probably due to the exposure temperature, which was RT (293 K) in this study, but 260 K in.[4] The observed 15 nm shift in doped sample may be due to several overlapping bands in the N_2 region.

REFERENCES

1. S. Girard and J. L. Doualan, *J. Phys.: Condensed Matter* **5**, 1811 (1993).
2. P. Raerinne and P. Ketolainen, *Solid State Comm* **86 (11)**, 699 (1993).
3. P. Raerinne, *Meas. Sci. Technol.* **3**, 75 (1992).
4. E. Georgiou and C. Pollock, *Phys. Rev.* **B44 (13)**, 6608 (1991).

Radiation Effects and Defects in Solids, 1995, Vol. 134, pp. 401–404
Reprints available directly from the publisher'
Photocopying permitted by license only

© 1995 OPA (Overseas Publishers Association)
Amsterdam B.V. Published under license by
Gordon and Breach Science Publishers SA
Printed in Malaysia

A LIGHT INDUCED CONFIGURATIONAL CHANGE OF F_A CENTRES IN Li DOPED KCl-KBr CRYSTALS

P. KETOLAINEN* and P. SILFSTEN**

**Department of Physics, University of Joensuu, P.O. Box 111, FIN-80101 Joensuu, Finland; **Department of Information Technology, Lappeenranta University of Technology, P.O. Box 20, FIN-53851 Lappeenranta, Finland*

Spectroscopic properties of F_A centres in Li doped KCl-KBr mixed crystals were studied. At low temperature light induced spectral shifts, for the F_{A1} band towards lower energy and for the F_{A2} band towards higher energy, were observed. The shifts are proposed to be due to a configurational change where the electron occupied vacancy finds a new location in relation to the neighbouring chlorine and bromine ions. The recovery to the original configuration, obtained in the $F \rightarrow F_A$ conversion, is a temperature activated process.

Key words: alkali halides, mixed crystals, colour centres, F_A centres.

1 INTRODUCTION

There has been a continuous research interest in F_A centres of alkali halides which have been used in laser applications. Their basic properties, as their type I and II classification, are well known,[1] but some structural problems, e.g. off-axis behaviour, have kept the interest vivid. In case of mixed alkali halides F_A centres have been studied only in Li doped KCl-KBr system. Asami and Ishiguro[2] showed that this system has both type I and type II emissions relating to different relaxed excited state (RES) configurations. However, they observed only one pair of absorption bands, namely F_{A1} and F_{A2}. At 1.6 K they measured a peak separation of F_A bands under applied pressure. In case of $KCl_{0.78}Br_{0.22}$ this band splitting showed abrupt changes that the authors related to transitions between off-centre and on-centre configurations.

In KCl-KBr mixed crystal the F_A(Li) centre electron is surrounded by five K^+ ions and the Li^+ ion. Further, the impurity Li^+ itself is surrounded partly by chlorine and partly by bromine ions, their relative numbers depending on the composition. The arrangement of the ions dictates, the Li^+ ion in an off-axis position or not, and accordingly the nature of the RES configuration. Following their emission measurements Asami and Ishiguro concluded, that the centre goes to the RES of type II via the RES type I with a thermally activated process.

The facts mentioned above led us to consider if there might be light induced configurational changes of F_A centres in Li doped KCl-KBr which should express themselves in absorption spectra. In this paper we show, that this was really the case.

2 EXPERIMENTAL

Five different compositions (14, 24, 49, 74, and 84 mole% KCl in the melt) as well as 'pure' KCl and KBr doped with one mole% of Li were crystallized by Czochralski method in Argon atmosphere. The crystals were coloured additively in a Mollenauer type heat pipe oven or electrolytically using the method developed in our laboratory.[3] Before measurements the coloured crystals were quenched from 500°C to RT on a copper plate. The sample was then mounted in an optical cryostat which allows to reach every

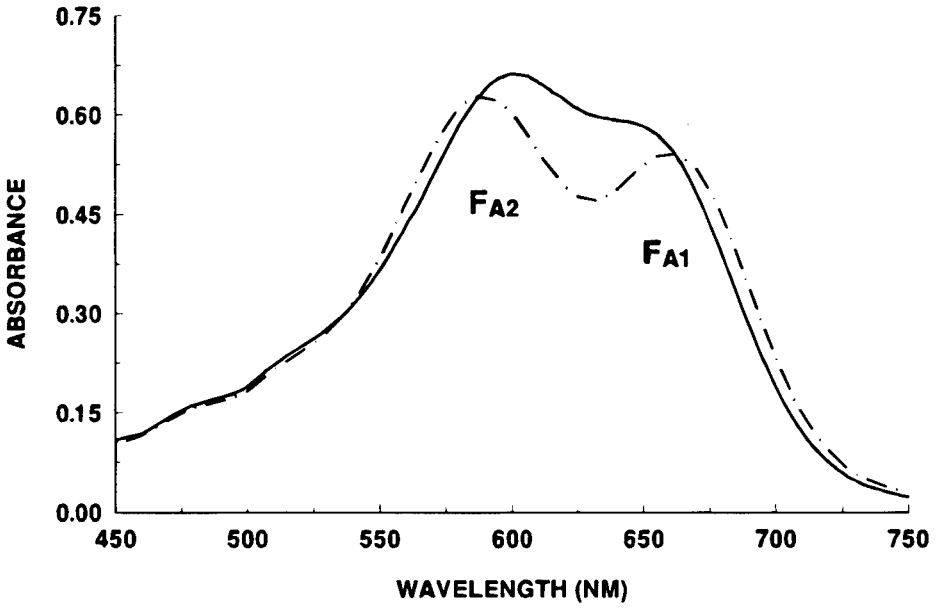

FIGURE 1 Absorption spectra of F_A centres in KCl-KBr mixed crystal containing 49 mole% KCl. The curves are recorded at LNT before (solid line) and after (dashed line) white light exposure.

temperature between RT and LNT. The $F \rightarrow F_A$ conversion was carried out at RT or at $-20°C$ without any significant difference between these two temperatures. The absorption spectra were recorded with a Perkin-Elmer Lambda 9 spectrophotometer, and for comparing and manipulating the spectra a Perkin-Elmer computerized spectroscopy software was applied. The light source for exposures was a projector lamp equipped with a set of Oriel filters with a half width of 10 nm and covering the range 400–740 nm with 20 nm intervals.

3 RESULTS AND DISCUSSION

After the $F \rightarrow F_A$ conversion the crystal was immediately cooled down to LNT and its absorption spectrum was recorded. Then it was exposed for 10 min with white light and the spectrum was recorded again. For every mixed composition, but not for 'pure' KCl and KBr, a clear shift for the F_{A1} band towards lower energy and for the F_{A2} band towards higher energy was observed. Figure 1 shows the spectra for the composition of 49 mole% KCl. In energy scale the shifts are of the size of 0.02 eV and 0.01 eV for F_{A1} and F_{A2} bands, respectively.

It is well known that if the F_A centres are exposed at low temperature with monochromatic light, polarized or even unpolarized one, the centres will reorient. After a prolonged exposure with unpolarized light a steady state is reached, where the distribution of the centres in the different crystal axis directions is dependent on the pumping wavelength, i.e. on the extent the two F_A bands overlap each other at that particular wavelength. This phenomenon was applied as follows when searching the explanation for the energy split.

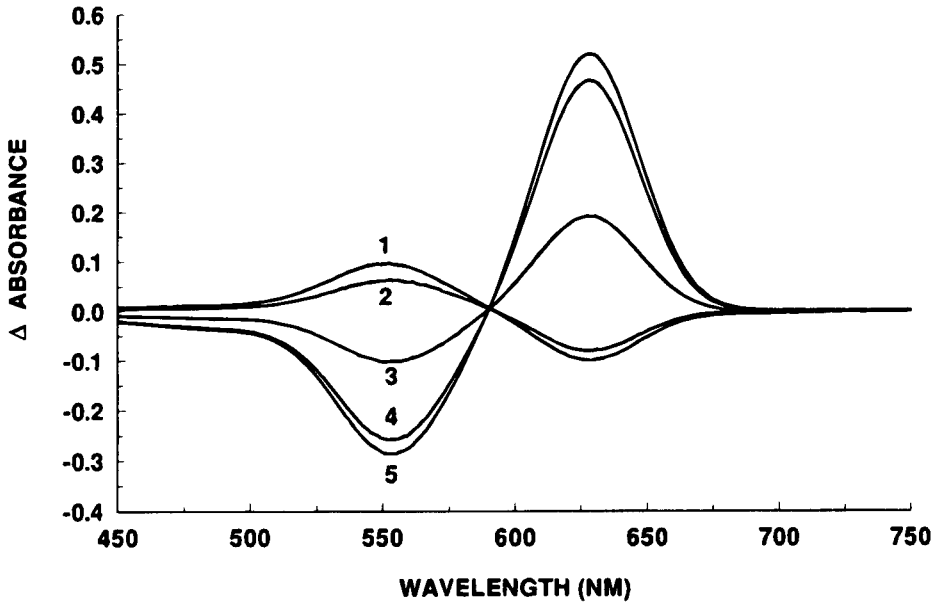

FIGURE 2 Differences of absorption spectra of oriented F_A centre distributions in unmixed KCl. Curves 1, 2, 3, 4, and 5 present differences between the original F_A spectrum and those obtained with unpolarized light exposure at 540, 580, 600, 620, and 680 nm, respectively.

At first an unmixed KCl crystal was cooled down to LNT, its absorption spectrum was recorded, whereafter it was successively exposed to a steady state pumping with the wavelengths of 540, 580, 600, 660, and 680 nm. Then each spectrum was subtracted from the original LNT one. Figure 2 presents the difference curves all of which have one common intersection point. This means that the exposures induce only reorientational changes for units of equal structure. Similar results were obtained also for unmixed KBr.

For mixed crystals the behaviour was different as shown in Figure 3. A mixed crystal containing 49% KCl was cooled down to LNT and then exposed to a steady state pumping with the wavelengths of 540, 600, 620, 640, and 700 nm. Each spectrum was then subtracted from that one corresponding to 600 nm. The difference curves do not intersect anymore at the same point and neither their maxima nor minima stay fixed. This behaviour is an evidence that there is a structural change in the F_A centres together with the reorientation. Most probably the electron occupied vacancy finds at low temperatures an energetically more favored position in relation to the neighbouring chlorine and bromine ions compared to that one obtained in the $F \rightarrow F_A$ conversion. The exposures with different wavelengths at LNT, described in Figure 3, induce jumps to these positions and away from them at different rates. The same type of behaviour was observed for all the other compositions. There is no hint to relate the spectral changes to transitions between on-axis and off-axis positions of the Li^+ ion.

When heating the sample, whose behaviour was described in Figure 1, back to RT in the dark and measuring its spectrum at LNT, the crystal gave the same spectrum as after the original $F \rightarrow F_A$ conversion. Thus the recovery is a temperature activated process, and it was observed starting to occur remarkably at about $-50°C$.

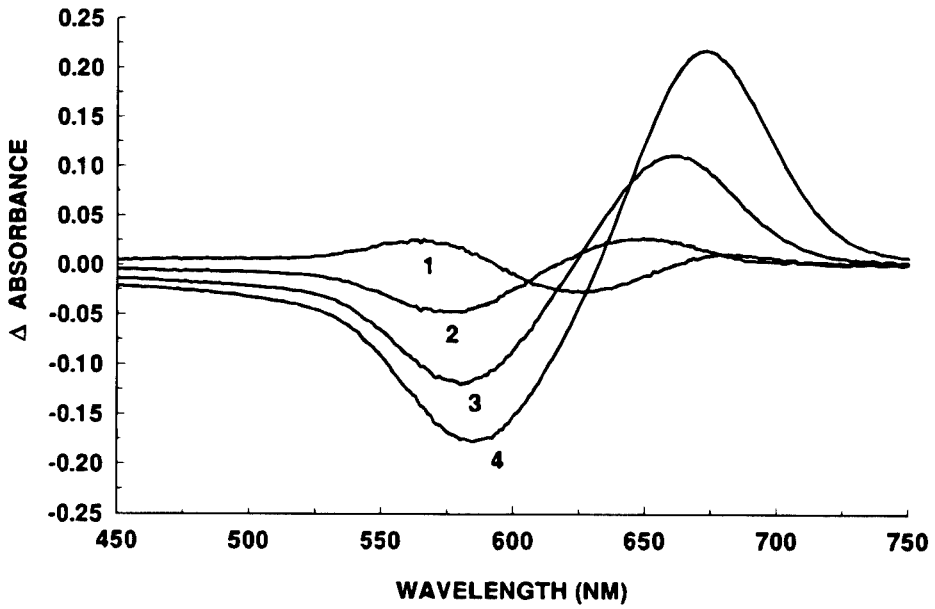

FIGURE 3 Differences of absorption spectra of F_A centre distributions in KCl-KBr mixed crystal containing 49 mole% KCl. The crystal was exposed with unpolarized light at the wavelengths of 540, 600, 620, 640, and 700 nm. The curves 1, 2, 3, and 4 present differences between the 600 nm spectrum and those of 540, 620, 640, and 700 nm, respectively.

Further, it was looked for the temperature range where the light induced shift of the F_A bands can be realized. The measurements show that starting from $-150°C$ downwards this is possible. Above this temperature the inverse reaction and the simultaneous formation of F_A' centres cancel the process.

REFERENCES

1. F. Lüty, *Physics of Color Centers*, ed. W. B. Fowler (Academic Press, New York, 1968), Chap. 3, pp. 181–242.
2. K. Asami and M. Ishiguro, *Phys. Rev.* **B34**, 4199 (1986).
3. P. Raerinne, *Meas. Sci. Technol.* **3**, 75 (1992).

Radiation Effects and Defects in Solids, 1995, Vol. 134, pp. 405–409
Reprints available directly from the publisher
Photocopying permitted by license only

© 1995 OPA (Overseas Publishers Association)
Amsterdam B.V. Published under license by
Gordon and Breach Science Publishers SA
Printed in Malaysia

E-V ENERGY TRANSFER IN THE $F_H(CN)$ CENTER IN KCl AND CSCl

L. F. CHEN* and K. S. SONG

*Dept. of Physics, Univ. Ottawa, Ottawa, Canada; *Dept. of Physics, Nanjing Normal Univ., Nanjing, China*

The electronic-to-vibrational energy transfer (e-v transfer) between the F center and CN^--molecule in $CsCl(CN^-)$ and $KCl(CN^-)$ is discussed in terms of nonradiative transitions between the electronic excited and ground states of the system. The role of dipole-dipole coupling between the F center and CN^- molecule in the e-v transfer is also considered.

Key words: defects, energy transfer, ionic solids.

1 INTRODUCTION

The F center-CN^- defect pairs, the $F_H(CN^-)$ centers, in alkali halides are of considerable interest and have been extensively studied.[1,2] The most novel and interesting effect appears in the case of $F_H(CN^-)$ in CsCl and CsBr. Electronic excitation of these centers by optical radiation produces an intense CN^- vibrational emission band and at the same time the electronic luminescence is quenched. The F luminescence in undoped caesium halides is not quenched. Although vibrational fluorescence of the CN^- molecule has been observed also in KCl, the efficiency of the conversion is only about 4%, and the electronic luminescence is hardly reduced.[1] Lüty and Dierolf observed that[2] the coupling between the two defects is stronger generally in the CsCl lattice than in the NaCl lattice. They also noted that despite such difference, the e-v transfer process produces always a maximum population in the $\nu = 3 \sim 4$ state of the associated CN^- in both types of materials.

In this paper, we attempt to explain some of the observed properties of $F_H(CN^-)$ in CsCl and KCl on the basis of the adiabatic potential energy surface (APES hereafter) recently obtained from first principles calculations.[3] The configuration coordinates used for the APES are the molecule bond length of CN^-, designated by Q_1, and the distance separating the F center and the CN^- molecule (its mid-point), designated by Q_2. The details of the calculation appeared in Ref. (3). This method treats the excited electron of the F center within the extended-ion approximation, while the CN^- molecule is treated by a CNDO (Complete Neglect of Differential Overlap) code. In the following section we discuss the possible mechanism and factors which are important in the e-v energy transfer process.

2 THE ELECTRONIC-TO-VIBRATIONAL ENERGY TRANSFER

The following points may be considered as important highlights of the experimental observations.

(1) While in KCl the e-v transfer is very weak and the F luminescence undiminished, in CsCl the e-v transfer is very strong, larger than 90% efficiency, and the F luminescence is almost completely quenched.

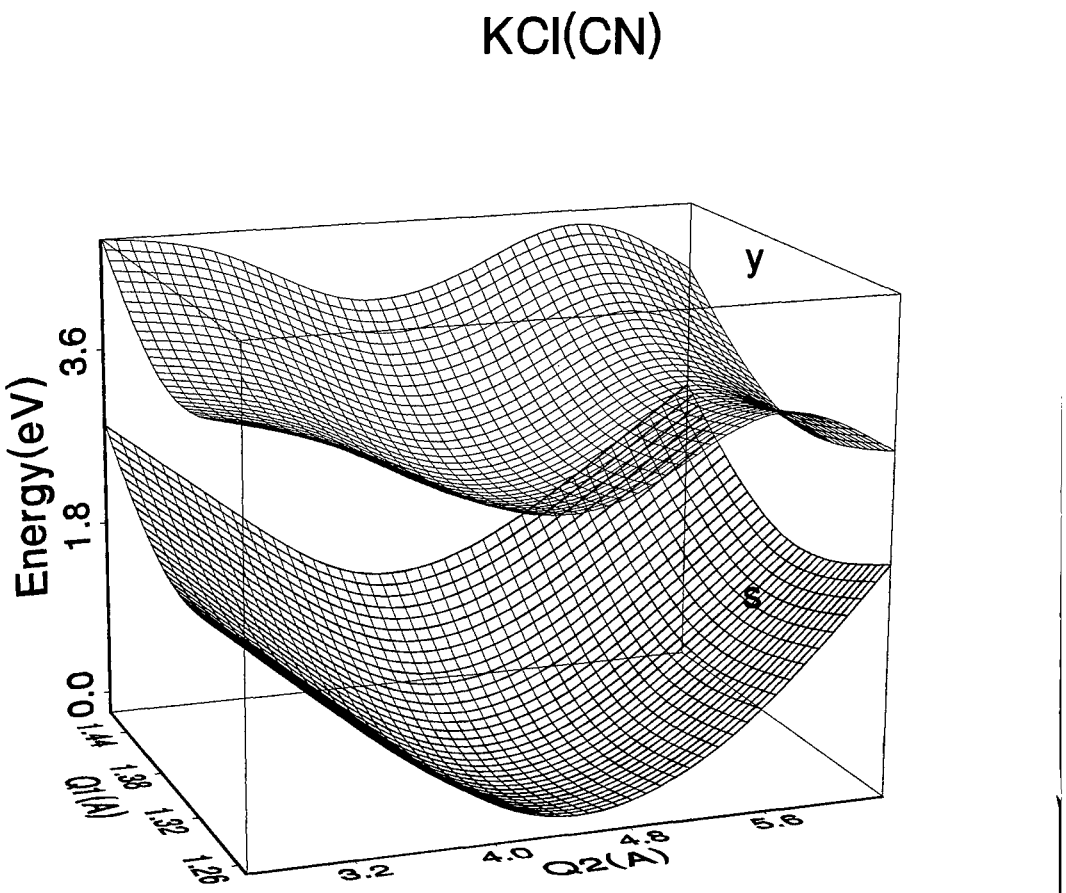

FIGURE 1 The APES of the F_H(CN) system for KCl and CsCl with the F center in p_y-like excited and Franck-Condon ground states. The ground state equilibrium occurs at ($Q_1 = 1.36$ Å, $Q_2 = 4.5$ Å) and ($Q_1 = 1.36$ Å, $Q_2 = 4.6$ Å), respectively for KCl and CsCl.

(2) In crystals of both structure, the strongest e-v transfer occurs to $\nu \cong 4$ level of the CN^- molecule. As the stretching mode phonon energy is about 0.25 eV, this is equivalent to a transfer of about 1 eV from electronic to vibration.
(3) A recent work[4] based on pulsed excitation shows that in CsCl, a very weak luminescence at energy 1.3 eV (the ordinary F luminescence is at 1.255 eV) decays with the same time constant as the vibrational emission rise time.
(4) In CsBr, excitation into the F_H^1 band (the p-orbital parallel to CN^- axis), induces a stronger e-v transfer than with the F_H^2 band (polarized perpendicular to the CN^- axis).

The defect is oriented along the ⟨100⟩ and ⟨110⟩ axes respectively in CsCl and KCl. The APES for the excited p_y state (CN^- along the y-axis) and the Franck-Condon ground state are presented in Figure 1 for KCl and CsCl. We present below two mechanisms

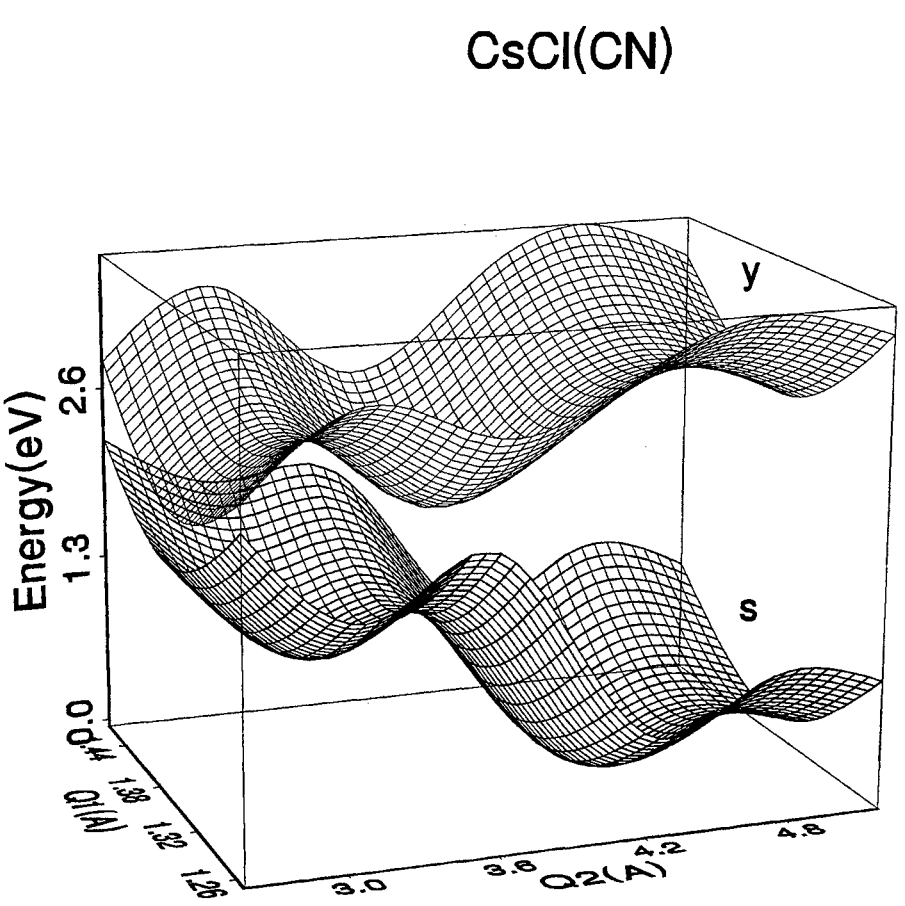

REFER to Figure 1

which could account for the observations enumerated above. One is the non-radiative transition (NRT) from the excited to the ground state and is based on the results shown in Figure 1. The other is the dipole-dipole coupling which was formulated by Dexter[5] in his study of sensitized luminescence and taken up by Halama *et al.*[6] in their papers on $F_H(CN^-, OH^-)$, centers.

Figure 1 shows that the most important difference between the two kinds of material is the intersecting of the excited and ground state APES. The crossing is indicated at about $Q_2 = 2$ Å for the entire range of Q_1 in CsCl, but no crossing occurs in KCl. This is true also for the p_x state.[3] It follows that luminescence is quenched in CsCl, but not in KCl in agreement with observation. The difference between KCl and CsCl is attributable to the lattice structure difference which exerts subtle influences on the interaction between the excited F electron and the nearby molecule. Because of the symmetry around the defect, there is strong interaction between the p_y and s states and result in more complex APES

than for the p_x state.[3] In particular, it is possible that for the p_y state a local minimum exist around $Q_2 \cong 3.6$ Å as seen in Figure 1-b. When the system reaches this region, it can either luminesce, with an energy of $\cong 1.3$ eV, or be transfered to the vibrationally excited states on the ground state APES. It seems quite natural to link the observed strong e-v transfer in CsCl to the crossing (or near crossing) of the APES.

We have also evaluated in an approximate way the permanent dipole moment μ of CN^- in CsCl and KCl on the excited and ground states APES: $\mu = Q_1 \delta q$. Here, δq is related to the Mulliken populations q_C and q_N obtained in Ref (3) as $\delta q = (q_C - q_N)/2$. It was found that in general μ varies monotonically as Q_2 varies from about 4 Å to about 2 Å. When the crossing region ($Q_2 \cong 2$ Å) is reached in CsCl it varies abruptly and substantially (by as much as 50%). At the same time there is substantial difference in the values of μ between the excited and ground states near the crossing. This is brought about by the rapid variation of q which depends on the Madelung potential acting on CN^-, but more importantly on the changing charge density of the excited F electron. Similar variation of μ is absent near the energy minimum in KCl. It is speculated that the dipole moment undergoes a fast fluctuation between the old and new values after reaching the ground state APES, which appears as an excitation of the Q_1 mode, the bondlength. The permanent dipole moment μ_{CN} varies in response to the change in the charge density of the F center (therefore the dipole moment of the F center μ_F). Within a simple model relying only on the NRT, it does not seem possible to explain the excitation of the stretching mode Q_1 and specifically the selective vibrational excitation to $\nu \cong 4$.

In their recent studies, Halama *et al.*[6] have adapted the mechanism which was originally proposed by Dexter to treat the e-e (electronic-to-electronic) energy transfer to that of the e-v transfer. According to this theory, the transition of the system from $|i> = |p;\ \nu = 0>$ to $|f> = |s; \nu = n>$ occurs as the result of the dipole-dipole coupling given by:

$$H' = [\vec{\mu}_{CN} \cdot \vec{\mu}_F - 3(\vec{R} \cdot \vec{\mu}_{CN})(\vec{R} \cdot \vec{\mu}_F)/R^2]/\varepsilon R^3 \qquad (1)$$

Here, R is the distance between CN^- and the F center and ε is the dielectric constant. The e-v transition probability is obtained with the matrix element of H' between the initial and final states. A numerical evaluation of the matrix element $\langle i|H'|f\rangle$ would be complex mainly because of that of μ_{CN}, due to the complexity of its wavefunction. Halama *et al.* have assumed that the electronic structure of CN^- does not change with the F center in the ground and excited states, which is contrary to our finding of very strong dependence of μ_{CN} on the F center state. We believe that there is a strong $\vec{\mu}_{CN} \cdot \vec{\mu}_F$ coupling in CsCl and a weak one in KCl. The stronger excitation obtained in CsBr(CN^-) with absorption into the $F_H(1)$ band (the p_y-like state)[2] can be analyzed in terms of the anisotropy contained in H'. We expect the vector of $\langle i|\vec{\mu}_{CN}|f\rangle$ to be along the molecular axis. With the excitation of the $F_H(2)$ band, $\vec{\mu}_F$ of the F electron would be perpendicular to $\vec{\mu}_{CN}$ resulting in $H' = 0$ effectively ($\vec{R}$ is also along the molecule axis). With the $F_H(1)$ band on the other hand, $\vec{\mu}_F$ is parallel to $\vec{\mu}_{CN}$, thereby resulting in $H' \neq 0$ and we expect a stronger e-v transfer. We have presented several aspects of the e-v transfer in the defect system $F_H(CN^-)$. It seems that the NRT process between the excited and ground states, as demonstrated in the calculated APES of Figure 1, is an important element. At the same time the calculated dipole moment μ_{CN} which depends strongly on the F electron state indicates the importance of the dipole-dipole coupling. In this sense the two mechanisms presented in this work are complementary.

REFERENCES

1. Y. Yang, W. von Osten and F. Lüty, *Phys. Rev.* **32** (1985) 2724.
2. F. Lüty and V. Dierolf, *Proceedings of LATDIM-92*, ed O. Kanert & J. M. Spaeth (1983, World Scientific Pub.), 17.
3. K. S. Song, L. F. Chen, P. Q. Tong, H. W. Yu and C. H. Leung, *J. Phys. Cond. Matt.* **6** (1994) 5657.
4. F. Lüty and V. Dierolf, (in the present proceedings).
5. D. L. Dexter, *J. Chem. Phys.* **21** (1953) 836.
6. G. Halama, K. T. Tsen, S. H. Lin, F. Luty and B. Page, *Phys. Rev.* **B39** (1989) 13457.

Radiation Effects and Defects in Solids, 1995, Vol. 134, pp. 411–415
Reprints available directly from the publisher
Photocopying permitted by license only

© 1995 OPA (Overseas Publishers Association)
Amsterdam B.V. Published under license by
Gordon and Breach Science Publishers SA
Printed in Malaysia

POINT DEFECT INTERACTION IN ALKALI HALIDE CRYSTALS

A. V. GEKTIN, V. YA. SEREBRYANNY and N. V. SHIRAN

Institute for Single Crystals, Ukraine, Kharkov, 310001

(Received 1 July 1994)

Molecular statics method is used to determine the energy and configuration peculiarities of vacancy-bivacancy interaction in alkali halide crystals. It is shown that high level of local vacancy supersaturation defines the possibility of cluster formation. The study of carrier traps by luminescence methods is used to reveal vacancy clusters.

Key words: point defect, vacancy, vacancy cluster, thermoluminescence.

1 INTRODUCTION

It was known that concentration of single vacancies measured by means of radiation coloration is by an order of magnitude smaller than the total vacancy concentration determined using flotation method [1]. This confirms the assumption that clusters are specific vacancy formations.

The development of computer methods for the calculation of crystal lattice parameters allows to perform a detailed investigation of the initial stages of point defect aggregation in alkali halides which is the aim of the present research. Crystals with NaCl and CsCl type lattice have been chosen as the objects of the study. The calculations are made for KCl and CsI, since their single point defect characteristics physical have been studied in detail [2]. Another aim of this study is to develop nondirect methods of vacancy and vacancy clusters separation.

2 POINT DEFECTS SIMULATION

The energies of various defect configurations have been calculated by means of the program MOLSTAT [3] using the same parameters of interionic interaction potentials as in [4].

An active interaction of the single v_a^+ and v_c^- must lead to a gradual prevalence of bivacancies $v_a^+v_c^-$. Therefore the main way of point defect aggregation is to be associated with the unification of divacancies. The simplest forms of such a unification leading to the appearance of tetravacancies. There are at least 10 various forms of such pairs for KCl. The formation energies for the tetravacancy configurations are in the region from 2.30 eV to 3.48 eV, i.e. some times the energy of the tetravacancy E4V is smaller in comparison with 2 $E_{v_a^+v_c^-}$ ($E_{v_a^+v_c^-}$ = 1.55 eV) and some times is higher.

Figure 1 shows the variation of the barrier value accompanying the junction of two bivacancies along the direction <100> perpendicular to the axis of $v_a^+v_c^-$. Such an interaction profile testifies to a certain repulsion of the defects. Therefore the junction of bivacancies cannot lead to the formation of tetravacancies in KCl crystals. As shown by calculations similar situation takes place in CsI, too. In other words, in both CsI and KCl crystals the junction of two bivacancies resulting in the formation of a tetravacancy is

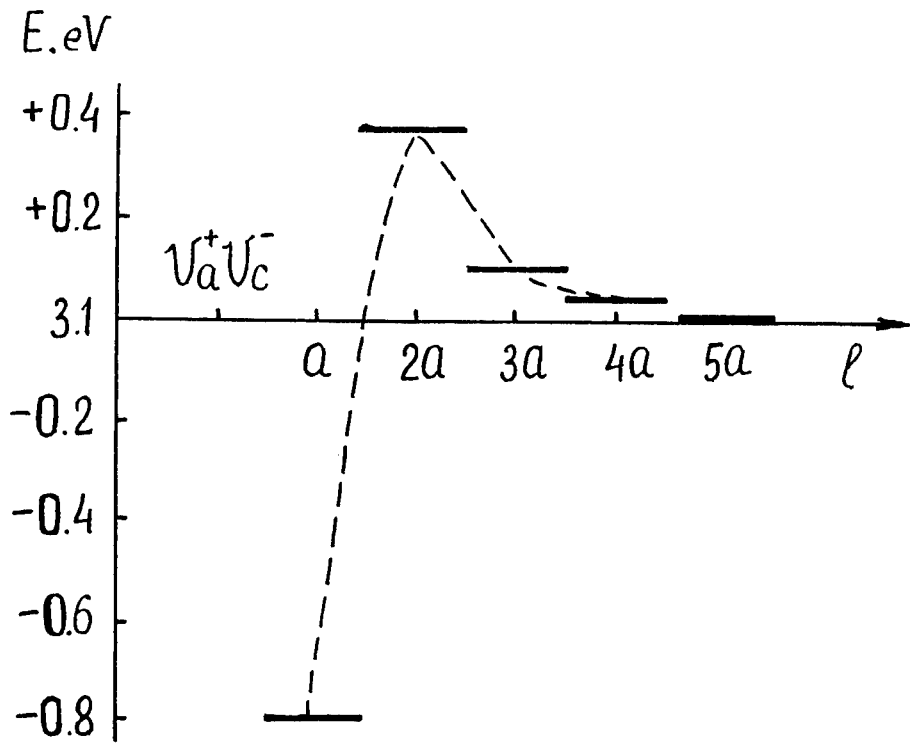

FIGURE 1 Variation of energy barrier value with distance between bivacancies. Direction <100>.

hardly probable, since in any case the barrier between neighbouring $v_a^+v_c^-$ must be overcome. It seems probable that vacancies may be positioned at certain distance from each other and form vacancy clusters.

It is obvious that vacancy clusters stability is limited because the final stable form has to correspond to the transformation of single point defects into dislocation loops, micropores. Probably it is possible to eliminate any traces of vacancies due to thermal annealing. It will depends on the parameters of interaction between bivacancies and single (charged) vacancies.

The first stage of the junction of v_a^+ and v_c^- is associated mostly with the Coulomb interaction. The next stage which consists in the junction of charged anionic or cationic vacancies to neutral divacancies was studied and stability of trivacancies was considered using the same method as described for the case of tetravacancy formation.

The calculations of the variation of bivacancy-vacancy system energy for all possible locations of both v_a and v_c with respect to the bivacancy show the potential relief around bivacancy. In the KCl crystal lattice any direction of the migration of a single vacancy requires to overcome the barrier up to 0.53 eV, though sometimes its value is small (+ 0.05 eV). The construction of the similar potential relief around divacancies in CsI reveals 'valleys'. Moving along the latter single vacancies may join with bi-, thre- and tetravacancies.

3 EXPERIMENTAL RESULTS

The investigation of the thermo-optical properties of the crystals irradiated with ionizing radiation was used for studying the state of the vacancy subsystem. The thermostimulated luminescence (TL) of KCl crystals with vacancy defects introduced by different methods was studied. The variation of bivacancy concentration has been determined using the method of radiation coloration.

Figure 2 shows the TL curves for the crystals KCl subjected to deformation. The crystal deformation leads to the appearance of an intensive «deformation» peak in the region 250–280°C. This peak is a superposition of several elementary ones and after the crystal annealing this peak is split at least into two ones with $T_m = 26°C$ (I) and $T_m = 285°C$ (II). In absorption spectra no additional increase of F-band absorption intensity has been revealed. Thus, in the deformed crystals (the curve a in Figure 3) the intensification of F-coloration corresponds to the appearance of about 10^{17} cm^{-3} additional bivacancies, whereas the annealing of the sample at 350°C during 2 hours restores the equilibrium bivacancy concentration. This means that I and II high temperature peaks (Figure 2, the

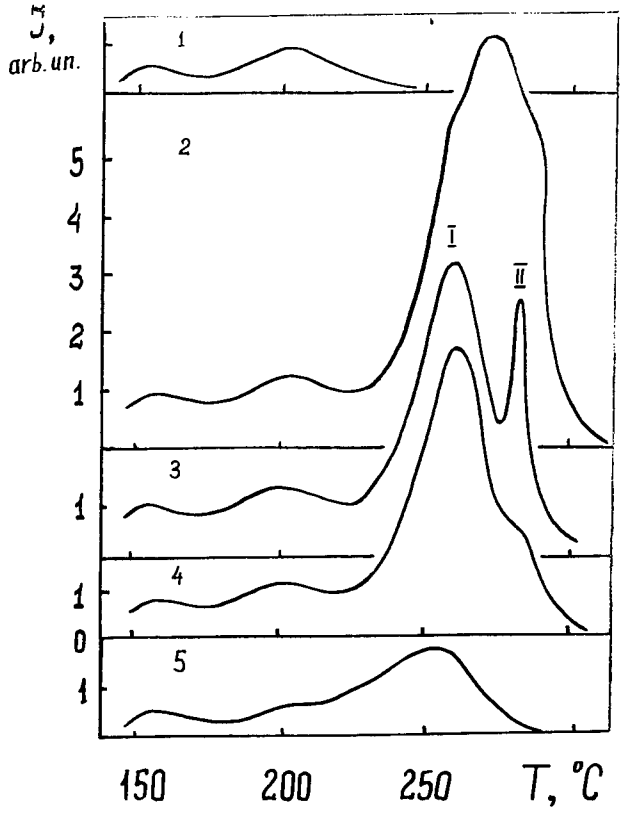

FIGURE 2 The influence of deformation and heat treatment on the shape and intensity of TL peaks in KCl. Dose 2 Mrad (^{60}Co). (1) Initial crystal; (2) strain $\varepsilon = 2.6\%$; (3) $\varepsilon = 2.6\%$ and annealed at 350°C, 2 h; (4) irradiated after measuring curve 3; (5) 100 Mrad dose (^{60}Co) and annealed (300°C, 15 min) and additionally irradiated with 1 Mrad.

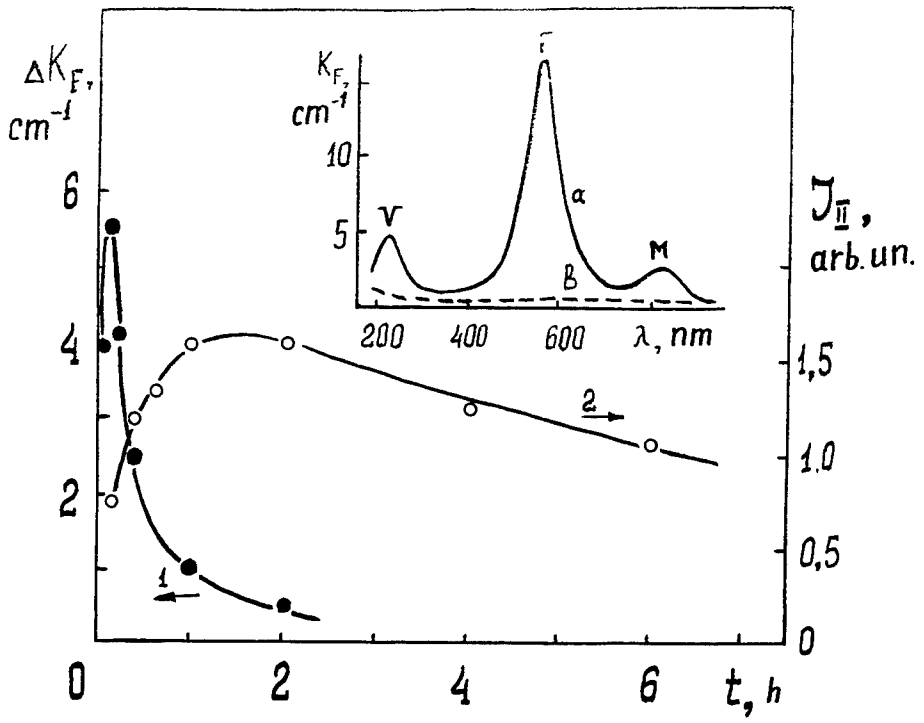

FIGURE 3 The dependences of additional coloration in F-band (1) ΔKf and (2) intensity of anomalous TL peak I_{II} on the post-deformation annealing time of KCl. ε = 2.6%, T_a = 350°C, 2 Mrad. Inset: absorption spectra of crystals a) deformed and b) annealed (350°C, 2 h) after deformation.

curve 3) are not connected with the presence of single vacancies in the crystal. This conclusion may be confirmed by the fact that we have not revealed any correlation between the variation of the intensity of the high temperature TL peak, induced by the annealing and the kinetics of bivacancy concentration recovery ($Cv_av_c \sim \Delta Kf$) (Figure 3). It is only the annealing at T > 400°C completely restoring the crystal density that leads to the disappearance of the «deformation» TL peak.

The curve 4 (Figure 2) presents the TL spectrum for the sample irradiated with the doses up to 100 Mrad and then annealed at 300°C during 15 min. This sample is also characterized by the presense of the high-temperature TL peak similar to that observed in the deformed crystals.

When the concentration of vacancies essentially exceeds the equilibrium value the behaviour of the vacancy subsystem cannot be described in the frames of the idea of charge carrier capture by single vacancies. The recovery of the equilibrium concentration of vacancies is conditioned first by their sink into clusters. The thermal stability of vacancy clusters within a fixed temperature range also testifies to a regular character of such structure defects. The described peculiarities of TL are associated with charge carrier capture by vacancy clusters. The nonelementary shape of the high-temperature TL peaks is evidently conditioned by a variety of cluster types.

4 CONCLUSION

The obtained results testify that the interaction of vacancies in alkali halide crystals has a rather complex character. The process of defect approach to a distance of about a lattice parameter is connected with the necessity to overcome a barrier. This peculiarity of point defect interaction leads to the fact that even if the crystals are greatly supersaturated with vacancies the junction of the latter resulting in the formation of micropores does not take place. The value of the energy barrier to be overcome for the junction of vacancies defines the level of stability of vacancy clusters which are metastable formations.

The TL investigations of KCl crystals with a high content of excessive vacancies reveal the light sum accumulation. The nonelementary character of high temperature TL peaks points to the variety of stable cluster forms.

REFERENCES

1. A. V. Gektin, I. M. Krasovitskaya and N. V. Shiran, *Fiz. tverd. Tela*, **26**, 2515 (1984).
2. P. V. Jacobs, *J. Chem. Soc. Faraday Trans.* **11, 85**, 415 (1989).
3. U. N. Kolmogorov and A. N. Varaksin, *Soviet Dep. VINITI N 2395-B89*, (1989).
4. C. R. A. Catlov, K. M. Diller, and L. W. Hobbs, *Phil. Mag.* **A42**, 123, (1980).

Radiation Effects and Defects in Solids, 1995, Vol. 134, pp. 417–420
Reprints available directly from the publisher
Photocopying permitted by license only

© 1995 OPA (Overseas Publishers Association)
Amsterdam B.V. Published under license by
Gordon and Breach Science Publishers SA
Printed in Malaysia

ULTRAFAST RELAXATION OF F_H-CENTRE IN KBr:OH^-

P. PROSPOSITO, M. CASALBONI,* F. IGNOZZA and U. M. GRASSANO

Dipartimento di Fisica, Università di Roma Tor Vergata; Via della Ricerca Scientifica 1, 00133 Rome—Italy

In this paper we present measurements of the lifetime of the optical cycle of the F_H center in KBr:OH^- obtained by means of a pump and probe technique with picosecond resolution. Different behavior has been observed before and after the $F \rightarrow F_H$ conversion. The temperature dependence of the nonradiative process shows that its activation energy is of about 100 cm^{-1}, the same order of magnitude of the local mode energy of the F center.

Key words: Ultrafast spectroscopy, Color centers, Alkali halides, Nonradiative processes.

1. INTRODUCTION

The F centers in KBr show, under optical excitation, a radiative decay with lifetime of the order of microseconds. The presence in the crystal of OH^- molecular-ions impurities reduces strongly the quantum efficiency of the luminescence.[1] The deexcitation occurs through very rapid nonradiative channels (of the order of picoseconds) whose origin is not yet completely clear.[2,3]

The experimental analysis of nonradiative processes can be carried out studying the recovery of the ground state population after optical excitation by means of measurements of the transient induced transparency.

Here we present some results on nonradiative processes of F and F_H (OH^-) centers in KBr. In particular, we studied the recovery times for this system as a function of the temperature and of the aggregation state of the centers ($F \rightarrow F_H$).

2 EXPERIMENTAL DETAILS

KBr samples were grown doping the melt with KOH in concentration of 0.5 or 1 mol %. These crystals have been additively colored in order to produce F centers in a concentration of about 10^{17} centers/cm^3. The samples have been exposed to monochromatic light (600 nm) at a temperature of 243 K for some minutes in order to convert the F in F_H centers, that is an F center with an OH^- molecule as next nearest neighbor. The conversion has been checked by measuring, before and after the irradiation, the low temperature ($T \sim 10$ K) absorption spectra.

In the induced transparency technique, a first laser pulse (*pump*) promotes some centers from the ground to the excited state; a second delayed pulse (*probe*) measures the ground state population. Information on the dynamics of the centers are obtained from the time evolution of the induced transparency.

Laser pulses of 3 ps, wavelength of 600 nm and peak power of about 200 W are provided by a dye laser synchronously pumped by the 2nd harmonic of a mode-locked Nd:YAG laser (high frequency repetition rate of 76 MHz).

* Permanent Address: Dipartimento di Matematica e Fisica, Università di Camerino, 62032 Camerino (MC) — Italy

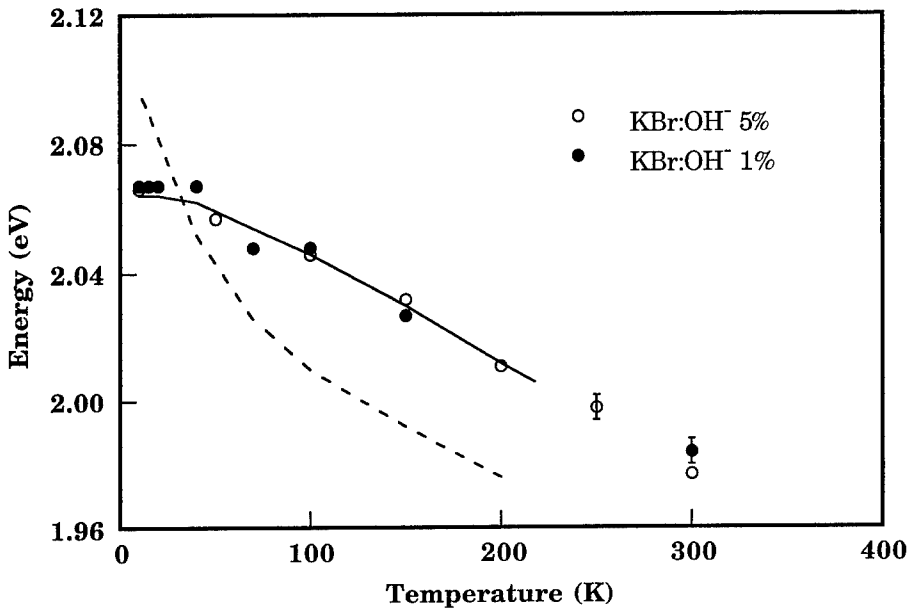

FIGURE 1 Absorption band peak energy of F centers in KBr:OH^- before F $\rightarrow$ F_H conversion, as a function of the temperature for two different OH^- concentration. Full line and dashed line report the energy peak for F and F_H center respectively after Ref. [4].

A detailed description of the experimental apparatus and of the double modulation lock-in amplifier detection system can be found in Ref. [2].

3 RESULTS AND DISCUSSION

Preliminary absorption measurements on samples with two different concentrations of OH^- ions as a function of the temperature have been carried out to verify the type of centers in the samples. In agreement with previous results[4] we found that the KBr:OH^- samples do not show presence of F_H centers, even for high concentrations of OH^- ions, unless they have been optically converted.

The presence of the F_H centers is monitored through the measurement of the peak of the absorption band, whose temperature dependence is shown in Figure 1. All data of doped, but not converted, samples follows the curve of the normal F centers in pure KBr and not that of the F_H centers.

The induced transparency depends strongly upon the numbers of F_H centers present after aggregation. This number can be varied by changing the F-light irradiation time. For low F_H concentration, the recovery time at LNT results hundreds of picoseconds, while in the case of higher F_H concentration it is of the order of tens of picoseconds, as shown in Figure 2.

In both cases an induced transparency signal remains for times much longer than those measurable with the variable delay line (1.3 ns). The origin of this slow temporary bleaching is still unclear and might be due to optical conversion between centers[4] or to some kind of $F_H \rightarrow F_H^-$ conversion.

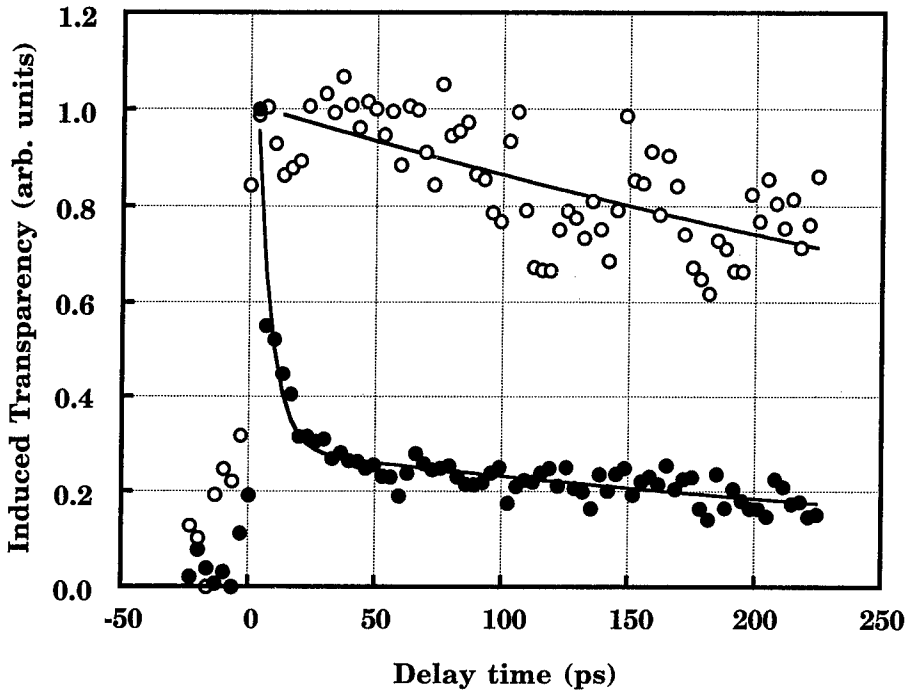

FIGURE 2 Induced transparency in KBr:OH^- 1 mol% at 77 K, (a) with partial $F \rightarrow F_H$ conversion; (b) after complete conversion.

A complete series of decay measurements was performed as a function of temperature. All curves show the simultaneous presence of two phenomena. The slower one, as indicated above, shows up only as a large background contribution. The faster one is temperature dependent. In particular the recovery time is constant ($\sim$ 200 ps) up to 40 K and becomes shorter on increasing temperature, reaching the limit value of our apparatus of about 10 ps at 150 K. The recovery times are shown in the Arrhenius plot of Figure 3. This plot allows us to calculate the thermal activation energy of the process $\Delta E \sim 100\ cm^{-1}$.

The value of this activation energy is of the order of magnitude of the local mode energy of the F center in alkali halides and one can suppose a configurational coordinate scheme for $F_H(OH^-)$ center in which a low lying crossing point between the ground and the excited state allows nonradiative transition between the RES and the ground state. These tunneling processes are responsible for the almost constant values of the recovery time below 40 K. For higher temperatures, the F_H centers in the electronic excited state can occupy higher vibrational levels with the consequent decrease of the potential barrier. As a result, an easier tunneling takes place: the higher the temperature, the faster the recovery of the ground state population.

An other thermal activated process has been observed for F center in KCl:OH^-[5] and in KBr:OH^-[2]. The activation energy is, in both cases, approximately equal to the librational energy of the OH^- ion. However we suppose that this higher activation energy reflects a different radiationless transition involving F center and OH^- ion far apart. Indeed a longer recovery time is sometime observed in the case of uncomplete $F \rightarrow F_H$ conversion.

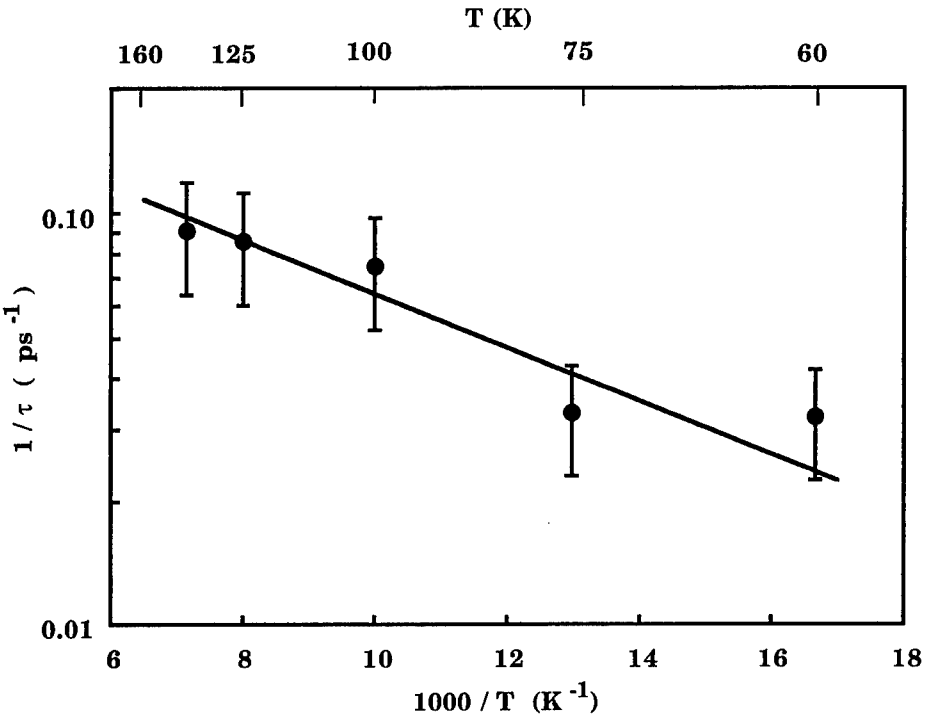

FIGURE 3 Arrhenius plot of the experimental values of the faster recovery time τ vs. 1/T.

REFERENCES

1. L. Gomes and F. Luty, *Phys Rev* **B30**, 7194 (1984).
2. M. Casalboni, P. Prosposito and U. M. Grassano, *Solid State Commun.* **87**, 305 (1993).
3. M. Leblans, E. Gustin, A. Bouwen and D. Schoemaker, *J. Luminescence* **58**, 388 (1994).
4. G. Baldacchini, S. Botti, U. M. Grassano, L. Gomes and F. Luty, *Europhys. Lett.* **9**, 735 (1989).
5. D. J. Jan, T. C. Corcoran, M. A. El-Sayed, L. Gomes and F. Luty, in *Ultrafast Phenomena V*, G. R. Flaming and A. E. Siegman eds. (Springer Verlag—Berlin 1986), p. 286.

Radiation Effects and Defects in Solids, 1995, Vol. 134, pp. 421–423
Reprints available directly from the publisher
Photocopying permitted by license only

© 1995 OPA (Overseas Publishers Association)
Amsterdam B.V. Published under license by
Gordon and Breach Science Publishers SA
Printed in Malaysia

CONFIGURATION OF F_A (Na) DEFECTS IN KF CRYSTALS

A. SCACCO,[1] C. GILIBERTI,[1] U. M. GRASSANO,[2] G. BALDACCHINI,[3] M. CREMONA,[3] R. M. MONTEREALI[3] and A. SHPAK[4]

[1]Dipartimento di Fisica, Universitá La Sapienza, P.le A. Moro 2, 00185 Roma, Italy; [2]Dipartimento di Fisica, Universitá di Roma Tor Vergata, Via della Ricerca Scientifica 1, 00133 Roma, Italy; [3]ENEA, Dipartimento Innovazione, Settore Fisica Applicata, CRE Frascati, C.P. 65, 00044 Frascati, Italy; [4]Institute of Semiconductors, Ukrainian Academy of Sciences, Pr. Nauki 45, 252028 Kiev, Ukraine

The configuration of F_A centres in KF:Na^+ crystals has been studied by means of spectroscopic measurements. The F_A(Na) dipoles are found to lie along the crystal axes, and this result is interpreted as the consequence of an on-centre position of the Na^+ ions in the lattice of KF, in good agreement with theoretical expectations.

Key words: F_A centres, Off-axis configuration, KF:Na^+.

1 INTRODUCTION

Optical studies, carried out on crystals of various alkali halides, showed that an off-centre position of Li^+ impurity ions in the lattice corresponds to an off-axis configuration of the F_A(Li) centre, formed by aggregation of the Li^+ ion with an F centre. Such a tilt of the F_A(Li) dipoles with respect to the crystal axes can be evaluated from their photostimulated reorientation through absorption or luminescence measurements.[1] However, the physical description of the F_A(Li) reorientation kinetics must take into account not only the off-axis geometry of the centres, but also the overlap of the F_{A1} and F_{A2} absorption bands.[2] Experimental values for the tilt angle of F_A(Li) dipoles, derived from optical measurements by means of an interpretation based on the above approach, were determined in several systems and found in quantitative agreement[3] with the values deduced from theoretical calculations, based on the shell model potentials, of the off-centre displacement of the Li^+ ion. In the frame of an investigation on aggregate centres in Na^+-doped crystals of KF, some measurements were specifically devoted to the determination of the possible off-axis geometry of such defects. The results are reported in this work.

2 EXPERIMENTAL PROCEDURE AND RESULTS

Samples of KF:Na^+ (0.25 mole % of the impurity in the melt) were additively coloured and contained typically about 10^{16} F centres/cm^3. The optical conversion to F_A(Na) centres has been performed at –40°C by irradiation with 438 nm light (namely in the F absorption band). The luminescence, excited by the various lines of an Ar ion laser, was revealed in the range 500–1200 nm by a cooled RCA7102 photomultiplier and in the range 1600–2500 nm by a cooled PbS detector.

Figure 1 shows the azimuthal dependence of the F_A(Na) luminescence. As it has been already reported,[4] the F_A(Na) centres in KF exhibit two different emissions depending on the crystal temperature: the first one, peaking at 920 nm (halfwidth 0.38 eV), is thermally quenched and vanishes above 50 K, whereas the second one, peaking at 2100 nm

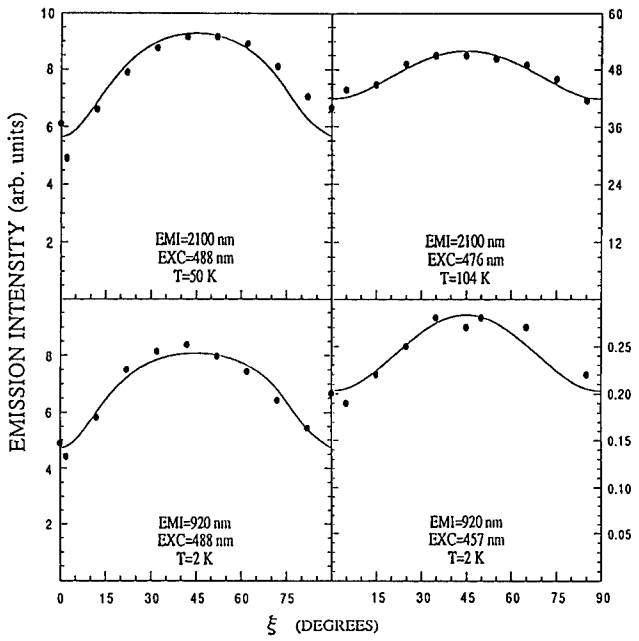

FIGURE 1 Azimuthal dependence of the F_A(Na) emission intensity in KF.

(halfwidth 0.08 eV), increases with temperature in the range 50–150 K. Data of the emission intensity are plotted as a function of the angle ξ formed by the polarization direction of the exciting light with the vertical axis in the front face of the crystal. The experimental points, describing bell-shaped curves, are fitted by equations 6 and 10 of Ref. 2 with three free parameters: the normalization factor K, dependent on the specific experimental conditions, the off-axis angle θ and the ratio R of the absorption cross sections for F_{A1} and F_{A2} transitions at the pumping wavelength. The results for the last two physical parameters are summarized in Table I. The values for R are in very good agreement with the experimentally observed overlap of F_{A1} and F_{A2} absorption bands at the various temperatures and pumping wavelengths. The values for θ are remarkably reproducible in all measurements and almost negligible within the uncertainties, so indicating that the F_A(Na) dipoles are practically almost completely aligned along the crystal axes. As a consequence, the Na^+ ions in KF are to be necessarily considered in an on-centre position.

Table I
Overlap R between F_{A1} and F_{A2} absorption bands and off-axis angle θ in KF:Na^+ obtained from luminescence measurements.

Emission (nm)	Temperature (K)	Excitation (nm)	R	θ (degrees)
2100	50	488	14.5 ± 0.1	1.0 ± 0.7
2100	104	476	19.5 ± 0.4	0.9 ± 0.8
920	2	488	3.9 ± 0.1	1.0 ± 0.4
920	2	457	0.3 ± 0.1	0.8 ± 0.5

3 DISCUSSION AND CONCLUSIONS

The results obtained in the above experiments show that Na^+ ions, substitutionally replacing K^+ ions in the lattice of KF, occupy regular lattice sites and therefore are not shifted to off-centre positions. Such a conclusion can be compared with the predictions of theoretical calculations concerning the configuration of alkali impurity ions in alkali halides. Most of the theoretical work deals with Li^+ ions, because their small size favours in some systems the off-centre displacement. However, some calculations were extended to the case of Na^+ ions in KF crystals and can be used here. The polarizable point ion model, widely adopted to describe the interactions between nearest neighbours induced by the impurity displacement, leads in the case of KF to some interesting conclusions. Whereas an off-centre position of Li^+ ions is strongly favoured because of the occurrence of pronounced minima in the potential energy curve far from the normal site, Na^+ ions exhibit a flat potential region around the lattice position and are then allowed to be on-centre or to undergo a small off-centre displacement with equal probabilities.[5] The alternative shell model,[6] modified by using suitable interionic potentials in order to take into account the elastic properties of the crystal lattice,[7] gives a more drastic indication: Na^+ ions in KF are definitely on-centre, at odd with Li^+ ions which again find their equilibrium configuration in off-centre position.[7] In conclusion, all theoretical predictions are in excellent agreement with our experimental results in KF:Na^+, which is a further support to the validity of both kinds of approach. In order to update the situation concerning the off-axis configuration of F_A centres in alkali halides, Table II shows the comparison between all experimental results and the corresponding calculated values of the off-axis angle in various systems. It is worth to remark the very good agreement between our results and the shell model predictions in all materials investigated up to now.

Table II
Theoretical and experimental values for the off-axis angle (degrees) of F_A centres.

Crystal	Theory			Experiment
	a	b	c	d
KCl:Li^+	5.4	11.9	14.6	5 ± 1
RbCl:Li^+	9.3	7 ± 1		
KF:Li^+	12.3	14.0	11.9	14 ± 2
KF:Na^+	0.0	–	≤ 6.0	0.9 ± 0.5

a: Ref. 7; b: Ref. 6; c: Ref. 5; d: Ref. 3 and this work.

REFERENCES

1. G. Baldacchini, G. P. Gallerano, U. M. Grassano, A. Lanciano, A. Scacco, F. Somma, M. Meucci and M. Tonelli, *Phys. Rev.* **B 33**, 4273 (1986).
2. G. Baldacchini, U. M. Grassano, A. Scacco, K. Somaiah and F. Somma, *Nuovo Cim.* **9D**, 1105 (1987).
3. F. De Matteis, M. Rossi, A. Scacco, F. Somma, G. Baldacchini, M. Cremona, U. M. Grassano, *Radiat. Eff. Def. Solids* **119–121**, 343 (1991).
4. G. Baldacchini, M. Cremona, R. M. Montereali, C. Giliberti, A. Scacco, U. M. Grassano, A. Shpak, *J. Lumin.* **58**, 278 (1994).
5. J. A. Van Winsum, T. Lee, H. W. Den Hartog and A. J. Dekker, *J. Phys. Chem. Solids* **39**, 1217 (1978).
6. M. J. L. Sangster, *J. Phys.* **C13**, 5279 (1980).
7. C. R. A. Catlow, K. M. Diller, M. J. Norgett, J. Corish, B. M. C. Parker, P. W. M. Jacobs, *Phys. Rev.* **B 18**, 2739 (1978).

Radiation Effects and Defects in Solids, 1995, Vol. 34, pp. 425–429
Reprints available directly from the publisher
Photocopying permitted by license only

© 1995 OPA (Overseas Publishers Association)
Amsterdam B.V. Published under license by
Gordon and Breach Science Publishers SA
Printed in Malaysia

TRIPLET STATE OF F_3^+ IN LiF

G. BALDACCHINI, M. CREMONA* G. D'AURIA,* V. KALINOV,*†
and R. M. MONTEREALI

ENEA, Dipartimento Innovazione, Settore Fisica Applicata, C.R.E. Frascati, C.P. 65, 00044 Frascati (Rome) Italy

Alkali halide crystals with intrinsic color centers are suitable media for solid state tunable lasers, and among them LiF is one of the most popular because of its good physical and optical qualities. The F_3^+ centers in this host crystal have absorption and emission properties with unusual time evolution effects after excitation. In order to clarify this particular optical cycle we investigated a γ-irradiated LiF crystal containing, besides F centers, mainly F_3^+ centers. The behaviour of emission and absorption as a function of temperature and pumping power confirms the existence of a triplet state.

Key words: LiF, Color Centers, Luminescence, Laser Material, Triplet State.

1 INTRODUCTION

The search for solid-state optically active media capable of generating radiation tunable in a wide spectral range is under way since long time, and alkali halide crystals with color centers are well known to be suitable media.[1] Colored LiF crystals are often preferred among them because they are not damaged by moisture, are more stable optically and can be operated at room temperature.[2] However also in these crystals there are some degradation effects under intense optical pumping. Up to now these effects, which cause efficiency losses in laser systems, have not widely investigated, while their understanding is very important for choosing the best pumping scheme and for basic research.

The excitation at ~ 450 nm of colored LiF crystals produces a green emission band peaked at 530 nm and a red one at 670 nm attributed to the F_3^+ and F_2 centers respectively,[3] which have the absorption bands almost coincident. This fortuitus overlapping provides the possibility of obtaining simultaneous lasing in the green and red spectral regions,[4] but hinders a laser emission of F_3^+ color centers alone. The use of ionizing radiation for coloring LiF crystals at RT produces a concentration of F_2 centers higher than that of F_3^+, and so in order to increase the efficiency of lasing in the green region of the spectrum or to study the green emission without optical interactions, it is necessary, at the initial stage of preparation of the active medium, to reduce the number of F_2 centers.[4,5]

Aim of the present work is to investigate the absorption and emission properties of F_3^+ centers in LiF crystals under pumping with a continuous Ar^+ laser light at 457 nm as a function of temperature and pump intensity. Apart the basic knowledge gained in this search, it is very interesting to verify whether F_3^+ centers, which are known to lase under pulsed pumping,[5] can also lase under cw pumping.

2 EXPERIMENTAL.

The F_2, F_3^+ and other color centers (F, F_3) in LiF were produced at dry ice temperature with γ rays from a Co^{60} source. Sample dimensions were about $(20 \times 40 \times 2)$ mm^3. A

* ENEA guest
† Permanent address: Inst. of Mol. and Atom. Phys., Acad. of Sciences of Belarus, Minsk, Belarus.

crystal containing mainly F and F_3^+ centers was obtained by destroying the F_2 centers at RT with the 308 nm light from an excimer laser.[6]

Emission measurements were taken in a collinear geometry of the pumping source and detector with the sample placed in a variable temperature cryostat. The 457 nm line of an Ar^+ laser was used to excite F_3^+ color centers, and a photomultiplier with S20 response monitored the emission filtered by a 25 cm focal length monochromator. The pumping light was modulated by a chopper and the signal analyzed by the lock-in technique and acquired by an A/D system. Absorption spectra were performed by using a Perkin Elmer 330 spectrophotometer.

The luminescence spectra were recorded at different powers and temperatures under cw excitation. During these measurements a change in the color of the light emitted from the crystal was clearly observed. The change occurs during the first seconds after the excitation, and strongly depends on the pump intensity and temperature. The time evolution of the luminescence intensity was monitored after switching on the excitation light with a mechanical shutter. An example of the time evolution of F_3^+ emission at 530 nm after switching on the 457 nm excitation is shown in Figure 1 at RT (a) and LNT (b). The initial intensity decays exponentially towards a steady-state value while the

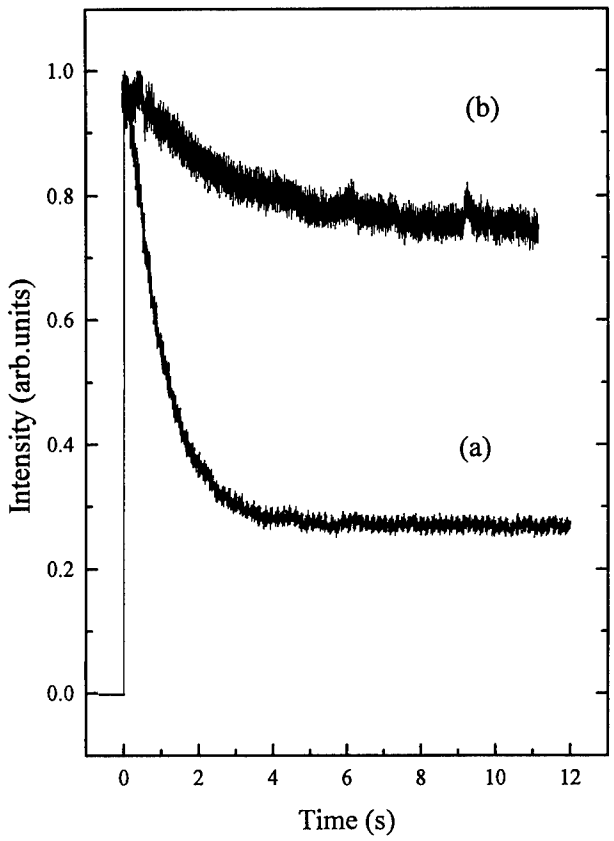

FIGURE 1 Time evolution of the F_3^+ emission intensity (normalized) under cw excitation with 42.5 mW of the 457 nm line of an Ar^+ laser at RT (a) and LNT (b).

pumping power is kept constant. This behaviour is similar for all the pumping powers but with different time scales. A comparison between the initial (transient), a, and the final (stationary), b, values of the spectral emission intensity at RT is reported in Figure 2.

The time evolution of the absorption band after switching on and off the laser exciting light has also been investigated. The absorption was measured at 460 nm, and the 457 nm line of an Ar^+ laser was used to excite the F_3^+ centers from the ground to the first excited state. After switching on the laser, the sample absorption decreases to a new equilibrium value. The removal of the laser light results in a spontaneous recovery toward the initial value of the absorption as shown in Figure 3 at RT (a) and LNT (b).

3 CONCLUSION

Previous investigations in colored LiF crystals[4,7] suggested the existence of a triplet state with characteristic lifetimes of a few seconds. The time evolution of the luminescence and absorption of our LiF sample containing mainly F_3^+ and F centers fully supports this model. The absorption of a photon by an F_3^+ center in the ground state excites it to a higher singlet state, from where it relaxes to the relaxed excited state. Afterwards the center can either decay radiatively to the ground state or transfer itself to a triplet manifold state with a radiationless transition. Eventually after some time the F_3^+ center reaches again the ground state. The kinetics of this last transition has been evidentiated by the transient absorption measurements as those reported in Figure 3. The recovery time of the absorption should be, accordingly to the previous model, the inverse exchange rate

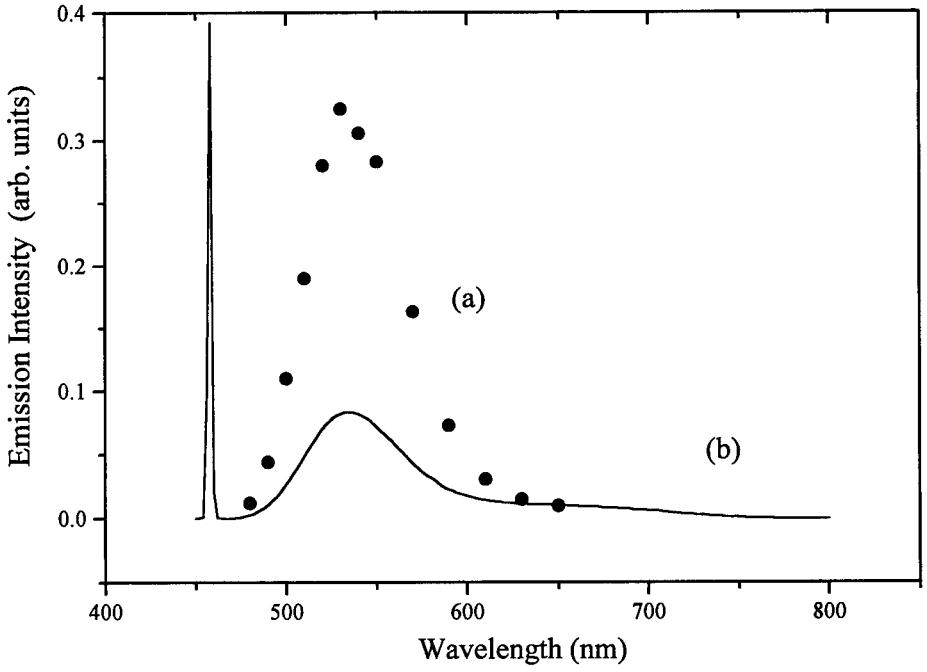

FIGURE 2 Transient (a) and stationary (b) luminescence spectra of F_3^+ centers in LiF under cw excitation with 42.5 mW of the 457 nm line of an Ar^+ laser at RT.

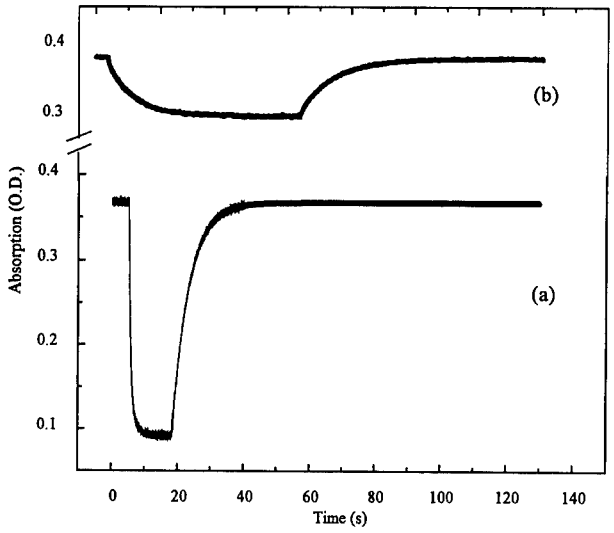

FIGURE 3 Time evolution of the F_3^+ absorption at 460 nm after switching on and off the cw laser excitation at 457 nm with 42.5 mW of power at RT (a) and LNT (b).

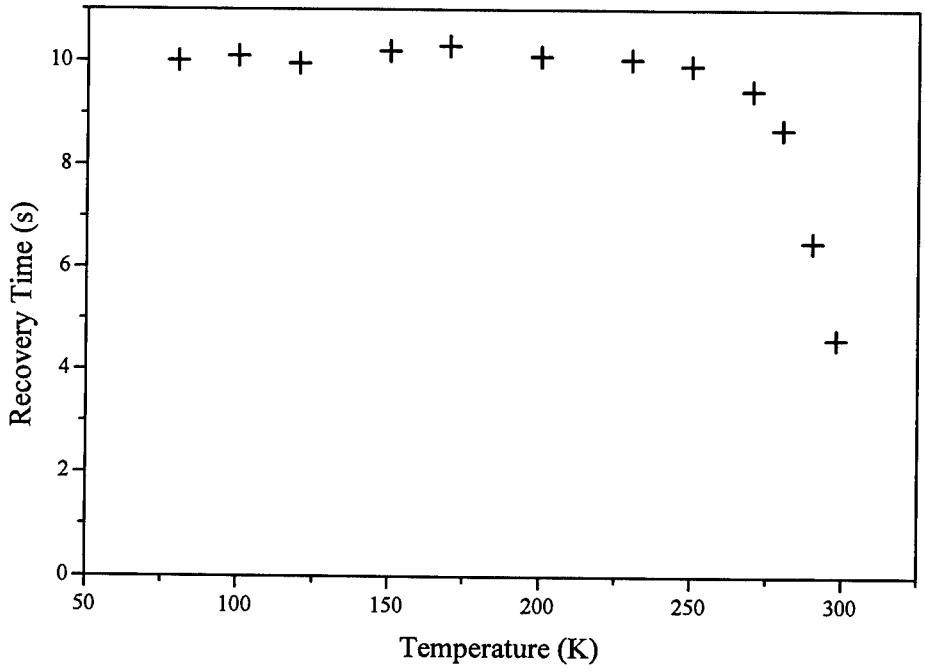

FIGURE 4 Temperature dependence of the absorption recovery time after switching off the Ar^+ laser.

between triplet state and ground state. The experimental values of the recovery time at different temperatures are shown in Figure 4, and they suggest that a multiphonon process is at work.

Moreover a first analysis of systematic experimental data shows that absorption and emission are strongly affected by the intensity of the exciting laser and the temperature, which implies an involvement of a triplet state in the optical cycle.

Such metastable state does not allow to maintain a high population in the upper singlet state especially at RT, and this is the main reason of the degradation of the F_3^+ luminescence intensity at RT by increasing the power of excitation. As a consequence it is practically impossible to obtain cw lasing of F_3^+ centers at RT, but our data indicate that such possibility may exist at lower temperatures.

REFERENCES

1. L. F. Mollenauer and J. C. White Eds., Tunable Lasers, Springer Verlag New York, 1987, p. 1–277.
2. T. T. Basiev, S. B. Mirov, V. V. Osiko, *IEEE Journal of Quantum Electronics*, **24** 6 (1988) 1052.
3. J. Nahum and D. A. Weigand, *Phys. Rev.*, **154** (1967) 817.
4. L. X. Zheng and L. F. Wan, *Opt. Commun.*, **55** (1985) 277.
5. G.Hongen, G. Shaozhang, R. Yongfeng, and W. Liangfeng, *Chinese Phys. Lett.* **5**, 241 (1988).
6. A. P. Voitovich, V. S. Kalinov, I. I. Kalosha. *Soviet Dokl. Akad. Nauk BSSR*, **30** (1986) 132.
7. S. Paciornick, R. A. Nunes, J. P. von der Weid, L. C. Scavarda do Carmo and V. S. Kalinov. *Applied Phys. D*, **24** (1991) 1811.

Radiation Effects and Defects in Solids, 1995, Vol. 134, pp. 431–435
Reprints available directly from the publisher
Photocopying permitted by license only

© 1995 OPA (Overseas Publishers Association)
Amsterdam B.V. Published under license by
Gordon and Breach Science Publishers SA
Printed in Malaysia

OPTICAL PROPERTIES OF F AND F^+ TYPE CENTERS IN BARIUM β-ALUMINA

D. GOURIER, B. VIANA, P. BELLENOUE, J. THERY and D. VIVIEN

Laboratoire de Chimie Appliquée de l'Etat Solide, URA-CNRS 1466 ENSCP 11 rue P et M Curie 75231 Paris Cedex 05 France

X-ray induced F and F^+ type centers in the conduction planes of Ba^{2+} β-alumina are characterized by optical absorption, Electron spin resonance (ESR) and time resolved fluorescence spectroscopies. These two centers exhibit similar optical absorption properties, although F centers are optically bleached by UV irradiation while F^+ centers are relatively stable under the same conditions. The latter are characterized by a strong fluorescence at 425 nm.

Key words: β-Alumina, F and F^+ centers, Electron Spin Resonance, Optical Properties.

1 INTRODUCTION

β-alumina family contains well-known superionic conductors. The hexagonal structure of these compounds can be described in terms of two spinel-like blocks separated by loosely packed mirror planes. These compounds are generally non-stoichiometric, and an excess of cations in the mirror planes is compensated by an excess of oxygen ions. The interstitial O^{2-} ions are stabilized by two aluminium Frenkel defects in the spinel blocks.

This linear cluster can be photolyzed under X-ray irradiation, resulting in a displacement of the interstitial oxygen and leaving one or two electrons in the vacant site according to the following mechanism:[1,2]

$$Al^{3+}–O^{2-}–Al^{3+}–\xrightarrow{-X-rays} Al^{3+}–e^{-}–Al^{3+}(F^{+}\text{ center})+O^{-}$$

$$\text{and } Al^{3+}–O^{2-}–Al^{3+}–\xrightarrow{-X-rays} Al^{3+}–e^{-}e–Al^{3+}(\text{F center})+O^{0}$$

where Al^{3+} represents the interstitial aluminium ions of the Frenkel defects in the spinel blocks. Strickly speaking, the two electron centers are not pure F^+ and F centers since the vacant site is that of an extra oxygen ion in an interstitial site. Both the O^- ion and the F^+ type center have been characterized by ESR.[2–4] The oxygen atom O^0 formed in the second reaction is thought to be responsible for the formation of superoxyde ion O_2^- in Na^+ and K^+ β-alumina[3] by a reaction of the type[2] $O^0 + O^- \rightarrow O_2^-$. The thermal stability of all these centers is very low in all the β-alumina compounds,[3,4] except in Ba^{2+} β-alumina where the centers are still detectable 4 years after the initial x-ray irradiation. This good stability allowed us to study the optical properties of the F^+ and F type centers in this compound.

The spinel blocks of β-alumina are not very sensitive to irradiation since only V type centers are formed, i.e. holes trapped at cationic defects, giving a yellow or brown color to the crystal.

2 OPTICAL ABSORPTION AND ESR SPECTROSCOPIES:

F^+ and F type centers are characterized by broad and intense absorption bands at 295 and 261 nm respectively. On Figure 2-a is presented the differential optical absorption

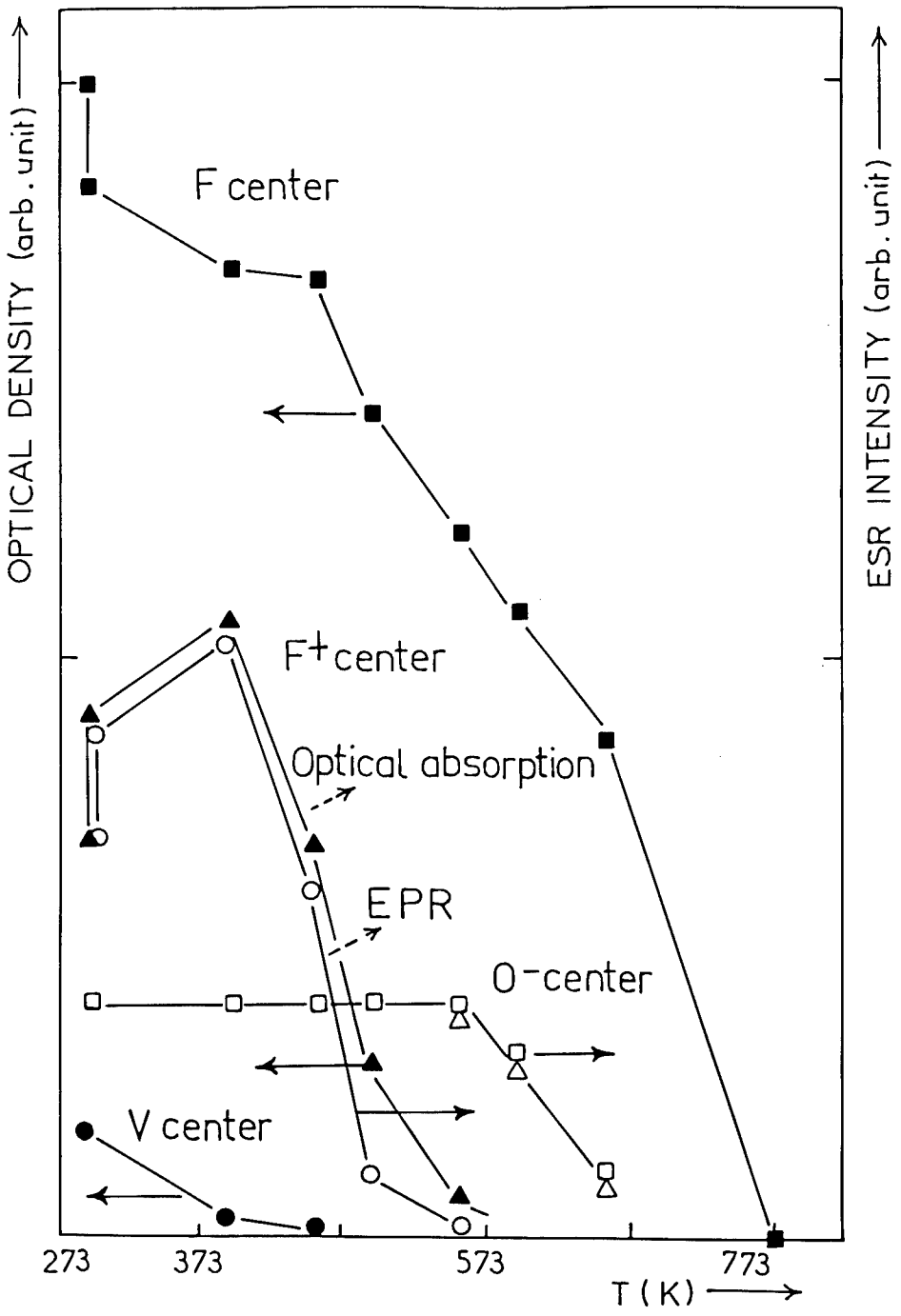

FIGURE 1 Temperature dependence of the defect concentration in Ba^{2+}-β-alumina measured by optical absorption and ESR spectroscopy.

spectrum of centers created by X-ray irradiation (difference between the spectra recorded before and after irradiation). An optical absorption band peaking at 295 nm represents the $^2S \rightarrow {}^2P$ transition of the F^+ center. In addition the F^+ center is paramagnetic and can be identified by its ESR spectrum.[2–4] The F centers are diamagnetic (electron spin $S = 0$) and are only characterized by an absorption band peaking at 261 nm representing the $^1S \rightarrow {}^1P$ transition of this center. The two absorption bands strongly overlap in the U.V. range. Correlations between optical densities and ESR intensities leads to the assignment of the centers (see Figure 1). A small fraction of F centers are thermally converted into F^+ centers by hole trapping from V-type centers of the spinel blocks,[2] characterized by an absorption band at 472 nm.[2] These V centers exhibit a high oscillator strength, therefore they are observed on the absorption spectrum even at very low concentration. At temperature higher than 770 K, thermal bleaching of F, F^+ and V centers is accompanied by an intense green thermally stimulated luminescence due to the Mn^{2+} impurities.[2]

3 FLUORESCENCE SPECTROSCOPY

Under C.W. excitation, the emission spectrum consists mainly in a band around 425 nm (2.9 eV). Increasing the temperature leads to a strong decrease of the fluorescence intensity and shifts the emission towards longer wavelengths. Both the F and F^+ centers are excited under UV illumination at 266 nm (fourth harmonic of a Q-switched Nd:YAG laser). The emission spectrum is presented in Figure 2. The F centers show only a weak emission around 500 nm (2.5 eV) attributed to the $^3P \rightarrow {}^1S$ transition of these centers, with a fluorescence lifetime τ of about 30 μs. The fluorescence of F^+ centers is characterized by the strong emission band at 425 nm ($^2P \rightarrow {}^2S$ transition) with a short lifetime $\tau < 30$ ns. In addition to this fluorescence, the F^+ centers present also a temperature dependent fluorescence band at the same wavelength with a lifetime value around 4 ms at room temperature. Its decay profile was observed with an intensified Optical Multichannel Analyser (O.M.A), a few microseconds after the laser excitation. This fluorescence can be attributed to the result of the thermal ionization of a shallow donor state, followed by the electron capture by a F^{2+} center and the $^2P \rightarrow {}^2S$ fluorescence of the resulting F^+ center summarized as follow:

$$F^{2+} + e^- \rightarrow F^+ + h\nu$$

F centers are optically bleached after a short excitation time, giving F^+ centers (detected by ESR) and free electrons which are trapped in shallow donor states while the F^+ centers are relatively stable. The long time stability of these centers against UV irradiation is explained by a good balance between their photo-ionization and their formation via photoionization of F centers according to:

$$F^+ \leftrightarrow F^{2+} + e^-$$
$$F \rightarrow F^+ + e^-$$

These absorption and emission properties from the two centers as well as the delayed emission are summarized on Figure 3. From our experiments it was not possible to observe the $^1P \rightarrow {}^1S$ allowed transition of the F centers. Therefore, from the ^1P level one can expect either a thermal ionization as shown in this paper or a non-radiative relaxation to the ^3P emitting level followed by the $^3P \rightarrow {}^1S$ emission peaking at about 500 nm.

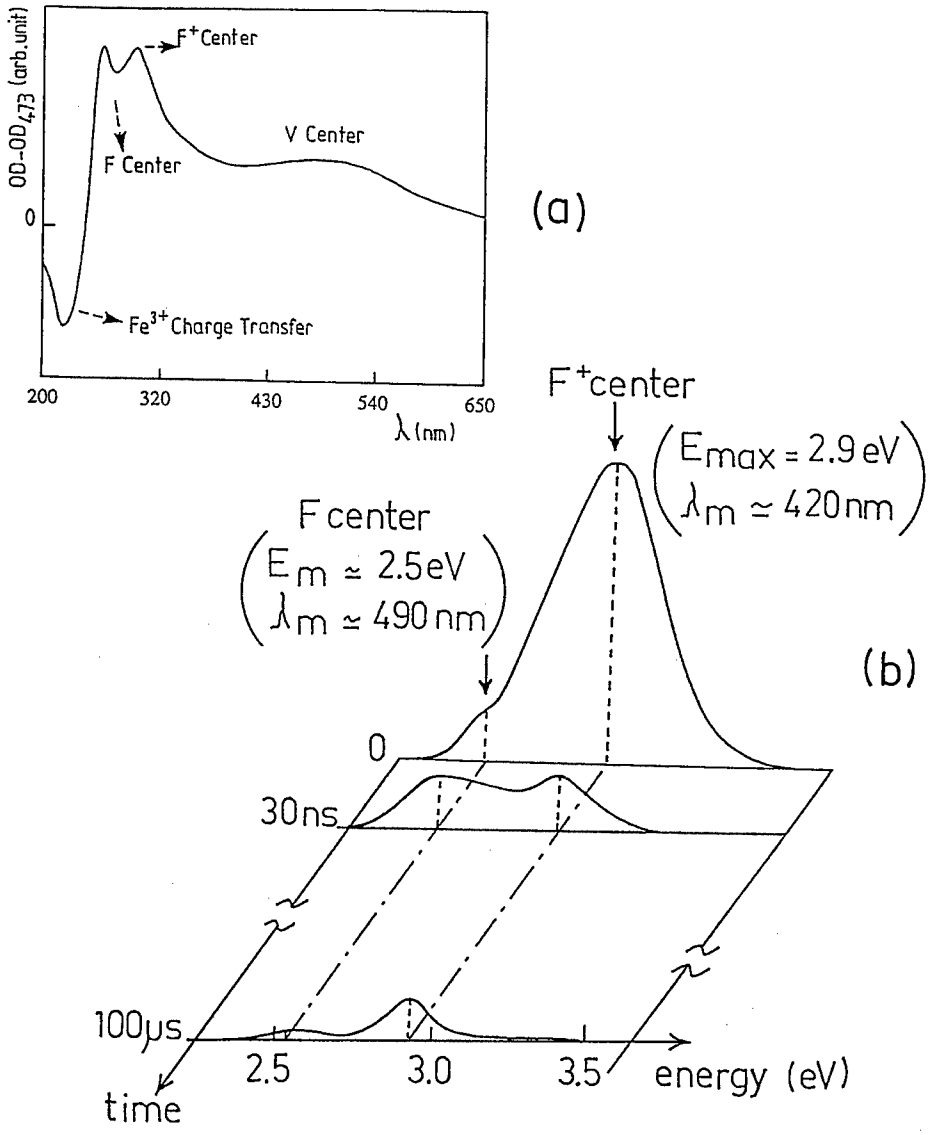

FIGURE 2 (a) Differential optical absorption spectrum obtained by substraction of the optical density after irradiation and thermal bleaching from the optical density just after irradiation. (b) Time resolved fluorescence spectra (λ ex = 266 nm). Emission spectra have been recorded at various time delays after the laser excitation.

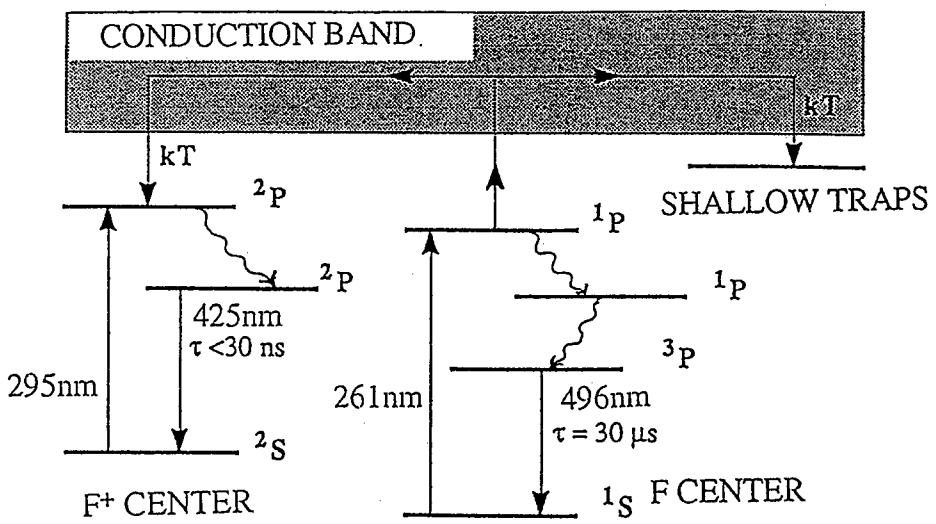

FIGURE 3 Schematic presentation of the energy level diagrams for F and F^+ centers in barium β-Alumina.

4 CONCLUSIONS

F and F^+ type centers produced by displacement of the interstitial oxygen ions in the mirror planes of Ba^{2+}-β-alumina are studied by Electron spin resonance, optical absorption and time resolved fluorescence spectroscopy. F centers are rapidly bleached by UV irradiation while F^+ centers are relatively stable. Thus the formation of F and F^+ type centers by ionizing radiation is a general property of the mirror planes of β-alumina compounds. The spinel blocks behave like other ionic oxides, where irradiation produces mainly V type centers.

ACKNOWLEGEMENTS

We are grateful to Marianne Salagnac and P. Delgado for their technical assistance.

REFERENCES

1. D. Gourier, P. Bellenoue and J. Théry, *Ann. Chem. Fr.* **16**, 391 (1991).
2. D. Gourier, T. Gbehi, R. Visocekas, J. Théry and D. Vivien, *Phys. Stat. Sol.* **B152**, 415 (1989).
3. D. Gourier, D. Vivien and J. Livage, *Phys. Stat. Sol.* **A56**, 247 (1979).
4. K. O'Donnell, R. C. Barklie and B. Henderson, *J. Phys.*. **C11**, 3871 (1978).

Radiation Effects and Defects in Solids, 1995, Vol. 134, pp. 437–441
Reprints available directly from the publisher
Photocopying permitted by license only

© 1995 OPA (Overseas Publishers Association)
Amsterdam B.V. Published under license by
Gordon and Breach Science Publishers SA
Printed in Malaysia

IDENTIFICATION OF I_3^- AND I_5^- CLUSTERS IN IRRADIATED KI BY X-RAY PHOTOELECTRON, RAMAN AND OPTICAL ABSORPTION SPECTROSCOPIES

J. D. COMINS,[O+] T. P. NGUYEN,[O] M-A. PARISELLE,[O] S. LEFRANT[O] and A. M. T. ALLEN[+]

[O]*Laboratoire de Physique Cristalline, Institut des Matériaux de Nantes, 2 rue de la Houssinière, 44072 Nantes Cedex 03, France;* [+]*Department of Physics, University of the Witwatersrand, Johannesburg, Wits 2050, South Africa*

Raman and XPS measurements have been performed on KI crystals irradiated near 200 K. The Raman studies show I_3^- and I_n^- (n = 5, 7, – – –) clusters which anneal together with F- and V- centres at 338 K. A small development of $(I_2)_n$ aggregates occurs during the anneal; these decay near 378 K and are responsible for a broad and weak residual V-band. The I $3d_{5/2}$ XPS peak has been fitted to reveal the presence of 3 components after low energy argon- ion bombardment. These are identified as due to normal lattice iodine, I_3^- and I_5^- whose behaviour is consistent with the Raman work.

Key words: Colour centres, XPS, Raman spectra.

1 INTRODUCTION

Our knowledge of the aggregated forms of H-centres formed in irradiated alkali halides has advanced by the application of optical absorption and Raman spectroscopies.[1–3] In the present studies X-ray photoelectron spectroscopy (XPS) has been used as well, the results being compared with previous XPS studies on iodine systems.[4–6]

2 EXPERIMENTAL DETAILS

The Raman and optical absorption experiments were carried out on KI samples which were γ- irradiated at 198 K to 5.6 Mrad. Isochronal anneals were performed in 10 K steps of duration 10 min. KI crystals were mounted in the XPS spectrometer and spectra were produced using Mg K_α X-rays as the stimulating radiation. The binding energies of the peaks were calibrated by the use of the Au $4f_{7/2}$ peak (84 eV) of a thin gold film deposited onto the crystal surface. In order to produce the defects in the the crystals, they were irradiated *in situ* at 200 K by means of the available argon-ion beam operated at 2 KV with a beam current of 8 mA.

3 RESULTS AND DISCUSSION

3.1 *Raman and Optical Absorption Studies*

During the isochronal anneal (Figure 1) the major V-band peaks at 3.8 and 4.4 eV decay in unison with the F-band in a major annealing step at 338 K. The residual V-band profile is weak and very broad suggesting a different form of defect. The Raman spectra obtained were fitted to reveal 3 major components near 113 cm^{-1}(I_3^-), 173 cm^{-1} (I_n^-) and

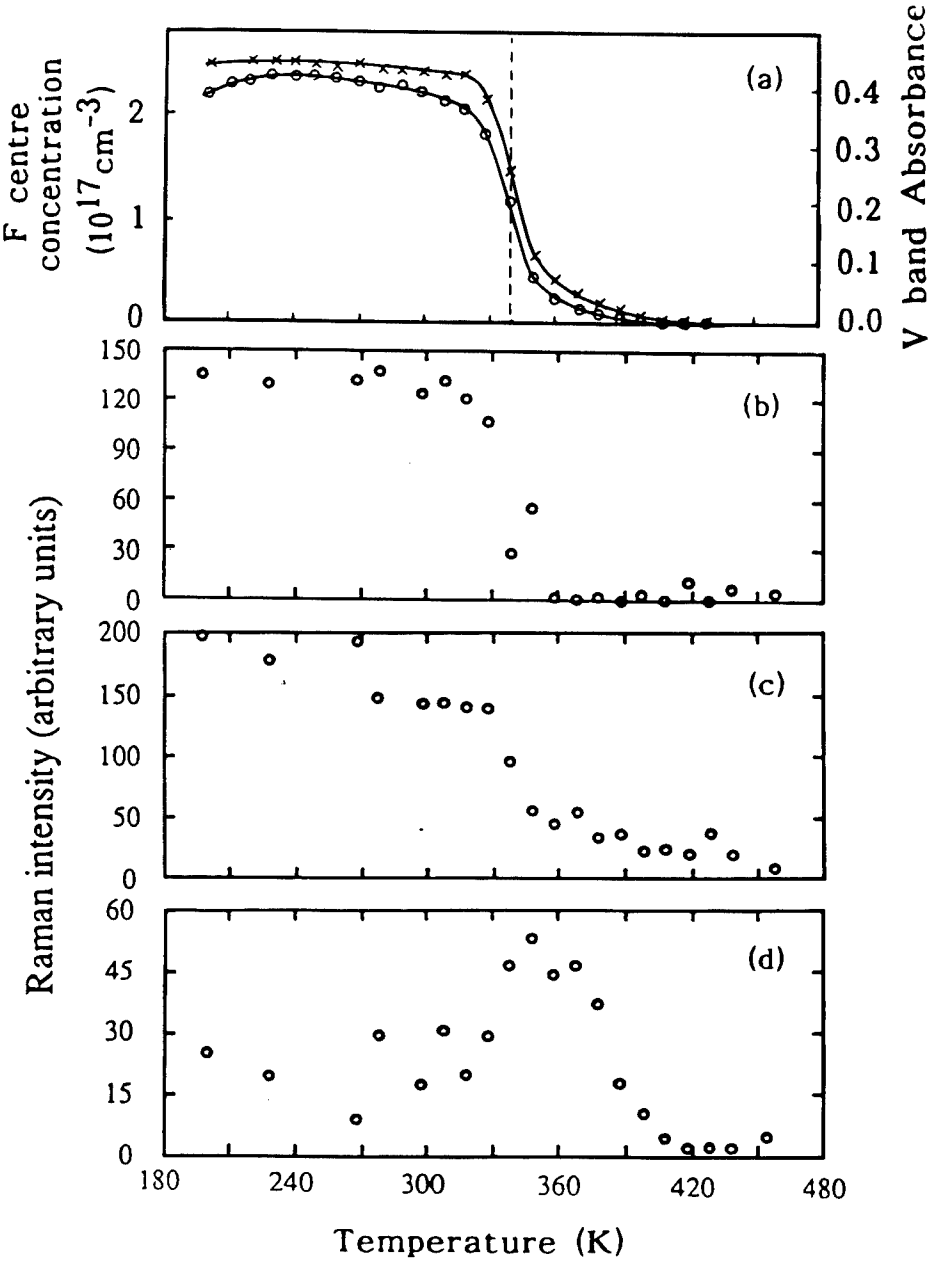

FIGURE 1 The results for isochronal annealing of samples of KI previously γ- irradiated at 198 K to a dose of 5.6 Mrad. The behaviour of the individual iodine components was obtained from fitting the Raman spectra. (a) Annealing of F-centres (crosses) and the V-band (circles). (b) Annealing of the 113 cm^{-1} Raman band due to I_3^- defects. (c) Annealing of of the 173 cm^{-1} Raman band due to I_n^- defects. (d) Evolution of the 181 cm^{-1} Raman band due to $(I_2)_n$ clusters.

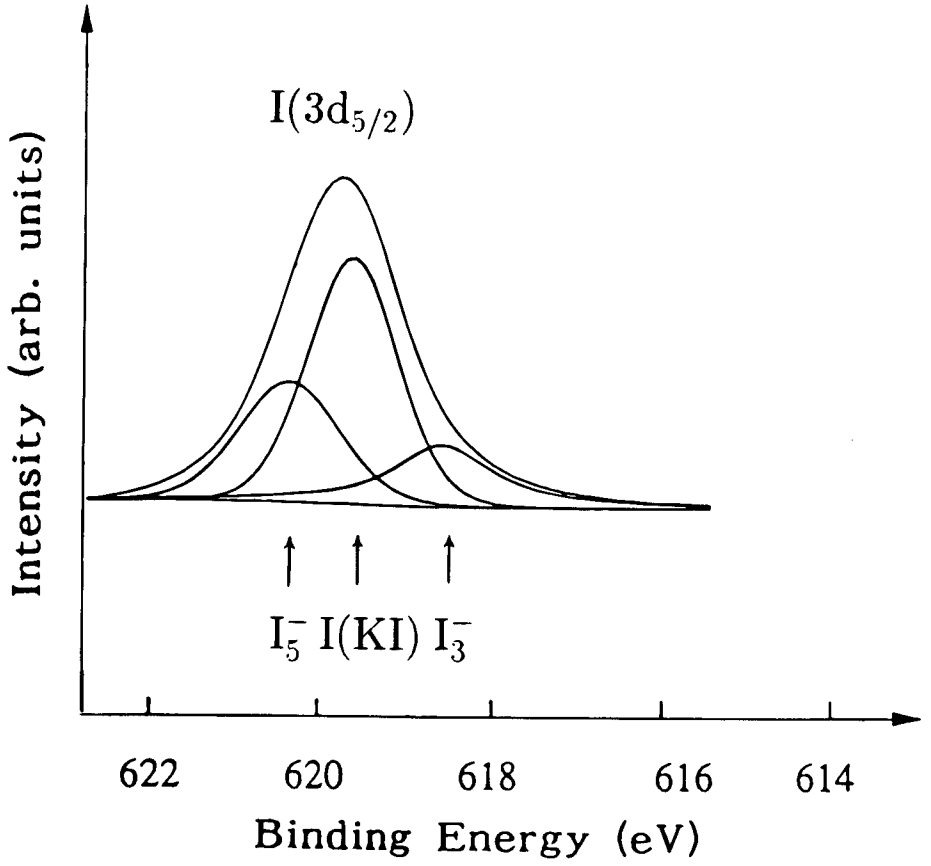

FIGURE 2 A fit of the I $3d_{5/2}$ XPS peak obtained after argon-ion bombardment of KI at 200 K showing 3 components at 618.5 eV (I_3^-), 619.5 eV (I in KI) and 620.3 eV (I_5^-).

181 cm^{-1} $(I_2)_n$. The 113 and 173 cm^{-1} features decay together in the 338 K annealing stage, while the 181 cm^{-1} band grows and subsequently decays in a separate stage near 378 K. An isothermal anneal[3] revealed that the 338 K annealing stage has close to second order kinetics and an activation energy of 1.4 eV. The results are consistent with the mutual annihilation of the F- and the small iodine aggregates I_3^- and I_n^- which contribute to the V-band absorption. The relative importance of each is uncertain, however, since the near resonance Raman conditions can selectively enhance one transition relative to another. The 181 cm^{-1} Raman band resulting from the decay of the I_3^- and I_n- aggregates is weak and broader than that observed when the $(I_2)_n$ clusters are in a crystalline form; the latter are small in number and probably have not self-organised into crystallites. They are responsible for the broad and weak V-band above the 338 K annealing stage.

3.2 *XPS Studies*

The behaviour of the I $3d_{5/2}$ peak was studied during the following procedures. The spectrum was first measured at 293 K, then re-measured at intervals during a 120 min.

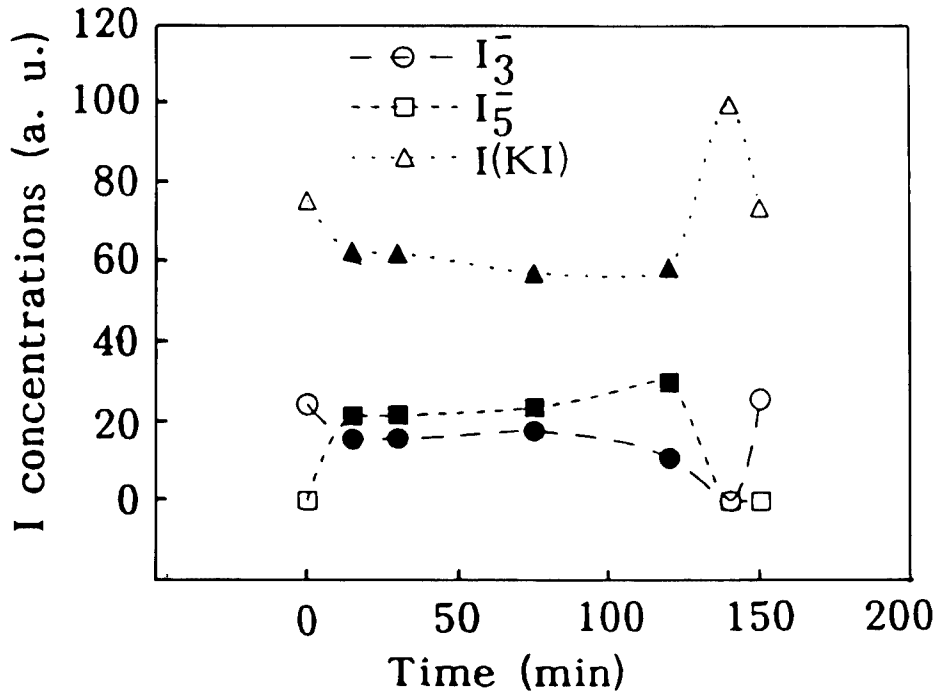

FIGURE 3 The evolution of the intensity of the various iodine components as a function of time using the XPS results. Circles: I_3^- defects; squares: I_5^- defects; triangles: (I in KI). The data at time 0 min. refer to the crystal measured at 293 K. Data between 0 and 120 min. (closed symbols) show the behaviour during the period of argon-ion irradiation at 200 K. Results plotted at 140 min. are after warming to 393 K. Data at 150 min. are after re-measuring at 293 K.

irradiation with argon-ions at 200 K as described above. The sample was then heated and measured at 393 K, followed by a measurement after cooling to 293 K. The I $3d_{5/2}$ peak broadens considerably during the the 200 K irradiation, suggesting the presence of more than one species. On heating the sample to 393 K, the spectrum becomes particularly narrow with a peak located at 619.3 eV and a FWHM of 1.4 eV. Recooling to room temperature resulted in a FWHM of 1.55 eV. The narrow spectrum produced at 393 K is considered to result from iodine in the KI lattice, since the Raman results show that iodine defect structures have all annealed out at this temperature. The 293 K spectrum is considered to have a contribution from I_3^- defects producing a component at 618.7 eV,[4–6] as evidenced by direct subtraction. These would be produced in small concentration by the X-ray beam of the XPS measurement. A fit of the I $3d_{5/2}$ peak resulting from argon-ion bombardment at 200 K is shown in Figure 2. The amplitudes of these features are very sensitive to the relative positions of the initial spectra and to the corrections of the binding energies. The positions of the peaks are 618.5 eV(I_3^-), 619.5 eV (I in KI) and 620.3 eV(I_5^-). These are in quite good agreement with those found by direct subtraction of the respective spectra and with the literature values[4–6] of 619.0 eV for I_3^- and 620.5 eV for I_5^-. Weak shake-up satellites[6] are also observed near 622.5 eV (I_3^-) and 624.0 eV(I_5^-).

Figure 3 shows the evolution of intensity of the various iodine components as a function of treatment. During the argon- ion irradiation there is an overall decrease of the I_3^- and an increase of the I_5^- defects. Warming to 393 K reduces these to zero, while the lattice iodine is enhanced. The final measurement at 293 K accords with the inital one in that I_5^- is absent and the spectrum is associated with lattice iodine with a contribution from I_3^-.

The Raman, optical absorption and XPS results show a self-consistency in that the dominant halogen aggregates formed near 200 K are of the form I_3^- and I_5^-, are responsible for the V-band and are the major complements of the F-centres.

REFERENCES

1. E. Rzepka, S. Lefrant, L. Taurel and A. E. Hughes, *J. Phys. C.* **14**, L767 (1981).
2. L. Taurel, E. Rzepka and S. Lefrant, *Radiat. Eff.* **72**, 115 (1983).
3. A. M. T. Allen, J. D. Comins and P. J. Ford, *J. Phys. C.* **18**, 5783 (1985).
4. S. L. Hsu, A. J. Signorelli, G. P. Pez and R. H. Baughman, *J. Chem. Phys.* **69**, 106 (1978).
5. I. lkemoto, M. Sakairi, T. Tsutsumi, H. Kuroda, I. Harada, M. Tasumi, H. Shirakawa and S. Ikeda, *Chem. Lett.* (1979) 1189.
6. W. R. Salaneck, H. R. Thomas, R. G. Bigelow, C. B. Duck, E. W. Plummer, A. J. Heeger and A. G. MacDiarmid, *J. Chem. Phys.* **72**, 3674 (1980).

Radiation Effects and Defects in Solids, 1995, Vol. 134, pp. 443–446
Reprints available directly from the publisher
Photocopying permitted by license only

© 1995 OPA (Overseas Publishers Association)
Amsterdam B.V. Published under license by
Gordon and Breach Science Publishers SA
Printed in Malaysia

VIBRONIC SCHEME OF THE FRANCK-CONDON STATE OF F CENTERS THAT CONSISTENTLY ELUCIDATES MCD AND RESONANCE RAMAN SCATTERING

S. MURAMATSU, Y. MORI* and H. OHKURA**

*Department of Electrical and Electronic Engineering, Utsunomiya University, Utsunomiya 321, Japan; *Department of Applied Physics, Osaka City University Sumiyoshi-ku, Osaka 558, Japan; **Department of Electronic Engineering, Okayama University of Science, Ridai-cho, Okayama 700, Japan*

The resonance Raman scattering (RRS) of F centers, particularly the photon-energy dependence of linear polarization of the RRS, has been studied on the basis of a vibronic viewpoint. With combinination of previous results that have explained magnetic circular dichroism (MCD) spectra, a vibronic scheme of the Franck-Condon state of F centers for KCl, KBr and KI crystals is established.

Key words: F centers, Resonance Raman scattering, Depolarization, Vibronic interactions.

1 INTRODUCTION

The resonance Raman scattering (RRS) of F centers provides us useful vibronic information about the Franck-Condon state (FCS) of F centers to which optical transitions occur. Hizhnyakov has developed a general theory of the resonant secondary radiation, and addressed that the validity of his theory could be verified by checking the dependence of the linear polarization ($P_1(\Omega_1)$) of the RRS on the photon energy $\hbar\Omega_1$ for the excitation.[1] Here, the $P_1(\Omega_1)$ is defined as $P_1(\Omega_1) = [I_{\|}(\Omega_1) - I_{\perp}(\Omega_1)]/[I_{\|}(\Omega_1) + I_{\perp}(\Omega_1)]$, where $I_{\|}$ and $I_{\perp}$ are the first-order Raman scattering intensities in parallel and perpendicular polarizations with respect to the incident polarization. Mori and Ohkura measured $P_1(\Omega_1)$ and proposed a simple model to explain qualitatively their experimental results on the basis of a semiclassical configuration-coordinate (CC) model.[2] After improving Mori-Ohkura's model, Muramatsu[3] derived the expression for the $P_1(\Omega_1)$ as a function of $x_1 = (\Omega_1 - \Omega_0)/\omega$, Ω_0 being the frequency of the first moment (peak) of the F absorption band, and ω an average vibrational frequency. It takes the following form,

$$P_1(x_1) = [\Delta E(x_1)^2 - C^{*2}]/[\Delta E(x_1)^2 + C^{*2}], \tag{1}$$

$$\Delta E(x_1) = 2\hbar\omega\,(\pi\alpha)^{-1/2}[1 + 2\int_0^{\beta x_1} (\beta x_1 - t)\,\exp\,(-\alpha t^2)dt],$$

where $\Delta E\,(x_1)$ denotes the energy separation between adiabatic potential energy surfaces (APES) associated with two components of 2p-like excited states coupled with two-dimensional e_g vibrational modes, α and β are parameters related to the strengths of the coupling with a_{1g} and e_g modes (See ref. 3 for detail), and C* a parameter corresponding to an interaction mixing the triply degenerate 2p-like states. In the previous work,[3] the values of α and β were taken from parameters (A and B) which could reproduce the MCD spectrum,[4] while C* was treated as a mere fitting parameter without discussing its physical meaning.

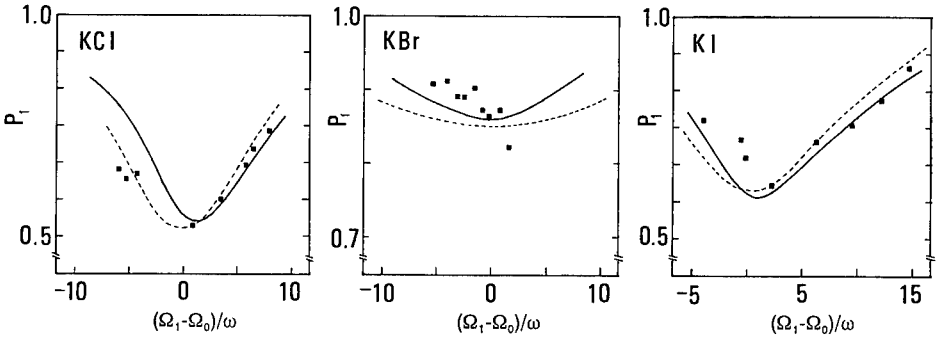

FIGURE 1 Calculated results for P_1 are compared with experimental data (■) for F centers in KCl, KBr and KI. The solid and broken lines represent results for QMC and CC model, respectively.

In the present work we recalculate the $P_1(\Omega_1)$ of the RRS of the F centers in KCl, KBr and KI based on a rigorous vibronic treatment, in which vibronic wavefunctions and their energies are directly used. The $P_1(\Omega_1)$ can be calculated quantum mechanically, if the whole vibronic structure of intermediate states in the Raman scattering process were known. In the F center, an excited 2p-like electron interacts with phonons with a_{1g}, e_g and t_{2g} symmetries. However, it is quite difficult to find general vibronic solutions, because of the complexity which arises mainly from high degeneracies in the vibrational states, particularly in t_{2g} modes. To avoid such a difficulty, we use the following model Hamiltonian:

$$\begin{aligned} H_{el} = &\{V_A Q_1 + V_E(Q_2 + Q_3/3^{1/2})\} \mid x><x \mid + \{V_A Q_1 + V_E(-Q_2 + Q_3/3^{1/2})\} \\ &\mid y><y \mid + \{V_A Q_1 - 2V_E Q_3/3^{1/2}\} \mid z><z \mid \\ &+ \{C^* (\mid x><y \mid + \mid x><z \mid + \mid y><z \mid) + \text{h.c.}\}, \end{aligned} \tag{2}$$

where the 1st and 2nd terms describe the coupling of electronic 2p-like excited states ($\mid x>$, $\mid y>$ and $\mid z>$) with the vibrational a_{1g} (Q_1) and e_g (Q_2, Q_3) modes. In the last term in eq. (2) a constant mixing parameter C* is introduced to minic the coupling with t_{2g} modes which causes mixing between the 2p-like excited states. For the H_{el} in (2), we can solve a secular equation numerically, and practically calculate the $P_1(\Omega_1)$ by a direct use of eigenvalues and eigenstates in the Heisenberg-Kramers formula for light scattering.[5]

Hereafter, the present calculation will be referred to as quantum mechanical calculation (QMC), to distinguish it from the previous semiclassical CC model.

2 QUANTUM MECHANICAL CALCULATION

In the calculation of $P_1(\Omega_1)$ we followed the procedure used in our previous work.[5] Input parameters, which characterize H_{el} in (2),are Huang-Rhys factors S_A ($= V_A{}^2/2\mu_A\hbar\omega_A{}^3$)

and S_E ($= V_E^2/2\mu_E\hbar\omega_E^3$), and C*. Throughout the present paper, $\omega_A = \omega_E = \omega$ is assumed for simplicity and $\hbar\omega$ was taken to be 15, 14 and 13 meV for KCl, KBr and KI, respectively.[4,6]

3 RESULTS AND DISCUSSION

First we have estimated three parameters, S_A, S_E and C* so as to reproduce optical F absorption bands. Then, using a set of parameters estimated, we have calculated the excitation spectrum $P(\Omega_1)$ for the RRS in the first-order Raman scattering region. The calculated results are plotted as a function of Ω_1 in Figure 1 with solid lines for QMC and with broken ones for C.C. model. Both are compared with experimental data indicated by closed squares. The coincidence between the calculated absolute value of the $P(\Omega_1)$ and experimental data[2,7] is fairly good for KCl and KI, and reasonable for KBr inspite of a few data. It should be noticed that almost the same results have been obtained by the two different approaches, one being based on a semiclassical framework and the other based on a quantum mechanical formula.

Let us discuss the result of QMC in comparison with that of the CC model.[3] In the CC model, the value of $C^*/\hbar\omega$ can be deduced from experimental data on the linear polarization. If we adopt the minimum value (P_{min}) of the experimental polarization and use the fact that the ΔE in eg. (1) yielding P_{min} is $2\hbar\omega/(\pi\alpha)^{1/2}$, the $C^*/\hbar\omega$ is given by the following simple relation:

$$C^*/\hbar\omega = 2[\rho_{max}/\pi\alpha]^{1/2}, \tag{3}$$

where ρ_{max} stands for the maximum depolarization ratio, $(I_\perp/I_\parallel)_{max} = (1 - P_{min})/(1 + P_{min})$. In the CC model the depolarization of the RRS intensity can be considered as the consequence of the following Raman process: $|g> \rightarrow |u> \rightarrow |g'>$ for x-polarized incident light with energy of $\hbar\Omega_1$. Here $|g>$ and $|g'>$ are initial and final states, and $|u>$ is an intermediate state described by $|u> = |x> + \{C^*/\Delta E(\Omega_1)\}|y>$. Therefore, the depolarization ratio is proportional to $|C^*|^2$, as in eq. (3). The value of $C^*/\hbar\omega$ obtained from this relation is compared with that of $C^*/\hbar\omega$ in the QMC in Table I. The value of $C^*/\hbar\omega$ of QMC, which has been determined so as to reproduce the experimental result for $P_1(\Omega_1)$, is quite close to the value of $C^*/\hbar\omega$ obtained from eq. (3), except for KBr. For KBr, the value of $C^*/\hbar\omega$ in the CC model is close to that of QMC, if the value of α obtained from values of A and B of Mauser *et al.*[8] is adopted. The A and B of Mauser *et al.* is well compatible with the QMC result as compared with A and B in Ref. 4, although both the sets of the parameters give almost the same MCD spectra. The degree of the polarization of the RRS is the complement to the MCD data in determining the vibronic scheme of FCS of the F centers.

Finally we compare the value of $C^*/\hbar\omega$ with that of a parameter C in Ref. 4, which represents the coupling strength for t_{2g} modes relative to a spin-orbit coupling constant λ. The latter was determined from the analysis of the MCD spectrum.[4] The $C^*/\hbar\omega$ can be related to $2^{1/2}(\lambda/\hbar\omega)$ C, since the former makes a contribution to the second moment of the absorption spectrum by the amount of $2|C^*|^2$, while the latter does by the amount of $4C^2|\lambda|$.[2] The values of $C^*/\hbar\omega$ of 1.6, 1.2 and 1.3 are extracted for KCl, KBr and KI, respectively, from the values of C and λ given in Ref. 4. They fairly well correspond to the values of $C^*/\hbar\omega$ in Table I.

Table I
The values of $C^*/\hbar\omega$ in QMC and CC model. The values of other parameters are also listed. α and β are determined by using values of A and B in Ref. 4 or in Ref. 8, where they are denoted by W_1 and W_3, respectively.

Crystal	S_A	S_E	$C^*/\hbar\omega$ (QMC)	α	β	$C^*/\hbar\omega$ (CC model)
KCl	10.0	3.6	1.4	0.24[a]	0.21[a]	1.5
KBr	15.0	1.3	0.8	0.58[a]	0.05[a]	0.4
				0.08[b]	0.18[b]	1.1
KI	10.0	3.0	1.3	0.21[a]	0.19[a]	1.3

[a] Reference 4
[b] Reference 8

4 SUMMARY

We have explained the observed photon-energy dependence of the linear polarization of the RRS of F centers in KCl, KBr and KI, by using vibronic solutions for a model Hamiltonian including a constant mixing interaction instead of interactions with t_{2g} modes. It is shown that the obtained result for the FCS is consistent with the previous one determined from the MCD spectra.

REFERENCES

1. V. Hizhnyyakov, *Phys. Rev.* **B30**, 3490 (1984).
2. Y. Mori and H. Ohkura, *J. Phys. Chem. Solids* **51**, 633 (1990).
3. S. Muramatsu, *J. Phys. Soc. Jpn.* **62**, 1078 (1993).
4. S. Muramstsu, N. Akiyama, Y. Mori and H. Ohkura, *J. Phys. Soc. Jpn.* **55**, 2811 (1986).
5. S. Muramatsu and K. Nasu, *J. Phys. Soc. Jpn.* **46**, 189 (1979).
6. W. B. Fowler, Physics of Color Centers, ed. W. B. Fowler (Academic Press, New York, 1968) p. 627.
7. Y. Kimura, *Master Thesis* [in Japanese], Osaka City University (1985).
8. K. E. Mauser, B. Niesert and A. Winnacker, *Z. Phys.* **B26**, 107 (1977).

Radiation Effects and Defects in Solids, 1995, Vol. 134, pp. 447–451
Reprints available directly from the publisher
Photocopying permitted by license only

© 1995 OPA (Overseas Publishers Association)
Amsterdam B.V. Published under license by
Gordon and Breach Science Publishers SA
Printed in Malaysia

LUMINESCENCE OF DEFECT CENTRES IN Hg_2Cl_2

Z. BRYKNAR,* P. PEKA,** A. KOŇÁKOVÁ,* J. KRÁL,*
and H.-J. SCHULZ**

**Czech Technical University in Prague, Břehová 7, CZ-11519 Prague 1, Czech Republic; **Fritz-Haber-Institut der Max-Planck Gesellschaft, Faradayweg 4–6, D-14195 Berlin, FRG*

Luminescence in Hg_2Cl_2 crystals excited with UV light is investigated in the spectral region 0.8–2.25 eV. Measurements are performed on as-grown samples and on samples previously exposed to UV light at RT. Six emission bands are found which depend on the concentration of the photochemical entities produced by irradiation of the crystals at RT. It is concluded that infra-red (IR) luminescence of Hg_2Cl_2 originates from crystal defects. The observed emission bands are tentatively attributed to the emission of $(HgCl_xBr_{3-x})^-$ and $(HgCl_xBr_{4-x})^{2-}$ complexes formed with residual Br impurities. Centres responsible for IR Hg_2Cl_2 emissions are excited: (i) via excitons of Hg_2Cl_2, (ii) via excited states of isolated Hg_2Br_2 molecules, and (iii) resonantly through the excitation bands of defect centres.

Key words: mercurous chloride, luminescence, exciton, chlorine-bromide complex of mercury.

1 INTRODUCTION

Mercurous chloride, Hg_2Cl_2, molecular crystals are highly promising for applications in opto-electronics because of the high value of birefringence, transparency up to 20 μm, and favourable acousto-optic figures of merit. The crystals are formed by linear chains of molecules Cl-Hg-Hg-Cl oriented parallel to axis *c*. The intramolecular bonding Hg-Hg is covalent while the bond of this core with the chlorine ions is ionic with a partially covalent character. The bond between adjacent molecules is of van-der-Waals type.

Hg_2Cl_2 crystals are photosensitive. If exposed to UV light at RT, they decompose into Hg and $HgCl_2$.[1] The aim of this work is to study the formation of luminescence centres responsible for IR emission between 0.80 and 2.25 eV.

2 EXPERIMENTAL TECHNIQUES

Hg_2Cl_2 crystals were prepared by crystallization from the vapour phase in the Institute of Physics, Prague. Using PIXE (Proton Induced X-ray Emission) analysis, the following impurities with atomic number $Z > 15$ were found in the crystals in concentrations higher than 1 ppm: K—700 ppm, Br—250 ppm, Cu—87 ppm, I—38 ppm, Fe—30 ppm, Sr—18 ppm, Ge—17 ppm, and Ti—14 ppm.

The samples were cleaved from a single crystal in the form of platelets with dimensions of approximately $1 \times 5 \times 12$ mm^3, the large faces being the tetragonal planes [110]. Two setups were used for the measurement of Hg_2Cl_2 luminescence. The first one, including an RCA 7103 cooled photomultiplier (S-1 photocatode), allowed to measure emission spectra in the range $h\nu > 1.22$ eV, the second one, with cooled Ge-detector, recorded emission in the spectral range 0.80–1.55 eV. All emission spectra were corrected.

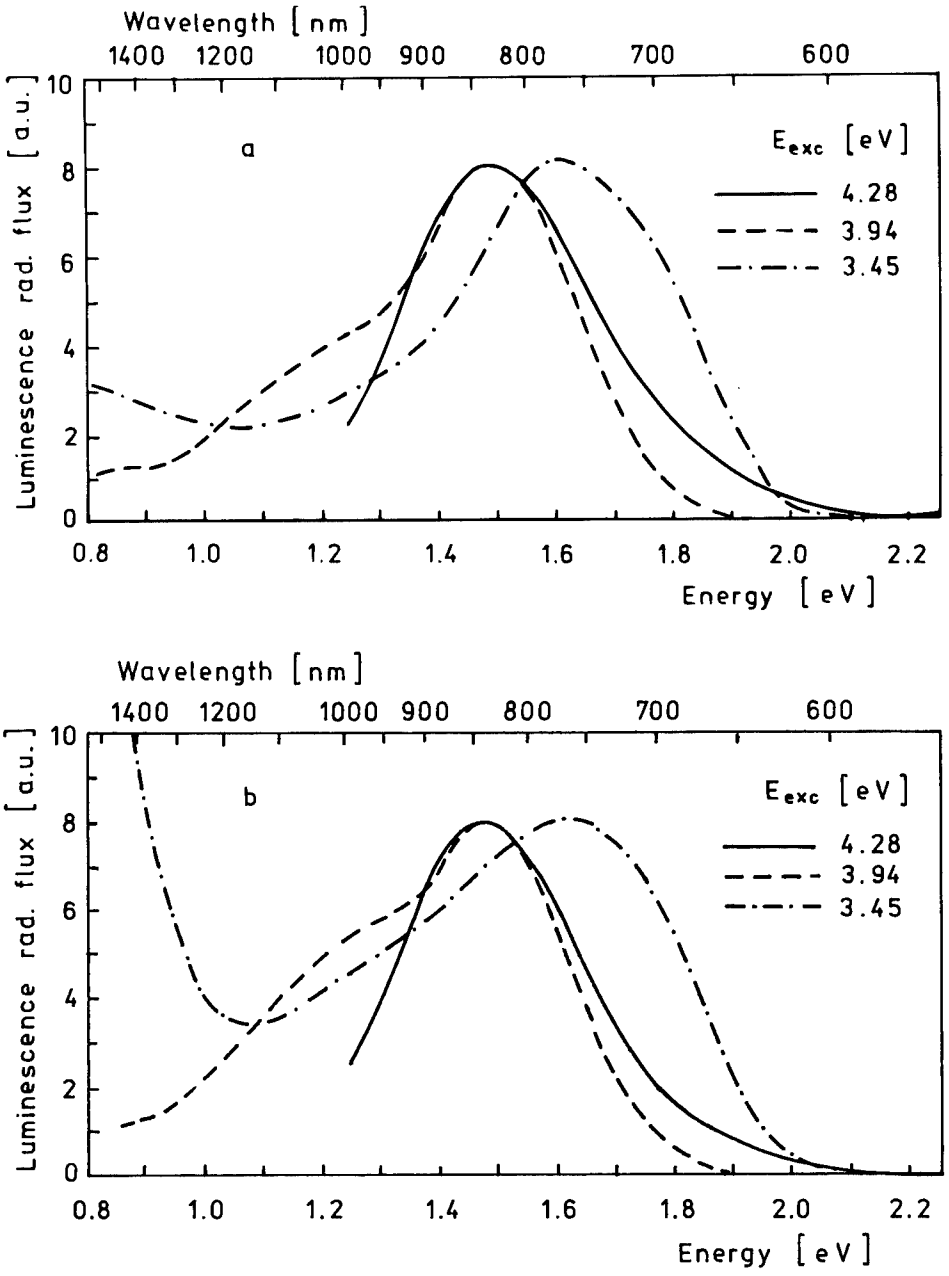

FIGURE 1 Normalized Hg_2Cl_2 emission spectra at 10 K taken for the excitation photon energy indicated in the figures a) as-grown crystal, b) crystal exposed at RT to unfiltered high-pressure xenon lamp (500 Watts) light in a distance of 10 cm for 30 sec.

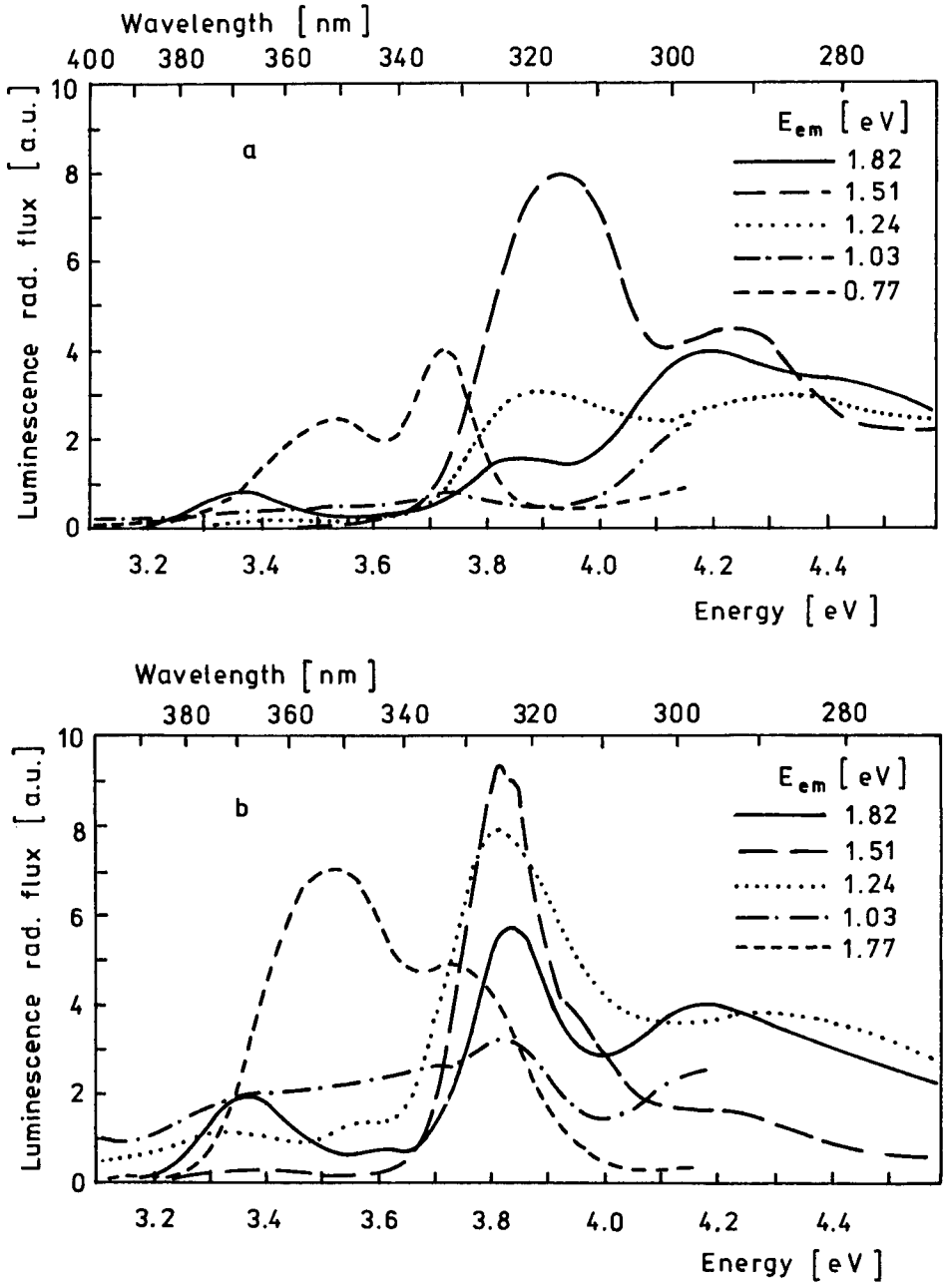

FIGURE 2 Hg_2Cl_2 excitation spectra at 10- K taken for the emission photon energy indicated in the figures a) as-grown crystal, b) an exposed crystal (exposure parameters–see Figure 1).

3 RESULTS AND DISCUSSION

Normalized Hg_2Cl_2 emission spectra at 10 K in Figure. 1 are shown for (a) the as-grown crystal and (b) the crystal exposed at RT to the unfiltered light of a high-pressure xenon lamp (500 Watts) at a distance of 10 cm for 30 sec. The spectra depend conspicuously on the indicated energies of exciting photons. The irradiation of crystals was performed at RT because at low temperature their photochemical decomposition is practically stopped. The changes in the emission spectra after irradiation are caused by the UV part of the xenon lamp light which decomposes the crystals[2]. The mentioned irradiation of crystal causes a three-fold increase of the luminescence intensity. This fact indicates that the red and IR emissions are mainly caused by the products of the photodecomposition. Using a non-linear least-squares approximation, all emission spectra shown in Figure 1 are fitted with linear combination of Gaussian curves. The parameters of Gaussians are found as follows: (1) maximal intensity at 1.72 eV (FWHM at 0.33 eV), (2) 1.51 eV (0.32 eV), (3) 1.39 eV (0.28 eV), (4) 1.23 eV (0.23 eV), (5) 1.06 eV (0.25 eV), and (6) 0.82 eV (0.21 eV). The most intensive emission is the band peaked at 1.51 eV under excitation at 4.28 and 3.94 eV.

If we consider the photodecomposition $Hg_2Cl_2 \rightarrow Hg + HgCl_2$, then the first candidate for IR emission could be $HgCl_2$ molecule. This free molecule has a broad-band fluorescence in the range of 2.21–3.65 eV under excitation by photons with energy higher than 6.5 eV[3], which is not in accordance with our excitation spectra.

The other possible photodissociation process can be described by reaction

$$2Hg_2Cl_2 \rightarrow (HgCl_3)^- + 3Hg + Cl,$$

where Hg(I) is converted to the Hg(II). A similar reaction can give rise to the $(HgCl_4)^{2-}$ complex. The existence of these complexes is known (e.g. Ref. 4) for aqueous systems. Because of a large concentration of Br in Hg_2Cl_2 crystals, one can suppose that some chlorine ions are substituted by bromide ions to form complexes $(HgCl_xBr_{3-x})^-$ and $(HgCl_xBr_{4-x})^{2-}$. These complexes are serious candidates for the IR luminescence, consequently a great variety of the IR emission spectra of Hg_2Cl_2 is to be expected, which is in accordance with Figure 1. For the time being an exact explanation of the nature of the IR luminescence is not possible.

Excitation spectra of Hg_2Cl_2 for as-grown and irradiated crystals are shown in Figure 2. The interpretation of these spectra is complicated because, to our knowledge, a calculation on the electronic band structure of the Hg_2Cl_2 crystals has not yet been performed. Kleier and Wadt[5] presented valence bond calculations for the ground states of Hg_2Cl_2 and Hg_2F_2 molecules only and they estimated the excitation energies for the some excited states of Hg_2Cl_2. These results support an interpretation of the observed spectra because in molecular crystals the electron levels of the free molecule will emerge as excitons. Due to crystal field, these electron levels will shift to lower energies. The exciton energies in Hg_2Cl_2[2] and Hg_2Br_2 crystals were determined from the polarized excitation spectra for the blue emission. These spectra are independent of the photochemical decomposition of the crystals.

A high energy part of the excitation spectra ($h\nu > 4.1$ eV, see Figure 2) is identical to the excitation spectrum for the blue Hg_2Cl_2 emission. Therefore we assume that the peculiarities close to 4.10, 4.15, and 4.40 eV can be assigned to the excitons, corresponding to the $\sigma_g \rightarrow \pi_u$, $\sigma_g \rightarrow \sigma_u$, and $\pi_g \rightarrow \sigma_u$ transitions of the free Hg_2Cl_2 molecule.[5] Comparisons of the calculated excitations giving rise to dipole-allowed transitions in a free Hg_2Cl_2 molecule, with experimentally determined exciton energies in

Hg_2Cl_2 and Hg_2Br_2 crystals are reported in Table I. It is worth to note that the band gap value of Hg_2Cl_2 was found[6] to be 4.8 eV.

Table I

Comparisons of the calculated excitation energies for the low-lying states of Hg_2Cl_2 molecule $\Delta E(molec)$[5] with experimentally determined exciton energies $E(Hg_2Cl_2)$ and $E(Hg_2Br_2)$ of the respective crystals. Directions of the transition moments are referred with respect to the molecule axis.

Excitation	ΔE(molec) [eV]	$E(Hg_2Cl_2)$ [eV]	$E(Hg_2Br_2)$ [eV]	Polarization
$4\sigma_g \rightarrow 3\pi_u$	6.35	4.15	3.59	$\perp$
$4\sigma_g \rightarrow 4\pi_u$	6.62	4.10	3.57	$\parallel$
$2\pi_g \rightarrow 4\sigma_u$	7.06	4.40	3.93	$\perp$

As Hg_2Cl_2 crystals contain a large concentration of bromine, the Hg_2Br_2 molecules are present in the Hg_2Cl_2 matrix and they can be excited separately. Therefore, the excitation bands near 3.54 and 3.94 eV were assigned to the excited states of the isolated Hg_2Br_2 molecules. The energies of these bands are close to the excitation band for blue emission of pure Hg_2Br_2 crystals.

The 3.35, 3.73, and 3.81 eV excitation bands are conspicuously enhanced after UV light exposure of the above crystal at RT (see Figure 2b). Therefore these bands are attributed to the specific excitation bands of the defect centres, probably $(HgCl_3)^-$ and $(HgCl_xBr_{4-x})^{2-}$ complexes, arising due to crystal photodecomposition.

REFERENCES

1. Č. Barta, J. Trnka, L. M. Beljajev, in: *Proc. Symposium on Mercury(I) Halides*, Liblice 1976, (Publ. Czechosl. Acad. Sci., Prague, 1977), p. 111.
2. Z. Bryknar, M. Holoubek, J. Walter, in: *Proc. Int. Conf. Defects in Insulating Materials*, Nordkirchen 1992, (Ed. O. Kanest and J. M. Spaeth, World Scientific Publ. Co., Singapore 1993), p. 1154.
3. K. Wieland, *Z. Phys.* **76**, 801 (1932).
4. S. Fujita, H. Horii, T. Mori, S. Taniguchi, *J. Phys. Chem.* **82**, 1693 (1978).
5. D. A. Kleier, W. R. Wadt: *J. Am. Chem. Soc.* **102**, 6909 (1980).
6. Z. Bryknar, W. Hersel, Č. Barta: *Crystal Res. Technol.* **17**, 425 (1982).

Radiation Effects and Defects in Solids, 1995, Vol. 134, pp. 453–455
Reprints available directly from the publisher
Photocopying permitted by license only

© 1995 OPA (Overseas Publishers Association)
Amsterdam B.V. Published under license by
Gordon and Breach Science Publishers SA
Printed in Malaysia

AUTLER-TOWNES SPLITTINGS OF PHOTO-EXCITED POINT DEFECTS

M. GLASBEEK, C. J. M. TAVARES, M. A. COSTA NETO and R. SITTERS

Laboratory of Physical Chemistry, University of Amsterdam, Nieuwe Achtergracht 127, 1018 WS Amsterdam, The Netherlands

Autler-Townes interactions are observed in the time domain by performing a modified echo experiment. Constructive and destructive interferences characteristic of the Autler-Townes components in electron spin triplet states are observed for two different color centers in calcium oxide and diamond crystals, respectively.

Key words: Autler-Townes effect, triplet states, point defects, ODMR, spin coherence.

In this paper we study multilevel coherences observed for defects in a photo-excited triplet state when the triplet state is simultaneously driven by two resonant microwave fields of different microwave frequency. It has long been known that when in a three-level system one of the possible transitions is coherently driven while probing a second transition, the latter will become split (Autler-Townes (AT) splitting).[1] In solids, however, inhomogeneous line broadening most often prevents that the AT splitting can be directly resolved in the spectrum. On the other hand, in a two-pulse echo decay experiment the influence of inhomogeneous broadening is averaged out. Here we show that the normal two-pulse sequence in the echo experiment can be modified in order to be able to resolve (for the first time in the microwave region for electron spin transitions in solids) Autler-Townes splittings using optical detection. Experimental results representative of constructive and destructive interference of the Autler-Townes components in triplet states will be presented for phosphorescent F-type defects in colored calcium oxide[2] crystals and the luminescent N-V center in diamond.[3]

In the experiment initially two microwave pulses resonant with one of the triplet state zero-field transitions (of frequency ω_{12}) with a time interval of τ are applied. The pulses give rise to a coherent response at 2τ (the echo), irrespective of the amount of inhomogeneous broadening. In the echo experiments of relevance here, during the rephasing interval (between τ and 2τ), a second microwave field is applied in order to coherently drive another transition of the three-level system (of frequency ω_{13}). As a result of the driving field at ω_{13}, levels 1 and 3 each will exhibit an Autler-Townes doublet splitting. As derived elsewhere,[4] this splitting manifests itself as amplitude modulation effects of the echo (detected at ω_{12}), the periodicity of the echo modulation being characteristic of the Autler-Townes doublet splitting.

The spectrometer for optical detection of spin coherence has been described previously.[2] Yellow colored calcium oxide crystals contain F_2^{2+} defects which consist of a nearest-neighbor oxygen divacancy containing two electrons.[2] Upon photo-excitation, the F_2^{2+} defect is excited into its phosphorescent $^3B_1$ state for which the no-phonon emission peaks at 683 nm. Zero-field resonance frequencies in the excited $^3B_1$ state of the F_2^{2+} defect occur at 1870 MHz ($|D| - |E|$ transition) and 2230 MHz ($|D| + |E|$ transition). Figure 1 shows typical optically detected spin echo amplitude decays generated (at 1.3 K) in the absence and in the presence of the driving second microwave frequency, ω_{13}. The inset shows the applied pulse sequences at the two microwave frequencies, ω_{12} and ω_{13}. As illustrated by Figure 1, the effect of the second microwave field when driving the $1 \leftrightarrow 3$ transition near resonance is to modulate the echo amplitude decay of the $|D| - |E|$

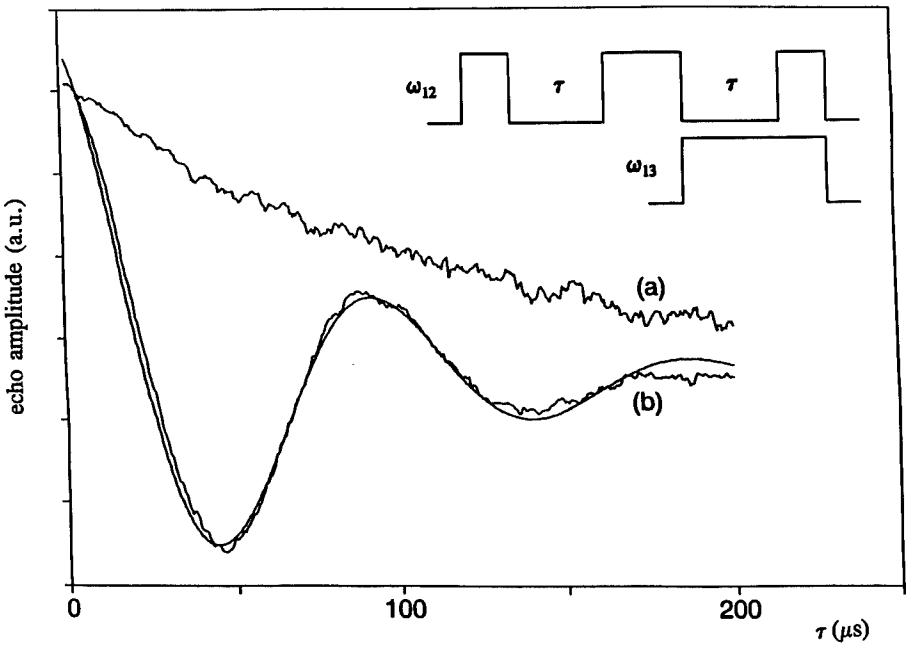

FIGURE 1 Optically detected Hahn echo decay of the |D| − |E| zero-field transition (at 1870 MHz) of the F_2^{2+} center in CaO in the photo-excited $^3B_1$ state at 1.3 K. (a) without pumping the |D| + |E| transition, (b) with the simultaneous pumping at $\tau < t < 2\tau$ of |D| + |E| transition (at 2230 MHz), see also insert. Drawn line is simulated Autler-Townes modulation.

transition of the F_2^{2+} center in its photo-excited triplet state. The result is explained as follows. During the rephasing interval, at $\tau < t < \tau$, the driving field ω_{13} gives rise to phase shifts of the spin coherent components which result in echo signals phase shifted by $(\Delta\omega/2 \pm \overline{\omega})\tau$ with respect to the phase of the echo in the absence of ω_{13}. $\Delta\omega = \omega - \omega_{13}$ and $\overline{\omega} = 1/2\{(\Delta\omega)2 + \omega_1^2\}^{1/2}$, where ω_1 characterizes the Rabi frequency for the coherently driven $1 \leftrightarrow 3$ transition. The final probe pulse samples the polarization at 2τ and is given by $R(2\tau) = R_0 \cos(\Delta\omega/2 \pm \overline{\omega})\tau$. The drawn line is a monoexponentially damped cosine function which fits the experimental data. Variation of the power of the driving microwave field at ω_{13} showed a change of the echo modulation periodicity: at higher powers the modulation frequency increased, as expected.

Similar results were obtained for another luminescent color center, the N-V center in diamond. The N-V center in diamond has a triplet electron spin ground state which previously has been studied by means of optically detected magnetic resonance (ODMR).[3] In the presence of a small magnetic field of $\approx$ 10 G along the [100] crystallographic direction, the degeneracy of the upper two zero-field spin levels in the ground state is lifted and, since all N-V centers are magnetically equivalent for the chosen direction of the magnetic field, two ODMR transitions at frequencies of 2862 MHz and 2895 MHz are observed. Upon driving the 2862 MHz transition while probing the echo amplitude decay of the 2895 MHz transition, Autler-Townes modulations could be observed. As for the photo-excited F_2^{2+} center, an increase of the driving field strength yielded an increase of the Autler Townes modulation frequency.

ACKNOWLEDGEMENT

This work was supported in part by the ECTS programm of the European Community Action Scheme and by the Netherlands Foundation for Chemical Research (SON) with financial aid from The Netherlands Organization for Scientific Research (NWO).

REFERENCES

1. S. H. Autler and C. H. Townes, *Phys. Rev.*, **100**, 703 (1955); R. M. Whitley and C. R. Stroud, *Phys. Rev. A.* **14,** 1498 (1976); Y. R. Shen, *The Principles of Nonlinear Optics,* (Wiley, New York, 1984), p. 418.
2. D. J. Gravesteijn and M. Glasbeek, *Phys. Rev. B* **19,** 5549 (1979); M. Glasbeek and R. Hond, *Phys. Rev. B,* 23, 4220 (1981).
3. E. van Oort and M. Glasbeek, *Phys. Rev. B,* **40**, 6509 (1989); *ibid Chem. Phys.*, **152,** 365 (1991).
4. C. J. M. Tavares, M. A. Costa Neto, R. Sitters, N. B. Manson, and M. Glasbeek, to be published.

Radiation Effects and Defects in Solids, 1995, Vol. 134, pp. 457–460
Reprints available directly from the publisher
Photocopying permitted by license only

© 1995 OPA (Overseas Publishers Association)
Amsterdam B.V. Published under license by
Gordon and Breach Science Publishers SA
Printed in Malaysia

PHOTOINDUCED COLOR CENTERS CREATION IN SUPERIONIC CRYSTALS $RbAg_4I_5$

N. KOVALEVA, A. BORIS, S. BREDIKHIN and *T. AWANO

Institute of Solid State Physics, Chernogolovka, Moscow dist., 142432 Russia;
**Department of Applied Physics, Tohoku Gakuin University, Tagajo 985, Japan*

A new phenomenon of a reversible photoinduced coloration caused by light irradiation is discovered and investigated in superionic $RbAg_4I_5$ crystals. The reversible photoinduced absorption is found to be a result of irradiation by light with wavelengths in the region from 420 nm to 450 nm. The proposed mechanism of the discovered effect is associated with ambipolar diffusion of screened by mobile ions optically excited electronic carriers. The processes of color centers creation in superionic crystals $RbAg_4I_5$ due to additive coloring in iodine vapours, ionic implantation and γ-ray irradiation are considered.

Key words: Superionic crystals, photoinduced color centers.

1 INTRODUCTION

Coexistence of a regular crystal lattice and a system of nonordered ions in superionic crystals leads to their unique physical properties. In superionic crystals one would expect the interaction between nonequilibrium electronic carriers optically generated to the conduction or valence bands and mobile ionic subsystem. Mobile ions because of high concentration and mobility should screen the electrostatic interaction between ionized centers and excited electronic carriers. For this reason one would expect considerable increasing of lifetime of nonequilibrium electronic carriers in superionic crystals. Due to the excess concentration the diffusion flow of these screened electronic carriers in the regime of ambipolar diffusion should appear from the irradiated region. As a result of these processes photoinduced defects can be produced in superionic crystals.

2 EXPERIMENTAL

Investigations were carried out on polycrystalline $RbAg_4I_5$ specimens grown from the melt by the zone melting method. The thickness of the samples was $0.2 \div 0.3$ mm. The irradiation of α—$RbAg_4I_5$ superionic crystals was performed at room temperature during 1–2 hours. Selective irradiation was produced by means of a high pressure Xenon lamp and a system of filter glasses. Optical measurements were fulfiled by automatic installation on the base of double grating monochromator in the transmission geometry.

3 RESULTS AND DISCUSSION

To study the structure of color centers we carried out detail investigations at low temperatures of absorption spectra additively colored in iodine vapours and affected to ionic implantation superionic crystals $RbAg_4I_5$. The ionic implantation of the sample surface was performed by positively charged ions of noble gase Kr^+ at room temperature. With the fluence $D \simeq 10^{14} \div 10^{15}$ cm^{-2} and the planting-ion energy $E \simeq 160 \div 180$ keV the surface of the samples acquired a stable red-orange color. The possible mechanisms of

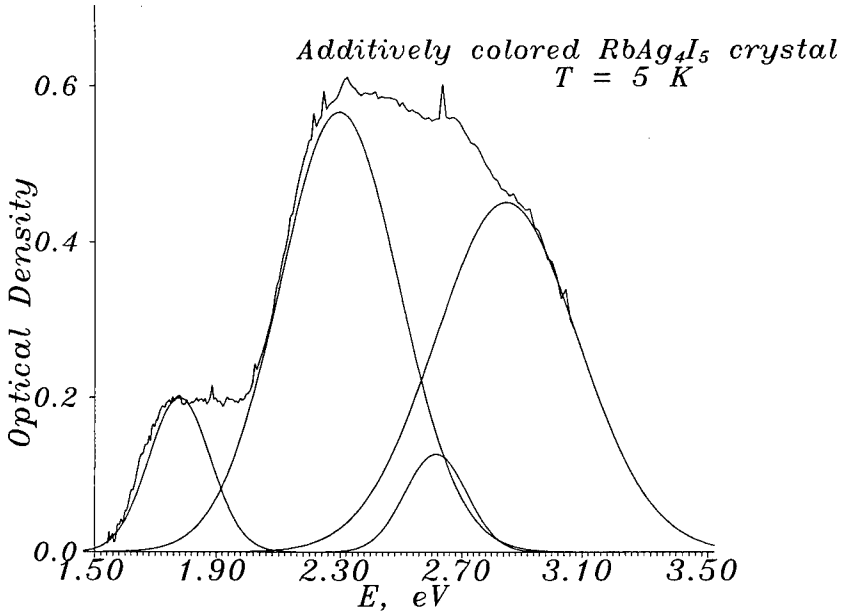

FIGURE 1 Absorption spectrum of additively colored $RbAg_4I_5$ superionic crystal.

defect formation caused by ionic implantation of $RbAg_4I_5$ superionic crystals are considered in [1]. Intensive additive coloring of $RbAg_4I_5$ in iodine atmosphere at room temperature is caused by the superionic properties of this material revealing high values of the Ag^+ diffusion coefficient [2]. Due to adsorpance of iodine molecules at crystal surface and formation of the AgI compound there the diffusion flows of Ag and holes adjacent to the silver vacancies appear correspondingly to the surface and into the sample. As a result color centers involving the hole adjacent to the silver vacancy can be created in the bulk. The typical optical density spectrum of additively colored $RbAg_4I_5$ superionic crystal at T = 5 K is shown in Figure 1. As can be seen there are four absorption bands in the optical density spectrum. The defined maxima, E_0, and halfwidths, W, after the spectrum was fitted into the sum of gaussian bands are listed in the Table I.

Table I
Absorption bands induced in $RbAg_4I_5$ by additive coloration, ionic implantation, γ-ray irradiation [3] and photoirradiation.

Additive Coloration		Ionic Implantation		γ-Ray Irradiation		Photocoloration	
E_0 (eV)	W (eV)	E_0 (eV)	W (eV)	E_0 (eV)	W (eV)	E_0 (eV)	W (eV)
1.82	0.12	1.91	0.12	1.80	0.12	1.83	0.12
		2.09	0.06	2.05	0.09	2.06	0.12
2.32	0.23	2.32	0.23	2.32	0.23	2.29	0.23
2.55	0.12	2.63	0.12			2.63	0.12
2.85	0.28	2.85	0.28	2.85	0.28	2.85	0.28

Comparing the observed absorption bands induced by γ-ray irradiation at 77 K [3] (see Table I) with those appearing in the additively colored and ion-implanted $RbAg_4I_5$ crystals we find similar absorption bands.

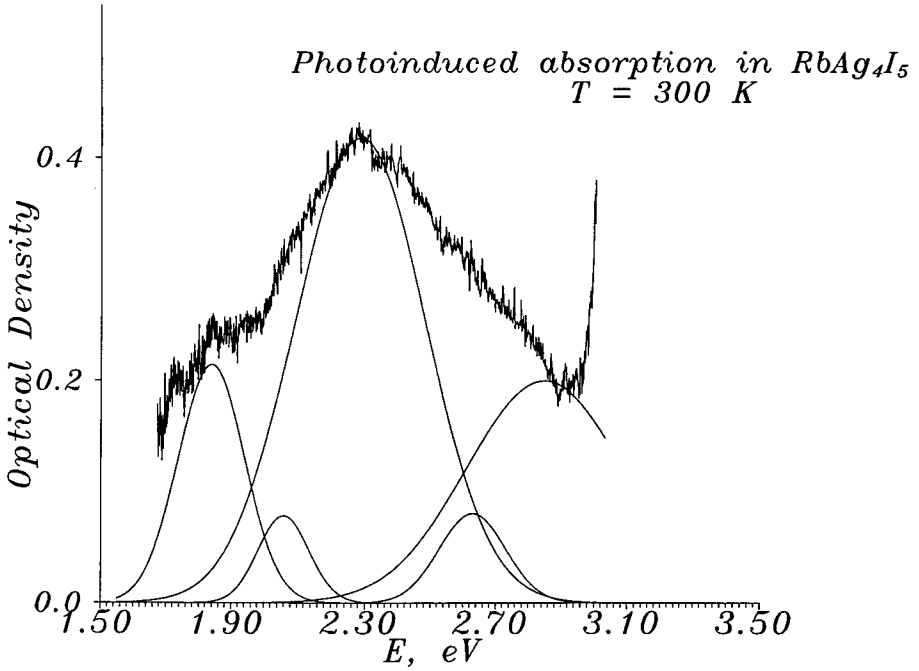

FIGURE 2 Photoinduced absorption spectrum of $RbAg_4I_5$ crystal.

In the present work the effect of reversible photoinduced coloration is discovered in $RbAg_4I_5$ superionic crystals under the irradiation by light with wavelengths in the spectral interval 420 nm $\div$ 450 nm. It is found that the photoinduced absorption depends on a wavelength and intensity of the irradiated light, the sample stoichiometry and time of irradiation. In Figure 2 is shown the typical photoinduced absorption spectrum in $RbAg_4I_5$ superionic crystals after two hours irradiation by light with wavelength λ = 425 nm ($\simeq$ 2.92 eV) at room temperature. The observed photoinduced absorption spectra have been fitted by assuming an overlapping of several Gaussian absorption bands (Figure 2). The defined parameters of maxima positions (E_0) and halfwidths (W) of separate absorption bands are listed in the Table I. As can be seen there are the same absorption bands in the optical density spectra of the photoirradiated, additively colored, ion-implanted and γ-ray irradiated crystals $RbAg_4I_5$ (see Table I).

To clarify the mechanism of the discovered effect and to study its reversibility the relaxation characteristics of photoinduced absorption was investigated. It was established that the time dependence of the light intensity transmitted through the irradiated $RbAg_4I_5$ crystal on the wavelegnth λ = 436 nm ($\simeq$ 2.85 eV) has an exponential character. The examined time dependence of photocoloration process in $RbAg_4I_5$ crystals was found to be described with two relaxation times $\tau_1 \simeq 3100$ sec and $\tau_2 \simeq 15400$ sec.

The similar absorption characteristics in additively colored and photoirradiated $RbAg_4I_5$ superionic crystals let us to propose that the mechanism of photocoloration effect is associated with the changes in a local concentration of mobile silver cations in the irradiated region. These local changes in crystal stoichiometry can be caused by the ambipolar diffusion process of optically excited electronic carriers screened by mobile

ions. Such a diffusion process can lead to creation of new color centers and also to some changes in structure and concentratration of color centers in $RbAg_4I_5$ superionic crystal exposed to light irradiation.

REFERENCES

1. S. I. Bredikhin, N. N. Kovaleva, I. Sh. Khasanov and N. V. Lichkova. *Solid State Ionics*, **28–30**, 280, 1988.
2. V. N. Andreev and V. G. Goffman, *Sov. Phys. Solid State* **25** (1984) 2004.
3. T. Awano, M. Ikezawa, T. Matsuyama and H. Yamaoka. *Solid State Ionics* **40/41** (1990) 324.

Radiation Effects and Defects in Solids, 1995, Vol. 134, pp. 461–463
Reprints available directly from the publisher
Photocopying permitted by license only

© 1995 OPA (Overseas Publishers Association)
Amsterdam B.V. Published under license by
Gordon and Breach Science Publishers SA
Printed in Malaysia

M-CENTRE LUMINESCENCE IN NaF AND LiF: TOWARDS A COMPREHENSIVE INTERPRETATION OF THE M-CENTRE EMISSION PROPERTIES IN ALKALI HALIDES

L. BOSI and D. GALLO

Dipartimento di Fisica del Politecnico di Milano, P.za Leonardo da Vinci 32, I-20133 Milano and Sede Staccata di Lecco

Emission and excitation spectra were accurately detected as a function of the temperature (in the range 18–300 K) in NaF and LiF samples containing unperturbed M-centres: different coloration techniques and ageing effects were tested in order to obtain the pure M-emission band. On the basis of collected data new trends and correlations are proposed between the halfwidth of the emission bands (H), the effective modes (ω), and the Huang-Rhys factors (S) for M and F centres: the H(M) values are roughly half the H(F) ones, M-emission S values are very similar in different crystals, ω and H values for the M- and F-emissions are proportional to the transverse optical frequency ω_T values.

Key words: colour centre, luminescence, emission band.

The aim of this work is to present new data about the M centre luminescence in NaF and LiF, together with a new analysis of peak energy (E), halfwidth (H), effective mode (ω), as well as transverse optical frequency (ω_T) in alkali halides, which leads us to propose new trends and correlations. Indeed, in recent years the analysis of the basic properties concerning the emission band has been somewhat disregarded. We also present a comparison between the observed properties of the M centre and those for the F centre in alkali halides: this comparison is very useful to obtain a comprehensive interpretation of the emission properties.

A pure M emission band was obtained in additively coloured NaF samples containing Li^+ substitutional impurities which favour coloration:[1,2,3] M_A formation was observed only after keeping the samples in the dark for a few days. Furthermore, in order to obtain a comparison, the M emission band was analysed in NaF and NaF:Li X-ray coloured samples: so we believe that the data collected in the Tables presented here refer to practically unpertubed M centres. The details of the measurements as a function of the temperature (T) and the data analysis were presented in a previous work.[4] The M emission was also investigated as a function of T in X-ray coloured LiF, which cannot be additively coloured.[4]

It is convenient to summarize some F centre emission properties. The halfwidths of the emission (and absorption) bands of the F and M centre are related to T according to the following classical formula:

$$H^2(T) = H^2(0)Coth(\hbar\omega/2kT) \qquad (1)$$

where ω is the effective mode.

Bosi and Nimis[5,6] discovered that the ω values of the F emission, here indicated as ω(F), are very close to the transverse optical frequency ω_T values. In Table I we present detailed data for ω(F) and ω_T, for the emission band halfwidth $H(0)$ at the lowest temperature employed in the experiments known in literature, and for the Huang-Rhys factor S(F), concerning the emission process, determined on the basis of the well-known relationship:

$$H^2(0) = 8\ ln2(\hbar\omega)^2\ S \qquad (2)$$

The ω(F) were obtained in ref. [8] by relationship (2) and, more correctly, in ref. [10], by using the shape function of the emission; finally, an accurate ω(F) value in RbCl was found by Brada,[11] by also taking into account the relative changes in the peak emission and halfwidth as a function of T.

Table I

Crystal	H(F) (eV)	$\omega_T(10^{13}s^{-1})$	ω(F) ($10^{13}s^{-1}$)	S(F)
RbI	0.148[7]	1.537	1.44[7]	43.94
RbBr	0.190[7]	1.780	1.89[7]	42.08
KI	0.185[8]	2.063	2.05[8]	33.91
	0.190[10]		2.14[10]	32.82
RbCl	0.237[8]	2.373	2.10[8]	53.03
	0.256[10]		2.00[10]	68.22
	0.229[11]		2.19[11]	45.53
KBr	0.215[8]	2.317	2.36[8]	34.56
	0.224[10]		2.54[10]	32.38
KCl	0.261[8]	2.844	2.86[8]	34.68
	0.294[10]		2.80[10]	45.90
NaCl	0.337[8]	3.353	3.71[8]	34.36
	0.360[10]		3.27[10]	50.47
KF	0.385[7]	3.796	3.48[7]	50.96
NaF	0.50[9]	4.936	4.86[9]	44.07

Furthermore, by inserting the mean of S(F) values (≈ 43.13) in rel. (2) we obtained[5,6] a new relationship between the $H(0)$ values for the F centre (here named $H(F)$) and ω(F):

$$H(F) = 15.465\ (\ \hbar\omega(F)\ )\ \ \text{(in eV)} \qquad (3)$$

This relationship seems to indicate a common behaviour concerning the F centre vibrational properties in the emission process (when clearly detectable): i.e. $H(F)$ is also proportional to ω_T. The occurrence $\omega(F) \approx \omega_T$ could be related to the dependence of the emission peak energy E(F) on the high frequency constant ε_∞ (which implies a similar one for the radiative lifetime); a full discussion is presented in ref. [6].

Our results for the M centre in NaF and LiF are as follows: emission and excitation spectra were detected as a function of T in the range 18.2–294 K. An accurate study of the band shapes and peak positions was carried out, and the degree of distortion was determined (see ref. [4]).

In Table II we list our data together with that known in literature: the quoted emission energies E(M) and halfwidths H(M) were determined at $T \leq 18$ K except for KF (at 77 K). The following correlations and trends can be observed:

i) the halfwidth of the F centre emission is roughly twice as wide as the one of the M centre;
ii) the S values for the M centre are very similar for different crystals, except in the KBr case, even if the discrepancy is not dramatic;
iii) the values $\omega(M)/\omega_T$ are practically the same for different crystals (mean value = 0.859) except in the KBr case (near to unity); obviously the same occurrence holds for $\omega(M)/\omega(F)$ values, since, as previously shown, $\omega(F) \approx \omega_T$; the data scattering is due, as expected, to the different methods adopted by the same authors[8,10] in analysing the F centre emission band;

iv) the trends commented above imply that $H(M)/\hbar\omega_T$ values are similar for different crystals, including the KBr case where the two above-mentioned anomalies seem to compensate each other; KF is only an apparent exception: indeed the H(M) value is necessarily high because, as anticipated, it was taken at an elevated temperature (77 K).

Table II

Crystal	E(M) eV	H(M) eV	ω(M) 10^{13} s^{-1}	S(M)	$\frac{H(F)}{H(M)}$	$\frac{\omega(M)}{\omega(F)}$	$\frac{\omega(M)}{\omega_T}$	$\frac{H(M)}{\hbar\omega_T}$
LiF	1.85	0.289	5.19	12.7			0.866	7.33
NaF	1.91	0.229	4.20	12.1	2.18	0.864	0.851	7.05
KF	1.579[12]	0.21[12]			1.83			8.40
NaCl	1.155[13]	0.14[13]			2.41			6.34
					2.57			
KCl	1.15[14]	0.130[14]	2.45[14]	11.4	2.01	0.857	0.861	6.94
					2.26	0.875		
KBr	1.04[14]	0.105[14]	2.39[14]	7.8	2.05	1.013	1.031	6.88
					2.13	0.941		
KI	0.818[13]	0.10[13]			1.85			7.36
					1.90			

REFERENCES

1. L. Bosi, M. Nimis and P. Gagliardelli, *Phys. Rev.* **B24**, 3600 (1981).
2. L. Bosi, P. Gagliardelli and M. Nimis, *Phys. Stat. Sol.* **B120**, 41 (1983).
3. L. Bosi, P. Gagliardelli and M. Nimis, *Nuovo Cimento Lettere* **35**, 292 (1982).
4. L. Bosi and D. Gallo, *Phys. Stat. Sol.* **B182**, 261 (1994).
5. L. Bosi and M. Nimis, *Phys. Stat. Sol.* **B98**, K151 (1980).
6. L. Bosi and M. Nimis, *Nuovo Cimento* **13D**, 1483 (1991).
7. P. Podini and G. Spinolo, *Solid State Comm.* **4**, 263 (1966) and Atti del Convegno Nazionale C.N.R., Proprieta' ioniche ed elettroniche degli alogenuri alcalini, Milano, July 4–6, 1966.
8. W. Gebhardt and H. Kuhnert, *Phys. Lett.* **11**, 15 (1964).
9. L. F. Stiles, M. P. Fontana and D. B Fitchen, *Phys. Rev.* **B2**, 2077 (1970).
10. W. Gebhardt and H. Kunhert, *Phys. Stat. Sol.* **B14**, 157 (1966).
11. Y. Brada, *J. Chem. Phys.* **58**, 3959 (1973).
12. W. C. Collins and I. Schneider, *J. Chem. Phys. Solids* **37**, 917 (1976).
13. R.W. Dreyfus, *Phys. Rev.* **B4**, 562 (1971).
14. M. Hirai and K. Hashizume, *J. Phys. Soc. Japan* **24**, 1059 (1968).

Radiation Effects and Defects in Solids, 1995, Vol. 134, pp. 465–470
Reprints available directly from the publisher
Photocopying permitted by license only

© 1995 OPA (Overseas Publishers Association)
Amsterdam B.V. Published under license by
Gordon and Breach Science Publishers SA
Printed in Malaysia

INVESTIGATION OF THE DYNAMICAL BEHAVIOUR OF THE $F_H(CN^-)$ CENTRE IN KCl WITH TEMPERATURE DEPENDENT ENDOR SPECTROSCOPY

TH. PAWLIK, R. BUNGENSTOCK, J. M. SPAETH and F. LÜTY*

Fachbereich Physik, Universität-GH Paderborn, 33095 Paderborn, Germany;
**Department of Physics, University of Utah, Salt Lake City, Utah 84112, USA*

The temperature dependence of the electron nuclear double resonance (ENDOR) spectra of $F_H(CN^-)$ centres in KCl was investigated in the temperature range between 10–220 K. At the lowest temperature of 10 K only one CN^- orientation with respect to the F centre electron is present, in which the nitrogen is thought to be nearer to the F-electron than the carbon. With the very small thermal activation energy of 2.9 meV the opposite orientation is occupied. The superhyperfine interactions of those first shell K nuclei nearest to CN^- and of the ^{13}C interaction of the CN^- molecule are strongly temperature dependent between 10 and 60 K, following an exponential law with a thermal activation energy of 4.2 meV. It is assumed that a soft local mode involving those two nearest K nuclei and the CN^- is causing the strong temperature dependence. The shf interactions of ^{14}N nuclei have not been seen, probably because of the dynamical effects.

Key words: ENDOR, defect dynamics, local modes, vibronic coupling, F-aggregate centres.

1 INTRODUCTION

F-aggregate centres in alkali halides consisting of F-centres associated with a CN^- molecule have attracted considerable interest because of a strong coupling between the F centre and the CN^- diatomic molecule resulting in an efficient transfer of the F centre electronic excitation energy to the CN^-vibrational energy [1,2]. In alkali halides CN^- is second nearest neighbour to the F centre electron in a (110) position. This microscopic structure, first inferred from optical measurements, was confirmed by electron nuclear double resonance (ENDOR) experiments, in which the superhyperfine (shf) interactions with the ^{13}C atom in the $^{13}CN^-$ molecule, however not with the ^{14}N nuclei, could be measured. From the ENDOR angular dependence the site of the CN^- could be confirmed [3]. From the failure to see the ^{14}N nuclei in the spectra, which should have a measurable shf interaction with the ^{14}N nucleus with I = 1, it was concluded that possibly even at the lowest measurement temperature (30 K) the CN^- dipole undergoes rapid orientation motions. Because of the expected quadrupole interaction of ^{14}N the ^{14}N NMR spectra are probably not observable then because of too short nuclear spin- lattice relaxation times. A strange doublet splitting of the ^{13}C spectra was observed, which was tentatively assigned to two possible orientations of the CN^- molecule [3].

In this paper we report on a detailed investigation of the temperature dependence of the ENDOR spectra of the ^{13}C nuclei and the nearest K nuclei of the $F_H(CN^-)$ centre in the temperature range between 10 K and 220 K. From this we show that CN^- has two orientations with respect to the F centre electron which differ in energy by only 2.9 meV and that the shf interactions of those first shell K neighbours, which are near to the CN^-, and of the ^{13}C nuclei in $^{13}CN^-$ have a strong temperature dependence which follows an exponential law with an activation energy of 4.2 meV.

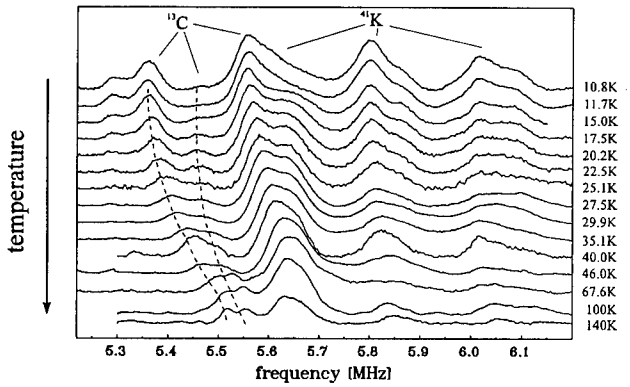

FIGURE 1 ENDOR spectra of $F_H(^{13}CN^-)$ centres in KCl for $B_0 \parallel [100]$ measured at various temperatures.

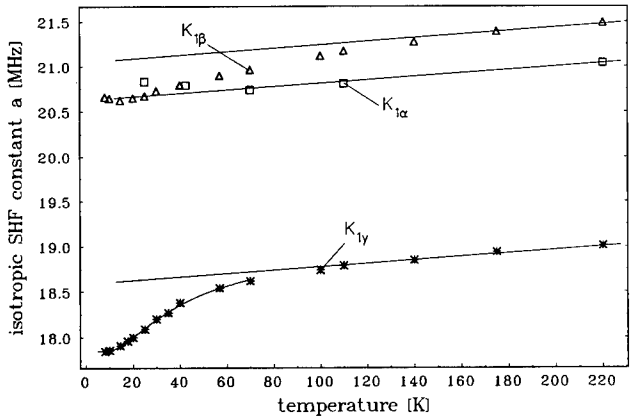

FIGURE 2 Temperature dependence of the isotropic shf constant of the three subshells K_α, K_β and K_γ of F_H ($^{13}CN^-$) centres in KCl.

2 EXPERIMENTAL

KCl single crystals were doped with K ^{13}CN and additively coloured. After quenching from 400°C to room temperature to disperse the F centres, aggregation of F centres and CN^-centres was done by optical bleaching at $\lambda = 514$ nm into the high energy flank of the F-band in the temperature range between 180–220 K. About 50% of the F centres could be aggregated with CN^-. The ENDOR measurements were performed in X-band with a computer controlled custom-built spectrometer operating between 10 and 300 K.

3 EXPERIMENTAL RESULTS

After aggregation of F centres to $^{13}CN^-$ new lines appear in the ENDOR spectrum: new lines of the first shell K nuclei and those due to ^{13}C (see Figure 1 of ref. [3]). No ENDOR

Table I
F centre—^{13}C shf interaction parameters at T = 180 K

	a/h [MHz]	b/h [MHz]	b′/h [MHz]
^{13}C (L)	3.975	0.106	0.043
^{13}C (H)	4.056	0.101	0.053

lines of ^{14}N have been observed. The angular dependence of the ^{13}C nuclei measured at 70 K was already shown in ref. [3], Figure 2. The assignment of the lines to ^{13}C and ^{39}K was made with the field shift method (see e.g. [4]). The ^{13}C lines exhibit a (110) symmetry, i.e. the principal axis of the ^{13}C shf tensor with the largest interaction is along a ⟨110⟩ direction indicating that the CN^- molecule is oriented along that orientation. As a surprising factor it was observed that each ^{13}C line is split into a doublet. The angular dependence consists of two parallel branches, each having the same ENDOR line intensity at that temperature. There are ^{13}C nuclei with a 'high' shf interaction (henceforth called $^{13}C(H)$) and those with a 'low' shf interaction ($^{13}C(L)$), whereby the shf interaction differs in the isotropic shf constant only by about 2%, practically not at all in the anistropic shf constants. The ^{13}C shf constants are given in Table I in terms of the isotropic shf constant a, the anistropic shf constants b and b′, which are related to the principal values of the shf tensor A by

$$A_{zz} = a + 2b \tag{1}$$

$$A_{xx} = a - b + b' \tag{2}$$

$$A_{yy} = a - b - b' \tag{3}$$

The doublet ENDOR lines change, however, when the temperature is lowered. The 'high' frequency ^{13}C line starts to decrease in intensity when cooling below approx. 40 K and is not observed anymore below 10 K. In Figure 1 two of the doublet ^{13}C ENDOR lines are shown as a function of temperature together with first shell K lines. There is not only an intensity change of the high and low frequency lines, but also a shift in frequency towards lower frequencies when cooling, observed for both ^{13}C lines and some of the ^{39}K lines.

When measuring the intensities of the $^{13}C(H)$ and $^{13}C(L)$ ENDOR lines as a function of temperature, an exponential law is found with a thermal activation energy of $\Delta E = 35$ K. The high frequency lines are thermally occupied with this low activation energy of 2.9 meV.

The presence of the CN^- is also seen by an effect on the shf interactions with the nearest shell of K neighbours, which are not equivalent anymore as in the F centre but split into three subshells K_α, K_β and K_γ. Those near to CN^- (K_γ, see Figure 3a in ref. [3]) have a significantly smaller shf interaction. The isotropic shf constant reduces by about 13% at 25 K, while the ansotropic constant is smaller by only 5%. The other two nearest K neighbours have only slightly different interactions compared to the isolated F centre. Table II gives the shf constants at various temperatures in comparison to those of the isolated F centre.

There is also an unusual temperature dependence of the shf interactions, both for the ^{13}C and for the K_γ nuclei. For the latter this is shown in Figure 2. Up to about 60 K the isotropic shf constant increases strongly with increasing temperature while above about

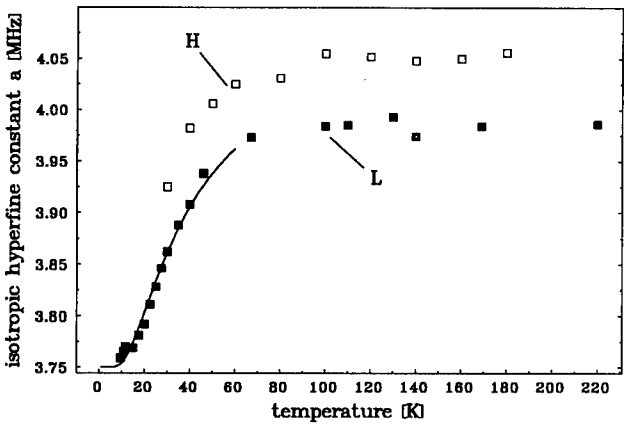

FIGURE 3 Temperature dependence of the isotropic shf constant of ^{13}C of $F_H(^{13}CN^-)$ centres in KCl. Solid squares: 'low frequency' centres (L); open squares: 'high frequency' centres (H) (see text).

80–100 K it shows the linear temperature dependence known from earlier investigations of the isolated F centre [5]. The K_α nuclei have the temperature dependence known from the isolated F centre. A similar behaviour is also found for ^{13}C (Figure 3).

Table II
shf interaction parameters of the first shell (^{39}K) of $F_H(CN^-)$ centres and of isolated F centres (last row, after [6])

T		a/h [MHz]	b/h [MHz]	b′/h [MHz]	q/h [MHz]	q′/h [MHz]	θq
25K	Kα	20.83	0.916		0.061		
	Kβ	20.67	0.90		0.061		
	Kγ	18.11	0.867	0.032	0.075	0.107	13°
42.5K	Kβ,α	20.79	0.909		0.063		
	Kγ	18.41	0.873	0.024	0.086	0.074	11°
70K	Kα	20.74	0.900		0.063		
	Kβ	20.99	0.901		0.061		
	Kγ	18.62	0.881	0.006	0.082	0.060	8°
110K	Kα	20.81	0.895		0.063		
	Kβ	21.20	0.891		0.061		
	Kγ	18.77	0.873	0.006	0.079	0.055	0°
220K	Kα	21.04	0.857		0.062		
	Kβ	21.52	0.878		0.062		
	Kγ	19.01	0.845	0.007	0.078	0.050	0°
77K	K	20.719	0.918		0.061		0°

4 DISCUSSION

The disappearance of the $^{13}C(H)$ line at low temperature (< 10 K) and its thermally activated occupation points to two orientations of the CN^- molecule with respect to the F-electron. Both orientations are energetically almost degenerate regarding the small activation energy of 2.9 meV. This agrees with the calculation made by Song *et al.*[7] who found that the total energies are very close, to within 0.1 eV, the precision position limit of the calculation.

The temperature dependence of the intensities of the $^{13}C(L)$ and $^{13}C(H)$ ENDOR lines follows an exponential law, which can be modelled assuming a two level system. If N_1 is

the population of the ground state, N_2 that of the excited state, the fraction N_2/N_1 should be proportional to $\exp(-\Delta E/kT)$, where ΔE is the energy difference between the two states. We can explain our data very well assuming $\Delta E = 35$ K (2.9 meV).

The temperature dependence of the isotropic shf constants above 80–100 K is practically the linear one known for the F centre, which is interpreted as being the difference of an increase because of higher vibrational amplitudes of the lattice ions and a decrease due to the lattice expansion. The strong temperature dependence found here for low temperature, points, however, to a soft local mode which is thermally excited. Following the explanation of an analysis of the temperature dependence found for atomic hydrogen centres in alkali halides [8] we analysed the temperature dependence in the following way:

If one assumes for the ground state a shf constant a_0 and for the vibrational excited state a shf constant a_1, which is larger because of the increased overlap with the F centre electron due to the higher vibrational amplitudes, one obtains:

$$a(T) = a_0 N_0(T)/N + a_1 N_1(T)/N \tag{4}$$

$$\text{with} \quad N = N_1 + N_2 \tag{5}$$

The two levels are occupied according to the Boltzmann statistics:

$$a(T) = \frac{a_0}{e^{-E/kT} + 1} + \frac{a_1}{e^{E/kT} + 1} \tag{6}$$

where ΔE is the thermal activation energy. We can explain our temperature dependence data for ^{13}C very well with $a_0/h = 3.75$ MHz, $a_1/h = 4.45$ MHz and $\Delta E = (50 \pm 5)$ K ((4.2 ± 0.04) meV). The temperature dependence of the isotropic constant of $^{39}K_\gamma$ can be explained similarily with $a_0/h = 17.85$ MHz, $a_1/h = 20.35$ MHz and $\Delta E = (55 \pm 5)$ K ((4.6 ± 0.04) meV). The solid lines in Figures 2 and 3 are the calculated temperature dependencies of the isotropic shf constants using equation (6). The two energies are the same within experimental error and suggest that a soft mode vibration exists which comprises the 2 K_γ neighbours and the CN^- molecules. Apparently those three ions are particularly coupled and this coupling may be the cause for the efficient energy transfer from the F-electron to the vibrations of the CN^- molecule [1].

The question arises which orientation of the CN^- is the low temperature orientation. From the temperature dependence of the shf interactions it is suggested that it is that orientation, in which the ^{13}C interaction is smaller, i.e. where C is further away and N nearer to the F-electron assuming, that the overlaps with ^{13}C s-orbitals are then lower.

The $F\text{-}NC^-$ configuration would be expected to be energetically slightly favoured if one assumes that due to the incomplete of the positive charge of the anion vacancy by the F-electron the more negative nitrogen compared to the carbon in the CN^- molecule [7] is attracted by Coulomb forces. Thus the $F\text{-}CN^-$ configuration is an excited state, which is, however, very close ($\Delta E = 2.9$ meV).

It is, however, difficult to understand why the isotropic ^{13}C interactions differ only so little (by 2%) and the anisotropic interactions are practically the same. This seems to be at variance with the calculations by Song *et al.* [7] who found the minimum of the total energy for both orientations to be for CN^- at the same distance from the F centre at 4.5 Å, which is about the distance of the centre of gravity of CN^- from the Cl^- vacancy centre (4.4 Å). When calculating the isotropic shf constant using the Schmidt orthogonalisation procedure with the F centre envelope functions [9] and the CN^- molecular wave functions [10], we obtain for $F\text{-}CN^-$ a/h = 19.3 MHz and for $F\text{-}NC^-$ a/h = 0.7 MHz: the difference comes out to be two orders of magnitude too large (a variation of the F centre wave

function alone would never explain the small difference observed for the two locations of carbon). In order to explain our experimental result (a/h $\approx$ 4 MHz) one would need to relax the CN^- ion for the low temperature F-NC^- configuration by about 0.53 Å towards the F centre, in the other orientation away by about the same amount. A relaxation by 12% of the regular distance seems quite a lot, and it seems surprising that this should not influence the energies much more than the experimentally found 3 meV. From the calculation of Song *et al.* [7] it seems that the total energy for the ground state depends much more on the separation of the CN^- ion from the centre of the vacancy. Whether or not CN^- is oriented with its axis along a $\langle 110 \rangle$ direction or whether it is 'jumping' about this axis with a frequency fast compared to our measurement frequency of a few MHz, we cannot say, because we would only measure a motionally averaged effect.

ACKNOWLEDGEMENT

The work of one of the authors (F. L.) was supported by NSF grant DMR 92–23230 and ONR grant N–00014–926–0140.

REFERENCES

1. Y. Yang and F. Lüty, *Phys. Rev. Letters* **51**, 419 (1983).
2. F. Rong, Y. Yang and F. Lüty, *Cryst. Latt. Defects and Amorph. Mat.* **18**, 1 (1989).
3. H. Söthe, M. Jordan and J. M. Spaeth, *Radiation Effects and Defects in Solids*, **119–121**, 931 (1991).
4. J. M. Spaeth, J. R. Niklas and R. H. Bartram, *Structure Analysis of Point Defects in Solids* (Springer Series of Solid State Sciences **43**) (1992).
5. W. T. Doyle and A. B. Wolbarst, *J. Phys. Chem. Sol.* **36**, 549 (1975).
6. R. Kersten, *Phys. Stat. Sol.* **29**, 575 (1968).
7. K. S. Song, L. F. Chen, P. Q. Tong, H. W. Yu and C. H. Leung, *Proc. Int. Conf. on Defects in Insulat. Materials*, Nordkirchen, Germany, ed. O. Kanert and J. M. Spaeth, World Scientific (Singapore), p. 449 (1992).
8. Ch. Hoentsch and J. M. Spaeth, *Phys. Stat. Sol.(b)* **94**, 479 (1979).
9. B. S. Gourary and F. J. Adrian, *Solid State Phys.* **10**, 127 (1960).
10. R. Bonaccorsi, C. Petronoglo, E. Scrocco and J. Tomasi, Chem. *Phys. Lett.* **3**, 473 (1969).

Radiation Effects and Defects in Solids, 1995, Vol. 134, pp. 471–475
Reprints available directly from the publisher
Photocopying permitted by license only

© 1995 OPA (Overseas Publishers Association)
Amsterdam B.V. Published under license by
Gordon and Breach Science Publishers SA
Printed in Malaysia

ODEPR OF INDIUM COLOUR CENTRES IN THE X- IRRADIATED STORAGE PHOSPHOR KBr:In

U. ROGULIS, J.-M. SPAETH,* I. TALE, E. RUZA

Inst. of Solid State Physics, University of Latvia, 8 Kengaraga str., LV1063, Rìga, Latvia;
** Universität-GH Paderborn, FB Physik, Postfach 1621, D–33095, Paderborn, Germany*

The results of measurements of the magnetic circular dichroism of the optical absorption (MCDA) and optically detected electron paramagnetic resonance (ODEPR) of X-irradiated KBr:In crystals are presented. The MCDA bands and ODEPR parameters of In°(1) centers and In^{2+} centres have been measured. The mechanism of the energy storage in KBr:In crystals is found not to be simply the formation of correlated F centre-In^{2+} centre pairs as was assumed previously. Considerable similarities to the storage phosphor BaFBr:Eu^{2+} were found for the photostimulated emission and read-out properties.

Key words: X-ray storage phosphor, In centres, paramagnetic resonance.

1 INTRODUCTION

Materials to produce X-ray storage phosphors have attracted much interest recently because of their higher sensitivity compared to X-ray films and because of the possibility to create digitized X-ray images. There is a search for new materials besides the well-known system BaFBr:Eu^{2+}. Recently it has been shown that KBr:In has an X-ray storage efficiency comparable to that of BaFBr:Eu^{2+} [1].

On the basis of recent extensive studies of optical absorption in the visible and near UV region and of optically and thermally stimulated recombination luminescence it was proposed that X-ray energy storage in KBr:In crystals is mainly due to the formation of close F center-In^{2+} centre pairs [2]. The question is, however, whether upon X-irradiation of KBr:In indeed spatially correlated F centre-In^{2+} centre pairs are formed and if so, whether only correlated pairs are generated.

According to recent investigations with optically detected electron paramagnetic resonance (ODEPR) the X-ray energy storage in BaFBr:Eu^{2+} is indeed based on aggregates involving F centres as electron trap centres, spatially correlated both to O_F^-- and Eu^{2+} centres [3,4].

Therefore an investigation of the radiation damage centres in KBr:In was undertaken using magneto-optical and optically detected electron paramagnetic resonance techniques. We show that indeed In^{2+} centres are formed, but that the mechanism for energy storage and read-out is more complicated than assumed by Plavina *et al.* [2] with the simple idea of correlated In^{2+}-F centre pairs.

2 EXPERIMENTAL RESULTS AND DISCUSSION

KBr:In ($1 - 5 \times 10^{17}$ cm^{-3}) crystals were X- irradiated at RT with a dose of 10^3 Gy. The magnetic circular dichroism of the absorption (MCDA) at 1.5 K (Figure 1) exhibits several bands in the UV and IR in addition to the strong MCDA of F-centres (derivative structure, transition through zero at 2.06 eV).

An ODEPR spectrum similar to that found for In°(1) centres in KCl:In crystals is obtained [5]. The ODEPR spectrum of the In°(1) centres in KBr:In is shown in Figure 2.

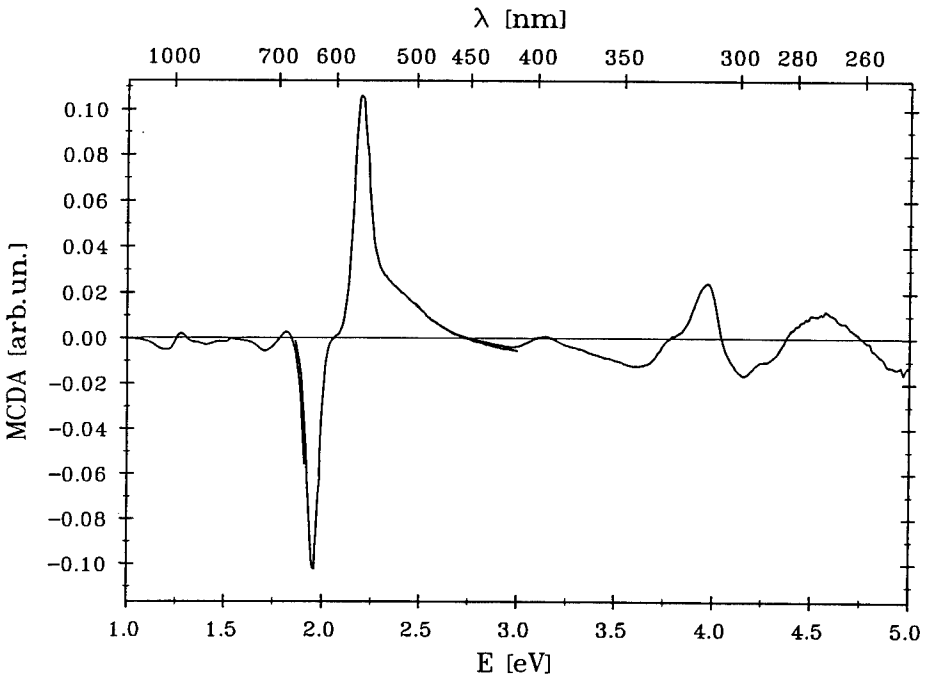

FIGURE 1 MCDA spectrum of a KBr:In crystal X-irradiated at room temperature, measured at T = 1.5 K, B = 2 T.

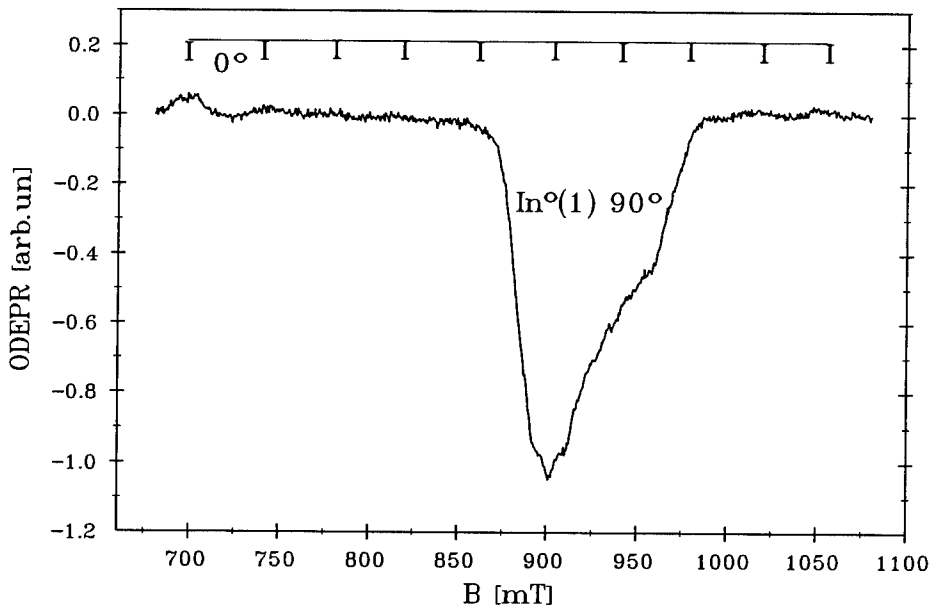

FIGURE 2 ODEPR spectrum of In°(1) centres in KBr measured as microwave-induced change of the MCDA spectrum of Figure I at λ = 1015 nm.
For $B_0 \| [100]$ (microwave frequency 24.21 GHz, T = 1.5 K) In°(1) centres were produced by X-irradiation at room temperature. The bars indicate the HF structure for parallel centres (I_{In} = 9/2), the strong line is due to perpendicular centres.

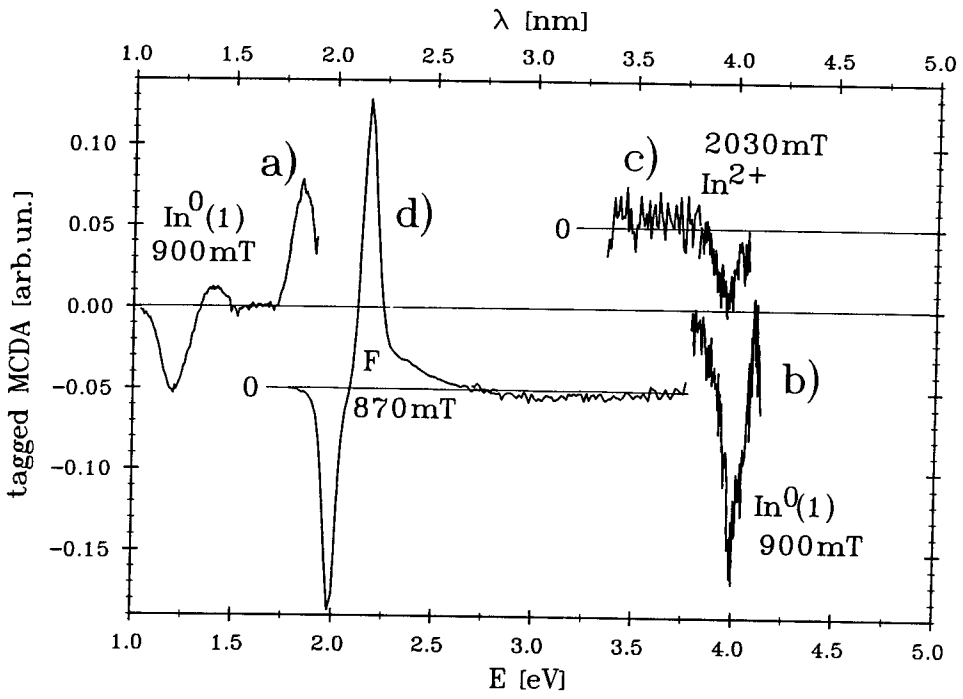

FIGURE 3 Tagged MCDA spectra of In°(1) centres (curves a and b, measured at 900 mT), F centres (curve d, measured at 870 mT) and In^{2+} centres (curve c), measured at 2030 mT) in KBr after X-irradiation at room temperature.

The values of the EPR parameters are as follows: $g_{\|} = 1.97 \pm 0.02$; In-hyperfine (HF) splitting constant $A_{\|} = (40 \pm 2)$ mT; $g_{\perp} = 1.88 \pm 0.02$; $A_{\perp} = (8 \pm 1)$ mT; $P = (-0.2 \pm 0.05)$ mT. The MCDA bands of In°(1) centres are located at 3.99 eV and 1.85 eV, 1.4 eV and 1.2 eV. They were determined by measuring the 'tagged' MCDA (see e.g. [6]). The 'tagged' MCDA spectrum (i.e. the excitation spectrum of the In°(1) ODEPR lines) is shown in Figure 3, curves a and b.

In the UV region several MCDA bands appear. The ODEPR line (Figure 4, curves a and b), detected in the 3.95 eV MCDA band, is located at 2040 mT. From the Breit-Rabi calculation (Figure 4, upper part c) this line is attributed to In^{2+} hole centres with an In-HF splitting constant of A = 13.2 ± 0.1 (GHz), g ~ 2. Only one EPR transition could be recorded with our microwave frequency of about 24 GHz. A hole is trapped on an In^{+}-ion on the cation site. A superhyperfine splitting from bromine nuclei could not be resolved in the weak EPR line. The 'tagged' MCDA spectrum in the UV region contains a MCDA band located at 3.95 eV which overlaps the MCDA band for In°(1) centres at 3.99 eV (halfwidth for both MCDA bands is above 0.1 eV) (see Figure 3, curves b and c).

Because of the strong overlap of the MCDA bands of both the In^{2+} and the In°(1) centres, both ODEPR signals are present simultaneously. However, up to now we have not observed any cross relaxation effects in the ODEPR spectra caused by an interaction between In^{2+} and In°(1) nor between In^{2+} and F centres.

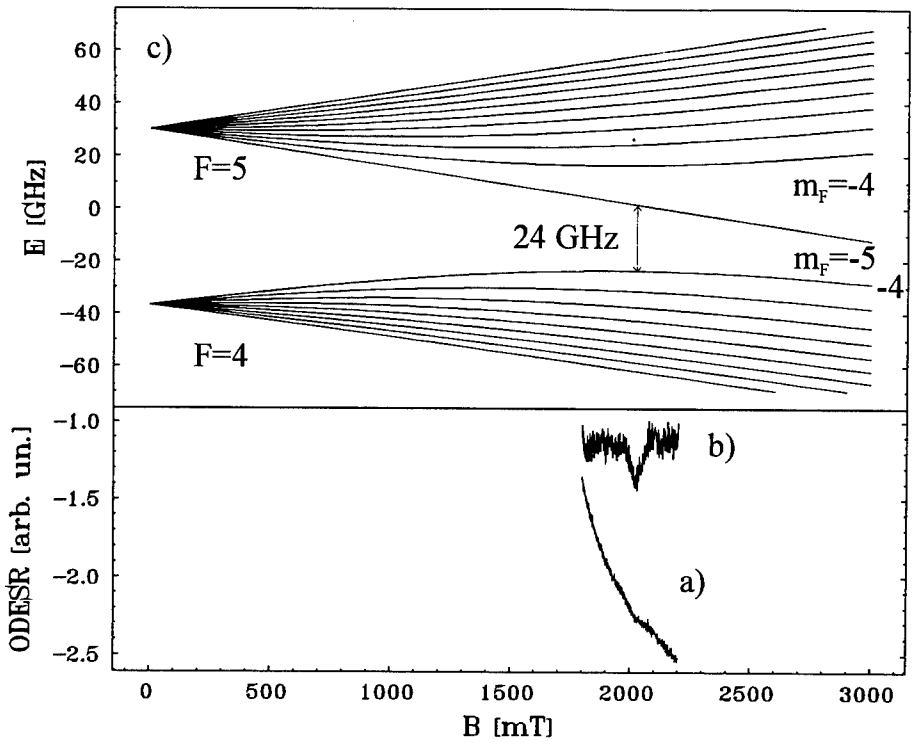

FIGURE 4 ODEPR spectrum of In^{2+} centres in KBr:In X-irradiated at room temperature (curve a: as measured, curve b: without MCDA background) The upper part c) represents the calculated Breit-Rabi diagram for the In^{2+} centres.

Such cross relaxation effects had been observed in the ODEPR spectra of F centres and Eu^{2+} centres in BaFBr:Eu^{2+} and gave direct experimental evidence for a spatial correlation between the radiation-induced F centres and the activator Eu^{2+} [4].

We have carried out preliminary experiments on the bleaching of F centres using the light of a He-Ne laser at RT as well as at low temperatures. These experiments show that the mechanism of the energy storage in KBr:In crystals is considerably more complicated than described by the assumption that only the F centre-In^{2+} centre pairs are formed and recombine during the read-out process. After exhaustion of the photostimulated emission at low temperature, only a fraction of the F centres is bleached, and very few In^{2+} centres have disappeared. Also the In°(1) centres remain.

Similarily to the observations in BaFBr:Eu^{2+} crystals [7], also in the KBr:In crystals the photostimulated luminescence can be exhausted by low temperature (4 K) read-out with the light of the He-Ne laser, and then be restored again partially by warming up to RT in the dark (so-called replenishment effect [7]).

Thus it may be speculated that similarily as in the case of BaFBr:Eu^{2+} there are aggregates of F centres, In+ centres and an unknown hole centre which leads to the photostimulated luminescence, if F centres are excited and recombine with the hole centres, upon which process the In^{+} is excited and emits the observed In^{+}-related luminescence

[1,2]. According to our results it seems unlikely that the dominating process is that of an F centres-In^{2+} center recombination, as was assumed by Plavina *et al.* [2].

According to a recent report [8], the spectrum of the excitation of the photostimulated luminescence significantly differs from the absorption band of the F centres and includes additionally a long wavelength region, where the absorption band of the In°(1) centres occurs.

The role of In°(1) centres is at present not clear. Since they are also electron trap centres, they may be excited similarily as F centres for a read-out process.

REFERENCES

1. A. Kalnins, I. Plavina, L. Trinklere, M. Trinklere, *Proc. of the LUMDETR'91*, Rìga, **E18** (1991).
2. I. Plavina, I. Tale, A. Tale, *Proc. of the LUMDETR'91*, Rìga, **D4** (1991).
3. R. S. Eachus, F. K. Koschnick, J.-M. Spaeth, R. H. D. Nuttall, M. T. Olm, W. G. McDugle. *Proc. of the ICDIM'92*, World Scientific, **1**, 267 (1993).
4. F. K. Koschnick, J. M. Spaeth, R. S. Eachus, W. G. Mc Dugle and R. H. D. Nuttall, *Phys. Rev. Letters* **67**, 3571 (1991).
5. F. J. Ahlers, F. Lohse, Th. Hangleiter, J. M. Spaeth and R. H. Bartram, *J. Phys.: Solid State Physics*, **17**, 4877 (1984).
6. J. M. Spaeth, J. R. Niklas, R. H. Bartram, *Structural Analysis of Point Defects in Solids* (Springer Series of Solid State Sciences 43) (1992).
7. T. Hangleiter, F. K. Koschnick, J.-M. Spaeth, R. H. D. Nuttall and R. S. Eachus, *J. Phys. C: Cond. Matter*, **2**, 6837 (1990).
8. I. Tale, V. Tale, P. Kulis, M. Springis and A. Veispals *Proc. of the ICDIM'92*, World Scientific, **2**, 1262 (1993).

Radiation Effects and Defects in Solids, 1995, Vol. 134, pp. 477–480
Reprints available directly from the publisher
Photocopying permitted by license only

© 1995 OPA (Overseas Publishers Association)
Amsterdam B.V. Published under license by
Gordon and Breach Science Publishers SA
Printed in Malaysia

THERMOACTIVATED SPECTROSCOPY OF HETEROVALENT IMPURITY TRAPS IN $CdWO_4$.

V. TĀLE*, I. TĀLE* and L. L. NAGORNAYA**

** Inst. of Solid State Phys. University of Latvia, 8, Kengaraga St., LV1063, Riga, Latvia;*
*** Institute for Single Crystals, Acad. Sci. of Ukraine, 60 Lenin Av., Charkhov, Ukraine*

Recombination luminescence emission spectra, TSL and trap spectra estimated by fractional glow technique (FGT), in nominally pure and Li-, Bi- and Ho-doped $CdWO_4$ crystals are reported. According to the investigations by FGT heterovalent impurities Li, Bi and Ho causes localized electronic states which act as traps for charge carriers. It is shown that TSL results in emission of known blue-green luminescence band by emptying of the Li^+-related traps in $CdWO_4$-Li and yellow luminescence band by emptying of the Bi^{3+}-related traps in $CdWO_4$-Bi. It is proposed that blue-green and yellow luminescence occur by recombination correspondingly of free holes and free electrons at different intrinsic tungstate group related luminescence centers.

Key words: $CdWO_4$; impurities; defects; electron traps; TSL; luminescence.

Like other tungstates two luminescence bands are observed in $CdWO_4$. Upon excitation into the optical band gap the blue-green emission occurs attributed to the intrinsic $^3T_1 \rightarrow {}^1A_1$ transitions within an octahedral WO_6 group [1]. Additional yellow luminescence band (excitation band at 355 nm shifted to the lower photon energies) is attributed to transitions in a tungstate group which lacks one oxygen ion [1]. Presence of impurities in $CdWO_4$ may cause the formation of the color centers. Local [2] or non-local [3] charge compensation of the Me^{3+} impurity dopands by V_{OH} centers has been discussed. It can be expected that heterovalent ions substituting cations can form either donor–acceptor type centers or complex centers which involve charge-compensating defects. The nature of the recombination luminescence due the presence of the intrinsic defects and the heterovalent impurities in $CdWO_4$ is discussed.

Nominally stoichiometric single crystals of $CdWO_4$, pure and doped by heterovalent Li^+, Ho^{3+} and Bi^{3+} ions were grown in air by Chochralsky technique. Cation deficient crystals were obtained from melt composition with non-stoichiometric excess of WO_3. Trap spectra were examined by fractional glow technique (FGT) as described in [4,5]. X-irradiated (up to 10^2 Gy) samples of dimensions about $5 \times 5 \times 0.5$ mm^3 were investigated.

Trap spectrum of nominally-pure $CdWO_4$ (Figure 1) is represented by 5 kinds of single monoenergetic traps (glow peaks and corresponding activation energies E at 120 K, 0.41 eV; 141 K, 0.44 eV; 160 K, 0.56 eV; 183 K, 0.61 eV and 207 K, 0.68 eV). Qualitatively similar trap spectrum occurs in cation deficient crystals (Figure 1). At equivalent X-ray excitation dose the main light sum is accumulated by traps represented by 120K TSL peak instead of the 183K TSL peak in nominally stoichiometric sample, the total accumulated light sum being slightly suppressed (see TSL intensities, Figure 2a). For various TSL peaks in undoped $CdWO_4$ the emission spectrum corresponds either the blue-green or yellow luminescence (see Figure 2a: 120 K and 183 K peaks) [5]. Thus, presence of the thermostimulated recombination processes of different nature shall be expected.

Presence of Li, Bi (Figure 2b,c) and Ho does not results in appearance of new luminescence bands additional to the blue-green and yellow ones. Under X-ray excitation the blue-green band in doped crystals is slightly suppressed with respect to the yellow one when compare to the nominally undoped crystals.

Comparative trap spectroscopy of the pure and Li, Bi, Ho doped $CdWO_4$ samples by FGT indicates that heterovalent impurities forms localized electronic states which act as

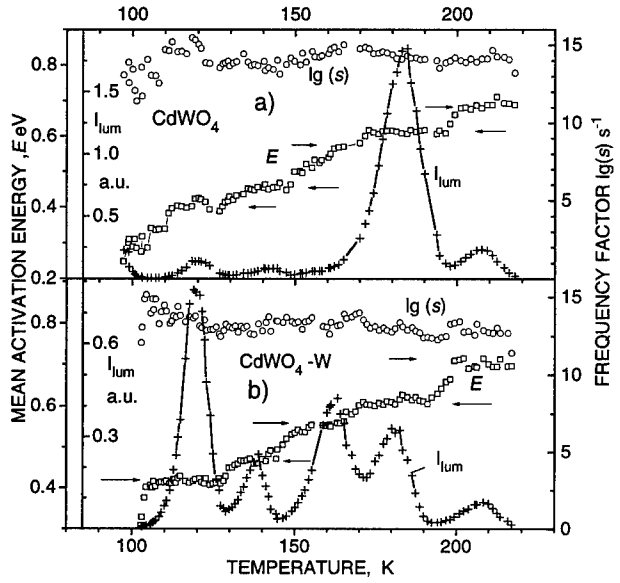

FIGURE 1 FGT spectra of undoped nominally stoichiometric (a) and WO_3-excess (b) $CdWO_4$, X-irradiated at 80 K. ++++—glow intensity; □□□□—mean activation energy; oooo—process frequency factor. Arrows indicate the value of the activation energy of corresponding traps.

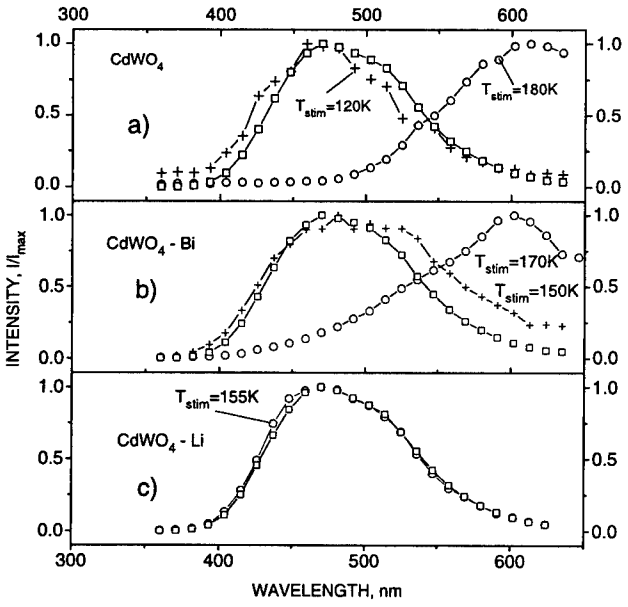

FIGURE 2 Luminescence spectra of nominally stoichiometric $CdWO_4$(a), $CdWO_4$-Bi (b) and $CdWO_4$-Li. □□□□—X-ray luminescence at 300 K; ++++—and oooo-TSL emission spectra at stimulation temperatures T_{stim}, indicated in Figure.

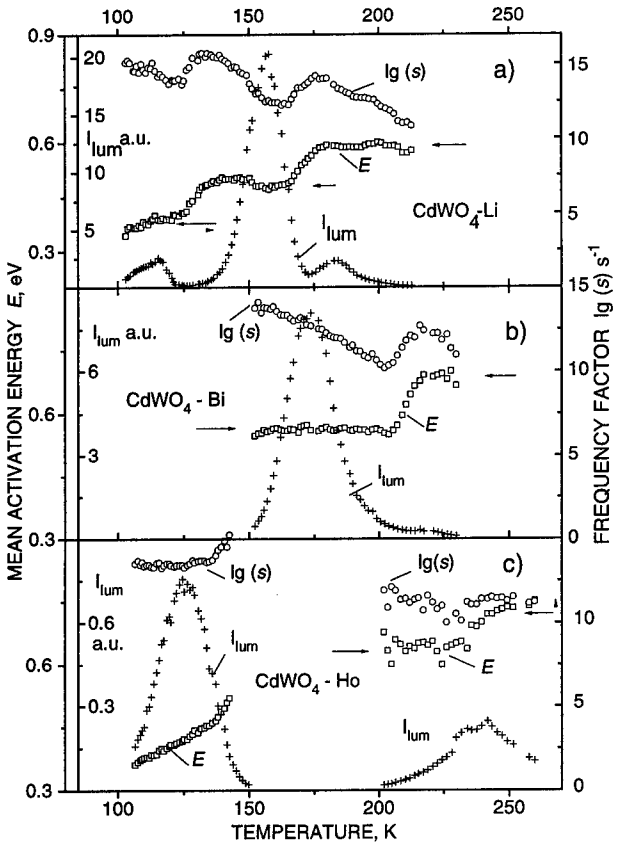

FIGURE 3 FGT spectra of $CdWO_4$-Li (a) $CdWO_4$-Bi (b) and $CdWO_4$-Ho, X-irradiated at 80 K. ++++—glow intensity; ****—mean activation energy; oooo—process frequency factor. Arrows indicate the value of the activation energy of corresponding traps.

traps for charge carriers. For each examined kind of impurities characteristic main glow peak occurs (Figure 3) at ~125 K, 155 K and 175 K in Ho-, Li- and Bi-doped samples correspondingly. According to the FGT the Li- and the Bi-related traps are mono-energetic, the activation energy E being 0.48 eV and 0.56 eV correspondingly. The Ho-related traps are distributed in depths in the E region ~0.37–0.47 eV. The values of the frequency factor, s for Li-, Bi- and Ho-related traps are of the order 10^{12}–$10^{13}s^{-1}$. Being close to the optical phonon frequency they are typical for thermostimulated recombination processes governed by release rate of free electrons or holes. Decrease of the frequency factor, when stimulation temperature rises, indicate that the order of the recombination process kinetics exceeds 1 [5]. Presence of the heterovalent impurities Li and Bi results in sufficiently enchanted efficiency of the light sum accumulation.

In the case of emptying of the Li-related traps at 155 K mainly blue-green luminescence band occurs (Figure 2c). Thus, the spectral composition of the glow corresponds to that of X-ray excited luminescence, whereas emptying of the Bi-related traps results in the yellow luminescence band (Figure 2b). In the case Li^+ and Bi^{3+} ions in CdWo4 substitute Cd correspondingly acceptor- and donor-like centers will be formed in doped crystals which

can act as hole and electron traps. Thus the difference in the TEL emission in the course of emptying of the Li- and Bi-related traps can be explained assuming that the blue-green luminescence occurs by recombination of holes with electrons localized at intrinsic defects related to the WO_6 group. The yellow luminescence occurs by recombination of free electrons with holes localized at tungstate groups which lacks one oxygen ion [1].

REFERENCES

1. Lammers M. J. J., Blasse, G. and Robertson D. S. *phys. stat. sol. (a)*, **63**, 569 (1981).
2. Foldvari I., Capelletti R, *et al. Sol. St. Commun.*, 1987, vol. **63**, 787 (1987).
3. Watterich A. *Defects in Insulat. Material*, ed. by O. Kanert, J.-M. Spaeth, World Scientific, Singapore, (1993).
4. Tāle I. *Phys. Status Solidi (a)*, **66**, 65 (1981).
5. Tāle I. *Proc. Sov. Acad. Sci. phys. sci.* **45**, 245 (1981) (in russ.).

Radiation Effects and Defects in Solids, 1995, Vol. 134, pp. 481–483
Reprints available directly from the publisher
Photocopying permitted by license only

© 1995 OPA (Overseas Publishers Association)
Amsterdam B.V. Published under license by
Gordon and Breach Science Publishers SA
Printed in Malaysia

POINT DEFECTS RELATED TO 260 K THERMOSTIMULATED LUMINESCENCE IN α-Al_2O_3

M. SPRINGIS, P. KULIS and I. TALE

Inst. of Solid State Physics University Latvia, 8 Kengaraga St., LV-1063 Riga, Latvia

Abstract Thermo- and photostimulated processes are studied in reduced hydrogen containing α-Al_2O_3 excited by UV light. It is found that UV excitation in F absorption band at 90 K results in a ionization of the F-centers and capture of released electrons at defects thus producing an anisotropy absorption band at 4.2 eV and the dominant thermoluminescence (TL) peak at 260 K. The 260 K TSL peak is accompanied by complete bleaching of the 4.2 eV absorption band and *vice versa*—by light stimulation in the region of the 4.2 eV band the 260 K TSL peak disappear and released electrons recombine with F^+-centers. Both the effect of the preliminary high-temperature thermal treatment of samples on formation of 4.2 eV-centers and the observed dichroism characteristics allows to conclude that corresponding complex defect contains hydrogen and can involve vacancy pair.

Key words: α-Al_2O_3, defects, thermoluminescence, photostimulation, radiation processes.

Anion deficient α-Al_2O_3 is one of materials intensively studied for thermoluminescence (TL) dosimetry applications. It is known that the sensitivity, amount and position of TL peaks in a α-Al_2O_3 are significantly dependent from crystal growth and treatment conditions.

We reported here on the optical properties of point defects related to the 260 K TL peak in α-Al_2O_3 crystals containing hydrogen and annealed in reducing atmosphere. The examined crystals were grown either by the Verneuil or Chochralsky technique. Annealing in hydrogen and then in reducing atmosphere were performed in hermetic Mo bomb.

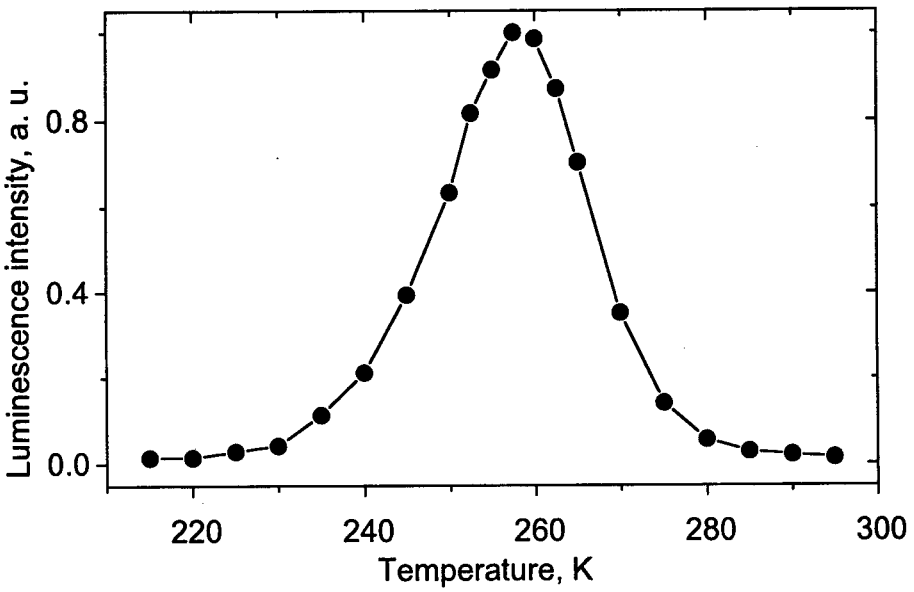

FIGURE 1 TL curve of α-Al_2O_3 crystals containing hydrogen and annealed in reducing atmosphere excited by UV light in F-center absorption band at 90 K.

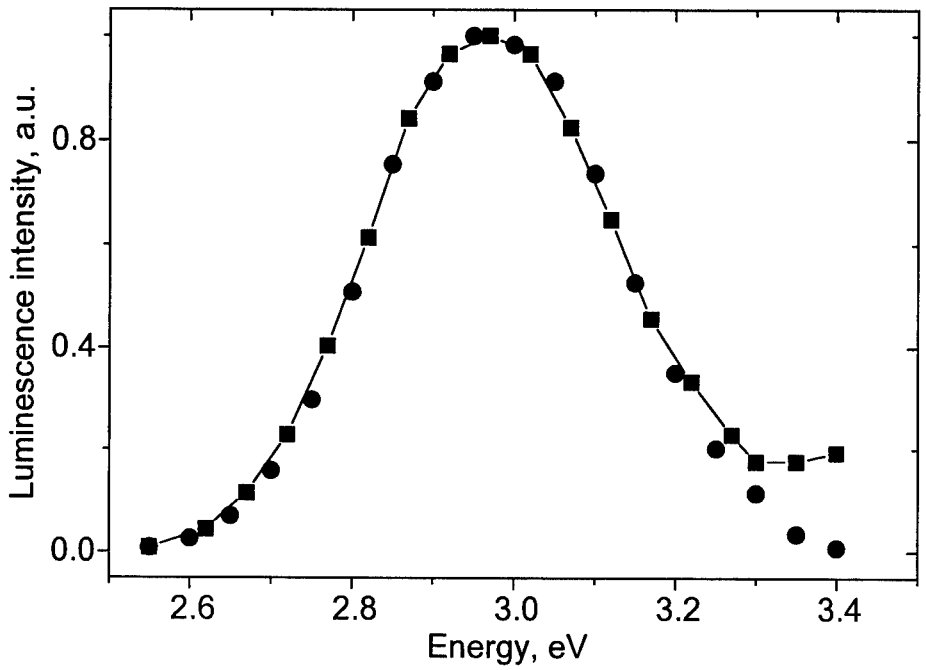

FIGURE 2 The spectral composition of 260 K TL peak (squares) and F- center emission excited in absorption band of F centers at 6.0 eV (circles).

According to the IR absorption spectra the Verneuil crystals especially those previously annealed in oxygen contains OH ions. Reducing in Al vapors destroys OH-centers and produces F–($h\nu_{abs}$ = 6.0 eV) and F^+-centers as main intrinsic defects (see, for example [1]).

The UV excitation in F-center absorption band at 90 K results in decrease of the F center absorption and proportionally increase of the F^+ center absorption. Simultaneously a new broad absorption band at $h\nu$ = 4.2 eV and $a_{\|}/a_{\perp}$ = 0.7 appears ($a_{\|}$ and $a_{\perp}$—absorption for light polarized parallel and perpendicular to the C_3 axis of crystal respectively).

In the course of the heating the 260 K TL peak dominates (Figure 1). The spectral composition of the TL (Figure 2) corresponds to the F-center emission ($h\nu_{max}$ = 3.0 eV). Thermostimulated recombination at 260 K destroys the 4.2 eV absorption band.

Optical stimulation at 90 K in the 4.2 eV band previously created by UV excitation in F-absorption band yields to the F-center emission. Photostimulation spectrum of F-luminescence is presented on Figure 3. Efficiency of photostimulation depends on light polarization. Light polarized perpendicular ($_{\perp}$) to the C_3 axis of crystal stimulates F-luminescence more effective than light polarized parallel ($\|$) to the C_3 axis the ratio being $\|/_{\perp}$ = 0.7 (Figure 3). Optical bleaching of the 4.2 eV absorption band is accompanied by complete disappearance of the 260 K TL peak. Maximum of the photo bleaching efficiency of the 260 K TL peak correlate with photostimulation maximum of the F-emission (Figure 3).

The experimental data obtained lead us to conclude that anion deficient α-Al_2O_3 crystals containing previously hydrogen or annealed in hydrogen contain defects able, below 240 K, to trap electrons released by photoionization of F-centers, thus resulting in

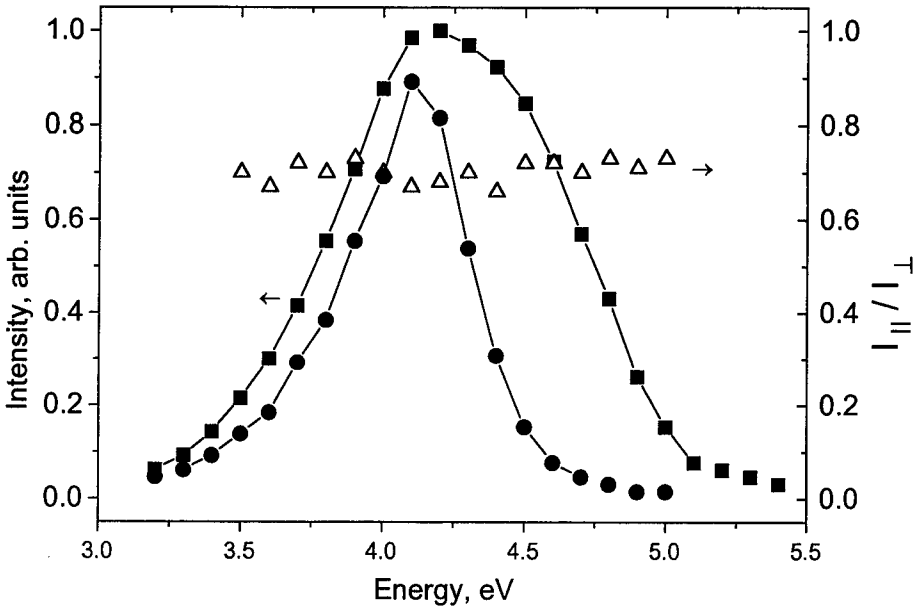

FIGURE 3 Photostimulation spectrum of F luminescence of α-Al_2O_3 crystal excited by UV light in F-center absorption band at 90 K (squares), photostimulation ratio $I_{\parallel}/I_{\perp}$ of F center emission (triangles) and 260 K TL peak quenching efficiency (circles).

production of color centers with anistropy absorption band at 4.2 eV. The 260 K TL is due to the release of electrons from these anistropy color centers with subsequent recombination to F^+-centers resulting in F-center emission.

Optical anistropy of 4.2 eV band in dipole approximation corresponds to the electric dipole oriented at 60° with respect to the C_3 axis. This angle approximately corresponds to nearest anion cation direction. In terms of the one anion vacancy center with three or more electrons it is difficult to explain the observed anisotropy. The latter however does not exclude the two-vacancy center as possible candidate for the 4.2 eV absorption. We speculate also on the role of hydrogen by formation of electron traps in reduced α-Al_2O_3. The considerations are based on fact that both dominant 260 K TL peak and 4.2 eV absorption band were obtained only in those thermochemically reduced α-Al_2O_3 crystals which before reduction either contains OH (crystals obtained by the Verneuil technique) or were preliminary annealed in hydrogen atmosphere. The optical anisotropy and thermal stability suggests that defect, responsible for 4.2 eV absorption band is probably complex occupying anion-cation sites and hydrogen nearby. A similar situation exists also in thermochemically reduced MgO where 260 K TL peak is attributed to the release of electrons from $[H_x^-]^\circ$ ions [2].

REFERENCES

1. J. H. Crawford, Jr. *Semiconductors and Insulators*, **5**, 599 (1983).
2. V. M. Orera, Y. Chen. *Phys. Rev.* **B36**, 6120 (1987).

Radiation Effects and Defects in Solids, 1995, Vol. 134, pp. 485–488
Reprints available directly from the publisher
Photocopying permitted by license only

© 1995 OPA (Overseas Publishers Association)
Amsterdam B.V. Published under license by
Gordon and Breach Science Publishers SA
Printed in Malaysia

A DEFECT MODEL FOR THE OPTICAL AND EPR ACTIVITY OF THE T-CENTER IN YTTRIUM-STABILIZED ZIRCONIA

C. B. AZZONI, L. BOLIS, P. CAMAGNI, G. C. CAMPAGNOLI and M. DE SIMONE

Dipartimento di Fisica 'A. Volta' Via A. Bassi, 6–27100 Pavia, Italy

Direct quantitative correlations have been recently observed between the T-centre EPR signal and an optical absorption band at 370 nm, in X-irradiated YSZ, suggesting that the colour centre and the paramagnetic centre might be the same entity. In order to confirm this hypothesis, theoretical modeling was undertaken, where by appropriate refinement the known electronic structure of the T-centre is shown to be compatible with an optical transition, having an oscillator strength of the correct magnitude.

1 INTRODUCTION

Yttria-stabilized zirconia (YSZ) is a well studied material in its cubic phase, which is stable at RT for yttria concentrations exceeding ~ 6.5 mol%. A variety of electronic centres, showing optical and/or paramagnetic activity, can be introduced in YSZ by irradiation or electro-reduction [1]. Study of the underlying structures is a goal of special interest, as it offers the way for probing the complex system of 'structural' or stoichiometric defects in these compounds.

Attention has been devoted recently to the electron-type T-centre. It appears to consist of an excess electron on a Zr^{4+} ion, midway between two vacancies at the opposite ends of the coordination cube (Figure 1). Elements of identification, coming from EPR analysis, include [2]: i) axial anisotropy of the g tensor, with $g_{//} = 1.989$ and $g_{\perp} \approx 1.84$ and a defect axis in the $\langle 111 \rangle$ crystal direction, giving rise to a fourfold multiplicity of the spectrum; ii) anisotropy of the linewidth ΔB, ranging from 0.7 mT to 6 mT as **B** rotates from the $\langle 111 \rangle$ direction to the orthogonal one: in the latter case the lineshape is gaussian;

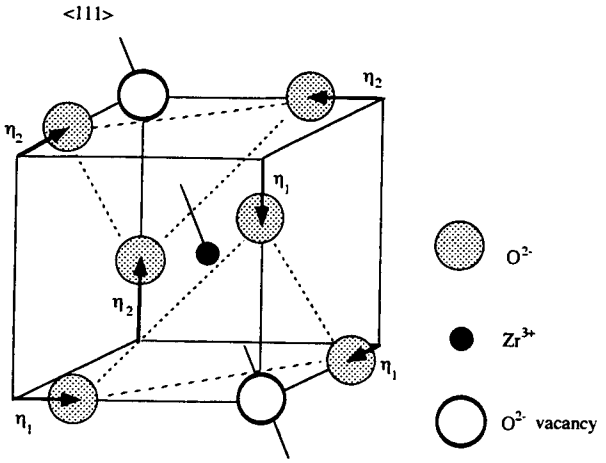

FIGURE 1 Structural model of T-centre used in the calculations.

iii) asymmetry of the line shape, evident when **B**//⟨111⟩. The main features of the EPR spectrum were shown to be compatible with a point-ion model of D_{3d} symmetry having a centre of inversion at the Zr site (Figure 1). Broadening was proposed to arise from an inhomogeneous spread of $g_\perp$ within ± 0.03 from its average value [2].

Direct quantitative correlations, for what concerns production yield and annealing, have been found between the EPR signal and a broad gaussian-like absorption band at 3.35 eV [3]. This suggested that the colour centre and the paramagnetic T-centre might well be the same entity. Checking this identification is of some importance, as it can improve our means of studying the behaviour of the precursor defect, i.e. the two vacancy complex described before. In the following, we sketch the main lines of a theoretical model, aimed to describe the optical activity as well. The model extends the lines of a previous treatment, in which the T-centre is schematized as a simple $4d^1$ system in the field of a central Zr ion, in the ligand field of six surrounding oxygen ions [2].

2 OPTICAL TRANSITIONS OF THE T-CENTRE

In the hypothesis that paramagnetic and optical properties are due to the same centre, one can equate the absolute densities measured by EPR with those, which one derives from the area under the optical absorption spectrum (Smakula's formula). In this way, a value of $f = 0.03$ was obtained for the oscillator strength of the T-centre. Theoretical modeling was undertaken to justify this sizeable figure.

As regards the optical activity of the T-centre, two possible level schemes have been tentatively proposed, namely intersystem transition to the conduction band [3] or intra-centre crystal-field (CF) transition of the Zr^{3+} ion [4]. Following the intra-centre interpretation the observed optical band should be associated with electronic dipole transitions within the $4d^1$ manifold. Local symmetry is crucial in determining the possibility of such transitions. Owing to parity selection rules, distortions of the D_{3d} defect structure are to be invoked: in fact, the existence of electric-dipole matrices determining the oscillator strength is compatible only with a lower symmetry, lacking the inversion centre (e.g. C_{3v}). Additional constraints must be imposed on the ionic configuration, if the model is to explain at the same time the EPR and optical spectrum and their inhomogeneous character. On the other hand, the picture should remain consistent with the previous modeling of paramagnetic activity, based on a symmetric configuration.

Starting from static dilatations of the coordination cube, with fixed D_{3d} symmetry, we have considered the effect of asymmetric rearrangements on the energy level scheme of the $4d^1$ system. Each configuration of the ligand field is now specified by a value a (side of the cube) and by displacements $\eta_1 a$, $\eta_2 a$, each of which describes the common relaxation of the three oxigens in a given coordination plane, towards the nearest vacancy (C_{3v} distortion, see Figure 1).

The explicit form of the crystal field potential was analysed in terms of spherical harmonics, separating the two distinct parts V_{even} and V_{odd}. The even terms, modified with respect to the symmetric situation by the presence of the distortion, were used to define new states, hence the g-factor and the ΔE splitting were re-evaluated as a function of the above defined variables. Actual calculations moved from diagonalization of the even part of CF Hamiltonian in the base of free-ion d states, under the assumption that these be well separated in energy from the excited p and f multiplets. This is the case as the separation between the $4d^1$ configuration and the next excited one $4d^05p^1$, for the Zr^{3+} free ion, is about 10 eV [5], to be compared with a calculated CF splitting of the ^2D multiplet, which is substantially less than 4 eV.

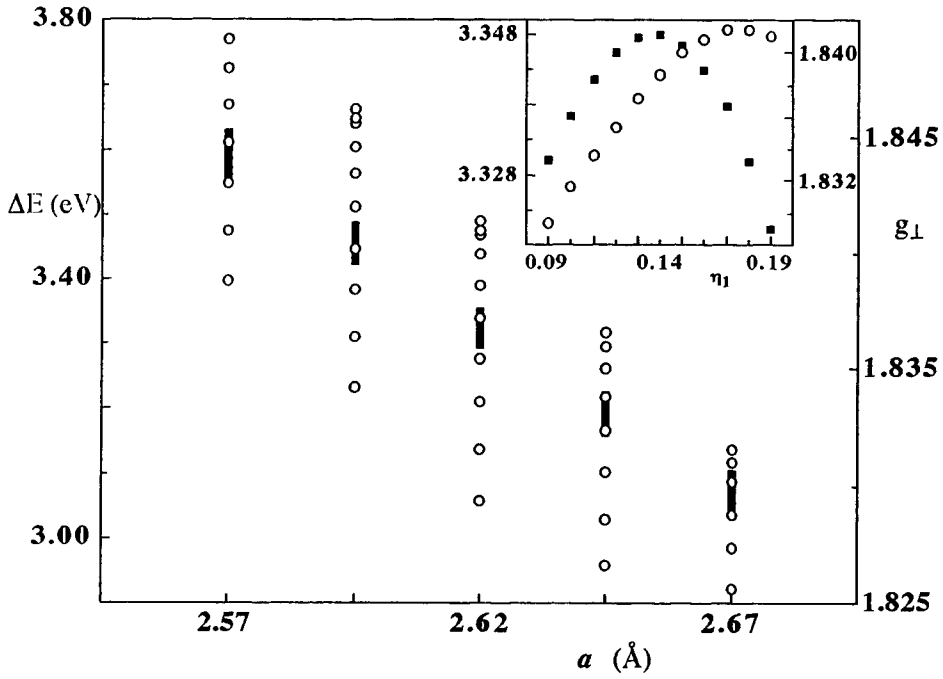

FIGURE 2 Plots of calculated energy values ΔE (full squares) and $g_\perp$-factors (open circles) for different distorted situations, characterized by 2.57 Å $\leq a \leq$ 2.67 Å and by $0.9 \leq \eta_1 \leq 0.19$, for fixed $\eta_2 = 0.14$ (in units of a).

Figure 2 shows for a number of configurations D_{3d}, with varying a, the spread of the calculated energy values ΔE and of the $g_\perp$-factor, consequent to different choice of η_1 (for fixed $\eta_2 = 0.14a$), i.e. of the C_{3v} distortion. Among other things, these data helped us in fixing the range of variation of the parameters a, η_1 and η_2 which is compatible with the spread of $g_\perp$-values already known from EPR, as well as with an energy of about 3.35 eV, needed to justify the observed optical transition at 370 nm. The insert illustrates in greater detail the data for a median configuration a = 2.62 Å, corresponding to a dilatation of 2% of the regular cube (a_0 = 2.57 Å).

Calculation of the oscillator strength, for CF optical transitions of the T-centre, was then carried out in the scheme of the effective dipole approximation. In the assumption that the odd-parity terms are perturbations of the D_{3d} crystal field, perturbation theory was applied to evaluate the non-vanishing matrix elements of the electric dipole **P**, by computing $\mathbf{P_{eff}} = V_{odd} \cdot \mathbf{P}$ in terms of unperturbed states. The oscillator strength f was calculated from the expression [6]:

$$f = \frac{8\pi^2 m}{3he^2} \nu \left(|P^x_{eff}|^2 + |P^y_{eff}|^2 + |P^z_{eff}|^2 \right)$$

where the symbols have the usual meaning, and P^k are the matrix elements of the dipole components, referred to orthogonal axes which are congruent with the principal axes of the local symmetry. These terms were evaluated considering each product operator $V_{odd} \cdot P_i$ in

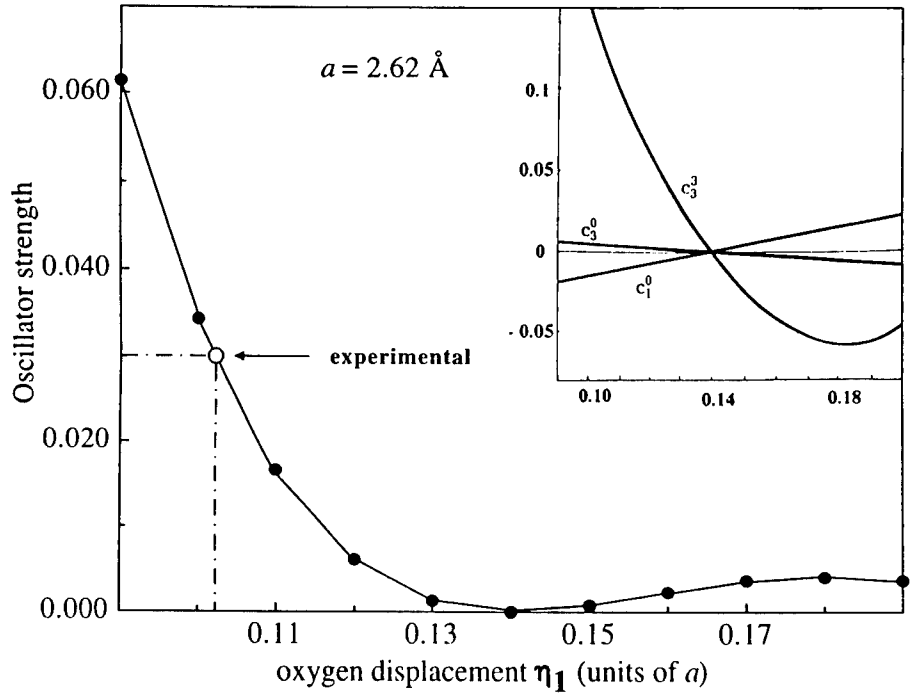

FIGURE 3 Plot of the calculated oscillator strength for different C_{3v} distortions, for a given size of the coordination cube. The insert shows the plots of spherical harmonic coefficients, used in the model.

terms of Stevens operators. The results are summarized in Figure 3, showing the calculated oscillator strength for various distorted configurations, around a median symmetric one with $a = 2.62$ Å. We notice that the experimental f-value of 0.03, reported here as an open circle, matches with a comfortable value of distortion C_{3v}, for the same a value which was shown compatible with the correct transition energy (see Figure 2). The insert illustrates the corresponding trend of the odd spherical harmonic coefficients, which were employed in these calculations. They show a common zero, which correctly corresponds to $\eta_1 = \eta_2$, i.e. to the absence of C_{3v} distortion.

REFERENCES

1. D. C. Nagle, V. R. PaiVerneker, A. N. Petelin, G. Groff; *Mater, Res. Bull.* **24**, 619, (1989).
2. C. B. Azzoni, A. Paleari; *Phys. Rev.* **B40**, 6518, (1989).
3. V. M. Orera, R. I. Merino, Y. Chen, R. Cases, P. J. Alonso; *Phys. Rev.* **B42**, 9782, (1990).
4. C. B. Azzoni, P. Camagni, G. Samoggia, A. Paleari; *Sol. State Ionics* **60**, 223, (1993).
5. C. C. Kiess, R. J. Lang; *Bur. Std. J. Research* **5**, 307, (1930).
6. see for instance S. Sugano, Y. Tanabe, H. Kamimura; *'Muliplets of Transition—Metal Ions in Crystals'* (Academic Press, New York, 1970), Vol. 33, p. 126.

Radiation Effects and Defects in Solids, 1995, Vol. 134, pp. 489–492
Reprints available directly from the publisher
Photocopying permitted by license only

© 1995 OPA (Overseas Publishers Association)
Amsterdam B.V. Published under license by
Gordon and Breach Science Publishers SA
Printed in Malaysia

INFLUENCE OF OH^- IMPURITIES ON THE RELAXATION OF *F* CENTERS STUDIED WITH PICOSECOND OPTICAL PULSES

E. GUSTIN, W. WENSELEERS, M. LEBLANS, A. BOUWEN
and D. SCHOEMAKER

Physics Department, University of Antwerp (U.I.A.), Universiteitsplein 1, B-2610 Wilrijk (Antwerp), Belgium

The relaxation of the two configurations of the $F_H(OH^-)$ center in KBr is studied with a time-resolved induced transparency technique. Multiple decay components are observed. The slowest of these is interpreted as conversion in the ground state between the red and blue configuration of the F_H center, on a longer than nanosecond time scale. A contribution of the order of 100 ps might be related to non-radiative electronic relaxation, but cannot be identified with certainty. An unresolved transient, faster than 10 ps, might be related to a cross-over process.

Key words: F centers, time-resolved measurements, energy transfer, non-radiative decay.

1 INTRODUCTION

The emission of F centers in alkali halides can be quenched by the presence of impurities, especially CN^- and OH^-. This quenching, with the associated radiationless decay and possible energy transfer from the F center to the impurity, has attracted much interest in the last years.[1] Our study is directed at clarifying the interaction between the F center and a neighboring OH^- in KBr. In this host two configurations of the $F_H(OH^-)$ aggregate center exist, with different orientations of the OH^- axis to the axis of the F_H center,[2] one with a blue-shifted and the other with a red-shifted absorption band.[3] Above 10 K, the configurations are thermally converted into one another. Below 5 K full optical bistability is found. Between 5 K and 10 K, the red centers decay; we observe a conversion rate of 24 minutes at 7 K.

We use a picosecond pump-probe induced transparency technique.[4] A small fraction of the *F* centers is excited by the pump pulse. The repopulation of the ground state is observed as a change in the absorption experienced by a delayed probe pulse. Double modulation and phase-sensitive detection are applied; the combination of the 82 MHz pulse repetition rate and the 10 MHz modulation can cause significant distortions of the amplitude of combined slow and fast decay signals, but the decay times are unaffected.[5] Because of the phase-sensitive detection, we do not know the absolute sign of the signal. A positive signal indicates a decrease of the absorption at the probe wavelength; a negative signal an increase.

2 OBSERVATIONS

To create $F_H(OH^-)$ centers, additively colored crystals were bleached at 240 K with 600 nm light of low intensity. The conversion was checked by monitoring the quenching of the luminescence and the position of the absorption band. Some samples had an absorption at low temperatures significantly different from that reported by Baldacchini *et al.*,

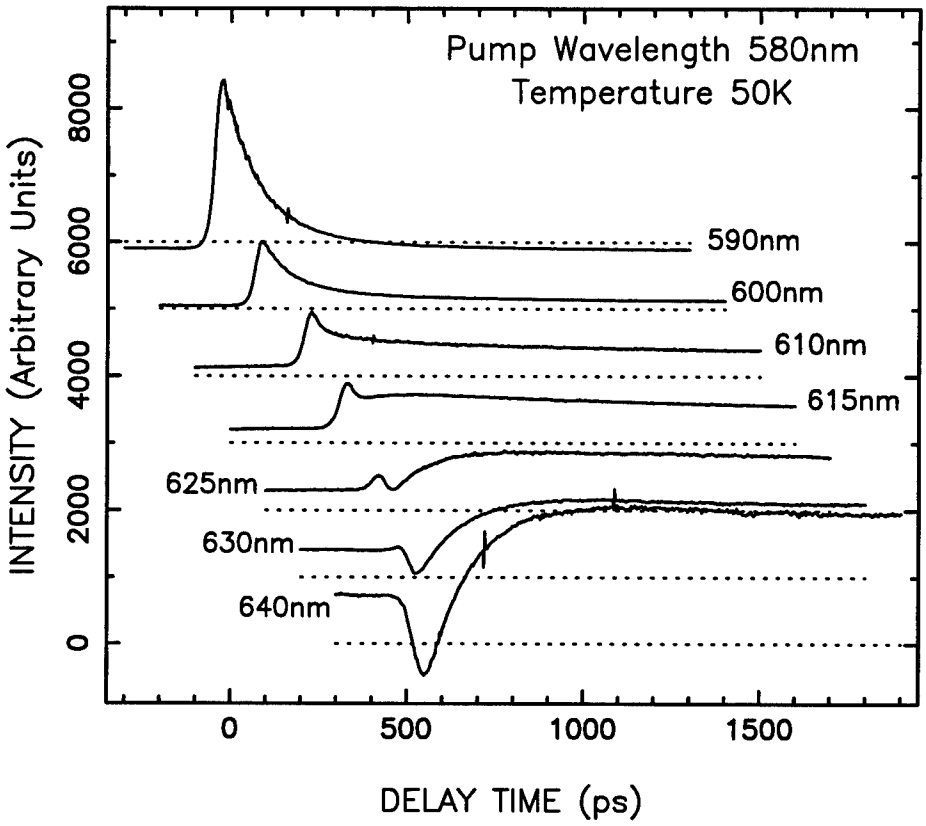

FIGURE 1 Decay signal at 50 K, recorded with the pump wavelength fixed at 580 nm, and probe wavelength as indicated. The dotted lines are at zero intensity. Resolution is 25 ps.

and these also have completely different decay spectra.[6] This might be caused by the stress we observed in these samples.

The decay spectra are strongly dependent on the wavelength of the pump and probe pulses. This is not unexpected, because the F_H center is present in two configurations that can be optically converted into each other at low temperatures. In Figure 1, decay spectra are shown, recorded at a temperature of 50 K and a fixed pump wavelength of 580 nm. There is a combination of at least three decay components: an unresolved transient at zero delay, a component with a decay time of the order of 100 ps that changes sign when the probe is scanned from the blue to the red, and a contribution on a time scale longer than the 1300 ps experimental range, that also changes sign.

A slow negative component can appear if F' or F_2 centers are present,[7] but their concentration is low enough to exclude this. We interpret the slowest decay as a relaxation to equilibrium of the concentrations of the red and blue centers in the ground state. The disturbance of the equilibrium could be caused either by conversion in the excited state, reorientation of the OH^- as part of the non-radiative decay process,[8] or reorientation related to dissipation of the vibrational energy released in this decay.[9] The gradual change

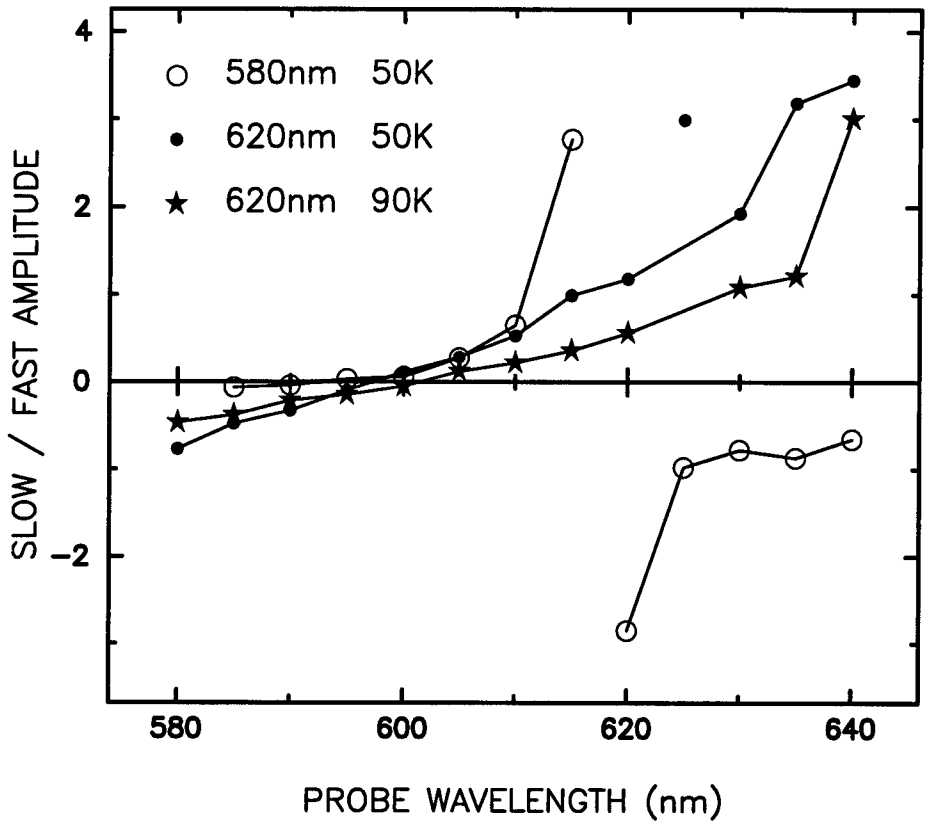

FIGURE 2 Relative amplitude of the slow component to the 100 ps component, as a function of probe wavelength, for fixed temperatures and pump wavelengths as indicated in the legend. The jump in the ○ series is caused by a sign change of the fast component; this does not occur with a 620 nm pump.

of the amplitude of this component relative to that of the 100 ps contribution, when scanning from the red to the blue, is plotted in Figure 2.

The 100 ps decay component is likely to be related to the non-radiative relaxation of the F center. This might be a horizontal vibronic tunneling process enhanced by energy transfer to the OH^- intramolecular vibration or libration, or a transition stimulated by reorientation of the OH^- dipole.[8] The observed change of the sign of this contribution can be related to excited state absorption or reorientation of the OH^- ion.

The amplitude of the fast transient might be larger than seen on the Figure, if its lifetime is significantly below the experimental resolution. Because its time scale is that of the vibrational relaxation of the F center, it may be related to a cross-over process.

Decay spectra at different temperatures are shown in Figure 3. At 10 K, the fast component has a relaxation time of 300 ps; at 50 K this is reduced to 75 ps. Each of these spectra reflects a different proportion of red and blue absorption, because of the strongly different thermal equilibrium concentrations,[3] therefore the relaxation rates should be analyzed with great care, because the red and blue center are likely to have different properties.

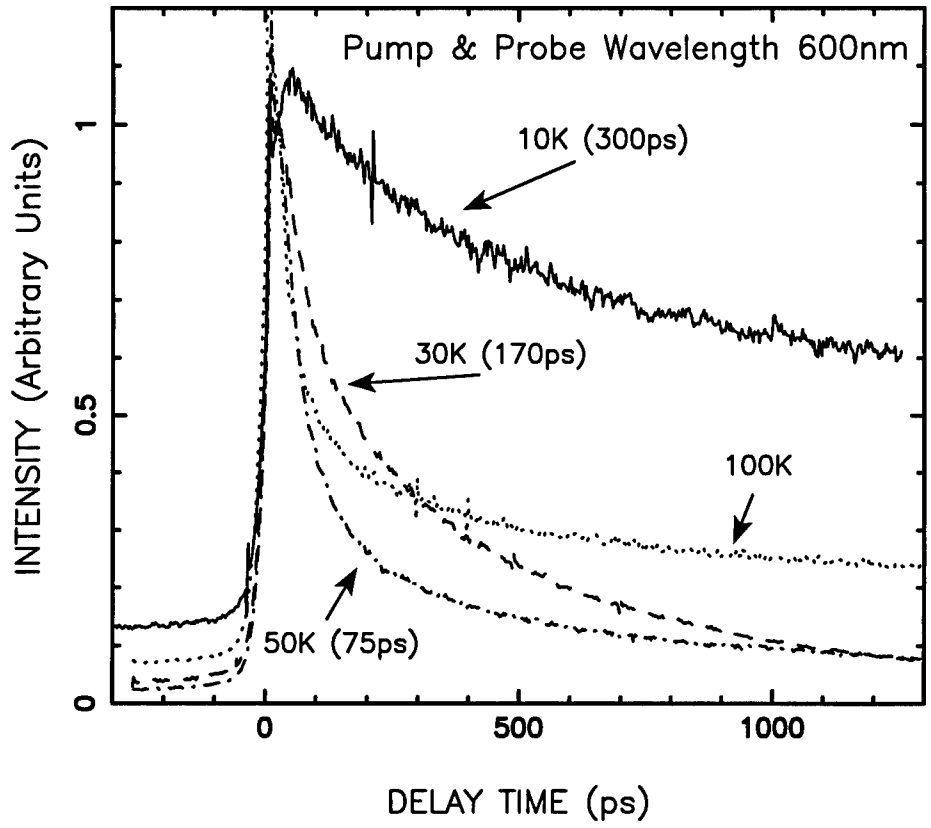

FIGURE 3 Decay signals recorded with pump and probe pulses at 600 nm, for varying temperatures. The indicated decay time is that of the fast component. Resolution is 7 ps.

REFERENCES

1. G. Halama, K. T. Tsen, S. H. Lin, F. Lüty, and J. B. Page, *Phys. Rev.* **B39**, 13457 (1989).
2. H. Söthe, J.-M. Spaeth and F. Lüty, *J. Phys. Condens. Matter* **5**, 1957 (1993).
3. G. Baldacchini, S. Botti, U. M. Grassano, L. Gomes and F. Luty, *Europhys. Lett.* **9**, 735 (1989).
4. C. Sierens, W. Joosen, and D. Schoemaker, *Phys. Rev.* **B23**, 28 (1981).
5. F. De Matteis, M. Leblans, W. Slootmans, and D. Schoemaker, *Phys. Rev.* **B**, to be published.
6. M. Leblans, E. Gustin, A. Bouwen, and D. Schoemaker, *J. Luminescence* **58**, 388 (1994).
7. J. De Kinder, W. Joosen, and D. Schoemaker, *Phys. Rev.* **B42**, 9674 (1989).
8. L. Gomes and F. Luty, *Phys. Rev.* **B30**, 7194 (1984).
9. C. Mungan, U. Happek and A. Sievers, *J. Lumin.* **58**, 33 (1994).

Radiation Effects and Defects in Solids, 1995, Vol. 134, pp. 493–497
Reprints available directly from the publisher
Photocopying permitted by license only

© 1995 OPA (Overseas Publishers Association)
Amsterdam B.V. Published under license by
Gordon and Breach Science Publishers SA
Printed in Malaysia

STABILIZATION OF H CENTRES IN IRRADIATED LiF:Mg CRYSTALS

S. MYSOVSKY, B. ROGALEV and V. CHERNOV

Institute of Geochemistry, P.O. Box 4019, 664033 Irkutsk, Russia

The paper is dedicated to investigation of possible ways of stabilization of the H centres created together with F and Mg^+ centres in a process of decay of selftrapped exciton. As a main mode of the H centres stabilizationa capture of the H centre by magnesium-vacancy dipole and creation of V-type centre was suggested. This process was theoretically studied in the frames of model of molecular cluster which electron structure was calculated by the semi-empirical version of the Hartree-Fock method. For experimental corroboration of this process the relations between dependences of magnesium dipoles decrease on dose of gamma irradiation and corresponding dose dependences of the Mg^+, Mg^o, and F centres radiation creation were used.

Key words: Lithium fluoride, dipole, H centre, stabilization, Hartree-Fock method.

1 INTRODUCTION

Storage of ionizing radiation energy in LiF crystals doped with magnesium is of a great interest because of wide using of these crystals (additionally doped with Ti or Cu, P) for thermoluminescent dosimetry. But the main attention is commonly paid to the study of radiation induced electron centres and their photothermal transformations. In particular, we have been studied in main features the mechanisms of radiation creation of the F, Mg^+, and Mg^o centres in these crystals.[1] According to this work the F and Mg^+ centres are created as a result of decay of selftrapped exciton in regular site of the lattice or near a magnesium-vacancy dipole (Mg^{2+} centre), respectively. Capturing of electron by Mg^+ centre caused creation of the Mg^o centre. At the exciton decay, in addition to creation of F and Mg^+ centres, equal amount of H centres are created.

The present paper is dedicated to investigation of possible ways of stabilization of the H centres. As a main mode of the H centres stabilization, according to experimentally observed processes in other alkali halides doped with divalent metals,[2–4] a capture of the H centre by magnesium-vacancy dipole and creation of V-type centre was suggested. This model was already formally used in works of Ramos *et al.*[5,6] for a kinetics calculations of radiation induced centres production in alkali halides. In the present work the process is theoretically studied in the frames of model of molecular cluster which electron structure was calculated by the semi-empirical version of the Hartree-Fock method. For experimental corroboration of this process the relations between dependences of magnesium-vacancy dipoles decrease on dose of gamma irradiation and corresponding dose dependences of the F, Mg^+, and Mg^o centres radiation creation were used.

2 CALCULATIONS

For research the intermediate neglect of differential overlap calculation procedure[7] and the embedded molecular cluster model have been chosen. The interaction of ions entering the molecular cluster and outside it is treated in terms of the nonpoint polarisible lattice model. The sheet of the adiabatic surface of the excited states has been studied. The energies of

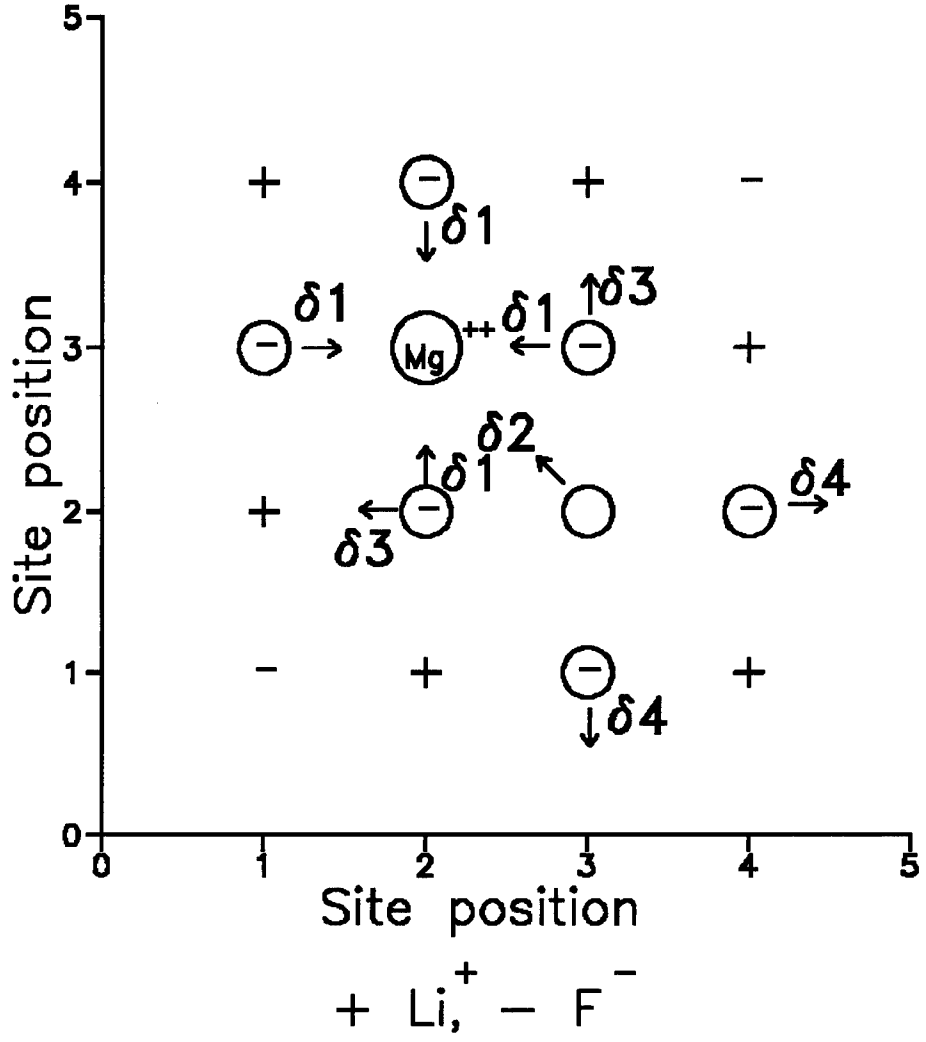

FIGURE 1 X-Y cross-section of the molecular cluster used. Final disposition. Total energy is equal to –522.807 a.u. σ are displacements of ions ($\sigma_1 = -0.02$a, $\sigma_2 = -0.13$a, $\sigma_3 = 0.07$a, $\sigma_4 = 0.05$a; a is lattice constant).

optical transitions are calculated using the restricted configuration interaction technique, it is the difference in total energies of self-consistent excited and ground states.

For simulation of H centre capture by magnesium-vacancy dipole molecular fragment $[F^-_{24}Li^+_{22}F^oMg^{2+}]$ was used. In starting position of H centre is situated in site (4, 4) and oriented in $\langle 111 \rangle$ direction (see Figure 1). Displacement of the centre in this direction is given by vector δ ($\delta_x = \delta_y = \delta_z$). Distance of equilibrium between the nucleus is equal to

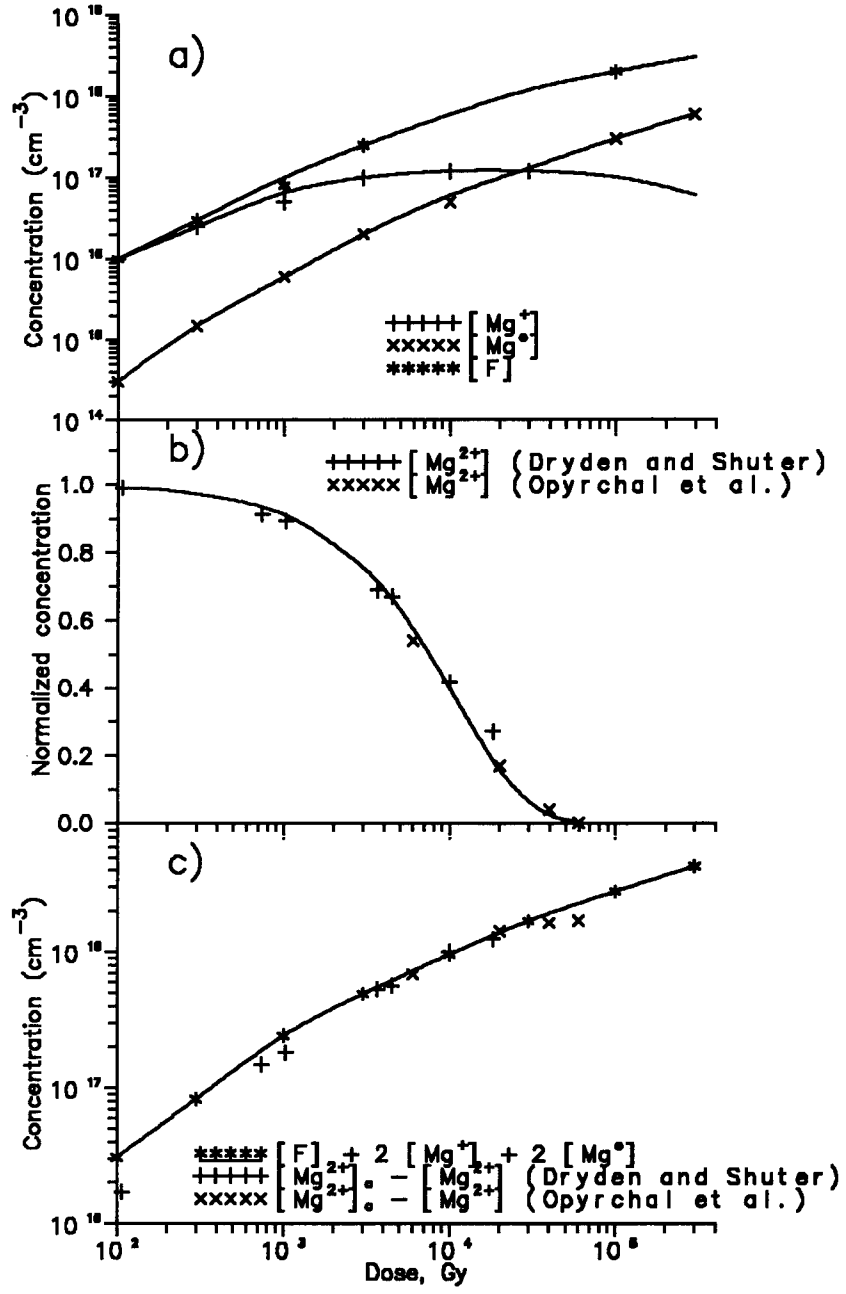

FIGURE 2 Dose dependences of : (a) creation of radiation induced centres in LiF:Mg (0.05 wt%),[1] (b) decrease of free dipole concentrations,[8,9] (c) correlation between concentration of transformed dipoles and sum of radiation induced centres. Symbols are experimental data, line are corresponding approximations.

3.22 a.u. Presence of magnesium-vacancy dipole decreases the system symmetry and effective charges of fluorine ions form H centre, obtained from population analysis are nonequal. The calculation shows that after transition of H centre from position (4, 4) to position (3, 3) total energy of the system decreases by approximately 0.4 eV. Following relaxation of the system leads to additional decrease of the total energy by approximately 1 eV. Configuration of the relaxed ground state corresponded to minimum of the total energy is shown in Figure 1. One of fluorine atoms is localized in cation vacancy with slight shift to magnesium. Its effective charge is –0.08e, this of magnesium is +1.92e. In one-electron spectrum of the system some states exist in which molecular orbitals main contribution is given by atom orbitals of magnesium and three nearest fluorines. Thus, as a result of interaction of H centre with magnesium-vacancy dipole a centre $Mg_c^{2+}F_a^-F_c^oF_a^-$ is appeared, which may be called Mg-H aggregate centre (Mg-H centre).

In the calculated spectrum of optical transitions we can set off by oscillator strength a slightly splitted band with maximums near 10.5 and 10.4 eV connected with electron transition from local state of Mg-H centre in valence band to free state of magnesium in forbidden gap. Two another more weak bands with maximums near 3.0 and 11.5 eV are governed by transitions to the one-fold occupied state caused mainly by states of three fluorines.

3 DISCUSSION

According to the mechanism of ionizing radiation energy accumulation, described in our previous work,[1] concentration of H centres created at the exciton decays is equal to sum of F, Mg^+, and Mg^o centres concentrations. If we assume that all H centres are captured by magnesium-vacancy dipoles than concentration of created Mg-H centres (neglecting the capture by magnesium-vacancy dipoles more than one H centre) will be equal to sum of F, Mg^+, and Mg^o centers concentrations. Furthermore, creation of Mg^+ and Mg^o centres leads to additional decrease of free dipoles concentration equal to sum Mg^+ and Mg^o centres concentrations. Therefore relation between magnesium-vacancy dipoles and radiation induced electron centres may be written as follows:

$$[Mg^{2+}]_0 - [Mg^{2+}] = [F] + 2 \circ [Mg^+] + 2 \circ [Mg^o], \quad (1)$$

where symbols in square brackets are concentrations of corresponding centres, $[Mg^{2+}]_o$ is initial (before irradiation) concentration of magnesium-vacancy dipoles.

Creation of Mg-H centres leads to decrease of free dipoles concentration, which can be determined experimentally from decrease of dielectric losses peak connected with these dipoles. Expression (1) gives principal possibility to test the validity of idea proposed because all the concentrations involved could be determined experimentally. Result of such test is shown in the Figure 2, where dose dependence of sum of radiation induced centres according to expression (1) (dose dependences of the centres concentrations shown in Figure 2a are borrowed from our previous work[1]), is correlated with dose dependences of magnesium-vacancy dipoles decrease adopted from the works[8,9] (Figure 2b). Because in these works the initial concentrations of dipoles were absent, we normalized it on initial value of $[Mg^{2+}]_o$ equal to $1.6 \cdot 10^{18}$ cm^{-3} for dose $3 \cdot 10^4$ Gy.[1] It is clear from the Figure 2c that in dose range of 10^2–$3 \cdot 10^4$ Gy decrease of magnesium-vacancy dipoles is reasonably fitted with increase of total concentration of the radiation induced centres. It is, in our opinion, evidence for idea that Mg-H centres are really created in gamma irradiated LiF:Mg crystals.

REFERENCES

1. B. I. Rogalev, S. Mysovsky, A. I. Nepomnyachikh, and V. G. Chernov, *Radiat. Prot. Dosim.* **33**, 15 (1990).
2. W. Puymbroeck and D. Schoemaker, *Phys. Rev.* **B23**, 1670 (1970).
3. N. Itoh, *Crystal Lattis Defects* **3**, 115 (1972).
4. T. Harami, *J. Phys. Soc. Japan* **57**, 3621 (1988).
5. S. Ramos B. *et al.*, *Phys. Rev.* **B31**, 8164 (1985).
6. J. Rubio O. *et al.*, *Phys. Rev.* **B34**, 5820 (1986).
7. E. V. Stefanovich, E. K. Shidlovskaya, A. L. Sluger, and M. A. Zakharov, *Phys. Status solidi*, **B160**, 529 (1990).
8. J. S. Dryden and B. Shuter, *J. Phys. D: Appl. Phys.* **6**, 123 (1973).
9. H. Opyrchal, B. Macalic, and A. Watterich, *Cryst. Res. Technol.* **22**, 291 (1987).

Notes for Contributors

TYPESCRIPTS

Submissions: Papers should be typed on good quality paper with double spacing and wide (3 cm) margins, using one side only, and submitted in duplicate to the Editor in Chief or to the appropriate Regional Editor:

J. P. Biersack, Editor in Chief, Hahn-Meitner-Institut, Glienickerstraße 100, 14109 Berlin, Germany

N. Itoh, Department of Physics, Faculty Of Science, Nagoya University, Furo-cho, Chikusa-ku, Nagoya 464, Japan

H. Kronmüller, Max-Planck-Institut für Metallforschung, Institut für Physik, Heisenbergstraße 1, 70569 Stuttgart 80, Germany

M. A. Kumakhov, Russian Research Center, Moscow 123182, Russia

N. Tolk, Department of Physics and Astronomy, Vanderbilt University, P.O.Box 1807-B, Nashville, Tennessee 37325, USA

The editors and publisher cannot be responsible for correcting English grammar, spelling, and idiom. Authors should ensure before submission that papers are correct in style and language.

Abstracts, key words, running heads: Each paper requires an abstract of 100-150 words summarizing the significant coverage and findings. Abstracts should be accompanied by up to six key words which between them characterize the contents of the paper. These will be used for indexing and data retrieval purposes. Please also provide an abbreviation of the paper's title (no more than 35 characters) for use as a running head.

Terms of Acceptance: Submission of a manuscript is taken to imply that the paper represents original work not previously published, is not being considered elsewhere for publication, and if accepted for publication will not be published elsewhere in the same form, in any language, without the consent of the publisher. It is also assured that the author has obtained all necessary permissions to include in the paper items such as quotations, reprinted figures, results of government-sponsored research, etc. It is a condition of acceptance for publication that the publisher acquires copyright of the paper throughout the world.

FIGURES

All figures should be numbered with consecutive arabic numbers, have descriptive captions, and be mentioned in the text. Keep figures separate from the text, but indicate an approximate position for each in the margin.

Preparation: Figures submitted must be of high enough standard for direct reproduction. Line drawings should be prepared in black (India) ink on white paper or tracing cloth, with all lettering and symbols included. Alternatively, good sharp photoprints ("glossies") are acceptable. Photographs intended for halftone reproduction must be good glossy original prints, of maximum contrast.

Clearly label each figure with the authors' names and figure number, indicating "top" where this is not obvious. Redrawing or retouching of unusable figures will be charged to authors.

Size: Figures should be planned so that they reduce to a 12.5 cm column width. The *preferred* width of submitted line drawings is 22 to 25 cm with capital lettering 4 mm high, for reduction by one-half. Photographs for halftone reproduction should be approximately twice the desired size.

Captions: A list of figure captions, with relevant figure numbers, should be typed on a separate sheet and included with the typescript.

COLOR PLATES

Whenever the use of color plates is an integral part of the research, the journal will publish color illustrations without charge to the authors.

EQUATIONS AND FORMULAE (MATHEMATICAL)

Whenever possible, mathematical equations should be typewritten, with subscripts and superscripts clearly shown. It is helpful to identify unusual or ambiguous symbols in the margin when they first occur. To simplify typesetting, please use: (1) the "exp" form of complex exponential functions; (2) fractional exponents instead of root signs; and (3) the solidus (/) to simplify fractions—e.g. $\exp x^{p/3}$

Marking: The printer will set mathematical symbols in italics, except for obvious groups like sin and log. Any symbols which are to be left in roman (upright) type should be encircled in pencil in the typescript; bold symbols should be underlined with a wavy line.

EQUATIONS AND FORMULAE (CHEMICAL)

Ring formulae, and other complex chemical matter, are extremely difficult to typeset. Please therefore, supply reproducible artwork for equations containing such chemistry. Long reaction sequences should be designated as "Schemes" and treated like figures: i.e. keep artwork separate from the text, indicate in the margin an appropriate position, and supply a separate list of scheme captions. Where necessary, individual chemical formulae can be identified with bold arabic numbers. Chemical equations referred to in the text should be indicated with arabic numbers set over to the right in parentheses.

Marking: Where chemistry is straightforward and can be set (e.g. single-line formulae), please help the typesetter by distinguishing between e.g., double bonds and equal signs, and single bonds and hyphens, where there is ambiguity. The printer finds it difficult to identify which symbols should be set in roman (upright), italic, or bold type, especially where the paper contains both mathematics and chemistry. Therefore, please help the printer as much as possible by adding marginal notes in pencil.

TABLES

Number tables consecutively with roman numerals, and give each a clear descriptive caption at the top. Avoid the use of vertical rules in tables.

UNITS

Metric units are preferred. Acceptable abbreviations of units are given in the *Style Manual* of the American Institute of Physics and similar publications.

REFERENCES AND NOTES

References and notes are indicated in the text by consecutive superior arabic numbers. The full list should be collected and typed at the end of the paper in numerical order. Listed references should be complete in all details but excluding article titles in journals. Authors' initials should precede their names: journal title abbreviations should conform to *Physical Abstracts*. Examples:

1. A. B. Smith and C. D. Jones, *J. Appl. Phys.* **34**, 296 (1965).
2. R. B. Brown, *Molecular Spectroscopy* (Gordon and Breach, New York, 1970), 3rd ed., Chap. 6, pp. 95, 106.

TEXT HEADINGS

Set first-level headings in the text over to the left, type all in capitals (upper-case); begin the text on the following line. Second-level headings should be typed in small (lower-case) letters with all main words capitalized. Underline the heading and start the text on the next line. For third-level headings, only the first letter should be a capital. Underline, then run on the text after three typewriter spaces.

FIRST LEVEL HEADING

Second-Level Text Headings

Third-level headings. With text run on.

PROOFS

Authors will receive proofs (including figures) by airmail for correction, which must be returned to the printer within 48 hours of receipt. Please ensure that a full postal address is given on the first page of the manuscript, so the proofs are not delayed in the post. Author's alterations in excess of 10% of the original composition will be charged to authors.

REPRINTS

The senior author of each paper will receive 25 complimentary reprints. Additional reprints may be ordered by completing the appropriate form sent with proofs.

PAGE CHARGES

There are no page charges to individuals or to institutions.

A FINAL NOTE

Typescripts which do not conform to the required standards of preparation for submission outlined here will be returned to authors for correction before review.

SCIENCE SPECTRA

THE INTERNATIONAL MAGAZINE OF CONTEMPORARY SCIENTIFIC THOUGHT

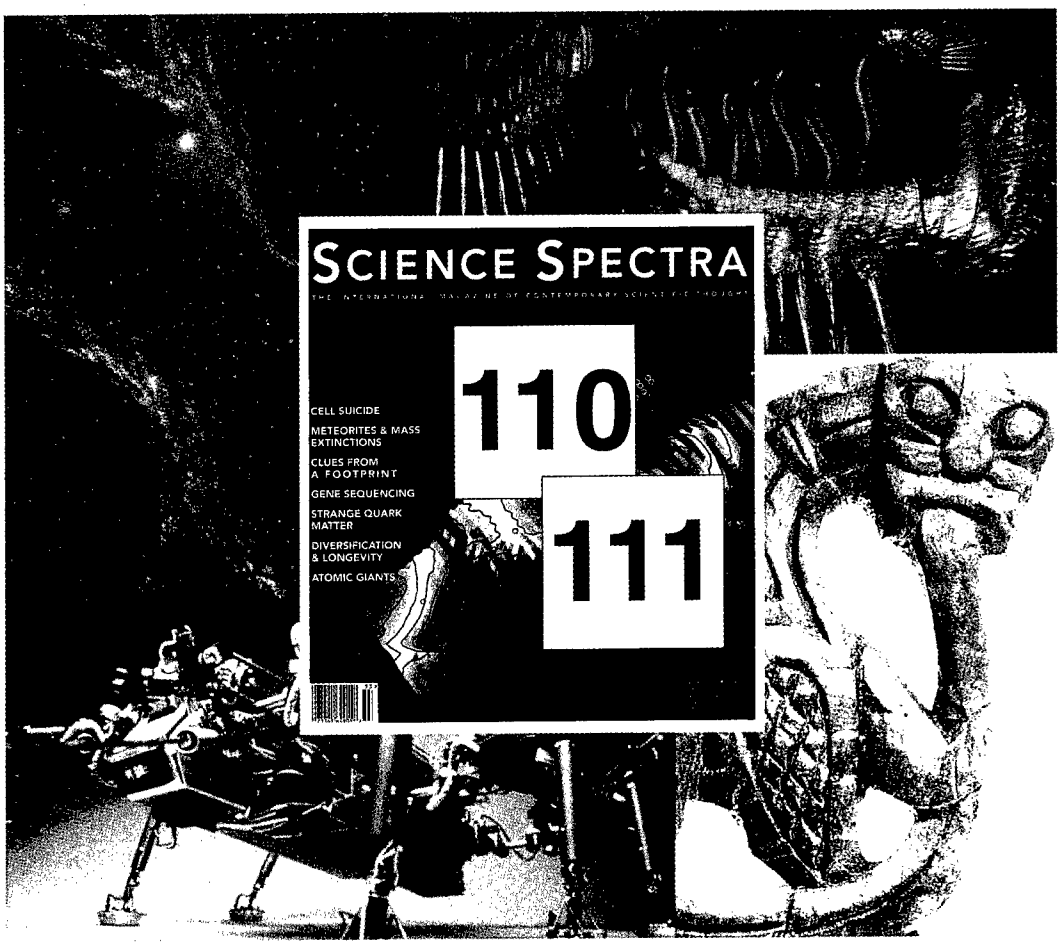

FROM CELLS TO SUPERNOVAS, FROM NUCLEAR CHEMISTRY TO ARTIFICIAL INTELLIGENCE, FROM ANCIENT HISTORY TO FUTURE THOUGHT...

Science Spectra is a magazine for scientists, by scientists, that takes you on a journey to the frontiers of research and contemporary scientific thought. With a team of editors who are leading scientists in their fields, and backed by the international science publishing house Gordon and Breach, *Science Spectra* is a cross-disciplinary magazine that brings you the full spectrum of today's science.

Subscribe now at US$32/£20/SFr48/Aus.$34 for four issues (15% off cover price), or at US$49/£32/SFr73/Aus.$52 for eight issues (35% off cover price). Your check or money order should be directed and made payable to:

North/South America:
c/o International Publishers Distributor
PO Box 41010,
Newark NJ 07101-8007, USA
or call 1-800-545-8398

Europe:
c/o International Publishers Distributor
Postfach, CH-4004 Basel,
Switzerland
or call (+44)0-73-456-8316

Asia:
c/o International Publishers Distributor
Kent Ridge Rd., PO Box 1180,
Singapore 911106
or call +65 741 6933

Australia:
c/o Fine Arts Press
PO Box 480 Roseville,
NSW 2069 Australia
or call +61 2 417 1033

GB
Gordon and Breach Publishers

(Continued from inside front cover)

© 1995 by OPA (Overseas Publishers Association) Amsterdam BV. Published under license by Gordon and Breach Science Publishers SA, a member of The Gordon and Breach Publishing Group. All rights reserved.

Except as permitted under national laws or under the Photocopy License described below, no part of this publication may be reproduced or transmitted in any form or by any means, electronic, mechanical, photocopying or otherwise or stored in a retrieval system of any nature, without the advance written permission of the Publisher.

ORDERING INFORMATION
Four issues per volume. 1996 Volumes: 137-139
Orders may be placed with your usual supplier or with International Publishers Distributor at one of the addresses shown below. Journal subscriptions are sold on a per volume basis only; single issues of the current volume are not available separately. Claims for nonreceipt of issues will be honored free of charge if made within three months of publication of the issue. Subscriptions are available for microform editions; details will be furnished upon request.

All issues are dispatched by airmail throughout the world.

SUBSCRIPTION RATES
Base list subscription price per volume: ECU 283.00 (US$368.00).* This price is available only to individuals whose library subscribes to the journal OR who warrant that the journal is for their own use and provide a home address for mailing. Orders must be sent directly to the Publisher and payment must be made by personal check or credit card.
Separate rates apply to academic and corporate/government institutions, and may also include photocopy license and postage and handling charges.

*ECU (European Currency Unit) is the worldwide base list currency rate; payment can be made by draft drawn on ECU currency in the amount shown or in local currency at the current conversion rate. The US Dollar rate is based upon the ECU rate and applies to North American subscribers only. Subscribers from other territories should contact their agents or the Publisher. All prices are subject to change without notice.

Publication Schedule Information: To ensure your collection is up-to-date, please call the following number for information about the latest issue published: USA (201) 643–7500 – Dial extension 290 – Enter the ISSN followed by # key. Note: If you have a rotary phone, please call our Customer Service at the numbers listed below.

*Orders and enquiries should be placed through **International Publishers Distributor** at one of the addresses below:*

Postfach, 4004 Basel
Switzerland
Telephone: (41-61) 261-01-38
Fax: (41-61) 261-01-73

820 Town Center Drive
Langhorne, PA 19047 USA
Telephone: (215) 750-2642
Fax: (215) 750-6343

Kent Ridge, PO Box 1180
Singapore 911106
Republic of Singapore
Telephone: 741-6933
Fax: 741-6922

Yohan Western Publications Distribution Agency
3-14-9, Okubo, Shinjuku-ku
Tokyo 169, Japan
Telephone: (03) 3208-0186
Fax: (03) 3208-5308

LICENSE TO PHOTOCOPY
This publication and each of the articles contained herein are protected by copyright. If the subscription price paid by the subscriber includes a fee for a photocopy license, then the subscriber is permitted to make multiple photocopies of single articles for the internal study or research purposes of the subscriber. The Photocopy License is not available to individuals or to certain other subscribers. The Photocopy License does not permit copying for any other purpose, such as copying for distribution to any third party (whether by sale, loan, gift or otherwise); as agent (express or implied) of any third party; for purposes of advertising or promotion; or to create collective or derivative works. All requests for permission to copy beyond the scope of the Photocopy License must be made to the Publisher. No copyright licensing organization in any territory has authority to grant such permission on the Publisher's behalf. Any unauthorized reproduction, transmission or storage may result in civil or criminal liability.

RIGHTS AND PERMISSIONS / REPRINTS OF INDIVIDUAL ARTICLES
Permission to reproduce and/or translate material contained in this journal must be obtained in writing from the Publisher. Copies of individual articles may be obtained from SCAN, the Publisher's own document delivery service. For either service, please write or fax to: International Publishers Distributor at one of the addresses listed above.

VOLUNTARY PAGE CHARGES
The United States National Science Foundation has extended the allowance of page charge funds for payments to journals regardless of the Publisher's commercial status. Previously this was reserved for only nonprofit society-sponsored journals. Voluntary page charge payments are now accepted for this journal, and authors may elect to pay any amount up to a maximum of $25.00 per page. Payments will be refunded in the form of a voucher at 100% value of total payment. This voucher can be used by the author or the author's university library for any product or service offered by the Publisher, and thereby can be used to supplement library funding.

NEGATIVE PAGE CHARGES
The principal author of each article will receive a voucher for his contribution in the amount of ECU 15.00 (US $20.00, Yen 3,000), which can also be used to purchase the Publisher's products directly or through university libraries, thereby reducing costs of publications to those authors supporting the journal.

Distributed by International Publishers Distributor.
Printed in Malaysia.

DECEMBER 1995